Measurement of the beam and helicity asymmetries in the reactions $\gamma p \to p\pi^0$ and $\gamma p \to p\eta$

Dissertation
zur
Erlangung des Doktorgrades (Dr. rer. nat.)
der
Mathematisch-Naturwissenschaftlichen Fakultät
der
Rheinischen Friedrich-Wilhelms-Universität Bonn

vorgelegt von

Farah Noreen Afzal
aus
Bonn

Bonn, Januar 2019

Angefertigt mit Genehmigung der Mathematisch-Naturwissenschaftlichen Fakultät der Rheinischen Friedrich-Wilhelms-Universität Bonn

1. Gutachter:	Prof. Dr. Reinhard Beck
2. Gutachter:	Prof. Dr. Bernd Krusche
Tag der Promotion:	06.08.2019
Erscheinungsjahr:	2019

Abstract

Nucleons are bound states composed of quarks and gluons. The study of the nucleon excitation spectra gives insight into the underlying dynamics between quarks and gluons that are governed by the strong interactions and described by Quantum Chromodynamics (QCD). However, the non-perturbative regime of QCD is not well understood, e.g. discrepancies exist between theoretically predicted and experimentally observed excited states. To solve this issue, the study of the photoproduction of mesons offers an important experimental tool to increase the sensitivity to resonances that couple only weakly to the πN channel. However, precise data regarding photoproduction reactions exist mostly for the unpolarized cross section, which can not determine all complex amplitudes needed to describe the photoproduction process unambiguously on its own. In order to achieve this goal in partial wave analyses (PWAs), a so-called complete experiment is needed. Here, single and double polarization observables have to be measured additionally, utilizing polarized photon beams, polarized targets and by measuring the polarization degree of the recoil nucleon.

For this work, data were taken with the CBELSA/TAPS experiment at the accelerator facility ELSA in Bonn and with the A2 experiment at the accelerator facility MAMI in Mainz. Both experimental facilities probe nucleons within a fixed target electromagnetically, using a real photon beam. The CBELSA/TAPS data were taken with a linearly polarized photon beam and an unpolarized liquid hydrogen target in order to access the beam asymmetry Σ for the reactions $\gamma p \to p\pi^0$ and $\gamma p \to p\eta$ at beam photon energies ranging from 1130 MeV to 1790 MeV. An elliptically polarized photon beam in combination with a polarized butanol target was used at the A2 experiment, which enabled the measurement of two double polarization observables, namely G and the helicity asymmetry E, at the same time for both the $p\pi^0$ and $p\eta$ final states. The simultaneous measurement of G and E has not been attempted before and offers the opportunity to significantly reduce the required beamtime to measure all single and double polarization observables involving beam and target polarization measurements.

After calibrating both data sets, the $p\pi^0$ and $p\eta$ final states were selected with low background contributions. Subsequently, the beam asymmetry Σ was determined using two different fit methods, firstly a binned χ^2-fit and secondly an unbinned maximum likelihood fit. The helicity asymmetry E was determined utilizing the carbon subtraction method, which required an intensive study of background contributions stemming from bound nuclei within the employed butanol target.

The new CBELSA/TAPS and A2 data provide one of the most precise data sets of measured polarization observables until now. The high statistical precision allows the observation of the $p\eta$ and $p\eta'$ cusp-effects in the data. Additionally, the extracted data for the beam asymmetry Σ have such a high statistical precision that sensitivity up to partial waves corresponding to an angular momentum quantum number $l = 4$ (G-waves) could be determined. Moreover, the data for the helicity asymmetry E close the existing gap of the database down to the $\Delta(1232)\frac{3}{2}^+$ (P_{33})

resonance in the $p\pi^0$ final state and show with high precision a good agreement to existing data, whereby the latter were taken using only circularly polarized photons. Thus, first experimental evidence is given in this work for the fact that the double polarization observable E can be measured with an elliptically polarized photon beam.

Contents

1 Introduction

In 1961 R. Hofstadter was awarded with the Nobel prize for discovering that the proton, which is the essential building block of all matter, is not a point-like object but has an inner structure. This insight was gained by means of electron-nucleon scattering experiments [Hof57]. Now, 57 years after that discovery, fundamental properties of the proton, e.g. the proton radius [Poh+10], or the proton spin [Ash88], or the excited states of the proton are not well understood and are therefore still vigorously investigated in hadron physics research. In particular the study of the latter topic aims at understanding the underlying dynamics of the constituents inside the nucleon, the dynamics between the so-called quarks and gluons. The present work is embedded within this topic.

This chapter gives a short overview of the relevant theoretical framework. It starts in Section 1.1 with a description of the most important aspects of the Standard Model of particle physics, followed by the nucleon excitation spectra and their description through lattice QCD and quark models (see Section 1.3). Afterwards, the study of meson photoproduction reactions (see Section 1.4.1) is introduced as an experimental tool to investigate the nucleon excitation spectra and the importance of measuring polarization observables is discussed in Section 1.4.2.

1.1 The Standard Model of particle physics

Most experimentally observed phenomena in the microscopic world, e.g. the binding of protons and neutrons in nuclei, or the binding of electrons in an atom, or radioactive decays can be explained through three fundamental interactions: the strong, the weak and the electromagnetic interactions. The fourth known fundamental interaction, the gravitational interaction, is negligibly small for the description of microscopic phenomena, and thus it is not relevant for this work. In the 1970s, the Standard Model (SM) of particle physics [Alt05; DGH14; AH13] was developed, which is a $\mathrm{SU}(3)_c \times \mathrm{SU}(2)_L \times \mathrm{U}(1)_Y$ gauge theory capable of describing most of the observed phenomena in nature.

According to the SM all matter in the universe is made up of twelve building blocks that are spin-1/2 fermions and therefore follow the Fermi-Dirac statistics. They consist of quarks of six different flavors (u, d, s, c, b, t) and six leptons of three different flavor types ((e, ν_e), (μ, ν_μ), (τ, ν_τ)), as well as their antiparticles. Both groups are subdivided into three generations which have similar properties but different masses. Within one generation of quarks or leptons, the particles are distinguished by their electric charge. Additionally, bosons with spin 1 mediate the corresponding interaction between the elementary particles. The number of bosons that exist for each interaction depends on the underlying gauge symmetry. The most important properties of all elementary particles and all gauge bosons are listed in Table 1.1.

	generation 1	2	3	color charge (c)	weak isospin (T)	electric charge (q)	mass [GeV/c^2] 1	2	3
quarks	u	c	t	r,g,b	+1/2	+2/3	2.2×10^{-3}	1.27	173.1
	d	s	b	r,g,b	−1/2	−1/3	4.7×10^{-3}	0.096	4.18
leptons	e	μ	τ	-	+1/2	−1	5.11×10^{-4}	0.11	1.78
	ν_e	ν_μ	ν_τ	-	−1/2	0	$< 0.2 \times 10^{-8}$	$< 1.9 \times 10^{-4}$	< 0.0182

	particle	c	acts on T	q	mass [GeV/c^2]
gauge bosons	g	yes	no	no	0
	$W^\pm$	no	yes	no	80
	Z^0	no	yes	yes	91
	γ	no	no	yes	$< 1 \times 10^{-27}$
	H^0				125.09 ± 0.24

Table 1.1: The elementary spin 1/2 fermions consist of quark and lepton which are grouped into three generations. Their properties regarding color charge, weak isospin (of left-handed fermions), electric charge and their (upper limit of) mass is given. Gauge bosons with spin 1 are listed as well. It is indicated on which property of a particle (color charge (c), weak isospin (T) or electric charge (q)) they act on according to the interaction they mediate (color charge → strong interaction, weak isospin → weak interaction, electric charge → electromagnetic interaction). The last line contains the Higgs boson which is a scalar boson with spin 0. All information is taken from [Pat+16].

The electromagnetic interaction, which is described theoretically by quantum electrodynamics (QED) [AH13], is a $U(1)_{em}$ gauge theory since the QED Lagrangian is invariant under local phase transformations. Since the phase factors commute, QED is an abelian gauge theory. It has one mediator, the photon, which acts on electrically charged fermions. The coupling strength of QED is given by the coupling constant $\alpha_{EM} \approx 1/137$ for low momentum transfers $Q \to 0$. Due to vacuum fluctuations, that consist of the creation of virtual charged fermion and anti-fermion pairs, the charge of a given charged particle is *screened*. This leads to the measurement of a larger charge at short distances, or equivalently at larger momentum transfers, than at larger distances. Hence, α_{EM} rises towards higher momentum transfers (see Figure 1.1 on the left). Therefore, the QED vacuum can be described as a dielectric medium. Since perturbation theory is well applicable for $\alpha_{EM} \ll 1$, it can be utilized to analytically solve the QED field equations with α_{EM} as expansion parameter up to a very good approximation. This allows precise predictions of QED phenomena, e.g. the anomalous magnetic moment of the electron up to an order of α_{EM}^5 [Aoy+15].
The electroweak interaction is described by a chiral gauge theory [Gla61; Sal68; Wei67] with the $SU(2)_L \times U(1)_Y$ symmetry group. Left-handed fermions form weak isospin doublets with the third component of the weak isospin T_3 being $\pm 1/2$ and right-handed fermions weak isospin singlets with weak isospin of 0. Y stands for the weak hypercharge. Only left-handed fermions participate in weak interactions, meaning that parity is violated maximally here. The so-called

Higgs mechanism [Hig64; GHK64] spontaneously breaks the $\mathrm{SU}(2)_L \times \mathrm{U}(1)_Y$ to $U(1)_{\mathrm{em}}$ in order to account for the fermion and weak exchange boson masses. In addition, it leads to the existence of a scalar boson with spin 0, the Higgs boson, which was discovered in 2012 [Aad+12; Cha+12].

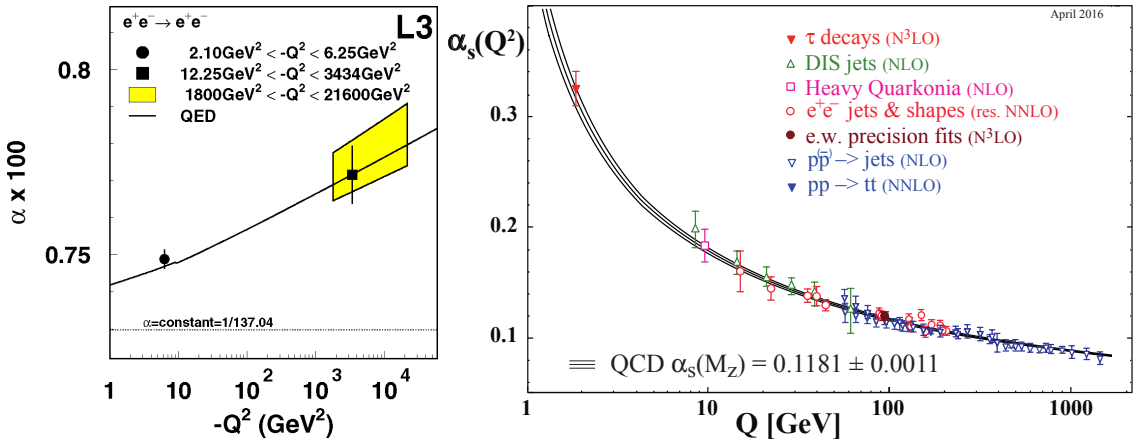

Figure 1.1: Left: The electromagnetic coupling constant α_{EM} is shown as a function of the momentum transfer $-Q^2$ as measured with the LEP experiment. The black line corresponds to the QED prediction. Taken from [Ach+05]. Right: Points represent the coupling constant α_s of the strong interaction as a function of the energy scale Q and as measured with different experiments. Taken from [Pat+16].

The strong interactions are responsible for the binding of the nucleons inside nuclei and act on color charged particles like quarks and gluons. As is experimentally verified, there are three different color charges: red (r), green (g) and blue (b). The fundamental theory that describes the strong interaction is called quantum chromodynamics (QCD) [Nar04; DGH14; AH13]. It is a non-abelian gauge theory with quarks and gluons as degrees of freedom. The structure of QCD is dictated by the $\mathrm{SU}(3)_c$ color symmetry group. This leads to 8 gauge bosons and therefore 8 possible gluons as mediators. Unlike photons, gluons themselves carry color charge and therefore can self-interact, which leads to the running of the strong coupling constant α_S which is demonstrated in Figure 1.1 on the right. The creation of virtual quark-anti-quark pairs in the QCD vacuum leads to similar color screening effect as observed in QED. However, since gluons carry color charge themselves, contributions from virtual gluon pairs dominate and lead to a total *anti-screening* effect of color charge in QCD (see Figure 1.2). This leads to a decrease of α_S with larger energy scales or shorter distances. Mathematically, the dependence of the strong coupling constant on the momentum transfer Q^2 is given by [DGH14]

$$\alpha_s(Q^2) = \frac{12\pi}{(11 \cdot N_C - 2n_f) \cdot \ln(Q^2/\Lambda^2_{\mathrm{QCD}})}, \tag{1.1}$$

where $N_C = 3$ is the number of different colors, n_f is the number of different quark flavors and Λ_{QCD} is the renormalization scale of QCD. As long as n_f does not exceed 16, which is fulfilled with $n_f = 6$, α_S decreases with larger energy scales. Thus, quarks behave asymptotically for $Q^2 \to \infty$ like free particles. This property of QCD is known as *asymptotic freedom*. For $\alpha_S \lesssim 0.1$, perturbation theory can be applied and used to make predictions.

Figure 1.2: Feynman diagrams demonstrating contributions from quark and anti-quark pairs (straight lines) which leads to a color charge screening effect like in QED (left). Since gluons (curly lines) carry color charge themselves, contributions from gluon loops are possible as well leading to an anti-screening of color charge (right).

However, at energy scales in the order of the proton mass ($\approx 1\,\mathrm{GeV}$), perturbation theory can not be applied anymore. This regime is called the *non-perturbative* regime of QCD. Here, the strong coupling constant becomes very large, which is attributed to the fact that no quark or gluon has ever been observed experimentally as an isolated particle. Instead, only color neutral bound states are realized in nature. This phenomenon is called *confinement*. Any attempt to separate e.g. a quark-antiquark pair from each other leads to a formation of many new quark antiquark pairs, a process known as hadronization [BDS16]. The mathematical description of *confinement* is one of the biggest open challenges in the SM.

1.2 Color neutral bound states in QCD

Color neutral bound states can be obtained through the formation of quark-antiquark ($q\bar{q}$) pairs or three quarks (qqq). These two groups are classified as mesons and baryons which build the group of hadrons. In principle other constellations e.g. $qqqq\bar{q}$ or $q\bar{q}q\bar{q}$ are possible as well [ADK16].

Each bound state is described by the total angular momentum J and parity P. The following inequality holds with the orbital angular momentum l and spin s: $|l - s| \leq J \leq |l + s|$ [Clo79; ADK16]. The parity is defined as $P = (-1)^{l+1}$ for mesons. Mesons are states of integer spin and baryons are states of half integer spin. Their total wave functions Ψ_{tot} are decomposed into space, spin, flavor and color components [ADK16]:

$$\Psi_{\mathrm{tot}} = \Psi_{\mathrm{space}} \cdot \Psi_{\mathrm{spin}} \cdot \Psi_{\mathrm{flavor}} \cdot \Psi_{\mathrm{color}}. \tag{1.2}$$

M. Gell-Mann [GM62], Ne'eman [Ne'61] and G. Zweig [Zwe64] suggested within the first quark model to organize the many experimentally found states based on a group-theoretical Ansatz. Assuming mass degeneracy of the three lightest quarks (u,d and s quarks) in the unitary symmetry limit, despite not being fulfilled exactly in nature (see Table 1.1), $\mathrm{SU}(3)_f$ flavor symmetry can be utilized to find all possible combinations of $q\bar{q}$ mesons and qqq baryons consisting of u, d and/or s quarks. For mesons, the total wave function contains a direct product of the $\mathrm{SU}(3)_f$ representation of the quark ($\mathbf{3}$) and the conjugate representation of the antiquark ($\bar{\mathbf{3}}$), which leads to a direct sum of an octet and singlet [Clo79; ADK16]:

$$\mathbf{3} \otimes \bar{\mathbf{3}} = \mathbf{8} \oplus \mathbf{1}. \tag{1.3}$$

Each multiplet contains mesons with the same quantum numbers according to J^{PC}, where C

denotes the C-parity. Figure 1.3 shows the nonets, a combination of an octet and singlet, of the ground state containing the lightest mesons with quantum numbers $J^{PC} = 0^{-+}$ (pseudoscalar mesons e.g. π^0 or η) on the left and $J^{PC} = 1^{--}$ (vector mesons e.g. ω or ρ) on the right. Here, the orbital angular momentum is $l = 0$ and the spins are oriented anti-parallel or parallel, respectively. Mesons are arranged according to their hypercharge $Y = B + S$, which is the sum of the baryon number ($B = 0$ for mesons and $B = +1$ for baryons) and strangeness ($S = -1$ for each s quark contained in the meson or baryon, $S = 0$ if no s quark is present and $S = +1$ for each anti-s quark), as well as the third component of the strong isospin I_3.

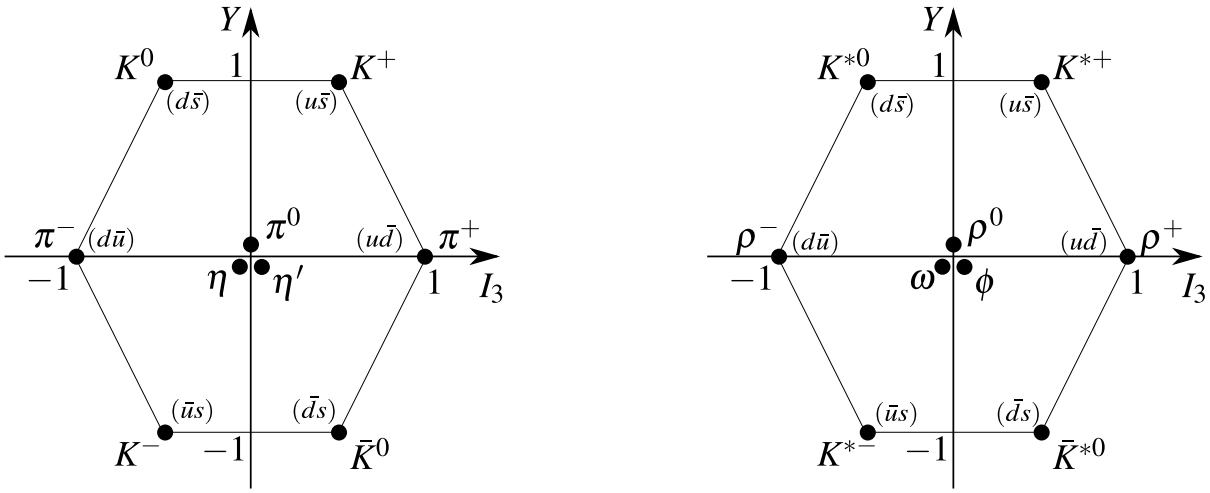

Figure 1.3: The nonets of the ground state: pseudoscalar ($J^{PC} = 0^{-+}$, left) and vector meson ($J^{PC} = 1^{--}$, right) nonets are shown. The mesons are placed according to their hypercharge $Y = S + B$, which is given by the sum of the strangeness and baryon quantum number, and the third component of the strong isospin I_3. The quark content of almost all mesons is given in brackets [Pat+16].

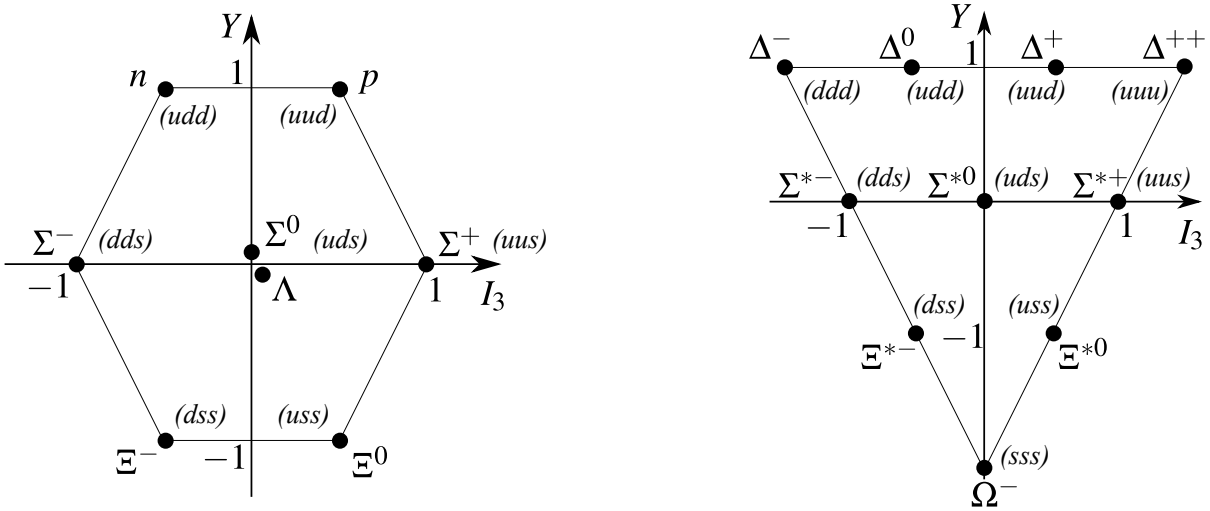

Figure 1.4: The baryon octet ($J^P = \frac{1}{2}^+$, left) and decuplet ($J^P = \frac{3}{2}^+$, right) are depicted. The baryons are placed according to their hypercharge $Y = S + B$, which is given by the sum of the strangeness und baryon quantum number, and the third component of the strong isospin I_3. The quark content is given in brackets [Pat+16].

The decomposition of baryons is given by a decuplet, two octets and a singlet [Pat+16]:

$$\mathbf{3} \otimes \mathbf{3} \otimes \mathbf{3} = \mathbf{10}_S \oplus \mathbf{8}_{MS} \oplus \mathbf{8}_{MA} \oplus \mathbf{1}_A. \tag{1.4}$$

The subscript denotes which symmetry (S = symmetric, MS = mixed symmetric, MA = mixed antisymmetric and A = antisymmetric) is present when interchanging any two quarks. Baryons have to follow the Pauli principle, which means that the total wave function (see Equation (1.2)) has to be antisymmetric. Thus, the existence of the A multiplet is forbidden for the ground state with $l = 0$ [Pat+16]. Therefore, only the octet multiplet with $J^P = \frac{1}{2}^+$ and decuplet with $J^P = \frac{3}{2}^+$ are present in the ground state. Figure 1.4 depicts these two baryon multiplets. Through changing of the orbital angular momentum, or with spin flips, it is possible to obtain excited states. In this case, also the other multiplets can be realized. While the proton (p) and neutron (n) belong to the octet, the $\Delta(1232)$ state belongs to the decuplet. Each flavor multiplet contains on the horizontal the isospin multiplets, e.g. the isospin doublet containing the n and p where they are interpreted as two eigenstates of the same particle, the nucleon. Due to the small u and d quark mass difference, isospin symmetry is considered to be approximate, leading to a small mass difference of proton and neutron. The mass difference of the s quark relative to the u and d quarks is not negligibly small, causing a breaking of $\mathrm{SU}(3)_f$ symmetry and therefore the masses within the baryon octet are not degenerate, but range from 939 MeV for the nucleons to 1318 MeV for the Ξ baryons. The same is true for the baryon decuplet, where the masses go from 1232 MeV for the Δ baryons to 1672 MeV for the Ω^- baryon [Pat+16].
The group-theoretical Ansatz of the quark model served as a classification scheme of the experimentally observed bound states that historically helped understanding the quark content of mesons and baryons and even predict the existence of the, at that time, missing baryon Ω^-. However, as a static quark model it has no predictive power concerning the masses of the states within the multiplets. The mass of e.g. the nucleons is of particular interest since only 5% of the nucleon mass of 939 MeV is accounted for through the u and d current quark masses (see Table 1.1), which are by themselves acquired through the Higgs mechanism. The remaining 95% is given by the strong interactions of quarks and gluons confined within the nucleons [Dür+08]. In order to predict the baryon mass states in the non-perturbative regime of QCD, it is necessary to take the dynamics between the quarks and gluons into consideration, e.g. by modeling the strong interactions in a phenomenological approach using constituent quark models, or e.g. by solving QCD numerically through lattice calculations. Both approaches are discussed in the following, concerning only the non-strange baryon sector where either isospin $I = \frac{1}{2}$ nucleon or $I = \frac{3}{2}$ delta states are present (see Figure 1.4).

1.3 Theoretical description of the nucleon excitation spectra

1.3.1 Constituent quark models

Constituent quark models assume baryons to be built up of three constituent quarks, which have the same properties as the current quarks (see Table 1.1). However, a sea of quark-antiquark pairs and gluons surrounds them, giving them an effective mass of $m_u \approx m_d \approx 350$ MeV and $m_s \approx 500$ MeV [CR00]. The constituent quarks are bound by a potential within the baryons. This potential is chosen to fulfill the QCD property of confinement which is implemented by a

linearly rising potential for large interquark distances[1] in all models. However, differences are present in the assumptions about the short-ranged residual interactions between quarks. While the residual interactions determine the ordering scheme of the excited states and the decay properties of each resonance e.g. its mass, width, etc., the effective degrees of freedom are responsible for the number of predicted states [Pat+16]. In literature, one distinguishes models which are based on a quantum mechanical or quantum field theoretical Ansatz and which are formulated either non-, semi- or fully relativistic. In the non-relativistic quark model of N. Isgur and G. Karl [IK77; IK79], the excited states of baryons correspond to energy eigenstates which are obtained by solving the Schrödinger equation. Here, the Hamiltonian contains a confining harmonic oscillator potential and includes a hyperfine-like interaction as a model for the short range forces. Spin orbit interactions due to one-gluon exchange are neglected. A detailed review about the different available models is given in [CR00; Pat+16]. Here, the emphasis is put on the fully relativistic Bonn model developed by Loering, Metsch, Petry and Ronninger [LMP01; RM11].

To account for the movement of the confined quarks within the baryons with a significant fraction of the speed of light [Met08], the Bonn model is formulated relativistically based on quantum field theory using the Bethe-Salpeter equation. It incorporates a linearly rising potential for confinement which is flavor- and spin independent. The residual interactions between quarks contain instanton induced two- and three body interactions among the quarks [LMP01]. The latest updated version of the Bonn model includes a flavor dependent interaction based on pseudoscalar meson exchange as well [RM11], which helps to predict the mass position of e.g. of the first radial excited state, the $N(1440)\frac{1}{2}^+$ (P_{11}) that is also known as the roper resonance. The resonance notation is given in the following way: $N(W)J^P((l_M)_{2I2J})$, where W is the mass of the resonance, l_M is the relative orbital angular momentum between the meson and the proton with values $l_M = 0, 1, 2, \ldots$ corresponding to $S, P, D, \ldots$ (see Section 1.4.1) and I and J are the isospin and the total angular momentum of the resonance.

Figure 1.5 shows the predicted nucleon and delta excitation spectra from the Bonn model with a strong isopin of $I = 1/2$ and $I = 3/2$, respectively (blue lines). Both spectra contain positive and negative parity states ordered by increasing total angular momentum from $J = 1/2$ to $J = 11/2$. The predicted states are compared to experimentally observed states (red lines) as listed in [Nak+10]. The yellow and orange boxes indicate the measurement uncertainty of the mass position. In addition, a star rating of the PDG [Pat+16] is given according to how well the resonance is established, e.g. four stars mean the resonance has been experimentally observed in several experiments. Thus, its existence is certain and its properties are well known.

The comparison between experimentally measured and predicted states shows a good agreement for low-mass resonances until 1800 MeV. Every predicted state can be assigned to an experimentally verified one. A detailed inspection reveals aspects that are not yet understood like the mass positions of the $N(1535)\frac{1}{2}^-$ (S_{11}) or $\Delta(1700)\frac{3}{2}^-$ (D_{33}) resonances, or the occurrence of some parity doublets, e.g. $N(1680)\frac{5}{2}^+$ (F_{15}) and $N(1675)\frac{5}{2}^-$ (D_{15}), two states with almost the same mass but different parity. The latter gave rise to a recent discussion whether chiral symmetry could be restored at higher masses[2] [Pat+16]. Nevertheless, a good qualitative description of the nucleon excitation spectra is achieved in the low-mass regime.

[1] Large distances in QCD means ≈ 2 fm [EHM09].

[2] The quark masses enter the QCD Lagrangian as free parameters. In the limit of massless quarks, chiral symmetry is fulfilled in QCD. However, the experimental evidence for the fact that not all hadrons belong to a parity doublet with degenerate mass, suggests that chiral symmetry is spontaneously broken [EHM09].

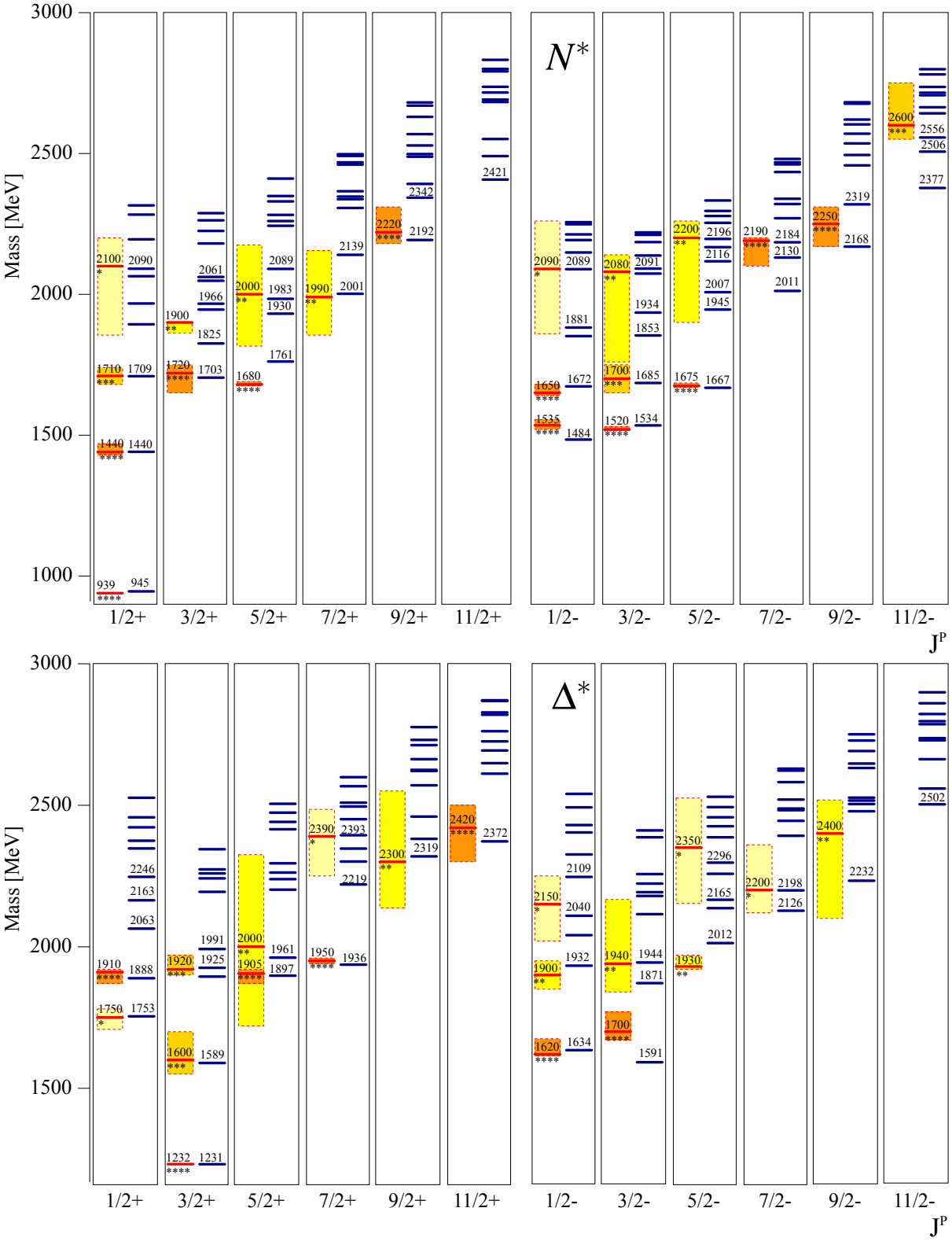

Figure 1.5: Blue lines depict the predicted excited nucleon N^* resonances with $I = 1/2$ (top) and delta Δ^* resonances with $I = 3/2$ (bottom) of the Bonn model [RM11]. Each state is characterized by the total angular momentum and parity J^P. The experimentally observed states are given by red lines and the yellow and orange boxes indicate their measurement uncertainty. The stars give the PDG rating [Nak+10]. Adapted from [RM11].

The situation is dramatically different for masses above 1800 MeV. Here, many more states are predicted than there have been measured experimentally. This feature, which is known as the problem of the *missing resonances*, is not only inherent to the Bonn model, but is also present in other quark models [CR00] as well. A possible explanation could be either that not all existing states have been found experimentally or that the underlying degrees of freedom in the Bonn model are not correct. An alternative approach suggests a quark-diquark formation within the baryons instead of a three quark model, where the diquark is in a relative S-wave state [Ans+93]. This leads to fewer degrees of freedom and therefore less states are predicted in such a scenario. However, recent experimental data indicate otherwise [Thi+15]. In addition, lattice QCD calculations do not find evidence for a quark-diquark model [Lei93; Edw+11].

1.3.2 Lattice QCD

QCD, which is described by quark and gluon fields, is defined for every four dimensional space-time point. Any physical quantity is calculated using path-integrals over field-configurations. As already mentioned before, perturbation theory can not be used to solve QCD exactly in the mass region of the nucleons. In the lattice QCD approach [Wil74; AH13], the QCD Lagrangian is discretized utilizing an approximation of the space-time continuum by a finite volume hypercubic space-time lattice with size L and lattice spacing a (see Figure 1.6). Lorentz-invariance is no longer fulfilled but can be restored in the continuum limit ($a \to 0$). Instead, a hypercubic symmetry, consisting of a sub-group of the Lorentz group, is present in lattice QCD. All integrals and differentials have to be reformulated using finite sums and difference expressions. The quark fields are placed on the lattice sites while the gluon fields live on the lattice links. Physical quantities, e.g. the baryon masses, are determined by solving the multi-dimensional integrals numerically using Monte Carlo simulations. Since the numerical evaluation requires an enormous computational effort, the parameters entering the lattice QCD simulations, containing the lattice size, lattice spacing and quark masses, have to be chosen carefully.

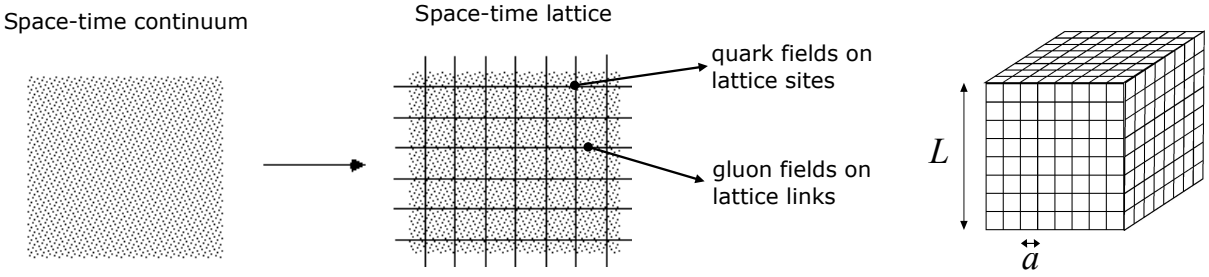

Figure 1.6: In lattice QCD, the space time continuum is discretized using a lattice of size L and lattice spacing a. Quark fields are placed on the lattice sites and gluon fields on the lattice links. Adapted from [Uka13].

The lattice size should ideally be chosen in such a way that the finite volume is larger than the size of hadrons. In reference [Dür+08] the following rule is given:

$$m_{\pi^0} \cdot L \gtrsim 4, \tag{1.5}$$

where m_{π^0} is the mass of the π^0 meson. Thus, finite volume errors become negligibly small. On the other hand, the lattice spacing a should be much smaller than the hadron size, so that discretization effects are not too evident. Typically, the calculations are not performed

in the continuum limit. Once the observables of interest are calculated, they are extrapolated towards the physical mass values of the u, d quarks and therefore also to the π^0 mass. In order to make the immense calculation process manageable, quark masses higher than the current quark masses have to be employed, which results in an unphysically large π^0 mass.

The first lattice QCD calculations regarding the nucleon and delta resonances were performed by Edwards et al. [Edw+11], using an unphysical high π^0 mass value of $m_{\pi^0} = 396\,\text{MeV}$. The results are displayed in Figure 1.7. Due to the unphysical π^0 mass, only a qualitative comparison to quark model predictions and experimental data can be done. The states are clustered into bands of levels with increasing total orbital momentum L and with alternating parity for each J, which is very similar to what non relativistic quark models predict. Furthermore, the occurrence of parity doublets is also not predicted by the lattice QCD calculations. At higher masses, many more states are predicted in comparison to experimentally found states, similar to the predictions of the Bonn model. In addition, no indication is given in favor of a quark-diquark interpretation of baryons. With advancing technology and better performing super computers, lattice QCD calculations near the actual π^0 mass will be possible and it remains to be seen how the lattice QCD predictions change.

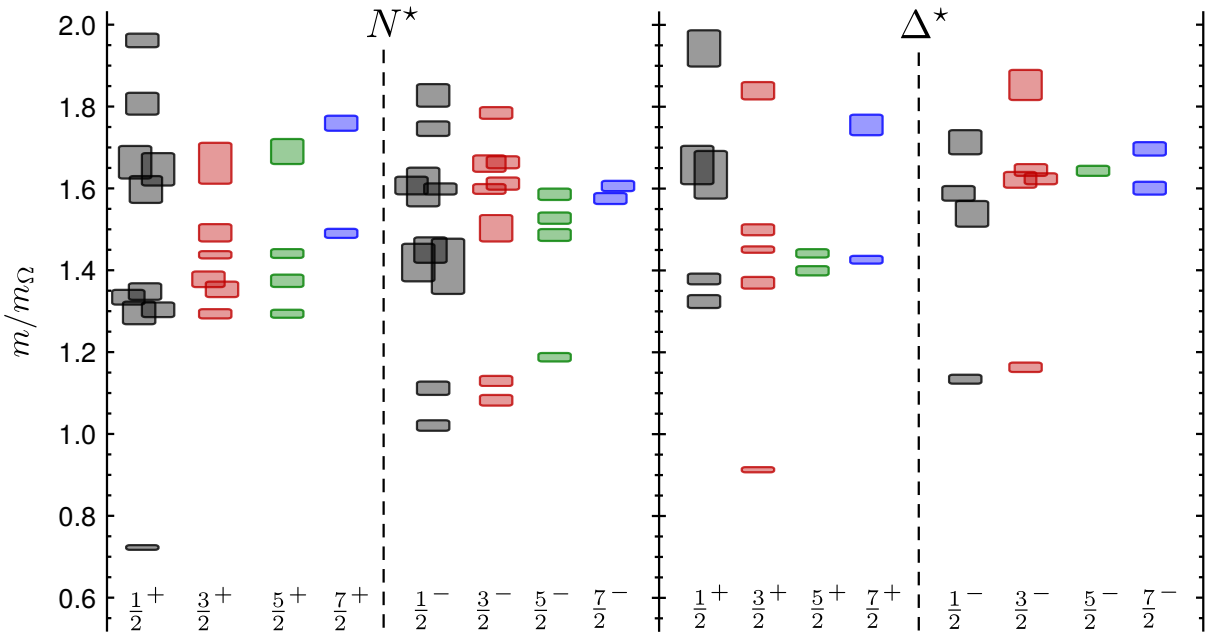

Figure 1.7: Lattice QCD calculation of the nucleon and delta excitation spectra are shown for different spin parity states J^P utilizing an unphysical π^0 mass of $m_\pi = 396\,\text{MeV}$. The masses are given in units of the Ω^- baryon mass. Taken from [Edw+11].

1.4 Experimental tools to determine the nucleon excitation spectra

As discussed previously, discrepancies exist between experimentally observed states and states predicted by quark models and lattice QCD calculations. To resolve this issue, it is paramount to ensure that all excited states, that exist, are found from the experimental side. Historically, most of the excited states that are listed in the PDG from 2010 [Nak+10] were obtained from πN scattering experiments. The $\pi^+ p \to X$ cross section is with $\sigma \approx 200$ mb [Pat+16] large

enough to obtain a good statistical database. However, there is the possibility that not all resonances couple strongly, or some do not couple at all, to the πN channel [Met08] and thus, have not been observed until now. Therefore, it is important to probe the nucleon excitation spectra with different initial and/or final states. In photoproduction reactions, the initial pion beam is replaced by a real photon beam. This offers the possibility to study many different final states, e.g. $N\pi^0$ or $N\eta$ or multi meson final states. However, the disadvantage here is that the cross section for $\gamma p \to X$ is with $\approx 0.5\,\mathrm{mb}$ [Pat+16] four hundred times smaller than the hadronic cross section and the measurement of a data sample with good statistics is more challenging.
Several experimental facilities like the CLAS experiment at Jefferson Lab, the CBELSA/TAPS experiment at ELSA and the A2 experiment at MAMI run dedicated programs to study photoproduction reactions. Data from the latter two facilities were analyzed during the scope of this thesis. The next sections explain in detail the photoproduction reactions, which physical quantities are necessary to measure and how information about excited states can be extracted from the measured observables.

1.4.1 Photoproduction of pseudoscalar mesons

At the CBELSA/TAPS and A2 experiments, a photon beam impinges on a target made of nucleons. In particle physics, three different possible scattering processes are distinguished involving two initial and two final state particles: s-, u- and t-channel processes. In all processes, an intermediate particle is exchanged. The corresponding Feynman diagrams are displayed in Figure 1.8. The energies, momenta and scattering angles of all particles involved are described by the Lorentz-invariant Mandelstam variables, s, t and u [Man58], e.g.

$$s = (p_1 + p_2)^2 \equiv W^2, \tag{1.6}$$

where p_1 and p_2 are the momenta of the initial state particles and W the center of mass energy. The s-channel processes can lead to resonant excitations in the intermediate state, e.g. N^* or Δ^* resonances, which decay via the strong interactions and emit at least one meson in the final state e.g. a π^0 or η meson. Aside from the resonant excitations in the s-channel, non-resonant background contributions are possible as well [KS03]. Non-resonant Born terms contribute to the s- and u-channel, where a nucleon is exchanged in the intermediate state. Furthermore, a background term contributes to the u-channel where a resonance is present in the intermediate state.

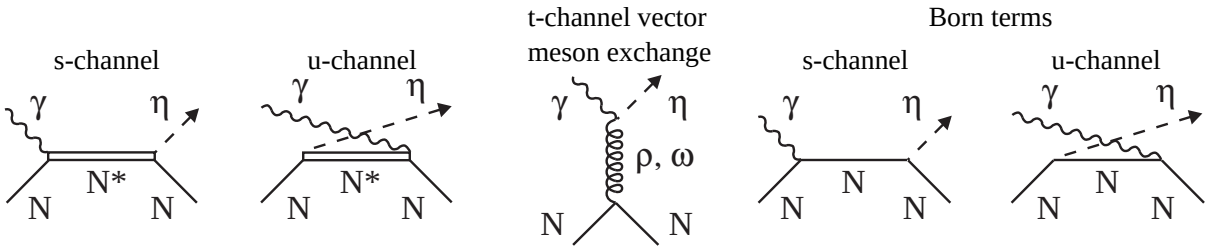

Figure 1.8: Tree-level diagrams show the resonant s-channel (first diagram from the left) and non-resonant contributions (all other diagrams) in case of η photoproduction. The latter consists of a u-channel term with a resonance, a t-channel term with a vector meson and Born s-or u-channel terms with a nucleon in the intermediate state. Adapted from [KS03].

In addition, t-channel processes, where a vector meson (e.g. ρ, ω) is exchanged in the intermediate state, are possible as well. Figure 1.8 illustrates the resonant and the non-resonant background contributions with tree level diagrams as an example for η photoproduction.

The most relevant process for this work is the resonant s-channel process which is discussed in the following in more detail. In the initial state, the photon has parity P_γ, isospin I_γ and a total angular momentum $L_\gamma = l_\gamma + S_\gamma$, consisting of a relative orbital angular momentum between the photon and the proton l_γ and spin $S_\gamma = 1$. Either electric (E) or magnetic (M) multipole radiation can be responsible for the nucleon excitation [DT92]. The photon parity is given by $P_\gamma = (-1)^{L_\gamma}$ for electric and by $P_\gamma = (-1)^{L_\gamma+1}$ for the magnetic photon multipoles [DT92]. The proton is in the ground state in the initial and final state with the following quantum numbers: spin $S_p = +1/2$, parity $P_p = +1$ and isospin $I_p = 1/2$ (see Figure 1.9). The intermediate state resonance is characterized by the total angular momentum $J_{\text{res.}}$, parity $P_{\text{res.}}$ and isospin $I_{\text{res.}}$. After the resonance decays, e.g. one pseudoscalar meson is emitted in the final state. Here, only the case of a single π^0 or η is relevant. Both mesons are spin $S_M = 0$ particles with a relative orbital momentum between meson and proton l_M and parity P_M. The meson parity consists of an intrinsic parity of $(-1)^{l_M}$ that has to be multiplied by the parity of the π^0 or η meson, which is in both cases (-1), since both mesons belong to the pseudoscalar octet (see Figure 1.3). However, the π^0 and the η meson differ in regards to the strong isospin quantum number: π^0 has an isospin of $I_{\pi^0} = 1$ while η has an isospin of $I_\eta = 0$. Since the resonances decay via the strong interactions, isospin is conserved at the strong interaction vertex. While in the case of the π^0 both $N^*(I_{N^*} = 1/2)$ and $\Delta^*(I_{\Delta^*} = 3/2)$ resonances can contribute to the intermediate state, only the N^* resonances are allowed in single η-photoproduction. Thus, the $p\eta$ channel acts as an isospin filter and offers the great opportunity to exclusively study N^* resonances with η-photoproduction reactions.

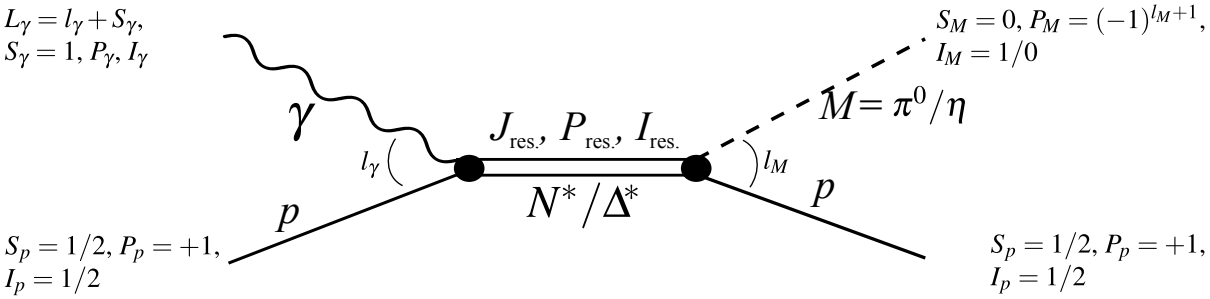

Figure 1.9: Feynman graph of the s-channel process with all important quantum numbers in the initial state (γp), the intermediate state (N^*, Δ^*) and the final state (pM, where M stands for the meson).

Total angular momentum and parity conservation have to be fulfilled which lead to the following selection rules [KS03] for the intermediate state resonance total angular momentum and parity quantum numbers, when taking into account the initial state

$$|L_\gamma - S_p| = |L_\gamma - 1/2| \leq J_{\text{res.}} \leq |L_\gamma + S_p| = |L_\gamma + 1/2|, \tag{1.7}$$

$$P_{\text{res.}} = P_p \cdot P_\gamma = P_\gamma, \tag{1.8}$$

and the final state

$$|l_M - S_p| = |l_M - 1/2| \leq J_{\text{res.}} \leq |l_M + S_p| = |l_M + 1/2|, \tag{1.9}$$

$$P_{\text{res.}} = P_p \cdot P_M = (-1)^{1+l_M}. \tag{1.10}$$

Table 1.2 gives an overview of all possible quantum numbers of the initial, the intermediate and the final state for $L_\gamma = 1$ and $L_\gamma = 2$.

Photon multipole $\mathbf{EL_\gamma/ML_\gamma}$	**initial state $(\mathbf{L_\gamma^{P_\gamma}}, \mathbf{S_p^{P_p}})$**	**intermed. state $\mathbf{J_{res.}^{P_{res.}}}$**	**final state $(\mathbf{S_p^{P_p}}, \mathbf{l_M^{P_M}})$**	**photoprod. multipole $\mathbf{E_{l\pm}}, \mathbf{M_{l\pm}}$**	**resonance $\mathbf{N/\Delta(M)J_{res.}^{P_{res.}}((l_M)_{2I2J})}$**
E1	$\left(1^-, \frac{1}{2}^+\right)$	$\frac{1}{2}^-$	$\left(\frac{1}{2}^+, 0^-\right)$	E_{0+}	$N(M)\frac{1}{2}^-(S_{11}), \Delta(M)\frac{1}{2}^-(S_{31})$
		$\frac{3}{2}^-$	$\left(\frac{1}{2}^+, 2^-\right)$	E_{2-}	$N(M)\frac{3}{2}^-(D_{13}), \Delta(M)\frac{3}{2}^-(D_{33})$
M1	$\left(1^+, \frac{1}{2}^+\right)$	$\frac{1}{2}^+$	$\left(\frac{1}{2}^+, 1^+\right)$	M_{1-}	$N(M)\frac{1}{2}^+(P_{11}), \Delta(M)\frac{1}{2}^+(P_{31})$
		$\frac{3}{2}^+$	$\left(\frac{1}{2}^+, 1^+\right)$	M_{1+}	$N(M)\frac{3}{2}^+(P_{13}), \Delta(M)\frac{3}{2}^+(P_{33})$
E2	$\left(2^+, \frac{1}{2}^+\right)$	$\frac{3}{2}^+$	$\left(\frac{1}{2}^+, 1^+\right)$	E_{1+}	$N(M)\frac{3}{2}^+(P_{13}), \Delta(M)\frac{3}{2}^+(P_{33})$
		$\frac{5}{2}^+$	$\left(\frac{1}{2}^+, 3^+\right)$	E_{3-}	$N(M)\frac{5}{2}^+(F_{15}), \Delta(M)\frac{5}{2}^+(F_{35})$
M2	$\left(2^-, \frac{1}{2}^+\right)$	$\frac{3}{2}^-$	$\left(\frac{1}{2}^+, 2^-\right)$	M_{2-}	$N(M)\frac{3}{2}^-(D_{13}), \Delta(M)\frac{3}{2}^-(D_{33})$
		$\frac{5}{2}^-$	$\left(\frac{1}{2}^+, 2^-\right)$	M_{2+}	$N(M)\frac{5}{2}^-(D_{15}), \Delta(M)\frac{5}{2}^-(D_{35})$

Table 1.2: All quantum numbers of the initial, the intermediate and the final state are given for $L_\gamma = 1$ and $L_\gamma = 2$. Additionally, all possible resonances with masses M are given for the $p\pi^0$ final state. In case of the $p\eta$ final state, the Δ^* resonances do not contribute. Adapted from [Afz12].

According to scattering theory, the probability for the photoproduction process of a pseudoscalar meson with a transition from an initial state i to a final state f is given by [Chu+95]

$$P(i \to f) = |S_{fi}|^2 \qquad \text{with} \qquad S = \mathbb{1} + iT. \tag{1.11}$$

Here, S is the scattering matrix, which consists of a term describing the case of no interaction with the unitarity matrix $\mathbb{1}$ and a term with the transition matrix T which contains all important information of the scattering process e.g. phase space, energy and momentum conservation and the spin and momenta of all particles [LB14]:

$$T_{fi} \propto i(2\pi)^4 \delta^{(4)}(p_f - p_i) \cdot M_{fi}. \tag{1.12}$$

The latter are contained within the invariant amplitude M_{fi} which is related to the photoproduction amplitude $\mathcal{F}$ evaluated in the center mass system. There are different parametrizations available to describe $\mathcal{F}$. One of these is given in Equation (1.13) by the four complex Chew-Goldberger-Low-Nambu (CGLN) spin amplitudes F_i with $i = 1 \ldots 4$ [Che+57]:

$$\mathcal{F} = i(\vec{\sigma} \cdot \vec{\epsilon})F_1 + (\vec{\sigma} \cdot \hat{q})(\vec{\sigma} \cdot (\hat{k} \times \vec{\epsilon}))F_2 + i(\vec{\sigma} \cdot \hat{k})(\hat{q} \cdot \vec{\epsilon}))F_3 + i(\vec{\sigma} \cdot \hat{q})(\hat{q} \cdot \vec{\epsilon})F_4, \tag{1.13}$$

where $\hat{k}$ and $\vec{\epsilon}$ are the momentum unit vector and the polarization vector of the initial state photon, $\hat{q}$ the momentum unit vector of the meson and $\vec{\sigma}$ denote the Pauli spin matrices. The CGLN amplitudes (see Equations 1.14 - 1.17 [Che+57]) can be expressed in a partial wave decomposition through photoproduction multipoles $E_{l\pm}$ and $M_{l\pm}$ and derivatives of Legendre polynomials [AS72], e.g. P_l', P_l''.

$$F_1 = \sum_{l=0}^{\infty} \left[lM_{l+}(W) + E_{l+}(W) \right] P'_{l+1}(\cos\theta) + \left[(l+1)\, M_{l-}(W) + E_{l-}(W) \right] P'_{l-1}(\cos\theta), \tag{1.14}$$

$$F_2 = \sum_{l=0}^{\infty} \left[(l+1)\, M_{l+}(W) + l M_{l-}(W)\right] P_l'(\cos\theta), \tag{1.15}$$

$$F_3 = \sum_{l=0}^{\infty} \left[E_{l+}(W) - M_{l+}(W)\right] P_{l+1}''(\cos\theta) + \left[E_{l-}(W) - M_{l-}(W)\right] P_{l-1}''(\cos\theta), \tag{1.16}$$

$$F_4 = \sum_{l=0}^{\infty} \left[M_{l+}(W) - E_{l+}(W) - M_{l-}(W) - E_{l-}(W)\right] P_l''(\cos\theta). \tag{1.17}$$

The nomenclature for the photoproduction multipoles takes into consideration not only the initial state, but also the final state to describe the transition. While E/M indicate the initial state photon multipole, $l\pm$ states the relative orbital momentum of the final state meson ($l = l_M$) to the recoil proton according to $J_{\text{res.}} = l \pm 1/2$. While the photoproduction multipoles contain the center of mass energy W dependence, the Legendre polynomials describe the dependence of the amplitude on the meson scattering angle $\cos\theta$ in the center of mass frame. Table 1.2 indicates which photoproduction multipoles and resonances are correlated. All resonances, except those with a total angular momentum of $J_{\text{res.}} = 1/2^-$ or $J_{\text{res.}} = 1/2^+$, can be excited by two multipoles, one electric and one magnetic multipole, e.g. resonances with $N(M)\frac{3}{2}^+$ (P_{13}) can be excited by the M_{1+} or the E_{1+} multipole.

1.4.2 Measurement of polarization observables

In order to achieve a full description of the photoproduction process of a single pseudoscalar meson, it is important to determine four complex amplitudes like the CGLN amplitudes. This means one has to determine the absolute values of the amplitudes as well as their three relative phases and an overall global phase[3] [CT97]. The question arises, how can theses amplitudes or photoproduction multipoles be related to experimentally accessible quantities that will enable the extraction of the contributing resonances' properties like mass, width and photon couplings. One possibility is to measure the unpolarized differential cross section $\frac{d\sigma}{d\Omega}_0(W,\theta)$, which can be written using the CGLN amplitudes as [FTS92]

$$\frac{d\sigma}{d\Omega}_0(W,\theta) = \frac{1}{4}\rho \sum_{\text{spins}} |< f|\mathcal{F}|i >|^2 \tag{1.18}$$

$$= \frac{q}{k}\text{Re}\Big\{|F_1|^2 + |F_2|^2 - 2\cos\theta F_2 F_1^* + \frac{1}{2}\sin^2\theta\left(|F_3|^2 + |F_4|^2 + 2F_4F_1^* + 2F_3F_2^* + 2\cos\theta F_4F_3^*\right)\Big\}, \tag{1.19}$$

by averaging over the initial state spin projections and summing over the final state spin projections. The phase space factor $\rho = \frac{q}{k}$ is given by the ratio of the final state meson and the initial state photon momenta in the center of mass system. Integrating over $d\Omega$ results in the total cross section $\sigma_0 = \int \frac{d\sigma}{d\Omega}_0 d\Omega$. It depends only on the moduli squared of the electric and magnetic multipoles [DT92]

$$\sigma_0 = 2\pi\frac{q}{k}\sum_{l=0}^{\infty}\left[(l+1)^2(l+2)|E_{l+}|^2 + (l-1)l^2|E_{l-}|^2 + l(l+1)^2|M_{l+}|^2 + l^2(l+1)|M_{l-}|^2\right]. \tag{1.20}$$

[3] The global phase can not be fixed by any observable quantity [CT97].

Thus, the measurement of the unpolarized cross section gives one real number which is clearly not sufficient to determine all four complex amplitudes. Furthermore, the total cross section is only sensitive to the square of the electric and magnetic multipoles and therefore to the dominating resonance contributions. This is demonstrated in Figure 1.10, which shows the total cross section of the $p\pi^0$ final state as a function of the beam photon energy E_γ and the center of mass energy W together with the contributing resonances up to $J_{\text{res.}} = \frac{7}{2}$. The dominating resonances consist of the $\Delta(1232)\frac{3}{2}^+$ (P_{33}) in the so called first resonance region ($1075\,\text{MeV} \lesssim W \lesssim 1350\,\text{MeV}$), the $N(1520)\frac{3}{2}^-$ (D_{13}) in the second ($1350\,\text{MeV} \lesssim W \lesssim 1600\,\text{MeV}$), the $N(1680)\frac{5}{2}^+$ (F_{15}) in the third ($1600\,\text{MeV} \lesssim W \lesssim 1800\,\text{MeV}$) and the $\Delta(1950)\frac{7}{2}^+$ (F_{37}) in the fourth resonance region ($1800\,\text{MeV} \lesssim W \lesssim 2250\,\text{MeV}$) [Pat+16]. Due to the short lifetime of around $10^{-24}\,\text{s}$ [Pat+16], the resonances have a broad width of around 100 MeV or more and overlap. Thus, the disentanglement of all contributing resonances is challenging.

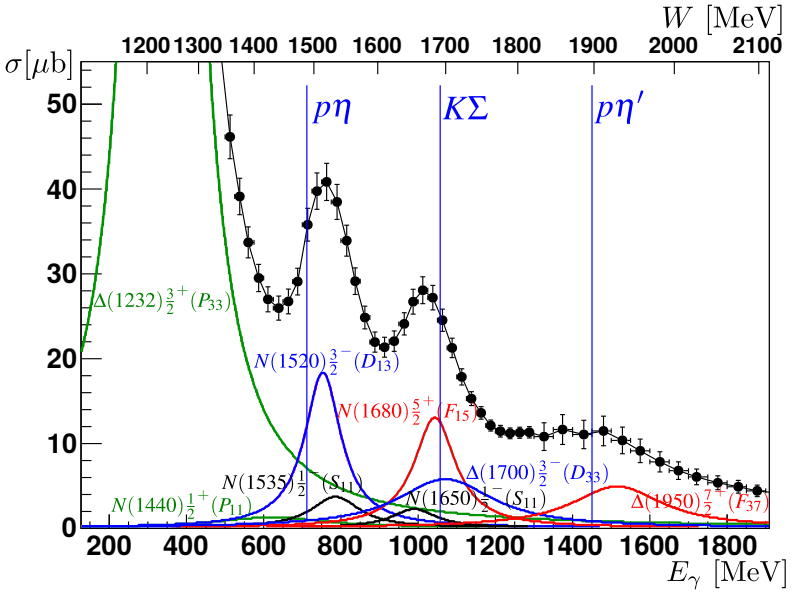

Figure 1.10: The unpolarized total cross section is plotted for the $p\pi^0$ final state together with the contributing resonances which are plotted using a Breit-Wigner parametrization. Here, S-wave resonances ($l = 0$) are plotted in black, P-wave resonances ($l = 1$) in green, D-wave resonances ($l = 2$) in blue and F-wave resonances ($l = 3$) in red. The blue lines indicate the $p\eta$, the $K\Sigma$ and the $p\eta'$ photoproduction thresholds. Taken from [WA+17].

As already mentioned, it is advantageous to study more than one final state since resonances can couple with different strength to the different final states (see Figure 1.10). In this work, the $p\pi^0$ and the $p\eta$ final states are both studied. In the $p\eta$ final state, the two S-wave resonances $N(1535)\frac{1}{2}^-$ (S_{11}) and $N(1650)\frac{1}{2}^-$ (S_{11}) [Pat+16] dominate until the η' photoproduction threshold ($W \approx 1900\,\text{MeV}$) (see Figure 1.11). At higher energies, D- and F-wave resonances become more important.

In order to find answers, especially for the missing resonances problem, it is important to measure observables that are sensitive also to the resonances which only couple weakly to a certain final state. This can be achieved by utilizing a polarized photon beam and/or a polarized target

and/or by measuring the polarization degree of the recoil nucleon. In total, sixteen different observables can be defined [San+11], the unpolarized cross section σ_0, three single (Σ, P, T) and twelve double polarization observables, which are listed in Table 1.3. The double polarization observables can be assigned to three different categories: beam-target (E, F, G, H), beam-recoil $(C_{x'}, C_{z'}, O_{x'}, O_{z'})$ and target-recoil $(L_{x'}, L_{z'}, T_{x'}, T_{z'})$. The measurement of the differential cross section, all three single polarization observables and four of the double polarization observables, which have to be selected carefully, lead to an unambiguous solution for the CGLN amplitudes up to one overall phase [CT97]. Such a set of eight observables is known as the *complete experiment* [BDS75; CT97; San+11].

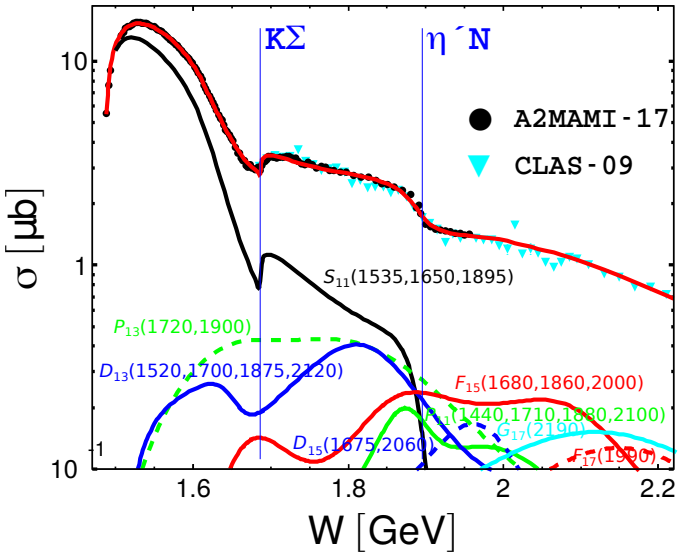

Figure 1.11: The unpolarized total cross section is plotted for the $p\eta$ final state in logarithmic scale together with the contributing partial waves and resonances in brackets according to the ηMAID-2018 PWA model [Tia+18]. The S_{11} partial wave is shown in black, the P_{11} and P_{13} partial waves in green, the D_{13} and D_{15} partial waves in blue, the F_{15} and F_{17} partial waves in red and the G_{17} partial waves in turquoise. Adapted from [Tia+18].

photon		**target**			**recoil nucleon**			**target and recoil**			
		x	y	z	-	-	-	x	z	x	z
		-	-	-	x'	y'	z'	x'	x'	z'	z'
-	σ_0	-	T	-	-	P	-	$T_{x'}$	$L_{x'}$	$T_{z'}$	$L_{z'}$
linear	$-\Sigma$	H	$(-P)$	G	$O_{x'}$	$(-T)$	$O_{z'}$	$(-L_{z'})$	$(T_{z'})$	$(L_{x'})$	$(-T_{x'})$
circular		F	-	$-E$	$C_{x'}$	-	$C_{z'}$	-	-	-	-

Table 1.3: Overview of all sixteen possible polarization observables that can be measured in pseudoscalar meson photoproduction reactions using photon beam, target and recoil nucleon polarization degrees. The unpolarized cross section is highlighted in green, the single polarization observables in blue and all double polarization observables in red. The observables in brackets show alternative ways on how to obtain the specific observable, e.g. P can be measured as a double polarization observable with linearly polarized photon beam and a transversely polarized target as well. The coordinate system (x',y',z') is depicted in Figure 1.12. All information are taken from [San+11].

The CBELSA/TAPS and A2 experiments are both capable of producing a linearly or circularly polarized photon beam as well as of employing a longitudinally or transversely polarized target. Using a polarized photon beam with a polarized target leads to the following expression for the now polarized differential cross section [San+11]:

$$\frac{d\sigma}{d\Omega}(W,\theta,\varphi) = \frac{d\sigma}{d\Omega}_0(W,\theta)\Big[1 - p_\gamma^{\text{lin}}\mathbf{\Sigma}\cos(2\varphi) + p_x\left(p_\gamma^{\text{lin}}\mathbf{H}\sin(2\varphi) + p_\gamma^{\text{circ}}\mathbf{F}\right) - p_y\left(p_\gamma^{\text{lin}}\mathbf{P}\cos(2\varphi) - \mathbf{T}\right) - p_z\left(-p_\gamma^{\text{lin}}\mathbf{G}\sin(2\varphi) + p_\gamma^{\text{circ}}\mathbf{E}\right)\Big]. \tag{1.21}$$

It contains the unpolarized cross section, which is multiplied by additional terms consisting of the polarization degree of the photon beam (p_γ^{lin} or p_γ^{circ}) and target (p_x, p_y or p_z with the target polarization vector $\vec{p}_T = (p_x, p_y, p_z)$) and the polarization observables of the beam-target category.

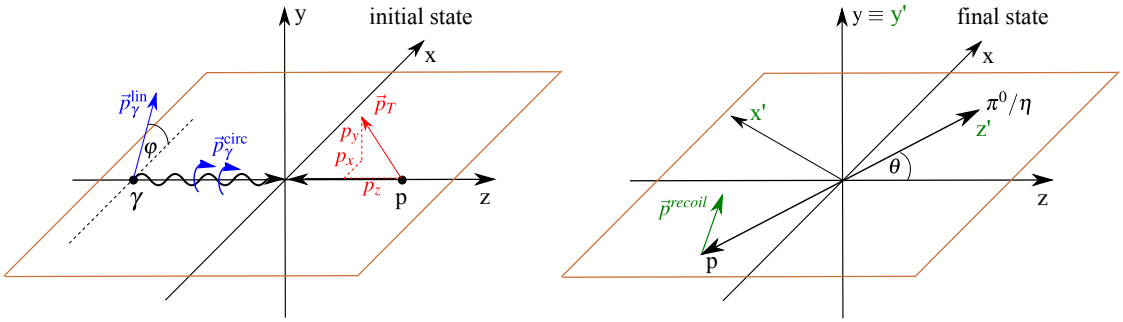

Figure 1.12: The coordinate system in the center of mass system is shown for the initial (left) and final state (right). In the initial state the photons can be polarized either linearly, circularly or both in case of elliptically polarized photons. For linearly polarized photons, the polarization vector has an angle φ to the reaction plane (brown), which is spanned by the photon and meson momentum vectors. The protons can be polarized either longitudinally (p_z) or transversely (p_x or p_y). In the final state, the meson (π^0 or η) flies back to back to the recoil proton. It encloses the angle θ to the z-axis in the center of mass system. For the measurement of recoil polarization observables, the coordinate system (x,y,z) has to be rotated by θ to the coordinate system (x',y',z'). Similar plots of the coordinate system can be found in [San+11].

Figure 1.12 depicts the coordinate system in the initial and final state for the center of mass system. The linear polarization vector encloses the angle φ with the reaction plane. The target polarization $\vec{p}_T$ can be placed either longitudinally or transversely to the beam direction ($+z$). In the final state, the produced meson and recoil proton fly back to back to each other. The scattering angle θ of the meson in the center of mass system is used to rotate the center of mass coordinates (x, y, z) into the primed coordinate system (x', y', z'), which is needed for the measurement of the recoil polarization observables.
The CBELSA/TAPS experiment was used in this work to obtain the beam asymmetry Σ by measuring the polarized cross section utilizing only a linearly polarized photon beam. In this case, Equation (1.21) reduces to

$$\frac{d\sigma}{d\Omega}(W,\theta,\varphi) = \frac{d\sigma}{d\Omega}_0(W,\theta)\left[1 - p_\gamma^{\text{lin}}\mathbf{\Sigma}\cos(2\varphi)\right]. \tag{1.22}$$

In addition, the goal of this work is to determine the helicity asymmetry E using the A2

experiment. According to Table 1.3, the helicity asymmetry E is accessible using a circularly polarized photon beam together with a longitudinally polarized target. While the circularly polarized photons can be right (r) or left (l) handed, the target has to be polarized in beam ($+z$) or against beam ($-z$) direction. Photons are called right handed, if the photons have a helicity of $h_\gamma = +1$ ($\uparrow_H$), otherwise left handed with $h_\gamma = -1$ ($\downarrow_H$). The spin of the proton in the target is oriented either in $+z$ direction with the z-component of the spin being $S_p^z = +1/2$ ($\uparrow_T$) or in $-z$ direction with $S_p^z = -1/2$ ($\downarrow_T$). Thus, the z-component of the spin of the resonance $J^z_{\text{res.}}$ in the intermediate state can have the values $\pm\frac{1}{2}$ or $\pm\frac{3}{2}$. Four different cross sections with corresponding spin configurations can be measured, out of which two represent the helicity dependent cross section $\sigma^{1/2}$ and the other two the cross section $\sigma^{3/2}$ (see Table 1.4). Resonances with $J_{\text{res.}} \geq \frac{3}{2}$ contribute to the helicity dependent cross sections $\sigma^{3/2}$ and $\sigma^{1/2}$, while resonances with $J_{\text{res.}} = \frac{1}{2}$ contribute only to the helicity dependent cross section $\sigma^{1/2}$.

$\mathbf{S}_\gamma$	$\mathbf{S_p}$	$\mathbf{S}^\mathbf{z}_\gamma$	$\mathbf{S}^\mathbf{z}_\mathbf{p}$	$\mathbf{J}^\mathbf{z}_{\text{res.}}$	σ	$\mathbf{J}_{\text{res.}}$
$\uparrow_H$	$\uparrow_T$	1	$\frac{1}{2}$	$\frac{3}{2}$	$\sigma^{3/2}$	$\geq \frac{3}{2}$
$\downarrow_H$	$\downarrow_T$	-1	$-\frac{1}{2}$	$-\frac{3}{2}$	$\sigma^{3/2}$	$\geq \frac{3}{2}$
$\uparrow_H$	$\downarrow_T$	1	$-\frac{1}{2}$	$\frac{1}{2}$	$\sigma^{1/2}$	$\geq \frac{1}{2}$
$\uparrow_H$	$\uparrow_T$	-1	$\frac{1}{2}$	$-\frac{1}{2}$	$\sigma^{1/2}$	$\geq \frac{1}{2}$

Table 1.4: There are four different spin configurations possible. The spins of the initial state photon S_γ and proton S_p can be either aligned parallel or anti-parallel to each other, giving two possible values for the z-component of the spin $S^z_\gamma = \pm 1$ and $S^z_p = \pm\frac{1}{2}$. The z-component of the intermediate state spin $J^z_{\text{res.}}$, the possible helicity dependent cross sections and the total angular momentum $J_{\text{res.}}$ of contributing resonances to the respective helicity dependent cross sections are given as well. Adapted from [Bös16].

Instead of using circularly polarized photons, elliptically polarized photons were utilized at the A2 experiment. Since in this case the photons have a linear and circular polarization component, and since a longitudinally polarized target was used in addition, it is possible to access three polarization observables: Σ, G and E. Equation (1.21) simplifies to

$$\frac{d\sigma}{d\Omega}(W,\theta) = \frac{d\sigma}{d\Omega_0}(W,\theta,\varphi)\left[1 - p_\gamma^{\text{lin}}\mathbf{\Sigma}\cos(2\varphi) + p_z p_\gamma^{\text{lin}}\mathbf{G}\sin(2\varphi) - p_z p_\gamma^{\text{circ}}\mathbf{E}\right]. \tag{1.23}$$

Each polarization observable Ω can be expressed with CGLN amplitudes, after multiplying it by the unpolarized differential cross section and thus obtaining the so-called profile functions $\check{\Omega}$, e.g. for the beam and helicity asymmetry it holds [FTS92]

$$\check{\Sigma} = \Sigma \cdot \frac{d\sigma}{d\Omega_0} = -\rho\,\frac{\sin^2(\theta)}{2}\,\text{Re}\left\{|F_3|^2 + |F_4|^2 + 2\left(F_1^* F_4 + F_2^* F_3 + \cos(\theta) F_3^* F_4\right)\right\}, \tag{1.24}$$

$$\check{E} = E \cdot \frac{d\sigma}{d\Omega_0} = \rho\,\text{Re}\left\{|F_1|^2 + |F_2|^2 - 2\cos(\theta) F_1^* F_2 + \sin^2(\theta)\left(F_4^* F_1 + F_3^* F_2\right)\right\}, \tag{1.25}$$

where $\rho = \frac{q}{k}$ denotes the phase space factor. According to Equations (1.14)-(1.17), all polarization observables can also be formulated with the photoproduction multipoles ($E_{l\pm}$,$M_{l\pm}$)

and associated Legendre polynomials ($P_l^m(x) = (1-x^2)^{\frac{m}{2}} \frac{d^m}{dx^m} P_l(x)$ with $x = \cos\theta$ [AS72]) to describe the energy and angular dependence. All polarization observables can be expanded directly into a series of partial waves, using the angular momentum cutoff $\mathrm{L_{max}}$. In a truncated partial wave analysis, the angular dependence of the profile functions is given by [WA+17; Tia12]

$$\check{\Omega}(W,\theta) = \rho \sum_{l=\beta}^{2\mathrm{L_{max}}+\beta+\gamma} (a_{\mathrm{L_{max}}})_l^{\check{\Omega}}(W)\, P_l^{\beta}(\cos\theta)\,, \tag{1.26}$$

where $(a_{\mathrm{L_{max}}})_l^{\check{\Omega}}$ are the Legendre coefficients. The remaining parameters β and γ determine the total number of Legendre coefficients N_a for each truncation order according to $N_a = 2\mathrm{L_{max}} + \gamma + 1$, which can be different for all polarization observables. Table 1.5 gives the parameters for the beam and helicity asymmetries. The parameters for all polarization observables are listed in reference [WA+17].

$\check{\mathbf{\Omega}}$	β	γ	$\mathbf{N_a}$
$\check{\Sigma}$	2	-2	$2\mathrm{L_{max}} - 1$
$\check{E}$	0	0	$2\mathrm{L_{max}} + 1$

Table 1.5: Parameters of the profile functions (see Equation (1.26)) are given for the beam and helicity asymmetries in accordance to L. Tiator [Tia12; WA+17]. N_a gives the total number of Legendre coefficients for each truncation order $\mathrm{L_{max}}$. It holds $N_a = 2\mathrm{L_{max}} + \gamma + 1$.

Inserting the parameters β and γ from Table 1.5 in Equation (1.26), yields

$$\check{\Sigma}(W,\theta) = \rho \sum_{l=2}^{2\mathrm{L_{max}}} (a_{\mathrm{L_{max}}})_l^{\check{\Sigma}}(W)\, P_l^2(\cos\theta)\,, \tag{1.27}$$

$$\check{E}(W,\theta) = \rho \sum_{l=0}^{2\mathrm{L_{max}}} (a_{\mathrm{L_{max}}})_l^{\check{E}}(W)\, P_l(\cos\theta)\,. \tag{1.28}$$

The expression of the Legendre coefficients in terms of multipoles read [WA+17]

$$(a_{\mathrm{L_{max}}})_l^{\check{\Omega}}(W) = \langle \mathcal{M}_{\mathrm{L_{max}}}(W)|\, \mathcal{C}_l^{\check{\Omega}}\, |\mathcal{M}_{\mathrm{L_{max}}}(W)\rangle\,. \tag{1.29}$$

Here, the hermitean matrices $\mathcal{C}_l^{\check{\Omega}}$ have the dimension $(4\mathrm{L_{max}}) \times (4\mathrm{L_{max}})$ and $|\mathcal{M}_{\mathrm{L_{max}}}(W)\rangle$ contains $4\mathrm{L_{max}}$ multipoles. Truncating at $\mathrm{L_{max}} = 1$, the Legendre coefficient $(a_1)_0^{\check{E}}(W)$ reads for example [WA+17]

$$(a_1)_0^{\check{E}}(W) = (E_{0+}^*, E_{1+}^*, M_{1+}^*, M_{1-}^*) \begin{pmatrix} 1 & 0 & 0 & 0 \\ 0 & 3 & 3 & 0 \\ 0 & 3 & -1 & 0 \\ 0 & 0 & 0 & 1 \end{pmatrix} \begin{pmatrix} E_{0+} \\ E_{1+} \\ M_{1+} \\ M_{1-} \end{pmatrix} \tag{1.30}$$

$$= |E_{0+}|^2 + 3|E_{1+}|^2 + 3E_{1+}^* M_{1+} + 3M_{1+}^* E_{1+} - |M_{1+}|^2 + |M_{1-}|^2, \tag{1.31}$$

which demonstrates that polarization observables are sensitive to not only the absolute value squared of the multipoles, but also to the interference terms of the photoproduction multipoles. Thus, weakly coupling resonances can be accessed, if there exists an interference term with strongly coupling resonances. The coefficient $(a_4)_0^{\check{E}}$ is sensitive, as demonstrated in Equation (1.31), to interference terms of the same l (see also Figure 8.12). Instead of expressing each Legendre coefficient with the full sum of bilinear products of multipoles up to a certain $\mathrm{L_{max}}$, a compact notation can be given, e.g. for $\mathrm{L_{max}} = 4$ [WA+17]

$$(a_4)_0^{\check{E}} = \langle S,S\rangle + \langle P,P\rangle + \langle D,D\rangle + \langle F,F\rangle + \langle G,G\rangle\,, \tag{1.32}$$

where e.g. $\langle P,P\rangle$ contains the sum of bilinear products of multipoles with $l = 1$. Figure 1.13 shows as an example the energy dependence of the Legendre coefficient $(a_4)_0^{\check{E}}$ as obtained from CBELSA/TAPS data [WA+17] and the analyzed A2 data of this work for the $p\pi^0$ final state. The dominant role of the $\Delta\,(1232)\,\frac{3}{2}^+(P_{33})$ resonance, which contributes to the M_{1+} multipole, is well visible in the data of the $p\pi^0$ final state from $W = 1180\,\mathrm{MeV}$ to $W = 1450\,\mathrm{MeV}$. At higher center of mass energies, the $N\,(1520)\,\frac{3}{2}^-(D_{13})$ resonance and the $N\,(1680)\,\frac{5}{2}^+(F_{15})$ resonance play an important role (see Figure 1.10). This is demonstrated through comparisons to continuous curves stemming from the BnGa-2014-02 model solution [Gut+14] (see Section 1.4.3), which are truncated at different $\mathrm{L_{max}}$. The word 'truncated' means in this context, that the respective coefficient has been evaluated using the BnGa-multipoles only up to a certain $\mathrm{L_{max}}$. The curve for $\mathrm{L_{max}} = 1$ describes the data very well until $W = 1450\,\mathrm{MeV}$, while at higher center of mass energies the $\mathrm{L_{max}} = 3$ curve describes the data and thus, corrections from the $\langle F,F\rangle$ interference term are needed. Table 1.6 lists the correlation between multipoles and partial waves for different relative orbital angular momentum of the meson l_M and parity P_M.

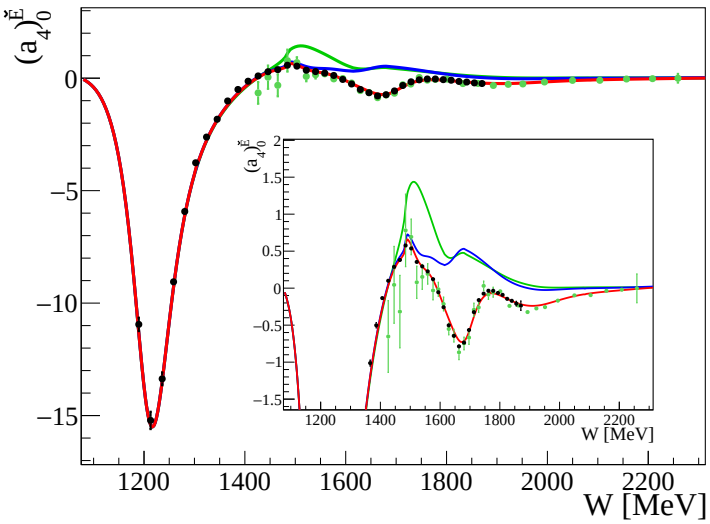

Figure 1.13: Left: The Legendre fit coefficients $(a_4)_0^{\check{E}}$ of the $p\pi^0$ final state are plotted for the new A2 data of this work (black points). They are compared to CBELSA/TAPS data (green points) [Got13; Got+14] and to continuous curves evaluated from the BnGa-2014-02 model solution [Gut+14], which are truncated at different $\mathrm{L_{max}}$ ($\mathrm{L_{max}} = 1$ (green line), $\mathrm{L_{max}} = 2$ (blue line) and $\mathrm{L_{max}} = 3$ (red line)).

In addition, Figure 1.13 emphasizes the high quality of the new A2 data analyzed in this work in comparison to the existing CBELSA/TAPS data. It closes the gap in the database down to the $\Delta\,(1232)\,\frac{3}{2}^+(P_{33})$ resonance and provides high precision data until $W \approx 1870\,\text{MeV}$.

$\mathbf{l_M}$	$\mathbf{P_M}$	**multipoles**	**partial wave states**
0 (S)	$-$	E_{0+}	$N\frac{1}{2}^-$, $\Delta\frac{1}{2}^-$
			$N\,(1535)\,\frac{1}{2}^-(S_{11})$
1 (P)	$+$	E_{1+}, $M_{1\pm}$	$N\frac{1}{2}^+$, $N\frac{3}{2}^+$, $\Delta\frac{1}{2}^+$, $\Delta\frac{3}{2}^+$
			$N\,(1440)\,\frac{1}{2}^+(P_{11})$, $\Delta\,(1232)\,\frac{3}{2}^+(P_{33})$
2 (D)	$-$	$E_{2\pm}$, $M_{2\pm}$	$N\frac{3}{2}^-$, $N\frac{5}{2}^-$, $\Delta\frac{3}{2}^-$, $\Delta\frac{5}{2}^-$
			$N\,(1520)\,\frac{3}{2}^-(D_{13})$, $\Delta\,(1700)\,\frac{3}{2}^-(D_{33})$
3 (F)	$+$	$E_{3\pm}$, $M_{3\pm}$	$N\frac{5}{2}^+$, $N\frac{7}{2}^+$, $\Delta\frac{5}{2}^+$, $\Delta\frac{7}{2}^+$
			$N\,(1680)\,\frac{5}{2}^+(F_{15})$, $\Delta\,(1905)\,\frac{5}{2}^+(F_{35})$
4 (G)	$-$	$E_{4\pm}$, $M_{4\pm}$	$N\frac{7}{2}^-$, $N\frac{9}{2}^-$, $\Delta\frac{7}{2}^-$, $\Delta\frac{9}{2}^-$
			$N\,(2190)\,\frac{7}{2}^-(G_{17})$
5 (H)	$+$	$E_{5\pm}$, $M_{5\pm}$	$N\frac{9}{2}^+$, $N\frac{11}{2}^+$, $\Delta\frac{9}{2}^+$, $\Delta\frac{11}{2}^+$
			$N\,(2220)\,\frac{9}{2}^+(H_{19})$, $\Delta\,(2420)\,\frac{11}{2}^+(H_{311})$

Table 1.6: An overview of the partial waves and the corresponding multipoles is given for different values of the relative orbital angular momentum between the meson and the proton l_M and parity P_M. In addition, the PDG notation for the resonances as well as examples for well established N- and Δ-resonances are given [Pat+16]. The table is taken from [WA+17].

1.4.3 Model dependent partial wave analyses

In order to extract the resonance parameters from the determined polarization observables, partial wave analyses (PWA) need to be performed. It is desirable to perform the analyses model-independently based on a complete experiment database. However, a complete database with infinite statistical precision is not available. In addition, the photoproduction multipoles do not only contain resonant but also non-resonant background contributions, e.g. from Born terms or from t-channel vector meson exchange which have been shown previously as examples in Figure 1.8. Therefore, different models exist which parametrize the resonant and non-resonant contributions in order to fit the existing data and are capable of making predictions for observables that have not yet been measured. The most relevant models for this work are the MAID, SAID, Bonn-Gatchina and Jülich-Bonn analyses, which will be collectively referred to as the PWA models. Before introducing the PWA models, general remarks are made on the parametrization of resonances in the following.

The scattering matrix S is an analytic function in the complex s-plane. Singularities of the function consist of branch-points and poles. Branching points emerge if a channel opens up, which happens at every production threshold of a massive particle, e.g. the thresholds for π^0 and η photoproduction are given at $\sqrt{s} = W = 1077\,\text{MeV}$ and $\sqrt{s} = W = 1486\,\text{MeV}$. Here, the number of Riemann sheets doubles (see Figure 1.14). A resonance is defined as a pole on the unphysical, second Riemann sheet [AHK16]. It is located at W_{pole} in the complex s-plane

[AHK16]:

$$W_{\text{pole}} = \sqrt{s_{\text{pole}}} = M_{\text{pole}} - i\frac{\Gamma_{\text{pole}}}{2}. \tag{1.33}$$

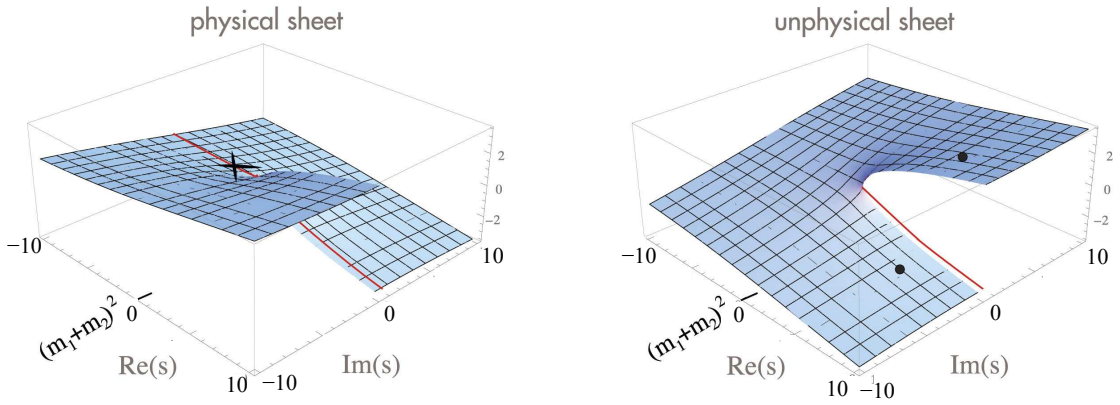

Figure 1.14: The physical (left) and unphysical (right) sheets are depicted as expected for the imaginary part of a single-channel amplitude. Bound states (cross) appear in the physical (first Riemann) sheet, while resonances (dots) appear in the unphysical (second Riemann) sheet in the complex s-plane. The physical axis is drawn as a solid line. Connection between the sheets is realized along the branch-cut. Taken from [AHK16].

The real part corresponds to the mass of the resonance M_{pole}, while the imaginary part determines the total width (Γ_{pole}) of the resonance. In case a resonance has only one decay channel and is isolated and therefore far away from threshold effects, a Breit-Wigner (BW) parametrization can be utilized to describe the resonance contributing to a physical amplitude A [AHK16]:

$$A = -\frac{g_a g_b}{s - M_{\text{BW}}^2 + i\sqrt{s}\Gamma_{\text{BW}}}, \tag{1.34}$$

where g_a, g_b are couplings to the initial (a) and final state (b), $\sqrt{s} = W$ the center of mass energy, M_{BW} the mass and Γ_{BW} the width of the resonance. Only in this case, which is applicable e.g. for the $\Delta(1232)\frac{3}{2}^+$ (P_{33}) resonance which is well isolated from other resonances, it holds $M_{\text{BW}} \approx M_{\text{pole}}$ and $\Gamma_{\text{BW}} \approx \Gamma_{\text{pole}}$. However, usually more than one resonance contribute to a single partial wave and the Breit-Wigner parameters do not agree with the pole parameters as they are reaction dependent. Equation (1.34) can not be utilized anymore.
Here, a K-matrix approach [Chu+95] is often used with a hermitean and real matrix K, which is related to the scattering matrix S in the following way [Chu+95]:

$$S = \mathbb{1} + iT = \frac{\mathbb{1} + iK}{\mathbb{1} - iK}. \tag{1.35}$$

Resonant and non-resonant contributions can be included as follows [Ani+12]:

$$K_{ab} = \sum_{\alpha=1}^{n} \frac{g_a^\alpha g_b^\alpha}{(M_\alpha^2 - s)} + f_{ab}, \tag{1.36}$$

where n denotes the number of resonances, M_α the mass of resonance α, g_a^α, g_b^α are couplings to the initial (a) and final state (b), and f_{ab} describes the non-resonant background. The photon couplings can be calculated with the contour integral around the pole position, e.g. they are related to the pole residues.

The available PWA models differ in the parametrization of the resonant and non-resonant contributions, as well as the fitted database. The differences of four different models are discussed in the following [Ani+16].

1.4.3.1 SAID

The *Scattering Analysis Interactive Dial-in* (SAID) model [Bri+] is based on the Chew-Mandelstam K-matrix approach, where the matrix elements are expanded as energy-dependent polynomials up to 5th order [Wor+12]. Resonances are dynamically generated except for the $\Delta(1232)$ resonance which is explicitly included as a K-matrix pole. Here, a minimal set of generated resonances is determined that is needed to describe data. The masses, widths and branching ratios of resonances are determined from fits to pion-induced reactions. These fits also determine the real and imaginary part of the partial waves for πN reactions. In a second step, photoproduction data are used to get the γN photon couplings. Thus, new resonances can not be found using photoproduction data. The latest SAID solution is the SAID-CM12 solution [Wor+12] for the $p\pi^0$ final state and the SAID-GE09 solution for the $p\eta$ final state [Bri+].

1.4.3.2 MAID

The Mainz Isobar model (MAID) [Tia+b; Tia+a] is a unitary isobar model that is based on a T-matrix approach. Resonances are parametrized as multi-channel Breit-Wigner amplitudes. As a starting point for the PWA, masses, widths and coupling strengths are taken from the PDG [Pat+16]. Background contributions from Born terms in the s- and u-channel, and t-channel exchanges are included as well. The latter contribution is described in the latest model utilizing a Regge-cut model [Kas+17; Tia+18]. The $p\pi^0$ and $p\eta$ data are fitted separately and independently from each other. Therefore, there is the MAID2007 solution [DKT07] for the $p\pi^0$ channel and the ηMAID solution for the $p\eta$ channel [Chi+02]. While the MAID2007 and old ηMAID solutions only included $\pi^0 p, \pi^+ n$ and $p\eta$ photo- and electroproduction data that were published until 2002, the ηMAID solution was recently updated using the latest published unpolarized cross section and polarization observables data of the $p\eta$, $n\eta$, $p\eta'$ and $n\eta'$ final states in their fit as well. This latest solution is called ηMAID-2018 [Tia+18].

1.4.3.3 BnGa

Partial wave amplitudes are described in the Bonn-Gatchina (BnGa) model [AKN+; Ani+16] based on the K-matrix/P-vector approach according to Equation (1.36). However, the K-matrix Ansatz has been modified recently by a dispersion-relation Ansatz which is based on the N/D technique [Ani+16]. Resonances are added by hand. Some resonances that have a higher mass than 2.2 GeV are described with relativistic multi-channel Breit-Wigner amplitudes. Background t- and u-channel exchange processes are included in the amplitude parametrization. The Bonn-Gatchina model is a multi-channel analysis, fitting simultaneously a large database of πN and photoproduction two- and three-body final states that is used to extract resonance parameters. It utilizes the SAID WI08 energy-dependent amplitude solution together with

different πN reactions: $\pi^- p \to \eta n, K^0\Lambda, K^0\Sigma^0, \pi^0\pi^0 n$ and $\pi^+ p \to K^+\Sigma^+$. The following photoproduction reactions $\gamma p \to p\pi^0$, $n\pi^+$, $p\eta$, ΛK^+, $\Sigma^0 K^+$, $\Sigma^+ K^0$, $p\pi^0\pi^0$ and $p\pi^0\eta$ are included in the fit as well. All data sets with their according weights in the fit are listed in [Ani+12]. Nineteen N^* and nine Δ^* are determined as a result of the fit. The two Bonn-Gatchina model solutions BnGa-2014-01 and BnGa-2014-02 [Gut+14] existed prior to the data analyzed in this work. The latest solution is the BnGa-2017 solution [Ani+18].

1.4.3.4 JüBo

The Jülich-Bonn (JüBo) model [Rön+] is a dynamical coupled-channel approach, which goes beyond a PWA. Nevertheless, the JüBo model is included in the collective reference of PWA models throughout this work. The scattering process from the initial state ν to the final state μ with the intermediate state κ is described via the Lippmann-Schwinger equation in the partial-wave basis [Rön+15; Ani+16]:

$$T_{\mu\nu} = V_{\mu\nu} + \sum_{\kappa} \int_0^\infty dp \quad p^2 V_{\mu\kappa} G_\kappa T_{\kappa\nu}, \tag{1.37}$$

where $T_{\mu\nu}$ is the hadronic T-matrix, $V_{\mu\kappa}$ the scattering potential and G_κ the propagator of the intermediate state. Here, the hadronic potential is constructed from an effective Lagrangian, consisting of a pole ($V_{\mu\nu}^{\text{pole}}$) and a non-pole contribution. The pole contribution includes bare resonances as s-channel states by hand, which are called genuine resonances and are parametrized in the following way in the complex energy plane [Rön+15; Ani+16]:

$$V_{\mu\nu}^{\text{pole}} = \sum_{i=0}^{n} \frac{\gamma_{\mu i}^a \gamma_{\nu i}^c}{W - m_i}. \tag{1.38}$$

The quantities $\gamma_{\mu i}^a$ and $\gamma_{\nu i}^c$ are the annihilation and creation vertices, m_i the bare mass of resonance i and n the total number of included resonances per partial wave. In the non-pole term u- and t-channel processes are considered with the help of an effective Lagrangian. In addition, it is possible to obtain dynamically generated resonances. Examples of dynamically generated resonances in the JüBo model are e.g. the roper resonance $N(1440)\frac{1}{2}^-$ (P_{11}) and the $\Delta(1600)\frac{3}{2}^+$ (P_{33}) resonance. Each resonance is characterized by a pole on the second Riemann sheet. Photoproduction processes are parameterized by energy-dependent polynomials, the photoproduction multipole amplitude $M_{\mu\gamma}$ reads [RDM18]

$$M_{\mu\gamma} = V_{\mu\gamma} + \sum_{\kappa} \int_0^\infty dp \quad p^2 T_{\mu\kappa} G_\kappa V_{\kappa\gamma}, \tag{1.39}$$

where γ gives the initial state γN. During the fitting procedure, data of multiple channels of pion- and photon-induced reactions are used. Eleven N^* and ten Δ^* resonances are present in the fit. A total of 761 free parameters need to be fixed in the fitting procedure. The extensive calculations are performed at the JURECA supercomputer in Jülich. The latest solution is the JüBo-2017 solution [RDM18].

1.5 Current data situation

Figures 1.15 and 1.16 give an overview of all existing data for all single and beam-target double polarization observables for the $p\pi^0$ and $p\eta$ final states, showing the coverage of the data in the beam photon energy E_γ and scattering angle $\cos\theta$ of the produced meson. They are accessible at [Bri+].

The $p\pi^0$ final state has the most available data with the highest statistical precision. Here, the beam asymmetry Σ is the most frequently measured observable apart from the unpolarized cross section [Fuc+96; Ahr+02; Ahr+04; Bar+05b; Bar+05a; Pee+07; Dug+07; Cre+11]. Until the year 2002, the database for the beam asymmetry Σ was comprised of the following data in the $p\pi^0$ final state [Bar+69; Gor+74; Gor+78; Bel+83; Bla+92; Bec+97; Ada+01; Bla+01], which are plotted in gray. The latest four data sets are from the GRAAL collaboration (magenta squares) [Bar+05a], the LEPS collaboration (yellow points) [Sum+07], the CBELSA/TAPS (red points) [Spa+10] and the CLAS collaboration (blue squares) [Dug+14]. However, only the CLAS data has a large angular coverage at energies $E_\gamma > 1500\,\text{MeV}$ with a high statistical precision and was published in parallel to this work.

In the last decade, with the possibility to get polarized targets, the measurement of additional polarization observables (T, P, G, E, F, H) became feasible. The main contributing data sets are from the CBELSA/TAPS (red points, T, P, H [Har+14; Har+15], G [Thi+12; Thi+17] and E [Got13; Got+14]) and the A2 (green squares, T, F [Ann+16]) collaboration for the $p\pi^0$ channel, covering all polarization observables of the beam-target category albeit not the entire energy and angular range.

There exist only scarce data with large energy and angular bins for the $p\eta$ final state. Important data sets for the beam asymmetry Σ in η-photoproduction are from [Aja+98], the GRAAL collaboration [Bar+07a], the CBELSA/TAPS data [Els+07] and at energies above 1450 MeV from the CLAS collaboration [Col+17], which were published in parallel to this work. The polarization observables T, P, G, E, H have been measured by the CBELSA/TAPS collaboration [Mül+17], the observables T, F by the A2 collaboration [Ako+14] and the helicity asymmetry E by the CLAS collaboration as well [Sen+16].

The red box indicates the energy range that is anticipated to be covered with the analyzed data for the beam asymmetry Σ using CBELSA/TAPS data and the green box for the helicity asymmetry E utilizing A2 data.

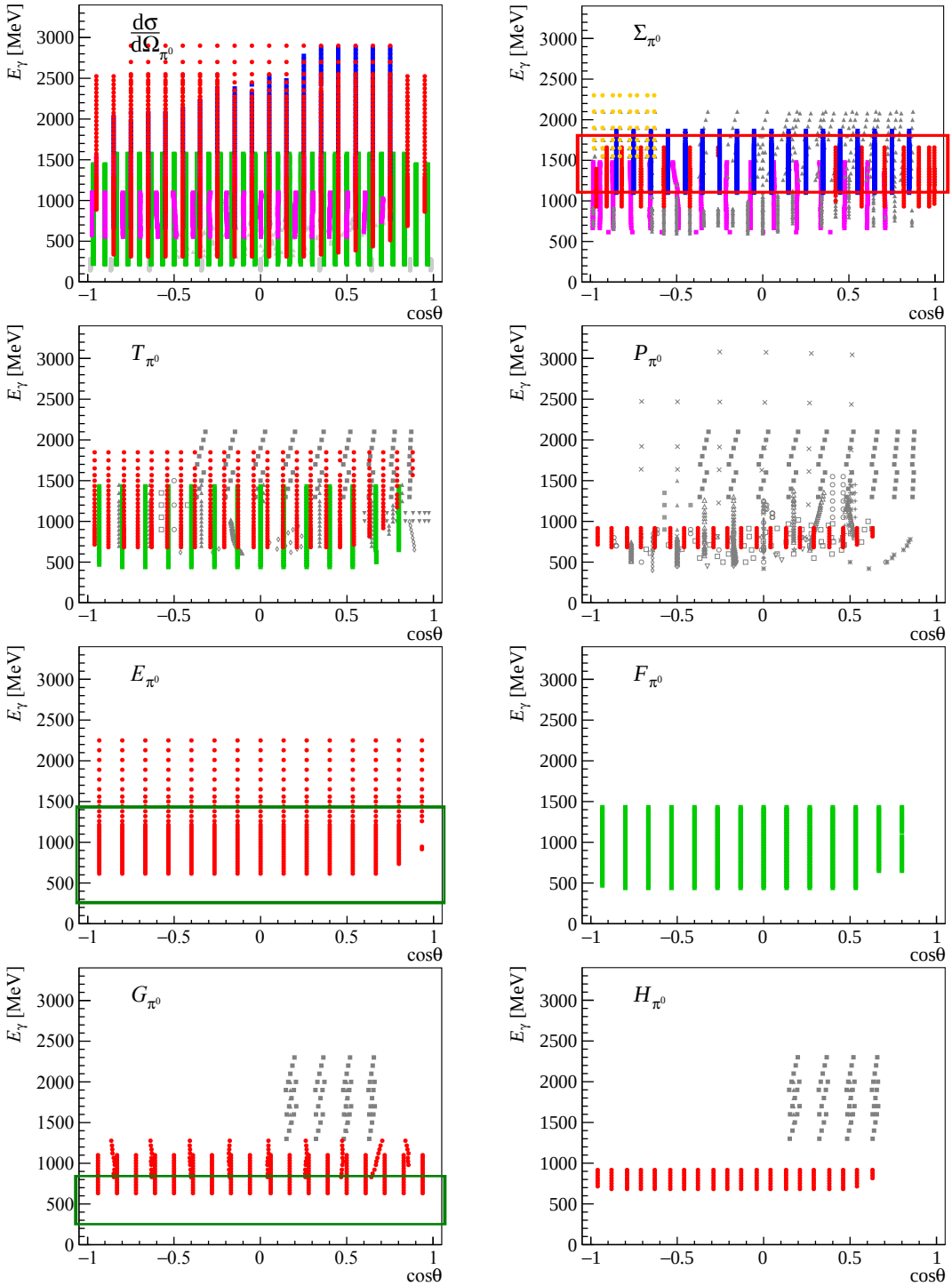

Figure 1.15: Database of the measured unpolarized differential cross section ($\frac{d\sigma}{d\Omega}$), single (Σ, T, P) and double (E, F, G, H) polarization observables in the $p\pi^0$ final state. The full database is accessible in reference [Bri+]. Data from the CBELSA/TAPS collaboration are plotted in red [Bar+05b; Pee+07; Spa+10; Cre+11; Thi+12; Thi+17; Got13; Got+14; Har+14; Har+15], from the A2 collaboration in green [Adl+15; Ann+16], from the CLAS collaboration in blue [Dug+07; Dug+14], from the GRAAL collaboration as magenta squares [Bar+05a] and from the LEPS collaboration in yellow [Sum+07]. Old data sets prior to year 2005 are shown in gray [Bar+69; Gor+74; Gor+78; Bel+83; Bla+92; Bec+97; Ada+01; Bla+01; Ahr+02; Ahr+04; Fuc+96]. The red and green box marks the energy and angular range covered by the analyzed CBELSA/TAPS and A2 data in this work, respectively.

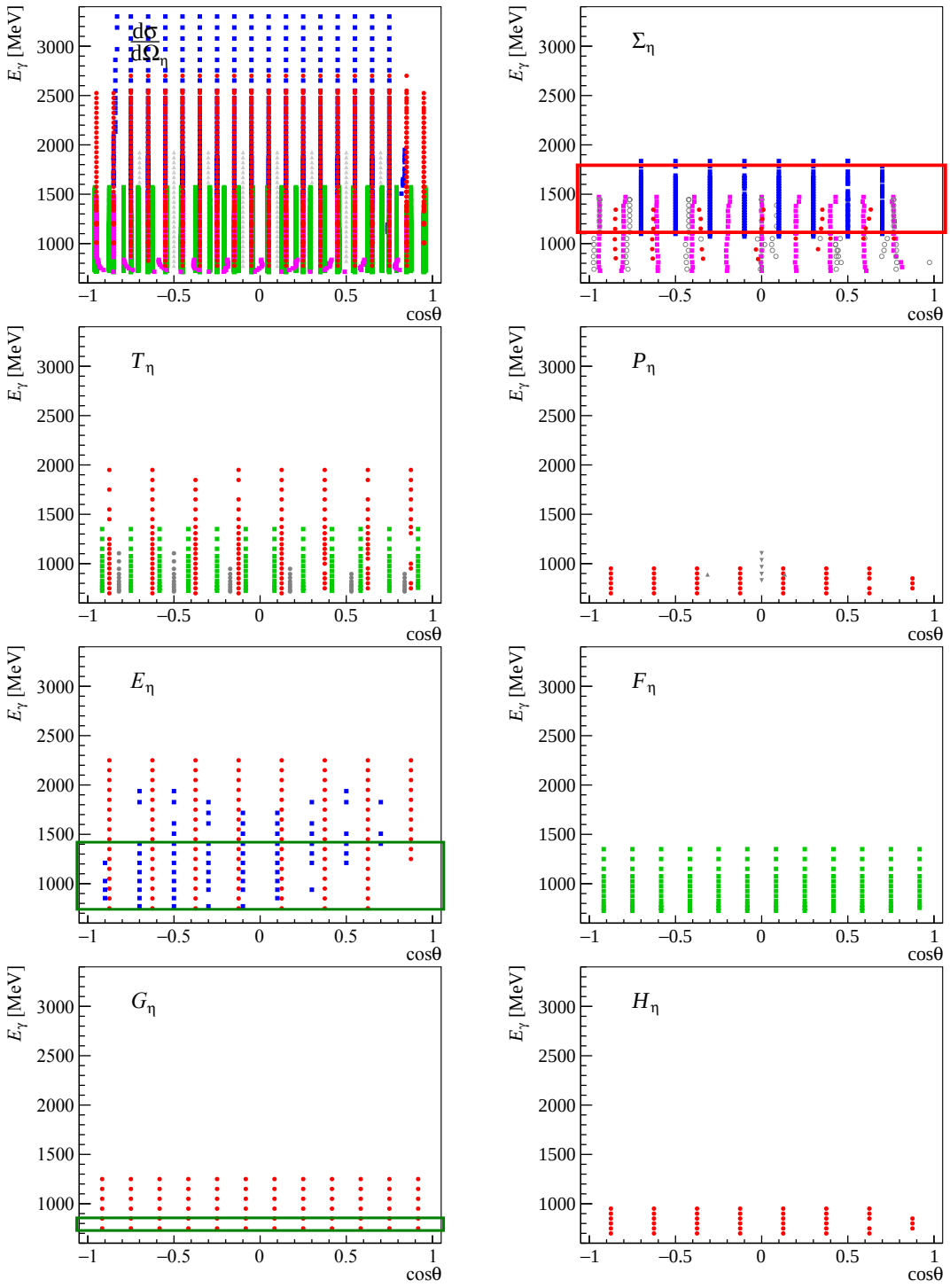

Figure 1.16: Database of the measured unpolarized differential cross section ($\frac{d\sigma}{d\Omega}$), single (Σ, T, P) and double (E, F, G, H) polarization observables in the $p\eta$ final state. The full database is accessible in reference [Bri+]. Data from the CBELSA/TAPS collaboration are plotted in red [Els+07; Bar+07b; Cre+09; Mül+17], from the A2 collaboration in green [McN+10; Ako+14; Kas+17], from the GRAAL collaboration in magenta [Bar+07a] and from the CLAS collaboration in blue [Wil+09; Sen+16; Col+17]. Older data sets are shown in gray [Aja+98; Dug+02]. The red and green box marks the energy and angular range covered by the analyzed CBELSA/TAPS and A2 data in this work, respectively.

1.6 Aim of this work

The goal of this work is on the one hand to determine the beam asymmetry Σ using the CBELSA/TAPS experiment at the electron stretcher accelerator ELSA (in Bonn) for the $p\pi^0$ and $p\eta$ final states, covering a beam photon energy range of $E_\gamma = 1100\,\text{MeV}$ - $1800\,\text{MeV}$ ($W = 1716\,\text{MeV}$ - $2064\,\text{MeV}$). This energy range is of particular importance to finding new resonances as not many data exist in this range, but a lot of missing resonances are predicted. A high statistical data set is desirable that will allow the sensitivity to resonances with high total angular momentum $J_{\text{res.}}$. The $p\eta$ final state serves as an isospin filter and enables the search of N^* resonances.

On the other hand, the aim is to extract the helicity asymmetry E from data taken at the A2 experiment at the accelerator facility MAMI (in Mainz) for the energy range of $E_\gamma = 270\,\text{MeV}$ - $1400\,\text{MeV}$ ($W = 1178\,\text{MeV}$ - $1872\,\text{MeV}$) and also for the $p\pi^0$ and $p\eta$ final states. Here, the database will be expanded down to the $\Delta(1232)\frac{3}{2}^+$ (P_{33}) resonance in the $p\pi^0$ channel, which is an energy range only covered insufficiently by double polarization observables. Moreover, data with high statistical precision will be obtained up to $E_\gamma = 1400\,\text{MeV}$ for both channels. In addition, an important goal is to show that the double polarization observables E and G can be measured simultaneously within one beamtime, using elliptically polarized photons, which has not been attempted before. This will have a great impact on future experiments since it allows to measure all polarization observables of the beam-target group within two separate beamtimes, which only need to differ in the target polarization orientation. Thus, the measurement of polarization observables will become more time efficient and feasible.

This work is structured in the following way: first the two experimental facilities CBELSA/-TAPS at ELSA and A2 at MAMI are introduced in Chapter 2. Afterwards, the reconstruction (see Chapter 3) and calibration (see Chapter 4) procedures of the data are explained. The work then proceeds in Chapter 5 with the selection process of the two $p\pi^0$ and $p\eta$ final states and the extraction of the beam asymmetry (see Chapter 6) and helicity asymmetry (see Chapter 7). In the end the results are discussed in Chapter 8.

2 Experimental setup

The analyzed data were taken at the CBELSA/TAPS experiment at the ELectron Stretcher Accelerator (ELSA) located in Bonn and the A2 experiment at the MAinzer MIcrotron (MAMI) accelerator located in Mainz. Both experiments use the bremsstrahlung process off a radiator to produce a photon beam. The photons can interact with the fixed target material via electromagnetic interactions and excite the nucleons. The excited states decay over the strong interactions by emitting mesons. The mesons and baryons are detected using a detector system comprised of electromagnetic calorimeters and scintillators.
The measured analog signals of all detectors are electronically processed using e.g. amplifiers, shapers and discriminators. Subsequently, the signals are digitized utilizing time to digital converters (TDCs) for timing signals and charge integrating ADCs[1] (QDCs) for the energy information. In addition, scalers monitor the count rates and the dead time of each detector.
The digitized information is then collected and stored by the data acquisition (DAQ). This digitization and storage is only started if a trigger signal is present. The trigger looks for predefined patterns in the detector signals and thereby decides which events are saved on disk for further offline-analysis. Here, unwanted background events are already suppressed during the data acquisition and the statistics for the wanted reactions is maximized.
In this chapter an overview is given about all detector components and their readout electronics used in both experiments, respectively.

2.1 The CBELSA/TAPS experimental setup

In this work the CBELSA/TAPS experiment was used to measure the beam asymmetry Σ in the photoproduction reactions $\gamma p \to \pi^0 p$ and $\gamma p \to \eta p$ from July 2013 to October 2013. This section provides information about the CBELSA/TAPS experimental setup as it was used during these four beamtimes. Unpolarized electrons from ELSA (see 2.1.1) were incident on a diamond crystal producing linearly polarized photons (see 2.1.2). The linearly polarized photons were energy tagged (see Section 2.1.3) and interacted with a liquid hydrogen target (see 2.1.4). The decay photons of the π^0 and the η mesons were measured with two calorimeters (see Section 2.1.5.2 and 2.1.5.3).

2.1.1 The electron stretcher accelerator (ELSA) facility

The ELSA facility [Hil06] is located underneath the Physics Institute in Bonn and provides high energetic unpolarized or longitudinally polarized electrons that are subsequently used to produce real photons via bremsstrahlung. The acceleration process of the electrons is performed in three steps. First of all free electrons are produced. In case of unpolarized electrons, a 48 keV thermal electron source is used.

[1] ADC stands for analog to digital converter.

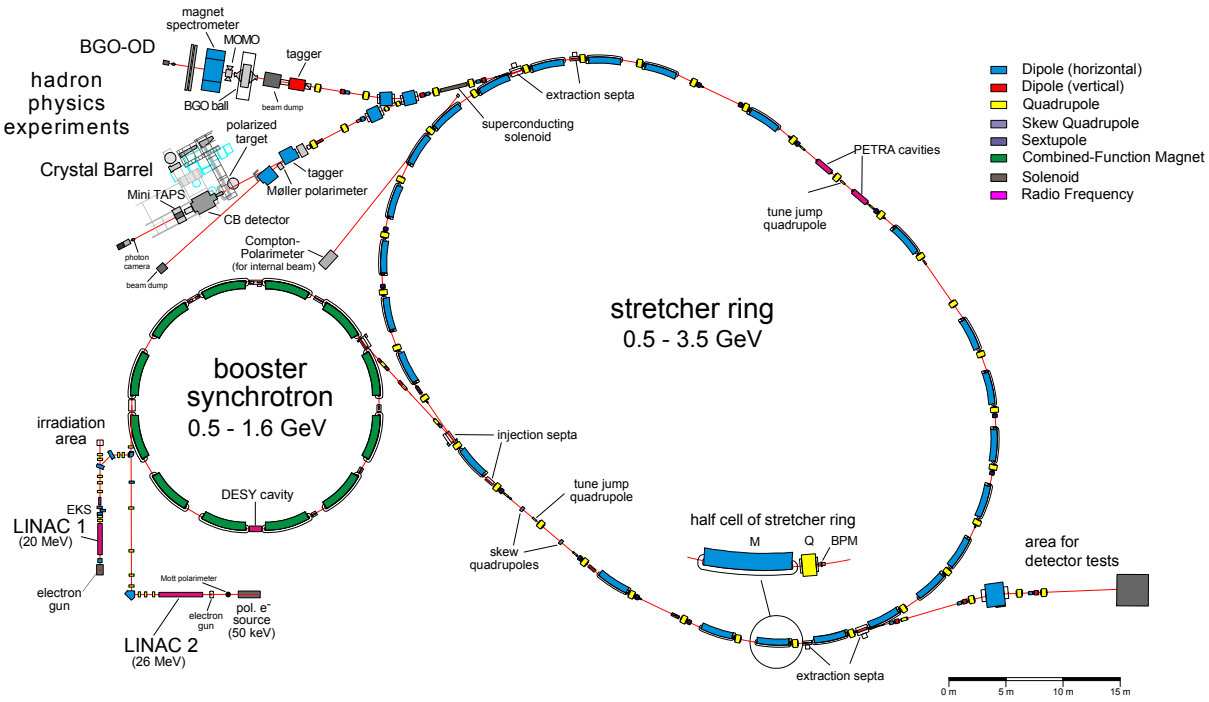

Figure 2.1: Overview of the ELSA facility in Bonn. Taken from [Fro].

For longitudinally polarized electrons circularly polarized laser light is incident on a GaAs photo-cathode which leads to photoemission. A Mott polarimeter (see Section 2.17) is utilized to measure the electron polarization degree which reaches up to 80 % [Hil00]. The electrons are pre-accelerated in the linear accelerator LINAC 2[2] (see Figure 2.1) up to an energy of 26 MeV before they are injected in four to five cycles with a repetition frequency of 50 Hz into the booster synchrotron. The synchrotron accelerates the electrons using the electromagnetic field of a radio-frequency (RF) cavity (DESY) [Pus12]. Ramping the magnetic field strength of the combined function bending magnets[3] synchronously to the electron energy gain ensures the remaining of the electrons on a constant orbit with a radius of 7.65 m.
The standing wave RF cavity is tuned by its design to a frequency of 500 MHz. Passing electrons with different energies and arriving at different times are accelerated or decelerated by the electromagnetic field of the cavities in order to match the desired energy. This process leads to a division of the beam into packets, so-called bunches. The beam bunches have a typical length of 100 ps and a time distance of 2 ns [Hil00]. At this acceleration step, energies between 0.5 and 1.6 GeV are achievable within 10 ms.
Afterwards, the electrons are injected slowly as a pulsed beam into the stretcher ring. Due to the different orbit lengths of the synchrotron and stretcher ring, many synchrotron cycles are needed to completely fill the stretcher ring which consists of two accelerating RF cavities (PETRA cavities), twenty-four dipole, thirty-two quadrupole and twelve sextupole magnets and beam injection and extraction tools. The two RF cavities are tuned to a frequency of 500 MHz driven by klystrons. Passing electrons are accelerated by the lowest fundamental mode TM_{010} of the cavities' electromagnetic field which has a longitudinal electric field component.

[2] LINAC 1 is not available at the moment.
[3] The combined function magnets are designed to achieve bending and focusing of the electron beam at the same time.

The dipole and quadrupole magnets are aligned in a FODO-cell structure [Hil06]. Each cell contains a horizontally focusing quadrupole (F), a drift pathway without any focusing (O), a horizontally defocussing quadrupole (D) and another drift pathway (O) in order to focus the beam horizontally and vertically. The sextupole magnets correct chromatic effects and allow the excitation of a third integer resonance needed for slow extraction of the beam to the experimental areas [Nec93]. It is possible to operate ELSA in different modes. The electron beam can be stored in the stretcher ring for several hours to study synchrotron radiation in the storage-mode. If operated in the stretcher-mode, the booster synchrotron pulses are injected into the stretcher ring and extracted slowly with a maximum energy of 1.6 GeV. In the post-accelerator mode the electrons are first accelerated further up to an energy of 3.5 GeV before the electron beam is extracted slowly within a few seconds to the experimental area. Additionally, the single bunch-mode has become available recently where only one (or a few) bunches are kept in the stretcher ring and slowly extracted. This mode is useful for low intensity beams that are needed to perform e.g. detector tests [Hon14]. In autumn 2016, a new beamline area for detector tests was put into operation.

2.1.2 Linearly polarized photons

Linearly polarized photons are needed for the measurement of the beam asymmetry. They are produced via coherent bremsstrahlung of electrons off a diamond radiator. The energy and time information of the produced real photons are determined with the tagging system 2.1.3 using the outgoing electrons.

2.1.2.1 Bremsstrahlung process

Electrons passing through matter lose energy due to either scattering (Møller, Bhabha), ionization or bremsstrahlung processes [Ams+08]. Since the electrons provided by ELSA have an energy of up to $E_0 = 3.5\,\text{GeV}$, the dominating process here is bremsstrahlung. The incoming electrons e^- with momentum $\vec{p_e}$ and energy E_0 are decelerated in the Coulomb field of a nucleus N and radiate real photons γ with momentum $\vec{k}$ and energy E_γ:

$$e^- + N \rightarrow e^- + N + \gamma. \tag{2.1}$$

The nucleus serves as recoil partner and absorbs the recoil momentum $\vec{q}$ due to momentum conservation:

$$\vec{q} = \vec{p_e} - \vec{p_{e'}} - \vec{k}, \tag{2.2}$$

where $\vec{p_{e'}}$ denotes the momentum of the outgoing electron. The recoil energy T is negligibly small ($T = q^2/(2M_N)$, where M_N is the mass of the nucleus). Kinematical constraints for the longitudinal and transverse recoil momentum transfer, q_l and q_t, can be calculated [Tim69; Ü56]:

$$\delta \leq q_l \leq 2\delta \tag{2.3}$$

$$0 \leq q_t \leq 2x. \tag{2.4}$$

The lower limit of the longitudinal momentum transfer q_l is given by

$$\delta = \frac{1}{2E_0}\frac{x}{1-x}, \qquad \text{with} \qquad x = \frac{k}{E_0}. \tag{2.5}$$

The allowed region in momentum space is known as the *pancake* region due to its shape (see Figure 2.2).

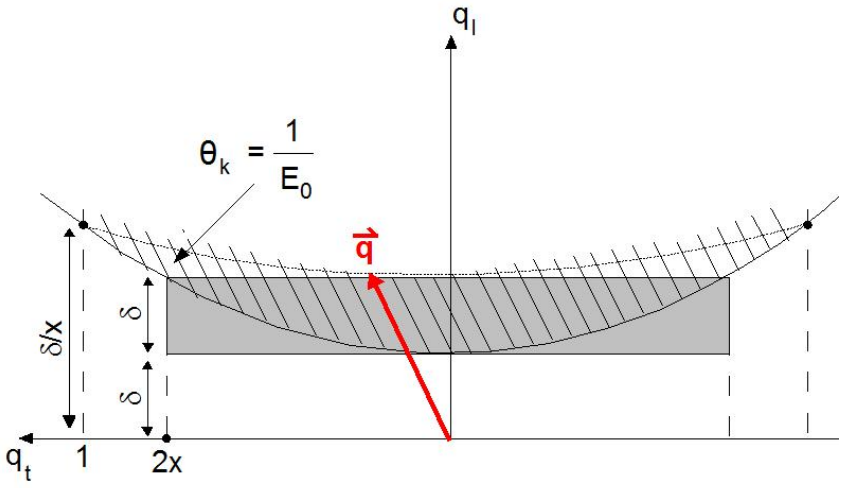

Figure 2.2: The allowed kinematic region for bremsstrahlung in momentum space (with q_l and q_t being the longitudinal and transverse momentum transfers) is depicted. It has the shape of a *pancake*. Taken from [Kam09].

2.1.2.2 Incoherent bremsstrahlung

In case of an amorphous radiator, the nuclei are non-periodically distributed and the recoil momentum is transferred to a single atomic nucleus as shown in Figure 2.3 on the left. There is no preferred direction of the outgoing photons relative to the incoming electrons. Due to the lack of periodicity, the electric field vectors are randomly orientated and on average the photons are unpolarized. The intensity spectrum of the bremsstrahlung photons is continuous and has a $\frac{1}{E_\gamma}$ dependence according to the Bethe-Heitler cross section [Hei54].

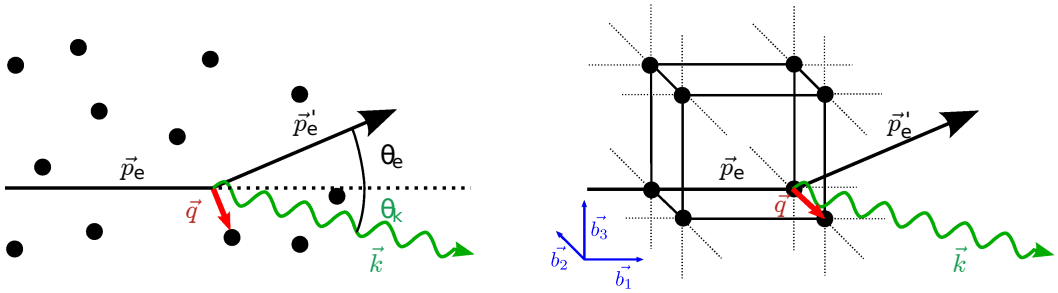

Figure 2.3: Left: In case of an amorphous radiator, incoherent bremsstrahlung is produced. The recoil momentum $\vec{q}$ is transferred to a single atomic nucleus. Right: In case of a crystal radiator and if the recoil momentum is equal to a reciprocal lattice vector, the recoil momentum is absorbed by the entire crystal lattice. Taken from [Gut10].

2.1.2.3 Coherent bremsstrahlung

During coherent bremsstrahlung [Tim69] the recoil momentum $\vec{q}$ is transferred to a crystal radiator. A diamond crystal, which has a cubic face-centred crystal structure as shown in Figure 2.3 on the right, is chosen as radiator. Depending on how the diamond is orientated relative to the electron beam and kinematic constraints according to Equation (2.3), the recoil momentum can be absorbed by the whole crystal lattice. This is only possible if the transferred recoil momentum $\vec{q}$ equals a multiple n of a reciprocal lattice vector $\vec{g} = \sum_{i=1}^{3} \vec{b}_i h_i$ [Els+09], where b_i are the basis vectors and h_i the Miller indices of the according reciprocal lattice vector [Els+09]:

$$\vec{q} = n \cdot \vec{g} \tag{2.6}$$

Thus, the Laue condition (Equation (2.6)) is fulfilled for discrete recoil momenta and constructive interference of the bremsstrahlung photons of single indistinguishable atoms occurs, leading to coherent bremsstrahlung. This fixes the plane of electron deflection and consequently, the produced photons are linearly polarized with the electric field vector oscillating in a fixed direction. An enhancement is observed in the bremsstrahlung spectrum (see Figure 2.4). All reciprocal lattice vectors within the pancake region contribute to the coherent bremsstrahlung process. As soon as x is high enough for the reciprocal lattice vector to leave the pancake region, the photon intensity drops dramatically. This discontinuity is known as the coherent edge. The coherent edge position is chosen to be at a certain energy through precise alignment of the diamond crystal to the incoming electron beam. It is achieved by using the Stonehenge Technique [Liv09], which was adapted for the CBELSA/TAPS experiment [Els07; Ebe12].

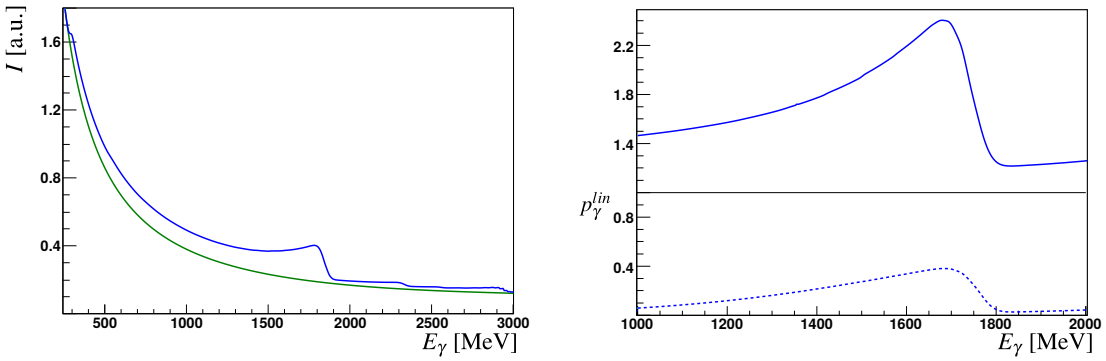

Figure 2.4: Left: The incoherent (green) and crystal (blue) bremsstrahlung intensities are plotted as a function of the beam photon energy. Right: The ratio of crystal to incoherent intensity spectra gives the enhancement spectrum. Below the calculated linear polarization degree is shown. Both spectra are based on ANB calculations.

Incoherent bremsstrahlung can still occur as well due to imperfections in the periodic crystal structure which leads to unpolarized beam photons. Therefore, the total bremsstrahlung cross section off a crystal radiator σ_{crystal} is given by

$$\sigma_{\text{crystal}} = \sigma_{\text{coherent}} + \sigma_{\text{incoherent}}, \tag{2.7}$$

where σ_{coherent} is the cross section of the coherent bremsstrahlung and $\sigma_{\text{incoherent}}$ the cross section

of the incoherent bremsstrahlung component. In order to determine the linear polarization degree, the ratio of the total crystal to incoherent bremsstrahlung intensity spectra is taken (see Section 6.1.1). The form of the produced enhancement spectrum depends strongly on the beam characteristics and the crystal properties [Liv09]. Moreover, collimation of the photon beam increases the relative coherent component of all bremsstrahlung photons that are incident on the target and thus, increases the amount of polarized photons [Liv09]. The enhancement spectrum and the degree of linear polarization p_γ^{lin} are analytically calculated based on the **AN**alytical **B**remsstrahlung (ANB) calculations [Nat+03]. Figure 2.4 shows on the right a typical enhancement spectrum and the energy dependence of the polarization degree as obtained from the ANB calculations.
To obtain the enhancement spectra, data are taken with two different radiators, a diamond and an amorphous copper radiator [Els+09]. The copper radiator is needed to describe the incoherent bremsstrahlung component. Both radiators are located inside the goniometer tank.

2.1.3 Goniometer and Tagging system

The goniometer [Els+09] consists of a rotational aluminum wheel inside a vacuum tank and contains different radiators. Four copper radiators of 12 µm, 50 µm, 150 µm and 300 µm thickness, which correspond to radiation lengths of $8.4 \times 10^{-4}\,X_0$, $3.5 \times 10^{-3}\,X_0$, $1.0 \times 10^{-2}\,X_0$, and $2.1 \times 10^{-2}\,X_0$ [Kam09], are mounted on the wheel along with beam diagnostic tools. In the center of the aluminum wheel a thin diamond crystal of 500 µm thickness is glued to a 12.5 µm thick Kapton foil. The goniometer can be moved horizontally, vertically and it can be rotated in azimuthal angle in order to precisely move the desired radiator with respect to the incoming electron beam of ELSA. For the measurement of the polarization degree of the circularly polarized photons a Møller radiator is used which is also located inside the goniometer tank as well. It is made of a 20 µm thick ferromagnetic foil which is surrounded by a solenoid [Kam09]. More information about the working principle of a Møller polarimeter can be found in Section 2.18.

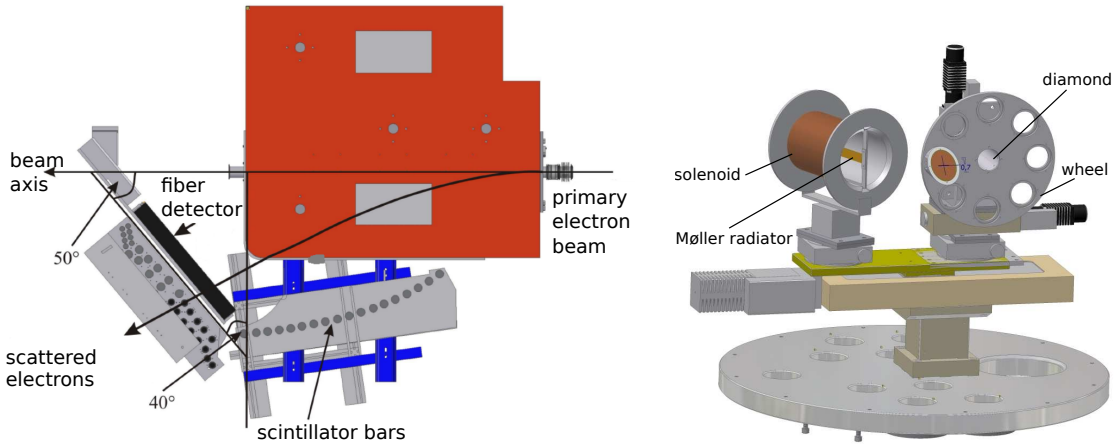

Figure 2.5: Left: The tagging system is made of a dipole magnet (red) and scintillating fibers and bars for the detection of the bent electrons. Taken from [FP09]. Right: The goniometer provides different radiators, e.g. a diamond or a Møller radiator. Taken from [Wal07].

The scattered electrons with energy E_e are deflected according to their momenta within the magnetic field of a dipole magnet of 1.5 T towards plastic scintillating bars and fibers of the

tagging system [FP09] (see Figure 2.5). Knowing the primary electron energy E_0 from ELSA allows the calculation of the energy of the produced bremsstrahlung photon E_γ:

$$E_\gamma = E_0 - E_e. \tag{2.8}$$

The recoil energy of the nucleus is negligibly small. The 96 plastic scintillation bars of 1.4 - 5 cm thickness are placed in three sections in an overlapping way. For a primary electron energy of $E_0 = 3.2$ GeV, they cover a photon energy range from 560 MeV to 3.1 GeV with an energy resolution of 0.1% E_γ - 6% E_γ. In addition to the tagger bars, 480 plastic scintillating fibers with a diameter of 2 mm are located in front of the tagger bars in the photon energy region of E_γ = 416 MeV - 2.67 GeV. This leads to an improvement of the energy resolution to 0.1% E_γ - 0.4% E_γ. Photomultipliers are utilized for the readout of the tagger bars and fibers. The time resolution is FWHM[4] = 635 ps for the scintillating bars and FWHM = 1.694 ns for the fibers [Har08]. The photomultiplier signals are passed to leading edge discriminators and afterwards to CATCH-TDCs for digitization of the time information. Additionally, 95 livetime-gated counters are used for the determination of the photon flux.
The linearly polarized photon beam is subsequently collimated with six hollow cylinders in order to, on the one hand increase the linear polarization degree [Tim69], and on the other hand to contain the photon beam inside the target cell. Each cylinder is made of a tungsten alloy and has a length of 4 cm, an inner diameter of 4 mm and an outer diameter of 20 mm [FP09]. The collimated photon beam was incident on the liquid hydrogen target after removing electron and positron pairs[5] with the help of a dipole magnet, which is located behind the collimator.

2.1.4 Liquid hydrogen target

The liquid hydrogen target [Ham09] is located at the center of the Crystal Barrel detector. The cylindric target cell is made of a thin Kapton foil (80 µm on the front and back and 125 µm on the sides) and has a diameter of 3 cm and a length of 5.1 cm. The target cell is filled with liquid hydrogen through two connecting tubules (see Figure 2.6). In order to keep hydrogen liquefied, a separate cooling circuit with hydrogen is used. In the cooling circuit, hydrogen gas is condensed at a cold head that provides temperatures down to 20 K. The liquid hydrogen flows to a heat-exchanger near the Kapton cell where it vaporizes and absorbs the heat energy from the target cell and thus cools the hydrogen in it. To ensure the working principle of the target, the pressure inside the target cell and the cooling circuit is monitored closely. More information about the cooling circuit is given in [Ham09].

The density of liquid hydrogen is $\rho_{\text{liquid}H_2} = 0.0708\,\text{g/cm}^3$ [PDG] and the target area density is $n_{T,H} = 2.16 \times 10^{23}\,\text{cm}^{-2}$ [Ham09]. It is high enough to ensure a high rate for hadronic reactions. Kapton has a low density of $\rho_{\text{Kapton}} = 1.42\,\text{g/cm}^3$ and a large radiation length of X_0 =28.6 cm [PDG]. The total target area density of both Kapton endcaps with 80 µm thickness is approximately $n_{T,\text{Kapton}} = 0.14 \times 10^{23}\,\text{cm}^{-2}$. Therefore, the rate of background reactions from the target cell material is much lower than from liquid hydrogen. The binding energy of the liquid hydrogen electrons is with 21.8 eV [Pat+16] negligibly small so that the protons can be regarded as free.

[4] FWHM stands for Full Width Half Maximum.
[5] Photons that do not pass the collimator can create electron and positron pairs trough electromagnetic interaction with the collimator.

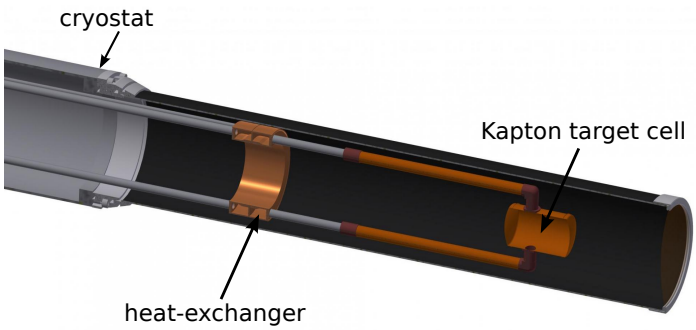

Figure 2.6: Schematic view of the liquid hydrogen target. The Kapton cell (orange) can be filled with liquid hydrogen via two tubules that are connected to a heat-exchanger. Taken from [Grü18].

2.1.5 Detector system

During the beamtimes of this work, the final state particles were measured with the detector system as shown in Figure 2.7. Two calorimeters, the Crystal Barrel and the forward detector 2.1.5.2 and the MiniTAPS 2.1.5.3 detectors, cover together 95% of 4π in solid angle and are highly efficient at detecting photons. For the identification of charged particles, an inner detector 2.1.5.1 is located inside of the Crystal Barrel detector. In addition, plastic scintillation plates are used as veto detectors which are placed in front of the forward detector and MiniTAPS crystals. The photon flux is monitored by the GIM and FluMo detectors 2.1.5.5.

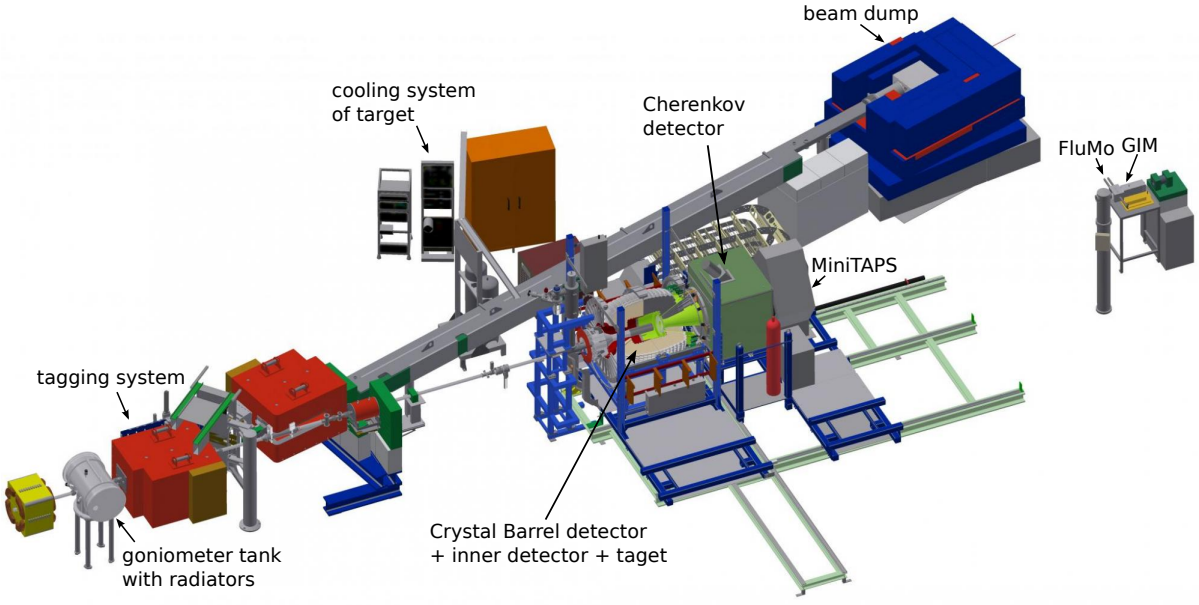

Figure 2.7: Overview of the CBELSA/TAPS experiment. The ELSA electron beam enters the goniometer tank containing radiators from the left. The photons are tagged with the tagging system and are incident on the liquid hydrogen target which is surrounded by the inner detector and is located at the center of the Crystal Barrel calorimeter. In forward direction, the MiniTAPS detector complements the detector system. The FluMo and GIM detectors monitor the photon flux. Taken from [Grü18].

2.1.5.1 Inner detector

The inner detector [Fös00; Suf+05] is a cylindrical plastic scintillation detector that encloses the target and covers the polar angular range from $23.1° \leq \theta \leq 166°$. It is 40 cm long and consists of 513 plastic scintillation fibers which are arranged on three different layers. The fibers of the inner layer are tilted by $-24.5°$ to the beam direction and the fibers of the middle layer by 25.7°, whereas the fibers of the outer layer are orientated in beam direction (see Figure 2.8). Thus, a charged particle's angular information is attainable by finding the intersection point of at least two of the three layers. The inner detector has an angular resolution of 0.4° in θ and 0.1° in ϕ angle [Got13]. The utilized fibers of type BCF-12 are round with a diameter of 2 mm. Polystyrene with a refractive index of n=1.6 [PDG] is used as the core of the fibers. Charged particles passing through the detector excite the polysterene molecules which de-excite via emission of scintillation light at around $\lambda = 435$ nm (blue light) [Fös00]. The short decay time ensures a fast time signal which allows the inner detector to provide a fast first level trigger (see Section 2.1.5.6). Polymethylmetacrylat ($C_5H_8O_2$, n=1.49 [PDG]) serves as the optical cladding material. The difference between the refractive indices enhances the transmission of the emitted scintillation light to lightguides where the light is transmitted via internal total reflection to photomultipliers. The time resolution is given by FWHM $= (2.093 \pm 0.013)$ ns [Har08].

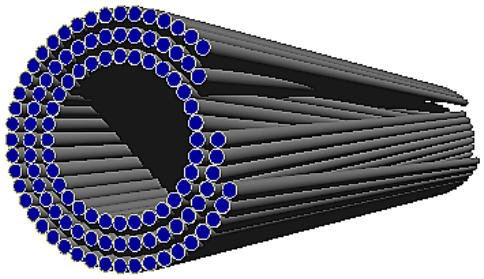

Figure 2.8: The inner detector consists of three layers of scintillating fibers that is tilted by $-24.5°$ or 25.7° towards the outer layer. Taken from [Wal07].

2.1.5.2 Crystal Barrel calorimeter

The Crystal Barrel calorimeter [Ake+92] consists of 1320 CsI(Tl) crystals which are arranged in 24 rings, building a barrel (see Figure 2.9). Thereby, all 90 crystals of the first three rings ($11.18° < \theta < 27.54°$) are placed in a cone and form the forward detector. While the rings $4-20$ contain 60 crystals each, the first three rings (forward detector) and the 24^{th} ring contain 30 crystals. Each crystal has the shape of a truncated pyramid with a trapezoidal base area which points to the target center. The crystal size is chosen in such a way that each crystal covers 6° in the azimuthal ϕ and polar angle θ. The crystals of the first three and last ring however cover 12° in the azimuthal angle ϕ. In total, the calorimeter covers a large solid angular range: the complete azimuthal angle ϕ and the polar angle from 12° to 156°. Photons from meson decays, that pass through the detector, mainly interact with the inorganic scintillator material via pair production. The electron positron pairs, however, lose their energy mainly due to the bremsstrahlung process, creating photons. Thus, an electromagnetic shower develops over several crystals with a lateral and transverse spread. It is possible to contain photons within the detector up to an energy of 2 GeV by using crystals of 30 cm length which corresponds to

16.22 radiation lengths X_0 [Ake+92].

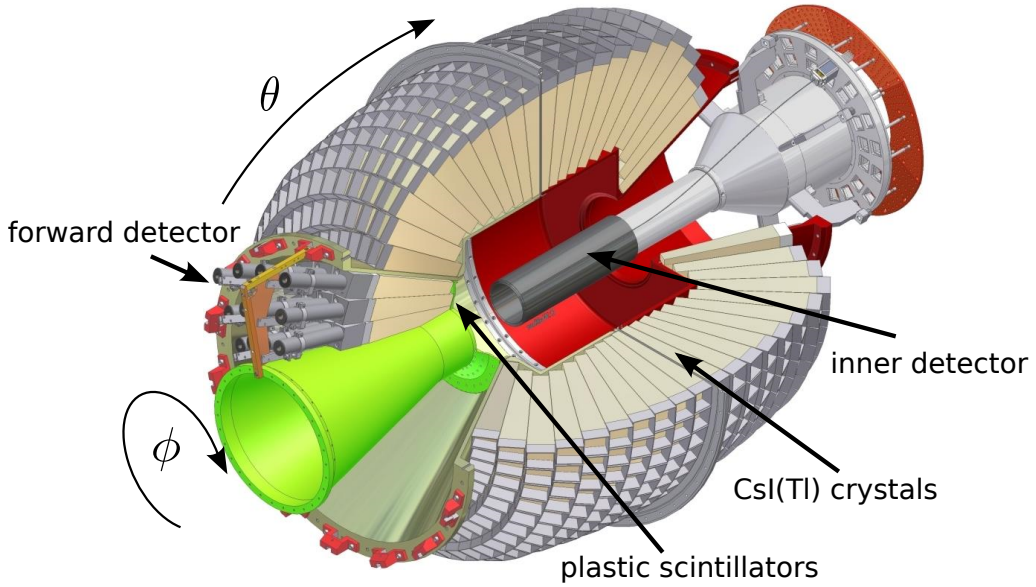

Figure 2.9: The Crystal Barrel detector encloses the target and the inner detector. It consists of 1320 CsI crystals which form 24 rings. The first three rings form the forward detector. These three rings are equipped with plastic scintillators on the front of the crystals and are read out with PMTs. Taken from [Wal07].

The transverse spread is described by the Molière radius which is 3.8 cm for CsI(Tl) [Ake+92]. The center of the electromagnetic shower can be determined which leads to a better angular resolution of less than 2° [Jun04].
The energy resolution is given by [Ake+92]:

$$\frac{\sigma_E}{E} = \frac{2.5\%}{\sqrt[4]{E/GeV}}, \tag{2.9}$$

where E is the energy of the primary photon.
Charged particles other than electrons lose energy in the calorimeter via ionization processes that can be described according to the Bethe-Bloch formula. They are only contained up to certain energies in the detector which depends on the mass of the charged particles. Protons are stopped up to a kinetic energy of 400 MeV. Higher energetic protons become minimum ionizing particles and deposit only a fraction of their initial energy before punching through the detector.
The deposited energy of a particle is absorbed by the CsI crystals through excitation of electrons to the conduction or exciton band, creating electron-hole pairs that drift through the crystal until they transfer their energy to an impurity center (thallium) that de-excites by emitting scintillation light in the wavelength range of 520-590 nm [Ake+92].
An overview of the readout electronics of one CsI(Tl) crystal not belonging to the forward detector is shown in Figure 2.10. First the emitted scintillation light has to be shifted with a wavelength shifter to the sensitive range of the used PIN-photodiodes (Hamamatsu of type S2575). The analog output signal is then preamplified and passed to a line driver. The signal is split and transferred to a charge to digital converter (QDC) where the signal is integrated and

digitized. In addition, the analog signal is discriminated and given to the Fast Cluster Encoder (FACE) [Fle01] that is used for trigger purposes (see Section 2.1.5.6).
Thallium doped CsI crystals have a long decay time of around 1 µs [Pat+16]. In addition, the design of the readout electronics is optimized for energy determination and the PIN-photodiodes do not allow a fast trigger shaping of weak signals because of their signal to noise ratio. Therefore, no timing information exists for detected particles.
The CsI crystals of the forward detector are readout with photomultipliers (PMTs) which provide a faster signal than the PIN-photodiodes and thus, allow the extraction of timing information for detected particles. The time resolution is given by FWHM $= (1.861 \pm 0.016)$ ns [Har08]. Furthermore, each crystal of the forward detector is equipped with two plastic scintillator plates [Wen04] of 3 mm thickness which are placed in an overlapping manner in front of the crystal. This makes it possible to distinguish between charged and uncharged particles, since charged particles deposit a small amount of their energy in the plastic scintillators. The detection efficiency for charged particle identification is approximately $\geq 72\%$ [Geh15]. The produced scintillation light of the plates is guided to photomultipliers with the help of optical fibers. The placement of the fibers between the 3rd and 4th ring of the Crystal Barrel detector creates a 5 mm gap. Starting from spring in year 2014 the readout of the Crystal Barrel detector has been upgraded by replacing the PIN-photodiodes with avalanche photodiodes. In the future timing information can be extracted from the signals of all Crystal Barrel crystals. This can be used to improve the trigger acceptance (especially for neutral particles) and offline analysis. Detailed information about the Crystal Barrel upgrade can be found in [Hon14; Urb17; Kla19].

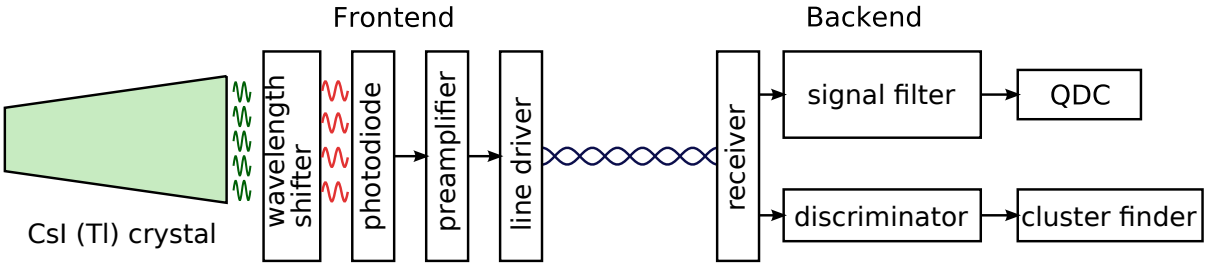

Figure 2.10: Overview of the readout system of each crystal of the Crystal Barrel detector. Taken from [Hon14].

2.1.5.3 MiniTAPS calorimeter

The Mini-Two Arm Photon Spectrometer (MiniTAPS) calorimeter [Gab+94; Str96] is composed of 216 hexagonally shaped BaF_2 crystals and positioned in a distance of 2.1 m from the target center (see Figure 2.11). It complements the Crystal Barrel detector by covering the forward θ angles from $1° - 12°$. BaF_2 has a high density of $4.89\,\mathrm{g/cm^3}$ [PDG] and is well suited to sustain high rates and detect high energetic photons. This is essential here since most of the produced particles are strongly boosted in forward direction. In addition, it is a high granularity detector with an angular resolution of 0.2° in the polar angle θ [Dah08]. Each crystal has a length of 25 cm which corresponds to 12 radiation lengths [Nov91]. Due to different possible scintillation mechanisms BaF_2 has two scintillating components, a fast component with a decay time of 0.9 ns and a slow component with a decay time of 620 ns. The readout system of one BaF_2 crystal is schematically shown in Figure 2.12. The emitted scintillation light of around $\lambda = 220$ nm for the fast and $\lambda = 310$ nm for the slow component is collected and processed by photomultipliers

and readout modules consisting of ADCs for the energy information and constant fraction discriminators and TDCs for the time information [Dre04]. An energy resolution [Gab+94] of

$$\frac{\sigma_E}{E} = 1.9\% + 0.59\% \cdot \sqrt{E/GeV} \tag{2.10}$$

and a time resolution of FWHM = 0.872±0.006 ns [Har08] are achievable.

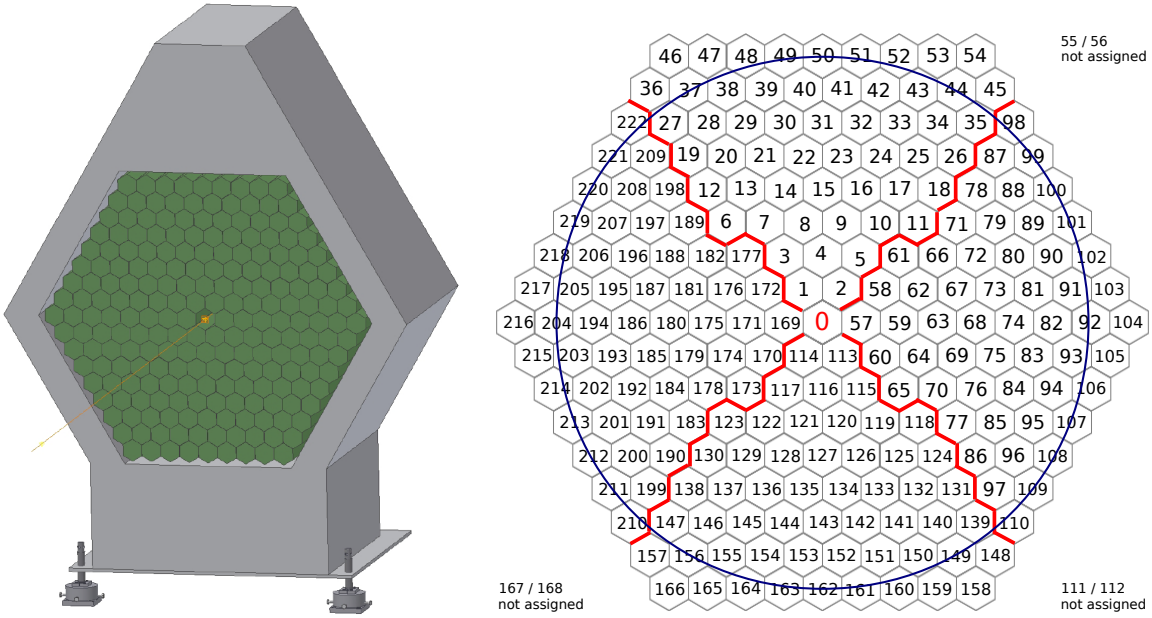

Figure 2.11: Left: 3D representation of the MiniTAPS detector. Taken from [Wal07]. Right: The MiniTAPS detector is segmented into four sectors for trigger purposes which are indicated by the red lines. The round circle marks the opening cone of the forward detector. Adapted from [Dah08].

Due to its fast readout system, the MiniTAPS detector is used in the first level trigger (see Section 2.1.5.6). For this purpose the MiniTAPS detector is divided into four sectors as shown in Figure 2.11 on the right. Two leading edge discriminators provide a trigger signal using two thresholds, the LEDHigh and LEDLow thresholds, which are both set to 80 MeV for all MiniTAPS crystals except for the two innermost MiniTAPS rings[6] [Har17]. In case at least one hit within a MiniTAPS sector fulfills the LEDHigh threshold or in each case one hit is detected in two different MiniTAPS sectors above the LEDLow threshold, a trigger signal is produced. Hexagonally shaped plastic scintillators of 5 mm thickness are placed as a wall in front of the MiniTAPS BaF_2 crystals. Their purpose is the identification of charged particles and additionally, it is possible to perform a $\Delta E - E$ measurement (see Section 2.2.7.3). Their scintillation light is guided via lightguides to photomultipliers. The time resolution is given by FWHM = 3.06±0.05 ns [Har08].

[6] The two innermost rings are not used in the trigger due to the high rate of electromagnetic background.

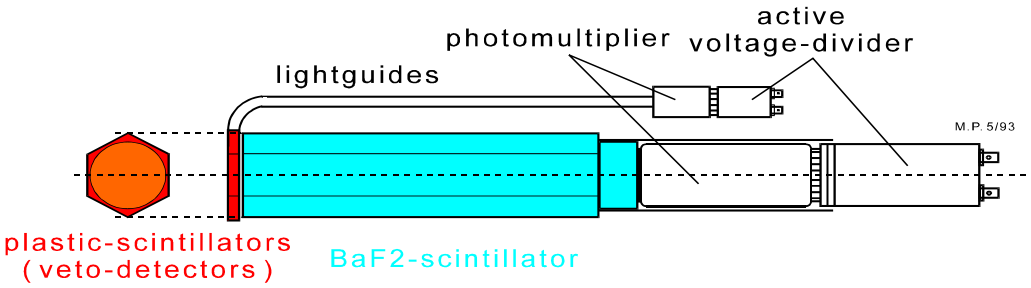

Figure 2.12: One typical hexagonally shaped TAPS BaF_2 crystal (lightblue) is shown. In front of each TAPS element a plastic scintillator is mounted (red). Both crystal and plastic scintillator are read out via photomultipliers. Taken from [Dre04].

2.1.5.4 Cherenkov detector

In order to reduce the amount of recorded electromagnetic background already on the trigger level, a gas Cherenkov detector [Kai07] is placed between the Crystal Barrel and the MiniTAPS detector. The Cherenkov detector is made of an aluminum box with a thin entrance and a thin exit window (see Figure 2.13) and is filled with CO_2, which has a refractive index of n= 1.00045 [PDG]. Only electrons and positrons with an energy higher than 17.4 MeV emit Cherenkov light when passing through the detector. The produced Cherenkov light is collected with a parabolic mirror and focused to a photomultiplier that is located on the top of the Cherenkov box. Based on simulations the detection efficiency of electrons or positrons is approximately 90%, if they have an energy of 19 MeV. It increases to maximal 99.97% for energies higher than 100 MeV [Kai07]. Experimentally, a maximum efficiency of $99.72 \pm 0.45\%$ was determined [Kai07]. The inclusion of the Cherenkov veto signal as a trigger condition improves the trigger efficiency of hadronic events by reducing the dead time caused by electromagnetic events.

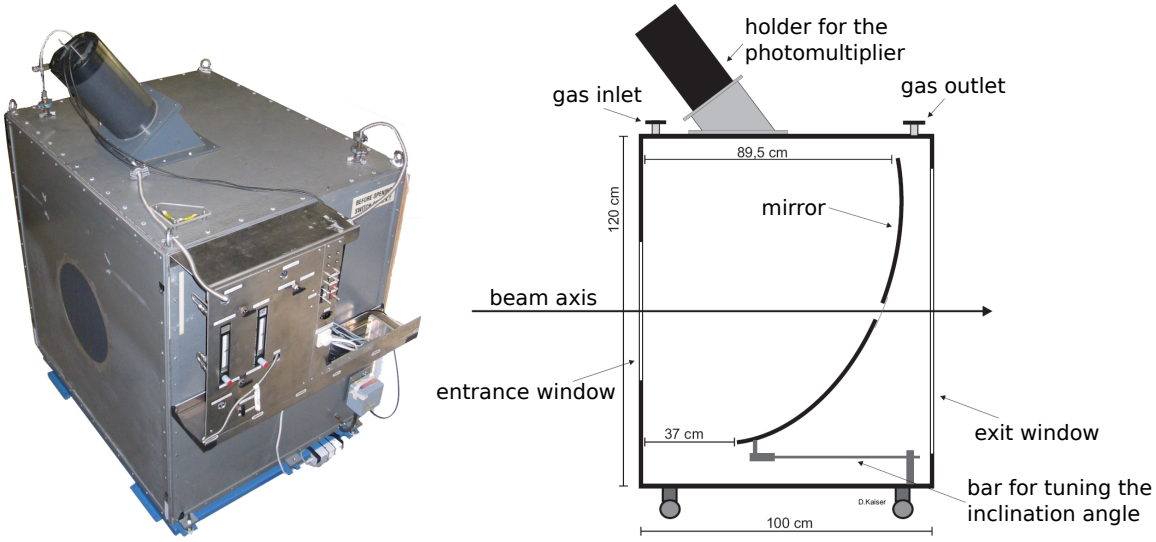

Figure 2.13: Left: The CO_2 Cherenkov detector consists of an aluminum box with a thin entrance and exit window. Taken from [Kai]. Right: Schematic view of the Cherenkov detector. Taken from [Kai07].

2.1.5.5 Flux monitoring

In order to determine the number of photons that went through the collimator and were incident on the target, two detectors, the Gamma Intensity Monitor (GIM) and the Flux Monitor (FluMo), are located behind the MiniTAPS detector at the end of the beam line.

The GIM detector [McG08] comprises 16 lead fluoride PbF_2 crystals that are arranged in a 4×4 array (see Figure 2.14). PbF_2 has a very high density $7.77\,\mathrm{g/cm^3}$ [PDG] and is resistive to high rates. The incoming photons interact with the crystal material creating an electromagnetic shower. The produced electron positron pairs emit Cherenkov light that is measured by photomultipliers. At rates higher than 5 MHz deadtime effects become important which cause a significant reduction of the GIM detector efficiency, e.g. more than 10% of events are not registered for a rate above 7 MHz [Har08].

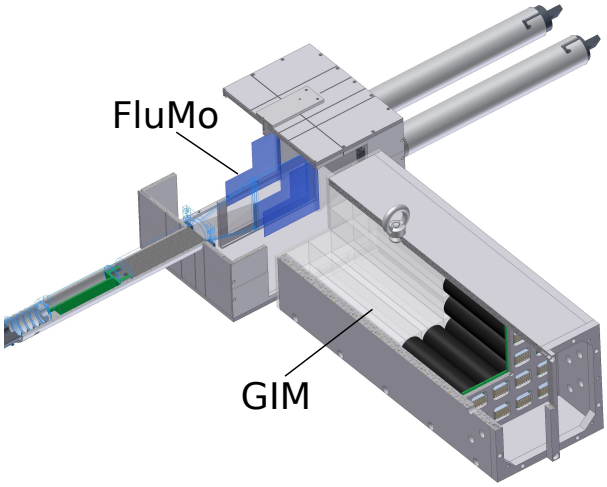

Figure 2.14: The GIM and FluMo detectors in Bonn. Taken from [Wal07].

Therefore, the FluMo detector [Die08] is used in order to determine the photon flux at higher rates. It consists of a converter plate made of lead, two plastic scintillation detectors and a veto detector. Incoming photons create with a small probability electron positron pairs that are detected in coincidence with the two plastic scintillation detectors. Another plastic scintillation detector is mounted in front of the converter plate to provide a veto signal if charged particles are incident on the converter plate which originate e.g. from the target.

2.1.5.6 Trigger system

The analyzed data sets were taken with the *vme_trig42c* trigger [Win06; Hof18] which can be configured using a Field Programmable Gate Array (FPGA) module. The goal of the trigger is to suppress background reactions, especially electromagnetic background and on the other hand to be sensitive for the desired photoproduction reactions $\gamma p \to p\pi^0$ and $\gamma p \to p\eta$. It consists of two levels. At the first level all detectors with a fast readout system (up to 250 ns) are included: the inner detector, the forward detector, the MiniTAPS and the Cherenkov detector[7]. The Crystal Barrel detector, however, is only used at the second level. The number of

[7] The tagger is left out since at high rates the tagger always sees a hit and therefore the inclusion of the tagger does not improve the trigger selection.

detected particles is determined for the Crystal Barrel detector using the Fast Cluster Encoder (FACE). This can take up to 10 µs [Fle01].

Table 2.1 gives an overview of the trigger configuration. Each trigger condition demands at least the detection of two particles since both π^0 and η meson decay with a high branching ratio by emitting two photons [Pat+16]. It is therefore crucial to detect the two photons in either the Crystal Barrel, the forward detector, the MiniTAPS detector or a combination of two detectors (see conditions 2-6 in Table 2.1). An anti-coincidental signal of the Cherenkov detector is demanded in addition in order to suppress electromagnetic background that involves the detection of electrons and positrons. Condition 1 covers the case where both photons are detected in the Crystal Barrel detector and the proton at least left a signal in the inner detector.

No.	**first-level trigger**				**second-level trigger**
	Inner	FD	MT	Cherenkov	# clusters (FACE)
1	≥ 1			0	≥ 2
2		1		0	≥ 1
3			1	0	≥ 1
4		≥ 2		0	-
5		1	1	0	-
6			≥ 2	0	-

Table 2.1: An overview is given regarding the different trigger conditions [Win06; Hof18] used in the *vme_trig42c*. At the first-level, all detectors with a fast readout system are checked for hits ($\geq$1) or no hit (0): the inner detector (Inner), the forward detector (FD), the MiniTAPS detector (MT) and the Cherenkov detector. Later the FAST Cluster Encoder (FACE) provides information about the number of clusters found in the Crystal Barrel detector which is used in the trigger conditions as well.

2.1.6 Data sets

The analyzed data were taken from July 2013 to October 2013. Unpolarized electrons were provided by ELSA which was operated in the post-accelerator mode. The extracted electron beam energy was $E_0 = 3.2\,\text{GeV}$ and a current of roughly 1 nA was used. The electron beam was incident on a diamond radiator of 500 µm thickness. Thus, linearly polarized photons were produced. In order to enhance the polarization degree a collimator with a diameter of 4 mm was used. The linearly polarized photon beam was incident on a liquid hydrogen target of 5.1 cm length. The *vme_trig42c* trigger was utilized in all four beamtimes.
Table 2.2 gives an overview of additional important parameters: the number of runs and measurement hours and the coherent edge position. While for the July and August beamtimes the coherent edge position was chosen to be at 1750 MeV, the coherent edge position was moved further to 1850 MeV for the September and October beamtimes. This allowed the coverage of the beam asymmetry for beam energies from $E_\gamma \approx 1100\,\text{MeV}$ to 1800 MeV. In total, 4919 runs were taken. Each run has a compressed file size of 820 MB, comprising 500000 raw events, and was measured for roughly 13 minutes. Thereby, the runs were taken alternately at the azimuthal angle $\pm 45°$ of the polarization vector (see Figure 6.1). In addition, data were taken twice per day with an amorphous copper radiator in order to obtain the enhancement spectra for the determination of the degree of linear polarization. Unfortunately, the GIM detector and the tagger encountered problems during all four beamtimes that remained undetected until the

end of the beamtime. The consequences of these problems regarding the determination of the polarization degree are described in Section 6.1.

beamtime	**number of runs (h)**	**coherent edge position**
July 2013	513 (111 h)	1750 MeV
August 2013	1832 (396 h)	1750 MeV
September 2013	1490 (323 h)	1850 MeV
October 2013	1084 (235 h)	1850 MeV

Table 2.2: Overview of important parameters of the beamtimes taken at the CBELSA/TAPS experiment for the measurement of the beam asymmetry Σ in Bonn.

2.2 The A2 experimental setup

From November 2013 to September 2015 data were taken within five separate beamtimes in order to attempt a first measurement of the double polarization observables G and E at the same time. For this purpose longitudinally polarized electrons from the accelerator MAMI (see Section 2.2.1) were incident on a thin diamond radiator, creating elliptically polarized photons (see Section 2.2.2) with a linear and a circular polarization component (see Section 2.2.2). The polarization degree of the electrons was measured with a Mott (see Section 2.2.3) and a Møller (see Section 2.2.4) polarimeter. The produced bremsstrahlung photons were incident on a frozen spin butanol target (see Section 2.2.6) that provided longitudinally polarized protons. The decay products of the desired hadronic reactions were measured with the A2 detector system (section 2.2.7).

2.2.1 The Mainz microtron (MAMI) electron accelerator facility

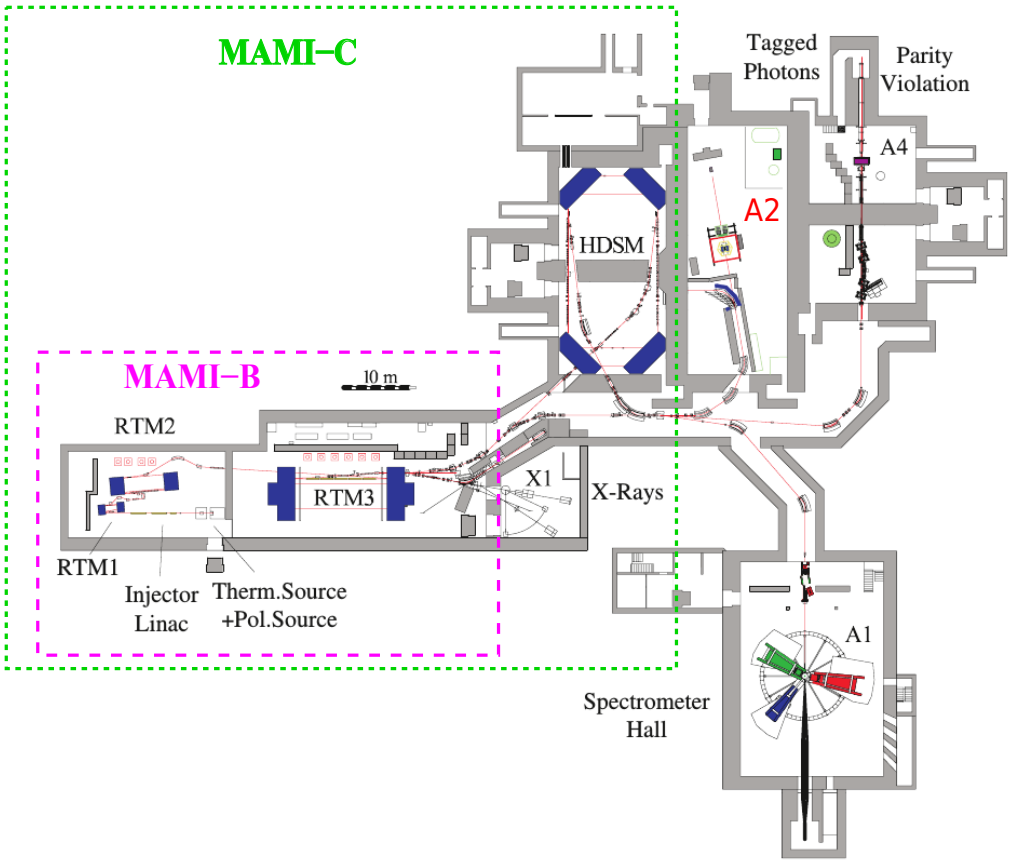

Figure 2.15: Overview of the MAMI facility in Mainz. Taken from [Jan06].

The electron accelerator facility MAMI [Jan+09] is located at the Institute for Nuclear Physics of the Johannes Gutenberg Universität Mainz. Similar to ELSA, MAMI provides either unpolarized or longitudinally polarized electrons. A thermionic electron gun (EKAN) delivers unpolarized electrons via thermionic emission off a hot cathode. For the production of lon-

gitudinally polarized electrons a pulsed titanium sapphire laser of 830 nm wavelength is used which is incident on a gallium-arsenide-phosphor (GaAsP) semiconductor photocathode [Aul11]. Through optical pumping with the laser light, electrons are transferred from the valence bands to the conduction band of GaAsP. The surface of the GaAsP is modified using Cesium-oxide layers to facilitate a state of negative electron affinity that allows electrons to be emitted from the crystal and not recombine. In order to achieve longitudinally polarized electrons the linearly polarized laser light has to be converted first into a circularly polarized light. This is accomplished by using a quarter-wave plate[8]. The quarter-wave plate is realized as a Pockels cell that allows to flip the laser light helicity and thus the electron polarization vector between parallel and antiparallel relative to the beam direction by changing the applied voltage polarity across the cell. During data taking the helicity flip was performed with a frequency of 1 Hz in order to keep artificial asymmetries and therefore systematic effects low [Aul+97].
After preaccelerating the electrons to an energy of 611 keV, they are accelerated further in the injector Linac up to an energy of 3.97 MeV. In subsequent three racetrack microtrons (RTM1-3) the electrons reach energies of up to 883 MeV with a current of up to 100 µA which is the MAMI-B beam [Jan+09]. Each RTM consists of two large dipole magnets and one Linac that is placed between both magnets. The electrons are accelerated by the electric field of the Linac RF cavities of 2.45 GHz and deflected by 180° in the magnetic field of the dipole magnets. Each turn the electrons gain a constant energy ΔE and thus, follow a larger deflection orbit. The RF frequency of 2.45 GHz means that the time distance between the electron bunches is around $t = 1/2.45\,\text{GHz} = 400\,\text{ps}$. Since the time resolution of the detector system of the A2 experiment is in the range of roughly 1 ns, MAMI is considered to be a continuous wave machine.
During the last acceleration step the electron energy is ramped up from 883 MeV up to 1.604 GeV (MAMI-C). It is achieved by the harmonic double sided microtron (HDSM) [Kai+08] which consists of two Linacs and four 90° bending magnets. It was chosen instead of a fourth RTM in order to lower the required magnet size and costs.
The preservation of the longitudinal electron polarization through all magnets of MAMI is a difficult task since the electron spin precesses in a magnetic field that is applied perpendicular to the electron beam direction. Thereby the precession frequency ω_s is proportional to the cyclotron frequency ω_c according to the Thomas-BMT equation [BMT59; TA06]:

$$\omega_s = (1 + a\gamma)\omega_c \quad \text{with} \quad a = \frac{(g-2)}{2} \quad \text{and} \quad \gamma = 1 + \frac{T}{m}, \tag{2.11}$$

where a is the anomalous magnetic moment, T the kinetic energy and m the mass of the electron. In general ω_s is not exactly an integer multiple of ω_c which leads to the electron spin not being longitudinal to the beam direction anymore once the electron beam reaches the experimental area [TA06]. In order to get a longitudinally polarized electron beam nonetheless a Wien filter [TA06] is installed near the preaccelerator. The Wien filter applies a homogeneous magnetic $\vec{B}$ and electric field $\vec{E}$ both perpendicular to the electron beam direction so that the following equation is fulfilled:

$$\vec{B} \times \vec{v} = \vec{E} \tag{2.12}$$

with $\vec{v}$ being the electron velocity. Through simultaneous variation of the electric and magnetic

[8] A quarter-wave plate is made of a birefringent material whose index of refraction depends on the orientation of the incoming light. If the linearly polarized laser light has an angle of 45° to the optical axis of the birefringent material, the light is split into two equal electric field components and one of them is delayed causing a phase shift of 90° between the two electric field components and thus, creating circularly polarized light.

fields in a way that Equation (2.12) is always fulfilled, the electron spin orientation can be rotated in the range from $-\pi/2$ to $\pi/2$. By choosing the right rotation angle of the spin and through precise calculation of the spin orientation throughout the MAMI accelerator, it is made sure that the electrons are longitudinally polarized when the electron beam is guided to the A2 experimental hall. Further spin depolarization effects are negligible for MAMI. The polarization degree of the electron can be determined by a Mott and a Møller polarimeter. Polarization degrees of around 80% are achievable.
The longitudinally polarized electron beam is guided towards a goniometer containing different radiators similar to the one used in Bonn.

2.2.2 Elliptically polarized photons

In order to measure the double polarization observables G and E at the same time, it is necessary to have on the one hand linearly polarized photons for G and on the other hand circularly polarized photons for E. Using the longitudinally polarized electron beam provided by MAMI and a diamond radiator enables the production of elliptically polarized photons with a linear and a circular polarization component. The diamond was positioned in such a way towards the electron beam that the produced coherent edge was located at 350 MeV, 450 MeV, 550 MeV, 650 MeV, 750 MeV and 850 MeV, respectively (see Figure 2.16 on the left). The polarization degree of the photons is discussed in Section 7.2.1. According to QED calculations it is assumed that the degree of linear and circular polarization can be determined in first approximation in the same way as in the case of using unpolarized electrons and a diamond or longitudinally polarized electrons with an amorphous radiator, respectively [Bos; Nad76]. However, this has not been experimentally verified. Therefore, an important goal of this measurement is not only to obtain the double polarization observables G and E, but to additionally experimentally confirm that the linear and circular polarization components do not or only little influence each other.

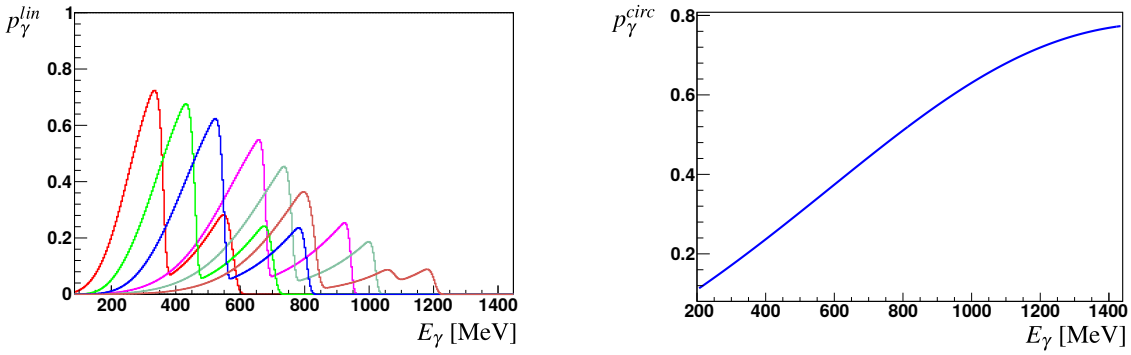

Figure 2.16: Left: The linear polarization degree is shown for six different coherent edge positions: 350 MeV (red), 450 MeV (green), 550 MeV (blue), 650 MeV (magenta), 750 MeV (darkgreen), 850 MeV (brown). Taken from [Afz+16; Spi19]. Right: The circular polarization degree as a function of the photon beam energy. Taken from [Afz+16].

While the PhD theses [Spi19][Mac17] focus on the double polarization observable G, this work focuses on the double polarization observable E. Usually, the double polarization observable E is measured with longitudinally polarized electrons and an amorphous radiator. During the incoherent bremsstrahlung process the electron transfers dependent on its energy its helicity to

the beam photon. This process is theoretically and experimentally well understood. According to Haakon Olsen [OM59] the degree of circular polarization p_γ^{circ} is given by

$$p_\gamma^{\text{circ}} = \frac{4x - x^2}{4 - 4x + 3x^2} \cdot p_e, \tag{2.13}$$

where x is the ratio of E_γ/E_0 and p_e is the electron polarization degree. The circular polarization degree rises with higher energy and reaches its maximum at $E_\gamma = 1400\,\text{MeV}$ with a polarization degree of around 80% (see Figure 2.16 on the right).

2.2.3 Mott polarimeter

In order to determine the electron polarization degree a spin dependent process e.g. Mott, Møller or Compton scattering is used. Mott scattering [Kes69; Ber09] is the elastic scattering of electrons in the Coulomb field of a heavy target nucleus. During the scattering process the electrons do not only experience the Coulomb field potential V_0 generated by the nucleus but also a spin-orbit potential V_{ls} due to the magnetic moment of the electron interacting with the magnetic field that the nucleus creates in the rest frame of the electron. The spin-orbit potential V_{ls} term is proportional to the coupling term $L \cdot S$ which has a different sign depending on the spin orientation (up or down) of the electron for the same angular momentum L and thus depending on whether the electrons pass the nucleus from the left or right side. This leads to a measurable left-right asymmetry A which is proportional to the electron polarization degree (see Equation (2.14)) [Ber09].

$$A = pS_0, \qquad A = \frac{N_L - N_R}{N_L + N_R} \tag{2.14}$$

with p being the transverse electron polarization degree and S_0 the Sherman function. The electron spin vector has to be rotated by the angle ϕ_{Wien} with the Wien filter from longitudinal to transverse orientation since the $L \cdot S$ coupling is zero for longitudinally polarized electrons. The Sherman function depends mainly on three parameters: the scattering angle θ of the electron, the electron beam energy E and the nuclear charge of the target material Z and it can be calculated theoretically. However, due to e.g. multiple scattering in the Mott-target the effective Sherman function S_{eff} and experimentally measurable asymmetry A_{exp} are lower [TAR11].
Experimentally, it is desirable to minimize the time required to accumulate high statistics for the asymmetry. This can be achieved by choosing the experimental parameter so that the Sherman function is maximal. For this reason a gold target is chosen as the Mott target since it has a high Z value. Figure 2.17 shows on the right the scattering angular dependence of the Sherman function for three different electron energies that are achievable by the MAMI injector Linac, where the Mott polarimeter is located. For the Mott measurement an electron energy of $3.65\,\text{MeV}$[9] is chosen and the asymmetry is measured for a backscattering angle of $\theta = 164°$ by two plastic scintillator detector at opposite azimuthal angle (see Figure 2.17 on the left). The electron polarization degree is then given by

$$p_e = \frac{A_{\text{exp}}}{S_{\text{eff}}} = \frac{A}{\sin(\phi_{\text{Wien}}) \cdot S_{\text{eff}}} \cdot f_{\text{trans}}^{\text{corr}}. \tag{2.15}$$

[9] This energy is chosen for $E_0 = 1557\,\text{MeV}$.

An additional correction factor $f_{\text{trans}}^{\text{corr}}$ is needed if the electrons have a small transverse polarization component to the longitudinal one before the polarization vector is rotated by the Wien filter [Ott12]. Since no important depolarization effects occur during the acceleration stages in the RTM and double sided microtrons, the measured electron polarization degree is still roughly the same at the position of target in the A2 experimental area (see section 7.2.1).

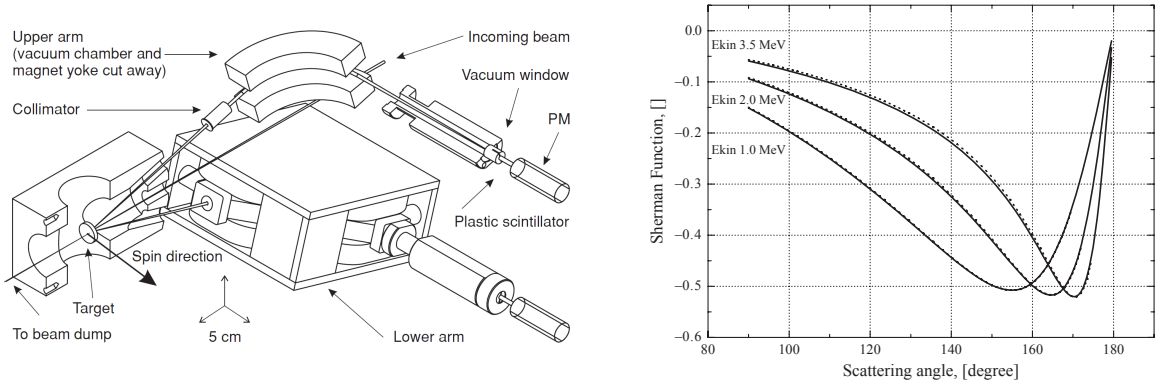

Figure 2.17: Left: Overview of the Mott polarimeter. The incoming transversely polarized electron beam scatters on a thin gold foil. The Mott asymmetry is measured at backward scattering angle $\theta = 164°$. Right: The Sherman function is shown as a function of the scattering angle θ for three different electron beam energies. Both figures taken from [TAR11].

2.2.4 Møller polarimeter

In addition to the performed Mott measurements, the electron polarization degree can be monitored using a Møller polarimeter [Wag+90] at the position of the Glasgow tagger spectrometer in the A2 hall. For this purpose data have to be taken with an amorphous Møller radiator which consists of a thin foil made of cobalt and iron alloy and a surrounding coil. Applying a magnetic field of 10 mT with the coil, the foil is magnetizable and the electron spins get aligned to the z-direction within the foil plane [Ott08]. Since the foil is tilted by $\alpha = 25°$ to the beam direction in the x-z plane (see Figure 2.18), the foil polarization vector reads $\vec{p}^T = p^T(\sin\alpha, 0, \cos\alpha)$. When the incoming longitudinally polarized MAMI-C electrons reach the Møller radiator, elastic electron electron scattering, Møller scattering, can occur.

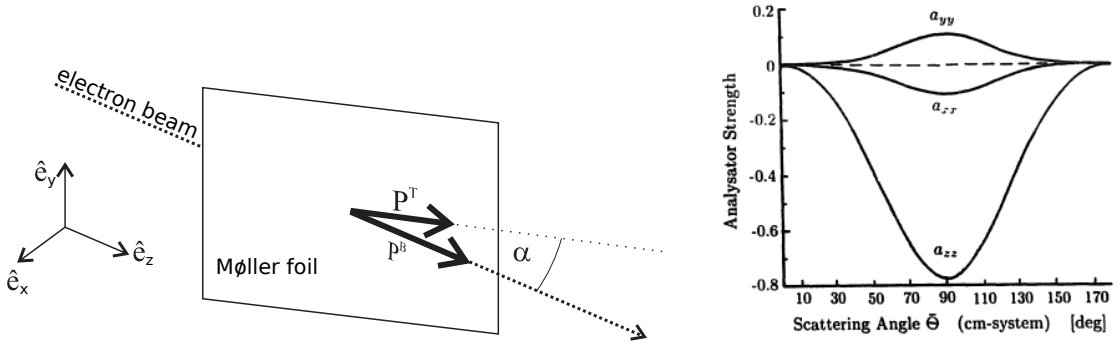

Figure 2.18: Left: The incoming longitudinally polarized electron beam scatters on a thin Møller foil where the electrons are polarized in the x-z plane. The angle between both polarization vectors is α. Taken from [Ott08]. Right: The Møller asymmetry is measured at scattering angle $\theta_{CM} = 90°$ in the center of mass frame. Here the asymmetry terms A_{xx}, A_{yy} and A_{zz} are maximal. Taken from [Wag+90].

The cross section depends on the longitudinal polarization degree of the incoming electron beam P_i^e and the polarization degree of the Møller foil electrons P_j^T [Wag+90; Arr+92]:

$$\frac{d\sigma}{d\Omega}_{(\uparrow\downarrow,\uparrow\uparrow)} = \frac{d\sigma}{d\Omega}_{unpol.} \cdot \left(1 \pm \sum_{i,j} a_{ij} P_i^e P_j^T\right), \quad i,j = x,y,z, \tag{2.16}$$

with a_{ij} being the tensor components which describe the corresponding analysator strengths. Due to parity conservation the components $a_{\mathrm{xy}} = a_{\mathrm{yx}} = a_{\mathrm{zy}} = a_{\mathrm{yz}}$ are zero [Ott08]. In the high-energy limit (which is the case of the MAMI-C beam the coefficients a_{xz}=a_{zx} become negligible and the coefficients a_{xx}, a_{yy} and a_{zz} become energy independent and only depend on the scattering angle θ_{CM} [Ott08] (see Figure 2.18 on the right). The maximum analysator strength is achieved for symmetric Møller scattering, when both electrons have the same energy of $E_0/2$ at the scattering of $\theta_{CM} = 90°$, due to the Pauli Principle. At this scattering angle the cross section for a parallel ↑↑ spin configuration is much smaller than for antiparallel (↑↓) aligned spins since the spatial wave function has to be antisymmetric[10] for parallel spin configuration in order for the total wave function of the Møller electrons to be antisymmetric.
Assuming the contribution of transverse electron beam polarization is negligible, the longitudinal electron polarization degree P_z^e is obtainable by taking the asymmetry of count rates of both spin configurations [Arr+92]:

$$A = \frac{N_{\uparrow\downarrow} - N_{\uparrow\uparrow}}{N_{\uparrow\downarrow} + N_{\uparrow\uparrow}} = \frac{N_{\uparrow\downarrow} - N_{\uparrow\uparrow}}{2 \cdot N_{unpol.}} = \sum_{i,j} a_{ij} P_i^e P_j^T \approx a_{zz} P_z^e P^T \cos\alpha. \tag{2.17}$$

$$P_z^e = \frac{A}{a_{zz} P^T \cos\alpha}, \tag{2.18}$$

with $P^T = 8.08 \pm 0.21\%$ and $a_{zz} \approx \frac{-\sin^2\theta_{CM} \cdot (8 - \sin^2\theta_{CM})}{(4 - <sin^2\theta_{CM})}$ which can be derived in a first order QED approximation [Wag+90].

2.2.5 Glasgow photon tagger

During data taking the longitudinally polarized MAMI-C electron beam impinged a radiator producing bremsstrahlung photons. As radiator either a thin diamond crystal or an amorphous Vacoflux 50 radiator made of a cobalt and iron alloy (Møller radiator) were used. In case of the Møller radiator incoherent bremsstrahlung is created with an energy distribution that follows a typical $1/E_\gamma$ dependency and with a small emittance angle [KM59]. Using the diamond radiator instead coherent and incoherent bremsstrahlung are produced.
The purpose of the Glasgow photon tagger [Ant+91] lies in determining the energy of each produced photon. It consists of a dipole magnet which deflects the scattered electrons momentum dependent towards the focal plane detector. Electrons that did not interact with the radiator are guided to a beam dump. For the MAMI-C electron beam energy of E_0 =1557 MeV the magnetic field was chosen to be 1.88 T using a maximum current of 440 A. Thus achieving a tagged photon energy range of 100 MeV to 1446 MeV. The energy of the beam photons is determined using Equation (2.8).

[10] Since it holds for the Legendre polynomials: $P_l(-\cos\theta) = (-1)^l P_l(\cos\theta)$, the spatial wave function ($\Psi_{spatial} \propto P_l(\cos\theta)$) is antisymmetric only if l is odd.

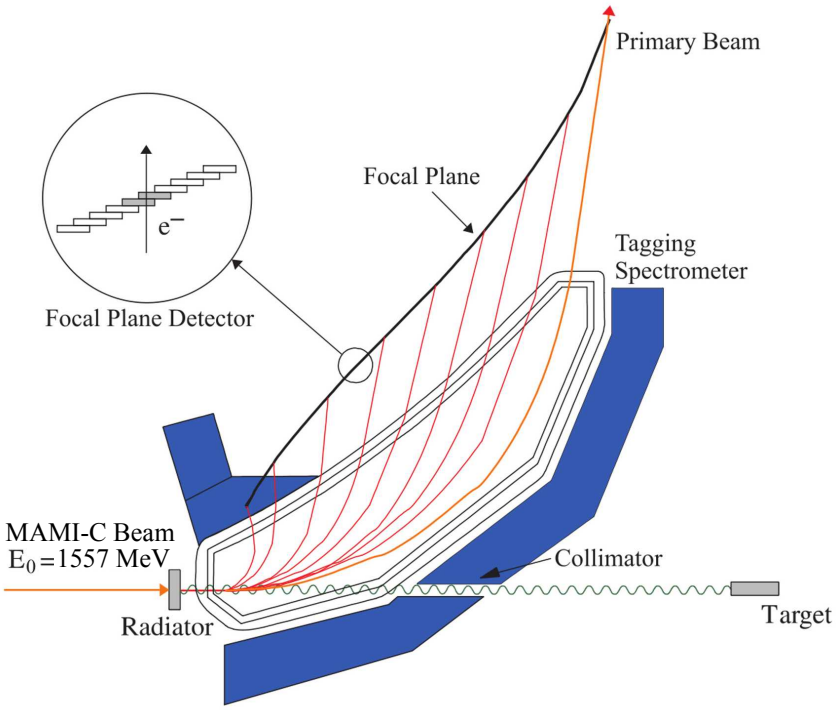

Figure 2.19: Overview of the Glasgow photon tagger. The MAMI-C electron beam hits a radiator creating bremsstrahlung photons. Electrons are deflected in the magnetic field of the tagging spectrometer. If an electron goes through two neighboring and overlapping scintillators in the focal plane detector, it is marked as a tagger hit. Taken from [Hor+09].

The focal plane detector [Hal+96] comprises 353 plastic scintillators of type EJ-200 and of 80 mm length, 2 mm thickness and varying widths of 9 mm to 32 mm that are arranged in an overlapping manner (see Figure 2.19). In order to reduce the counting of accidentals in the tagger a tagger hit is saved only if an electron passes through two neighboring and overlapping ladders giving a coincident signal. Therefore, the tagger has 352 channels whereby each channel covers an energy of 2-5 MeV. Each scintillator is connected to a Hamamatsu R1635 photomultiplier tube for readout [McG+08] which are shielded from the magnetic field with the help of steel plates. The signals of the photomultiplier are passed to a discriminator and subsequently to CATCH multi-hit TDCs in order to record the times of the electrons. Furthermore, the signals are transferred to FASTBUS and VUPROM scalers. While the FASTBUS scalers count the hits in the corresponding focal plane detector only when a trigger signal (see section 2.2.7.6) is present, the VUPROM scalers count the hits as free running scalers independent of the trigger signal. These rates are important for determining the photon flux.
The produced bremsstrahlung photons were collimated with a 2 mm collimator and guided towards the frozen-spin butanol target as shown in Figure 2.19.

2.2.6 Frozen spin butanol target

In principle an ensemble of particles with spin s can be polarized as long as the particles have a magnetic dipole moment μ different from zero. In an external magnetic field the energy levels split into $2s + 1$ levels according to the Zeeman effect (with the magnetic quantum number

$m = -s, -s+1, \cdots +s$), e.g. for protons or electrons with spin $s = 1/2$ there are two energy levels that are populated. The population number N of the levels is described in thermal equilibrium by the Boltzmann distribution [Mes05]:

$$\frac{N(E+\Delta E)}{N(E)} = e^{-\frac{\Delta E}{k_B T}}, \qquad \Delta E = g\mu B \Delta m \tag{2.19}$$

with $N(E)$ and $N(E+\Delta E)$ being the population number of the states with energy E and $E+\Delta E$, where ΔE is the energy difference between two energy levels with the magnetic quantum number m_i and m_j. T describes the temperature, k_B the Boltzmann constant, B the magnetic field, g the Landé factor, μ the Bohr or the nuclear magneton and $\Delta m = m_i - m_j$. The population number ratio and thus, the net polarization of the ensemble can be increased by increasing the magnetic field and by lowering the temperature.
In order to measure the double polarization observables G and E in π^0 and η photoproduction off protons, a longitudinally polarized target is needed. A polarizable liquid or solid hydrogen target containing only free protons and providing a high production rate would be desirable for this purpose. However, one is faced with two challenges regarding the polarization process of such a target:

- The magnetic moment of protons is low in comparison to e.g. electrons due to its high mass. A magnetic field of more than 10 T and a temperature of lower than 20 mK would be needed to polarize free protons [Bra+99]. Such high magnetic fields are not feasible for this experiment.

- Hydrogen atoms are not realized as single atoms in nature but as diatomic molecules. This means the total spin of hydrogen H_2 nuclei can either couple to 0 or 1, resulting in parahydrogen or orthohydrogen, respectively. At room temperature, 25 % of hydrogen gas consists of parahydrogen and 75% of orthohydrogen. At very low temperatures this ratio changes to almost 100% parahydrogen [TV02]. However, only orthohydrogen can be used for polarization purposes. Additionally, hydrogen has a fast relaxation time due to the exothermic ortho-para conversion which results in only very low polarization degrees.

For this reason pure H_2 targets are not used. Instead, hydrocarbon compounds, e.g. butanol (C_4H_9OH) are the preferable choice of material. Here, only the hydrogen nuclei (free protons with spin 1/2) are polarizable whereas the carbon and oxygen nuclei are not polarizable since both nuclei contain an even number of protons and neutrons, resulting in a total spin of zero and no magnetic moment. Thus, the background reactions off the bound protons and neutrons of carbon and oxygen nuclei is unpolarized background.
To avoid the first challenge, as mentioned above, the butanol target is polarized via Dynamic Nucleon Polarization (DNP) process [AP57; AG78]. The butanol compound is doped with paramagnetic radicals (Tetra-Methyl-Piperidin-1-Oxyl (TEMPO $C_9H_{18}NO$)) that provide quasi-free electrons. The electrons are polarized using a 2.5 T magnet. Due to their high magnetic moment the electrons are polarized nearly to 100%. Dipole-dipole interaction between the electrons and the neighboring hydrogen nuclei lead to a hyperfine splitting of the energy levels (see Figure 2.20) in the magnetic field. Considering in addition, dipole-dipole interactions between the paramagnetic radicals themselves causes the splitting of the Zeeman levels to continuous bands. This phenomenon is described by the Soild State Effect theory [AG78] and the Equal Spin Temperature theory [Red55]. Using irradiation of microwaves of frequency $\nu_e \pm \nu_N$

(ν_e =70.04 GHz and ν_N =106.4 MHz) allows simultaneous spin flips of electrons and protons [Ott15]. Both electrons and protons go back to their ground states after their spin relaxation times. The spin relaxation time of electrons is by a factor 10^6 smaller than the one of protons and therefore the electrons are quickly available to induce more simultaneous spin flips and ensure a faster building up of the polarization than its destruction. Thus, the polarization is slowly transferred dynamically from the electrons to the nucleons.

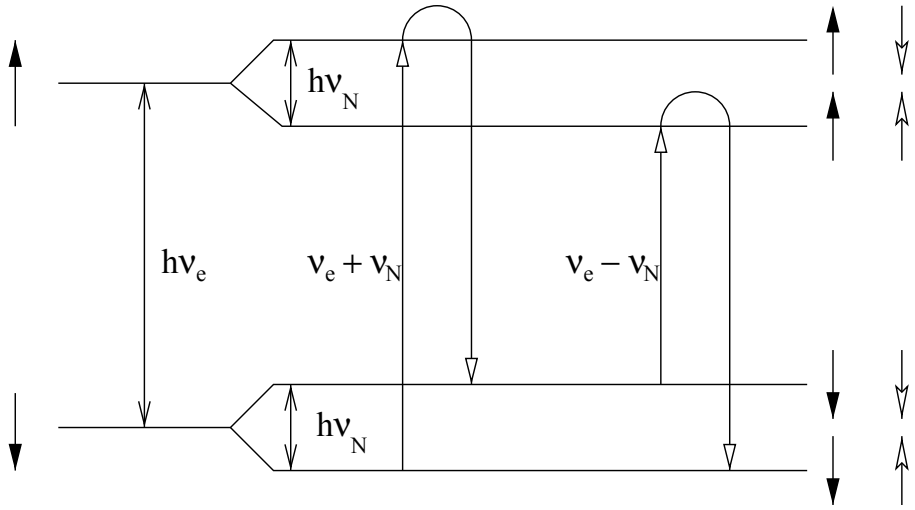

Figure 2.20: The hyperfine interaction between electrons and protons causes a splitting of the Zeeman levels into four energy levels. With the correct frequency of irradiated microwaves simultaneous spin flips of electrons (black arrows) and protons (white arrows) are induced. After certain relaxation times electrons and protons return to the state of thermal equilibrium. Taken from [Roh03].

During the beamtimes frozen butanol pallets (see Figure 2.21) of around 1.87 mm diameter were placed into the cylindric Teflon target cell that has a diameter and length of 2 cm [Roh03]. In order to polarize the butanol target via DNP a magnet of 2.5 T strength is moved over the target. For the maintaining of the polarization over a long time of ideally a few days it is necessary to cool the butanol target and to "freeze" the longitudinally oriented proton spins. This is achieved with a ^{3}He/^{4}He dilution refrigerator developed in cooperation with the Joint Institute for Nuclear Research (JINR) Dubna. It lowers the target temperature down to 25 mK within approximately 8 h.
The cooling process is done in three steps. First the ^{3}He and ^{4}He gas is liquefied in a separator and evaporator cryostat. It uses the phase transition from liquid to vapor to decrease the temperature down to 1.5 K by lowering the vapor pressure in the cryostat. Further cooling to 0.7 K is achieved via thermal contact with a still [Mar07]. Then the ^{3}He and ^{4}He enter the mixing chamber where a temperature of 25 mK is gained. Pure liquid ^{4}He becomes superfluid at 2.17 K. An admixture of ^{3}He shifts the critical temperature towards lower temperatures. Below a temperature of 0.867 K two phases are formed, a concentrated ^{3}He-rich phase and a diluted ^{3}He-poor phase. Since the density of ^{3}He is lower than the one of ^{4}He, the concentrated ^{3}He-rich phase swims on the diluted ^{3}He-poor phase. When ^{3}He atoms cross over to the diluted ^{3}He-poor phase energy is removed from the system and the temperature is lowered. This process is stimulated through the removal of ^{3}He atoms from the diluted ^{3}He-poor phase which causes

an imbalance[11]. At around 25 mK there is a concentration of 6% ^{3}He and 94% ^{4}He in the diluted ^{3}He-poor phase. [Roh03; Mar07].
After the polarization and cooling process, the magnet is moved away and the Crystal Ball detector is placed over the butanol target. Together with the small magnetic field of the holding coil of 0.68 T inside the refrigerator and the low temperature of 25 mK, relaxation times of more than 1000 h which allows continuous measurements for more than a week. Polarization degrees of up to 89% are achievable.

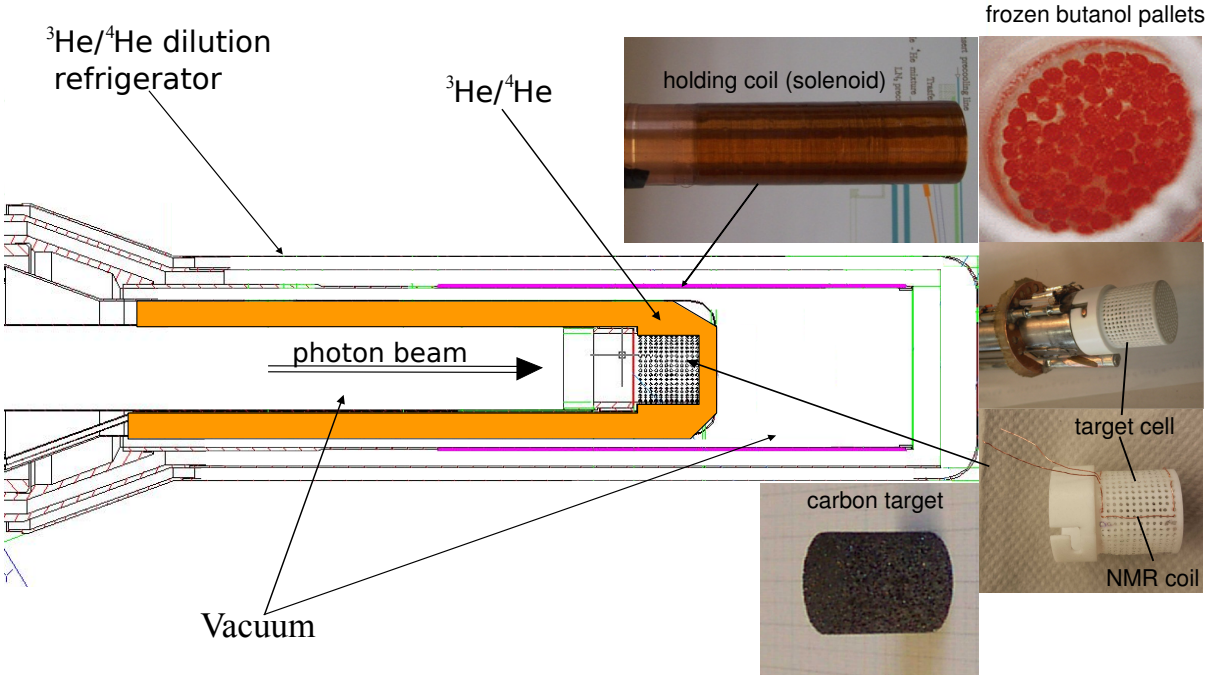

Figure 2.21: Schematic view of the ^{3}He/^{4}He dilution refrigerator (cryostat). The cylindric Teflon target cell is filled with butanol pallets that are cooled with ^{3}He/^{4}He gas mixture. The holding coil provides a magnetic field of 0.68 T. For the measurement of the polarization degree a NMR coil is used. The Pictures are adapted from [Tho13].

In order to study the unpolarized background of the butanol target, data were also taken with a carbon foam target made of POCO Graphite [Poc] which was placed in the same Teflon target cell, target holding structure and target cryostat as the butanol pallets. The density of the carbon foam target was chosen to match the number of all bound nuclei of the frozen spin butanol target. In addition, tests were performed in the September 2015 beamtime to investigate the influence of the ^{3}He/^{4}He mixture that is used to cool the butanol target (see Table 2.5). For this purpose the carbon target was cooled once with the same ^{3}He/^{4}He mixture and once no cooling was used. Moreover, data were taken with only the helium mixture in the target cell. The target area densities of all target materials are discussed in Section 7.1.2.1.

[11] Since ^{3}He and ^{4}He have different vapor pressure curves, it is possible to vaporize ^{3}He in the vaporization chamber that is connected to the dilution cryostat. In this way gaseous ^{3}He can be pumped out.

2.2.7 Detector system

Similar to the CBELSA/TAPS setup the A2 experimental setup (see Figure 2.22) is equipped with two calorimeters, namely the Crystal Ball (see Section 2.2.7.2) and in forward direction the TAPS detector (see Section2.2.7.3), for the detection of photons. Both detectors provide an energy, timing and spacial information of the photons. In addition, the Particle Identification Detector (PID), two multi-wire proportional chambers (MWPCs) (see Section 2.2.7.1)) and the TAPS veto detectors are used to identify charged particles.

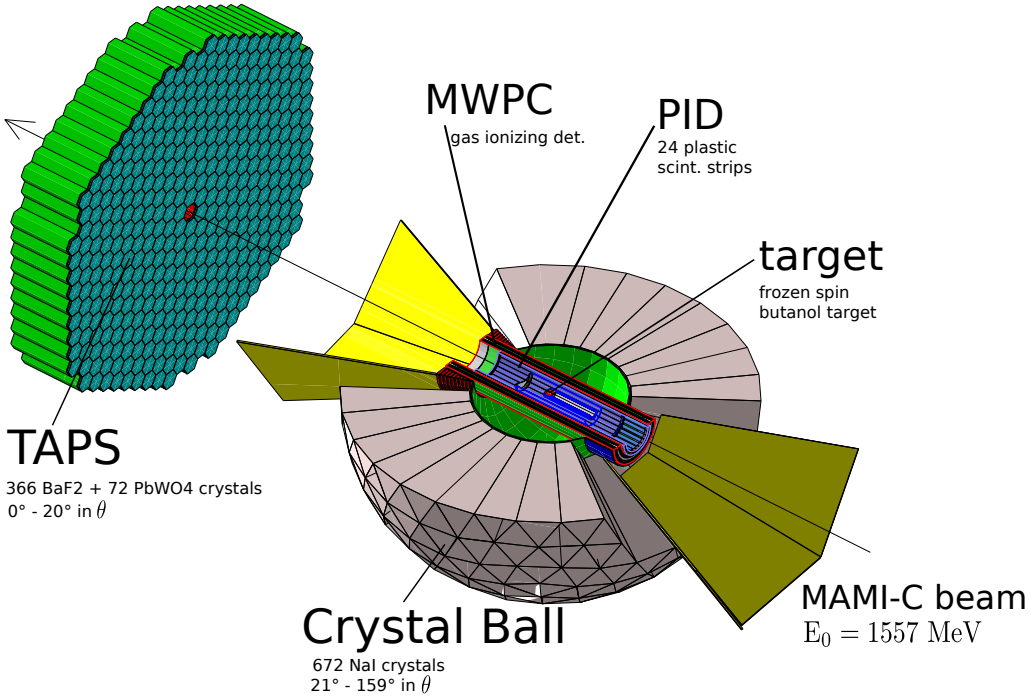

Figure 2.22: The A2 experiment in Mainz consists mainly of two calorimeters: the Crystal Ball and the TAPS detectors. The PID and MWPCs, which enclose the target cylindrically, are located in the center of the Crystal Ball detector. Taken from [Wit+13].

2.2.7.1 PID and MWPCs

For the identification of charged particles a Particle Identification Detector (PID) [Wat05] and two multi-wire proportional chambers (MWPCs) are installed surrounding the target [Dow06]. The PID consists of 24 plastic scintillator strips (type EJ-204) which have a length of 500 mm, a width of 15.3 mm and a thickness of 4 mm. They are arranged in a cylindrical manner around the target with a diameter of 116.5 mm, covering each 15° in the azimuthal angle ϕ and 15° - 159° in the polar angle θ (see Figure 2.23). Each scintillator strip is read out via photomultipliers of the type Hamamatsu H3164-10, providing an energy and time information of the detected particles.
The PID analog signals are first amplified and then split and fed to a timing and an energy branch. In the timing branch the signals are discriminated and sent to CATCH TDCs for a time measurement. In the energy branch the signals are delayed and processed by ADCs in order to measure the deposited energy in the PID elements.
While charged particles passing through the detector deposit a small amount of energy ΔE_{PID}

in the strips, neutral particles such as photons or neutrons will not leave any signal in the PID. This allows the separation of charged and neutral particles. Furthermore, electrons and charged pions are minimizing particles for the PID, whereas low energetic protons are mostly not. Therefore, electrons and charged pions leave a constant amount of energy in the PID. Low energetic protons, however, deposit more energy in the PID than high energetic protons (>400 MeV). Therefore, it is possible to distinguish between electrons, charged pions and protons when plotting the deposited energy in the PID ΔE_{PID} against the deposited energy in the Crystall Ball detector E_{CB} (see Figure 2.23 on the right).

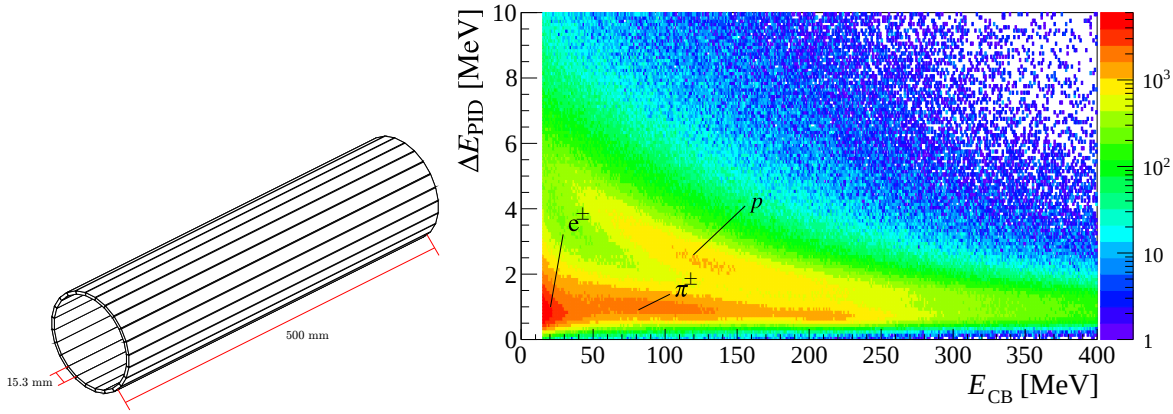

Figure 2.23: Left: Schematic view of the Particle Identification detector (PID). It consists of 24 scintillator stripes that have a length of 500 mm, a width of 15.3 mm and a thickness of 4 mm. Taken from [Mar13]. Right: The deposited energy in PID ΔE_{PID} is plotted against the deposited energy in the Crystal Ball detector E_{CB}. Electrons, charged pions and protons leave different fractions of their energy in the PID and Crystal Ball detector.

Two Multi-Wire Proportional Chambers (MWPCs) enclose the PID and the target which are both build up as shown schematically in Figure 2.24. Each chamber has two 1 mm thick cylindrical Rohacell tubes that are coated with 25 µm Kapton on the internal surfaces. Cathode strips, that are 4 mm wide and 0.1 µm thick and made of aluminum, are helically spiraled around the internal surfaces of the Rohacell tubes at ±45° to the beam direction with a gap of 0.5 mm between them. Consequently, each of the inner cathode strips has two intersection points with each of the outer cathode strips (see Figure 2.24 on the right). The external surfaces of the tubes are coated with 0.1 µm aluminum for shielding of electrical fields. Anode wires, which are 20 µm thick and are made of tungsten, are placed between the two Rohacell tubes parallel to the beam direction with a gap of 2 mm. A voltage of typically 2400 V - 2500 V is applied between the cathode strips and the anode wires.
In addition, the two chambers are filled with a gas mixture consisting of 67.1% argon, 29 % ethane, 0.5% freon and 3.5% methyl alcohol [Ott15]. When charged particles with an energy higher than 15.2 eV [Pat+16] pass through the detector, they will ionize the argon gas creating Ar^{+} and e^{-} pairs which create a charge avalanche. The electrons drift to the anodes and the ions to the cathodes causing a measurable voltage that is proportional to the initial gas ionization. Since the Ar^{+} and e^{-} have enough energy, X-rays or new electrons can be released from the electrodes as well. While the X-rays are absorbed by the ethane gas, the electrons are absorbed by the freon gas. The admixture of methyl alcohol is necessary in order to prevent

the occurrence of polymer chains from broken up ethane molecules, that can create an isolation layer around the cathode and prevent the ions from reaching the cathode [Ott15].
Using the information of the cathode strips and anode wires of both chambers, two particle trajectory points can be reconstructed. Through interpolation the origin of the particle at target position can be determined. All in all, the MWPCs provide not only information about whether the particle is charged or not, but also give angular information in θ and ϕ direction and thereby improve the angular resolution for charged particles ($\sigma_\theta = 2.4° \cdot \sin\theta$ and $\sigma_\phi = 2°$) that usually deposit their energy in only a few Crystal Ball crystals [Ott15]. Demanding that at least one of the chambers has detected the particle the detection efficiency of protons is typically around 90% and of charged pions around 80% [Ott15].

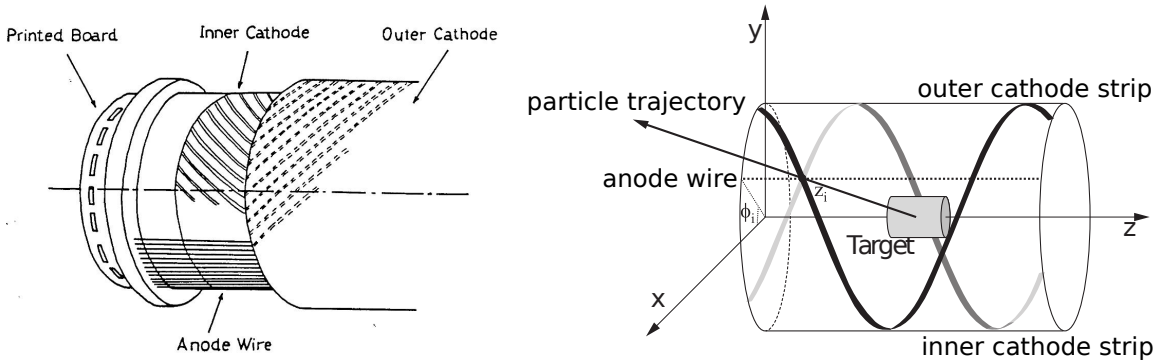

Figure 2.24: Left: Schematic view of one Multi-Wire Proportional chamber. Taken from [Dow06]. Right: A particle trajectory is reconstructed with a hit in an anode wire and through an intersection point between the inner and outer cathode strips. Taken from [Ott15].

2.2.7.2 Crystal Ball calorimeter

The main electromagnetic calorimeter, the Crystal Ball detector [Blo+75; Ore81; Sta+01], encloses the MWPCs, the PID and the target. The detector has the geometrical shape of an icosahedron and consists of 672 thallium doped sodium iodide (NaI(Tl)) crystals. They are each 40.6 cm long and have a shape of a tapered truncated triangular pyramid. While nine crystals form a minor triangle, four minor triangles are grouped to a major triangle. Lastly, 20 major triangles form the Crystal Ball detector (see Figure 2.25). Furthermore, the Crystal Ball detector is segmented horizontally into two parts, leaving a small inactive region consisting of steel plates and an air gap in-between them. Due to the hygroscopic nature of the (NaI(Tl)) crystals the two hemispheres are kept under vacuum. In order to leave space for the beam line a hexagonally shaped "tunnel region" is present (see Figure 2.25).
Passing photons create an electromagnetic shower in the crystals which is usually contained within 13 neighboring crystals when considering the Molière radius of $r_m = 4.11$ cm (see Table 2.3). In contrast, heavier charged particles propagate through the crystal as minimum ionizing particles, not creating a shower. Due to the limited length of the crystals, protons can be stopped up to 400 MeV and $\pi^\pm$ up to 240 MeV.
Each crystal is read out by a photomultiplier of type SRC L50B01. The energy resolution is given by $\sigma_E/E = 2\%/(E/\text{GeV})^{0.36}$ and the angular resolution is 2-3° for the polar angle θ and by $\sigma_\phi = \sigma_\theta/\sin\theta$ for the azimuthal angle ϕ [McN+10]. The Crystal Ball detector covers the polar angular range between 20° and 160° and almost the entire azimuthal angular range excluding the small gap region.

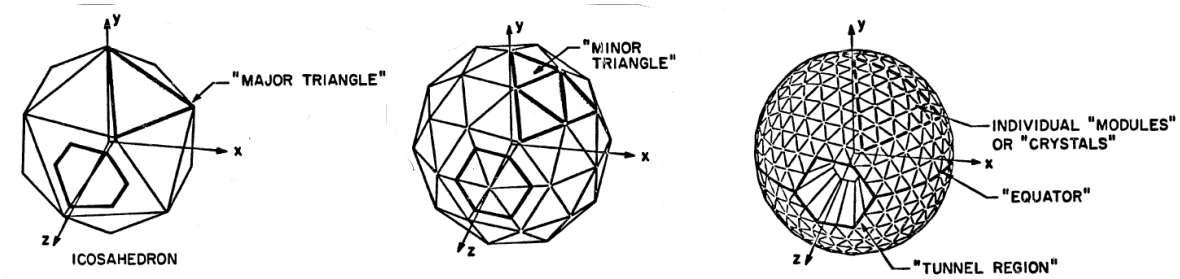

Figure 2.25: The Crystal Ball detector has the shape of a icosahedron. It is segmented in 20 major triangles. Each of the major triangles comprise four minor triangles which themselves contain 9 crystals. Taken from [Ore81].

Properties	**Crystal Ball (NaI(Tl))**	**TAPS (BaF_2)**	**TAPS ($PbWO_4$)**
density [g/cm^3]	3.67	4.89	8.3
radiation length X_0 [cm]	2.59	2.03	0.89
Molière radius r_m [cm]	4.11	3.1	2
decay time [ns]	245	0.9 (fast)	10 (fast)
		250 (slow)	30 (slow)
wavelength of	410	220 (fast)	420 (fast)
emission max. [nm]		300 (slow)	425 (slow)

Table 2.3: Overview of important properties of the scintillators used in the Crystal Ball and the TAPS calorimeters. Values are taken from [Pat+16; PDG].

The 672 photomultiplier output signals are split with 42 modules (16 channel analog fan out) and sent to a timing, trigger and to an energy branch. In the trigger branch, the analog signals are internally summed up in a cascade-like manner. The resulting analog signal is proportional to the total deposited energy in the Crystal Ball detector and is referred to as the Crystal Ball energy sum. This signal is transferred to its ADC channel for digitization and to two leading-edge discriminators where it is compared to a low and a high threshold. Since the NaI(Tl) crystals have a slow rise-time, the Crystal Ball energy sum trigger is used at the first and second trigger level. On the first trigger level the LED low threshold is set at around 48 mV which corresponds to roughly 20 MeV in order to have a fast trigger signal. On the second level a higher energy sum threshold value can be chosen according to the desired reactions.
In the timing branch the analog signals are passed to dual-threshold discriminators where the signals are compared to two threshold values. The low threshold is set at a few MeV and is used to suppress noise. In case the signal is higher than the lower threshold, a trigger signal is provided and each analog signal is passed to a CATCH-TDC in order to get a timing information. Since LED discriminators are used the trigger times are dependent on the signal amplitudes and hence to the deposited energy, which is known as time walk. The higher threshold is used to check the multiplicity (number of clusters) which can be utilized as a second level trigger.
In the energy branch the analog signals are delayed by 300 ns and given to sampling ADCs which are capable of sampling the signal with a frequency of 38.88 MHz [Wer14] and subtracting the

baseline directly during data acquisition.

2.2.7.3 TAPS calorimeter

The TAPS (Two Arm Photon Spectrometer) detector [Gab+94; Nov91] was located at a distance of 178.35 cm from the target center during all beamtimes of this work[12]. The detector covers the forward angular range from $2° < \theta < 17.48°$ and the full azimuthal angle ϕ. 9 out of 11 hexagonally arranged rings consist of 366 BaF_2 crystals (compare 2.26). The two innermost TAPS rings comprise 72 $PbWO_4$ crystals due to their higher density compared to BaF_2 (see Table 2.3) and therefore high rate capability.

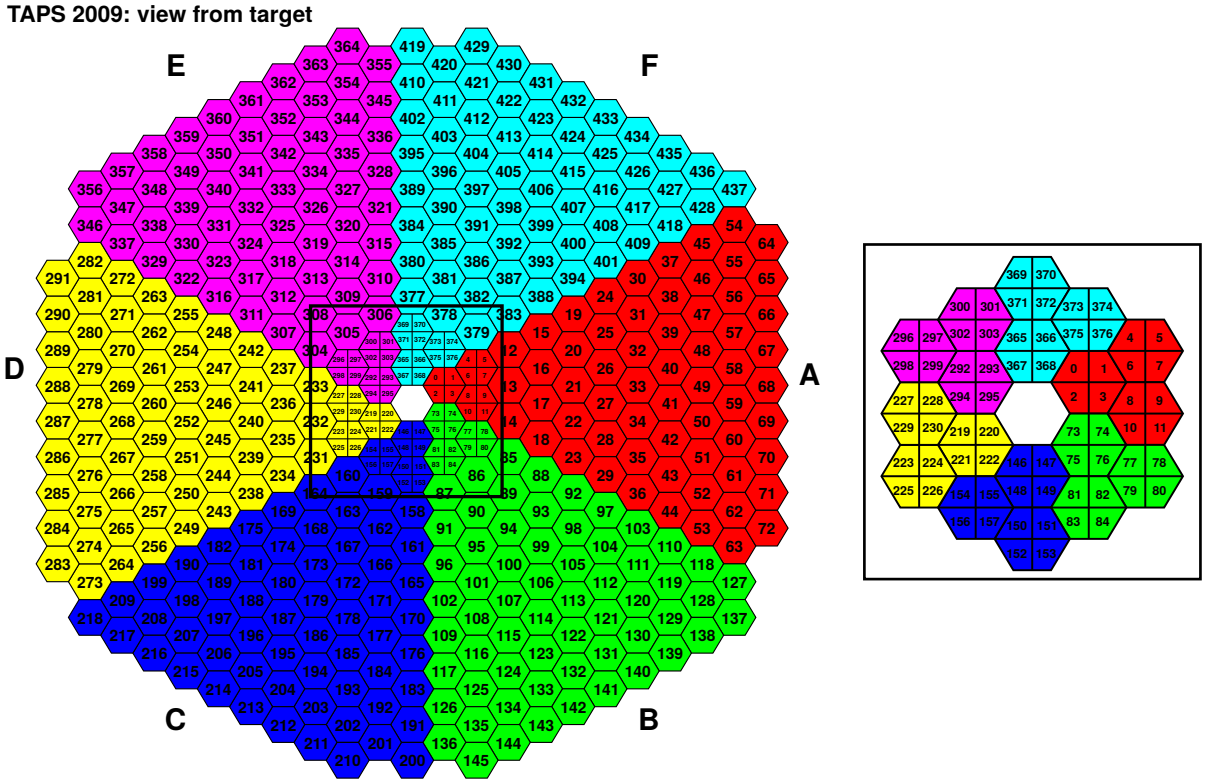

Figure 2.26: The hexagonally shaped TAPS detector is segmented into six sectors A-F. The inner two rings consists of $PbWO_4$ crystals. The remaining rings are made of BaF_2 crystals. Taken from [Wer14].

This is necessary because most of the particles are boosted in forward direction, especially electromagnetic background that occurs with a higher cross section than the hadronic reactions [Pat+16]. Each BaF_2 crystal is hexagonally shaped, has a length of 25 cm, a front face diameter of 5.9 cm and is read out via a Hamamatsu R2059-01 photomultiplier. BaF_2 crystals have two scintillation light components, a fast (0.9 ns) and a slow (250 ns) component. While the fast component leads to a good time resolution of Δt =170 ps [Wer14], the slow component is important for achieving a good energy resolution (see Equation (2.10)). Since photons deposit their energy faster than protons or neutrons, it is possible to distinguish photons from hadrons by their different pulse shapes. Integrating the signal over two different time intervals (one

[12] Depending on whether the Cherenkov detector is needed or not the TAPS detector is located at either 146.35 cm or 178.35 cm from the target center [Ros12].

short and one long interval) and comparing the two energies allows to separate photons from hadrons (see Section 4.2).
Each $PbWO_4$ crystal has a trapezoidal shape with a length of 20 cm. A group of four $PbWO_4$ crystals form a hexagon that matches the shape of one BaF_2 crystal (see Figure 2.26). The $PbWO_4$ crystals are read out by Photonis XP 1911 PMTs.
All BaF_2 crystals and each group of four $PbWO_4$ crystals are equipped with plastic scintillator plates which are placed in front of the crystals. The plastic scintillators of type EJ-204 have a thickness of 5 mm, a hexagonal shape and are read out via photomultipliers of type Hamamatsu H6568. Only charged particles deposit a small amount of their energy $E_{\text{TAPS VETO}}$ in the scintillator plates and therefore provide a veto signal for charged particles. In addition, a $E_{\text{TAPS VETO}} - E_{\text{TAPS}}$ plot can help to distinguish between charged particles as described for the PID. However, the resolution is worse in comparison of the PID due to a bad optical coupling [Wer14].
The TAPS photomultiplier signals are processed similar to the MiniTAPS signals of the CBELSA/-TAPS experiment with VME (Versa Module Eurocard) boards. Constant fraction discriminators are utilized to decide whether or not the according channel has seen a hit. In order to suppress noise the thresholds are set at a few MeV. In addition, two leading edge discriminators are available per channel for trigger selection purposes. While the timing of the TAPS signals are measured with time to amplitude converters (TAC), the energy is determined with a combination of charge to amplitude converters (QAC) and ADCs.
The TAPS veto signals are passed to LEDs which provide the start signal for the time measurement and a gate signal of 110 ns for the integration of the anolog signals in order to measure the deposited energy.

2.2.7.4 Cherenkov detector

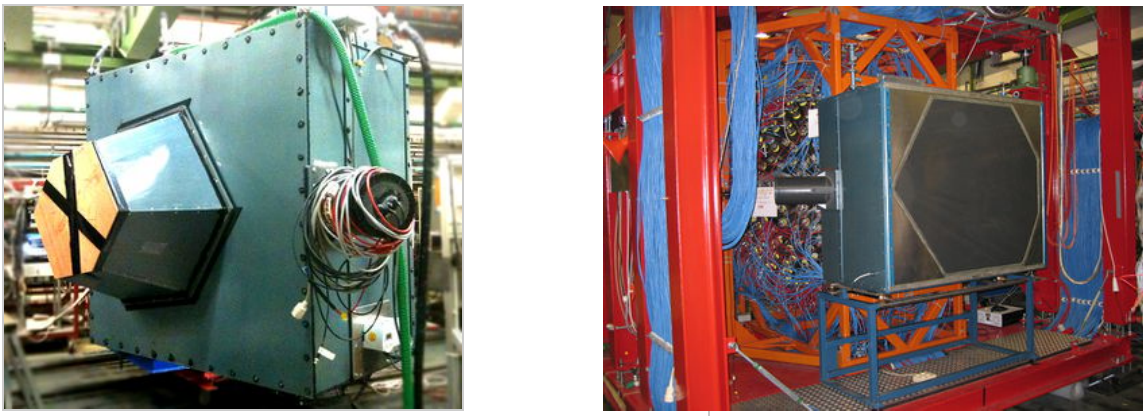

Figure 2.27: Left: The front side of Cherenkov detector. The nose of the Cherenkov detector is moved into the tunnel region of the Crystal Ball detector. The PMT is located on the right side of the detector. Right: The back side of the Cherenkov detector. Pictures taken from [Ros12].

In order to filter out the desired hadronic events a Cherenkov detector [Ros12] can be placed between the Crystal Ball and the TAPS detector and used in the trigger as veto. Thereby, the hexagonally shaped nose of the Cherenkov detector (see Figure 2.27) is moved into the tunnel region of the Crystal Ball detector. The TAPS detector has to be moved further away at the

position of 178.35 cm from the target center which causes a small gap of 2° between the Crystal Ball and the TAPS detector that is not covered in the θ-angle range. The Cherenkov detector is filled with Freon-C-318 (C_4F_8) which has a refractive index of n=1.0013 [Ros12]. Cherenkov light is produced if electrons or positrons with an energy higher than 10 MeV pass through the detector. For charged pions the threshold is much higher at 2.7 GeV. The Cherenkov light is collected by a large ellipsoidal mirror and focused to a photomultiplier which is located on the side of the Cherenkov detector. The detection efficiency of electrons and positrons is up to 99.95% [Ros12].

2.2.7.5 Flux monitoring

For the monitoring of the beam quality and relative photon flux, a parallel-plate ionization chamber (P2) is located behind the TAPS detector. It consists of converter plates where the photons can create an electromagnetic shower which ionizes the air between the plates. The produced charged particles are collected using 40 V between the plates [Ott15]. The chamber counts the number of photons that did not interact with the target material. The ratio of the P2 count rates to the tagger count rates gives an estimation about how well the electron beam is guided from MAMI to the A2 hall and later how well the photon beam is guided through the collimator. A small value is desirable which is controlled throughout the beamtime. In addition, the ratio gives a good estimation of the tagging efficiency. The tagging efficiency describes the count rate of photons reaching the target to the count rate of detected electrons in the tagger spectrometer.

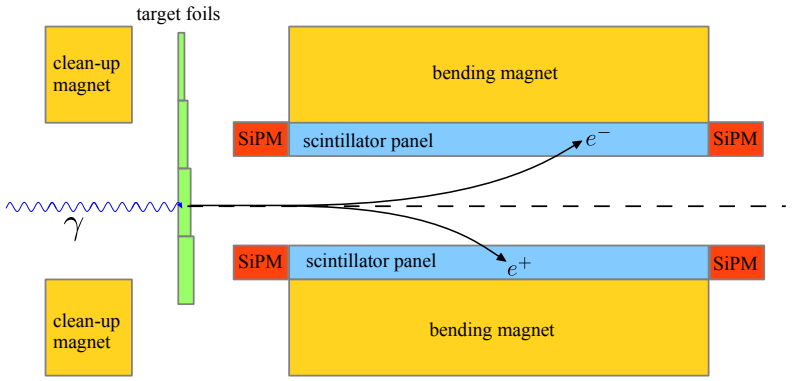

Figure 2.28: The pair spectrometer is shown here. The photon beam can interact with the molybdenum target foil via pair production. The produced electron and positron pair are deflected in the magnetic field of the bending magnet and detected in scintillator panels, which are read out by silicon photomultiplier. Taken from [Pau16].

For the precise measurement of the tagging efficiency dedicated runs are taken with a very low intensity beam and using a lead glass detector which can be moved into the beam line. These runs were taken with a rate of 10 kHz in the lead glass detector which has a nearly 100% detection efficiency [Ann08]. At this low rate dead-time losses are negligibly small.
Another possibility to monitor the photon flux is given by the pair spectrometer [Pau16] which is depicted in Figure 2.28. It is mounted shortly after the collimator. Four different molybdenum foils with a thickness of 5 µm, 10 µm, 15 µm or 20 µm can be moved into the beam line. Beam photons can interact with the foil material with a probability of 0.15% via pair production [Pau16]. The electron and position pairs are deflected by the bending magnet in opposite

direction towards scintillator detectors which are connected to silicon photomultipliers. Upon receiving a coincidence signal, a gating signal is generated for the tagger scalers. In addition, a delayed gating signal is provided in order to immediately subtract random background.

2.2.7.6 Trigger system

Similar to the CBELSA/TAPS trigger, the A2 trigger [Dow06] is divided into two levels. At the first level the analog sum of all Crystal Ball elements, known as the Crystal Ball energy sum, is used to get a fast trigger signal by setting the CB energy sum low threshold to roughly 20 MeV (48 mV). At the second level a higher energy sum threshold can be set in order to be selective for the wanted reactions. In addition, the LED1 and LED2 thresholds can be set for each TAPS crystal of all six sectors to generate a trigger signal in case the reaction products are detected mainly in the TAPS detector. Moreover, the number of detected particles in both the Crystal Ball and the TAPS detector are roughly estimated with the multiplicity trigger that can be set also at the second level.

beamtime	**coh. edge position**	**tagger sectors**	**CB energy sum high threshold**	**TAPS LED 1 threshold**
Nov. 2013	350 MeV, 450 MeV, 550 MeV 650 MeV, 750 MeV	A - H	40 MeV	40 MeV
April 2014	350 MeV, 450 MeV, 550 MeV 650 MeV, 750 MeV, 850 MeV	A - F	90 MeV	60 MeV
May 2014	850 MeV	A - F	90 MeV	60 MeV
May 2015	750 MeV, 850 MeV	A - G	120 MeV	120 MeV
Sep. 2015	450 MeV	A - G	70 MeV	60 MeV
	650 MeV		90 MeV	80 MeV
	850 MeV		90 MeV	80 MeV

Table 2.4: Overview of the configured trigger used at the A2 experiment: On the one hand the CB energy sum was used to trigger on events detected in the Crystal Ball detector. On the other hand the TAPS LED1 trigger is used as well. In addition, some tagger sectors (see Figure 4.22 for the corresponding beam photon energy) were switched off during data taking in order to enhance the statistics at higher energies.

For the analyzed data, the trigger had to select not only the $\pi^0 \to \gamma\gamma$ and $\eta \to \gamma\gamma$ final state but also e.g. $n\pi^+$ channel [Spi19]. Therefore a multiplicity ≥ 1 was demanded in order to access many different final states. The desired beam photon energy range for the double polarization observables G and E starts already at the $\Delta(1232)$ resonance region where the mesons have low energies. For that reason a CB energy sum high threshold of ≤ 120 MeV was chosen for all beamtimes (see Figure 2.29). In addition, it is crucial to cover the entire θ angular range for the observables. The case where e.g. both decay photons or a π^+ are detected in the TAPS detector, and therefore only very small energy is deposited in the Crystal Ball detector, can be covered by the additional usage of the TAPS LED1 trigger.
The TAPS LED1 thresholds were chosen similarly low as the CB energy sum thresholds. In case the TAPS LED1 trigger fired, an anti-veto signal was demanded from the Cherenkov detector in order to suppress electromagnetic background in the forward angular region. Due to a small gas leak in the Cherenkov detector during the May 2015 beamtime the TAPS LED1 threshold had to be increased to 120 MeV in order for the TAPS LED1 trigger rate to not outweigh the

CB energy sum trigger rate (see Table 2.4). Moreover, tagger sectors were switched off once enough statistics was acquired in the low beam photon energy region. This helped to increase the rate and maximize the statistics for higher energies which is especially important for the $p\eta$ channel. Thereby, the position of the coherent edges were taken into account as well. During all beamtimes difficulties were encountered regarding the TAPS LED1 trigger. The inclusion of the TAPS trigger lead to difficulties in the data acquisition system and the total lifetime was not estimated correctly.

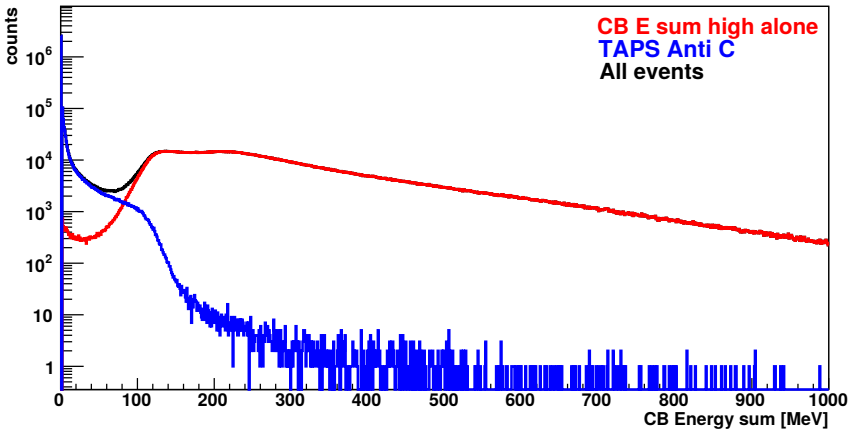

Figure 2.29: The Crystal Ball energy sum is shown for a run of the May 2015 beamtime in red for the trigger condition *CB E sum high alone* and in blue for the trigger condition *TAPS Anti C*. The total Crystal Ball energy sum spectrum is plotted in black.

2.2.8 Data sets

The analyzed data was taken in five separate beamtimes in November 2013, April 2014, May 2014, May 2015 and September 2015 as listed in Table 2.5. In all four beamtimes a longitudinally polarized electron beam of 1557 MeV energy was provided by MAMI, whereby the electron helicity was switched with a frequency of 1 Hz. Typical MAMI currents were around 3-5 nA. Elliptically polarized photons were produced by employing a thin diamond radiator. In addition, data were taken with a Møller radiator instead in order to have a reference measurement for the double polarization observable E with only circularly polarized photons. The photon beam impinged on a frozen spin butanol target. The target was polarized in or against beam direction which is indicated by $+$ or $-$ in Table 2.5. Moreover, data were taken in April 2014 and September 2015 with a carbon foam target to study the unpolarized background of the butanol target. Thereby, dedicated tests were performed with and without the addition of helium (He), and by using only helium in the target cell.
During each beamtime not every detector was functioning ideally. The November 2013 beamtime was the first beamtime after a DAQ upgrade. The DAQ upgrade compromised the $E_{\mathrm{PID}} - E_{\mathrm{CB}}$ spectrum resolution and the overall PID efficiency significantly due to gate timing problems of the PID signals [Wat]. This issue worsened over time until the May 2014 beamtime where the $E_{\mathrm{PID}} - E_{\mathrm{CB}}$ spectrum became completely not usable (see Figure A.3). The problem was identified and fixed after the May 2014 beamtime. In addition, gate timing problems occurred for the TAPS $PbWO_4$ ADCs in the November 2013 and May 2014 beamtimes [Ros].

While the PID was working well in the May 2015 and September 2015 beamtimes, a small gas leakage of the Cherenkov detector was discovered that slightly compromised the TAPS trigger efficiency. Here, the effect was smaller for the September 2015 beamtime. In the offline analysis it was concluded that the target polarization degree as determined by the target group was not correct for the November 2013, May 2014 and May 2015 beamtimes. This was investigated and fixed by the target group at the beginning of the last September 2015 beamtime. Detailed information are given in Section 7.2.2.2. Throughout all beamtimes difficulties remained with the TAPS LED1 trigger as already explained in Section 2.2.7.6.

beamtime	**# runs (h)**	**radiator**	**target**	**coh. edge position [MeV]**	**issues**
Nov. 2013	70 (35 h)	diamond	butanol (+/−)	350	PID, trigger, target pol.
	62 (31 h)	diamond	butanol (+/−)	450	PID, trigger, target pol.
	140 (69 h)	diamond	butanol (+/−)	550	PID, trigger, target pol.
	136 (68 h)	diamond	butanol (+/−)	650	PID, trigger, target pol.
	56 (28 h)	diamond	butanol (+/−)	750	PID, trigger, target pol.
	71 (34 h)	Møller	butanol (+/−)	-	PID, trigger, target pol.
April 2014	122 (61 h)	diamond/Møller	carbon (no He)	350, 450, 550 650, 750, 850	PID, trigger, target pol.
May 2014	120 (60 h)	diamond	butanol (−)	850	PID, trigger, target pol.
	51 (26 h)	Møller	butanol (−)	-	PID, trigger, target pol.
May 2015	110 (55 h)	diamond	butanol (+/−)	750	trigger, Cherenkov ,target pol.
	155 (74 h)	diamond	butanol (+)	850	trigger, Cherenkov, target pol.
	85 (43 h)	Møller	butanol (+/−)	-	trigger, Cherenkov, target pol.
Sep. 2015	86 (44 h)	diamond	butanol (+/−)	450	Cherenkov, trigger
	143 (72 h)	diamond	butanol (+/−)	650	Cherenkov, trigger
	34 (17 h)	diamond	butanol (+)	850	Cherenkov, trigger
	106 (53 h)	Møller	butanol (+/−)	-	Cherenkov, trigger
	89 (45 h)	diamond/ Møller	helium	850	Cherenkov, trigger
	8 (4 h)	diamond/ Møller	carbon (no He)	850	Cherenkov, trigger
	82 (41 h)	diamond/ Møller	carbon (with He)	850	Cherenkov, trigger

Table 2.5: Overview of important parameters of the beamtimes taken at the A2 experiment for the measurement of the double polarization observables G and E.

The tagger, the Crystal Ball detector and the TAPS detector were running stable during all beamtimes.

3 Event reconstruction

After data taking the data undergoes an offline analysis. The recorded raw digital ADC and TDC values are converted to energy and time information by applying detector calibrations (see Chapter 4). In addition the impact point of a particle can be reconstructed from the positions of the hit detector elements. Combining all available information of each detector e.g. energy, time, charge and spatial information, it is possible to reconstruct all particle's four-momenta involved in an event.
In this chapter the utilized software is introduced and the reconstruction process is described for both experiments.

3.1 Event reconstruction using CBELSA/TAPS data

3.1.1 Software

3.1.1.1 ExPlORA

The CBELSA/TAPS collaboration uses a self-developed software named *Extended Plugable Object-oriented Root Analysis* (*ExPlORA*) [Pio07] which is based on the object-oriented CERN-framework *ROOT* [BR97]. *ROOT*, which has become a standard analysis tool in the data analysis of particle physics experiments, uses *C++* libraries and object-oriented programming. *ExPlORA* is used for the reconstruction of particle four-momenta from the raw data, the application of detector calibrations and is easily extendable by a user through the usage of plugins for further data analysis e.g. applying cuts and filling histograms. It is controlled by *xml* files allowing to structure the reconstructed event information in form of *containers*.

3.1.1.2 Monte Carlo simulation

In particle physics experiments it is standard practice to study particle detection efficiencies through simulation of the according detector setup geometry and using the Monte Carlo (MC) technique [MU49] to track the particle interaction with the detector materials. The *Geant3* (geometry and tracking) software package [Bru+87] provided by *CERN* is based on *FORTRAN*. It models the energy losses of particles when passing through matter using hadronic and electromagnetic interactions based on experimental data. The simulation package provides information about the particle interaction e.g. the electromagnetic showers of the photons etc. and estimates the deposited energies in each detector element. For the CBELSA/TAPS experiment the CBGeant package [Cre01] was developed to model the experimental setup with all its detector components using the *Geant3* software package.
Recently, F. Kalischewski developed a new simulation package for the CBELSA/TAPS experiment using the Virtual Monte Carlo technique [Kal11]. It is written in *C++* and offers the possibility to easily exchange the underlying simulation package from *Geant3* to the latest *Geant4* [Ago+03] package and to modify part of the detector setup simulation.

For this work the Virtual Monte Carlo with the *Geant3* simulation package was used to generate different final states. The photon beam spot was simulated with a Gaussian distribution of $\sigma_x = 0.25\,\text{cm}$ width in both x- and y- direction (see Figure 3.1 on the left). In z-direction a flat distribution over the length of the target (5 cm) was assumed. Within this volume the primary reaction vertex was generated. The target was placed at the center of the Crystal Barrel detector at $z = 0\,\text{cm}$. The beam energy was distributed according to the Bethe-Heitler bremsstrahlung cross section [Hei54] and the final state particles were distributed according to phase-space.

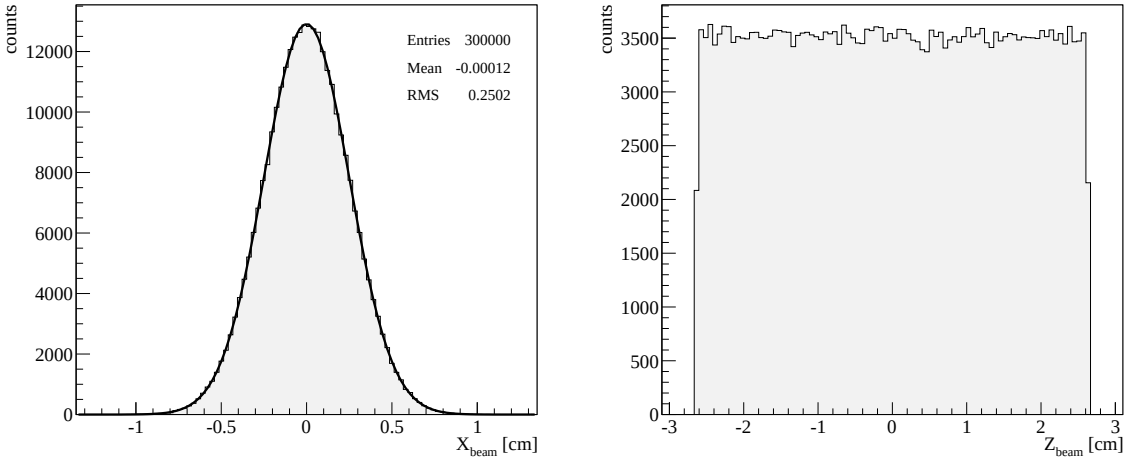

Figure 3.1: The simulated beam properties are shown for the analysis of CBELSA/TAPS data. Left: A Gaussian distribution with a width of $\sigma = 0.25\,\text{cm}$ was used for the x- and y- direction. Right: A flat distribution was utilized in z-direction for the length of the target, whereby the target was placed at $z = 0\,\text{cm}$).

analyzed reaction	**simulated reactions**	**events**
$\gamma p \to p\pi^0$	$\gamma p \to p\pi^0$	60×10^6
	$\gamma p \to p\omega \to p\pi^0\gamma$	30×10^6
	$\gamma p \to n\pi^+$	60×10^6
	$\gamma p \to n\pi^0\pi^+$	30×10^6
	$\gamma p \to p\pi^+\pi^-$	30×10^6
$\gamma p \to p\eta$	$\gamma p \to p\eta$	30×10^6
	$\gamma p \to p\pi^0$	60×10^6
	$\gamma p \to p\pi^+\pi^-$	30×10^6
	$\gamma p \to n\pi^+$	60×10^6
	$\gamma p \to n\eta\pi^+$	30×10^6
	$\gamma p \to p\omega \to p\pi^0\gamma$	30×10^6
	$\gamma p \to p\pi^0\pi^0$	30×10^6
	$\gamma p \to p\pi^0\eta$	30×10^6

Table 3.1: Overview of the simulated reactions for the analysis of CBELSA/TAPS data.

Table 3.1 shows a list of all simulated reactions for signal and background events. All reactions were distributed according to phase-space. The generated output *ROOT* files were processed with *ExPlORA* in the exact same way as experimental data. This allows to check for a correct event reconstruction, the study of possible background reactions and particle detection, reconstruction and analysis efficiencies. An energy calibration was performed for MC data as well. Here, the determination of global gain factors[1] utilizing $\gamma p \to p\pi^0$ MC events was enough since MC data does not contain any background events.

3.1.2 Clustering of detector hits

Particles passing through a detector deposit a certain amount of energy through interaction with the detector material. Photons for example create an electromagnetic shower in the Crystal Barrel, forward detector and the MiniTAPS detector that is spread over several detector elements. For the determination of the correct number of detected particles per event it is necessary to group the individual detector hits to clusters that are spatially and timely correlated. This section gives an overview of the used cluster algorithms for the different detectors.

3.1.2.1 Tagger

An electron hit is accepted as a tagger hit if at least two overlapping bars have registered a hit (see Figure 3.2). This reduces the occurrence of accidentals. In the region, where the tagger fibers overlap with the tagger bars, additionally up to three fibers can register the electron hit. The first step of clustering consists of grouping neighboring tagger bars and also fibers that have seen a signal to clusters. A time difference of less than 6 ns is required for the first and last hit within a cluster of the tagger bars and less than 7 ns for the fibers. After identifying all tagger bar and all tagger fiber clusters, the clusters can be combined in the overlapping region ($E_\gamma \leq 2.6\,\text{GeV}$ for $E_0 = 3.2\,\text{GeV}$) demanding a time coincidence within 4 ns. While pure tagger bar clusters are accepted in the non-overlapping region, pure fiber clusters are not used further. The finally reconstructed clusters are saved as *beam photons* in *ExPlORA*. Each beam photon has an energy and a time information.

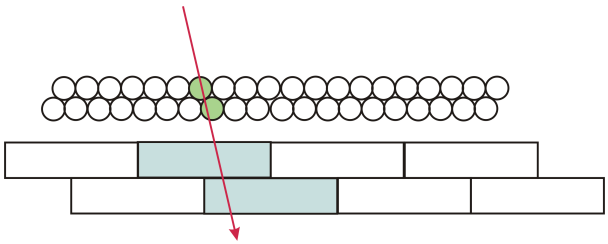

Figure 3.2: An electron leaves a signal in two overlapping fibers and two overlapping bars. Taken from [Thi11].

[1] Gain factors are determined for each detector element of the Crystal Barrel, forward and MiniTAPS detectors. The gain factor is multiplied to the measured energy deposition of the according detector element in a way that the invariant mass of two clusters is in agreement with the expected π^0 mass. It compensates photon shower losses in inactive detector material. For more detail see Section 4.1.2.

3.1.2.2 Crystal Barrel and forward detector

The Crystal Barrel and forward detector both consist of CsI crystals and are only separated from each other by a small gap that is needed for cables. Electromagnetic showers can spread over the Crystal Barrel and the forward detectors crystals. Therefore, all CsI crystals are used together to identify clusters and the same cluster algorithm is applied for both detectors.
The first step consists of listing all detector hits and grouping all neighboring hits with an energy deposition higher than 1 MeV locally to clusters. The algorithm iteratively checks for a signal in all direct neighbors of a hit crystal and continues the search until all connecting hits are grouped together. The threshold of 1 MeV allows the suppression of electronic noise. Additionally, it is demanded that the total cluster energy and the central cluster crystal, which is the one with the highest energy, is higher than 20 MeV. This threshold is chosen to be higher than the FACE threshold of 15 MeV in order to suppress any effects of the set trigger thresholds during data taking.

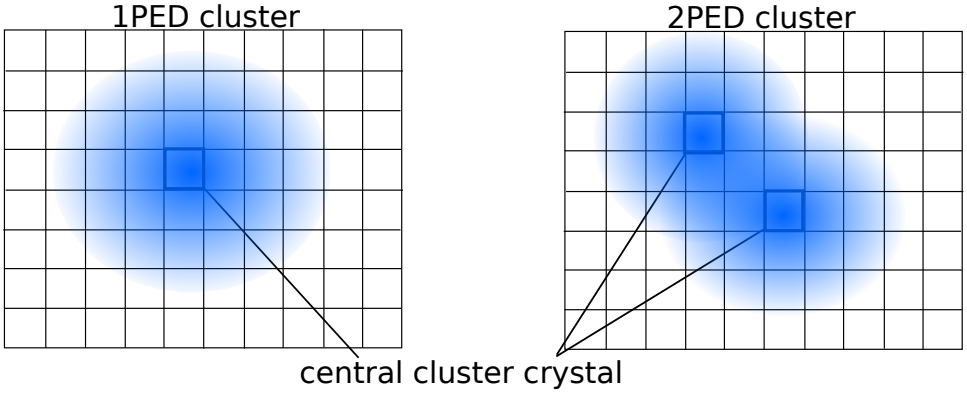

Figure 3.3: Left: The Crystal Barrel crystals are shown as as a grid. A cluster is found containing only one PED. Right: A cluster is found containing two local maxima and therefore this is a two PED cluster. The central crystal cluster is marked in dark blue.

In case the opening angle of two particles is very small, their clusters can overlap. Hence, one cluster does not necessarily correspond to one detected particle. A search for local energy deposition maxima within clusters is performed to take this into consideration. Subsequently, all identified maxima within clusters are saved as a particle energy deposition (PED). Only clusters with maximal two PEDs are accepted for the analyzed reactions $p\pi^0 \rightarrow p\gamma\gamma$ and $p\eta \rightarrow p\gamma\gamma$ since more than two particles will not be found within the same angular range in the analyzed kinematic region of this work. Each PED corresponds to a detected particle.

3.1.2.3 MiniTAPS detector

The cluster algorithm of the MiniTAPS detector works very similar to the one of the Crystal Barrel detector. However, the applied thresholds are chosen differently: The single crystal energy threshold is set to 13 MeV[2] except for the inner two MiniTAPS rings where it is 17 MeV. Since the majority of the electromagnetic background is boosted strongly in forward direction and the Cherenkov threshold for vetoing on electrons is 17.4 MeV, the inner two rings contain

[2] 13 MeV corresponds to the minimum energy electrons start creating showers.

a lot of background hits at energies lower than 17 MeV. Similar to the Crystal Barrel detector, a threshold of 25 MeV is used for the total cluster energy and 20 MeV for the central cluster crystal. Since the MiniTAPS detector has a fast time response and since CFDs are used, clusters can be identified better than for the Crystal Barrel detector by demanding a time correlation of all detector hits within 5 ns. This is especially useful for high detector rates which is the case for the MiniTAPS detector due to its location in forward direction. Afterwards clusters are rechecked spatially in order to account for emerged gaps within clusters due to the applied time correlation.

3.1.2.4 Forward detector and MiniTAPS detector vetoes

The clustering of the forward detector and MiniTAPS detector veto hits is done in the same way as for the BaF_2 crystals of the MiniTAPS detector. An energy deposition higher than 100 keV is considered as a hit.

3.1.2.5 Inner detector

If a particle passes through the inner detector depositing more than 150 keV energy per fiber, it is saved as a hit. For each layer of the inner detector clustering of hits is achieved in a similar way as for the MiniTAPS detector. First neighboring hits are locally grouped, then their time correlation within 14 ns is checked, and finally they are spatially grouped again in case of newly emerged gaps as demonstrated in Figure 3.4. A maximum of 20 clusters per layer are allowed.

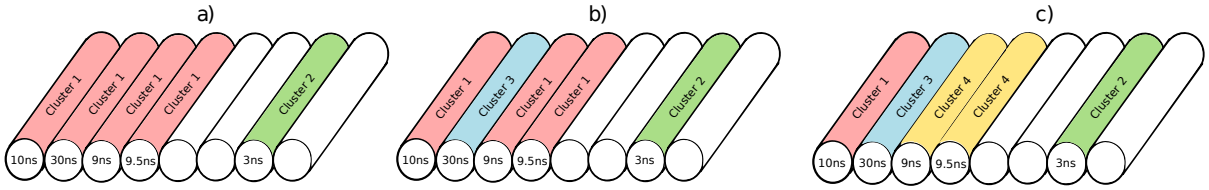

Figure 3.4: The clustering process of the inner detector is depicted in three steps: a) First hits are grouped locally. b) Then the time correlation of the fibers within clusters is checked. c) Clusters are grouped again locally. Taken from [Thi11].

Afterwards, the clusters of all layers are scanned for correlation by demanding a time coincidence of 14 ns and an angular difference of less than 10° in polar and azimuthal angles θ and ϕ. If a correlation is successfully found between at least two layers, it is saved as a so called *route* in *ExPlORA*.

3.1.3 Particle energy information

3.1.3.1 Tagger

Electrons are momentum analyzed in the magnetic field of the tagger magnet. The hit tagger bar or tagger fiber index is correlated to an energy through an energy calibration (see Section 4.1.2). The beam photon energy is determined from the average value of all corresponding fiber or bar cluster hit energies E_i:

$$E_\gamma = \frac{1}{n_{\text{fiber/bar}}} \sum_{i=1}^{n_{\text{fiber/bar}}} E_i, \tag{3.1}$$

where $n_{\text{fiber/bar}}$ is the number of all fiber or bar hits. Since the fibers provide a better energy resolution in comparison to the tagger bars, the energy information is obtained from the fibers in the overlapping region of tagger bars and fibers. In the non-overlapping region the bar energy information is taken instead. The four momentum vector of the beam photon $p_{\gamma,\text{beam}}$ reads

$$p_{\gamma,\text{beam}} = \begin{pmatrix} E_\gamma \\ 0 \\ 0 \\ E_\gamma \end{pmatrix}. \tag{3.2}$$

3.1.3.2 Crystal Barrel, forward and MiniTAPS detector

All particles detected in the Crystal Barrel, the forward or the MiniTAPS detector have an energy information. The particle energy is the sum of all energy depositions E_i of all n crystals belonging to a PED. For a single PED cluster the energy is given by

$$E_{\text{PED}} = \sum_{i=1}^{n} E_i. \tag{3.3}$$

In the case of a two PED cluster detected in the Crystal Barrel or forward detector the individual crystal energies have to be divided to the two PEDs. This is achieved by taking into account the CsI(Tl) Molière radius of $r_M = 3.57\,\text{cm}$ [Pat+16] and thus, the exponentially decreasing energy depositions in transverse direction of the shower spread. The energies of the central crystals of both PEDs $E^{\text{cent.}}_{\text{PED1}}$ and $E^{\text{cent.}}_{\text{PED2}}$ are corrected in the following way [Sei10]:

$$E^{\text{cent.}}_{\text{PED1,corr}} = E^{\text{cent.}}_{\text{PED1}} - E^{\text{cent.}}_{\text{PED2}} e^{-d_{12}/r_M}, \qquad E^{\text{cent.}}_{\text{PED2,corr}} = E^{\text{cent.}}_{\text{PED2}} - E^{\text{cent.}}_{\text{PED1}} e^{-d_{21}/r_M}, \tag{3.4}$$

where d_{12} and d_{21} are the distances between the central crystals of the PEDs. The energy of a crystal i, which is a direct neighbor of both PEDs' central crystals, is weighted by the ratio of the expected fraction of energy deposition according to the Molière theory. Here, the fraction of energy that is assigned to e.g. PED1 is [Sei10]:

$$E_{\text{PED1},i} = E_i \cdot \frac{E^{\text{cent.}}_{\text{PED1}} e^{-d_{i1}/r_M}}{E^{\text{cent.}}_{\text{PED1}} e^{-d_{i1}/r_M} + E^{\text{cent.}}_{\text{PED2}} e^{-d_{i2}/r_M}}, \tag{3.5}$$

where E_i is the measured energy in crystal i and d_{i1} and d_{i2} are the distances of crystal i to the central crystal of PED1 and PED2.
Two PED clusters are rarely detected in the MiniTAPS detector since it has a better polar angular resolution than the Crystal Barrel or forward detector. However, if a two PED cluster is present in the MiniTAPS detector the cluster energy is evenly divided between the two PEDs. Due to energy losses in insensitive material surrounding the crystals, the PED energy is usually smaller than the original particle energy. Therefore, energy correction functions were derived for both detectors based on comparisons of generated and reconstructed events in MC simulations [Mül18][Dah08]:

$$E^{\mathrm{CB/FD}}_{\mathrm{PED,corr}} = E^{\mathrm{CB/FD}}_{\mathrm{PED}} \left(f_{\mathrm{Landau}}(E^{\mathrm{CB/FD}}_{\mathrm{PED}}) + p_1 \cdot \left(1 - e^{-(E^{\mathrm{CB/FD}}_{\mathrm{PED}})^{p_2}/p_3} \right) + p_4 \cdot E^{\mathrm{CB/FD}}_{\mathrm{PED}} \right) \tag{3.6}$$

$$E^{\mathrm{MT}}_{\mathrm{PED,corr}} = E^{\mathrm{MT}}_{\mathrm{PED}} \left(p_0 e^{-\frac{1}{2}\left(\frac{E^{\mathrm{MT}}_{\mathrm{PED}} - p_1}{p_2}\right)^2} - p_3 e^{-p_4 {E^{\mathrm{MT}}_{\mathrm{PED}}}^{p_5}} + p_6 \cdot E^{\mathrm{MT}}_{\mathrm{PED}} + p_7 \right), \tag{3.7}$$

with $E^{\mathrm{CB/FD}}_{\mathrm{PED}}$ being a Crystal Barrel or forward detector PED energy, $E^{\mathrm{MT}}_{\mathrm{PED}}$ being a MiniTAPS PED energy and $p_1 \cdots p_7$ are fit parameters which strongly depend on the PED energy and polar angle θ of the located PED. Both functions contain a Gaussian/Landau function part together with a decreasing exponential function and a linear function.
All other detectors do not provide any energy information.

3.1.4 Particle angular information

3.1.4.1 Crystal Barrel, forward and MiniTAPS detector

The reconstruction of the impact point of a particle is done for the Crystal Barrel, the forward and MiniTAPS detectors in a similar way. In case the reconstructed PED consists of exactly one crystal hit, the θ and ϕ angles of the crystal center position relative to the target position are assigned to the PED. If the electromagnetic shower is spread over several crystals, a higher angular resolution is achieved through weighting each crystal position in spherical coordinates θ_i and ϕ_i with the weight $W_i = \max\{0, P + \ln \frac{E_i}{E_{\mathrm{PED}}}\}$ [Dah08] in the following way:

$$\theta_{\mathrm{PED}} = \frac{\sum_{i=1}^{n} W_i \cdot \theta_i}{\sum_{i=1}^{n} W_i} \qquad \text{and} \qquad \phi_{\mathrm{PED}} = \frac{\sum_{i=1}^{n} W_i \cdot \phi_i}{\sum_{i=1}^{n} W_i}. \tag{3.8}$$

The parameter P was determined for the Crystal Barrel and forward detector as $P = 4.25$ [Jun04] and for the MiniTAPS detector as $P = 4$ [Dah08] based on Monte Carlo simulations.

Since the MiniTAPS crystals are not mounted radially to the target position but are arranged horizontally flat, the θ angle obtained from the shower center does not give the correct impact point of a particle as demonstrated in Figure 3.5. Therefore, it is necessary to correct the x- and y-components of the shower center by a distance d and correct the polar angle θ by applying a shower depth correction as described in [Dah08].
Combining the energy and angular information of a PED, it is possible to calculate the four-momentum of a detected particle in spherical coordinates assuming it is a photon:

$$p_{\mathrm{PED}} = \begin{pmatrix} E_{\mathrm{PED}} \\ E_{\mathrm{PED}} \cos\phi_{\mathrm{PED}} \sin\theta_{\mathrm{PED}} \\ E_{\mathrm{PED}} \sin\phi_{\mathrm{PED}} \sin\theta_{\mathrm{PED}} \\ E_{\mathrm{PED}} \cos\theta_{\mathrm{PED}} \end{pmatrix}. \tag{3.9}$$

They are saved in form of *ExPlORA* containers of the according detector, namely *CBGammas, FWPlugGammas and MiniTAPSGammas*. In case the particle in question is not a photon but e.g. a proton the reconstructed four-momentum is wrong. Since protons often do not deposit their entire energy in the calorimeters but punch through the detectors, the reconstructed PED energy is not always correct. In addition, the applied energy correction function is only valid for

photons and does not give reasonable corrections for protons. Therefore, the energy information of a proton candidate is not utilized but only the angular information. Hence, it is not always possible to determine the correct four-momentum of a proton.

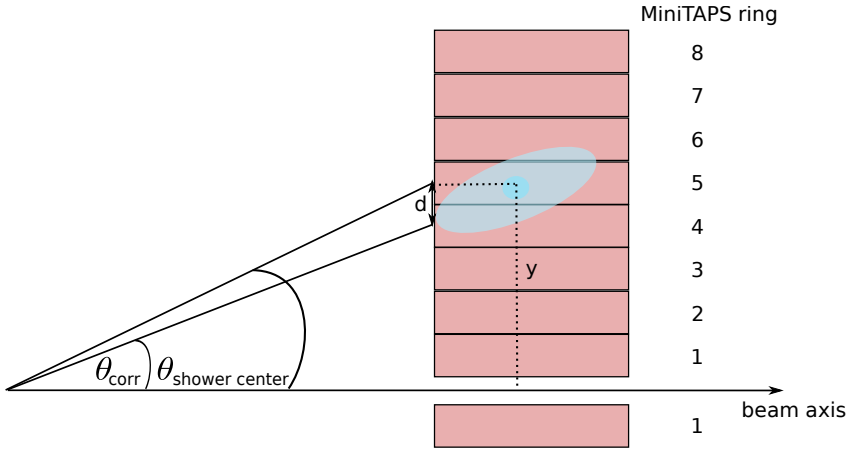

Figure 3.5: The reconstructed θ angle based on the shower center according to Equation (3.8) does not necessarily correspond to the correct impact point of a particle due to the horizontal alignment of the MiniTAPS crystals. The x- and y-coordinate of the determined shower center needs to be corrected by a distance d in order to calculate the correct polar angle θ.

3.1.4.2 Inner detector

Polar and azimuthal angles θ and ϕ are assigned to all routes of the inner detector. This is achieved through calculation of the intersection point of two timely coincident fiber clusters [GP08]. Here, the geometrical curve of each fiber is parametrized by an equation. More detailed information are given in [GP08].

3.1.5 Particle charge information

3.1.5.1 Inner detector

Depending on the number of inner detector layers that have registered the hit of a particle a charge quality value q is assigned to each detected particle. The value q is 2/3 if two and 1 if all three layers saw the hit. A cut of $q \geq 2/3$ is applied during the reconstruction. Using the θ and ϕ angular information, the routes are checked for correlation to reconstructed PEDs of the Crystal Barrel and forward detector. The angular correlation has to be smaller than 12° for the azimuthal angle ϕ and 12° for the polar angle θ[3] (compare upper row of Figure 3.6) which corresponds to the angular ranges covered by two Crystal Barrel crystals. In addition, a time correlation of 15 ns is demanded if a time information exists.

3.1.5.2 Forward detector vetoes

The scintillating plates of the forward detector are arranged in an overlapping manner. Only if at least two overlapping plates fired a signal it is saved as a cluster. Moreover, a time coincidence

[3] The polar angular correlation has to be optimized for the hydrogen target. More information are given in [Bar19].

within 20 ns is required. A charge quality is also assigned here to each cluster based on the number of plates that fired: $q = 0.45$ for one, $q = 1$ for two, $q = 0.75$ for three and $q = 0.5$ for more than three plates per cluster. A cut of $q > 0.45$ is chosen for the forward detector. For the correlation with the CsI(Tl) crystals further cuts are applied on the angular differences: $\Delta\phi \geq 14°$ and $\Delta\theta \geq 10°$ (compare bottom row of Figure 3.6).

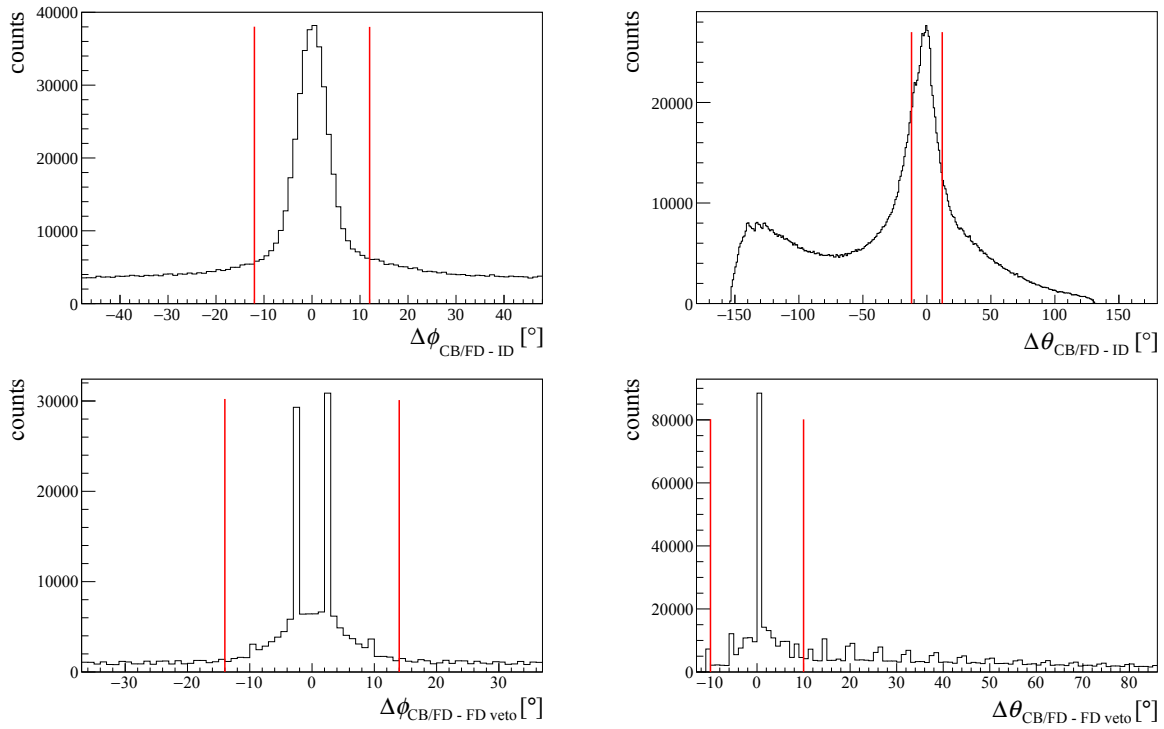

Figure 3.6: The angular correlation between inner detector (ID) and the Crystal Barrel (CB) or forward detector (FD) clusters are shown in the upper row. The bottom row depicts the polar and azimuthal angular difference between CB/FD and FD veto clusters. Since charged particles often make small clusters, e.g. only deposit their energy in one crystal, the impact point is reconstructed to the crystal center which leads to discrete peaks in the spectra. The applied cuts are displayed as red lines.

3.1.5.3 MiniTAPS vetoes

To correlate MiniTAPS veto clusters to MiniTAPS BaF_2 clusters, a spatial correlation of the impact points within the distance of 6.51 cm is required (see Figure 3.7) which corresponds to the outer diameter of a BaF_2 crystal. A time coincidence within 15 ns is demanded as well. Depending on the number of veto hits in a cluster a charge quality is assigned to each MiniTAPS veto cluster according to

$$q = \frac{1}{\text{number of veto hits per cluster}} \tag{3.10}$$

and marked as a charged hit. If no correlation is found, the MiniTAPS veto cluster is saved as a route. Figure 3.8 shows the charged quality q that is assigned to the reconstructed PEDs of the Crystal Barrel, forward and MiniTAPS detector. Using the charge information new

ExPlORA containers are formed: *Charged* and *UnCharged*. If one chooses to ignore the charge information, all PEDs are grouped to the *DontCareCharged* container.

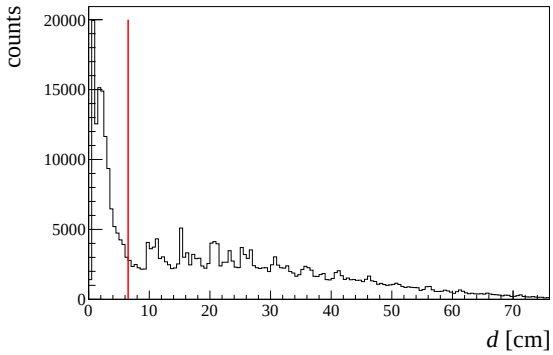

Figure 3.7: The distance of the impact points of MiniTAPS crystal and veto clusters is plotted. The applied cut is indicated by the red line.

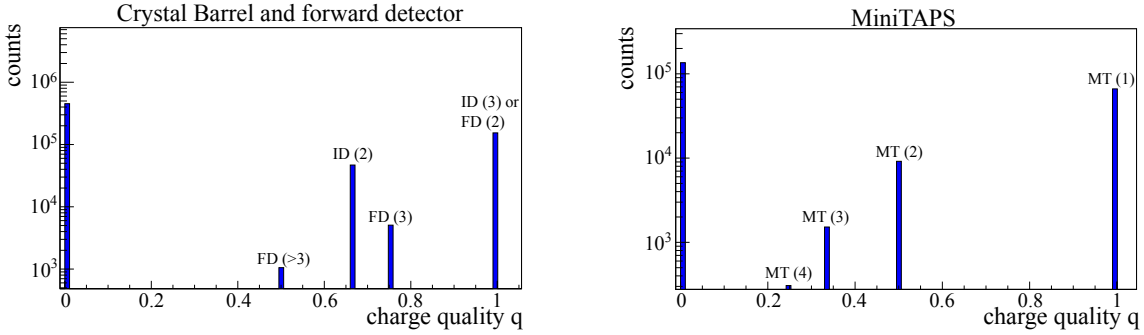

Figure 3.8: The charge quality q is plotted for all PEDs detected in the Crystal Barrel or forward detector (left) and in the MiniTAPS detector (right). The PEDs of the Crystal Barrel and forward detector are marked as charged if the inner detector (ID) has seen a hit in at least 2 layers or if two forward detector vetoes (FD) have registered a hit. For the MiniTAPS detector the charged quality is given according to Equation (3.10).

3.1.6 Particle time information

3.1.6.1 Tagger

The time of each beam photon is calculated by taking a weighted average value obtained from all involved fibers and bars per electron hit [Har08]:

$$t = \frac{w_{\text{fiber}} \cdot \sum_{i=1}^{n_{\text{fibers}}} t_i + w_{\text{bar}} \cdot \sum_{j=1}^{n_{\text{bars}}} t_j}{w_{\text{fiber}} \cdot n_{\text{fibers}} + w_{\text{bar}} \cdot n_{\text{bars}}}, \tag{3.11}$$

where the weights are determined using the corresponding time resolutions $w = 1/\text{FWHM}^2$ (compare Table 4.1), t_i and t_j are the measured times of the corresponding fiber i and bar j and n_{fibers} and n_{bars} are the total number of fibers and bars involved in the electron hit.

3.1.6.2 Inner detector

For the inner detector an average value of the individual hit fiber's time is taken.

3.1.6.3 Crystal Barrel, forward and MiniTAPS detector

For the forward and the MiniTAPS detector the time information of the central crystal element of a PED is assigned as the time of the PED[4].
Since the Crystal Barrel detector was read out with photo-diodes and therefore did not provide any time information, the neutral clusters of the Crystal Barrel detector do not have a time information[5]. However, if a charged particle passed the inner detector and also deposited energy in the Crystal Barrel detector, the time information provided by the inner detector is then assigned to the Crystal Barrel PED as well. Therefore, all charged particles have a time information.

3.1.7 Preselection of data

In order to avoid having to apply the detector calibrations and reconstruction procedure each time the data is analyzed, the data is saved as a reduced *ROOT* tree file after a preselection. The data is preselected based on the number of total reconstructed PEDs per event. This work only focused on two or three PED events since the decay modes $\pi^0 \to \gamma\gamma$ and $\eta \to \gamma\gamma$ [Pat+16] are used to reconstruct π^0 and η candidates. Additionally, a cut on each available final state particle's time is applied from $-20\,\text{ns}$ to $50\,\text{ns}$ to ensure that the particle is detected in time close to the trigger time at $0\,\text{ns}$. The cut is applied asymmetric due to jitter effects in the trigger signals [Har17].

[4] Charged particles, that are detected in the forward detector or MiniTAPS detector crystals, have two time information, one from the detector crystals and one from the vetoes. Since the time resolution of the detector crystals is better, the time information of the detector crystals is assigned to the charged particle.

[5] An exception exists for 2 PED clusters where one PED is detected in the forward detector and the other is assigned to a Crystal Barrel PED. The time information of the forward detector is then assigned to both PEDs. This only occurs in the θ angular range from 28° to 35°.

3.2 Event reconstruction using A2 data

3.2.1 Software

3.2.1.1 AcquRoot

The A2 collaboration uses mostly a self-developed software called *AcquRoot* which is, like *ExPlORA*, based on *ROOT* and uses *C++* programming. *AcquRoot* is structured in a hierarchy of classes that process the obtained raw data files and decode all ADC and TDC information of all detector elements and converts them into an energy and time information through application of detector calibrations. Each detector has its own class that handles the reconstruction of detector hits to identify clusters. Config files are used for each detector to specify useful information e.g. the number of detector elements, the number of neighboring detector elements and the analysis thresholds that can be applied. Once the individual detector reconstruction is finished, the detector information are combined to form particle tracks, e.g. the *TA2CentralApparatus* class relates clusters of the Crystal Ball detector to hits or clusters found in the PID and the MWPCs. The reconstructed particle tracks are saved with the *TA2GoAT* class in form of *ROOT* trees containing information about time, energy and angular information for each event. Moreover, useful information like the photon helicity and photon polarization degree and trigger pattern are saved as well.

3.2.1.2 Monte Carlo simulation

For the simulation of the A2 detector setup the *A2Geant* [ZWG15] simulation package was used which utilizes the *Geant4* [Ago+03] simulation package. It contains the Crystal Ball and the TAPS detectors, the PID and the MWPCs, but not the Cherenkov detector. Therefore, as a first step the existing setup in the simulation was extended by the Cherenkov detector. The steel frame and outer dimensions information of the Cherenkov detector were taken from existing CAD images. However, the dimensions of the parabolic mirror and the mirror frame had to be approximated using real life images of the Cherenkov detector. The results are depicted in Figure 3.9.

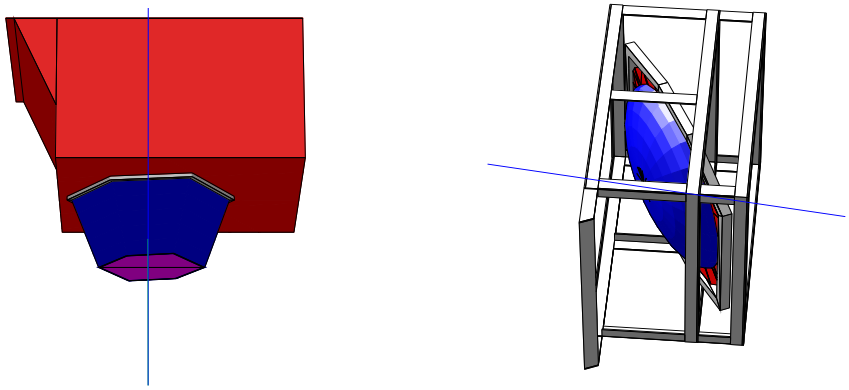

Figure 3.9: The simulated Cherenkov detector is shown here on the left from the top view looking from the target direction at the Cherenkov detector and on the right a top side view of the Cherenkov frame and the parabolic mirror inside the the detector. The blue line represents the z-direction.

As event generator the AcquMC software was used. 30×10^6 events were generated for the

reactions $\gamma p \to p\pi^0 \to p\gamma\gamma$ and $\gamma p \to p\eta \to p\gamma\gamma$ using phase space distributions for the final sate particles. In addition, several reaction channels can contribute as background in the analyzed data. A complete list of all simulated reactions are given in Table 3.2.

analyzed reaction	**simulated reactions**	**events**
$\gamma p \to p\pi^0$	$\gamma p \to p\pi^0$	30×10^6
	$\gamma p \to n\pi^+$	15×10^6
	$\gamma p \to n\pi^0\pi^+$	15×10^6
	$\gamma p \to p\pi^+\pi^-$	15×10^6
$\gamma p \to p\eta$	$\gamma p \to p\eta$	30×10^6
	$\gamma p \to p\pi^0$	30×10^6
	$\gamma p \to n\pi^+$	15×10^6
	$\gamma p \to n\eta\pi^+$	15×10^6
	$\gamma p \to p\eta\pi^-$	15×10^6
	$\gamma p \to p\pi^0\pi^0$	15×10^6
	$\gamma p \to p\pi^0\eta$	15×10^6

Table 3.2: Overview of the simulated reactions for the analysis of the A2 data.

The energy of the beam photons was distributed with a $1/E_\gamma$ dependence to account for the bremsstrahlung spectrum. The position of the reaction vertex was randomly chosen within a cylindical volume around the target center using the target and beam spot dimensions. The target position needed to be shifted from the center to $z = -0.33\,\text{cm}$ to match data of the May 2015 and September 2015 beamtimes[6].
The output *ROOT* files contain all particle's four-momenta and can be processed further with the *A2Geant* software which estimates the amount of energy each particle deposits in the sensitive detector elements of the A2 experimental setup. The deposited energies and the time information of each hit is saved as a *ROOT* file. It can be processed subsequently with *AcquRoot* like the data files. Furthermore, the deposited energies and time information were smeared to match the energy and time resolutions of the experimental data and the MC data were calibrated.
To account for the deflection of charged particles in the magnetic field of the target holding coil, a map of the magnetic field was used in the simulation (see Figure 3.10). There are two possibilities to change the polarization direction of the frozen spin target. Either the magnetic field direction or the frequency of the irradiating microwaves has to be changed. The first option causes charged particles to be deflected in opposite directions for the different target polarization directions. A comparison of the generated and the reconstructed azimuthal angle ϕ of protons shows a shift of around $\pm 0.6°$ (see Figure 3.11). Therefore, it was decided to take data only with the negative magnetic field direction and to change the frequency of the irradiating microwaves instead. Hence, it was not necessary to analyze the data with different target polarization directions separately. A match of data and simulation was achieved using the negative magnetic field map in the simulation.

[6] During the experiment an uncertainty remains regarding the precision with which the target is placed in the center of the Crystal Ball detector. Different target positions were simulated and the polar angle difference spectra (see Section 5.3.2.3) were used to ascertain the target position as achieved during each data taking period. While the target was positioned correctly at $z = 0\,\text{cm}$ for the November 2013 and May 2014 beamtimes, a shift occurred for the other two beamtimes.

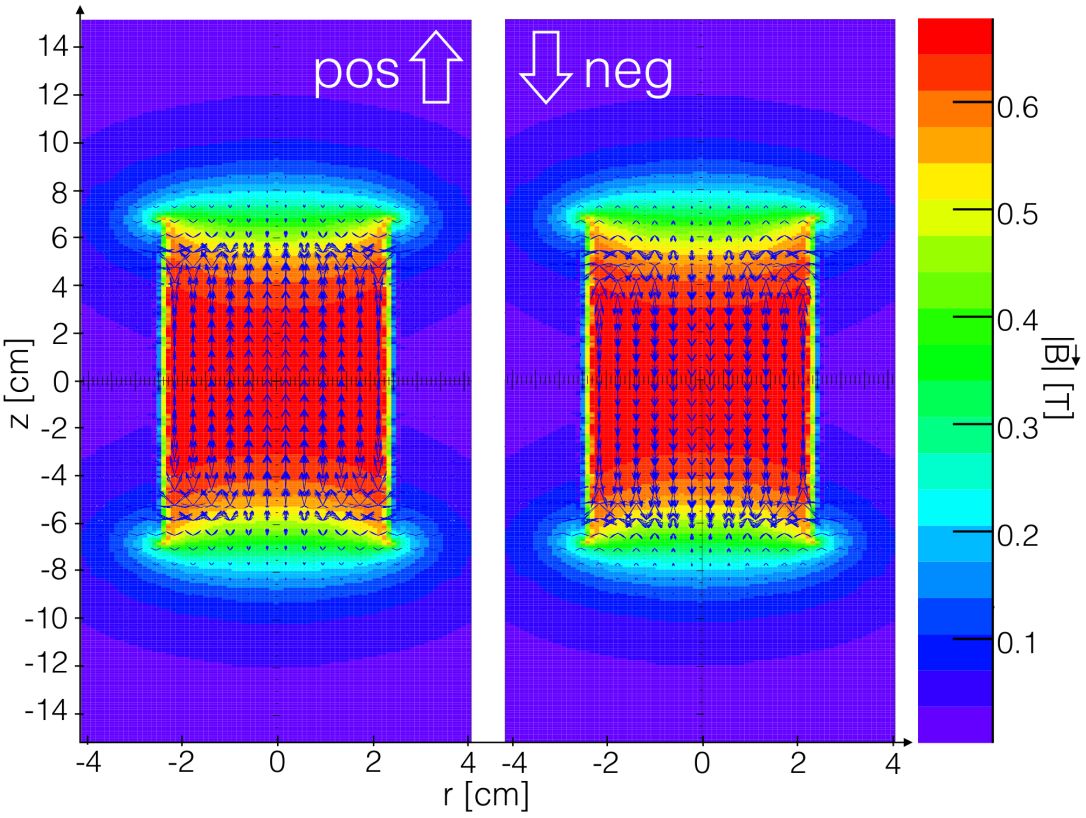

Figure 3.10: The simulated magnetic field map of the butanol target holding coil is shown as a function of the z-coordinate and the the distance from the target center in radial direction r for the magnetic field orientation in and against z-direction (pos and neg). Taken from [Die15].

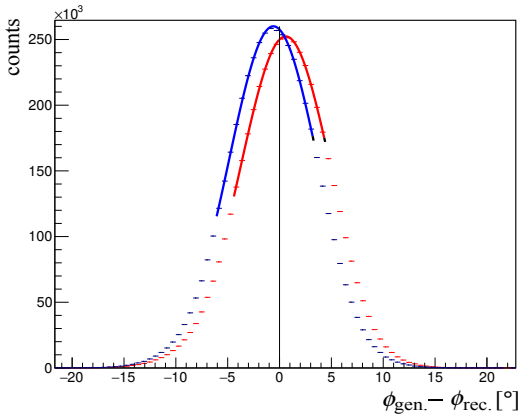

Figure 3.11: The difference of the generated and the reconstructed azimuthal angle ϕ of protons is plotted. It is caused by the magnetic field in $+z$-direction (red MC data points) and in $-z$-direction (blue MC data points). The red and blue lines represent Gaussian fits to the MC data. The magnetic field leads to a shift of around $\pm 0.6°$. The black line marks the 0° point.

Despite all these efforts it should be mentioned that the Monte Carlo data can not precisely reproduce experimental data since e.g. not all insensitive material is present in the simulated setup, especially in the Crystal Ball tunnel region [Wer14]. This leads to uncertainties in the calculation of detection efficiencies especially for low energetic protons.

3.2.2 Clustering of detector hits

3.2.2.1 Tagger

The multi-hit TDCs allow the reconstruction of up to eight hits in each tagger channel per event. A hit in the tagger requires the electron to have passed coincidentally two overlapping adjacent tagger ladders. A clustering of tagger hits is not performed since electrons pass up to two tagger ladders in general. Sometimes secondary delta electrons are produced which leave a signal in more than two adjacent tagger ladders and hence are cause for double counting. This needs to be accounted for in case a flux determination is needed. However, this work's aim is to extract asymmetries where such effects cancel out. Therefore, they were not considered in this work and no clustering of hits was performed. The energy and four momenta of each reconstructed beam photon is given by Equations (2.8) and (3.2).

3.2.2.2 Crystal Ball detector

The clustering of Crystal Ball hits is performed in the same way as for to the Crystal Barrel detector. The algorithm scans iteratively the nearest neighbors of a hit crystal for an energy deposition higher than 2 MeV. However, the algorithm search is limited to the maximal twelve direct neighbors since an electromagnetic shower is contained with a certainty of 98% [Wat05] within these twelve crystals which form a larger triangle (see Figure 3.12). In addition, each cluster needs to have a higher total energy than 15 MeV. A search for local maxima is not performed since the restriction to 13 crystal elements per cluster avoids having large clusters that could be originated from two particle tracks. Therefore, each cluster corresponds to exactly one particle.

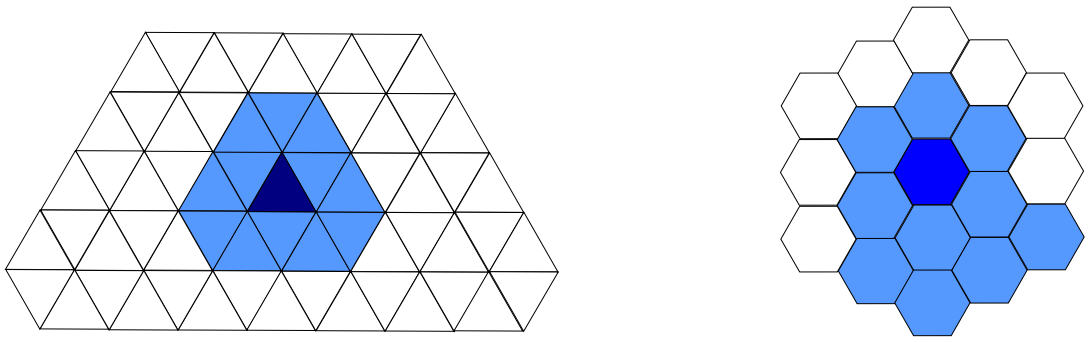

Figure 3.12: Left: A particle typically deposits energy in the Crystal Ball detector within twelve direct neighbors of a crystal (light blue). Right: An electromagnetic shower is spread over the typical six direct neighbor crystals of a TAPS crystal and a few adjacent crystals (light blue). The central cluster crystal is shown in dark blue.

3.2.2.3 PID

No cluster algorithm is used for the PID since a particle usually leaves a signal only in one of the 24 elements. The PID hits are required to have an energy deposition higher than 350 keV.

3.2.2.4 MWPCs

The clustering of all MWPCs hits is performed in the same way for both wire chambers. First a clustering of adjacent inner and outer cathode strips is done by grouping locally all hit strips and calculating the center of gravity of the cluster by determining the weighted average of all measured charge amplitudes $\bar{s}$:

$$\bar{s} = \frac{\sum_{i=1}^{N_s} c_i s_i}{\sum_{i=1}^{N_s} c_i}, \tag{3.12}$$

where s_i is the strip index and c_i is the measured charge amplitude of strip i and N_s is the total number of all hit strips within a cluster.
Additionally, all hit anode wires are locally grouped to clusters as well. The center of gravity of each wire cluster is given by the average value of all adjacent hit wire indexes:

$$\bar{w} = \sum_{i=1}^{N_w} w_i, \tag{3.13}$$

where w_i is the ith hit wire index and N_w is the sum of all hit adjacent wires of a cluster.
Afterwards, all possible combinations of intersection points between internal and external strip clusters are determined. In general each internal strip has two intersection points with an external strip. Only the inclusion of the anode wires allows an unambiguous determination of the intersection point (see Figure 3.13). At the end of the clustering procedure the reconstructed clusters from both wire chambers are combined to a particle track. However, a charged particle passing through the MWPCs does not always leave a hit signal in both wire chambers. Detailed information about all possible scenarios are given in [Spi19].
To reduce the possible combinations of internal strip, external strip and wire intersections and hence the possible reconstructed tracks using both wire chambers two conditions are demanded for the so called pseudo vertex which is the interpolation of the determined intersection point to the target center:

$$r_{\mathrm{PS}} \leq r_{\mathrm{max}} \tag{3.14}$$

$$-L/2 \leq z_{\mathrm{PS}} \leq L/2. \tag{3.15}$$

Here, r_{PS} and z_{PS} are the coordinates of the pseudo vertex in a cylindric coordinate system and r_{max} is chosen to be the radius and L the length of the butanol target. These conditions ensure that any possible reconstructed track lies within the dimensions of the MWPCs and the origin point of the track within the target volume. Since the MWPCs length exceeds the covered θ angle of the Crystal Ball detector an additional constraint is applied to the distance of both intersection points that are reconstructed in the two wire chambers. It should not exceed 0.55 cm in order to avoid correlations between the MWPCs and the TAPS detector.

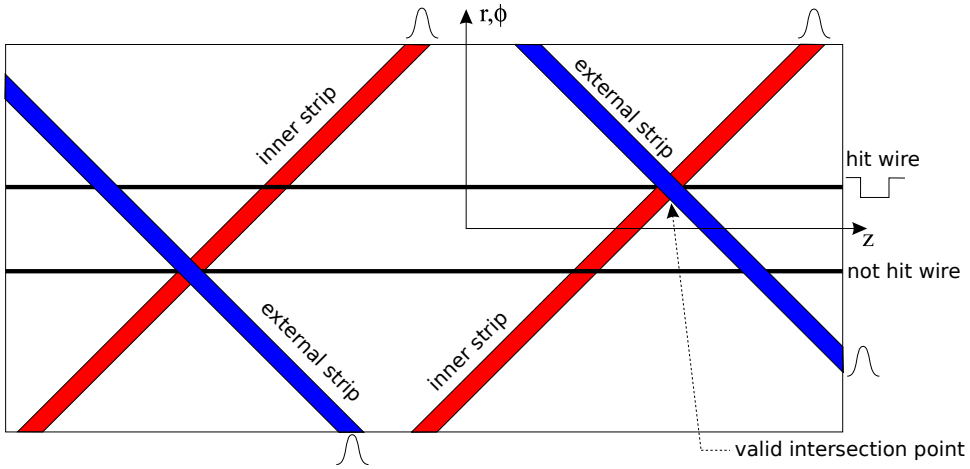

Figure 3.13: Schematic layout of the internal and external MWPCs cathode strips and the anode wires. Each internal strip has two intersection points with an external strip. The additional information of the wires helps to resolve this ambiguity. Adapted from [Lan04].

3.2.2.5 TAPS detector

The clustering algorithm of the TAPS detector is performed in the same way as for the Mini-TAPS detector. A TAPS hit is required to have a higher energy deposition than 3-5 MeV which is set through CFDs. A threshold of 20 MeV is applied to the total cluster energy. Unlike the Crystal Ball cluster algorithm no limit is set on the maximal number of hit elements per cluster (see e.g. Figure 3.12).

3.2.2.6 TAPS vetoes

A threshold of 150-300 keV is set for the TAPS veto LEDs defining a hit. Similar to the PID no clustering is needed as particles usually deposit their energy in only one veto element.

3.2.3 Particle energy information

3.2.3.1 Crystal Ball and TAPS detector

Each cluster that is reconstructed in the Crystal Ball or TAPS detector has an energy information which is determined through the sum of all cluster crystal energy depositions according to Equation (3.3).

3.2.3.2 PID

The energy of a PID hit is weighted by the polar angle θ_{CB} of the corresponding Crystal Ball cluster since particles passing through the PID traverse a larger distance for lower or higher polar angles than for $\theta = 90°$:

$$\Delta E_{\mathrm{PID}} = \Delta E_{\mathrm{PID},i} \cdot \sin\theta_{\mathrm{CB}}. \tag{3.16}$$

$\Delta E_{\mathrm{PID},i}$ is the deposited energy in PID element i. In this way the deposited energy is normalized to the distance d_{PID} which is the distance for $\theta = 90°$ (see Figure 3.14).

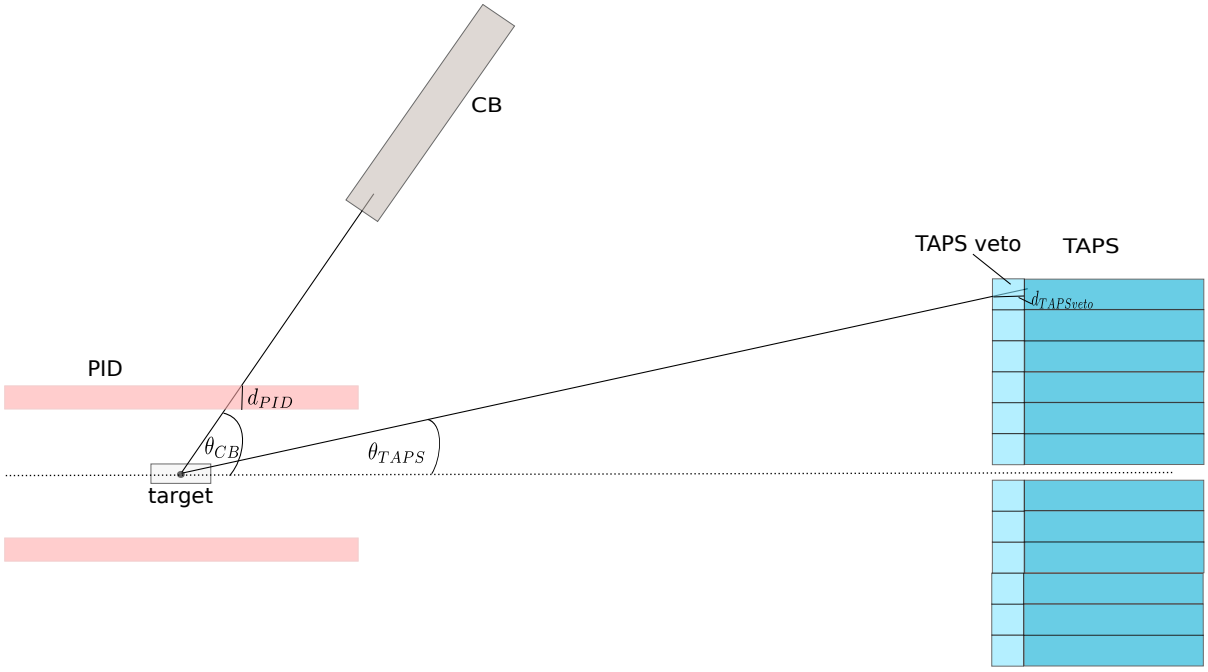

Figure 3.14: The deposited energy in PID or TAPS vetoes is corrected by $\sin\theta_{\mathrm{CB}}$ or $\cos\theta_{\mathrm{TAPS}}$ in order to normalize the deposited energy to the distances d_{PID} and $d_{\mathrm{TAPS\ veto}}$.

3.2.3.3 MWPCs

The MWPCs strips are not thick enough to achieve a high resolution $\Delta E - E$ spectrum like it is possible with the PID. Nevertheless, the deposited energy of a charged particle in the MWPCs strips can be used to make a very rough charged particle identification. The deposited energy E_{MWPCs} is given by the sum of all energy depositions within a MWPCs cluster.

3.2.3.4 TAPS vetoes

All veto elements that are in front of a TAPS cluster element are checked for a hit. The maximal deposited energy in one of these veto elements is saved as the veto energy $\Delta E_{\mathrm{TAPS\ VETO}}$. Additionally the veto energy is weighted by $|\cos\theta_{\mathrm{TAPS}}|$ of the according TAPS cluster:

$$\Delta E_{\mathrm{TAPS\ VETO}} = \Delta E_{\mathrm{TAPS\ VETO},i} \cdot |\cos(\theta_{\mathrm{TAPS}})|, \tag{3.17}$$

where $\Delta E_{\mathrm{TAPS\ VETO},i}$ is the energy of veto element i that contains the maximal energy deposit and that belongs to one TAPS cluster element. This ensures the comparability of the veto energies independent of the particle path through a veto element (see Figure 3.14).

3.2.4 Particle angular information

3.2.4.1 Crystal Ball detector

The flight direction of a particle detected in the Crystal Ball detector is reconstructed by weighting each crystal position $\vec{r}_i$ with the root of the corresponding energy deposition E_i:

$$\vec{r} = \frac{\sum_{i=1}^{n} \sqrt{E_i} \cdot \vec{r}_i}{\sum_{i=1}^{n} \sqrt{E_i}}. \tag{3.18}$$

3.2.4.2 TAPS detector

The impact point position in θ and ϕ of a particle detected in TAPS is calculated utilizing Equation (3.8) with a parameter of $P = 5$, which was determined using Monte Carlo simulations [Mol92].

3.2.4.3 PID

The PID only provides information about the azimuthal angle ϕ of a detected particle but gives no information about the polar angle θ. Therefore, no particle track is reconstructed based on the PID alone. The PID hits are matched to the reconstructed Crystal Ball clusters by demanding an azimuthal angle difference of less than $\pm 15^\circ$ since each PID element covers $360^\circ/24 = 15^\circ$ in the azimuthal angle ϕ. Due to the bad angular resolution of the PID detector, the ϕ and θ angles of the reconstructed Crystal Ball cluster are taken to reconstruct the particle track.

3.2.4.4 MWPCs

As already mentioned it is possible to reconstruct two trajectory points using both wire chamber information. The combined vector gives a θ and a ϕ angular information. All reconstructed MWPCs tracks are checked for correlation to PID hits and Crystal Ball clusters. Here, a cut is applied on the azimuthal angle difference between the PID and the MWPCs hit at $\pm 50^\circ$ and between the MWPCs and Crystal Ball cluster at 20° if both MWPCs reconstructed an intersection point and at 60° if only one MWPC registered the hit. Additionally, a cut is applied on the opening angle between the MWPCs track and the Crystal Ball cluster position at $\pm 20^\circ$. If a correlation is successfully found, the θ and ϕ angles provided by the MWPC are assigned to the reconstructed particle since the MWPCs angular resolution is better than the Crystal Ball resolution. If the MWPCs are not used in the analysis, the Crystal Ball angles are utilized.

3.2.5 Particle charge information

3.2.5.1 PID and MWPCs

Charged tracks are only saved in *AcquRoot* if a correlation of a PID and/or a MWPCs hit with a Crystal Ball cluster is found as described in Section 3.2.4.3 and Section 3.2.4.4. Additionally, only MWPCs or PID-MWPCs correlated tracks without a cluster in the Crystal Ball detector are saved as well as charged tracks.

3.2.5.2 TAPS vetoes

To correlate a TAPS veto hit to the TAPS BaF_2 clusters all cluster crystals's vetoes are checked for hits. If at least one of these vetoes has registered a hit within the time window of ± 16 ns, it is saved as a charged cluster.

3.2.6 Particle time information

The time of the central crystal of a cluster is taken as the particle's time. All reconstructed particles have a time information.

3.2.7 Preselection of data

The output *ROOT* files from *AcquRoot* were further processed with the *Generation of Analysis Trees* (*GoAT*) analysis software [Col15] developed by Cristina Collicott and Phil Martel. *GoAT* was first of all used to reduce the amount of events that need to be accessed during physics analysis procedure in order to save time. Since this analysis focuses on the π^0 and η mesons in the final state, only events containing two or three final state particle tracks were analyzed further.

4 Calibration of detectors

In order to reconstruct all particle's four-momenta it is necessary to relate the recorded raw digital ADC and TDC values to physical properties such as the deposited energy, time and spatial information. In Section 4.1 the calibration procedure steps, as applied to the CBELSA/TAPS raw data, are explained. In Section 4.2 all time and energy calibration steps are given for each detector of the A2 experiment.

4.1 Calibration procedure using CBELSA/TAPS data

The calibration process of the CBELSA/TAPS data was divided into three parts for the analyzed beamtimes: time calibration of all detectors, energy calibration of the Crystal Barrel and the energy calibration of the MiniTAPS detector. The time calibration of all detector components was performed by Jan Hartmann [Har08], while the Crystal Barrel energy calibration was carried out by Jonas Müller [Mül18]. Within the scope of this thesis, a new root macro was written in order to improve the existing MiniTAPS energy calibration software.

4.1.1 Time calibration

The goal of the time calibration is the assignment of the same time to simultaneously measured hits provided that the hits originated from photons which travel at the speed of light. Thereby the time of flight of photons to the different distant detectors is not considered. This means an electron detected in the tagger and any final state photon detected in the Crystal Barrel, in the forward detector or in the MiniTAPS detector are defined to be simultaneous [Har08].
All timing signals of detector hits were recorded with Single- or Multi-Hit-TDCs. TDCs measure time intervals between a start and a stop signal and give a digital output signal, that is proportional to the measured time interval and is saved in the form of a channel value. As a start signal the trigger time is used while the stop signal is given by the according detector element that registered a hit. Only for the MiniTAPS detector, where Single-Hit TDCs are used, this is reversed.
All detectors of the CBELSA/TAPS experiment, except for the MiniTAPS detector, use Multi-Hit CATCH TDCs that count the pulses of a voltage-controlled oscillator during the time measurement [Har08]. The voltage is regulated with the help of a phase-locked loop (PLL). This ensures that the output frequency remains stable and thus the TDC channel width corresponds to a fixed time interval. Knowing the channel width, it is possible to convert the TDC channel $\mathrm{ch}_{\mathrm{TDC}}$ to a physical time: $t = g_{\mathrm{TDC}} \cdot \mathrm{ch}_{\mathrm{TDC}}$ using a conversion factor g_{TDC}. The CATCH TDCs have a known conversion factor of $g_{\mathrm{TDC}} = 0.114\,42\,\mathrm{ns/ch}$ [Har08]. Through coupling of two TDC channels the conversion factor of the 96 tagger bars and the GIM detector is reduced by a factor of two to $g_{\mathrm{TDC}} = 0.057\,21\,\mathrm{ns/ch}$ [Har08]. The MiniTAPS TDCs, however, do not use a reference frequency for synchronization. Therefore, the conversion factors can be different for each MiniTAPS detector element TDC. On average the conversion factor was $g_{\mathrm{TDC}} = 0.1\,\mathrm{ns/ch}$. Detailed information about the determination process is given in [Har08].

In order to account for different cable lengths and different processing time of the electronic components, time offsets o are determined for each detector element and the time is corrected by them: $t = g_{\mathrm{TDC}} \cdot \mathrm{ch}_{\mathrm{TDC}} + o$. As a first step, all prompt peaks of the TDC spectra are moved to 0 ns in order to roughly align all detector elements in time. For a precise determination of the offsets the time differences of two detector hits are used. This has the advantage that the trigger time, which can be affected by jitter effects, cancels out and a much better time resolution is achieved: $t_1 - t_2 = t_{\mathrm{det1}} - t_{\mathrm{trigger}} - (t_{\mathrm{det2}} - t_{\mathrm{trigger}}) = t_{\mathrm{det1}} - t_{\mathrm{det2}}$. Since the Cherenkov detector has a good time resolution and consists of a single channel, it is used as a reference detector to calibrate the tagger bars. Afterwards, the tagger bars are used as a reference to calibrate the remaining detectors since a Cherenkov signal is not necessarily present for each event. Table 4.1 gives an overview of the time resolutions of all detectors.

detector	**time resolution FWHM [ns]**
Scint. bars of tagger	0.635 ± 0.003
Scint. fibers of tagger	1.694 ± 0.006
Scint. fibers of inner detector	2.093 ± 0.013
CsI crystals of forward detector	1.861 ± 0.016
Vetos of forward detector	4.434 ± 0.013
BaF_2 crystals of MiniTAPS	0.872 ± 0.006
Vetos of MiniTAPS	3.06 ± 0.05
CO_2 - Cherenkov	1.194 ± 0.014
PbF_2 crystals of GIM	3.1 ± 0.3

Table 4.1: Overview of the time resolution of the different detectors using the tagger bars as reference [Har08].

All timing analog signals are first digitized with the help of a discriminator before they are passed to the TDCs. For the forward detector Leading-Edge-discriminators are used which lead to a pulse height dependence and thus, an energy dependence of the output signal. Therefore, the measured time needs to be corrected by an energy dependent factor $f(E)$:

$$t = g_{\mathrm{TDC}} \cdot \mathrm{ch}_{\mathrm{TDC}} + o + f(E). \tag{4.1}$$

For the MiniTAPS detector CFDs are used which already correct this effect at hardware level.

4.1.2 Energy calibration

Deposited energy in the Crystal Barrel or MiniTAPS detector is measured by integrating an analog signal over a certain amount of time and thus producing a measurable electrical charge which is approximately proportional to the deposited energy. The measured charge is assigned to a digital channel with the help of QDCs. Due to the linear relationship between the ADC channel $\mathrm{ch}_{\mathrm{ADC}}$ and the deposited energy, the deposited energy E is then given by:

$$E = g_{\mathrm{ADC}} \cdot (\mathrm{ch}_{\mathrm{ADC}} - \mathrm{ped}), \tag{4.2}$$

where g_{ADC} is the conversion gain and ped the pedestal which marks the channel with zero deposited energy. The conversion gain factor depends on the crystal, the used wavelength

shifter, pre-amplifier and ADC and needs to be determined individually for all detector elements [Bös06].

4.1.2.1 Crystal Barrel and forward detector energy calibration

The Crystal Barrel and the forward detector are both equipped with 12 bit dual-range ADCs ($2^{12} = 4096$ channels) [Mül18]. These ADCs possess two energy ranges and are therefore capable of measuring low energies of only a few MeV in the low range as well as high energy depositions of up to 2 GeV in the high range with a high energy resolution. Technically this is realized by damping large incoming signals with a ratio of 1:8 before digitizing them. The switching between low and high range is done for the Crystal Barrel detector at about 125 MeV and for the forward detector at about 260 MeV. For both energy ranges the knowledge of the pedestal position and the conversion gain factor is important in order to convert the measured ADC channel $\mathrm{ch}_{\mathrm{ADC}}^{\mathrm{low}}$ or $\mathrm{ch}_{\mathrm{ADC}}^{\mathrm{high}}$ to a physical energy. For this purpose light pulses generated by a Xenon flash lamp are guided to the CsI crystals via light guides. The utilization of 13 different filter combinations leads the damping of the light transmission by known factors and the comparison to the corresponding measured ADC channel values.

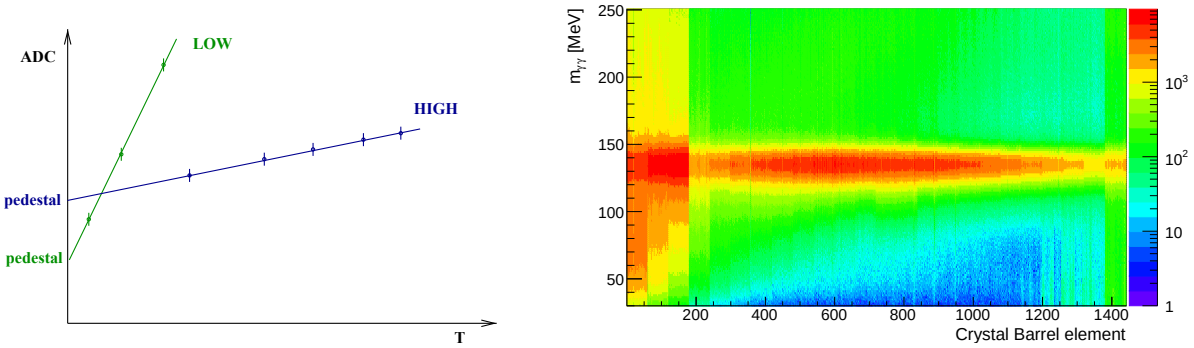

Figure 4.1: Left: The ADC channels are plotted for different light transmissions T of the Xenon flash lamp. The green line shows the correlation for the low range and the blue line for the high range of the dual-range ADCs. Taken from [Bös06]. Right: The two photon invariant mass $m_{\gamma\gamma}$ versus the Crystal Barrel detector elements is shown as an example for the September 2013 beamtime. The first three rings (from element 1 to 180) form the forward detector. Together with the last ring they each consist of 30 crystals which cover 12° in the polar angle ϕ, twice as much as the other crystals. The forward detector is subject to higher electromagnetic background which is visible at lower invariant masses.

Figure 4.1 shows on the left the correlation between the ADC channels and the different light transmissions T of the Xenon flash lamp for both low and high range. Linear fits to the data points are used to obtain the conversion gains g_{low} and g_{high} which are given by the slopes of the linear functions. The pedestal positions $\mathrm{ped}_{\mathrm{low}}$ and $\mathrm{ped}_{\mathrm{high}}$ of both ranges are determined using separate pedestal runs, which were taken regularly during the beamtimes. The low range energies E_{low} are calculated according to Equation (4.3). The ratio of the two gain factors g_{LP} is used to determine the high range energies E_{high} as given in Equation (4.4) [Bös06].

$$E_{\mathrm{low}} = g_{\mathrm{ADC}}(\mathrm{ch}_{\mathrm{ADC}}^{\mathrm{low}} - \mathrm{ped}_{\mathrm{low}}) \tag{4.3}$$

$$E_{\mathrm{high}} = g_{\mathrm{ADC}}(\mathrm{ch}_{\mathrm{ADC}}^{\mathrm{high}} - \mathrm{ped}_{\mathrm{high}}) \cdot g_{\mathrm{LP}}, \quad g_{\mathrm{LP}} = \frac{g_{\mathrm{high}}}{g_{\mathrm{low}}}. \tag{4.4}$$

During the beamtimes special light-pulser runs were taken that allowed the monitoring of the gain ratio g_{LP}. It is approximately $g_{\mathrm{LP}} \approx 1/8$. The light-pulser system has been renewed recently by using LED light instead of the Xenon flash lamp in order to reduce data taking time of the light-pulser runs. More information are given in [Urb17].

For a precise determination of the conversion gain g_{ADC}, two uncharged PEDs detected in the Crystal Barrel and/or the forward detector are combined and their two photon invariant mass squared is calculated using the deposited energies of both photons $E_{\gamma 1}$ and $E_{\gamma 2}$ and the opening angle between the two photons $\alpha_{\gamma_1,\gamma_2}$:

$$m^2_{\gamma\gamma} = 2E_{\gamma 1}E_{\gamma 2}(1 - \cos\alpha_{\gamma_1,\gamma_2}). \tag{4.5}$$

Using the well known π^0 mass as a reference point, new gain factors g_{new} are determined for each central PED element (see Equation (4.6)) by comparing the fitted π^0 peak position $m_{\gamma\gamma,\mathrm{fit}}$ to the PDG π^0 mass of $m_{\pi^0,\mathrm{PDG}}$ =134.977 MeV [Pat+16]:

$$g_{\mathrm{new}} = g_{\mathrm{old}} \cdot \left(\frac{m^2_{\pi^0,\mathrm{PDG}}}{m^2_{\gamma\gamma,\mathrm{fit}}} \cdot (1-d) + d \right). \tag{4.6}$$

Here, g_{old} is the initial gain factor and d is a damping factor. Afterwards, the data is reanalyzed with the new gain values and iteratively the π^0 peak positions are shifted to the desired PDG value. The damping factor is needed in case all gain factors are systematically shifted in one direction. Figure 4.2 shows the deviation of the determined π^0 peak position from the desired $m_{\pi^0,\mathrm{PDG}}$ value for each performed iteration in case of using a damping factor (right) and without a damping factor (left). In both cases the scattering of the π^0 peak mean values is significantly reduced until the last iteration. The deviation from the desired π^0 peak position oscillates from positive to negative values from one to the next iteration. However, the average π^0 peak position remains systematically shifted if no damping factor is used. Utilizing a damping factor leads to a damped oscillation of the average π^0 peak position around the desired value and convergence is achieved after several iterations. A damping factor of $d = 0.3$ was used for the Crystal Barrel and forward detector energy calibration [Mül18].

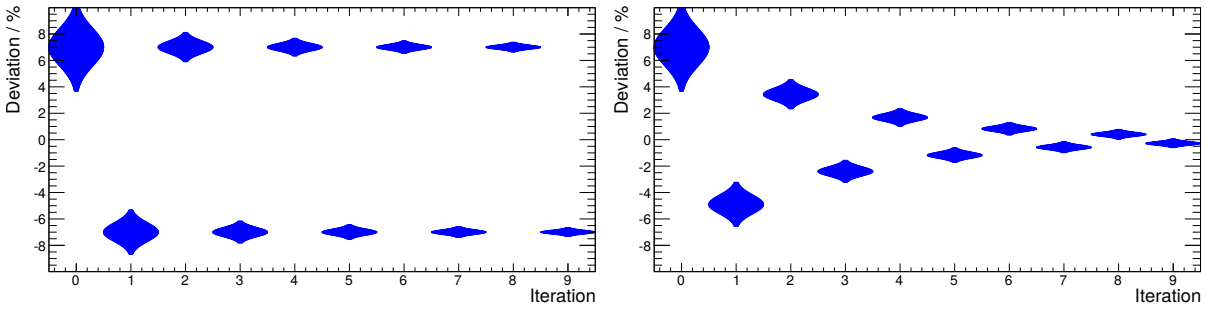

Figure 4.2: The deviations of the reconstructed π^0 peak position to the desired PDG value is depicted for several iterations. In case all gain values are systematically shifted in one direction and no damping factor is used, the systematic deviation of the reconstructed π^0 peak position remains (left). With the damping factor the mean position of the π^0 peak performs a damped oscillation around the desired value and reduces the deviation after several iterations. Taken from [Mül18].

On average the gain value is $g = 0.0826$ for the forward detector and $g = 0.033$ for the

Crystal Barrel detector elements [Mül18]. Figure 4.1 shows on the right the result of the energy calibration for the September 2013 beamtime. On average the π^0 mass peak is located at 134.973 ± 0.010 MeV after the calibration [Mül18]. This agrees with the PDG π^0 mass with a deviation of significantly less than 1%.

4.1.2.2 MiniTAPS energy calibration

Deposited energies in the MiniTAPS detector are also calculated according to Equation (4.2). Before data acquisition a rough energy calibration is performed in order to be able to set all discriminators thresholds correctly. Due to the horizontal alignment of the MiniTAPS crystals and their exact same shape and size, cosmic muon radiation is suitable for this purpose. When passing through the MiniTAPS crystals, cosmic muons lose energy via ionization according to the Bethe-Bloch formula. They deposit on average an energy of 37.6 MeV as minimum ionizing particles over the diameter of 5.9 cm for each BaF_2 crystal [Röb91]. This is used as a reference point together with the pedestals to perform the rough energy calibration of MiniTAPS. While the cosmic calibration may be precise enough to determine the energy in the low MeV range, a precise calibration procedure is performed after data taking to get a more precise gain calibration for energy depositions of several hundred MeV which is the case for the desired reactions $\gamma p \to p\pi^0/p\eta$. The next paragraphs describe in detail the pedestal and gain calibration procedures.

Pedestal calibration During each data run a pulser with a frequency of 1 Hz was used to trigger the readout of the BaF_2 crystals. In the case of no real energy signal being measured by the BaF_2 crystals, the QDCs start integrating the noise of the system (Gaussian around 0 MeV) for the given times of the slow and fast gates.

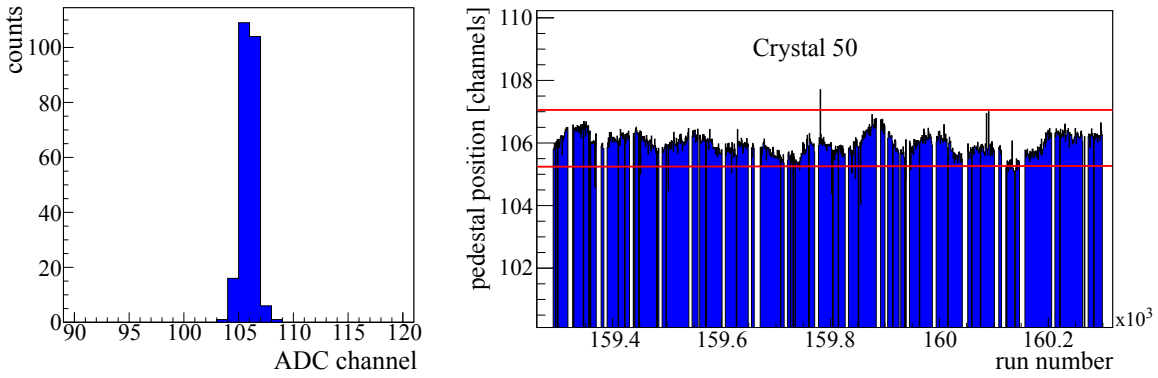

Figure 4.3: Left: The raw ADC spectrum is shown for MiniTAPS element 50 selecting only pulser entries. A pedestal peak is visible at around ADC channel 106. Right: The pedestal position of MiniTAPS element 50 is shown in dependence of the run number during the September 2013 beamtime. The fluctuations are related to temperature fluctuations in the experimental hall.

The output QDC channels correspond to an energy deposition of 0 MeV and determine the pedestal position. The pulser entries can be selected in the data through specification of the pulser trigger condition. A typical ADC spectrum containing only the pulser entries is shown in Figure 4.3 on the left. With the help of a Gaussian fit the pedestal position was determined for each MiniTAPS detector element. The pedestal positions were monitored throughout the

beamtimes. Figure 4.3 shows the pedestal position for MiniTAPS detector element 50 for the September 2013 beamtime. The pedestal position fluctuates due to temperature changes in the experimental hall and are therefore determined for each run. Overall, the pedestal position of MiniTAPS element 50 did not differ by more than 2 ADC channels for the duration of 3 weeks of beamtime.
The high rates (12 MHz in the GIM detector) used in the analyzed beamtimes revealed that not enough statistics is obtained for a precise pedestal determination of the inner MiniTAPS ring elements when using a 1 Hz pulser frequency. Utilizing the pulser during the spill break of ELSA solves the problem. This method was successfully applied during the beamtimes from November 2013 to January 2014. Alternatively, it is possible to take separate pedestal runs for a few minutes with the pulser as trigger.

Gain calibration To obtain a precise gain calibration, the invariant mass of two photon candidates (uncharged PEDs), one detected in the Crystal Barrel and the other detected in the MiniTAPS detector, is calculated (see Equation (4.5)). This requires the Crystal Barrel and the forward detector energy calibration to be finished. The π^0 peak position is iteratively shifted towards the PDG π^0 mass by determining new gain values according to Equation (4.6) using a damping factor of $d = 0.3$ similar to the case of the Crystal Barrel detector. The initial gain values are taken from the cosmic calibration. In order to have enough statistics for a precise fit for all MiniTAPS elements, this calibration process is not applied on a run-by-run basis, but several runs are accumulated. According to J. Müller's investigations [Mül18] it is reasonable to combine runs of around one month together for a precise calibration. If one chooses larger subsets of data, the variation of the π^0 peak position over time becomes larger than the statistical uncertainty of the determined peak position. Based on these findings, the analyzed data were divided into four data sets for the calibration process according to the four months (July, August, September and October). In the framework of this thesis a new root macro was written with the main goal of automatically fitting all invariant mass spectra successfully. This goal was achieved employing the following strategy:

- Choice of fit function: The π^0 invariant mass squared was fitted with a Novosibirsk function of the form [Got+09]

$$f(m) = A \cdot e^{0.5\left(\ln^2\left(1+\Lambda\tau\cdot(m-m_{\text{peak}})\right)/\tau^2+\tau^2\right)} \quad \text{with} \quad \Lambda = \frac{\sinh(\tau\sqrt{\ln(4)})}{\sigma\tau\sqrt{\ln(4)}}, \tag{4.7}$$

  where A describes the amplitude, m_{peak} the π^0 peak position, σ the peak width and τ the tail of the peak. A simple Gaussian can not be used since the peak shape deviates from a Gaussian by having a tail to lower masses which is caused by energy losses in insensitive material between the crystals or at the edge of the detector. A Chebychev polynomial of third degree is used for the description of the background. This choice of this fit function additionally ensures that any occurring systematic effects in the energy calibration of the MiniTAPS detector are in the same order as the ones for the Crystal Barrel detector where the same fit function is used.

- Fitting procedure: First the background is fitted with a Chebychev polynomial within the ranges [low1,low2] and [high1,high2] that exclude the π^0 peak range (see Figure 4.5 on the right). Then the background is subtracted and a Novosibirsk function is fitted

to the remaining events. To evaluate if a fit was successful, several parameters e.g. the χ^2/ndf and the fit parameters were monitored. The success rate of the fit of the spectrum is highly dependent on the chosen ranges that are set to fit the background which are indicated by the red lines in Figure 4.5 on the right. Since the invariant mass spectra are very similar in each hexagonal MiniTAPS ring due to the geometrical symmetry of the detector, the ranges were set individually for each ring. This enabled an automatized fitting procedure with a very high success rate of nearly 100%[1].

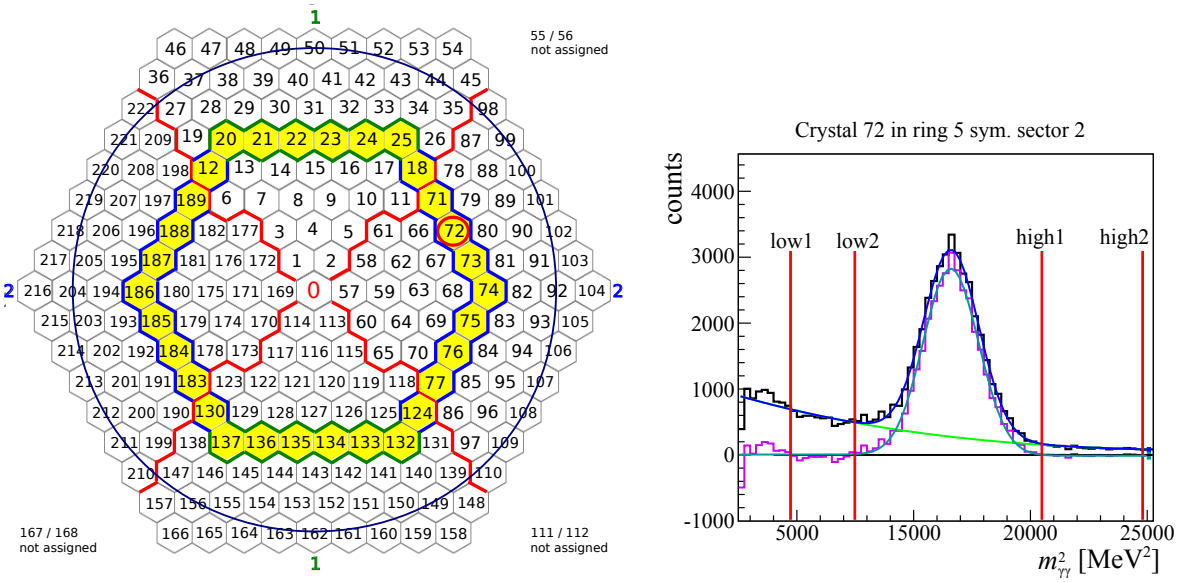

Figure 4.4: Left: The MiniTAPS detector can be divided into 8 different hexagonal rings. Ring 5 is highlighted in yellow. Each MiniTAPS ring can be segmented into two symmetric sectors: 1 (up and down part of the ring) and 2 (left and right part of the ring). The black circle indicates the opening cone of the forward detector. Adapted from [Dah08]. Right: The obtained fit result is shown for the MiniTAPS element 72 which is located in ring 5 in the symmetry sector 2. The green line represents the fit to the background performed between ranges [low1,low2] and [high1,high2] and the blue line the fit to the background subtracted histogram (violet).

- Customizability: In case of a failed fit result the macro offers several possibilities: The user can choose to refit the spectrum by setting new fit ranges for the background fit. Thereby, it is sometimes prudent to reset the ranges for an entire ring, or subsector of a ring based on the ring symmetry. They are referred to as the symmetry sectors 1 and 2 (see Figure 4.4). To facilitate the setting of the fit ranges and avoid setting them individually for each MiniTAPS element, the user can choose the according option (see upper left corner in Figure 4.5).

Employing this strategy the fit results are satisfactory for almost all MiniTAPS elements. Exceptions consist of the innermost and the outermost elements as highlighted in yellow in Figure 4.6.

[1] In the past, the success rate was only around 70% since only one fit range was used for all elements. For the remaining 30% of the MiniTAPS elements the ranges had to be set individually and the fit repeated which was a time consuming tedious work.

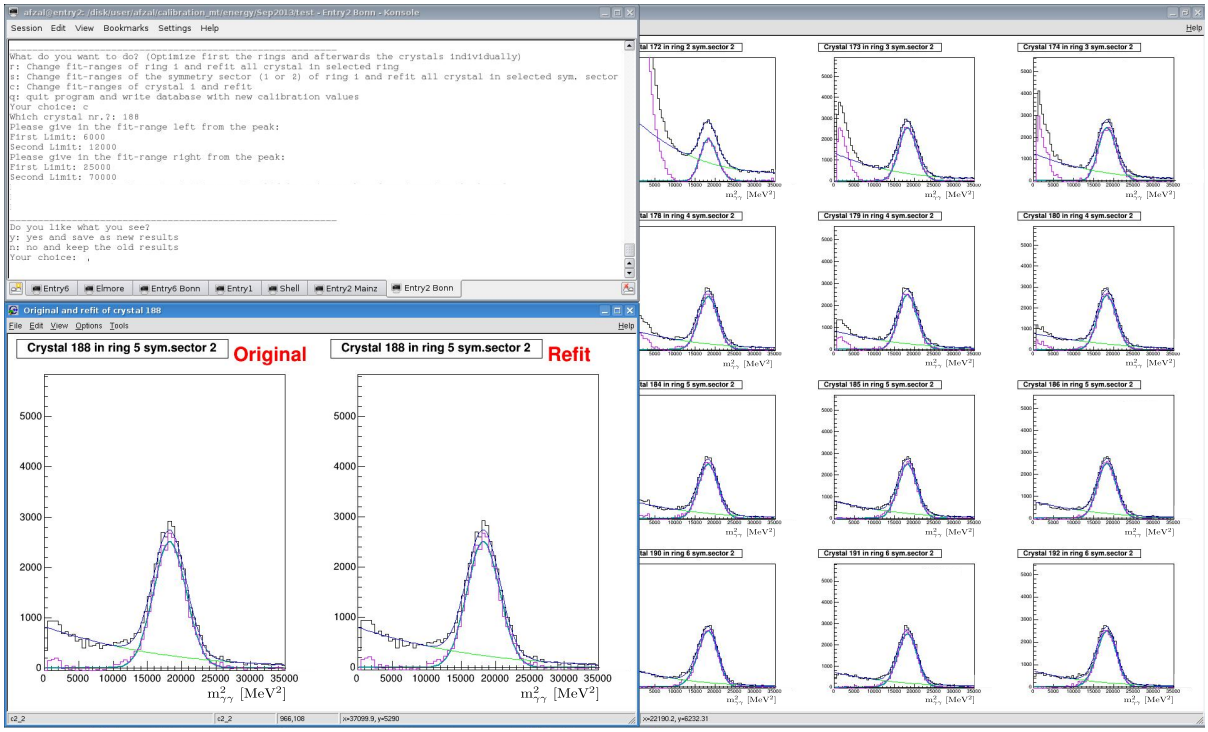

Figure 4.5: Overview of the MiniTAPS energy calibration macro. It is controlled via the terminal as shown in the upper left side. In the background (right side) some of the fit results are displayed. It is possible to refit the spectrum of a MiniTAPS element and compare it to the previous result (lower left side).

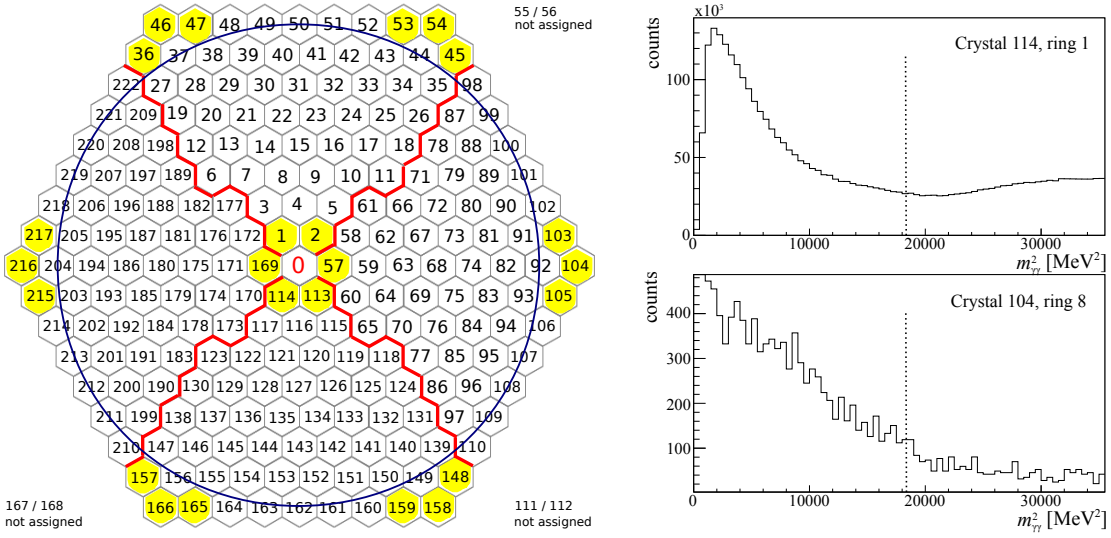

Figure 4.6: Left: The innermost MiniTAPS ring and the outermost crystals are highlighted here in yellow. Adapted from [Dah08]. Right: Two invariant mass spectra are shown as examples for ring 1 and ring 8, demonstrating that a fit can not be performed since a π^0 peak is not present at the expected value of $m^2_{\gamma\gamma} \approx 18\,219\,\mathrm{MeV}^2$ (dotted line).

While the elements of the innermost ring are subject to a large amount of electromagnetic

background, the outermost elements do not have enough π^0 candidates for a successful fit since the opening cone of the forward detector is smaller than the detector as indicated by the circle in Figure 4.4 and 4.6. Figure 4.6 shows on the right two spectra for the innermost and outermost crystals where a π^0 peak is not visible. For those elements the new gain value is set using the gain values from the cosmic calibration and assuming that on average the gain of all elements have changed similarly:

$$g_{\text{new}} = g_{\text{cosmics}} \cdot \frac{1}{n} \sum_{i=1}^{n} \frac{g_{\text{fit},i}}{g_{\text{cosmics},i}}, \tag{4.8}$$

where $g_{\text{fit},i}$ is the gain value of the i-th element obtained through a successful fit and $g_{\text{cosmics},i}$ being the according gain value taken from the cosmic calibration and n represents the number of MiniTAPS elements minus the innermost and outermost elements as highlighted in Figure 4.6 on the left.

Quality check At the end of the calibration procedure the π^0 and η mass peak resolutions for each MiniTAPS ring were determined (see Figure 4.7 and Table 4.2).

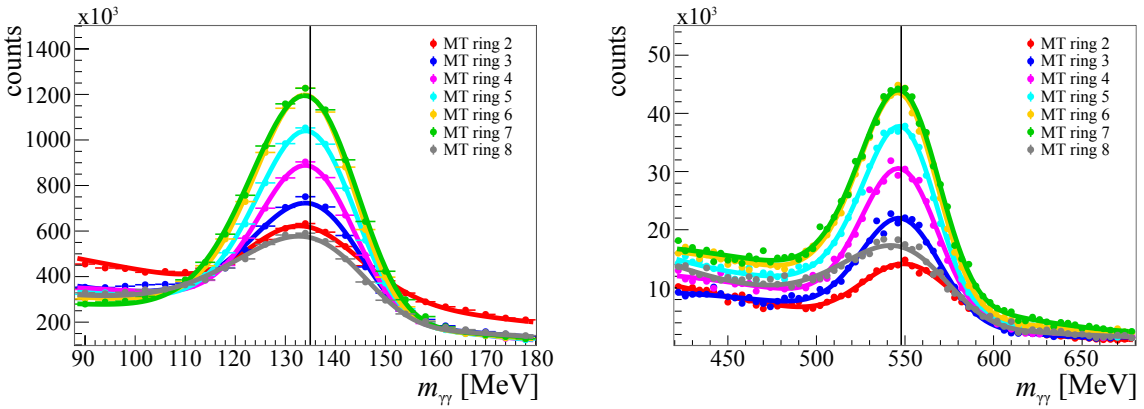

Figure 4.7: The two photon invariant mass, using one photon detected in the Crystal Barrel and the other one in the according MiniTAPS ring, is depicted for each MiniTAPS ring. The mass range around the π^0 mass of 134.977 MeV [Pat+16] is shown on the left and around the η mass of 547.862 MeV [Pat+16] on the right.

It is noteworthy that the best mass resolution is achieved for the MiniTAPS rings 4-6 with roughly FWHM = 22 MeV for the π^0 and FWHM = 54 MeV for the η invariant mass peak. Meanwhile rings 2, 3, 7 and 8 have a worse mass resolution. Here, ring 8 is the worst with 30 MeV for the π^0 and 70 MeV for the η invariant mass peak. The reason for this behavior is that in the central rings of the MiniTAPS detector the clusters are fully contained, while the inner and outer two rings sometimes only cover a part of the electromagnetic shower of a particle. As a result the invariant mass peaks are broader and have a larger tail towards lower masses. In addition, the deviations of the peak positions to the PDG mass values were determined, which are less than 1%, indicating a successful calibration.
As demonstrated in Figure 4.2 the deviation of the average π^0 peak position to the PDG mass value performs a damped oscillation. After eight iterations the deviations are systematically below the PDG mass (see Table 4.2). Applying another iteration would lead to a systematic shift above the expected π^0 mass value. Since the deviations are already less than 1% not more

than eight iterations were done.

ring	m_{π^0} [MeV]	dev. to PDG	FWHM$_{\pi^0}$ [MeV]	m_η [MeV]	dev. to PDG	FWHM$_\eta$ [MeV]
2	133.85 ± 0.03	0.8%	25.74 ± 0.07	551.98 ± 0.12	0.8%	66.64 ± 0.40
3	134.87 ± 0.02	0.1%	24.77 ± 0.05	547.89 ± 0.11	0.01%	58.77 ± 0.16
4	134.44 ± 0.01	0.4%	21.95 ± 0.02	547.74 ± 0.09	0.02%	53.78 ± 0.11
5	134.41 ± 0.01	0.4%	22.70 ± 0.02	547.42 ± 0.08	0.08%	54.89 ± 0.14
6	134.18 ± 0.01	0.6%	22.91 ± 0.02	547.17 ± 0.08	0.1%	53.92 ± 0.09
7	134.09 ± 0.01	0.7%	24.54 ± 0.02	547.64 ± 0.08	0.04%	55.95 ± 0.12
8	133.98 ± 0.02	0.7%	29.62 ± 0.05	545.36 ± 0.17	0.5%	69.84 ± 0.02

Table 4.2: The achieved π^0 and η mass resolution are listed for each MiniTAPS ring together with the relative deviation from the PDG mass values.

All in all, it can be said that a reliably working root macro was written for the MiniTAPS energy calibration that automatically fits all invariant mass spectra successfully within a few minutes, and thus, enables a fast and reliable fitting procedure. In the future a graphical interface will facilitate the energy calibration of the Crystal Barrel and the MiniTAPS detector further [Sal16; Got19].

4.1.2.3 Tagger energy calibration

In order to assign an energy to a hit found in the scintillating bars or fibers of the tagger an energy calibration was performed. Thereby, different low intensity beams of ELSA with known energies (E_0 = 650 MeV, 800 MeV, 1270 MeV, 1800 MeV and 2400 MeV) were guided directly, without the presence of a radiator, to the scintillating bars and fibers of the tagger. In addition, the magnetic field of the tagger magnet was varied to get more data points. Through polynomial fits to the data an energy is assigned to a hit in the scintillating bar or fiber (see Figure 4.8).

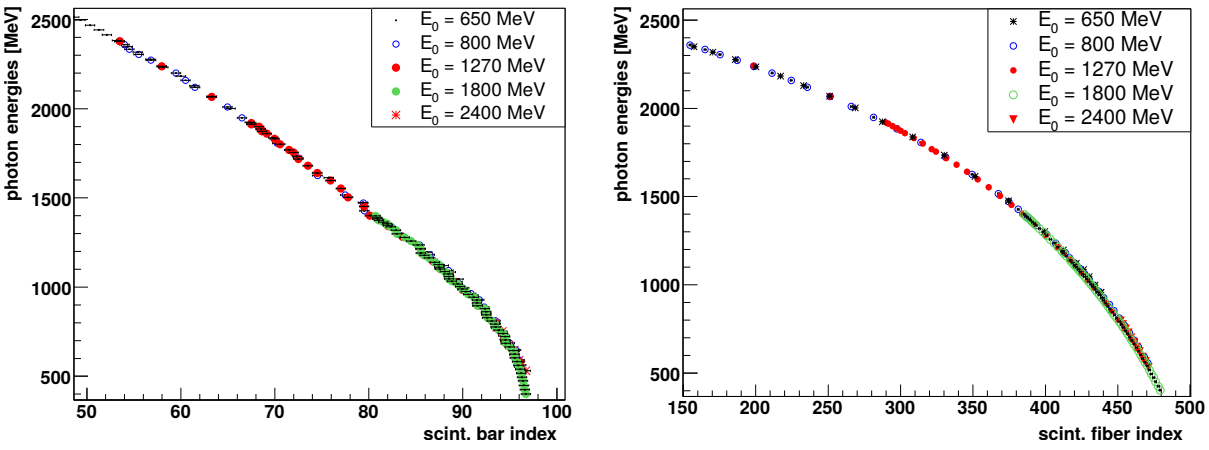

Figure 4.8: The beam photon energy is depicted as a function of the tagger bar (left) and the tagger fiber (right) index. Data was taken for several ELSA energies E_0 and for different tagger magnetic field strengths. Taken from [FP09].

4.2 Calibration procedure using A2 data

The calibration of the A2 data was performed using the *CaLib* software [Wer+13; Wer14] provided by the University of Basel group. The raw data was analyzed and necessary histograms were produced using the *AcquRoot* physics class *TA2MyCaLib*. A Graphical User Interface (GUI) within *CaLib* allows to display the relevant spectra and evaluate the fit results for each detector element. After each iteration, new calibration parameters are calculated based on the fit results and saved to a database.
All five beamtimes were calibrated in cooperation with Karsten Spieker and Peter Pauli, whereas most of the November 2013, May 2014 and May 2015 beamtime calibration steps were performed by this author. The calibration was done using the *CaLib* software, but the fitting functions and the fitting procedure were improved before the start of the calibration.
The following sections give an overview of the different steps involved in the time and energy calibration of all detector components exemplarily for the May 2015 beamtime. Each beamtime data was divided into subsets whenever a longer break due to e.g. target change occurred due to related temperature changes.

4.2.1 Time calibration

Similar to the CBELSA/TAPS time calibration procedure, the aim of the time calibration lies in determining the time offsets o and the conversion gains g_{TDC} in order to convert a given detector TDC channel $\mathrm{ch}_{\mathrm{TDC}}$ to a time information: $t = g_{\mathrm{TDC}} \cdot (\mathrm{ch}_{\mathrm{TDC}} - o)$. The tagger, Crystal Ball and PID CATCH TDCs as well as the TAPS $PbWO_4$ and TAPS VETO TDCs have a fixed gain as listed in Table 4.3.
The TAPS TDC gains were determined before the start of the November 2013 beamtime by Tigran Rostomyan using the TAPSMaintain software. The applied procedure consists of delaying the TDC stop signal with the help of different long cables and thus by fixed amount of times. Several runs were taken in the TAPS Standalone mode and the channel number of the TAPS pedestal pulser signals have a linear relation to the set time delays. The slope of a linear fit allows the extraction of the TDC gains for every TAPS detector element.

detector	**measured time**	$\mathbf{g_{TDC}}$ **[ns/ch]**
Tagger	$t_{\mathrm{trigger}} - t_{\mathrm{detector,\ elem}}$	0.117
CB	$t_{\mathrm{trigger}} - t_{\mathrm{detector,\ elem}}$	0.117
PID	$t_{\mathrm{trigger}} - t_{\mathrm{detector,\ elem}}$	0.117
TAPS (BaF_2)	$t_{\mathrm{detector,\ elem}} - t_{\mathrm{trigger}}$	0.10
TAPS ($PbWO_4$)	$t_{\mathrm{trigger}} - t_{\mathrm{detector,\ elem}}$	0.10
TAPS vetos	$t_{\mathrm{detector,\ elem}} - t_{\mathrm{trigger}}$	0.05

Table 4.3: The time of each detector element hit $t_{\mathrm{detector,\ elem}}$ is measured in reference to the trigger time t_{trigger}. The fixed gain values of the Multi-Hit TDCs of the tagger, Crystal Ball (CB), PID, the TAPS vetos and TAPS ($PbWO_4$) are taken from [Mar13]. Average TDC gain values of TAPS (BaF_2) are given.

With all TDC gains known, only the offsets o remain to be determined for all detector elements. The offsets are adjusted in a way that time differences between all elements of one detector are zero and that simultaneous hits of different detectors have the same time. This can be best

achieved by using two photon candidate clusters whenever possible since photons travel with the speed of light.
It is important to note that all detector times t_{det} are measured to a reference time, the trigger Level 1 time t_{trigger}. Depending on the detector which measured the hit, t_{trigger} either starts or stops the time measurements. Table 4.3 gives an overview of the time measurement for all detectors. For the calibration of the TDC offsets it is important to combine the time information of different detectors in the correct way to cancel out the trigger time, especially since either the Crystal Ball or the TAPS detector could have been responsible for the trigger and because the trigger time could be affected by jitter effects.
As a first step all time peaks of all detectors are roughly shifted to 0 ns. Then the Crystal Ball, PID, TAPS and Veto detector elements are aligned in time with respect to themselves. Subsequently, simultaneous tagger and TAPS hits are aligned. In the end the Crystal Ball detector is aligned in time to the tagger and thus also to the TAPS detector.

4.2.1.1 Crystal Ball time offset calibration

For the determination of the Crystal Ball time offsets a two dimensional histogram was filled with the time difference between all possible two neutral clusters (no PID hit) detected in the Crystal Ball detector $\Delta t_{\mathrm{CB}} = t_{\mathrm{CB},i} - t_{\mathrm{CB},j}$ versus the Crystal Ball central cluster element number (see Figure 4.9 left) with i and j being two different Crystal Ball element numbers. During calibration the projected time difference spectrum of each element is fitted with a Gaussian for the coincident peak and a linear function for the background. The peak positions p_i are used to calculate new offset values $o_{\mathrm{new},i}$:

$$o_{\mathrm{new},i} = o_{\mathrm{old},i} + \frac{p_i}{g_i}, \tag{4.9}$$

where g_i is the gain of the element and $o_{\mathrm{old},i}$ the old offset value.

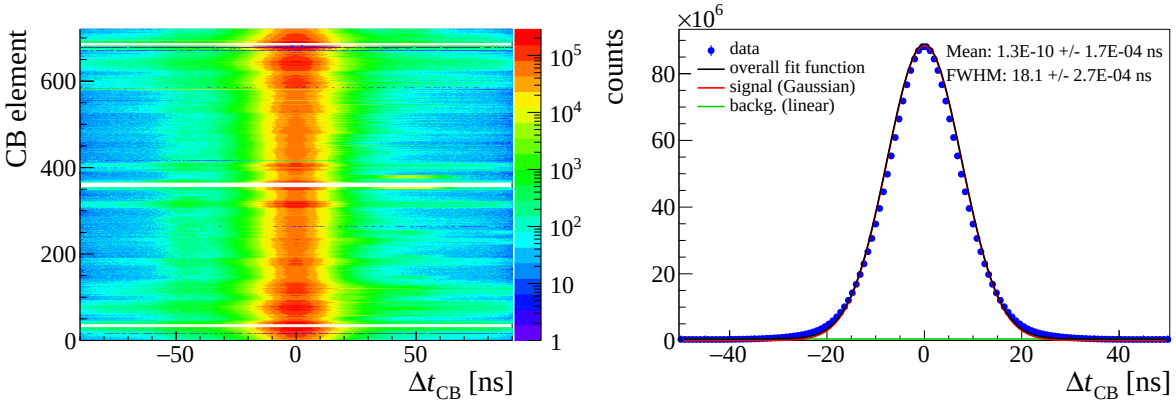

Figure 4.9: Left: Time difference of two CB elements vs. CB elements. Right: Projection of the CB time difference summed over all elements together with a combined Gaussian and linear function fit describing the spectrum.

Since the time differences are always dependent of two detector elements, this calibration step was done iteratively until all time coincidence peaks were aligned to 0 ns. The fit of the projected time difference integrated over all Crystal Ball elements gives an average time resolution of

FWHM=18.2 ns (see Figure 4.9 right). This time resolution is improved further through a time walk correction (see Section 4.2.1.5).

4.2.1.2 PID time offset calibration

The PID time offset calibration is done similar to the CB time calibration, only now all combinations of two charged hits have to be used for calculating the time differences. Figure 4.10 shows on the left the time of two PID hits plotted against the according PID elements and on the right the time difference spectrum summed over all 24 PID elements. After several iterations, a time resolution of FWHM=3.4 ns was achieved.

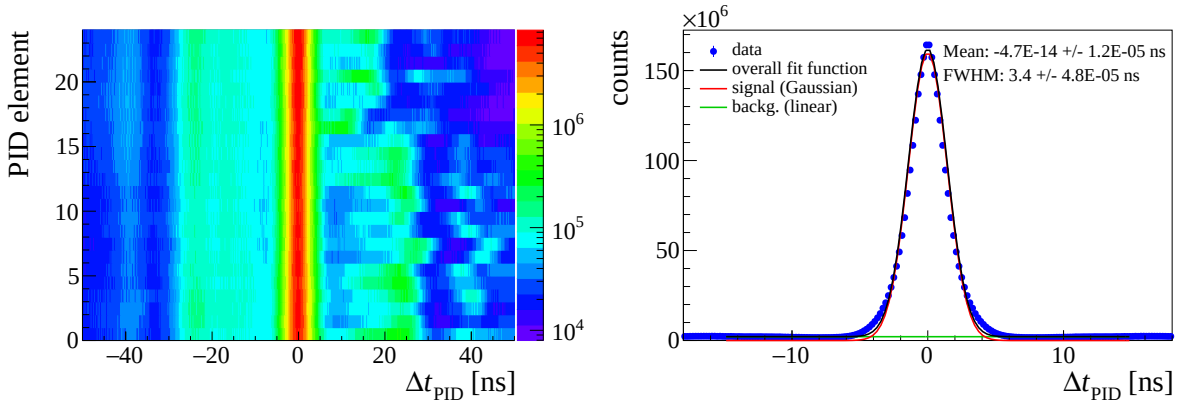

Figure 4.10: Left: Time difference of two PID hits versus the PID elements. Right: PID time difference spectrum summed over all elements (blue points). A Gaussian (red line) and linear (green line) fit function describe the spectrum (black line).

4.2.1.3 TAPS and veto time offset calibration

Similar to the Crystal Ball calibration, a histogram was created plotting the time difference between all combinations of two neutral hits in TAPS, that left no signal in the vetoes, versus the central cluster element number, respectively for both neutral hits (see Figure 4.11 left).

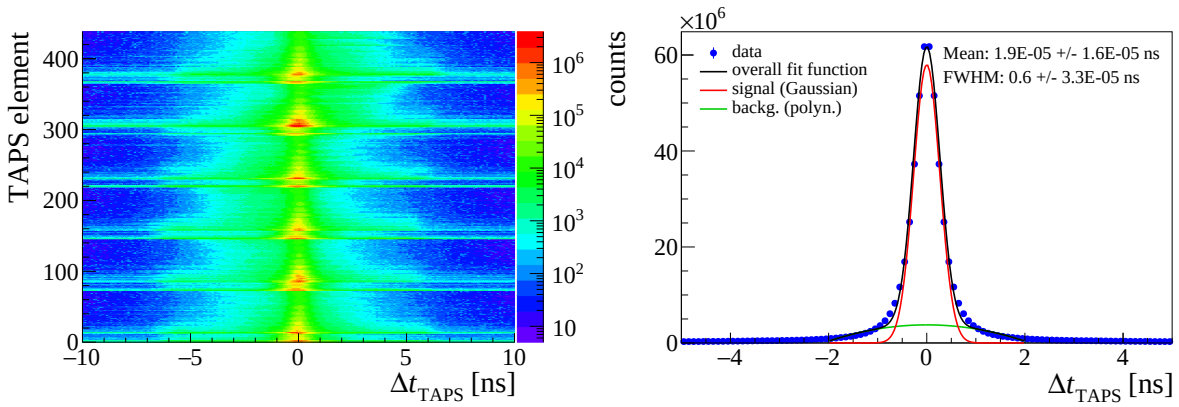

Figure 4.11: Left: Time difference between two neural TAPS hits versus the TAPS elements. Right: TAPS time difference spectrum summed over all elements is shown (blue points). A Gaussian (red line) and a polynomial (green line) function describe the spectrum (black line).

The peak positions of the resulting time difference spectra of all TAPS elements are fitted with Gaussians for the time peaks and polynomials for the background. New offset values are calculated using the old and new peak positions according to Equation (4.9). After seven iterations all peaks could be aligned to 0 ns. In comparison to the Crystal Ball detector, the TAPS detector has a notably better time resolution of 0.6 ns.
The veto time calibration is performed in the same way as the PID TDC offset calibration by fitting the time difference spectra of all possible VETO hits (see Figure 4.12). The time resolution of the vetoes of 3.4 ns is comparable to the PID time resolution as both detectors are scintillation detectors of type EJ-204 and are read out by photomultipliers.

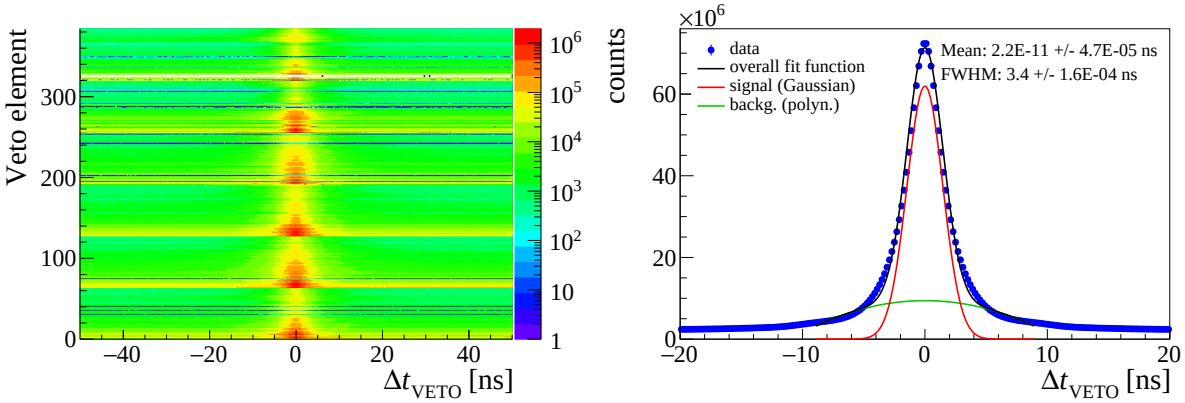

Figure 4.12: The 2D histogram (left) shows the time difference of all possible two VETO hits against the corresponding veto element number. The time difference spectrum (blue points) is fitted with a Gaussian (red line) and a polynomial (green line). The overall fit function is shown in black.

4.2.1.4 Tagger time offset calibration

Since the TAPS detector has a much better time resolution than the Crystal Ball detector, the TAPS detector is well suited to be used as a reference detector in order to calibrate the tagger time. For this purpose the time differences between all tagger hits and all neutral hits in TAPS are calculated and plotted against the corresponding tagger elements of the hits (see Figure 4.13). The $PbWO_4$ elements are not used here, so that the TAPS and tagger hit times needed to be added up in order for the trigger time to cancel out (see Table 4.3):

$$\begin{aligned} & t_{\mathrm{TAGGER}} + t_{\mathrm{TAPS}} \\ & = t_{\mathrm{trigger}} - t_{\mathrm{TAGGER,elem}} - t_{\mathrm{TAPS,elem}} - t_{\mathrm{trigger}} \\ & = t_{\mathrm{TAPS,elem}} - t_{\mathrm{TAGGER,elem}}. \end{aligned} \tag{4.10}$$

The coincident time peak of tagger and TAPS hits is fitted with a Gaussian function. As not just one but up to 100 tagger hits are assigned to each event depending on the tagger rate, an evenly distributed, flat background of random hits is visible around the coincident peak which is described with a linear function. The remaining background at the left side of the time coincident peak is fitted with a polynomial of 3rd degree (see Figure 4.13 right). This background is most likely to be attributed to neutral TAPS hits that are not originating from photons but probably from neutrons or from falsely neutral assigned proton hits since nucleons with a low energy can have a time of flight of up to 13 ns before they reach the TAPS detector.

Note: The tagger elements of section H (see Figure 4.13) were turned off during most of the runs of the May 2015 beamtime.

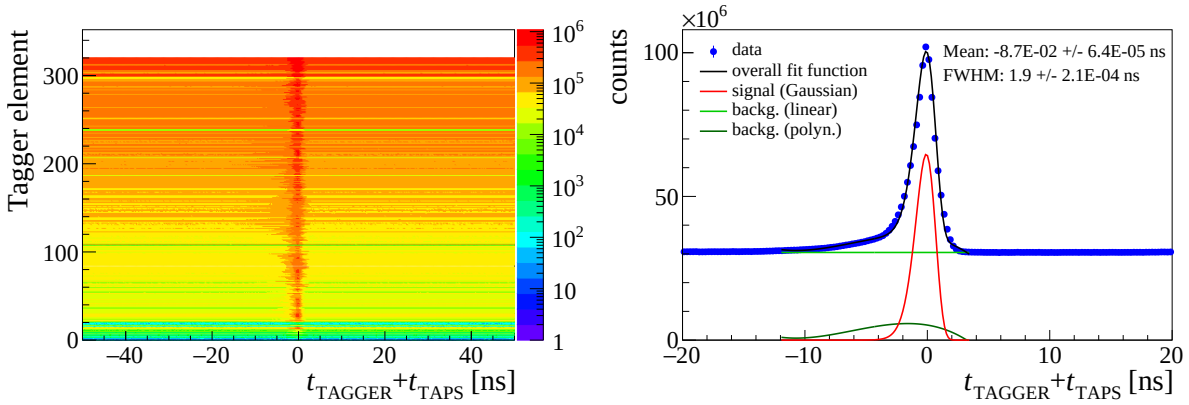

Figure 4.13: The 2D histogram (left) shows the time differences of all tagger hits and all neutral TAPS hits against the corresponding tagger element number. The time difference spectrum summed over all elements (blue points) is fitted with a Gaussian function (red line) for the coincident peak and a linear function (green line) and polynomial of 3rd degree (dark green) for the background. The overall fit function (black line) describes the spectrum well.

After only one iteration, the time coincident peaks of tagger and TAPS hits are moved to 0 ns as the tagger hit elements do not depend on each other since no clustering of tagger hits is done. The time resolution was determined as FWHM=1.9 ns.

4.2.1.5 Crystal Ball time walk correction

The time of a Crystal Ball hit is not independent of the deposited energy because of the slow rise-time of the NaI crystal signals and the utilized LEDs. This phenomenon is known as time walk and needs to be corrected for. It is accomplished by plotting the time difference between a Crystal Ball hit and a tagger hit as a function of the deposited energy E for all Crystal Ball elements (see Figure 4.14 left). Thereby, the Crystal Ball hit corresponds to a photon candidate which can be combined with another photon candidate of the Crystal Ball detector to a π^0 within an invariant mass range of 110-155 MeV. Furthermore, the missing mass (see Section 5.1.1.2) is calculated and a cut of 839-1039 MeV is applied. Random time background is reduced by applying also a time cut of -10 - 30 ns on the time difference of the reconstructed π^0 and the tagger hit and by subtracting random time background underneath the prompt peak. The energy dependence of the Crystal Ball time t_{CB} is fitted with the following function:

$$t_{\mathrm{CB}}(E) = a + \frac{b}{(E+c)^d}, \tag{4.11}$$

where a,b,c and d are fit parameters and E the deposited energy in the Crystal Ball detector. After applying the time walk correction, the time resolution of Crystal Ball-tagger hits is immensely improved (see Figure 4.14 right). In addition, the Crystal Ball and tagger time coincident peaks are shifted to 0 ns. However, the shifts are sometimes imprecise when e.g. the fit did not work very well. Therefore, the parameter a in Equation (4.11) was redetermined precisely in one last iteration.

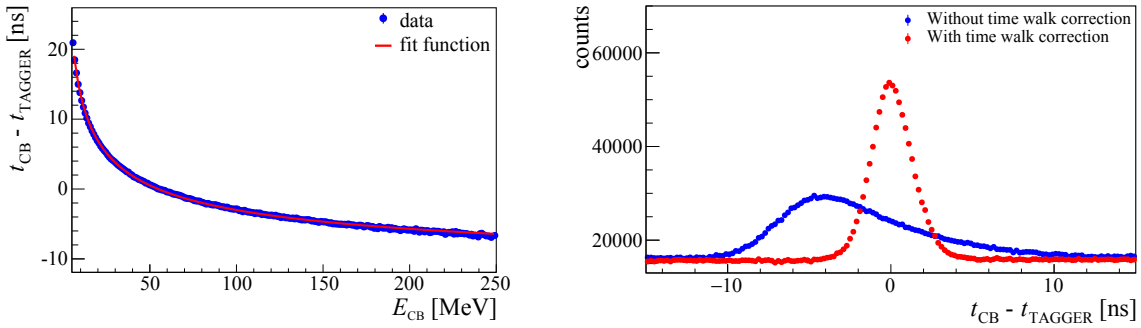

Figure 4.14: Left: The time difference of all neutral CB hits and all tagger hits is shown as a function of the deposited energy in Crystall Ball for one Crystal Ball element together with a fit function according to Equation (4.11) (red line). Right: Comparison of the Crystal Ball and tagger time difference spectrum before (blue points) and after (red points) applying the time walk correction.

Figure 4.15 shows on the left the Crystal Ball and tagger hit time differences versus the Crystal Ball elements and on the right the time difference spectrum summed over all Crystal Ball elements. Unlike for TAPS hits, the Crystal Ball hits originating from nucleons do not have a much larger time of flight than photon hits. Thus, the entire spectrum is well described with a combination of a Gaussian and a linear function. A time resolution of FWHM=2.9 ns was achieved.

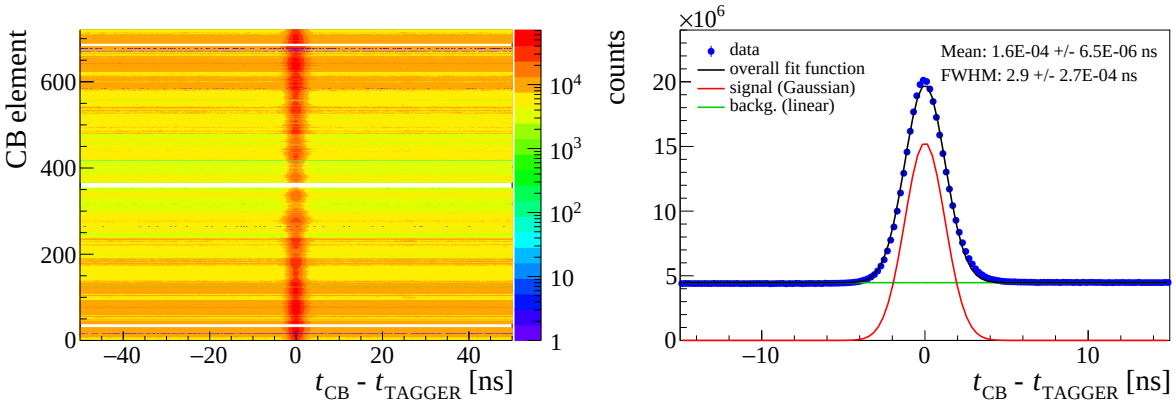

Figure 4.15: Left: Time difference of neutral Crystal Ball hits and tagger hits versus the Crystal Ball elements. Right: The time difference spectrum summed over all elements is shown together with a Gaussian (red line) and linear fit function (green line) describing the spectrum (blue points). The overall fit function is shown as a black line.

After this calibration step, the Crystal Ball detector and the tagger and therefore also the TAPS detector are all aligned in time. Since the time coincident peaks of the PID and TAPS vetos are shifted to 0 ns as well, the PID detector is aligned in time with the Crystal Ball detector and the TAPS vetos with the TAPS detector which is important for a correct charge identification of Crystal Ball and TAPS clusters.

4.2.2 Energy calibration

The energy calibration consists of five parts. First the energy calibration of the Crystal Ball detector (see Section 4.2.2.1) is performed followed by the long gate (LG, see Section 4.2.2.3) and short gate (SG, see Section 4.2.2.4) energy calibration of the TAPS detector (see Section 4.2.2.4). In the end the TAPS veto (see Section 4.2.2.5) and PID (see Section 4.2.2.6) energy calibration is done.

4.2.2.1 Crystal Ball energy calibration

During data acquisition the pedestals of all Crystal Ball elements were already subtracted due to the usage of sampling ADCs. Therefore, only the ADC gain values need to be determined. Before the start of each beamtime a rough gain calibration was performed with a ^{241}Am^{9}Be source which emits 4.438 MeV photons [Unv04]. Using the source it was possible to adjust the high voltages and thereby the gains of the NaI photomultipliers so that the 4.438 MeV photons left a signal at approximately the same ADC channel for all detector elements. A more precise energy calibration needs to be performed after data taking. This is achieved iteratively by aligning the invariant mass of two photon candidates (see Equation (4.5)) detected in the Crystal Ball detector to the π^0 PDG mass for each Crsytal Ball element (see Figure 4.16). The invariant mass spectrum is fitted first with a polynomial of third order excluding the π^0 peak range in order to describe the background. Afterwards, the background subtracted spectrum is fitted with a Novosibirsk function which determines the peak position. Due to the symmetric geometry of the Crystal Ball detector the same fit range could be used for all detector elements. After several iterations all the mass peaks could be aligned to the π^0 mass with a deviation of less than 1%. An average energy resolution of FWHM=20 MeV was achieved.

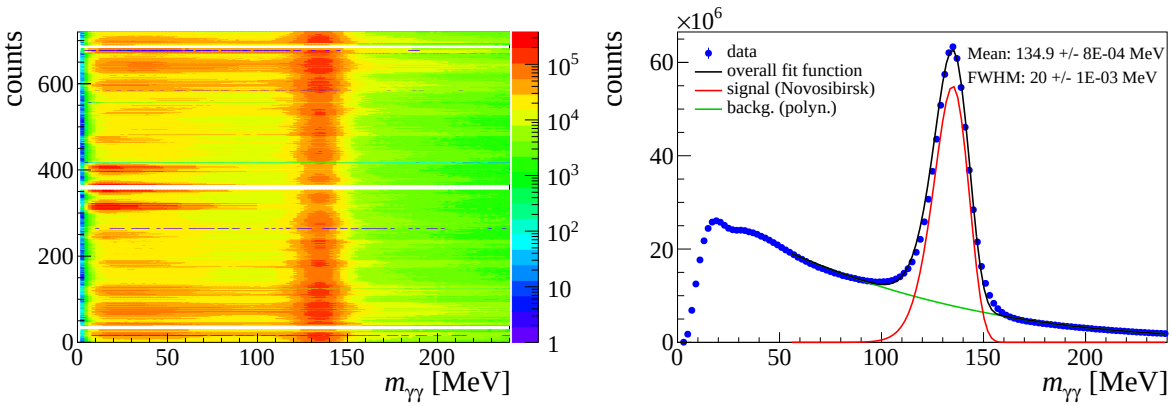

Figure 4.16: All possible pairs of two neutral Crystal Ball hits are combined and the invariant mass is fitted with a Novosibirsk for the π^0 signal and a polynomial of third order for the background and aligned to the π^0 PDG mass.

4.2.2.2 TAPS LG, SG and veto pedestal calibration

During the beamtimes additional runs were taken for the determination of the TAPS LG, SG and the VETO pedestals. The stability of the pedestals was checked for all three cases and it was found that the pedestal positions do not change for more than 0.5 channels over the time

span of the pedestal runs. The pedestals were determined using the LG, SG and veto ADC raw spectra of each element and fitting a Gaussian to the first visible peak in the spectrum at around ADC channel 100. An example is shown for the LG and SG pedestal calibration for one TAPS element in Figure 4.17.

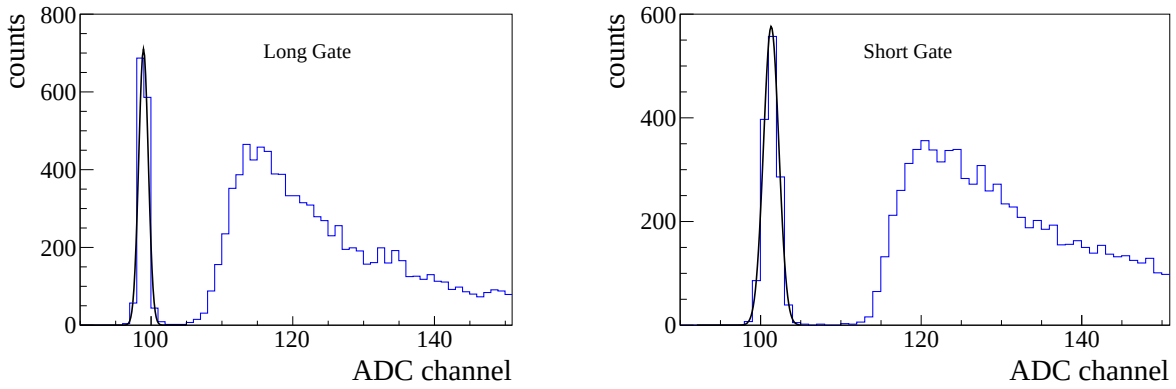

Figure 4.17: This plot shows the ADC raw spectrum for the TAPS LG (left) and TAPS SG (right) pedestal calibration. The peak visible around channel 100 is the pedestal peak which is fitted with a Gaussian.

4.2.2.3 TAPS LG energy calibration

The TAPS detector elements are roughly calibrated before the start of each beamtime. This is accomplished using muons from cosmic radiation in the same as it is done for the MiniTAPS detector (see Section 4.1.2.2). The 37.8 MeV deposited energy of muons [Röb91] was used as a reference point to adjust the BaF_2 high voltages and thus their gains. After this rough energy calibration, the CFD, LED 1 and LED 2 thresholds were set to the desired values.

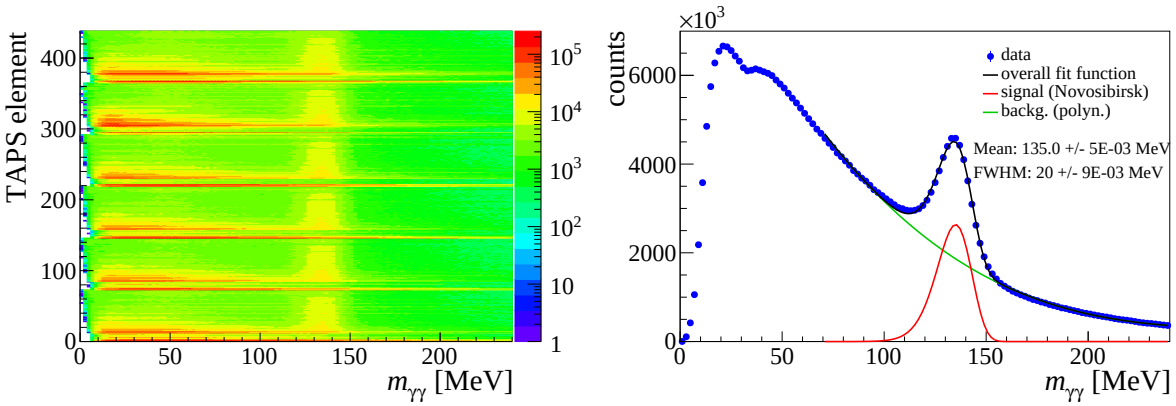

Figure 4.18: One neutral hit from CB is combined with one neutral hit from TAPS and the invariant mass spectra are fitted with a Novosibirsk for the π^0 signal and a polynomial of third order for the background and aligned to the π^0 PDG mass.

After finishing the Crystal Ball energy calibration, the TAPS LG energy calibration is performed in the same way as the Crystal Ball energy calibration. Two neutral clusters, one detected in the Crystal Ball and one in the TAPS detector, are combined and the resulting invariant mass

peak is shifted iteratively to the π^0 mass. Figure 4.18 shows on the left the invariant mass plotted against the TAPS cluster central element and on the right the invariant mass spectrum summed over all TAPS elements. Using the TAPS detector symmetry, the ranges defining the area of the π^0 peak, that is excluded for the background fit, and the total fit range were set separately for each TAPS ring since all spectra belonging to the same ring display a similar background (see Section 4.1.2.2). After several iterations all mass peaks were aligned to the π^0 mass. An average energy resolution of FWHM=20 MeV was achieved.

4.2.2.4 TAPS SG energy calibration

Unlike the LG ADCs, where the entire analog signal is integrated, the SG ADCs leave out part of the signal. Therefore, the SG gain calibration is done in a different way from the TAPS LG gain calibration. The short gate energy is compared to the long gate energy in the polar coordinate system with the pulse shape analysis (PSA) angle ϕ_{PSA} and radius r_{PSA}:

$$\phi_{\mathrm{PSA}} = \arctan\frac{E_S}{E_L}, \quad r_{\mathrm{PSA}} = \sqrt{E_S^2 + E_L^2}. \tag{4.12}$$

In this calibration step the energy from the SG ADC E_S is enforced to equal the energy from the LG ADC E_L for photons:

$$E_S = E_L. \tag{4.13}$$

This means that the PSA angle of photons should be 45°. Therefore, the PSA angle of the photons is shifted in this calibration step to 45°. Thereby, two different PSA radius ranges: 0-110 MeV and 350-600 MeV were used to determine the TAPS SG gain and pedestal[2] values with a Gaussian fit to the photon peak positions (see Figure 4.19). The PSA angle positions together with their corresponding central radii values (ϕ_1, r_1) and (ϕ_2, r_2) are used to calculate the short gate energies:

$$r = \sqrt{E_S^2 + E_L^2} = E_L\sqrt{\frac{E_S^2}{E_L^2} + 1} \quad |\tan\phi = \frac{E_S}{E_L} \tag{4.14}$$

$$= E_L\sqrt{\tan^2\phi + 1} \quad |E_L = \frac{E_S}{\tan\phi} \tag{4.15}$$

$$= \frac{E_S \cdot \sqrt{\tan^2\phi + 1}}{\tan\phi} \tag{4.16}$$

$$\Leftrightarrow E_S = \frac{r \cdot \sqrt{\tan^2\phi + 1}}{\tan\phi} \tag{4.17}$$

$$E_{S1} = \frac{r_1 \cdot \sqrt{\tan^2\phi_1 + 1}}{\tan\phi_1} \quad E_{S2} = \frac{r_2 \cdot \sqrt{\tan^2\phi_2 + 1}}{\tan\phi_2} \tag{4.18}$$

The ADC channels adc_1 and adc_2 corresponding to the SG energies E_{S1} and E_{S2} are given by the gain and pedestal values according to Equation (4.2):

$$\mathrm{adc}_1 = \frac{E_{S1}}{g} + \mathrm{ped} \quad \mathrm{adc}_2 = \frac{E_{S2}}{g} + \mathrm{ped}. \tag{4.19}$$

[2] Even though the pedestals were already determined in a previous step, they are allowed to be redetermined here because the absolute SG energy is irrelevant and only the LG energy is used to determine the deposited energy.

The gain and pedestal values g and ped have to be changed in such way that the new values g_{new} and ped_{new} and hence $E_{S1,\text{new}}$ and $E_{S2,\text{new}}$ fulfill condition (4.13) for photons. For the calculation of the new gain value the radius range 1 is used and for the pedestal determination the second radius range[3]:

$$E_{S1,\text{new}} = g_{\text{new}}(\text{adc}_1 - \text{ped}_{\text{new}}) = E_{L1} = \frac{E_{S1}}{\tan\phi_1} \tag{4.20}$$

$$\Leftrightarrow g_{\text{new}} = \frac{E_{S1}}{\tan\phi_1(\text{adc}_1 - \text{ped}_{\text{new}})} \tag{4.21}$$

$$\text{ped}_{\text{new}} = \text{ped} + \frac{E_{S2}}{g}\frac{1 - a\frac{E_{S1}}{E_{S2}}}{1-a}, \quad a = \frac{E_{L2}}{E_{L1}} = \frac{E_{S2}\tan\phi_1}{E_{S1}\tan\phi_2} \tag{4.22}$$

Since both pedestal and gain values are changed, this calibration step was performed iteratively. Figure 4.19 shows the result of this calibration step for one TAPS element. A clear peak is visible at the PSA angle of 45° which can be assigned to photons. At smaller PSA angles protons and neutrons signal is visible. The sudden increase in the count rate at r_{PSA} =110 MeV, which is indicated in Figure 4.19) can be explained by the used TAPS LED 1 threshold in the trigger.

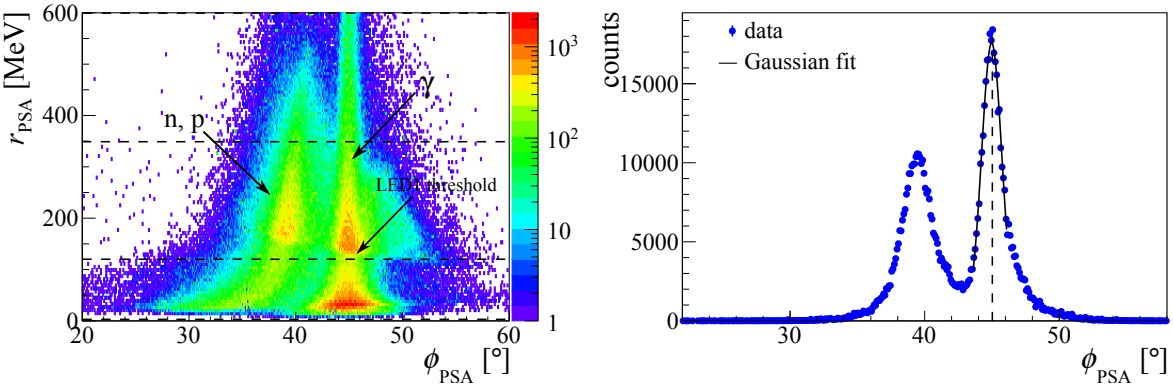

Figure 4.19: Left: The TAPS PSA radius versus the PSA angle is shown for one TAPS element. The peak at 45° can be assigned to photons and the left banana like shape to protons and neutrons. Right: Projection of the PSA angle for a PSA radius range of r_{PSA}: 110-600 MeV.

4.2.2.5 TAPS veto energy calibration

For each veto element the deposited energy of the veto element is plotted versus the corresponding TAPS cluster energy. Figure 4.20 shows on the left a histogram for one veto element. Using the deposited energy in the vetoes allows to distinguish between $e^{\pm}, \pi^{\pm}$ and protons in the TAPS detector.

A y-axis projection of the two dimensional histogram for TAPS cluster energies of 50 MeV to 60 MeV was performed for each veto element. The position of the proton banana in the data, which is visible as a peak in the veto energy spectrum, is shifted to 6 MeV in order to match the banana position in Monte Carlo simulations. For some veto elements the proton banana was very difficult to identify due to the already mentioned bad optical coupling to the

[3] The photon peak is much smaller for high PSA radii than for smaller values. Therefore this range enables a precise determination of the pedestal position.

photomultipliers.

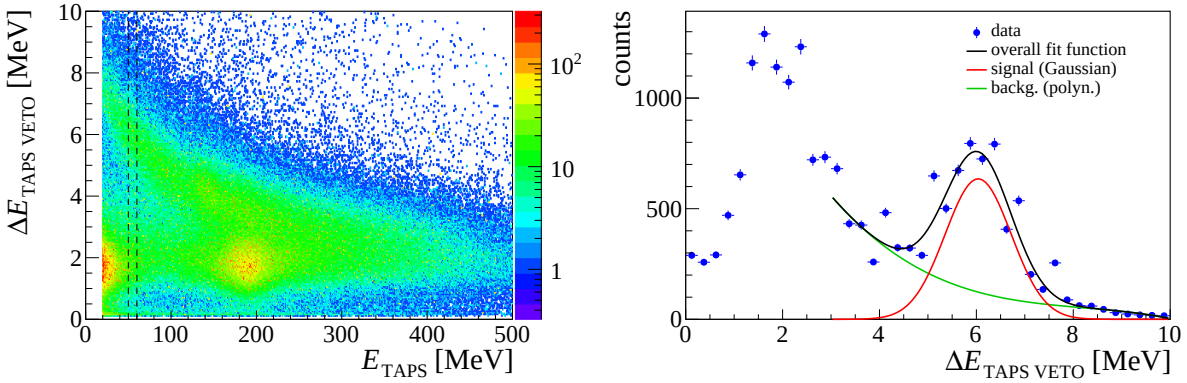

Figure 4.20: Left: The deposited energy of one veto element is plotted against the deposited energy of the corresponding cluster in TAPS. It is possible to distinguish between $e^{\pm}, \pi^{\pm}$ and protons. Right: The proton signal is visible as a peak in the veto energy spectrum at around 6 MeV. The spectrum was fitted with a Gaussian (red line) and a polynomial (green line). The overall fit function is depicted as a black line.

4.2.2.6 PID energy calibration

The PID energy calibration is carried out in a similar way as the TAPS Veto energy by plotting the deposited energy in the PID detector ΔE_{PID} versus the energy detected in the Crystal Ball detector. The proton banana is shifted than to match the proton banana position in the Monte Carlo simulation. This calibration step was performed by the Edinburgh group that is responsible for the detector. More information of the PID calibration are given in [Spi19].

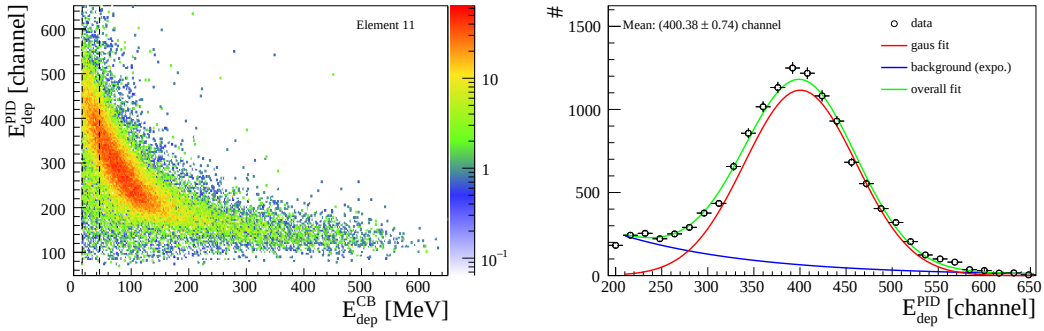

Figure 4.21: Left: The deposited energy in the PID detector is plotted as a function of the deposited energy in the Crystal Ball detector for PID element 11. The proton banana is clearly visible. Right: The projection of the PID energy for a Crystal Ball energy range from 15 MeV to 45 MeV is shown. Taken from [Spi19].

4.2.2.7 Tagger energy calibration

The tagger energy calibration was performed by guiding low intensity MAMI electron beams of different known energies directly without impinging on any radiator to the tagger ladders with a fixed tagger magnetic field strength in order to assign the known electron energies to

certain tagger elements. After doing this for several electron energies, the data is extrapolated to cover the full energy range with the program *ugcalv2ua* [Wer+13]. Before each beamtime the magnetic field strength is set according to the chosen MAMI electron beam energy. Here, a MAMI beam energy of $E_0 = 1557\,\text{MeV}$ and a magnetic field of $B = 1.888\,\text{T}$ were utilized.

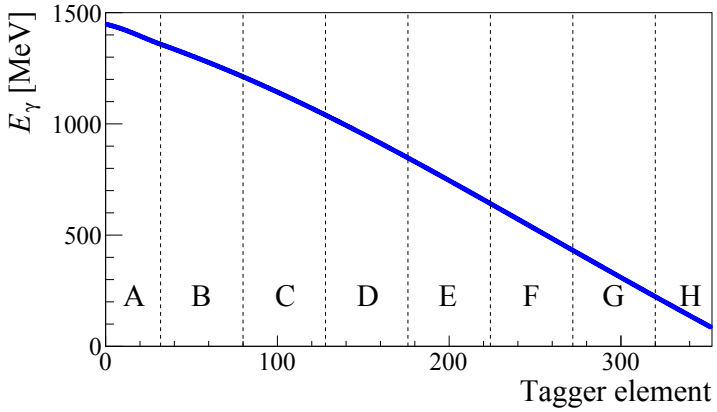

Figure 4.22: Energy of the beam photons as a function of the tagger element number. The dashed lines indicate the division of the tagger into sectors A-H.

4.2.2.8 Quality check

The achieved time and energy resolutions are listed in Table 4.4.

detector	**mass resol. FWHM [MeV]**
Crystal Ball	20.1 ± 0.3 (m_{π^0}), 46.3 ± 0.5 (m_η)
TAPS	20.3 ± 0.2 (m_{π^0}), 46.0 ± 0.7 (m_η)

detector	**Time resolution FWHM [ns]**
Tagger - TAPS	1.9 ± 0.0002
Tagger - Crystal Ball	2.9 ± 0.0003
TAPS - TAPS	0.6 ± 0.0003

Table 4.4: The achieved π^0 and η mass resolutions and the time resolutions of different detector combinations are given.

Note: The mass resolutions determined for the TAPS detector are better for the A2 data in comparison to the CBELSA/TAPS data due to the shorter butanol target (2 cm) used in the A2 experiment than the longer hydrogen target of the CBELSA/TAPS data (5 cm). Therefore, the θ-resolution and thus, the mass resolution of the A2 data is better.

5 Event Selection

Having calibrated the data and having accomplished the best possible mass and time resolutions, the preselected data was analyzed to select the desired reactions $\gamma p \to p\pi^0$ and $\gamma p \to p\eta$ and to reduce background contributions. This chapter gives an overview of all the cut conditions that were applied during the event selection process. Since both experiments are fixed target experiments and are equipped with a similar set of detectors, the kinematic variables of interest are the same. They are introduced first in Section 5.1 before the individual event selection is explained in detail for the CBELSA/TAPS data in Section 5.2 and for the A2 data in Section 5.3.

5.1 Kinematic constraints

The beam photons move along the z-direction and impinge on the target. The free protons of the target have a negligible momentum and are therefore assumed to be at rest. Thus, the initial state is fixed by the beam photon energy E_γ and the proton mass m_p:

$$p_{\text{initial}} = p_{\gamma,\text{beam}} + p_{\text{target}} = \begin{pmatrix} E_\gamma \\ 0 \\ 0 \\ E_\gamma \end{pmatrix} + \begin{pmatrix} m_p \\ 0 \\ 0 \\ 0 \end{pmatrix}, \tag{5.1}$$

with $p_{\gamma,\text{beam}}$ being the four-momentum of the beam photon, p_{target} being the four-momentum of a free proton of the target and p_{initial} the total four-momentum of the initial state.

For the detection of the final state particles both experiments are equipped with two main calorimeters that are highly efficient at detecting photons. Therefore, the π^0 or η meson was reconstructed using the according decay mode with the highest branching ratio that contained only photons in the final state, namely $\pi^0 \to \gamma\gamma$ (98.823%) and $\eta \to \gamma\gamma$ (39.41%) [Pat+16]. The final state total four-momentum p_{final} is given by the meson and recoil proton four-momenta p_{meson} and p_{recoil}:

$$p_{\text{final}} = p_{\text{meson}} + p_{\text{recoil}} \tag{5.2}$$

Keeping in mind that the important parameters for the extraction of the partial wave contributions from the polarization observables are the center of mass energy W

$$W = \sqrt{m_p^2 + 2 \cdot E_\gamma m_p} \tag{5.3}$$

and the center of mass angle $\cos\theta_{\text{CMS}}$ of the meson, it is essential to reconstruct the meson four-momentum. This was accomplished by retaining only events where at least both decay photons were detected. Events were discarded where one or both decay photons are lost.

Within the time window of the trigger usually more than one beam photon can be assigned to the same set of final state particles. The number of random tagger hits depends on the chosen beam current and the radiator thickness. Figure 5.1 shows on the left the number of tagger hits per event for the four beamtimes taken with the CBELSA/TAPS experiment and on the right for the four butanol beamtimes taken with the A2 experiment. Note: the diamond radiator with a thickness of 30 µm was exchanged after the May 2014 beamtime and replaced by a diamond of 100 µm thickness. This lead to an increase of the number of tagger hits in the A2 data for the May and September 2015 beamtimes.
In addition, there are three different combinations possible to combine two of the three particles to the meson if all three final state particles are detected. In order to find the correct beam photon and the right combination of particles, several cuts were applied to the data.

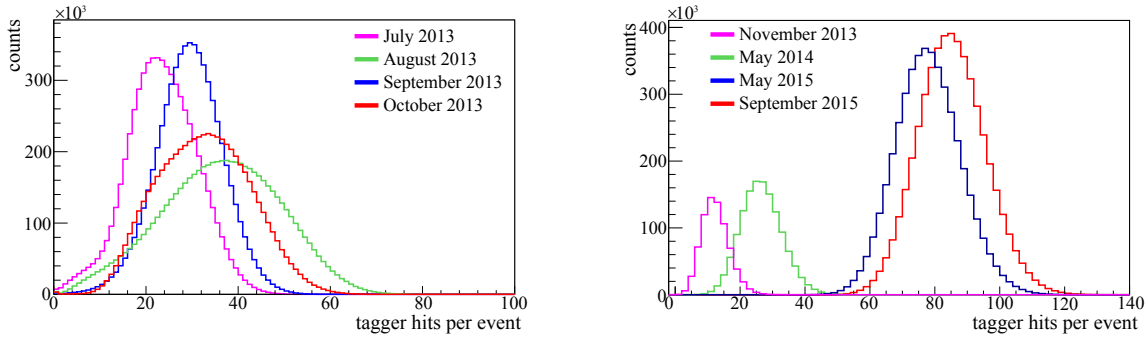

Figure 5.1: The number of tagger hits that were detected within the trigger time window is shown on the left for the CBELSA/TAPS and on the right for the A2 data. The number of tagger hits depends on the chosen beam current, which varied for the different beamtimes. In addition, the diamond radiator was exchanged after the May 2014 beamtime at the A2 experiment leading to an increase in the number of tagger hits.

5.1.1 Mass cuts

This section demonstrates how the meson and recoil momenta are determined from the measured data.

5.1.1.1 Invariant mass

The π^0 and η meson's four-momenta p_{meson} are given by the sum of the four-momenta of two reconstructed photon candidates p_{γ_1} and p_{γ_2}:

$$p_{\text{meson}} = p_{\gamma\gamma} = p_{\gamma_1} + p_{\gamma_2}. \tag{5.4}$$

The invariant mass of the two photons $m_{\gamma\gamma}$ reads

$$m_{\text{meson}} = m_{\gamma\gamma} = \sqrt{2E_{\gamma_1}E_{\gamma_2}(1 - \cos\alpha_{\gamma_1,\gamma_2})}, \tag{5.5}$$

where E_{γ_1} and E_{γ_2} are the energies of the photons and $\alpha_{\gamma_1,\gamma_2}$ the opening angle between the two photons. In case of correct assignment of the two decay photons, the invariant mass should correspond to the meson mass of π^0 (134.98 MeV [Pat+16]) or η (547.86 MeV [Pat+16]).

Using a Lorentz transformation, the meson four-momentum and the initial state information, it is possible to boost the meson from the lab system (LAB) to the center of mass system (CMS) and to determine $\cos\theta_{\mathrm{CMS,meson}}$. If not otherwise mentioned it holds $\cos\theta_{\mathrm{CMS,meson}} \equiv \cos\theta$ for all shown plots from now on and $\cos\theta$ refers to the center of mass polar angle of the meson.

5.1.1.2 Missing mass

As already mentioned the recoil protons do not always deposit their entire energy when passing through the calorimeters (see Figure 5.3). Therefore, the recoil protons are treated as the missing particle X of the system $\gamma p \to \mathrm{meson} + X$. Knowing the meson four-momentum allows the determination of the missing particle's four-momentum p_X. Its mass m_X can be calculated in the following way:

$$p_X = p_{\gamma,\mathrm{beam}} + p_{\mathrm{target}} - p_{\mathrm{meson}} \tag{5.6}$$

$$m_X = \sqrt{(E_\gamma + m_p - E_{\mathrm{meson}})^2 - p_{x,\mathrm{meson}}^2 - p_{y,\mathrm{meson}}^2 - (E_\gamma - p_{z,\mathrm{meson}})^2}, \tag{5.7}$$

where E_{meson} is the total meson energy and $p_{x,\mathrm{meson}}$, $p_{y,\mathrm{meson}}$ and $p_{z,\mathrm{meson}}$ are the three components of the meson momentum vector. The missing mass should be equal to the proton mass of m_p =938.27 MeV [Pat+16].

5.1.2 Angular cuts

While the recoil proton energy information can not be reliably used, the azimuthal angle $\phi_{\mathrm{recoil}}^{\mathrm{LAB}}$ and the polar angle $\theta_{\mathrm{recoil}}^{\mathrm{LAB}}$ of the detected recoil proton in the LAB frame were utilized to put further constraints on the data, if available.

5.1.2.1 Coplanarity

In the initial state the total transverse momentum $\vec{p}_{\mathrm{initial},xy}$, which is attainable through a projection of the three dimensional momentum to the $x-y$-plane, is zero since the beam photons move along the z-axis towards the fixed target protons (see Equation (5.1)). Due to momentum conservation the transverse momentum has to vanish in the final state as well:

$$\vec{p}_{\mathrm{final},xy} = \vec{p}_{\mathrm{meson},xy} + \vec{p}_{\mathrm{recoil},xy} \stackrel{!}{=} \vec{0} \tag{5.8}$$

This is only fulfilled if the meson and recoil proton xy-momenta lie back to back (coplanar) in the $x-y$-plane and have an opening angle of 180°. As the azimuthal angle ϕ^{LAB} runs in the $x-y$-plane, it holds

$$\Delta\phi = \phi_{\mathrm{recoil}}^{\mathrm{LAB}} - \phi_{\mathrm{meson}}^{\mathrm{LAB}} \stackrel{!}{=} 180°, \tag{5.9}$$

where $\phi_{\mathrm{meson}}^{\mathrm{LAB}}$ is the azimuthal angle of the meson and $\phi_{\mathrm{recoil}}^{\mathrm{LAB}}$ is the azimuthal angle of the measured recoil proton in the LAB frame.

5.1.2.2 Polar angle difference

The measured polar angle of the recoil proton in the lab frame $\theta_{\mathrm{recoil}}^{\mathrm{LAB}}$ should be equal to the reconstructed missing particle's θ_X^{LAB} angle (see Equation (5.6)). This leads to the following

cut condition:

$$\Delta\theta = \theta_X^{\mathrm{LAB}} - \theta_{\mathrm{recoil}}^{\mathrm{LAB}} \stackrel{!}{=} 0. \tag{5.10}$$

5.2 Event selection using CBELSA/TAPS data

An *ExPlORA* plugin was written for the analysis of the CBELSA/TAPS data that handled the application of cut conditions and the filling of necessary histograms and *ROOT* trees.
The linear polarization degree is higher than 10% in the beam photon energy range of 1130 MeV - 1770 MeV. Thus, the beam asymmetry Σ can only be extracted for this energy range (see Section 6.1). Therefore, all beam photons were rejected that did not lie in this energy range at the beginning of the selection process.

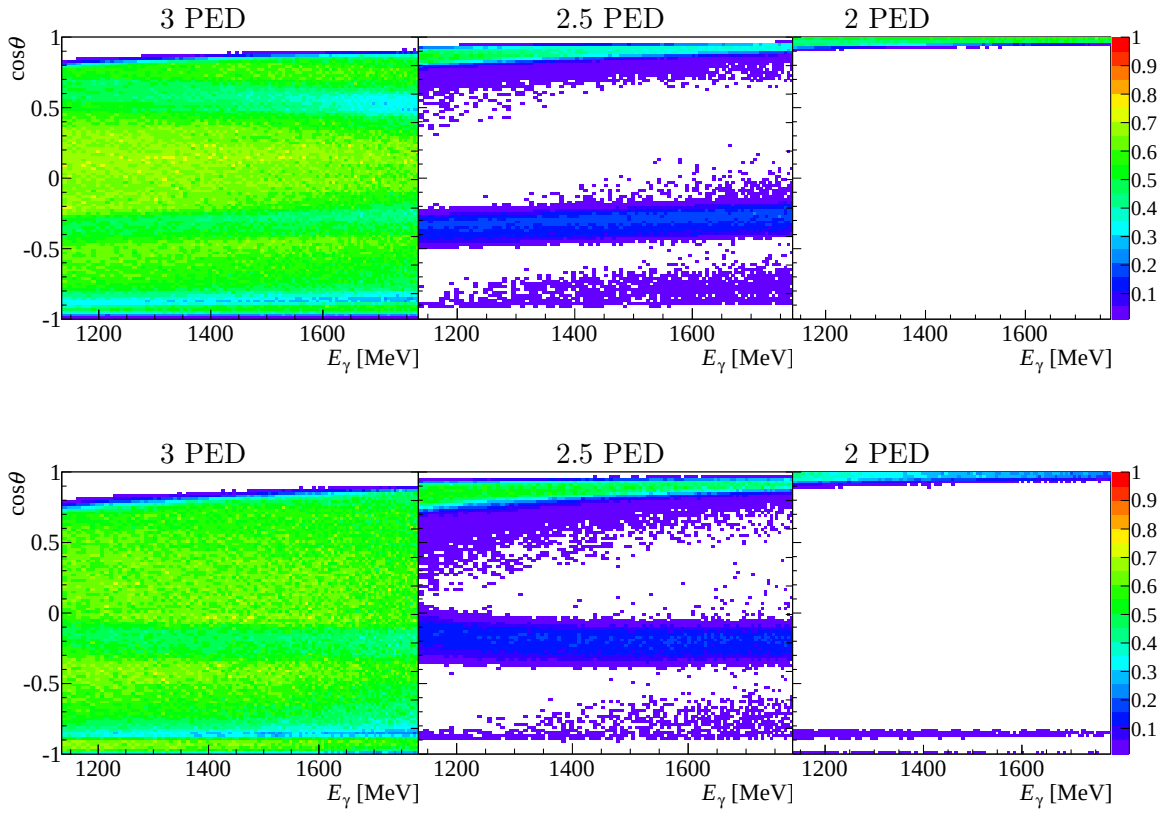

Figure 5.2: The detector and analysis acceptance is shown for the kinematic regions (beam energy E_γ and $\cos\theta$) of the three different event classes: 3 PED, 2.5 PED and 2 PED according to Monte Carlo simulations. The upper row shows the acceptance for the $p\pi^0 \to p\gamma\gamma$ and the lower row for the $p\eta \to p\gamma\gamma$ final state.

All events with exactly two or three reconstructed particles were chosen for the reconstruction of the final state. In case all three particles (p_1, p_2 and p_3) were detected in the calorimeter crystals (3 PED event), they were selected from the *DontCareCharged* container and combined pairwise to a meson candidate. The remaining third particle was assigned as the recoil proton candidate:

$$p_{\text{meson}} + p_{\text{recoil}} = p_{\gamma_1} + p_{\gamma_2} \quad + p_{\text{recoil}} = \begin{cases} p_{p_1} + p_{p_2} & + p_{p_3} \\ p_{p_2} + p_{p_3} & + p_{p_1} \\ p_{p_1} + p_{p_3} & + p_{p_2}. \end{cases} \tag{5.11}$$

Since low energetic protons do not always reach the calorimeters but are stopped either in the inner detector or in the forward detector or in the MiniTAPS vetoes, events were also analyzed with two particles selected from the *Uncharged* container, which were assigned as the decay photon candidates. The recoil proton candidate was selected from either the inner detector, forward detector or MiniTAPS *routes*. This event class is referred to as the 2.5 PED class.

In addition, inclusive reactions, where the recoil proton is not detected, were analyzed as well. The recoil proton is not detected if the proton has such a low kinetic energy that it is not able to reach the crystals of the Crystal Barrel or the MiniTAPS detector. Additionally, a particle can be lost in inactive material or acceptance gaps of the detector setup, e.g. between the forward detector and the MiniTAPS detector, or they can be absorbed in the target material. In this case, exactly two reconstructed particles were selected from the *Uncharged* container and were assigned as the two decay photons. This event class is called the 2 PED event class. Figure 5.2 shows the detector and analysis acceptance $\epsilon(E_\gamma, \cos\theta)$ for the three different event classes in the upper row for the $p\pi^0$ and in the lower row for the $p\eta$ final state. The detector acceptance is given by the ratio of the reconstructed events after applying all cuts $N^{rec}(E_\gamma, \cos\theta)$ to all generated Monte Carlo events $N^{gen}(E_\gamma, \cos\theta)$:

$$\epsilon(E_\gamma, \cos\theta) = \frac{N^{rec}(E_\gamma, \cos\theta)}{N^{gen}(E_\gamma, \cos\theta)}. \tag{5.12}$$

Most of the angular range is covered by the 3 PED events. An acceptance hole is visible at $\cos\theta \approx -0.8$ which can be attributed to the gap between the forward and the MiniTAPS detector where protons can be lost. At very forward $\cos\theta$ angles ($\cos\theta > 0.8$) the 2.5 PED and 2 PED events dominate.

5.2.1 Application of time cut and time background subtraction

As a first step the detected particles were checked for time coincidence. The tagged beam photons need to be coincident in time with the detected decay photons of the meson. The decay photons only have a time information if they are detected either in the forward or the MiniTAPS detector. The meson time t_{meson} is given by

$$t_{\text{meson}} = \begin{cases} t_{\gamma_1} & \text{only } \gamma_1 \text{ has a time} \\ t_{\gamma_2} & \text{only } \gamma_2 \text{ has a time} \\ \frac{1}{2}(t_{\gamma_1} + t_{\gamma_2}) & \gamma_1 \text{ and } \gamma_2 \text{ have a time,} \end{cases} \tag{5.13}$$

where t_{γ_1} and t_{γ_2} are the times of the decay photons. To check for coincidence with the beam photons, the reaction time t_{reaction} is formed using the time difference between the beam photon time t_{beam} and the meson time t_{meson}, if it is available. In case both decay photons were detected in the Crystal Barrel calorimeter, no meson time exists. Then, the time difference of the beam photon was checked to the recoil proton time t_{recoil}, if the recoil proton was detected (see Equation (5.14)).

$$t_{\text{reaction}} = \begin{cases} t_{\text{beam}} - t_{\text{meson}} & \text{meson time exists (3PED, 2.5PED or 2PED)} \\ t_{\text{beam}} - t_{\text{recoil}} & \text{meson time does not exist (3PED or 2.5 PED).} \end{cases} \tag{5.14}$$

All 2 PED events with no meson time were rejected from further analysis. Figure 5.6 shows the reaction time for the 3 PED and 2.5 PED events. The events fulfilling time coincidence between the beam photon and the meson or the recoil proton form the prompt peak around 0 ns. The time cut limits were selected based on the time resolution of the according detector that provided the particle time information. The MiniTAPS detector has the best time resolution of all detectors (see Table 4.1) and therefore allows to apply a narrower time cut in general. But in case of the proton being detected in the MiniTAPS detector, one has to consider time of flight effects as well due to the high proton mass. Protons with a low kinetic energy need more time to reach the MiniTAPS detector than higher energetic protons or photons. A time-span of up to 16 ns is needed [Har08].

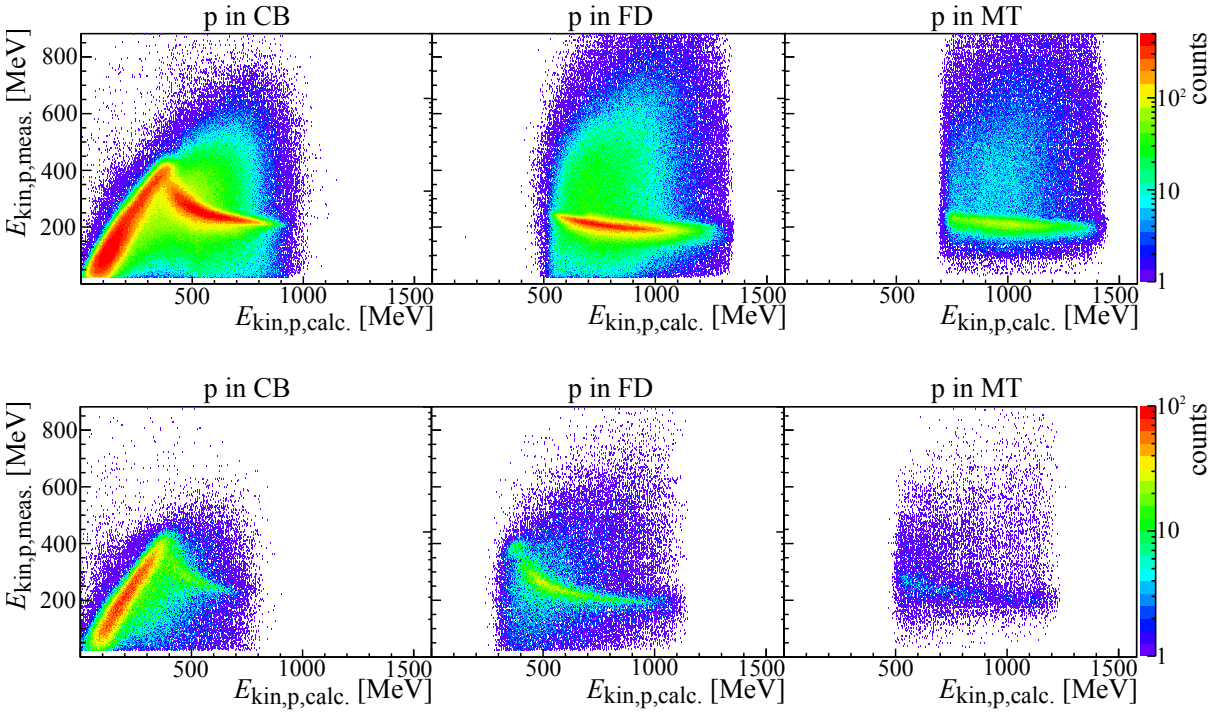

Figure 5.3: The measured proton energy is plotted as a function of the calculated proton energy in case the proton is detected in the Crystal Barrel detector (CB), the forward detector (FD) or in the MiniTAPS detector (MT). The upper row shows the 3 PED events for the $p\pi^0$ final state and the lower row for the $p\eta$ final state.

However, in the beam photon energy range considered here (1130 MeV - 1770 MeV), only high energetic protons are boosted towards the very forward θ angles where the MiniTAPS detector is located. This is demonstrated in Figure 5.3 which shows the measured kinetic energy of the recoil proton as a function of the calculated proton energy for 3 PED events after all cuts are applied to the data. It is given by $E_{\text{kin,p,calc.}} = E_\gamma - E_{\text{meson}}$. Low energetic protons are completely stopped in the Crystal Barrel detector up to a kinetic energy of around 400 MeV.

Higher energetic protons behave like minimum ionizing particles and deposit a constant energy of approximately 250 MeV. These protons are dominantly detected in the forward detector and in the MiniTAPS detector. Therefore, time of flight effects were neglected for both $p\pi^0$ and $p\eta$ analyses of the 3 PED events.
The detector dependent cut ranges are shown for the beam photon and meson time differences in Figure 5.4 on the left according to the detector the decay photons were detected in. The structures visible in 2 ns steps are correlated to the ELSA bunches. It should be noted here that a Crystal Barrel time information does not exist. Only if the according photon cluster is spread not just over the Crystal Barrel but also over the forward detector, or in case of a two PED cluster detected very close to the forward detector, or if the time information is provided by the inner detector in case of a false charge identification, a time information exists for a Crystal Barrel PED.

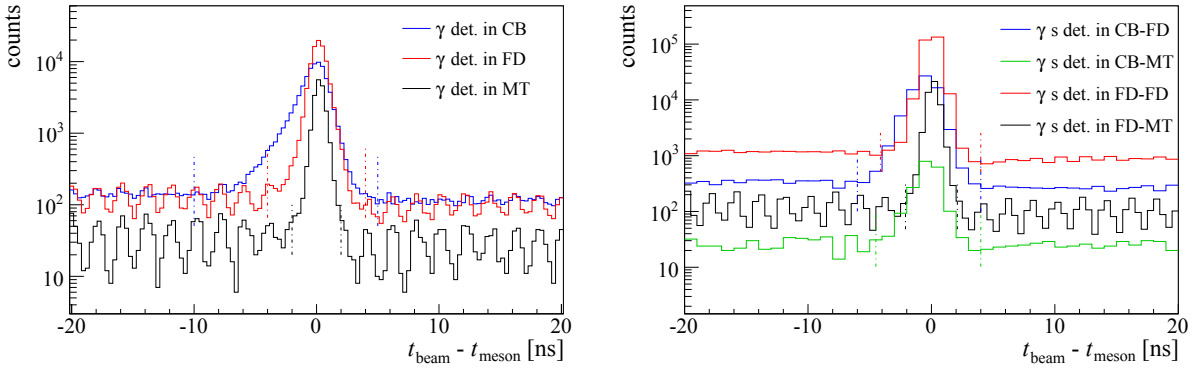

Figure 5.4: Left: The time difference between the beam photon and the meson is plotted after applying all other cuts. If the according decay photon was detected in the Crystal Barrel detector (CB, blue), in the forward detector (FD, red) and in the MiniTAPS detector (MT, black) for all event classes. Right: In case both photons have a time information, the applied time cut range varies depending on which detectors both photons were detected in. The following combinations are possible: CB-FD (blue), CB-MT (green), FD-FD (red) and FD-MT (black). The dashed lines mark the accepted cut ranges.

If both decay photons of the meson have a time information, the time cut was applied depending on the combination of detectors that provided the time information (see Figure 5.4 on the right). The following combinations of detectors (Crystal Barrel (CB), forward detector (FD) and MiniTAPS (MT)) can have measured the two photons: CB-CB, CB-FD, CB-MT, FD-FD, FD-MT and MT-MT. However, the latter case is not realized in this beam photon energy range and for the case CB-CB there are never time information available for both photons, leaving four possible combinations. The individual cut ranges were set broad enough to contain all of the prompt peak events and are listed in Table 5.1.

Figure 5.5 depicts the time of both decay photons. The timely correlated decay photons are located on the diagonal. After applying all cuts to the data, only the events on the diagonal are left which indicates a correct event selection (see Figure 5.5 on the right). A cut of $-6\,\text{ns} \leq t_{\gamma_1} - t_{\gamma_2} \leq 6\,\text{ns}$ was chosen to ensure only timely correlated decay photons are selected for further analysis.

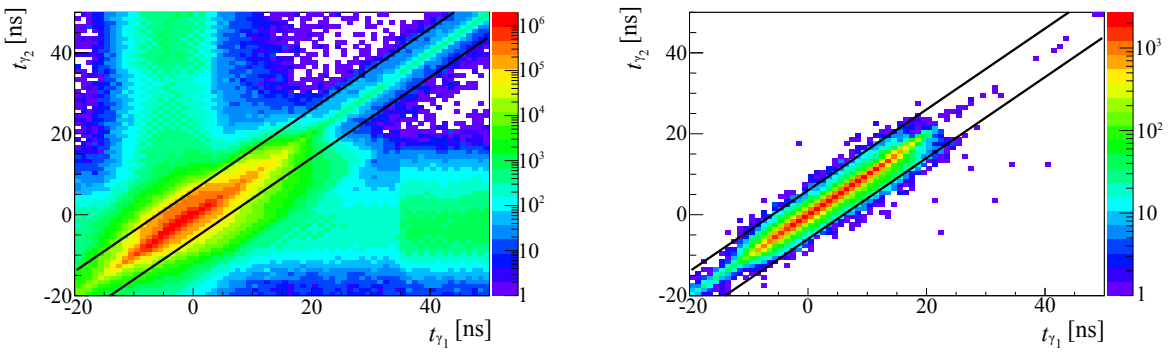

Figure 5.5: The time of one decay photon is plotted vs. the time of the other decay photon. Timely correlated photons are located on the diagonal. The cut range is indicated by the black lines. Left: No cuts are applied to the data. Right: All cuts except for the cut shown here are applied to the data.

In addition, the recoil proton time was checked for time coincidence to the meson. A clear time coincidence peak is visible after applying all cuts to the data which is shown in Figure 5.6 on the right. A broad cut of $-6\,\text{ns} \leq t_{\text{meson}} - t_{\text{recoil}} \leq 6\,\text{ns}$ was selected here.

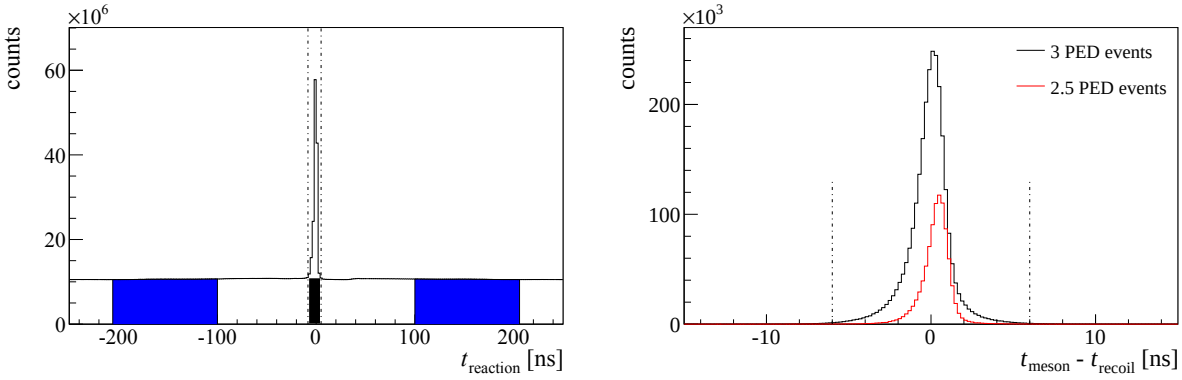

Figure 5.6: Left: The reaction time is plotted before any cuts are applied. The time background underneath the prompt peak (black area) is subtracted using the side bands (blue area). Right: The time difference between the meson and recoil proton in case both information are available and after applying all other cuts to the data.

Figure 5.7 depicts the time difference between the beam photon and the recoil proton separately for each detector in case no meson time exists for 3 PED events on the left and for 2.5 PED on the right. The MiniTAPS detector gives the best time resolution, followed by the inner detector and lastly the forward detector crystals. Note: the small peak at around 5 ns is also stemming from punch through protons and belongs to signal events. The according forward detector veto times can be compared to the forward detector crystals time which is depicted in Figure A.1 in the appendix.

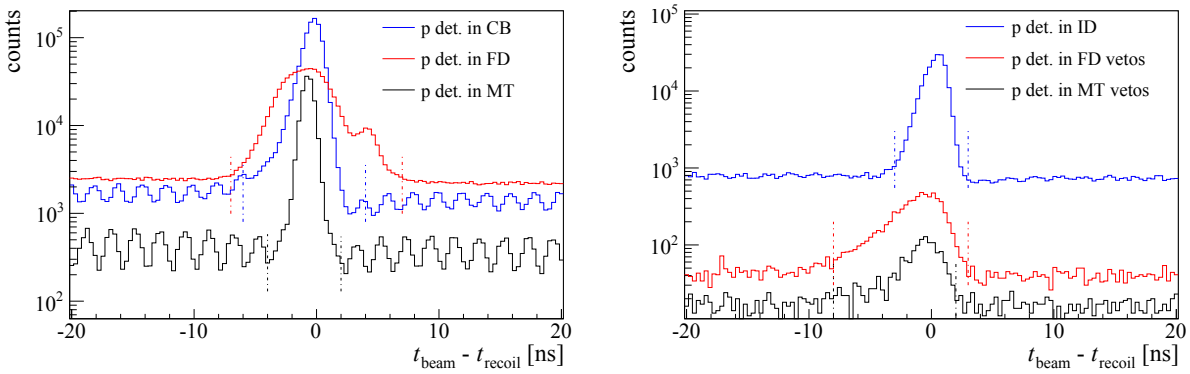

Figure 5.7: Left: The time difference between the beam photon and the recoil proton is plotted in blue if the inner detector detected the recoil proton, in red if the forward detector and in black if the MiniTAPS registered the recoil proton candidate for the 3PED events. Right: The time difference between the beam photon and the recoil proton is plotted for the 2.5 PED events. The proton time information is provided either by the inner detector (blue), the forward detector vetoes (red) or the MiniTAPS vetoes (black).

While for the 3 PED events the protons are high energetic and no time of flight effects need to be considered, this is differently for the 2.5 PED events. Protons stemming from 2.5 PED events do not always have enough kinetic energy to reach the detector crystals and are therefore in general low energetic. If the protons were detected in the forward detector vetoes or in the MiniTAPS vetoes, a broader cut range was chosen. Table 5.1 sums up the time coincidence cut.

particle with time	**which detector**	**time cut**	**additional constraints**
only γ_1 or γ_2	CB	$-10 \leq t_{\text{reaction}} \leq 5$	
	FD	$-4 \leq t_{\text{reaction}} \leq 4$	$-6 \leq t_{\text{meson}} - t_{\text{recoil}} \leq 6$
	MT	$-2 \leq t_{\text{reaction}} \leq 2$	
both γ_1 and γ_2	CB-FD	$-6 \leq t_{\text{reaction}} \leq 4$	
	CB-MT	$-4 \leq t_{\text{reaction}} \leq 4$	$-6 \leq t_{\text{meson}} - t_{\text{recoil}} \leq 6$
	FD-FD	$-4 \leq t_{\text{reaction}} \leq 4$	$-6 \leq t_{\gamma_1} - t_{\gamma_2} \leq 6$
	FD-MT	$-2 \leq t_{\text{reaction}} \leq 2$	
only proton	CB	$-6 \leq t_{\text{reaction}} \leq 4$	
	FD	$-7 \leq t_{\text{reaction}} \leq 7$	
	MT	$-4 \leq t_{\text{reaction}} \leq 2$	
	FD vetoes	$-8 \leq t_{\text{reaction}} \leq 3$	
	MT vetoes	$-8 \leq t_{\text{reaction}} \leq 2$	

Table 5.1: This table gives an overview about the used time cuts. If at least one decay photon has a time information, t_{reaction} is given by the time difference of the beam photon and the meson time (see Equation (5.14)). Additionally, time coincidence is demanded between the meson and recoil proton. In case both decay photons have a time, they are required to be coincident in time as well. If only the proton time is available, the time cut is applied on the time difference between beam photon and the recoil proton.

Since the tagger registers many hits during the trigger window of 1 µs, a flat random time background is visible in Figure 5.6. The random time background is not only present at the

sides of the prompt peak but also underneath it. This time background was subtracted using the sidebands from −205 ns to −100 ns and from 100 ns to 205 ns and assuming the background is flat underneath the prompt peak:

$$N_{\text{sub}} = N_{\text{prompt}} - s \cdot N_{\text{sideband}}, \tag{5.15}$$

where N_{prompt} is the yield in the prompt peak, N_{sideband} is the yield of the sidebands as depicted in Figure 5.6 and N_{sub} is the time background subtracted yield of the prompt peak. The scaling factor s, that is used to scale the sideband yields, is given by the ratio of prompt peak time window to sideband time windows. It differs according to the applied time cut windows, e.g. s equals $-\frac{15}{210}$ for the the first case in Table 5.1. Thus, each event of any histogram was either weighted with 1, if it is a prompt peak event or with s, if it is a sidebend event in order to subtract the random time background.
It is worth noting, that from this section forward the mentioning of the time cut includes the random background subtraction as well.

5.2.2 Application of kinematic constraints

After applying the time cut, the event selection and thus the signal to background ratio was further improved by using the kinematic constraints as explained in Section 5.1.
While the invariant mass and missing mass cuts are applicable for all three event classes, the angular cuts (see Section 5.1.2) can only be applied for the 3 PED and 2.5 PED events due to the missing recoil proton information. Therefore, the selection of the 2 PED events is more difficult and additional constraints become necessary to ensure a good signal to background ratio. These constraints are discussed in Section 5.2.5.
The kinematic constraints are applied for 3 PED and 2.5 PED events in the same way since in both cases all three final state particles were measured and are therefore not discussed separately.
The influence of each cut on each kinematic variable is demonstrated in Figure 5.8 for the 3 and 2.5 PED events of both final states, the $p\pi^0$ final state in the left column and the $p\eta$ final state in the right column. Each kinematic cut is discussed in the following.

5.2.2.1 Invariant mass cut

The invariant mass spectrum of the two detected photons (see Figure 5.8) shows very clearly the π^0 peak at 135 MeV and the η peak at around 547 MeV after all other kinematic and time constraints are applied to the data. Additionally, an ω peak is visible at about 783 MeV which is a result of a lost photon from the decay mode $\omega \to \pi^0\gamma \to \gamma\gamma\gamma$ and an η' peak at about 958 MeV which decays into two photons as well [Pat+16]. Especially the missing mass and coplanarity cuts improve the signal to background ratio significantly.

The cut limits were determined depending on E_γ and $\cos\theta$ since the detector energy and angular resolutions are different and since the final state particles are boosted to different polar angles θ depending on their energies. Figure 5.9 shows on the left the invariant mass as a function of the beam photon energy E_γ and integrated over the entire angular range for the $p\pi^0$ final state. In the energy region 1239 MeV-1671 MeV data of both coherent edges 1750 MeV (July and August 2013 beamtimes) and 1850 MeV (September and October 2013 beamtimes) were added up leading to an increased statistics in this region.

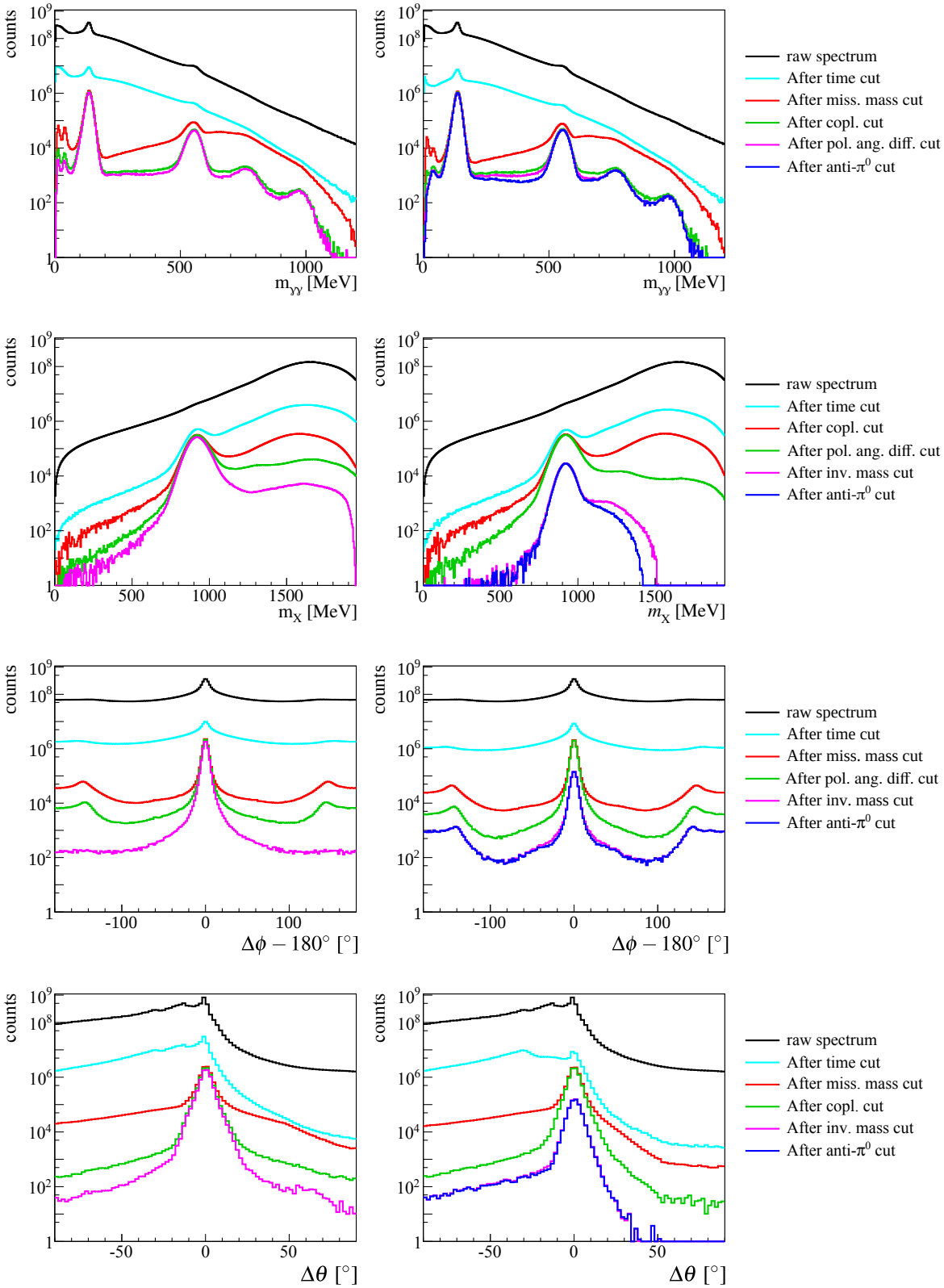

Figure 5.8: The impact of each kinematic constraint on each kinematic variable (invariant mass (first row), missing mass (second row), coplanarity (third row) and polar angle difference (bottom row)) are demonstrated for both final states $p\pi^0$ on the left and $p\eta$ on the right. The anti-π^0 cut is only applied for the $p\eta$ final state (see Section 5.2.2.2).

Only a small energy dependence is present since the energy range of interest is more than 1 GeV above the π^0 photoproduction threshold at around 142 MeV. Nevertheless, the cut limits were determined beam energy dependent due to the energy dependence of the differential cross section of signal and background contributions. For the energy bin region 1419 MeV $\leq E_\gamma <$ 1455 MeV the $\cos\theta$ dependence of the invariant mass is shown in Figure 5.9 on the right. The statistics has two minima at $\cos\theta \approx -0.4$ and $\cos\theta \approx 0.5$. They reflect the two minima of the differential cross section (see Figure A.2 on the left). The invariant mass position and width shows a strong dependence on $\cos\theta$ due to a not pefectly working energy correction function [Sta16] and since the ϕ-resolution is worst when the decay photons are detected in the forward detector ($0.5 < \cos\theta < 0.85$).

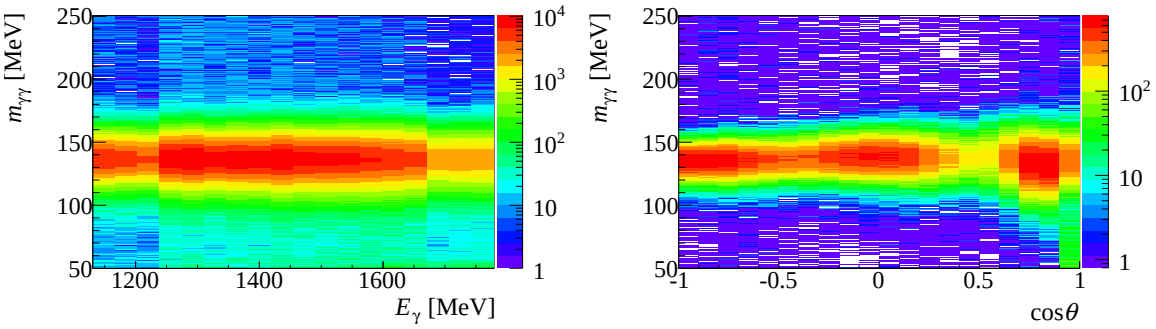

Figure 5.9: Left: The invariant mass of the two reconstructed photons is plotted as a function of the beam photon energy E_γ and integrated over the entire angular range for the $p\pi^0$ final state. In the energy region 1239 MeV-1671 MeV data of both coherent edges 1750 MeV (July and August 2013 beamtimes) and 1850 MeV (September and October 2013 beamtimes) are added up leading to an increased statistics in this region. Right: The $\cos\theta$ dependence of the invariant mass is shown for the energy bin 1419 MeV $\leq E_\gamma <$ 1455 MeV. The selection cuts (time, missing mass, coplanarity and polar angle difference) are applied.

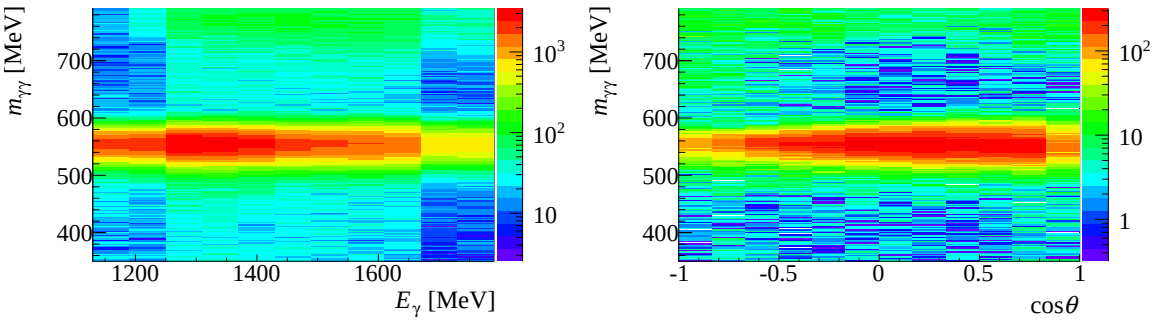

Figure 5.10: Left: The invariant mass of the two reconstructed photons is plotted as a function of the beam photon energy E_γ and integrated over the entire angular range for the $p\eta$ final state. In the energy region 1250 MeV-1670 MeV data of both coherent edges 1750 MeV (July and August 2013 beamtimes) and 1850 MeV (September and October 2013 beamtimes) are added up leading to an increased statistics in this region. Right: The $\cos\theta$ dependence of the invariant mass is shown for the energy bin 1370 MeV $\leq E_\gamma <$ 1430 MeV. The selection cuts (time, missing mass, coplanarity and polar angle difference) are applied.

Similar observations hold true for the $p\eta$ final state (see Figure 5.10). However, here, the

differential cross section increases continuously from $\cos\theta = -1$ to $\cos\theta \approx 0.9$ (see Figure A.2 on the right).
Figure 5.12 shows the invariant mass for all $\cos\theta$ bins as an example for the beam energy region of $1419\,\text{MeV} \leq E_\gamma < 1455\,\text{MeV}$ for the $p\pi^0$ final state and Figure 5.13 shows the according spectra of the $p\eta$ final state for the energy region of $1370\,\text{MeV} \leq E_\gamma < 1430\,\text{MeV}$. The data points are plotted as filled black circles and MC data spectra are depicted as a red line for comparison. In the $p\pi^0$ channel a clean signal is visible after applying all other cuts to the data. Therefore, a good agreement between data and MC spectra (red lines) is visible. An exception is the angular range $0.9 \leq \cos\theta < 1.0$ where mostly 2 PED events are present. As already mentioned, the angular cuts are not applied for the 2 PED events leading to an increased background. This background can be attributed mainly to electromagnetic background. An estimation of the background contribution within the cut ranges is discussed in Section 5.2.5.
The $p\eta$ invariant mass spectra, however, exhibit background contribution from the reactions $p\pi^0$ (light blue line), $n\pi^+$ (magenta line), $p\omega \to \pi^0\gamma$ (violet line) and $p\pi^0\pi^0$ (black line), especially at backward angles ($\cos\theta < -0.5$) and the very forward angles ($\cos\theta > 0.8$) as a fit of the MC spectra to the data reveals (see Figure 5.13). The majority of this background contribution is later removed with an additional anti-π^0 cut (see Section 5.2.2.2). The sum of signal and background Monte Carlos is depicted as a green line, which agrees well with the data. The dashed lines mark the $\pm 2\sigma$ cut range[1], that are chosen with the help of a Novosibirsk fit to the MC invariant mass spectra for both final states. This choice of cut width presents a compromise between retaining high statistics and obtaining a good signal to background ratio.

5.2.2.2 Anti-π^0 cut in the $p\eta$ analysis

As demonstrated in Figure 5.13 the $p\pi^0$ channel significantly contributes with up to 36% as background underneath the η invariant mass peak, especially at very backward and forward angles. According to Monte Carlo simulations this background can be traced back to the case where one low energetic photon of around 20 MeV energy belonging to the π^0 meson is lost due to the applied cluster reconstruction thresholds (see Section 3.1.2) or insensitive material.

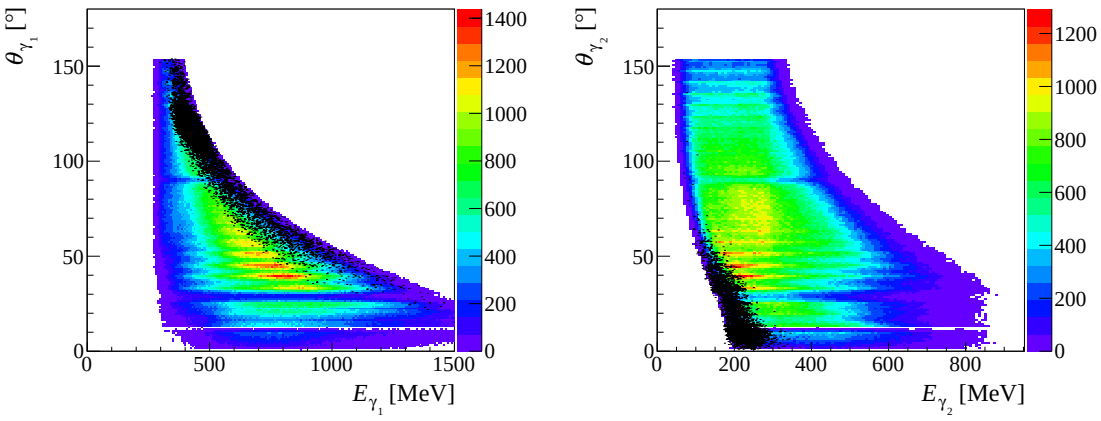

Figure 5.11: The energy and polar angle θ of both reconstructed photon candidates γ_1 and γ_2 in the lab system are shown for the $p\eta$ final state (MC). The background contribution from the $p\pi^0$ final state is overlayed using black points (MC).

[1] Due to a small tail parameter of the Novosibirsk function, the cut was performed symmetrically.

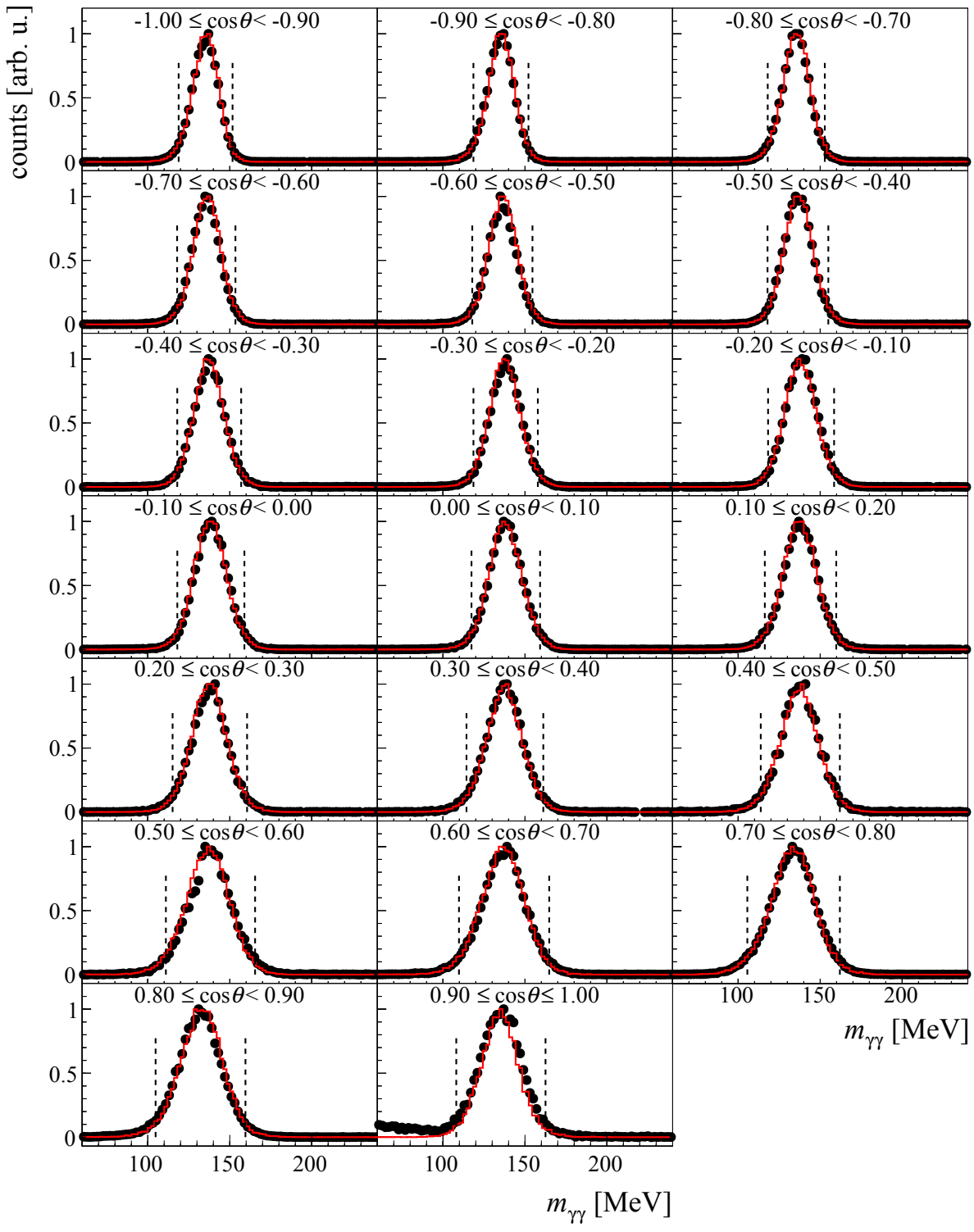

Figure 5.12: Invariant mass spectra are depicted for all $\cos\theta$ bins of the $p\pi^0$ final state and for the energy bin 1419 MeV $\leq E_\gamma <$ 1455 MeV after applying all selection cuts (time, missing mass, coplanarity and polar angle difference) to the data. The black points represent the data and the red line the $p\pi^0$ MC. The dashed lines show the chosen $\pm 2\sigma$ cut range for each bin.

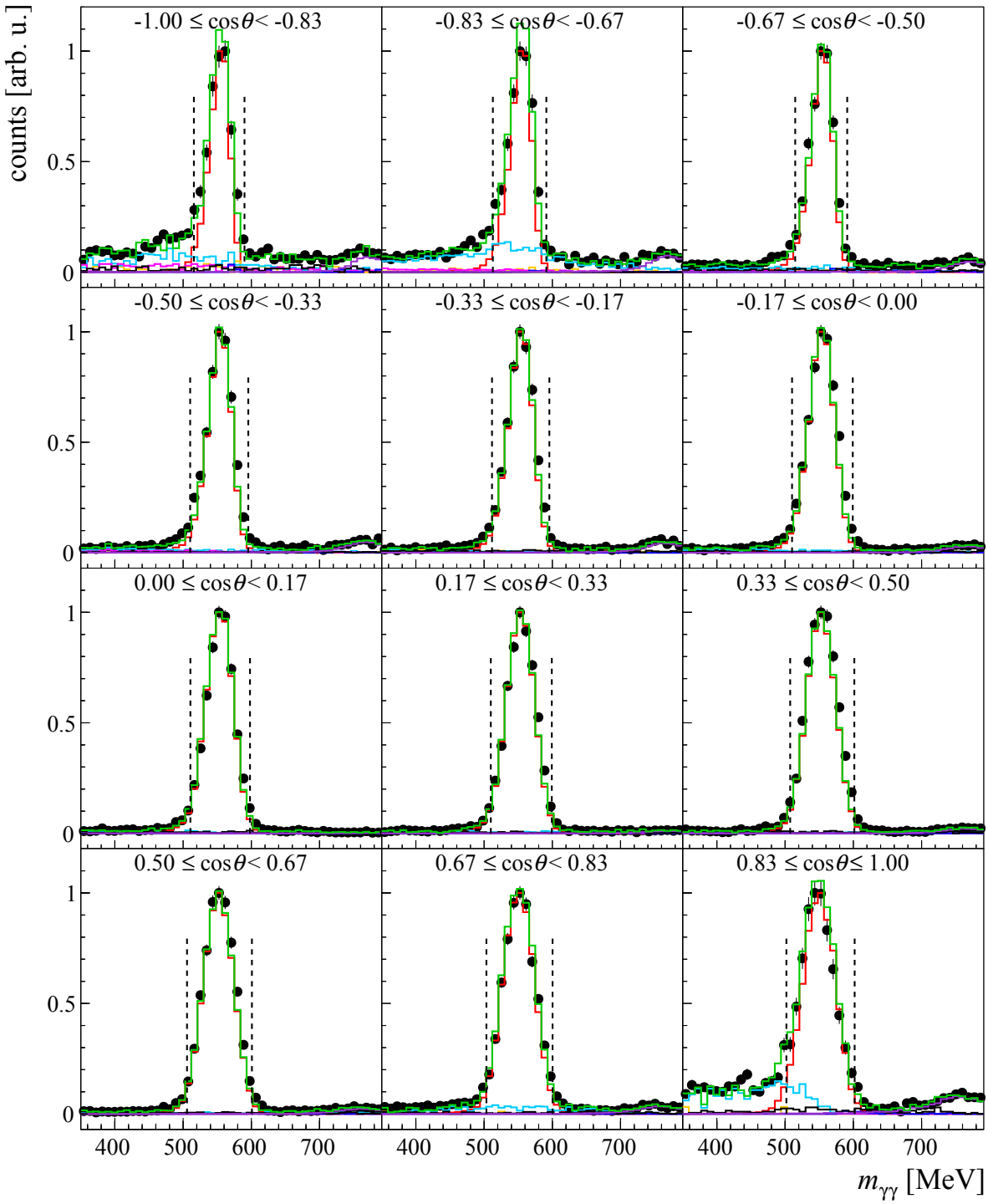

Figure 5.13: Invariant mass spectra are depicted for all $\cos\theta$ bins of the $p\eta$ final state and for the energy bin 1370 MeV $\leq E_\gamma <$ 1430 MeV after applying the selection cuts (time, missing mass, coplanarity and polar angle difference) to the data. The black points represent the data and the red line the $p\eta$ MC, violet line the $p\omega \to p\pi^0\gamma$, light blue line the $p\pi^0$, the black line the $p\pi^0\pi^0$ and magenta the $n\pi^+$ Monte Carlo background contributions and the green line the sum of all Monte Carlo spectra together. The line shape of the MC spectra were fitted to the data. The dashed lines show the chosen $\pm 2\sigma$ cut range for each bin.

The proton creates two tracks mostly in the forward detector ($11.18° < \theta < 27.54°$) and in the MiniTAPS detector ($1° \leq \theta \leq 12°$). Thereby, the proton is high energetic ($> 500\,\text{MeV}$), e.g. it sometimes punches through the forward detector and reaches also the MiniTAPS detector. One of these proton tracks is wrongfully combined with the detected photon to an η meson candidate. In order to filter out these events their kinematics was studied. First of all, the two photon candidates, that were reconstructed to the η meson, were sorted by their energy. The higher energetic photon candidate is referred to as γ_1 and the lower energetic photon as γ_2. Figure 5.11 shows the kinematic region of both reconstructed decay photons for the $p\eta$ final state using MC data. the $p\pi^0$ background contribution is overlayed utilizing black points.
In order to reject these events, three different kinematic conditions were used. The cut conditions were only applied for the relevant kinematic region (see Figure 5.11) of $E_{\gamma_1} > 350\,\text{MeV}$, $E_{\gamma_2} < 300\,\text{MeV}$ and $\theta_{\gamma_2} \leq 55°$:

- 1st condition: Since the proton creates two tracks (its own and the one of γ_2), the angles of the measured recoil proton candidate and γ_2 should not deviate a lot from each other. Figure 5.14 shows the polar and azimuthal angular difference between the reconstructed γ_2 and recoil proton on the left for data, in the middle for the $p\eta$ final state (MC) and on the right for the $p\pi^0$ final state (MC). While the $p\pi^0$ MC distribution shows a clear correlation around $(0°, 0°)$, the $p\eta$ MC shows no correlation. An anti-cut of $|\theta_{\text{recoil}} - \theta_{\gamma_2}| \leq 15°$ and $|\phi_{\text{recoil}} - \phi_{\gamma_2}| \leq 40°$ was applied to remove the $p\pi^0$ background contribution. It is additionally demanded that the recoil proton candidate is detected in either the forward or the MiniTAPS detector in order to not lose unnecessary good $p\eta$ events.

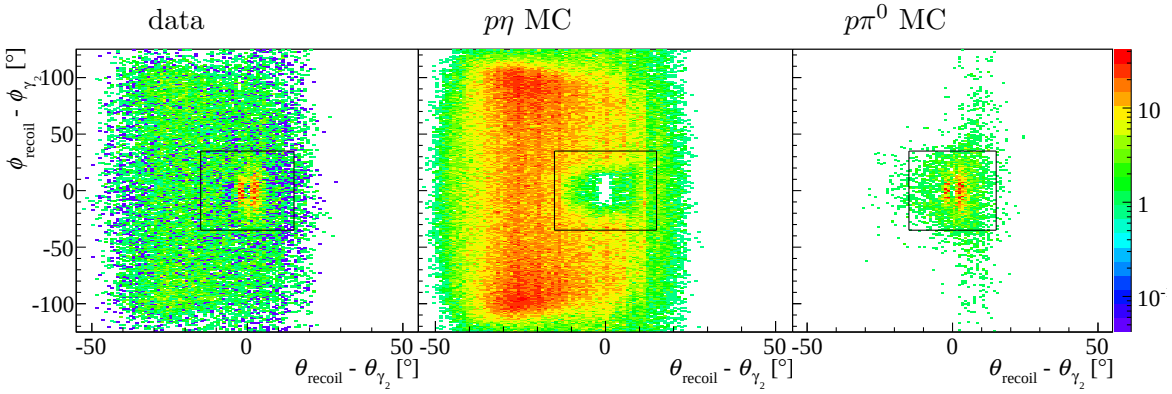

Figure 5.14: The polar and azimuthal angular difference of the recoil proton and γ_2 candidate are plotted on the left for data, in the middle for the $p\eta$ final state MC data and on the right for the $p\pi^0$ final state MC data. The black rectangular marks the anti-cut region.

- 2nd condition: As already mentioned the proton creates two tracks. One reason for this is a wrong identification of a one PED cluster to a two PED cluster. This happens dominantly in the gap region between the Crystal Barrel and the forward detector. Figure 5.15 shows the number of reconstructed PEDs per cluster in black without and in blue after applying the first condition. While almost only one PED cluster are present for the $p\eta$ final state, the $p\pi^0$ background has a much higher percentage of two PED cluster. If the proton candidate and γ_2 are part of a 2PED cluster, then the event is most likely a wrongfully reconstructed $p\pi^0$ event. After applying the first anti-π^0 cut condition, only

4% $p\eta$ events are omitted but also 70% of the $p\pi^0$ background. Utilizing an additional cut by retaining only one PED cluster events, 58% of the remaining $p\pi^0$ background can be removed (blue histogram) while only 7% $p\eta$ events are lost. In total, the first two conditions remove 87% of the $p\pi^0$ background.

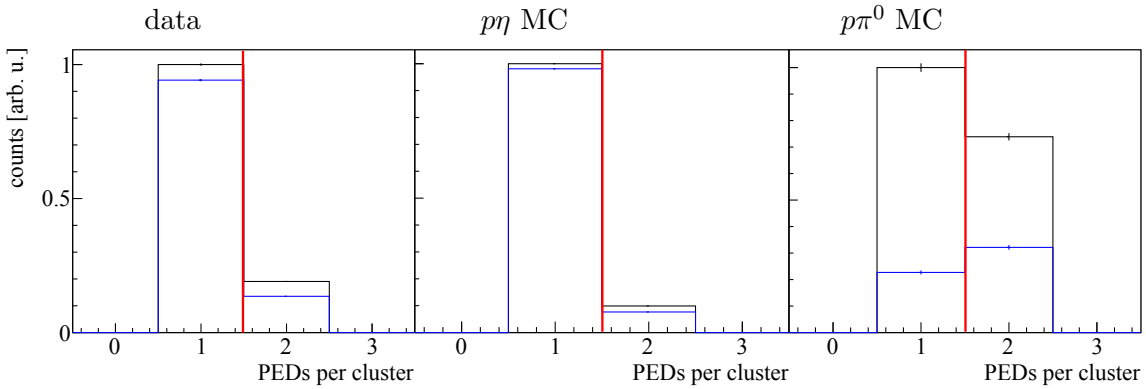

Figure 5.15: The number of PEDs per cluster is plotted on the left for data, in the middle for the $p\eta$ final state (MC) and on the right for the $p\pi^0$ final state (MC) without applying the first anti-π^0 cut condition (black) and after applying it (blue).

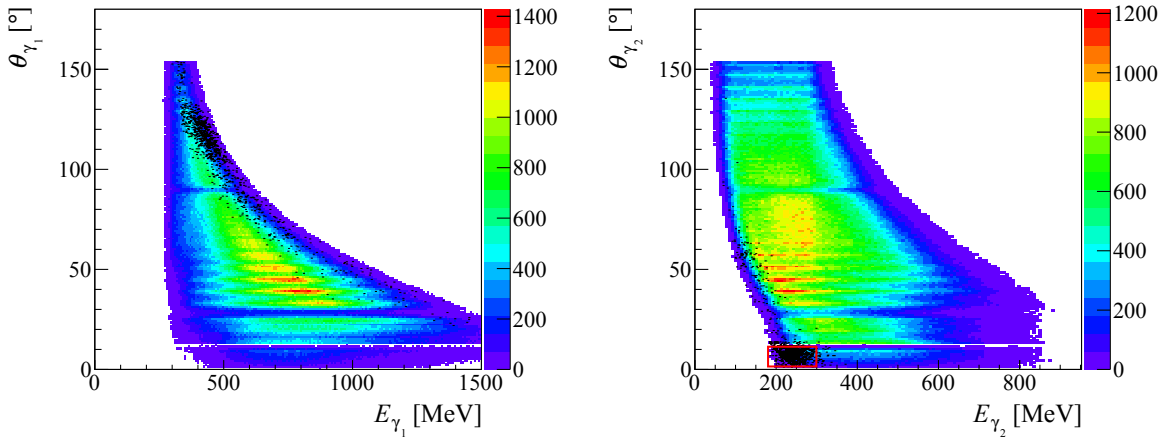

Figure 5.16: The energy and polar angle θ of both reconstructed photon candidates γ_1 and γ_2 are shown for the $p\eta$ final state (MC). The background contribution from the $p\pi^0$ final state is overlayed using black points (MC). After applying the first two anti-π^0 cut conditions most of the remaining $p\pi^0$ background is located at $\theta_{\gamma_2} < 12°$ (when it is detected in the MiniTAPS detector) and for $E_{\gamma_2} < 300\,\text{MeV}$ (red box).

- Figure 5.16 shows the kinematic region of both reconstructed photon candidates γ_1 and γ_2 after applying the first two anti-π^0 cut conditions. Almost all of the remaining background is located at $\theta_{\gamma_2} < 12°$, which is the region covered by the MiniTAPS detector and for the energy region $E_{\gamma_2} < 300\,\text{MeV}$ (see red box in Figure 5.16). If γ_2 is detected in the MiniTAPS detector and has an energy smaller than 300 MeV, then a cluster size higher than 2 is demanded to ensure the reconstructed photon candidate is really a photon

belonging to the $p\eta$ reaction and not to a wrongly reconstructed $p\pi^0$ event. This removes 90% of the remaining $p\pi^0$ background and 65% $p\eta$ events (see Figure 5.17). This third condition removes a lot of $p\eta$ events but only within a small kinematic region. Overall, no acceptance gaps are created using this cut (see Section 5.2.5).

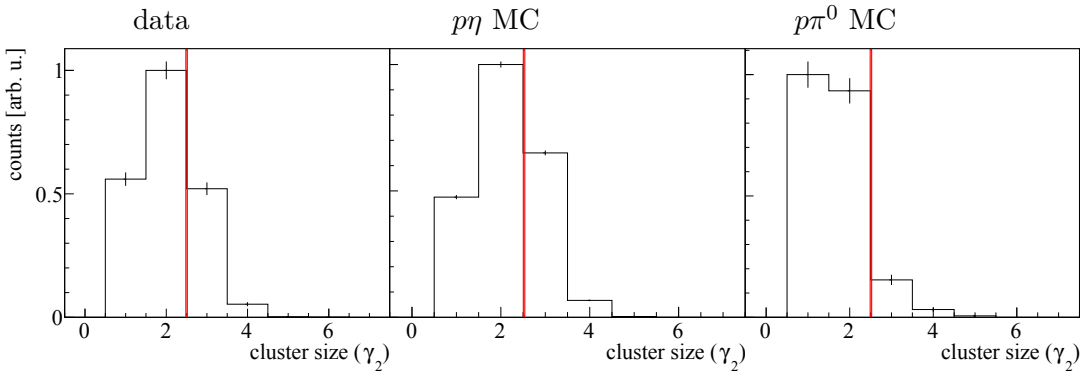

Figure 5.17: The cluster size of γ_2 is plotted on the left for data, in the middle for the $p\eta$ final state (MC) and on the right for the $p\pi^0$ final state (MC) for the case that γ_2 is detected in the MiniTAPS detector and it has an energy smaller than 300 MeV (compare the red box in Figure 5.16).

All in all, the anti-π^0 cut removes 98% of the $p\pi^0$ background underneath the η invariant mass peak. It is more efficient than using a charge cut which can remove only 66% of the background according to Monte Carlo simulations. All invariant mass spectra for the energy range of 1370 MeV $\leq E_\gamma <$ 1430 MeV are depicted in Figure 5.19 after applying in addition the anti-π^0 cut. As expected the $p\pi^0$ background is no longer contributing significantly underneath the η mass peak.

5.2.2.3 Missing mass cut

The missing mass spectra exhibit a clear peak as expected around the proton mass of 938 MeV (see Figure 5.8 second row).

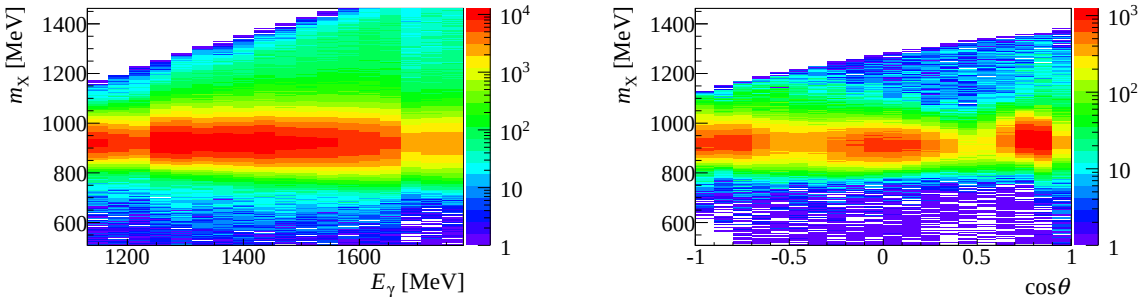

Figure 5.18: Left: The missing mass is plotted as a function of the beam photon energy E_γ and integrated over the entire angular range for the $p\pi^0$ final state. In the energy region 1239 MeV-1671 MeV data of both coherent edges 1750 MeV (July and August 2013 beamtimes) and 1850 MeV (September and October 2013 beamtimes) are added up leading to an increased statistics in this region. Right: The $\cos\theta$ dependence of the missing mass is shown for the energy bin 1419 MeV $\leq E_\gamma <$ 1455 MeV. The selection cuts (time, invariant mass, coplanarity and polar angle difference) are applied.

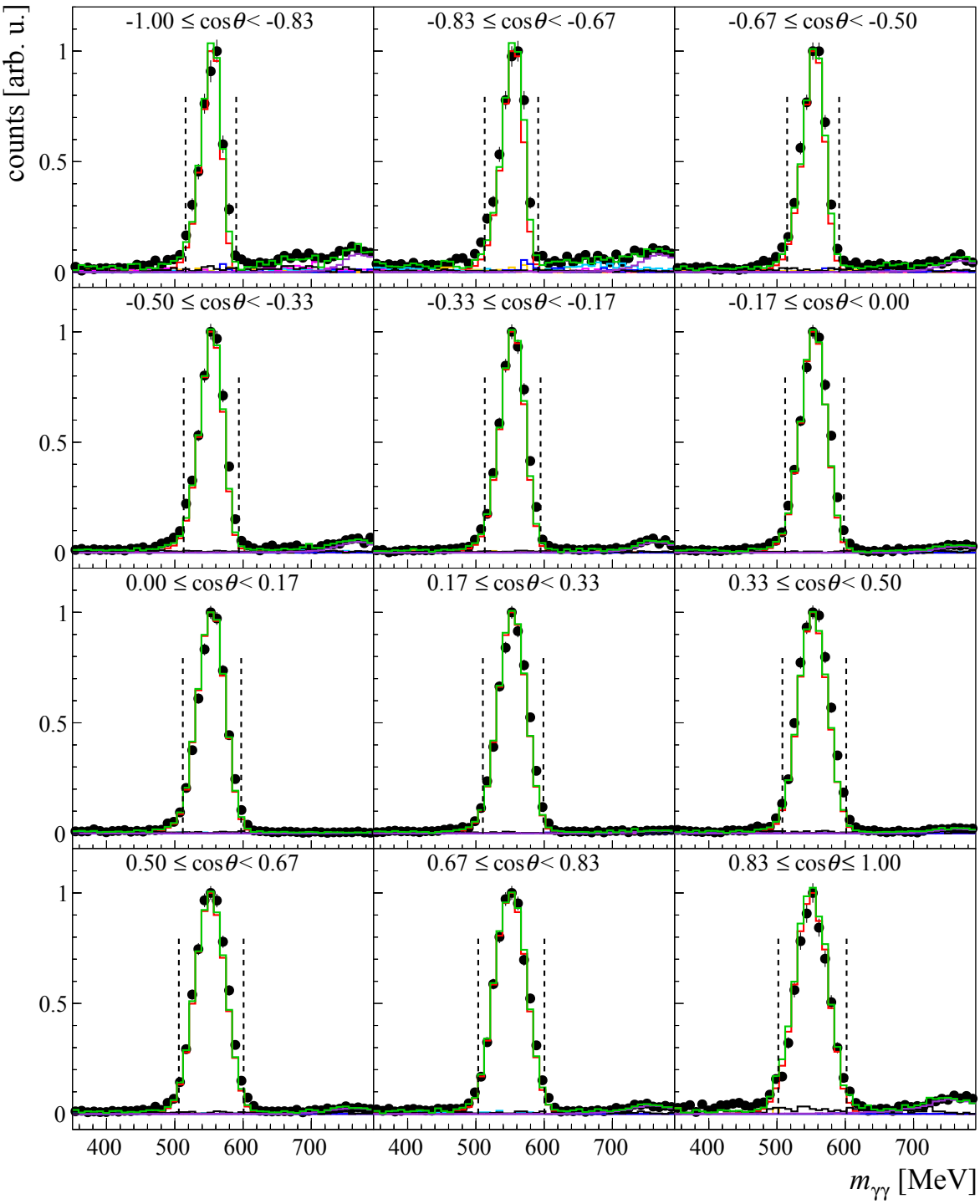

Figure 5.19: Invariant mass spectra are depicted for all $\cos\theta$ bins of the $p\eta$ final state and for the energy bin 1370 MeV $\leq E_\gamma <$ 1430 MeV after applying all other selection cuts (time, missing mass, coplanarity and polar angle difference) including the anti-π^0 cut to the data. The black points represent the data and the red line the $p\eta$ MC, violet line the $p\omega \to p\pi^0\gamma$, light blue line the $p\pi^0$, black line the $p\pi^0\pi^0$ and magenta the $n\pi^+$ Monte Carlo background contributions and the green line the sum of all Monte Carlo spectra together. The dashed lines show the chosen $\pm 2\sigma$ cut ranges.

Moreover, a broad shoulder is visible at higher masses which originates from different final states where one or more particles are lost. Figure 5.18 shows on the left the missing mass as a function of the beam photon energy and on the right the $\cos\theta$ dependence of the missing mass for the energy bin 1419 MeV $\leq E_\gamma <$ 1455 MeV and for the $p\pi^0$ final state. Similar as in the case of the invariant mass, the missing mass shows a strong $\cos\theta$ dependence. However, the missing mass peak position is shifted from the expected value to the opposite direction of the shifts observed in the invariant mass, since the meson four-momentum is subtracted from the initial state four-momentum to calculate the missing mass. The missing mass spectra of all $\cos\theta$ bins are plotted in Figure 5.21 for the $p\pi^0$ final state for an energy range of 1419 MeV $\leq E_\gamma <$ 1455 MeV. After all time and kinematic constraints are applied to the data, only small background contributions from the $p\omega \to p\pi^0\gamma$ final state are visible at higher masses, e.g. for the angular range of $-0.9 \leq \cos\theta < -0.4$. For these angular bins one photon of the final state $p\omega \to p\pi^0\gamma$ is lost which results in higher missing masses than the proton mass. The fit of the missing mass spectra with Monte Carlo distributions (green line) agrees well with the data. Small deviations in position and width of the spectra are due to imperfect agreement between the calibration procedure of data and MC and an uncertainty due to the unknown exact target position. In addition, the tagger is not present in the simulation and no clustering of bar and fiber hits is performed.
Figure 5.20 depicts the energy and angular dependence for the $p\eta$ final state. The missing mass spectra for all $\cos\theta$ bins are depicted after applying all other kinematic cuts for the $p\eta$ final state and for an energy range of 1419 MeV $\leq E_\gamma <$ 1455 MeV in Figure 5.22. The shoulder at higher masses at backward angles is described well using the $n\pi^+\eta$ (blue line), the $p\pi^+\pi^-$ (orange line), the $p\omega \to p\pi^0\gamma$ (violet line) and the $p\pi^0\pi^0$ (black line) final state Monte Carlo distributions. After applying the anti-π^0 cut negligibly small contributions from the $p\pi^0$ and the $n\pi^+$ final states remain under the selected missing mass peak range and thus, are not shown. The background contributions of $n\pi^+\eta$ occur due to a lost π^+. Therefore, the missing mass is larger than the proton mass.

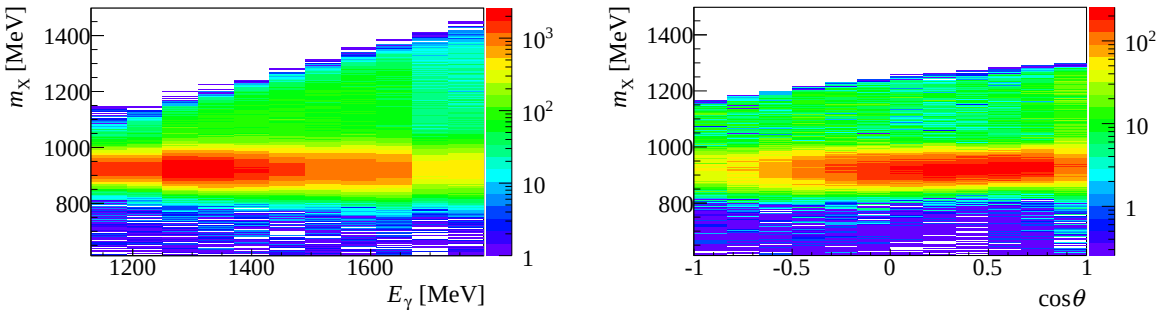

Figure 5.20: Left: The missing mass is plotted as a function of the beam photon energy E_γ and integrated over the entire angular range for the $p\eta$ final state. In the energy region of 1250 MeV-1670 MeV data of both coherent edges 1750 MeV (July and August 2013 beamtimes) and 1850 MeV (September and October 2013 beamtimes) are added up leading to an increased statistics in this region. Right: The $\cos\theta$ dependence of the missing mass is shown for the energy bin 1370 MeV $\leq E_\gamma <$ 1430 MeV. The selection cuts (time, invariant mass, anti-π^0, coplanarity and polar angle difference) are applied.

Since the background contributions are located at larger masses than the proton mass, but are close to the signal mass peak, a narrower cut of $(-1.7\sigma, +1.7\sigma)$ was chosen for each energy and angular bin and for both final states.

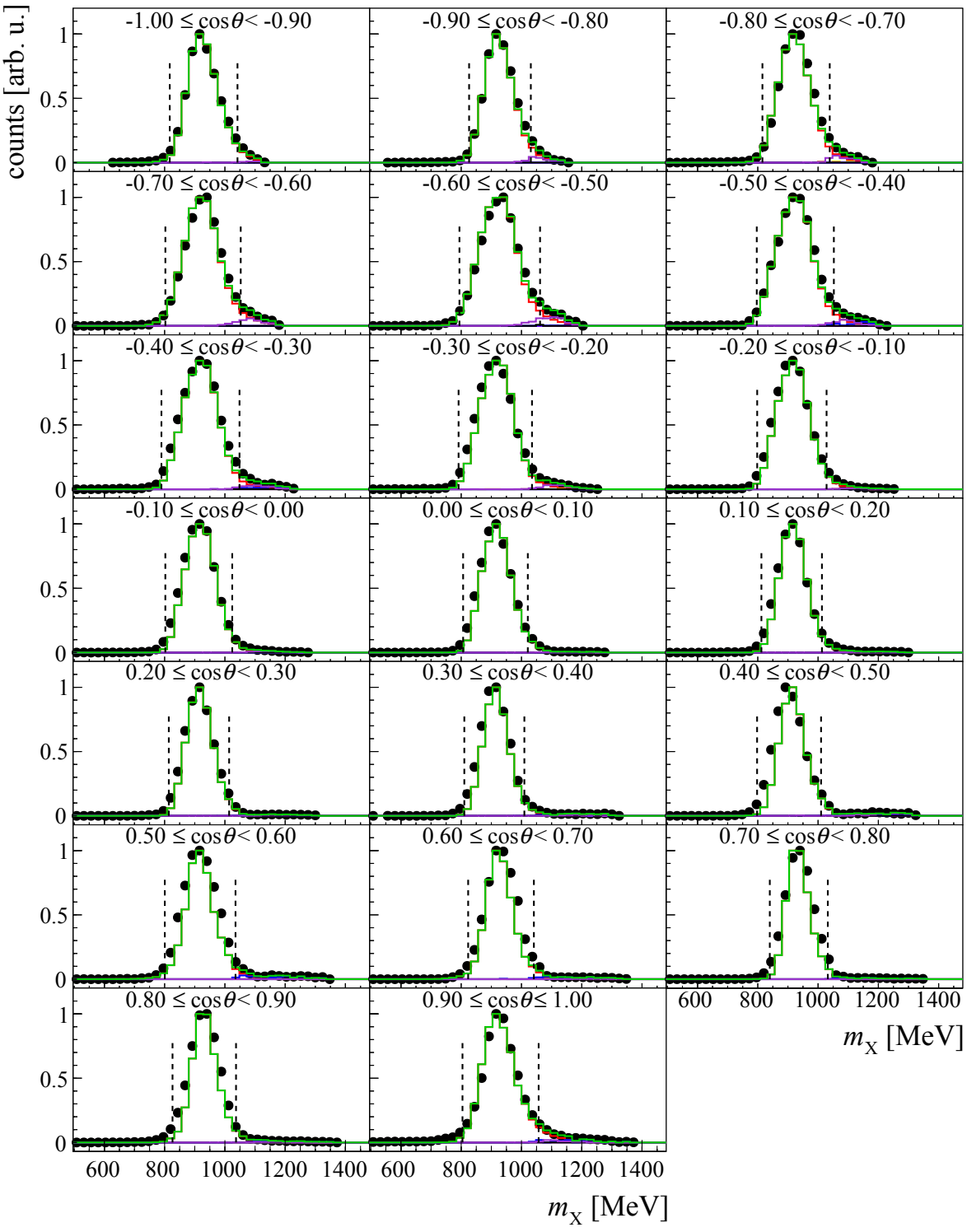

Figure 5.21: Missing mass spectra of the $p\pi^0$ final state are shown for all $\cos\theta$ bins of the energy bin 1419 MeV $\leq E_\gamma <$ 1455 MeV. All other cuts are applied to the data (time, invariant mass, coplanarity and polar angle difference). The black points represent the data and the red line the $p\pi^0$ MC, violet line the $p\omega \to p\pi^0\gamma$ background contribution and the green line the sum of all Monte Carlo spectra together. The dashed lines show the $\pm 1.7\sigma$ cut ranges.

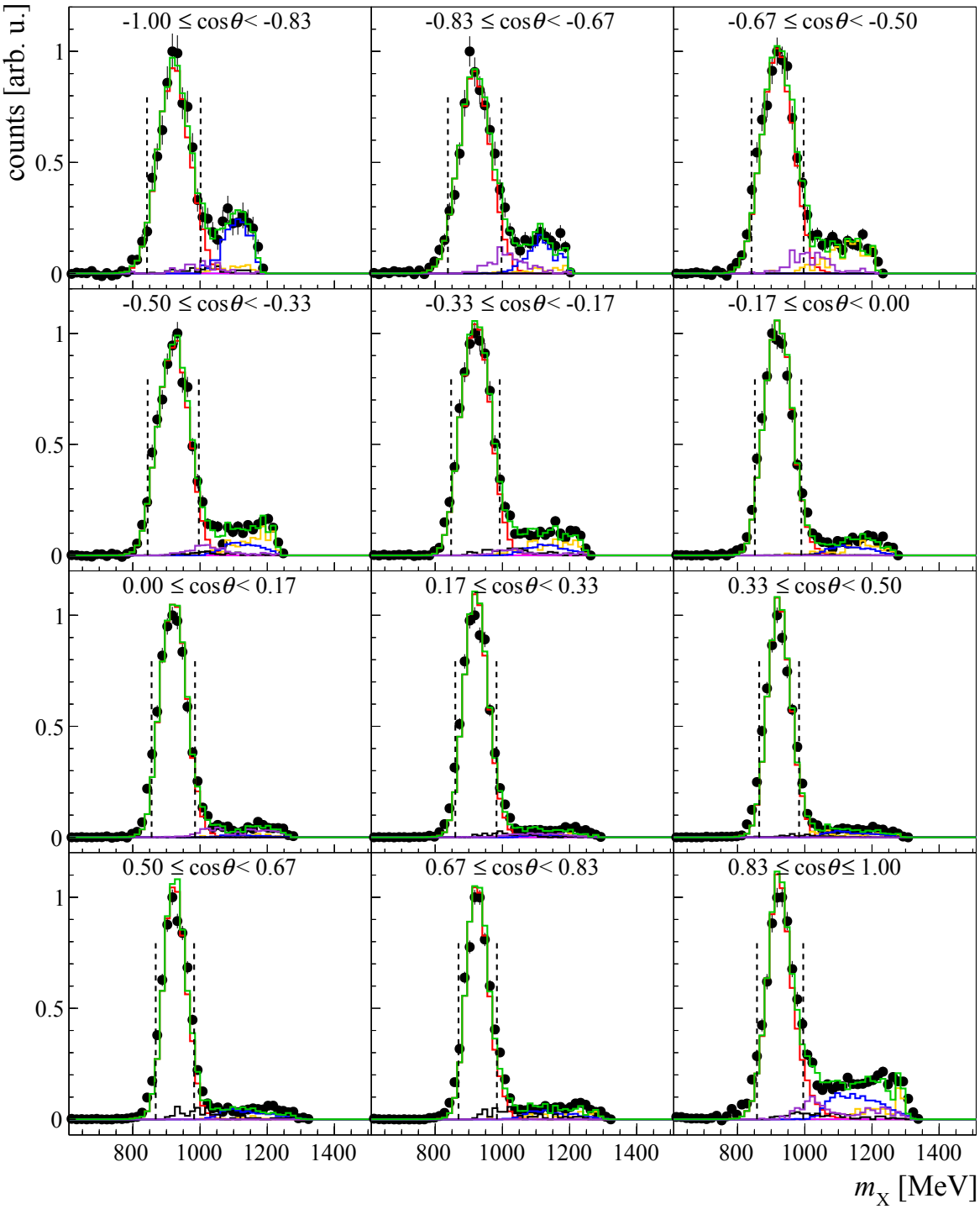

Figure 5.22: Missing mass spectra of the $p\eta$ final state are shown for all $\cos\theta$ bins of the energy bin 1370 MeV $\leq E_\gamma <$ 1430 MeV. All other cuts are applied to the data (time, invariant mass, anti-π^0, coplanarity and polar angle difference). The black points represent the data and the red line the $p\eta$ MC, violet line the $p\omega \to p\pi^0\gamma$, blue line the $n\pi^+\eta$, light blue the $p\pi^0$, black the $p\pi^0\pi^0$ and orange the $p\pi^+\pi^-$ simulated background contributions and the green line gives the sum of all Monte Carlo spectra together. The dashed lines show the chosen $\pm 1.7\sigma$ cut ranges.

Here, the background is almost completely suppressed since the background contributions visible in the missing mass spectra start at around 1000 MeV and are removed by the missing mass cut.

5.2.2.4 Angular cuts

The coplanarity distributions show the coplanar relation between the measured meson and recoil proton with a peak at $\Delta\phi - 180° = 0°$. The energy and $\cos\theta$ dependence of the coplanarity is depicted in Figure 5.23 for the $p\pi^0$ and in Figure 5.24 for the $p\eta$ final state. In both cases the width of the spectra is largest for the angular range of $-0.9 \leq \Delta\phi - 180° < -0.4$, since the proton is detected in the forward detector in this angular range where each crystal covers 12° in ϕ and since protons deposit energy in only a few crystals leading to an imprecise determination of the impact point of the protons compared to photons. When all three particles are detected in the Crystal Barrel detector the best ϕ-resolution is achieved and a more narrow cut can be applied.

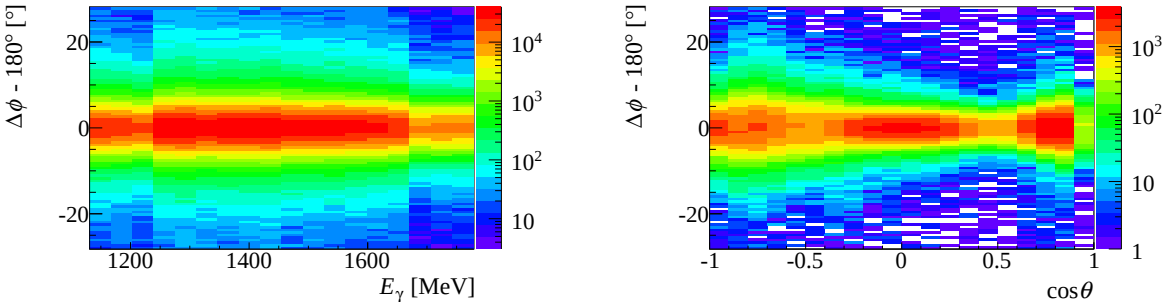

Figure 5.23: Left: The coplanarity is plotted as a function of the beam photon energy E_γ and integrated over the entire angular range for the $p\pi^0$ final state. In the energy region 1239 MeV-1671 MeV data of both coherent edges 1750 MeV (July and August 2013 beamtimes) and 1850 MeV (September and October 2013 beamtimes) are added up leading to an increased statistics in this region. Right: The $\cos\theta$ dependence of the coplanarity is shown for the energy bin 1419 MeV $\leq E_\gamma <$ 1455 MeV. The selection cuts (time, invariant mass, missing mass and polar angle difference) are applied.

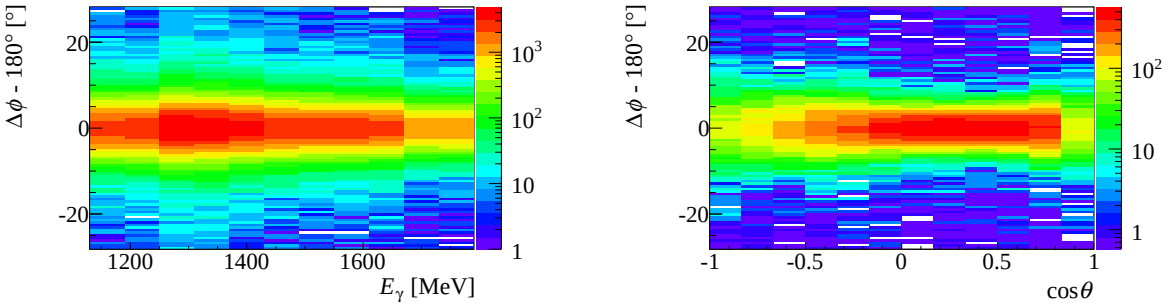

Figure 5.24: Left: The coplanarity is plotted as a function of the beam photon energy E_γ and integrated over the entire angular range for the $p\eta$ final state. In the energy region 1250 MeV-1670 MeV data of both coherent edges 1750 MeV (July and August 2013 beamtimes) and 1850 MeV (September and October 2013 beamtimes) are added up leading to an increased statistics in this region. Right: The $\cos\theta$ dependence of the coplanarity is shown for the energy bin 1370 MeV $\leq E_\gamma <$ 1430 MeV. The selection cuts (time, invariant mass, anti-π^0, missing mass and polar angle difference) are applied.

The influence of the other kinematic cuts on the coplanarity spectra is demonstrated in Figure 5.8 (third row). The two enhancement at $\pm 140°$ are caused through a combinatorial mismatch of a decay photon with the recoil proton, which are removed through the utilization of all kinematic constraints (see Figure 5.8 third row). Only in the spectrum of the $p\eta$ final state the enhancements nevertheless persist. They are not caused by combinatorial background of the $p\eta$ final state itself but mostly by the background channel $p\pi^0$. The anti-π^0 cut removes 98% of the $p\pi^0$ background underneath the coplanarity peak at 0° (see Figure 5.25 on the left). The two enhancements at $> 100°$ and at $< -100°$ are finally removed by a $\pm 2\sigma$ coplanarity cut. Figure 5.25 shows on the right the over all energy and $\cos\theta$ bins integrated coplanarity spectrum of the $p\eta$ final state in data (black points). After all kinematic cuts, small background contributions remain from $p\pi^0$, $n\pi^+$, $n\pi^+\eta$, $p\pi^0\pi^0$ and $p\omega \to p\pi^0\gamma$. The $p\pi^+\pi^-$ background is completely removed by the missing mass cut. The sum of all MC spectra describes the data well indicating that all significant background contributions are taken into consideration.

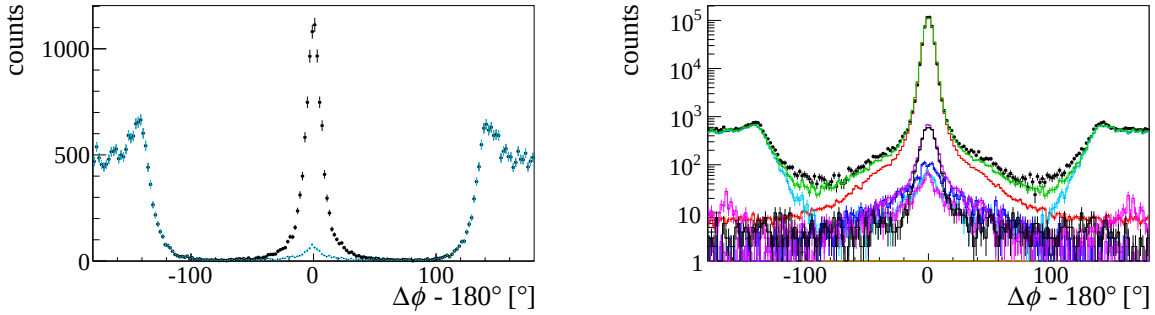

Figure 5.25: Left: The coplanarity spectrum is depicted using $p\pi^0$ MC data as obtained after all kinematic cuts are applied for a $p\eta$ analysis with (light blue) and without (black) utilizing the anti-π^0 cut. Right: The coplanarity spectrum is plotted after all kinematic cuts including the anti-π^0 cut and integrated over all energy and $\cos\theta$ bins of the $p\eta$ final state (black points: data). The following MC distributions are used to fit the data (red: $p\eta$, magenta: $n\pi^+$, light blue: $p\pi^0$, blue: $n\pi^+\eta$, violet: $p\omega \to p\pi^0\gamma$, black: $p\pi^0\pi^0$, yellow: $p\pi^+\pi^-$ and green: sum of all MC distributions).

The coplanarity spectra for all $\cos\theta$ bins of the energy range $1419\,\text{MeV} \leq E_\gamma < 1455\,\text{MeV}$ are depicted in Figure 5.26 for the $p\pi^0$ final state. Likewise, the coplanarity spectra of the $p\eta$ final state are shown in Figure 5.27. Since the background contributions are low after all other kinematic cuts are applied to the data, the data is only compared to $p\pi^0$ and $p\eta$ final state MC, respectively. A very good agreement between data and MC data is present. A cut of $\pm 2\sigma$ was chosen for both final states using Gaussian fits to each energy and $\cos\theta$ bin spectrum.

The polar angle difference spectra are like the missing mass spectra slightly asymmetric. After all kinematic constraints are applied, a peak at 0° is well visible in the over all energy and $\cos\theta$ bins integrated spectrum (compare 5.8 (fourth row)). The energy and $\cos\theta$ dependence is demonstrated in Figure 5.28 for the $p\pi^0$ final state and in Figure 5.29 for the $p\eta$ final state. The width of the polar angle difference spectrum is narrowest when the proton is detected in the MiniTAPS detector ($-1 \leq \cos\theta < -0.8$) since the detector has the better polar angular resolution than the Crystal Barrel or the forward detector. The width is largest for 2.5 PED events when the proton is detected only in the inner detector for $\cos\theta > 0.8$.

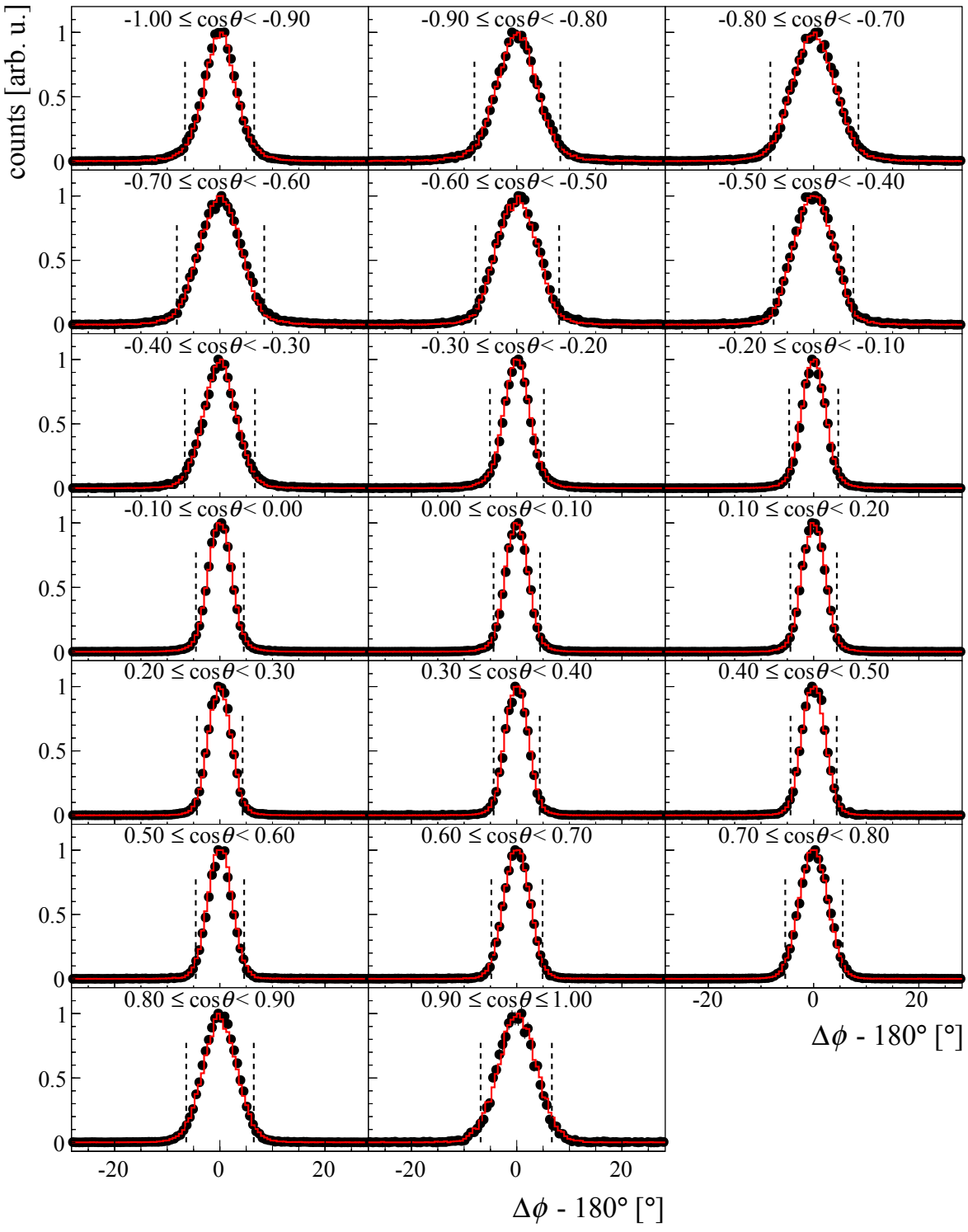

Figure 5.26: Coplanarity spectra of the $p\pi^0$ final state (3 PED and 2.5 PED) are shown for the energy bin 1419 MeV $\leq E_\gamma <$ 1455 MeV. All $\cos\theta$ bins of this energy bin are depicted. All cuts except for the coplanarity cut are applied to the data (time, invariant and missing mass and polar angle difference). The black points represent the data and the red line the $p\pi^0$ Monte Carlo distributions. The dashed lines show the chosen $\pm 2\sigma$ cut ranges.

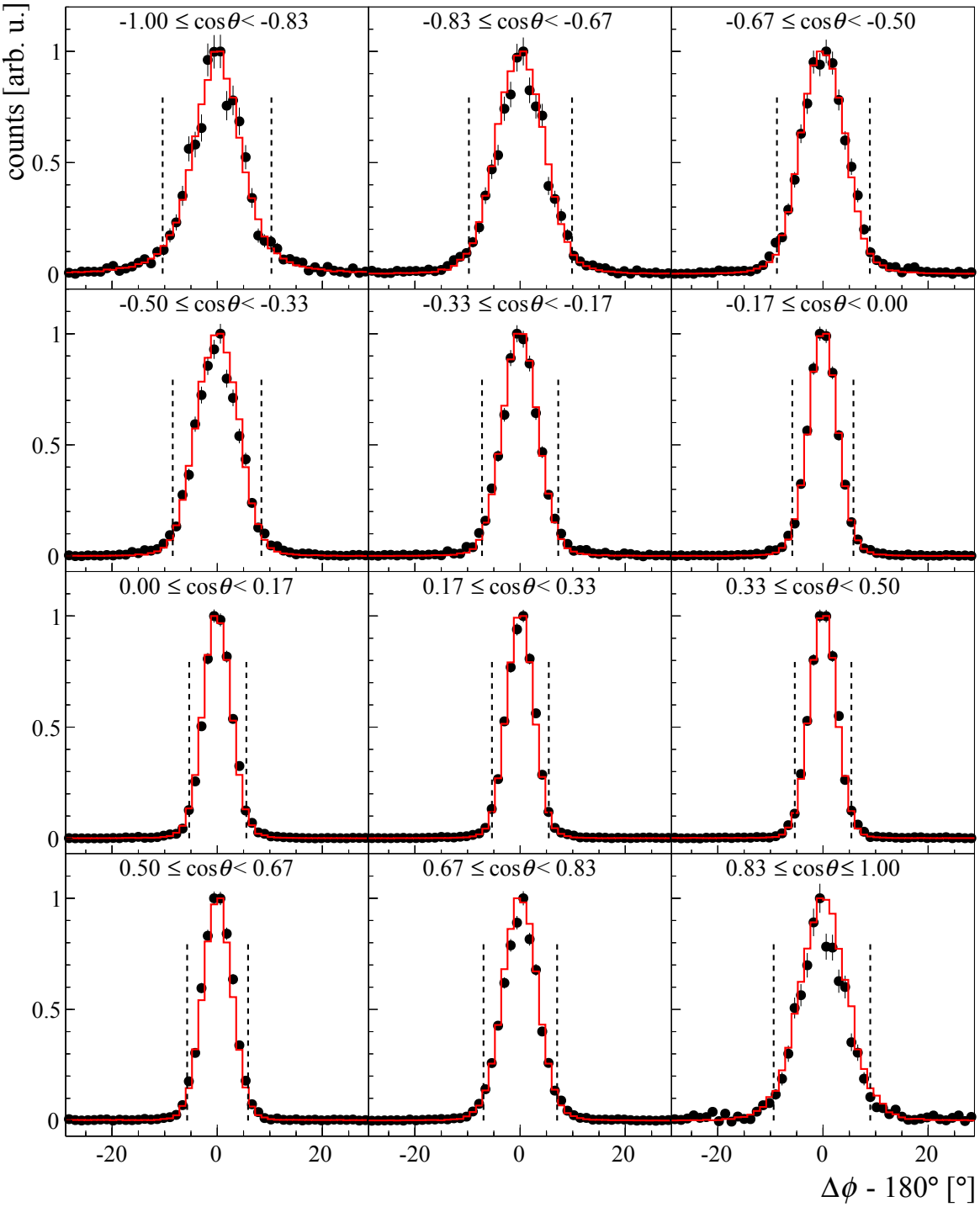

Figure 5.27: Coplanarity spectra of the $p\eta$ final state (3 PED and 2.5 PED) are shown for the energy bin 1370 MeV $\leq E_\gamma <$ 1430 MeV. All $\cos\theta$ bins of this energy bin are depicted. All cuts except for the coplanarity cut are applied to the data (time, invariant and missing mass, anti-π^0 and polar angle difference). The black points represent the data and the red line the $p\eta$ Monte Carlo distributions. The dashed lines show the chosen $\pm 2\sigma$ cut ranges.

The projections for each $\cos\theta$ bin of one energy bin are depicted in Figure 5.30 for the $p\pi^0$ and in Figure 5.31 for the $p\eta$ final state. For some angular bins e.g. $-0.8 \leq \cos\theta < -0.7$, $-0.6 \leq \cos\theta < -0.3$ of the $p\pi^0$ final state (see Figure 5.30) two peaks are visible. This observation can be attributed to the small cluster sizes of protons, especially if the proton deposits its energy only in one crystal. Then the impact position is assumed to be the crystal center. However, if the proton's true impact point is the edge of a crystal and not its center, the polar angle difference spectra reveal two peaks at $\pm 3°$. Small deviations to MC simulated spectra (red line) are observed in the transitional regions from MiniTAPS to the forward detector ($-0.8 \leq \cos\theta < -0.7$) and forward detector and Crystal Barrel detector ($-0.4 \leq \cos\theta < -0.2$). This indicates that the simulated setup can be improved in the transitional regions in the future. A $\pm 2\sigma$ cut is applied for each energy and angular bin utilizing a Novosibirsk fit function and for those bins with a two peak structure a combination of two Novosibirsk functions.

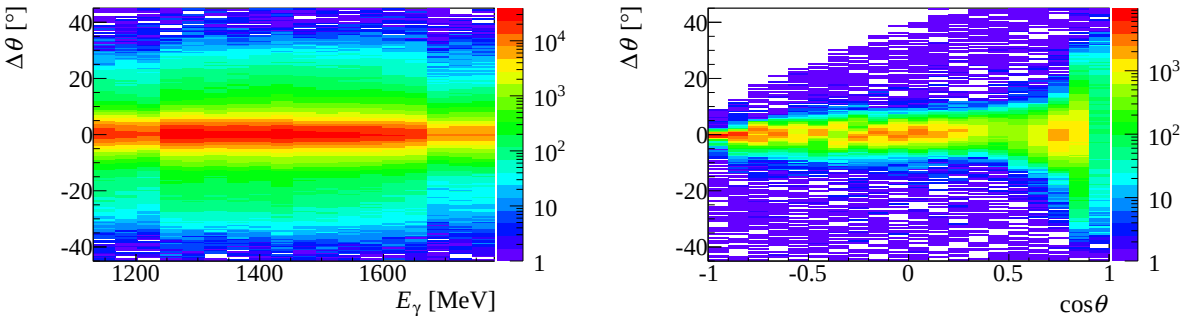

Figure 5.28: Left: The polar angle difference of the calculated and reconstructed recoil proton is plotted as a function of the beam photon energy E_γ and integrated over the entire angular range for the $p\pi^0$ final state. In the energy region 1239 MeV-1671 MeV data of both coherent edges 1750 MeV (July and August 2013 beamtimes) and 1850 MeV (September and October 2013 beamtimes) are added up leading to an increased statistics in this region. Right: The $\cos\theta$ dependence of the polar angle difference is shown for the energy bin 1419 MeV $\leq E_\gamma <$ 1455 MeV. The selection cuts (time, invariant mass, missing mass and coplanarity) are applied.

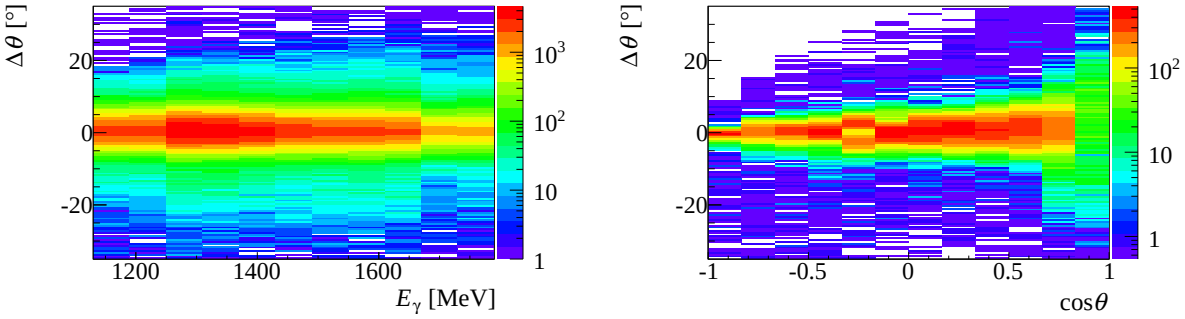

Figure 5.29: Left: The polar angle diff. of the calculated and reconstructed recoil proton is plotted as a function of the beam photon energy E_γ and integrated over the entire angular range for the $p\eta$ final state. In the energy region 1250 MeV-1670 MeV data of both coherent edges 1750 MeV (July and August 2013 beamtimes) and 1850 MeV (September and October 2013 beamtimes) are added up leading to an increased statistics in this region. Right: The $\cos\theta$ dependence of the polar angle difference is shown for the energy bin 1370 MeV $\leq E_\gamma <$ 1430 MeV. The selection cuts (time, invariant mass, anti-π^0, missing mass and coplanarity) are applied.

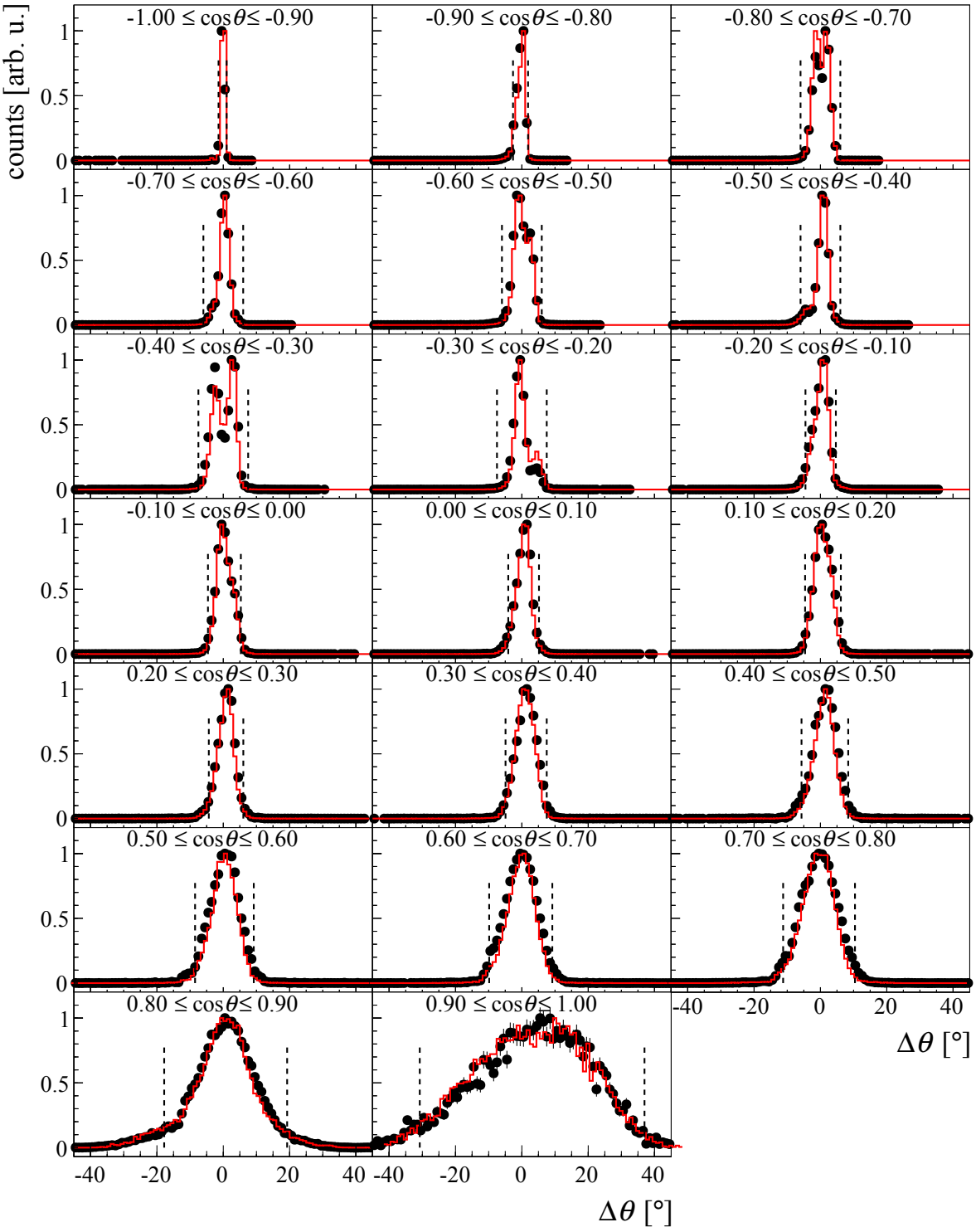

Figure 5.30: The polar angle difference spectra of the $p\pi^0$ final state (3 PED and 2.5 PED) are shown for the energy bin 1419 MeV $\leq E_\gamma <$ 1455 MeV. All $\cos\theta$ bins of this energy bin are depicted. All cuts except for the polar angle difference cut are applied to the data (time, invariant and missing mass and coplanarity). The black points represent the data and the red line the $p\pi^0$ Monte Carlo distributions. The dashed lines show the chosen cut ranges.

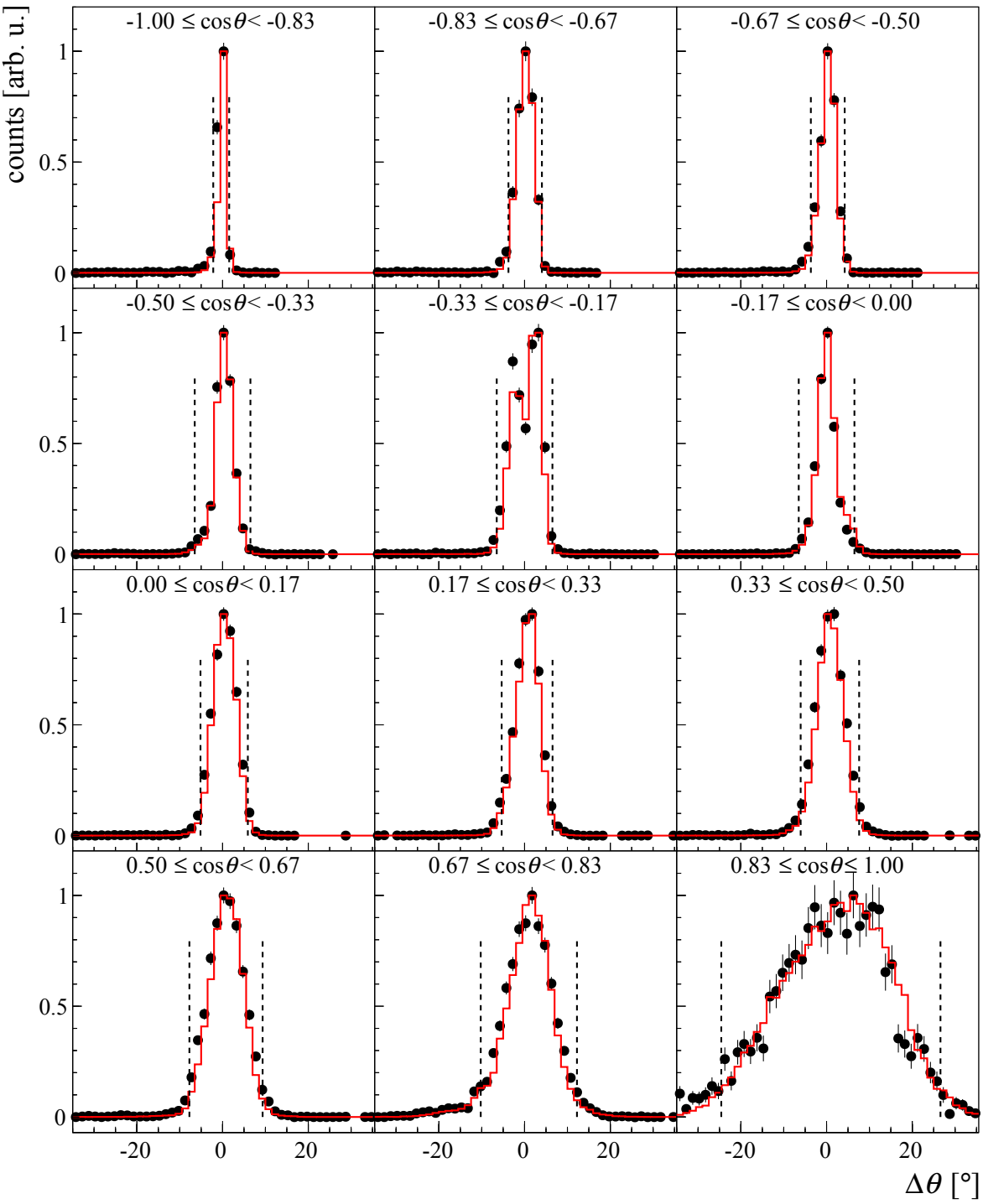

Figure 5.31: The polar angle difference spectra of the $p\eta$ final state (3 PED and 2.5 PED) are shown for the energy bin 1370 MeV $\leq E_\gamma <$ 1430 MeV. All $\cos\theta$ bins of this energy bin are depicted. All cuts except for the polar angle difference cut are applied to the data (time, invariant and missing mass, anti-π^0 and coplanarity). The black points represent the data and the red line the $p\eta$ Monte Carlo distributions. The dashed lines show the chosen cut ranges.

5.2.3 Charge cut

Using the charge information of all 3 particles and demanding exactly one charged and two neutral particles for the 3 PED events can remove ≈ 66% of the observed $p\pi^0$ background in the $p\eta$ analysis and it can also reduce the background seen in the missing mass spectra, e.g. the $p\pi^+\pi^-$ channel would not contribute at all. However, a charge cut does not only remove the background contributions but also signal events due to inefficiencies of the charge sensitive detectors. The charge detection efficiency can be determined by taking the ratio of the number of events with the charge cut to events selected without it and assuming that after the application of time and kinematic cuts no significant background is left. Figure 5.32 shows on the left the efficiency for marking the two decay photon candidates of the $p\pi^0$ analysis as uncharged. Over a large polar angular range the photons are identified as uncharged with an efficiency higher than 85%. However, with increasing beam photon energy, the efficiency is reduced to around 70% for $\theta_\gamma < 30°$ which is covered by the forward detector and MiniTAPS detector. Investigations revealed a charge detection efficiency of 85-90% [Her18] to not mark a photon wrongfully as charged in the MiniTAPS detector which is consistent with a combined charge detection efficiency for both photons to be recognized as uncharged of 72-81% and agrees well with the found efficiency here. The recoil proton candidate is marked as charged with an efficiency of higher than 80-85% for the polar angular ranges of $2° < \theta_p < 10°$ and $17° \leq \theta_p \leq 50°$. Larger inefficiencies are present for $10° \leq \theta_p \leq 17°$ and $\theta_p > 50°$[2]. If one of the decay photon and the proton are both detected in the region of the forward detector, a charge cut requesting two uncharged photons candidates and a charged proton candidate can lead to a loss of around 50% of the statistics. Therefore, it was decided to not use a charge cut for the 3 PED event class. Instead, a charge cut is advantageous for 2 PED events since in this kinematic region the $p\pi^+\pi^-$ channel dominates over the $p\pi^0$ or $p\eta$ final states due to its four or ten times larger cross section, respectively.

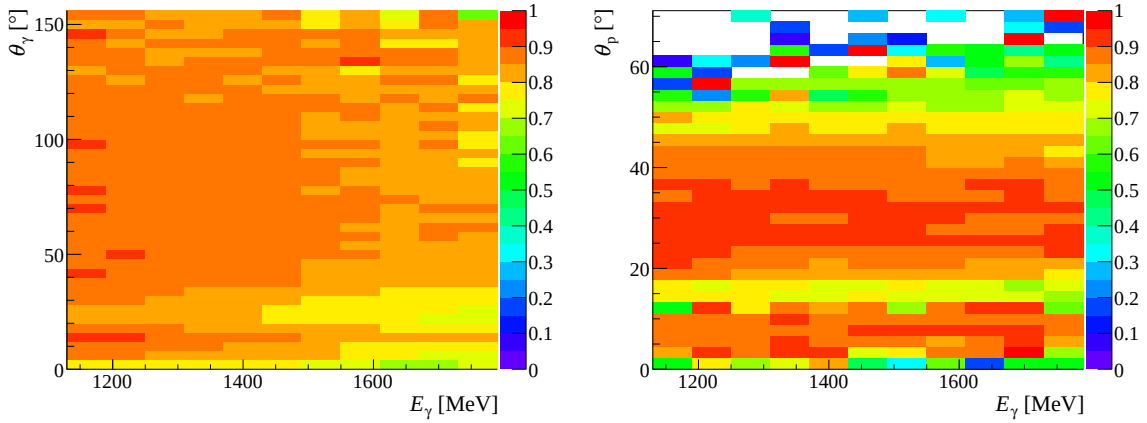

Figure 5.32: Left: The efficiency for marking a decay photon as uncharged is plotted as a function of the beam photon energy and the polar angle of the photon in the lab system. Right: The efficiency for marking a proton candidate as charged is shown. Both efficiencies are determined for a $p\pi^0$ analysis.

[2] The determined charge detection efficiencies for $\theta_p > 50°$ and $2° < \theta_p$ have to be taken with caution since only very few proton candidates are detected in this angular region. For a precise determination e.g. the $p\pi^+\pi^-$ final state would be more suitable as the $\pi^\pm$ are allowed to fly in the full polar angular range. In addition investigations are performed to improve the reconstruction software of the inner detector [Bar19].

5.2.4 Additional cuts for 2 PED events

The time, invariant and missing mass cuts were applied for the 2 PED events just like for the 3 PED events. To reduce background contributions, additional conditions were demanded based on MC data. Firstly, only events, where both decay photons have a larger kinetic energy than 130 MeV, were retained. Moreover, in the $p\pi^0$ final state both decay photons are so strongly boosted in forward direction that they only reach the forward or the MiniTAPS detector. However, in the $p\eta$ final state, the combination of one photon detected in the forward and one in the MiniTAPS detector or that both photons are detected in the MiniTAPS detector is not present in the analyzed kinematic range. This knowledge was used to reject background events. The largest impact on improving the signal to background ratio for the $p\eta$ final state has a cut on the cluster size of the decay photon candidates. Here, a cluster size larger than three (CB) or ten (FD) or two (MiniTAPS) was required for both decay photons since the events with smaller cluster sizes do not originate from the desired reaction as a comparison with MC data shows (see Figure 5.33).

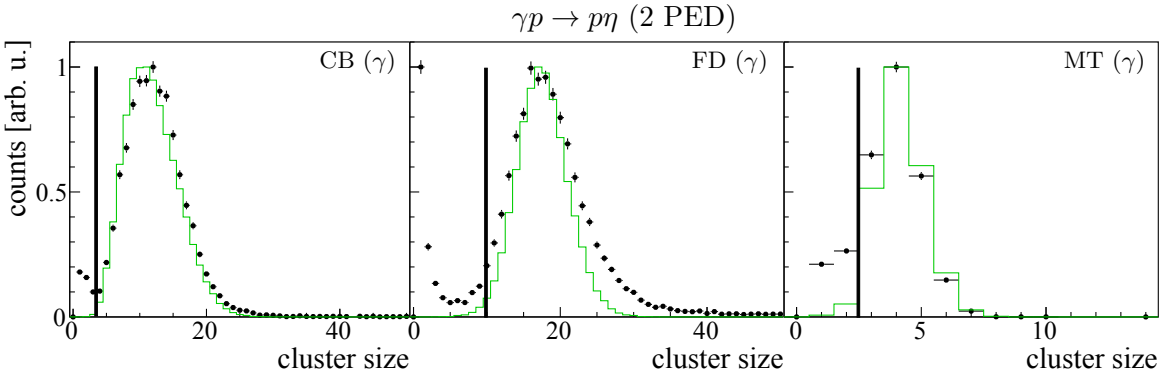

Figure 5.33: The cluster size of the reconstructed decay photons (γ) that are detected in the Crystal Barrel (CB), forward detector (FD) or MiniTAPS (MT) detector are depicted for 2 PED events for the $p\eta$ final state (black points). The MC spectra are compared to the data as well (green). The applied cut is indicated by the black line.

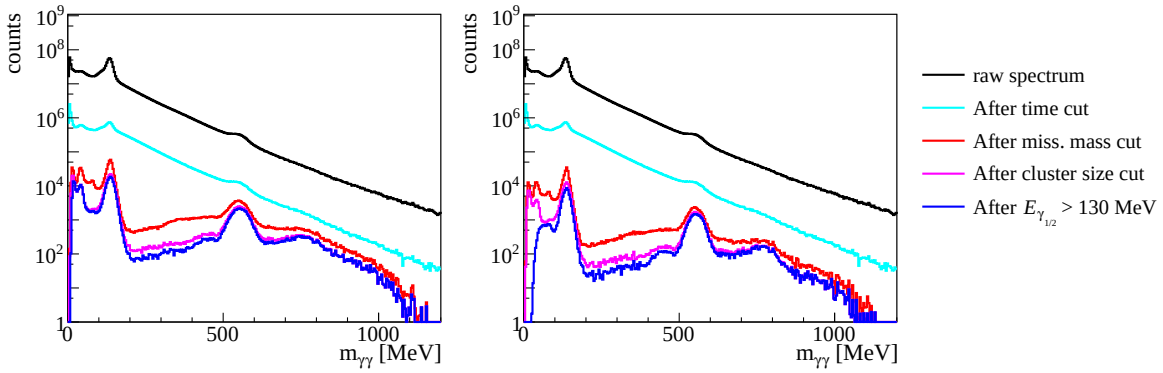

Figure 5.34: The impact of each cut condition that is applied is shown for the invariant mass of 2 PED events in the $p\pi^0$ (left) and $p\eta$ (right) final state.

A cluster size larger than three is demanded for the decay photons of the $p\pi^0$ final state as well.

Figures 5.34 and 5.35 show the influence of all cut conditions on the invariant and missing mass spectra of the 2 PED events. The signal to background ratio is improved with the applied cuts, especially with the cluster size cut.

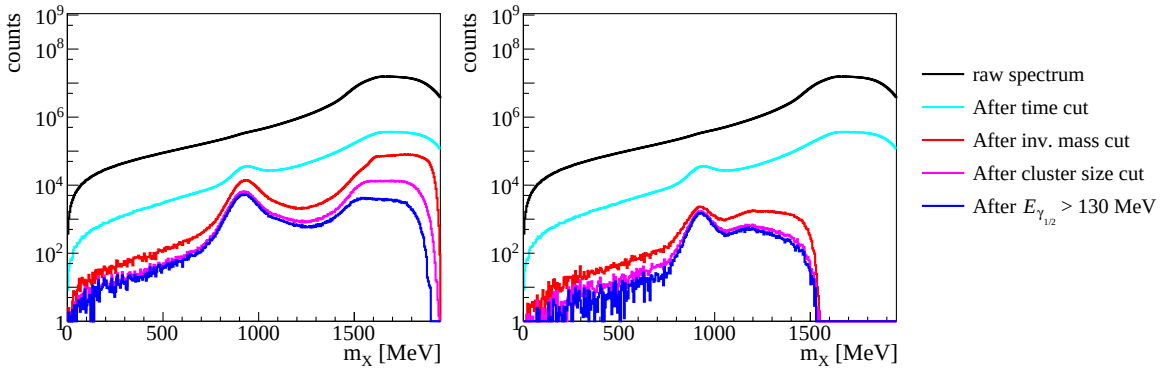

Figure 5.35: The impact of each cut condition that is applied is shown for the missing mass of 2 PED events in the $p\pi^0$ (left) and $p\eta$ (right) final state.

5.2.5 Quality of event selection

After applying all time and kinematic cuts to the data, 6.28×10^6 events were retained for the $p\pi^0$ final state and 5.24×10^5 events for the $p\eta$ final state. The acceptance after the selection process is depicted for all three event classes in Figure 5.36 on the left for the $p\pi^0$ and on the right for the $p\eta$ final state. In both cases the maximal acceptance is approximately 63%. This can be understood when taking into consideration that photons have a detection efficiency of 90% [Har17] and that three times 2σ cuts and one time a 1.7σ cut are applied to the data, which retain 95% of all events with each 2σ cut and 91% with the 1.7σ cut: $0.9^2 \cdot 0.95^3 \cdot 0.91 \approx 0.63$. As already stated the anti-π^0 cut does not remove too many good $p\eta$ events.

In addition, it is important to estimate the remaining background contributions after the event selection process. There are different origins of background possible: On the one hand it is possible to have combinatorial background for the 3 PED events as no charge cut was used and moreover, background from other reaction channels can occur. According to Monte Carlo simulations combinatorial background contributes with significantly less than 1% and thus, plays no important role in either final state. Different background channels have already been discussed and the cuts were optimized to remove these in the best possible way to increase the signal to background ratio. The comparisons to MC data show that only a flat background remains underneath the invariant mass peak after applying all cuts. Therefore, the background contributions in the different energy and angular bins were accessed using a fit function consisting of a Novosibirsk for the signal mass peak and a linear function for the description of the flat background. The fit results are shown in Figure 5.37 for one energy bin of the $p\pi^0$ final state and in Figure 5.38 for one energy bin of the $p\eta$ final state. The estimated background contributions within the applied invariant mass ranges are given in Figure 5.39 for the $p\pi^0$ and in Figure 5.40 for the $p\eta$ final state. In the $p\pi^0$ final state the background contribution is less than 1% for almost the entire angular range. Only for the 2 PED events at $\cos\theta \leq 0.9$ the background amounts to 5-9%. This background is caused mainly by electromagnetic reactions that create

two clusters in the MiniTAPS detector. The background is lower than 4% for almost all energy and angular bins for the $p\eta$ final state. At backward and very forward angles the background is slightly less than 7%. The selected events are used to determine the beam asymmetry Σ (see Chapter 6).

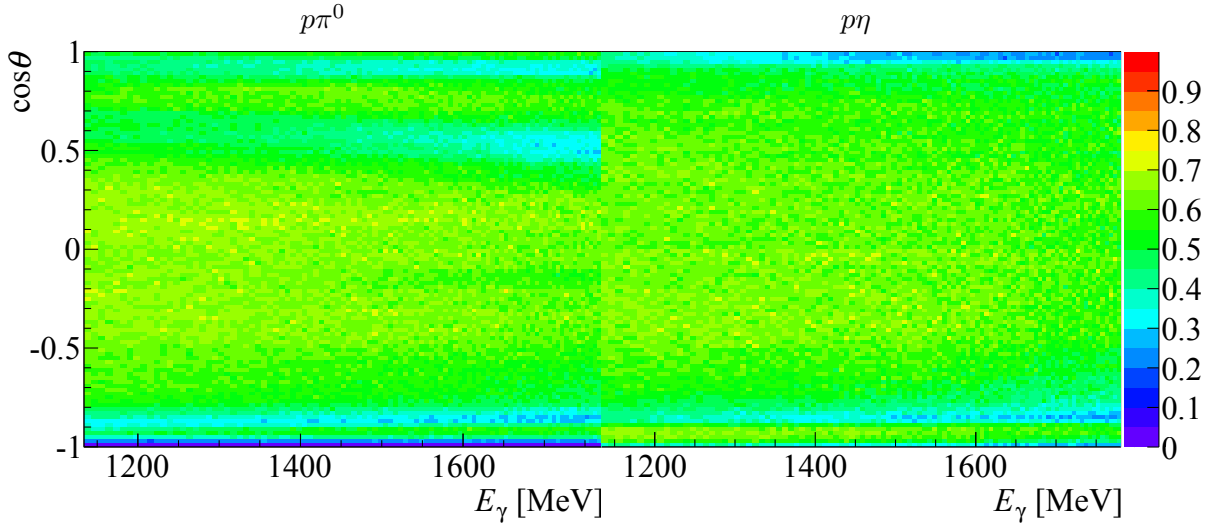

Figure 5.36: The acceptance $\epsilon(E_\gamma, \cos\theta)$ (see Equation (5.12)) is plotted for all three event classes together as a function of the beam photon energy E_γ and the center of mass angle $\cos\theta_{\text{meson}}$ for the $p\pi^0$ (left) and for the $p\eta$ (right) final state.

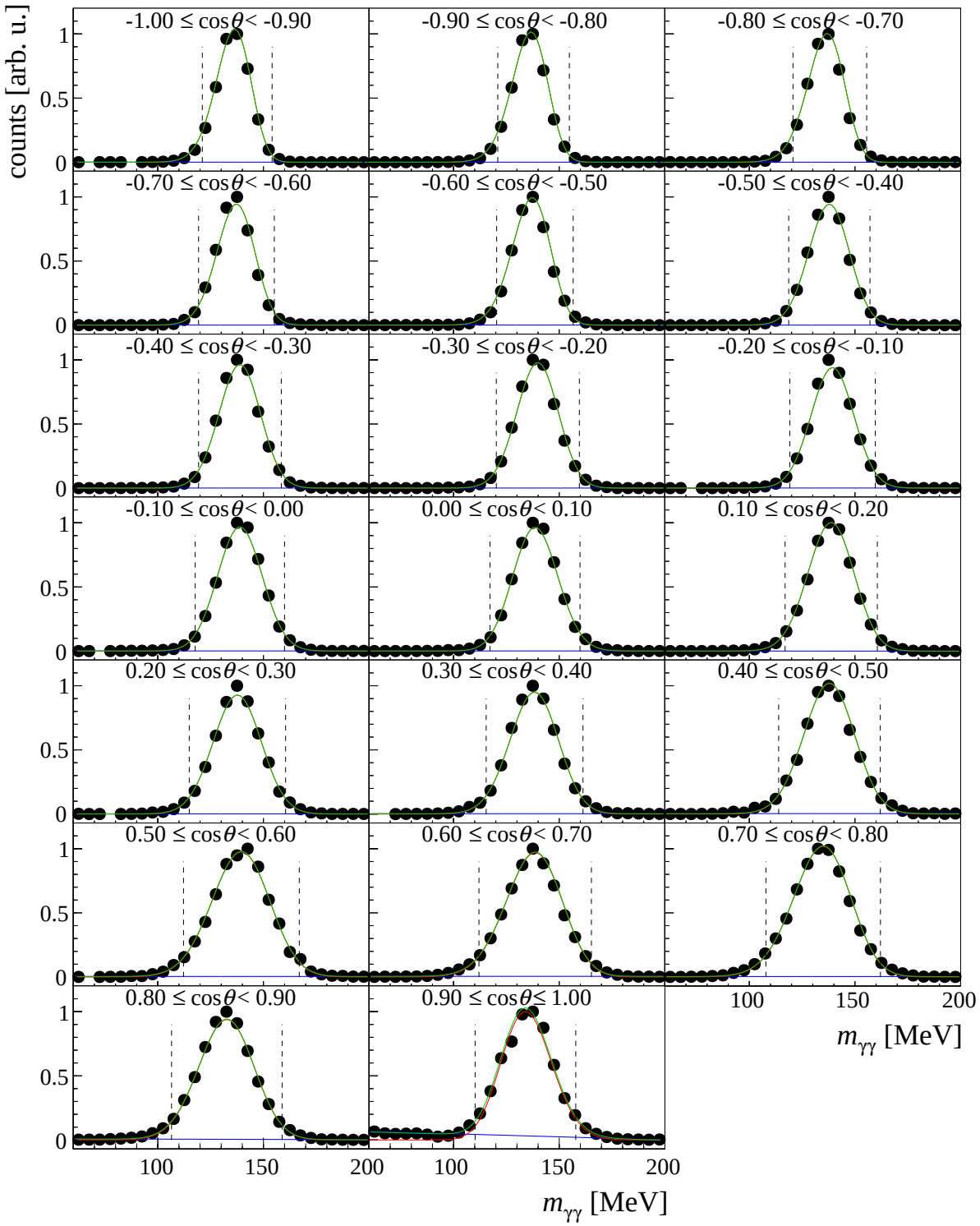

Figure 5.37: Invariant mass spectra are shown for the energy bin (1455 MeV $\leq E_\gamma <$ 1491 MeV) for the $p\pi^0$ final state. The black points represent the data, the red line a Novosibirsk function, the blue line a linear function and the green line the total fit function.

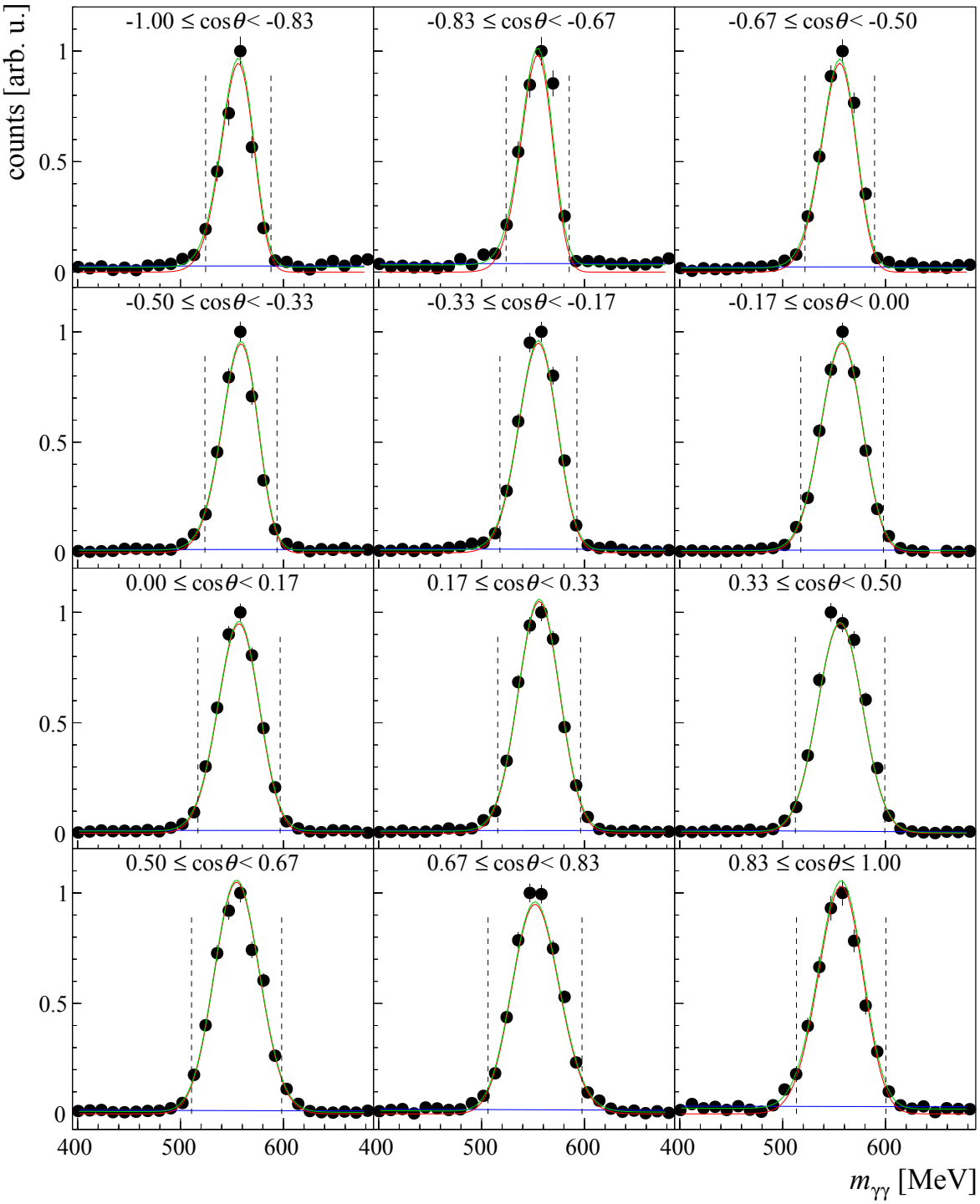

Figure 5.38: Invariant mass spectra are shown for the energy bin (1430 MeV $\leq E_\gamma <$ 1490 MeV) for the $p\eta$ final state. The black points represent the data, the red line a Novosibirsk function, the blue line a linear function and the green line the total fit function.

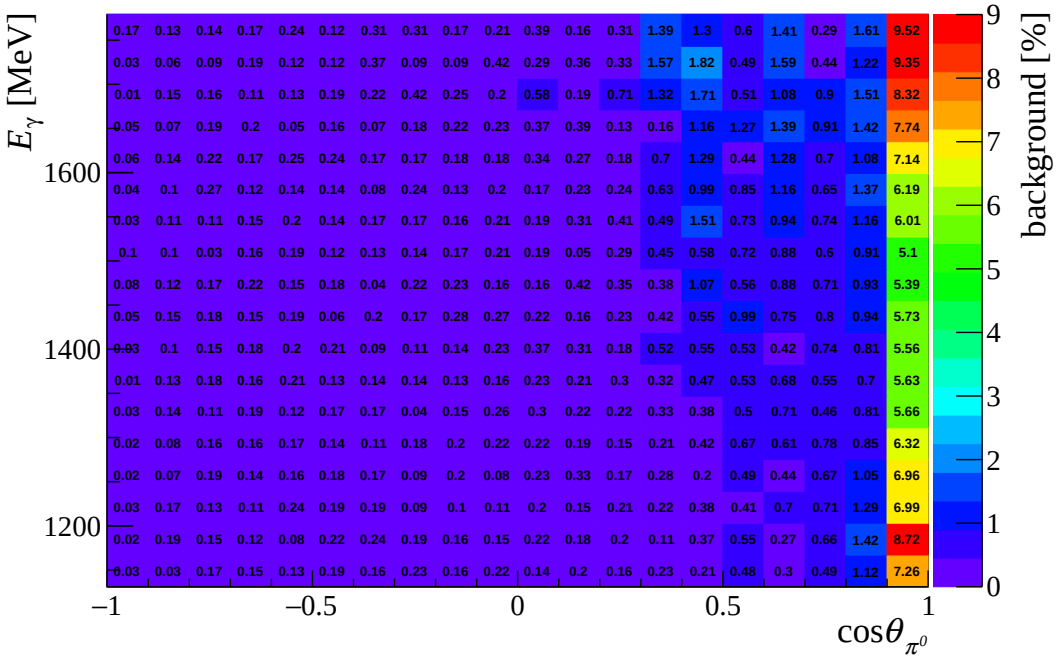

Figure 5.39: The background contributions are given as a function of the beam photon energy E_γ and the center of mass angle $\cos\theta_{\pi^0}$ after all selection cuts are applied to the data.

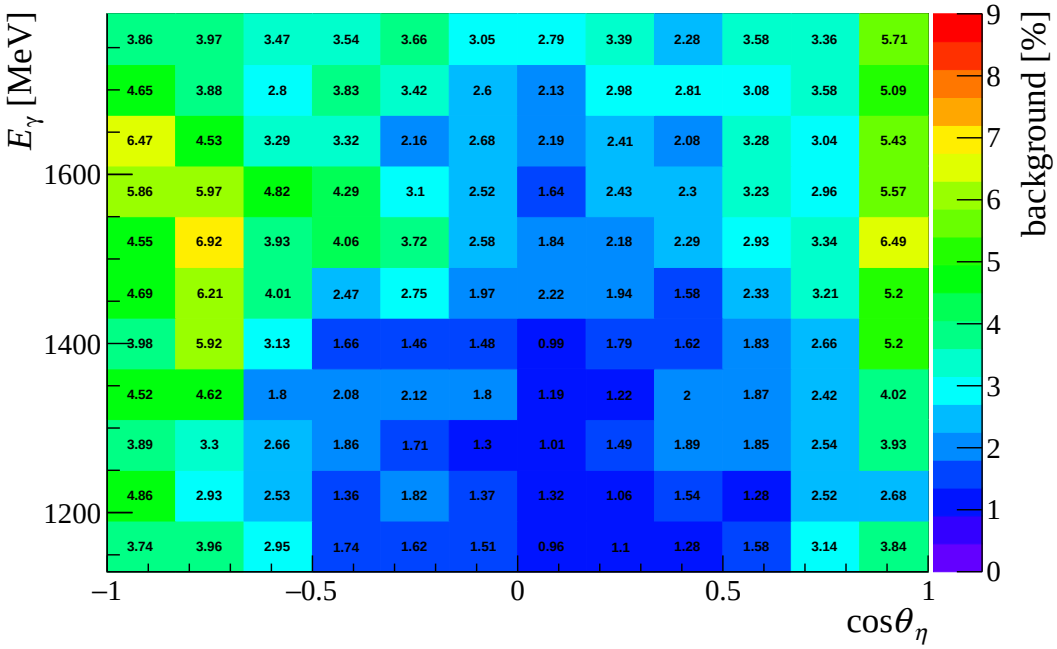

Figure 5.40: The background contributions are given as a function of the beam photon energy E_γ and the center of mass angle $\cos\theta_\eta$ after all selection cuts are applied to the data.

5.3 Event selection using A2 data

An analysis class was implemented within the *GoAT* software for the analysis of the A2 data. Similar to the CBELSA/TAPS data, the events were subdivided into different classes: into the 3 PED event class (exclusive reaction) and into the 2 PED class (inclusive reaction). Figure 5.41 shows the detection and analysis acceptance as a function of the beam photon energy E_γ and $\cos\theta$ for 3 PED (left) and 2 PED (right) events as selected for the $p\pi^0$ final state.

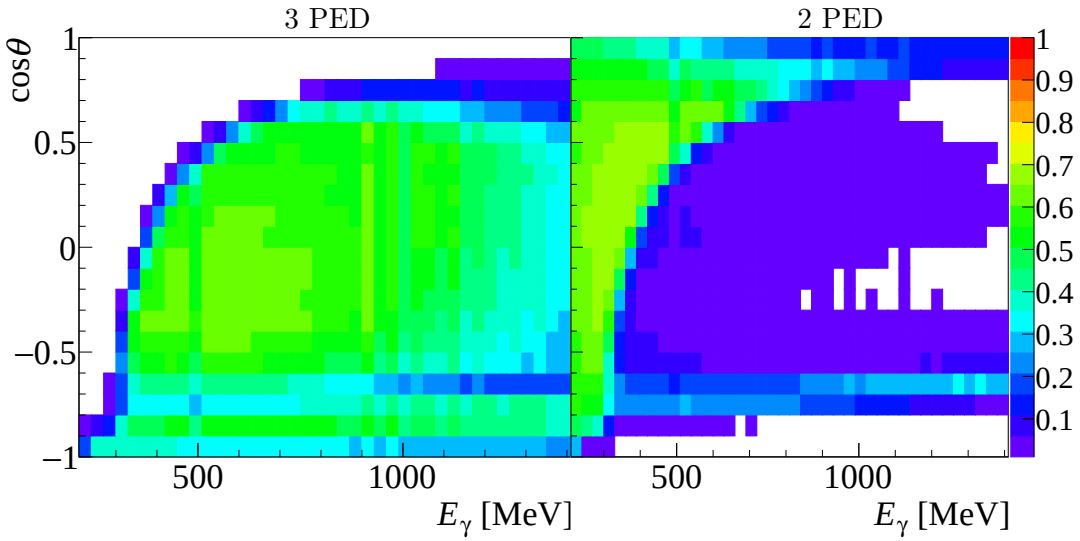

Figure 5.41: The detection, reconstruction and analysis acceptance $\epsilon(E_\gamma, \cos\theta)$ (see Equation (5.12)) is shown separately for the 3 PED (left) and 2 PED (right) event classes as a function of the beam photon energy and $\cos\theta$ for the $p\pi^0$ final state. All selection cuts are applied.

The 2 PED events of the $p\pi^0$ final state dominate below $E_\gamma = 400\,\text{MeV}$, since here the low energetic protons do not often reach the Crystal Ball detector. In addition, protons are lost in the gap region between the Crystal Ball and the TAPS detector ($-0.8 < \cos\theta < -0.6$), which leads to a reduction of the acceptance down to 20% in the 3 PED event class. Furthermore, the acceptance is reduced for $\cos\theta < -0.9$ and $\cos\theta > 0.9$ since the inner two rings of the TAPS detector ($PbWO_4$ crystals) could not be used in the analysis. Therefore, protons or photons could not be reconstructed in this angular region. The acceptance for the $p\eta$ final state is shown in Figure 5.42. Here, the gap region between the Crystal Ball and the TAPS detector leads to a decrease in the acceptance most prominently for the energy region 750 - 800 MeV and for higher energies in the angular region of $-0.7 < \cos\theta < -0.5$. The 2 PED events of the $p\eta$ final state are located mostly at $\cos\theta > 0.8$.

In this analysis, no charge information was used at all, e.g. due to the existing PID problems in the November 2013 and May 2014 beamtimes. The MWPCs are in principle usable, but investigations showed that the calibration of the MWPCs before the start of the May 2015 and September 2015 beamtimes was not done precisely enough so that the reconstructed angular information of charged particles detected in the MWPCs are not reliable. More information

about the MWPCs calibration problems are given in [Spi19]. In addition, not all TAPS vetoes were working properly during the beamtimes and since the TAPS veto energy resolution is bad (see Figure 4.20), the TAPS veto information was not used. Thus, no 2.5 PED event class is present in the A2 data analysis. Since MC simulations confirm that no charge cut is needed for the removal of combinatorial background for 3 PED events similar as in the case of the CBELSA/TAPS data, the exclusion of the PID, MWPCs and TAPS vetoes from the analysis has no negative impact.

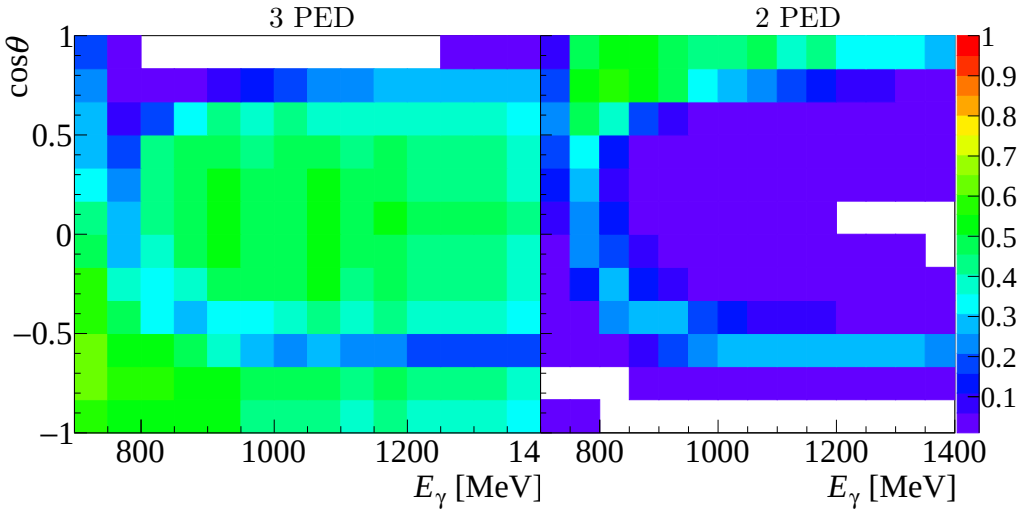

Figure 5.42: The detection, reconstruction and analysis acceptance $\epsilon(E_\gamma, \cos\theta)$ (see Equation (5.12)) is shown separately for the 3 PED (left) and 2 PED (right) event classes as a function of the beam photon energy and $\cos\theta$ for the $p\eta$ final state.

For the 3 PED event class all three detected particles were combined as described in Equation (5.11) and all three combinations together with all the detected beam photons were processed for each event. For the 2 PED events, the two detected particles were assigned as the two decay photons. In contrast to the CBELSA/TAPS data, a charge cut was not used for the analysis of 2 PED events as well, due to the afore mentioned detector problems[3].

5.3.1 Application of time cut and time background subtraction

All detected particles have a time information, simplifying the application of the time cut. Therefore, the meson time t_{meson} is always given by the average of both decay photon times and the reaction time t_{reaction} is given by

$$t_{\text{reaction}} = t_{\text{beam}} - t_{\text{meson}}, \qquad \text{with} \qquad t_{\text{meson}} = \frac{1}{2}(t_{\gamma_1} + t_{\gamma_2}) \tag{5.16}$$

Figure 5.43 depicts on the left the reaction time. The utilized cut limits to obtain the prompt peak events are drawn as dashed lines. They were set depending on the two detectors that

[3] In general, the four beamtimes can be analyzed separately with different cut conditions. However, this can lead to problems concerning the *carbon+helium* background subtraction (see Section 7.1) and thus, was avoided.

contained the decay photons. Here, one has to distinguish only between three cases: CB-CB, CB-TAPS and TAPS-TAPS (see Figure 5.43 on the right). Table 5.2 gives an overview of the chosen time cut windows.

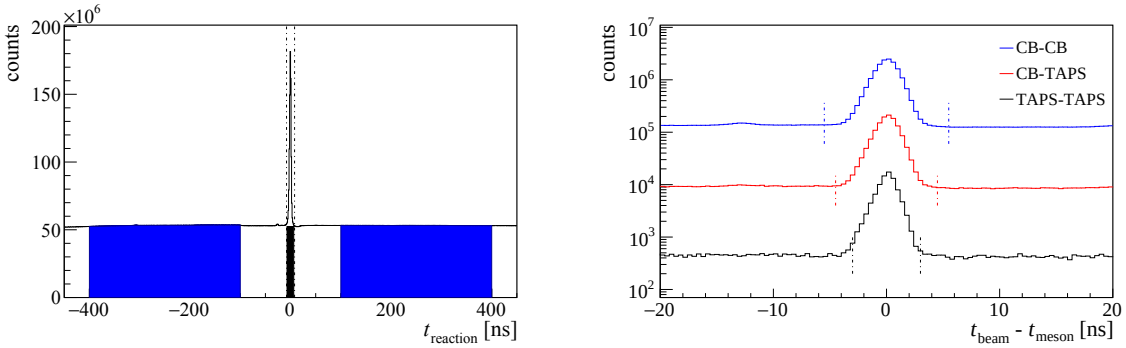

Figure 5.43: Left: The reaction time is plotted before any cuts are applied. The time background underneath the prompt peak within the dashed lines (black area) is subtracted using the side bands (blue area). Right: The reaction time is plotted after applying all kinematic cuts to the data (3 PED and 2 PED events) according to the detectors that contained the two decay photons: CB-CB, CB - TAPS and TAPS-TAPS together with the chosen cut limits (dashed lines).

The random time background subtraction was performed in the same way as for the CBELSA/-TAPS data according to Equation (5.15). The sideband range was selected from −400 ns to −100 ns and from 100 ns to 400 ns.

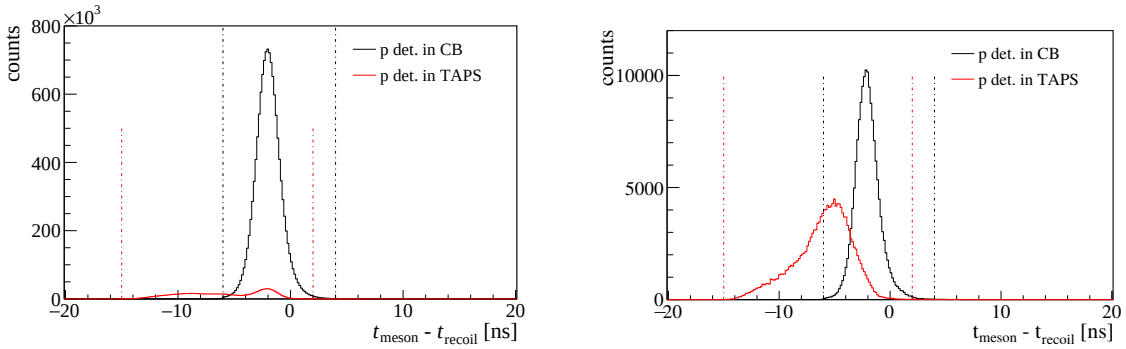

Figure 5.44: The time correlation between the meson and the recoil proton is plotted after applying all other cuts to the data (3 PED events) for the two cases that the proton is detected either in the Crystal Ball (black) or in the TAPS (red) detector for the $p\pi^0$ (left) and for the $p\eta$ (right) final state.

In addition, a constraint was put on the time difference between the meson and the recoil proton candidate of the 3 PED events. In contrast to the CBELSA/TAPS data, here the beam photon energy range covers the range near the $p\pi^0$ and $p\eta$ photoproduction thresholds, where low energetic protons can reach the TAPS detector. Therefore, time of flight effects are not negligible. Thus, an asymmetric cut window from −15 ns to 5 ns was chosen for protons detected in the TAPS detector. If the protons were detected in the Crystal Ball detector, the cut limits were set at −6 ns and 4 ns (see Figure 5.44). Moreover, time coincidence was required for both decay photons. The time of both decay photons is plotted before and after all cuts

are applied to the data (see Figure 5.45). After applying all selection cuts only time correlated decay photons remain on the diagonal.

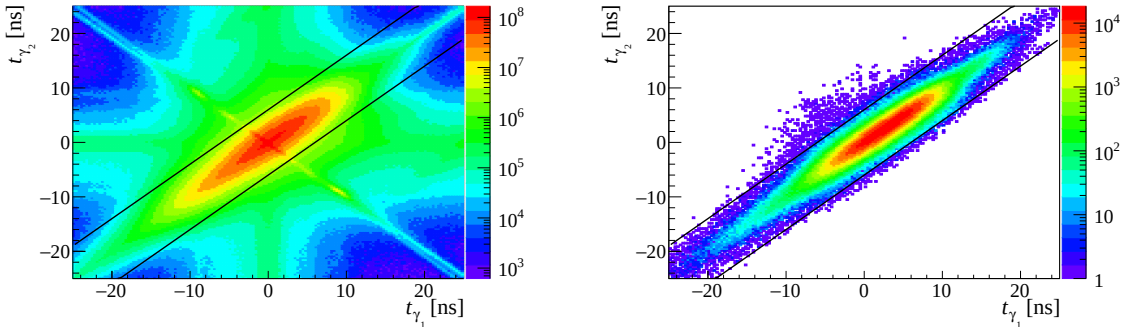

Figure 5.45: The time of one decay photon is plotted vs. the time of the other decay photon. Timely correlated photons are located on the diagonal. The cut range is indicated by the black lines. Left: No cuts are applied to the data. Right: The time correlation is plotted after applying all other cuts to the data.

Table 5.2 summarizes all applied time cut conditions.

which detector	**time cut**	**additional constraints**
CB-CB	$-5.5 \leq t_{\text{reaction}} \leq 5.5$	$-6 \leq t_{\text{meson}} - t_{\text{recoil}} \leq 4$ (p in CB)
CB-TAPS	$-4.5 \leq t_{\text{reaction}} \leq 4.5$	$-15 \leq t_{\text{meson}} - t_{\text{recoil}} \leq 2$ (p in TAPS)
TAPS-TAPS	$-3 \leq t_{\text{reaction}} \leq 3$	$-6 \leq t_{\gamma_1} - t_{\gamma_2} \leq 6$

Table 5.2: This table gives an overview about the used time cuts. Both decay photons always have a time information. Three cases were distinguished: Both decay photons were detected and reconstructed either in CB-CB, CB-TAPS or in TAPS-TAPS. Additionally, time coincidence was demanded between the meson and the recoil proton and between both decay photons. Different cut limits were chosen depending on whether the recoil proton was detected in the Crystal Ball or in the TAPS detector.

5.3.2 Application of kinematic constraints

Similar to the CBELSA/TAPS data selection, the kinematic variables: invariant mass (see Section 5.3.2.1), missing mass (see Section 5.3.2.2), coplanarity and polar angle difference (see Section 5.3.2.3) were used to maximize the desired $p\pi^0$ and $p\eta$ events and to suppress background contamination. Furthermore, a pulse shape analysis (PSA) (see Section 5.3.2.4) was performed for particles detected in the TAPS detector and the size of each cluster of the 2 PED events were used to ensure a correct assignment of the detected particles (see Section 5.3.2.5).

One difficulty arises in the analysis of the A2 data in comparison to the CBELSA/TAPS data due to the usage of the butanol (C_4H_9OH) target. The photoproduction reactions can take place not only off the free protons of the hydrogen nuclei, but also off the bound carbon, oxygen and helium nuclei. The background contribution caused by the bound nuclei was subtracted using data spectra taken with a *carbon+helium* target. The exact approach of scaling the *carbon+helium* spectra to the butanol spectra is explained in detail in Section 7.1.1. The cut limits were set in a way that events involving free protons are maximized.

5.3.2.1 Invariant mass cut

The invariant mass is plotted as a function of the beam photon energy for the butanol data and for the $p\pi^0$ final state in Figure 5.46 on the left and for the the $p\eta$ final state in Figure 5.47 on the left. The $\cos\theta$ dependence is depicted on the right for one energy bin, the energy bin $450\,\text{MeV} \leq E_\gamma < 480\,\text{MeV}$ for the $p\pi^0$ and the energy bin $800\,\text{MeV} \leq E_\gamma < 850\,\text{MeV}$ for the $p\eta$ final state. The 2 PED events were only added to the 3 PED events whenever not enough statistics of the 3 PED events was available. This corresponds to the angular range of $\cos\theta > 0.4$ for the $p\pi^0$ and $\cos\theta > 0.7$ for the $p\eta$ final state for their respective energy bins shown here. In this way, background contamination, especially from bound nuclei, are kept to a minimum[4].

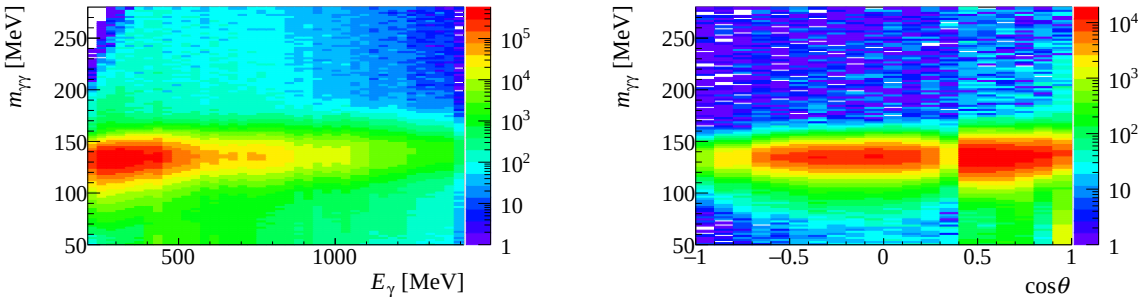

Figure 5.46: Left: The invariant mass of the two reconstructed photons is plotted as a function of the beam photon energy E_γ and integrated over the entire angular range for the $p\pi^0$ final state and for the butanol data. Right: For the energy bin $450\,\text{MeV} \leq E_\gamma < 480\,\text{MeV}$ the $\cos\theta$ dependence of the invariant mass is shown. Starting at $\cos\theta > 0.4$, 2 PED events are added to the 3 PED events to cover the forward angular region. The selection cuts: time, missing mass, coplanarity, polar angle difference, PSA and cluster size cuts are applied to the data.

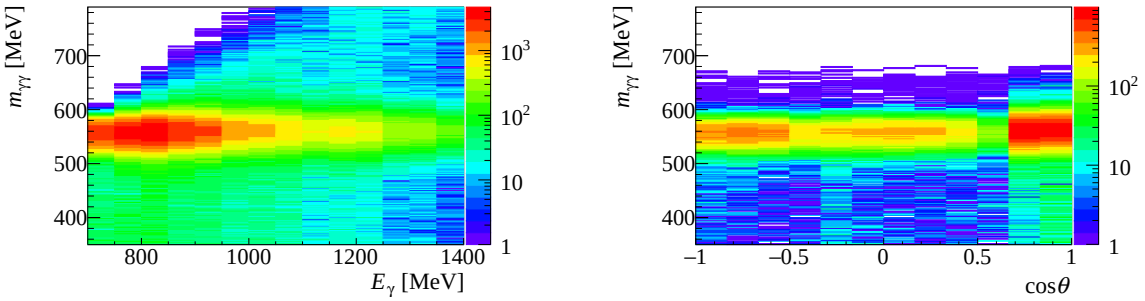

Figure 5.47: Left: The invariant mass of the two reconstructed photons is plotted as a function of the beam photon energy E_γ and integrated over the entire angular range for the $p\eta$ final state and for the butanol data. Right: For the energy bin $800\,\text{MeV} \leq E_\gamma < 850\,\text{MeV}$ the $\cos\theta$ dependence of the invariant mass is shown. Starting at $\cos\theta > 0.7$, 2 PED events are added to the 3 PED events to cover the forward angular region. The selection cuts: time, missing mass, coplanarity, polar angle difference, PSA and cluster size cuts are applied to the data.

The invariant mass spectra of all $\cos\theta$ bins of the before mentioned energy bins are shown in

[4] Since no angular cuts were applied for the 2 PED events, the background contribution from bound nuclei is by a factor ~ 3 larger for the 2PED events compared to the 3 PED events.

Figure 5.48 for the $p\pi^0$ final sate and in Figure 5.49 for the $p\eta$ final state. The black points represent the butanol data, the red points the *carbon+helium* data and the blue points the *carbon+helium* subtracted data, which corresponds to the free hydrogen nuclei component of the butanol target. The latter are compared to MC distributions which were simulated disregarding Fermi motion of the bound nuclei and thus, should describe the free nuclei contribution of the total butanol data (green line shape). A very good agreement is visible between the *carbon+helium* subtracted spectra and the MC spectra for both final states. The invariant mass peak positions and widths of the free and bound nuclei spectra are very similar since the calculation of the invariant mass only takes into account the measured energy depositions and the reconstructed angles of the decay photons in the calorimeters and disregards the initial state.
Typical spectra for the beam photon energy range of $E_\gamma = 1000\,\text{MeV}$ - $1400\,\text{MeV}$ are shown in Figure A.4 for the $p\pi^0$ and in Figure A.5 for the $p\eta$ final state. The *carbon+helium* subtracted spectra of the $p\pi^0$ final state indicate only background contribution for the angular range of $\cos\theta > 0.9$ very similar to the CBELSA/TAPS data. Here, also electromagnetic background contributions can not be fully eliminated after applying all kinematic cuts to the data. The invariant mass spectra of the $p\eta$ final state show no significant background contribution for the energy bin of 800 - 850 MeV. In the energy range of $E_\gamma = 1000$ - $1400\,\text{MeV}$ the invariant mass spectra reveal signs of $p\pi^0$ background contributions at backward and at forward angles. However, this background seems to mostly contribute to the *carbon+helium* spectra. After subtracting the *carbon+helium* background, almost no $p\pi^0$ contribution is left. This is also confirmed by looking at the coplanarity spectra (see Section 5.3.2.3). The amount of $p\pi^0$ background contamination is much smaller in the A2 data than in the CBELSA/TAPS data. Possible reasons are:

- two PED cluster do not exist according to the reconstruction algorithm of the Crystal Ball detector (see Section 3.2.2.2);
- the reconstruction threshold for a cluster is set at 15 MeV for the Crystal Ball detector so that a low energetic photon is not lost as often as in the case of the CBELSA/TAPS data, where a threshold of 20 MeV was chosen (see Section 3.2.2.2);
- each decay photon has a time information and therefore misidentifications of a photon with a proton are less probable for A2 data;
- a PSA was performed for the A2 data which helps to avoid misidentifications in the polar angular range of $\theta^{\text{LAB}} < 20°$ in the lab frame.

Therefore, it was not necessary to apply an anti-π^0 cut for the A2 data. A detailed background estimation is given in Section 5.3.3. Novosibirsk fits to the *carbon+helium* subtracted spectra were used to apply a $\pm 2\sigma$ cut on the invariant mass. Thereby, the cut limits were set for each energy and angular bin until $E_\gamma = 1000\,\text{MeV}$. The energy range $1000-$ $1400\,\text{MeV}$ was added up due to the lack of high *carbon+helium* statistics at higher energies. The width of the invariant mass peak increases slightly from $\sigma \approx 7.8\,\text{MeV}$ to $\sigma \approx 10.5\,\text{MeV}$ with increasing beam photon energy. This is caused by a worsening of the absolute energy resolution σ_E of the Crystal Ball calorimeter with higher energy depositions. In addition, the decay photons have higher kinetic energies with higher beam photon energies and are therefore boosted more strongly to forward angles ($\theta < 40°$) where the azimuthal angular resolution is decreased since the resolution is given by $\sigma_\phi = \sigma_\theta / \sin\theta$ [McN+10].

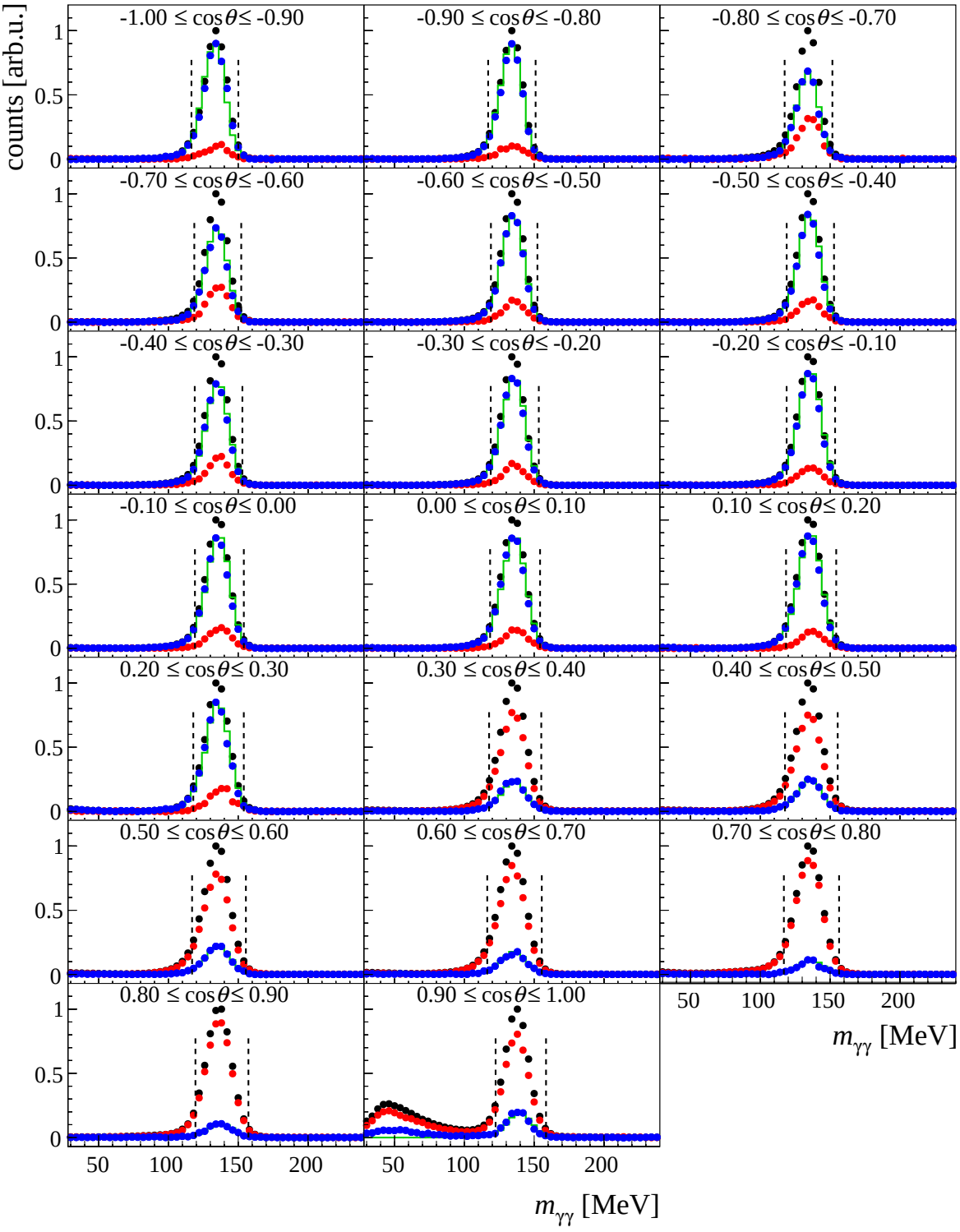

Figure 5.48: Invariant mass spectra are shown for the $p\pi^0$ final state and for all $\cos\theta$ bins of the energy bin 450 MeV $\leq E_\gamma <$ 480 MeV. The selection cuts: time, missing mass, coplanarity, polar angle difference, PSA and cluster size cuts are applied to the data. The black points represent the butanol data and the red points the *carbon+helium* data. The *carbon+helium* subtracted data are plotted in blue and are compared to Monte Carlo distributions (green). The $\pm 2\sigma$ cut ranges are marked as dashed lines.

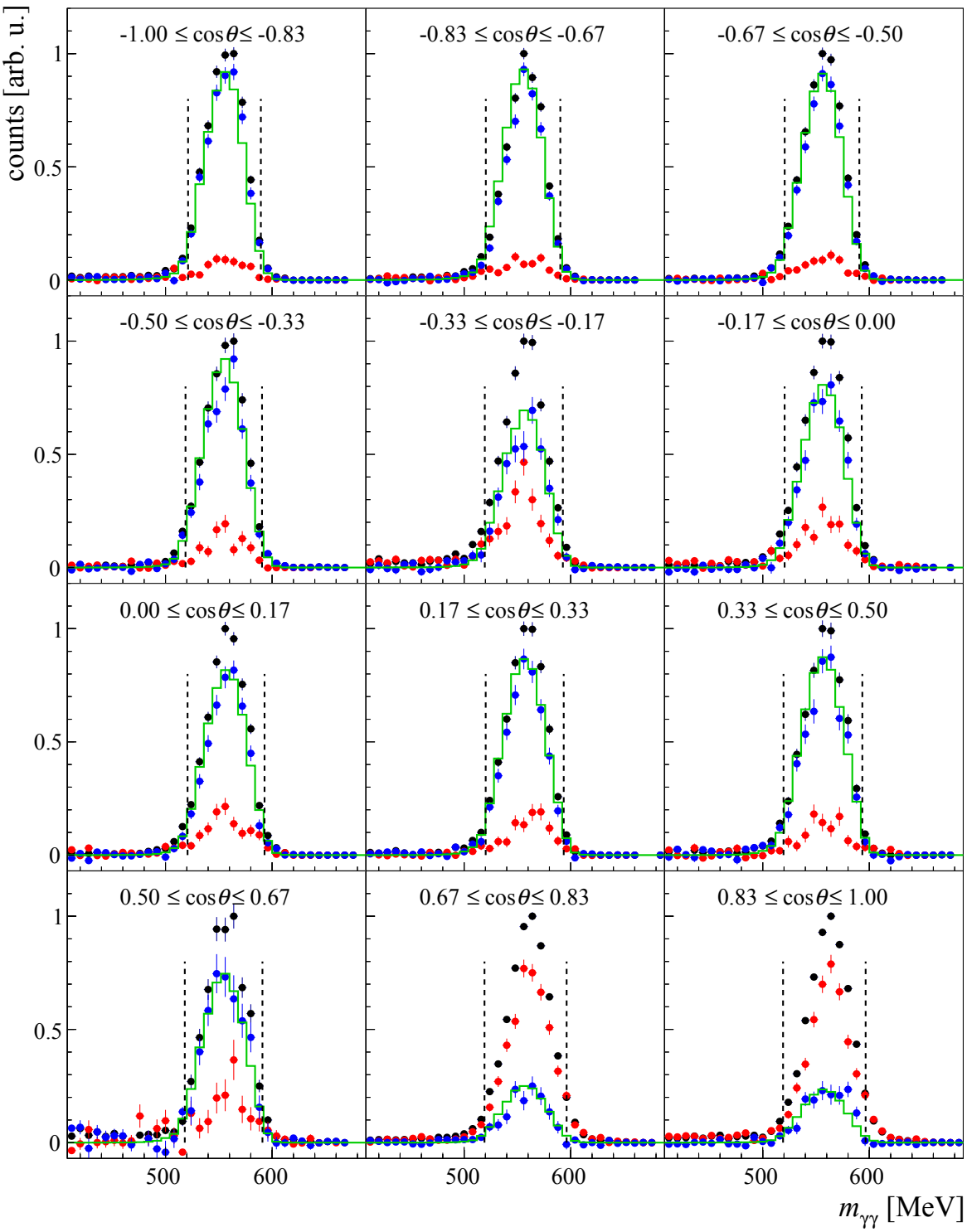

Figure 5.49: Invariant mass spectra are shown for the $p\eta$ final state and for all $\cos\theta$ bins of the energy bin 800 MeV $\leq E_\gamma <$ 850 MeV. The selection cuts: time, missing mass, coplanarity, polar angle difference, PSA and cluster size cuts are applied to the data. The black points represent the butanol data and the red points the *carbon+helium* data. The *carbon+helium* subtracted data are plotted in blue and are compared to Monte Carlo distributions (green). The $\pm 2\sigma$ cut ranges are marked as dashed lines.

The azimuthal angular resolution decreases also for large polar angles ($\theta > 120°$) [Wit15]. Therefore, an angular dependence of the invariant mass peak width is present and it is prudent to place the cut limits also angular dependent as demonstrated.

5.3.2.2 Missing mass cut

The missing mass spectra exhibit a clear peak around the expected proton mass of 938 MeV after applying all other kinematic and time cuts to the butanol data. The beam photon energy and $\cos\theta$ dependence of the missing mass are depicted in Figure 5.50 for the $p\pi^0$ and in Figure 5.51 for the $p\eta$ final state. The position and width of the missing mass peak show a strong beam photon energy and angular dependence for both final states. While the peak moves from 938 MeV to 921 MeV, the width increases with higher beam photon energy from $\sigma_{m_X} = 18$ MeV to $\sigma_{m_X} = 57$ MeV for the *carbon+helium* subtracted data. In addition, the width decreases from $\cos\theta = -1$ to $\cos\theta = 0.3$ for the 3 PED events and increases slightly for the 2 PED events. The amount of *carbon+helium* background is much higher for the 2 PED events due to the lack of angular cuts that can be applied, resulting in broader butanol spectra.

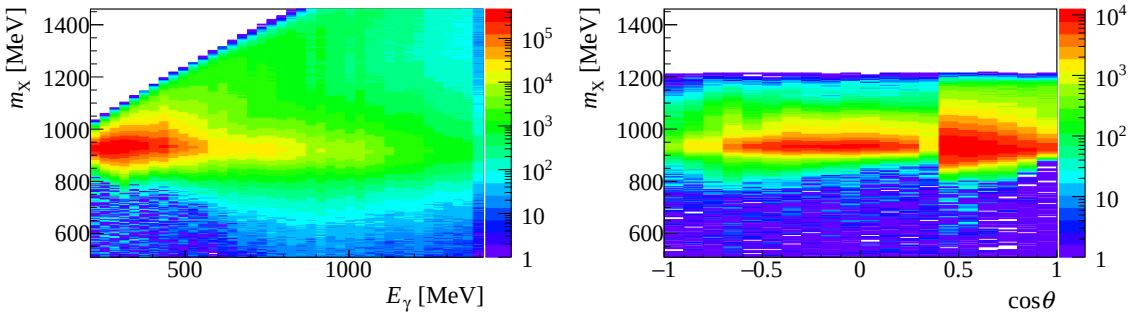

Figure 5.50: Left: The missing mass is plotted as a function of the beam photon energy E_γ and integrated over the entire angular range for the $p\pi^0$ final state and for the butanol data. Right: For the energy bin 450 MeV $\leq E_\gamma <$ 480 MeV the $\cos\theta$ dependence of the missing mass is shown. Starting at $\cos\theta > 0.4$ 2 PED events are added to the 3 PED events to cover the forward angular region. The selection cuts: time, invariant mass, coplanarity, polar angle difference, PSA and cluster size cuts are applied to the data.

Figure 5.52 shows the missing mass spectra for the energy bin of 450 MeV $\leq E_\gamma <$ 480 MeV for the $p\pi^0$ and in Figure 5.53 for the energy bin of 800 MeV $\leq E_\gamma <$ 850 MeV for the $p\eta$ final state. Since the calculation of the missing mass is done for free protons that are at rest, the missing mass peak distributions of the bound nuclei, for which Fermi motion and final state interaction need to be considered, are located at higher masses. In addition, the width of the peaks is higher for the *carbon+helium* spectra ($\sigma_{m_X} \approx 53$ MeV on average) than for the *carbon+helium* subtracted spectra ($\sigma_{m_X} \approx 24$ MeV on average). Thus, the missing mass cut suppresses the unwanted *carbon+helium* background well. The $\pm 2\sigma$ cut limits were set through fitting the *carbon+helium* subtracted spectra using a Novosibirsk function. The MC spectra describe the *carbon+helium* subtracted spectra very well for both final states, indicating that no significant background contribution is left after the *carbon+helium* subtraction.

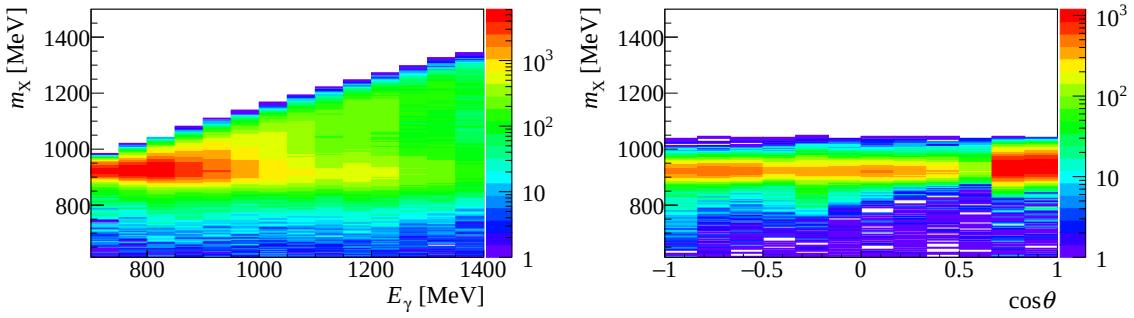

Figure 5.51: Left: The missing mass is plotted as a function of the beam photon energy E_γ and integrated over the entire angular range for the $p\eta$ final state and for the butanol data. Right: For the energy bin 800 MeV $\leq E_\gamma <$ 850 MeV the $\cos\theta$ dependence of the missing mass is shown. Starting at $\cos\theta > 0.4$ 2 PED events are added to the 3 PED events to cover the forward angular region. The selection cuts: time, invariant mass, coplanarity, polar angle difference, PSA and cluster size cuts are applied to the data.

Typical missing mass spectra for the beam photon energy range of E_γ = 1000 - 1400 MeV are depicted in Figure A.6 for the $p\pi^0$ and in Figure A.7 for the $p\eta$ final state. While the MC spectra are in agreement with the data also at higher beam photon energies for the $p\pi^0$ final state, the *carbon+helium* subtracted spectra of the $p\eta$ final state exhibit small background contributions located on the right side of the missing mass peak. This background contribution can be described using the combination of $p\pi^0\eta$, $p\pi^-\eta$, $n\pi^+\eta$ and $p\pi^0\pi^0$ MC distributions. If one or two final state particles are lost, e.g. a π^+, π^- or γ, all of these channels can pass the invariant mass, coplanarity and polar angle difference cuts. However, with the help of the missing mass cut this background is suppressed almost completely ($\approx$ 97%). It starts to contribute above $E_\gamma >$ 950 MeV and increases towards E_γ = 1400 MeV since the $p\eta$ unpolarized cross section decreases with higher beam photon energies.

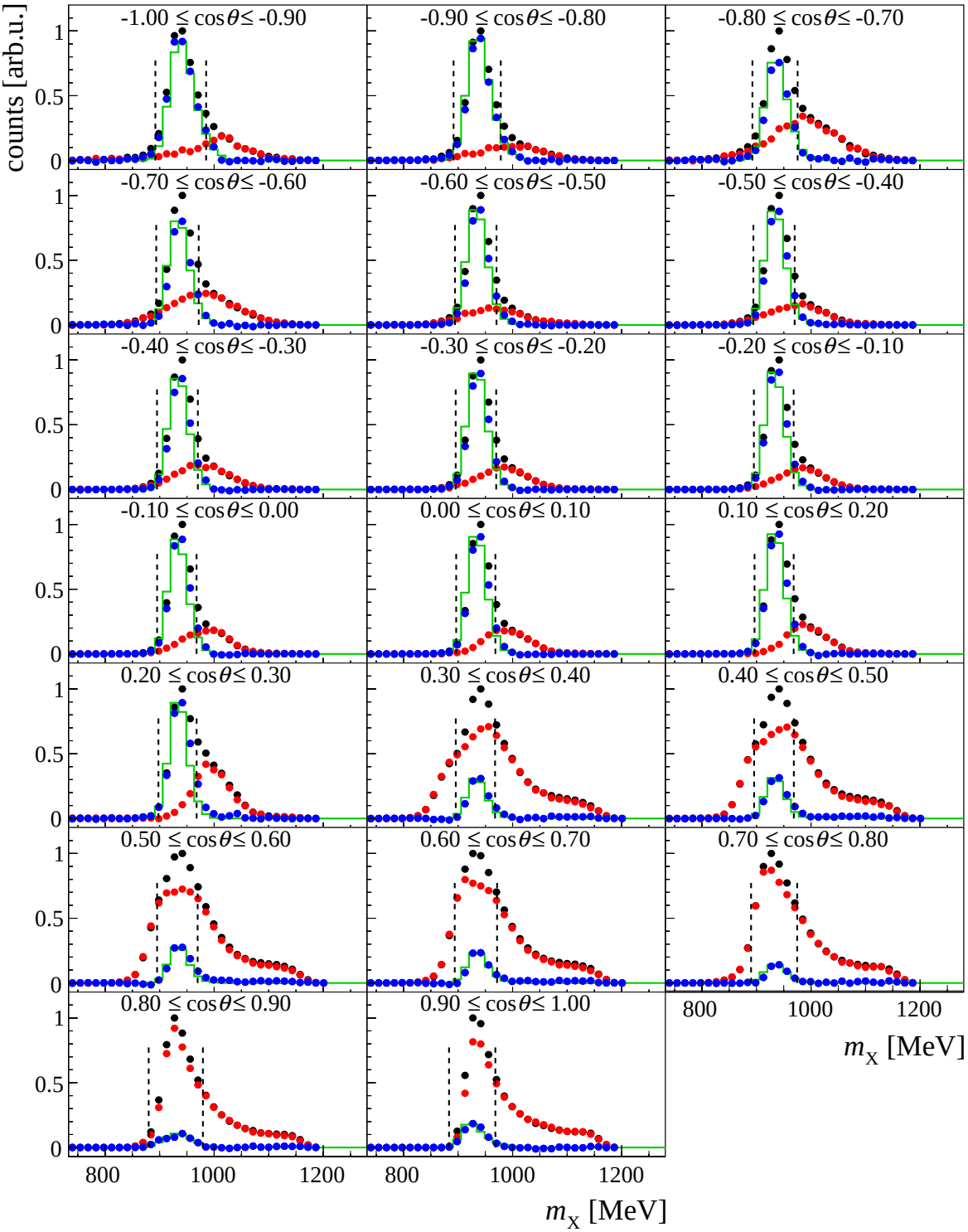

Figure 5.52: Missing mass spectra are shown for the $p\pi^0$ final state and for all $\cos\theta$ bins of the energy bin 450 MeV $\leq E_\gamma <$ 480 MeV. The selection cuts: time, invariant mass, coplanarity, polar angle difference, PSA and cluster size cuts are applied to the data. The black points represent the butanol data and the red points the *carbon+helium* data. The *carbon+helium* subtracted data are plotted in blue and are compared to Monte Carlo distributions (green). The cut ranges are marked as dashed lines.

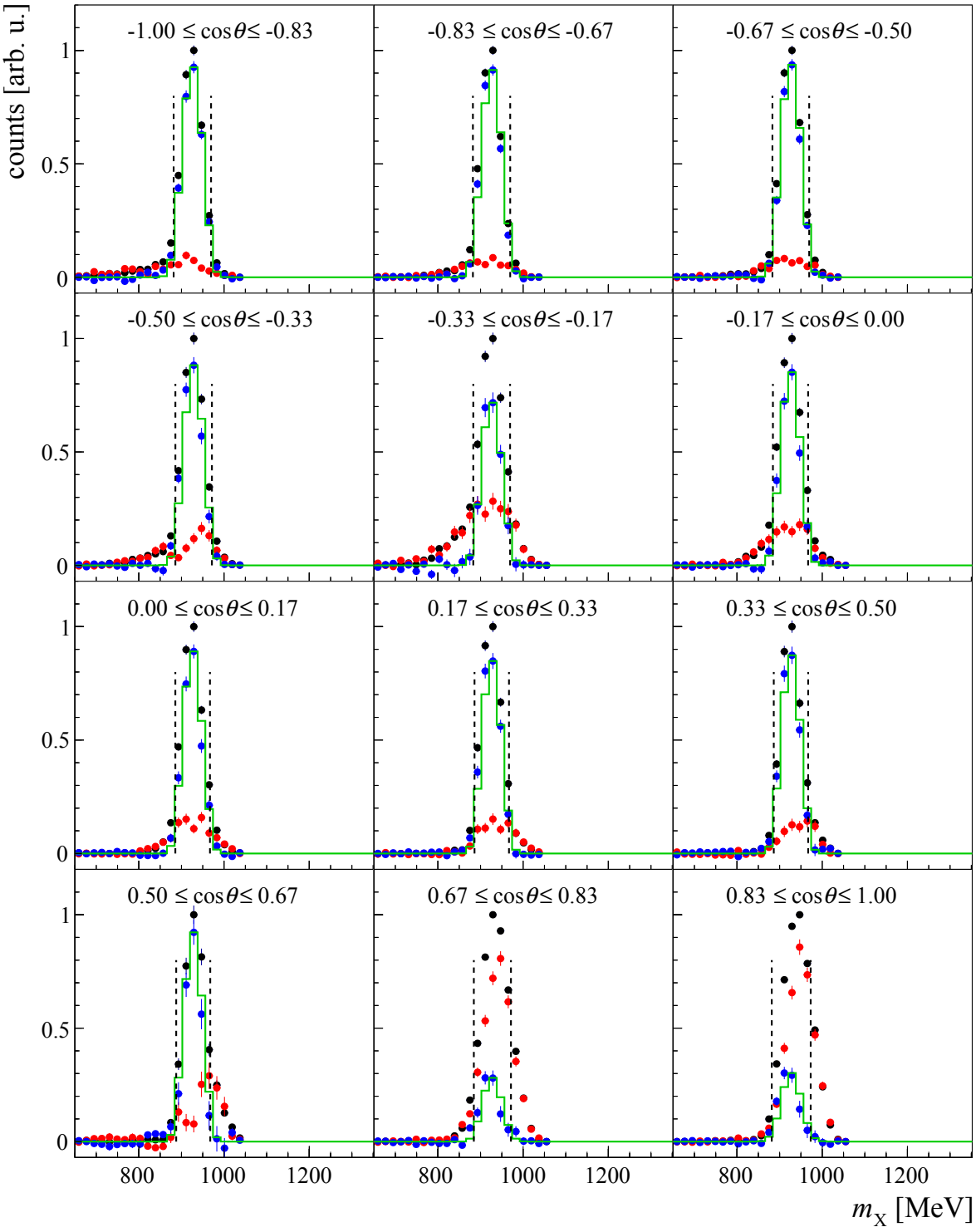

Figure 5.53: Missing mass spectra are shown for the $p\eta$ final state and for all $\cos\theta$ bins of the energy bin 800 MeV $\leq E_\gamma <$ 850 MeV. The selection cuts: time, invariant mass, coplanarity, polar angle difference, PSA and cluster size cuts are applied to the data. The black points represent the butanol data and the red points the *carbon+helium* data. The *carbon+helium* subtracted data are plotted in blue and are compared to Monte Carlo distributions (green). The cut ranges are marked as dashed lines.

5.3.2.3 Angular cuts

The coplanarity spectra show a clear peak around $\Delta\phi - 180° = 0.6°$. It is not exactly positioned at 0° since the protons are deflected by the magnetic field of the holding coil of the polarized frozen spin butanol target. The width of the coplanarity peak has a strong energy dependence for both final states (see Figure 5.54 and Figure 5.55). Due to multiple scattering of low energetic protons in the target material, the coplanarity of the *carbon+helium* subtracted data is broader with $\sigma_{\text{copl.}} \approx 12°$ near the π^0 or η photoproduction threshold than at energies above 1000 MeV with $\sigma_{\text{copl.}} \approx 4°$. A $\cos\theta$ dependence is also present due to the $\sin\theta$ dependence of the ϕ-resolution of the Crystal Ball detector and the different ϕ-resolutions of the Crystal Ball and TAPS detectors. Therefore, the cut limits were set beam photon energy E_γ and $\cos\theta$ dependent. Due to Fermi motion and final state interaction, the *carbon+helium* spectra have a much broader width ($\sigma_{\text{copl.}} \approx 17°$ on average). Thus, the coplanarity cut helps to increase the number of selected events on polarized protons.

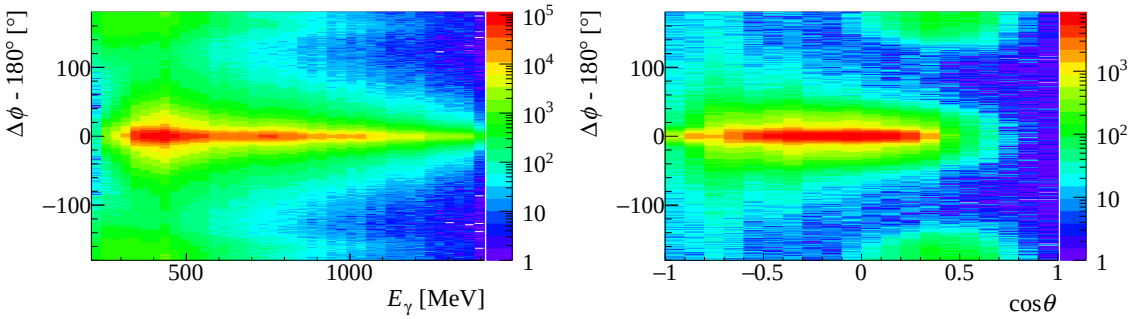

Figure 5.54: Left: The coplanarity is plotted as a function of the beam photon energy E_γ and integrated over the entire angular range for the $p\pi^0$ final state and for the butanol data. Right: For the energy bin 450 MeV $\leq E_\gamma <$ 480 MeV the $\cos\theta$ dependence of the coplanarity is shown. Above $\cos\theta > 0.5$, no more 3 PED events exist. The selection cuts: time, invariant mass, missing mass, polar angle difference, PSA and cluster size cuts are applied to the data.

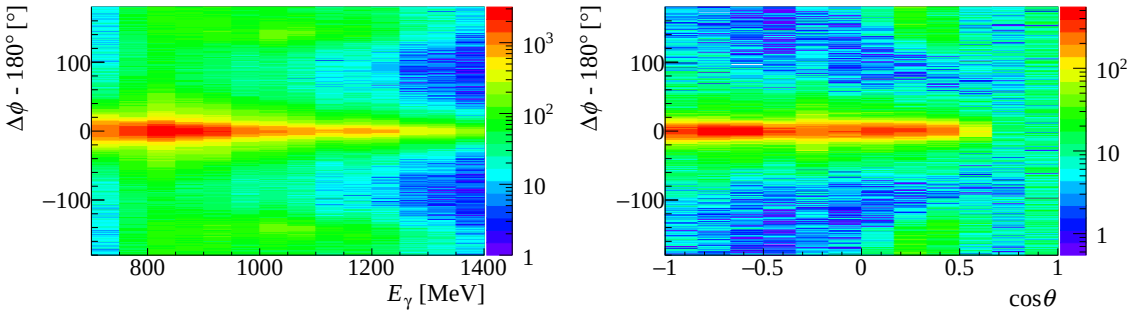

Figure 5.55: Left: The coplanarity is plotted as a function of the beam photon energy E_γ and integrated over the entire angular range for the $p\eta$ final state and for the butanol data. Right: For the energy bin 800 MeV $\leq E_\gamma <$ 850 MeV the $\cos\theta$ dependence of the coplanarity is shown. Above $\cos\theta > 0.7$, no more 3 PED events exist. The selection cuts: time, invariant mass, missing mass, polar angle difference, PSA and cluster size cuts are applied to the data.

Apart from the coplanarity peak of the signal, background contributions are present at ($\Delta\phi -$

$180°) < -100°$ and $(\Delta\phi - 180°) > 100°$, which contribute at the angular range of $\cos\theta > 0$ for both final states. This background can be attributed to mostly *carbon+helium* and a small part to combinatorial background for the $p\pi^0$ final state. Figure 5.56 shows on the left the colanarity as a function of $\cos\theta$ for the energy bin 450 MeV $\leq E_\gamma <$ 480 MeV and for $p\pi^0$ MC data. The total coplanarity spectrum of the butanol data can be described using the $p\pi^0$ MC and the *carbon+helium* data. In the case of the $p\eta$ final state, the background in the coplanarity spectra is described with *carbon+helium* data and wrongfully reconstructed $p\pi^0$ events, similar as found in the CBELSA/TAPS data, using $p\pi^0$ MC. The majority of this background is removed through a cut on the coplanarity. Only a small amount ($\sim 6\%$) of $p\pi^0$ events are located underneath the coplanarity signal peak (see Figure 5.57 on the right). As already mentioned, an anti-π^0 cut is consequently not needed for the A2 data selection.

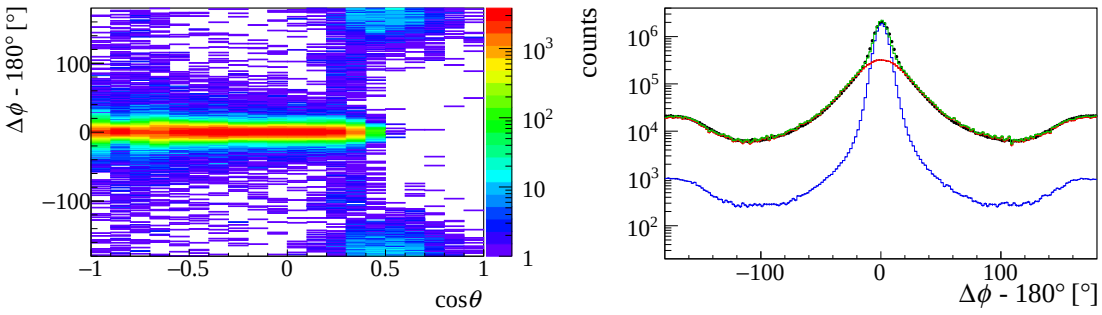

Figure 5.56: Left: The $\cos\theta$ dependence of the coplanarity is plotted for the energy bin 450 MeV $\leq E_\gamma <$ 480 MeV and for $p\pi^0$ MC data. The selection cuts: time, invariant mass, missing mass, polar angle difference, PSA and cluster size cut are applied to the MC data. Right: The over all energy and angular bins integrated coplanarity spectrum in the $p\pi^0$ analysis of the butanol data (black points) is described using the $p\pi^0$ MC data (blue line) and the *carbon+helium* data (red line). The sum of the latter two is shown in green.

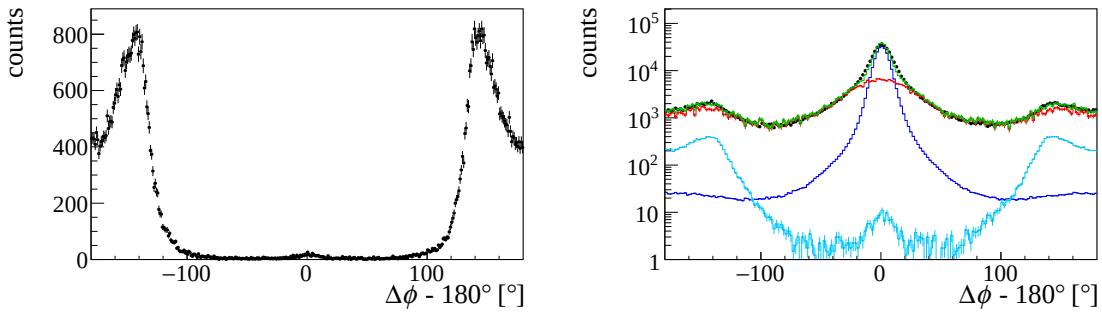

Figure 5.57: Left: The over all energy and angular bins integrated coplanarity spectrum in the $p\eta$ analysis is plotted for the $p\pi^0$ MC data after applying the selection cuts: time, invariant mass, missing mass, polar angle difference, PSA and cluster size cut to the MC data. Right: The over all energy and angular bins integrated coplanarity spectrum in the $p\eta$ analysis of the butanol data (black points) is described using the $p\eta$ MC data (blue line), the $p\pi^0$ MC data (light blue line) and the *carbon+helium* data (red line). The sum of the latter three is shown in green.

Example butanol, *carbon+helium* and *carbon+helium* subtracted coplanarity spectra are shown in Figure 5.58 for the $p\pi^0$ and in Figure 5.59 for the $p\eta$ final state. The MC distributions agree

well with the *carbon+helium* subtracted spectra. Gaussian fits to the latter spectra were used to apply $\pm 2\sigma$ cuts on the 3 PED events.

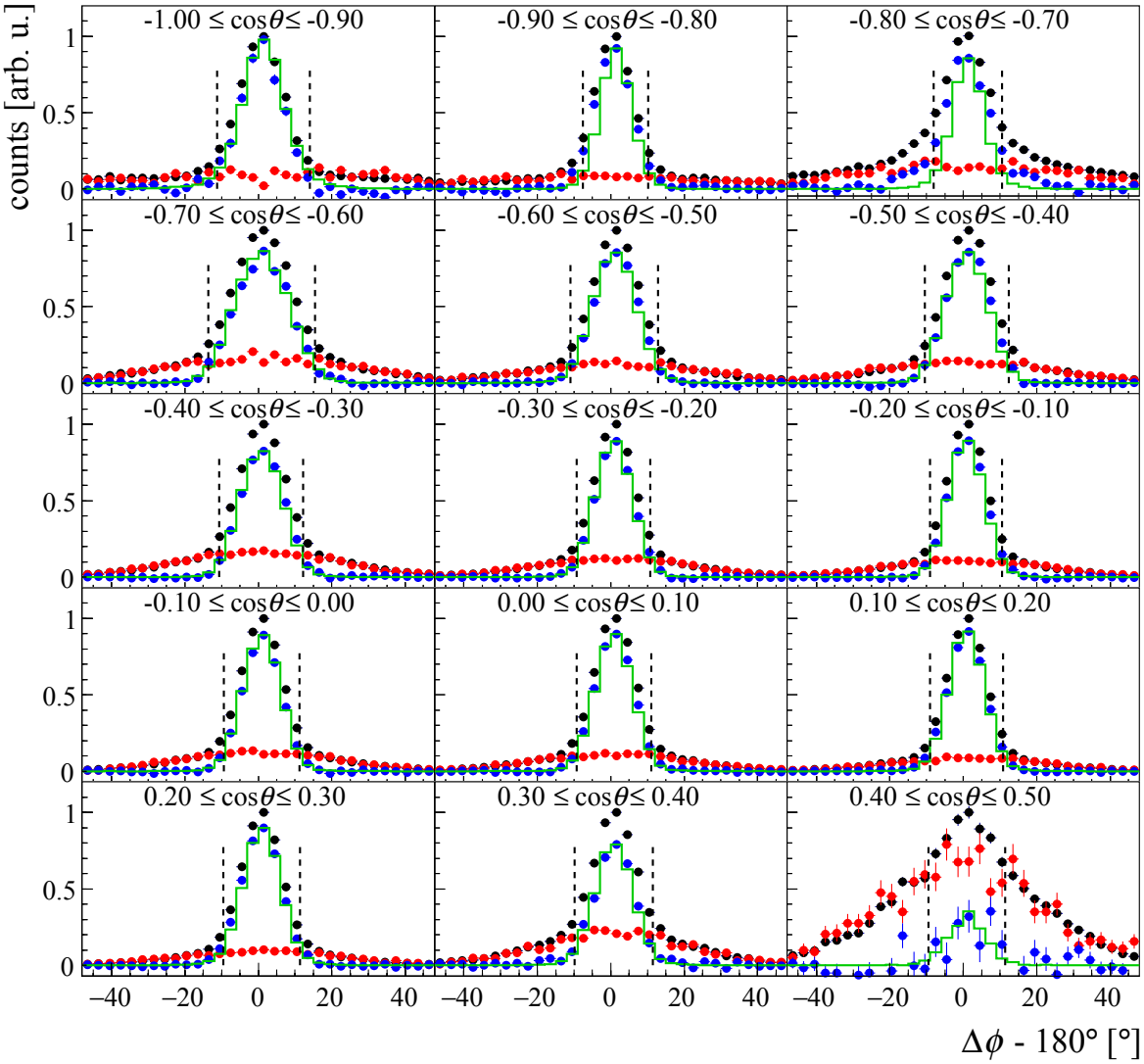

Figure 5.58: Coplanarity spectra are shown for the $p\pi^0$ final state and for all $\cos\theta$ bins of the energy bin 450 MeV $\leq E_\gamma <$ 480 MeV. Note: Above $\cos\theta > 0.5$, no 3 PED events exist for this energy bin. The selection cuts: time, invariant mass, missing mass, polar angle difference, PSA and cluster size cuts are applied to the data. The black points represent the butanol data and the red points the *carbon+helium* data. The *carbon+helium* subtracted data are plotted in blue and are compared to Monte Carlo distributions (green). The $\pm 2\sigma$ cut ranges are marked as dashed lines. The protons are lost above $\cos\theta > 0.5$.

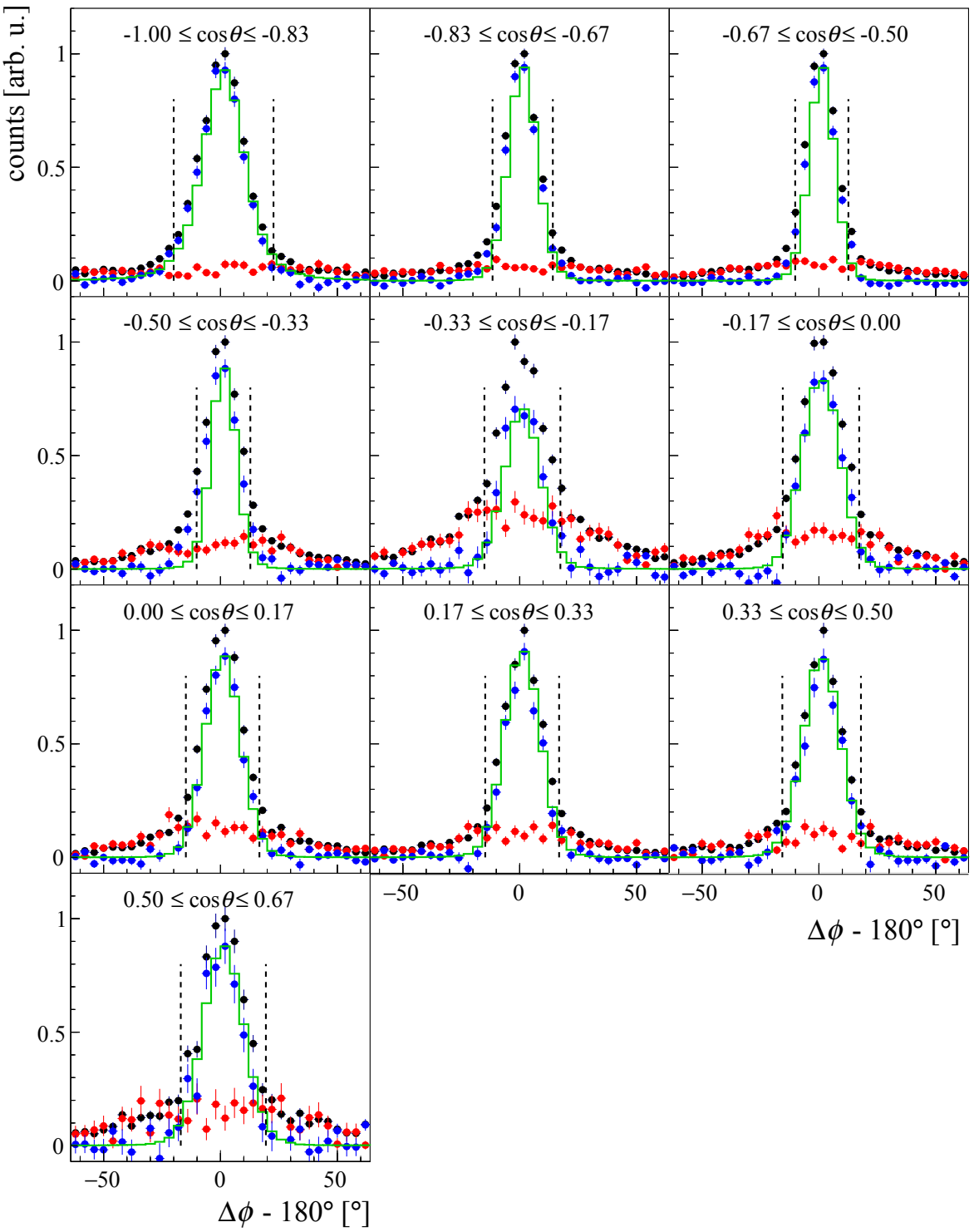

Figure 5.59: Coplanarity spectra are shown for the $p\eta$ final state and for all $\cos\theta$ bins of the energy bin 800 MeV $\leq E_\gamma <$ 850 MeV. Note: Above $\cos\theta > 0.7$, no 3 PED events exist for this energy bin. The selection cuts: time, invariant mass, missing mass, polar angle difference, PSA and cluster size cuts are applied to the data. The black points represent the butanol data and the red points the *carbon+helium* data. The *carbon+helium* subtracted data are plotted in blue and are compared to Monte Carlo distributions (green). The $\pm 2\sigma$ cut ranges are marked as dashed lines. The protons are lost above $\cos\theta > 0.67$.

The polar angle difference of the measured and calculated recoil proton is plotted as a function of the beam photon energy and $\cos\theta$ for the same energy bins as for the other kinematic variables in Figure 5.60 for the $p\pi^0$ and in Figure 5.61 for the $p\eta$ final state. A clear peak at around $\Delta\theta = 0°$ is visible in the over all angular bins integrated spectra. The $\cos\theta$ dependent spectra (see Figure 5.62 for the $p\pi^0$ and Figure 5.63 for the $p\eta$ final state) show, similar to the CBELSA/TAPS data spectra, two peak structures that can be explained by the small cluster sizes of protons. The cut limits were set again energy and $\cos\theta$ dependent at $\pm 2\sigma$. This cut enables the reduction of *carbon+helium* background contributions, especially in the angular region where the protons are detected in the TAPS detector ($\cos\theta < -0.7$) since the polar angular resolution of the TAPS detector allows to place a narrow cut. The *carbon+helium* subtracted spectra are described well with the MC distributions. An exception is given by the angular range $-0.8 \leq \cos\theta < -0.7$ where the Crystal Ball tunnel region and the gap between Crystal Ball and TAPS detector is relevant for the recoil protons. Here, the MC detector setup simulation needs improvement [Wer14].

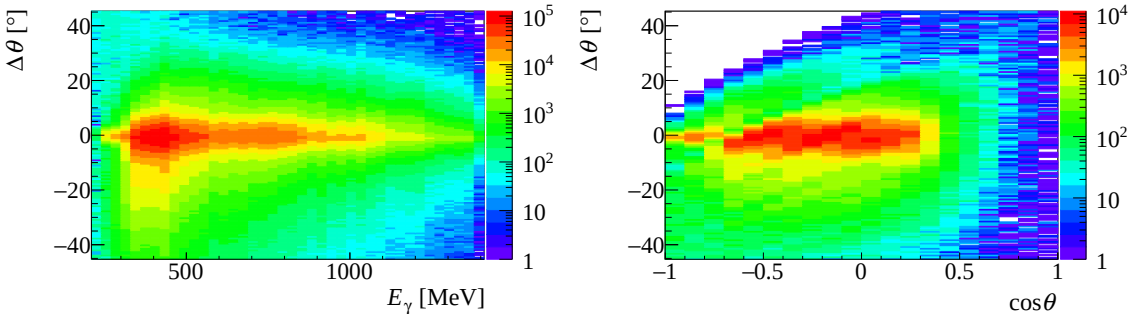

Figure 5.60: Left: The polar angle difference is plotted as a function of the beam photon energy E_γ and integrated over the entire angular range for the $p\pi^0$ final state and for the butanol data. Right: For the energy bin $450\,\text{MeV} \leq E_\gamma < 480\,\text{MeV}$ the $\cos\theta$ dependence of the polar angle difference is shown. Note: Above $\cos\theta > 0.5$, no 3 PED events exist for this energy bin. The selection cuts: time, invariant mass, missing mass, coplanarity, PSA and cluster size cuts are applied to the data.

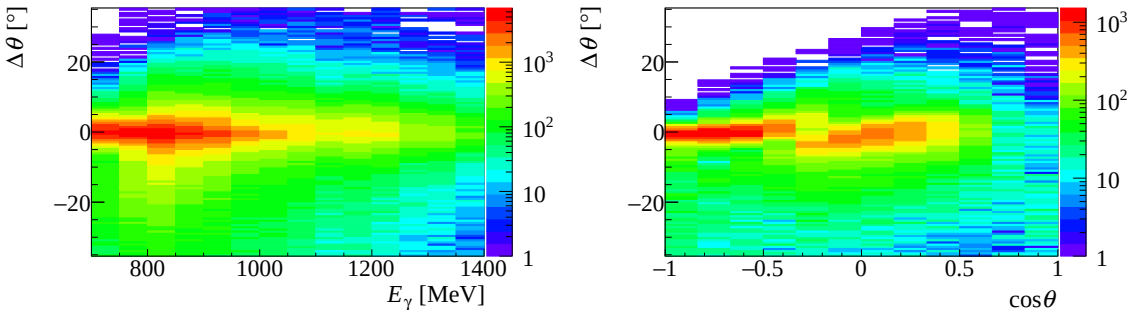

Figure 5.61: Left: The polar angle difference is plotted as a function of the beam photon energy E_γ and integrated over the entire angular range for the $p\eta$ final state and for the butanol data. Right: For the energy bin $800\,\text{MeV} \leq E_\gamma < 850\,\text{MeV}$ the $\cos\theta$ dependence of the polar angle difference is shown. Note: Above $\cos\theta > 0.7$, no 3 PED events exist for this energy bin. The selection cuts: time, invariant mass, missing mass, coplanarity, PSA and cluster size cuts are applied to the data.

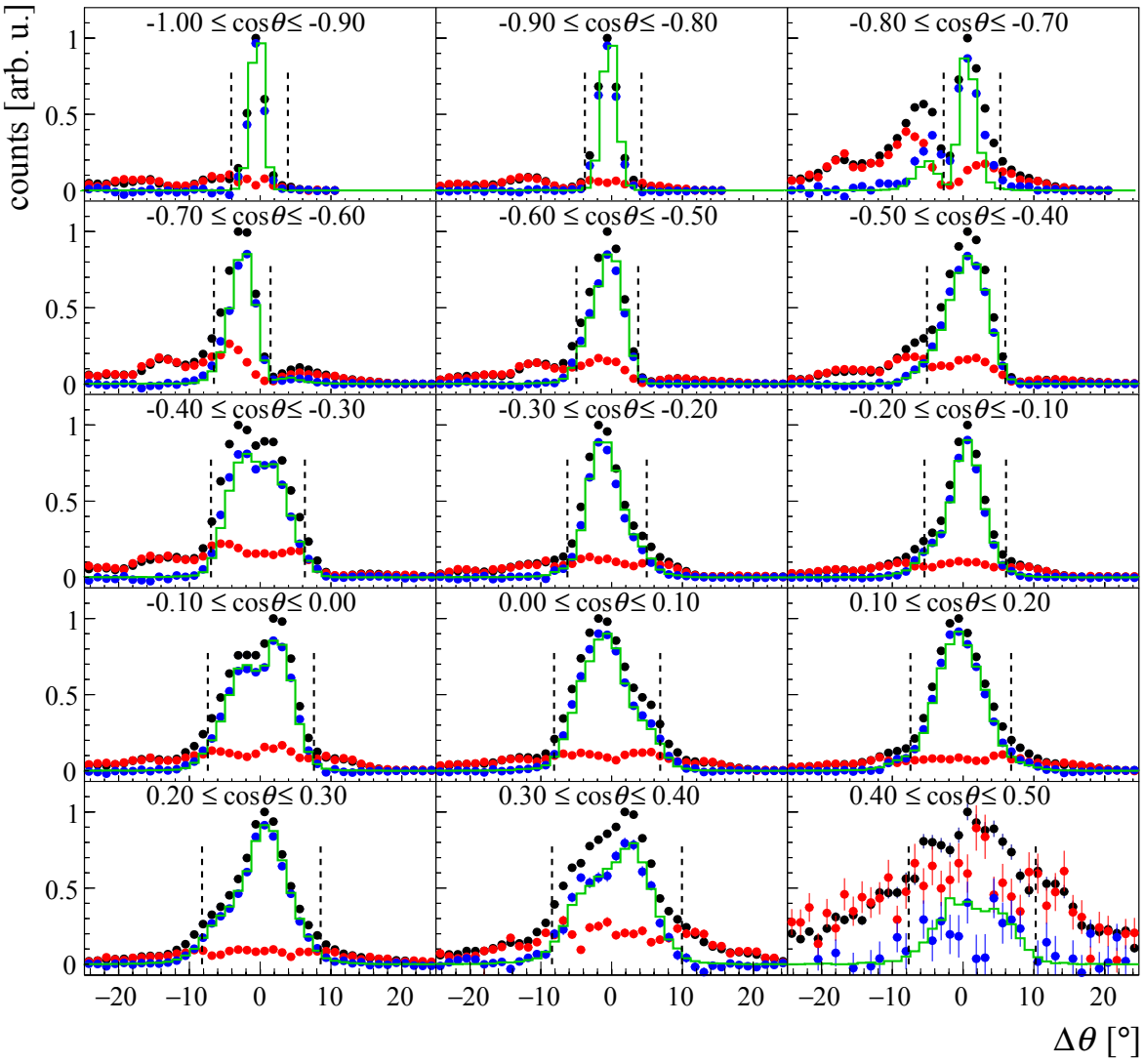

Figure 5.62: Polar angle difference spectra are shown for the $p\pi^0$ final state and for all $\cos\theta$ bins of the energy bin 450 MeV $\leq E_\gamma <$ 480 MeV. Note: Above $\cos\theta > 0.5$, no 3 PED events exist for this energy bin. The selection cuts: time, invariant mass, missing mass, coplanarity, PSA and cluster size cuts are applied to the data. The black points represent the butanol data and the red points the *carbon+helium* data. The *carbon+helium* subtracted data are plotted in blue and are compared to Monte Carlo distributions (green). The $\pm 2\sigma$ cut ranges are marked as dashed lines. The protons are lost above $\cos\theta > 0.5$.

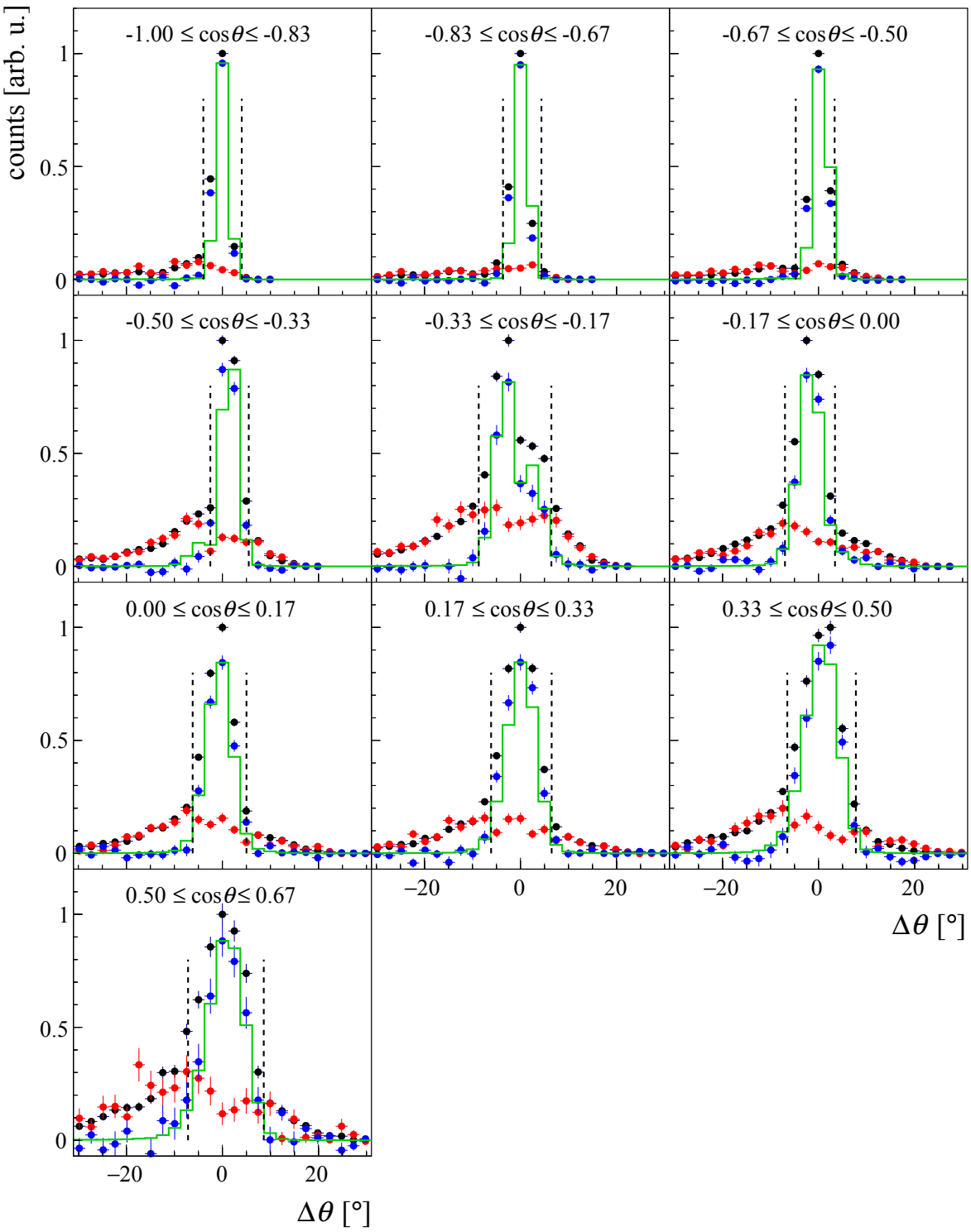

Figure 5.63: Polar angle difference spectra are shown for the $p\eta$ final state and for all $\cos\theta$ bins of the energy bin 800 MeV $\leq E_\gamma <$ 850 MeV. Note: Above $\cos\theta > 0.7$, no 3 PED events exist for this energy bin. The selection cuts: time, invariant mass, missing mass, coplanarity, PSA and cluster size cuts are applied to the data. The black points represent the butanol data and the red points the *carbon+helium* data. The *carbon+helium* subtracted data are plotted in blue and are compared to Monte Carlo distributions (green). The $\pm 2\sigma$ cut ranges are marked as dashed lines. The protons are lost above $\cos\theta > 0.67$.

5.3.2.4 PSA cut

A pulse-shape analysis (PSA) was performed for all particles that were detected in the TAPS detector. After applying the time, invariant and missing mass, coplanarity, polar angle difference and cluster size cuts to the data, the PSA radius r_{PSA} is plotted as a function of the PSA angle ϕ_{PSA} in Figure 5.64 for the $p\pi^0$ and in Figure 5.65 for the $p\eta$ final state.

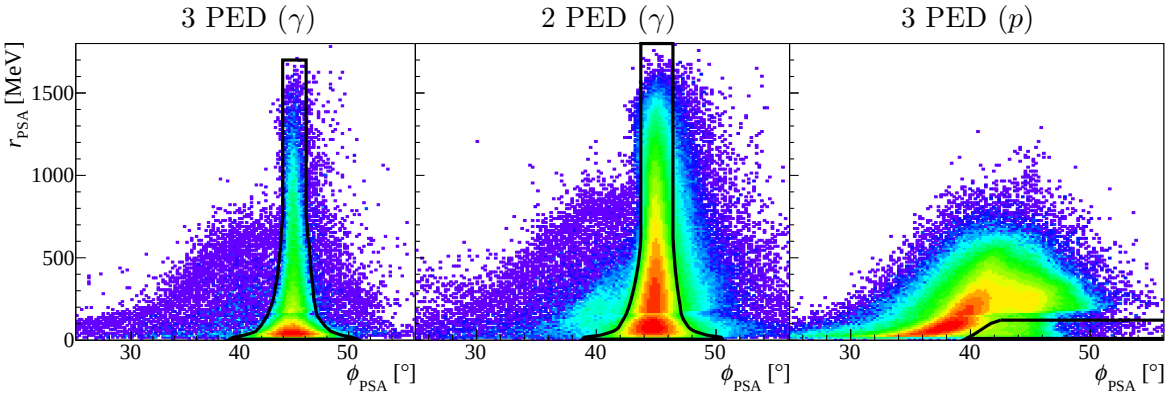

Figure 5.64: The PSA radius r_{PSA} is plotted as a function of the PSA angle ϕ_{PSA} for photon candidates of the 3 PED events (left), photon candidates of the 2 PED events (middle) and proton candidates of the 3 PED events (right) after applying the time, invariant and missing mass, coplanarity and polar angle difference and cluster size cuts to the data. The accepted (in case of photons) or the exclusion (in case of protons) cut range contours are shown by the black line. All plots are shown for the $p\pi^0$ analysis. Note: All PSA spectra are plotted in logarithmic scale.

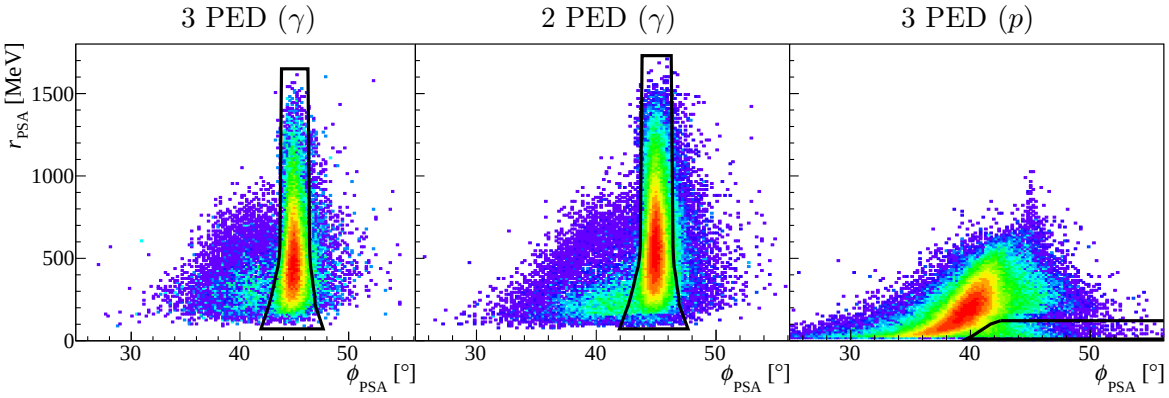

Figure 5.65: The PSA radius r_{PSA} is plotted as a function of the PSA angle ϕ_{PSA} for photon candidates of the 3 PED events (left), photon candidates of the 2 PED events (middle) and proton candidates of the 3 PED events (right) after applying the time, invariant and missing mass, coplanarity and polar angle difference and cluster size cuts to the data. The accepted (in case of photons) or the exclusion (in case of protons) cut range contours are shown by a black line. All plots are shown for the $p\eta$ analysis. Note: All PSA spectra are plotted in logarithmic scale.

As already explained in Section 4.2.2.4, photons have typical PSA angles of around $\phi_{\mathrm{PSA}} = 45°$. A clear almost straight band is visible for the selected photon candidates at $\phi_{\mathrm{PSA}} = 45°$ for both 2 and 3 PED events and for both final states. No significant background contamination is visible for photons of the 3 PED events of the $p\pi^0$ final state. The PSA spectra of the $p\pi^0$ 2

PED events and of the $p\eta$ final state show small contamination of falsely selected nucleons as photons. Projections of the PSA angle for different PSA radii were used to set 3σ cut limits. The resulting TcutG was applied as demonstrated by the black line and all photon candidates within the area were retained for further analysis. The PSA spectrum of selected proton candidates shows the typical banana like shaped band below $\phi_{\mathrm{PSA}} = 45°$ which corresponds to low energetic protons that are stopped within the detector. However, protons that punched through the detector are located mostly in the range of $40° \leq \phi_{\mathrm{PSA}} \leq 50°$. Figure 5.66 shows the PSA spectrum of proton candidates separately for punch-through protons (middle) and not punch-through protons (right).

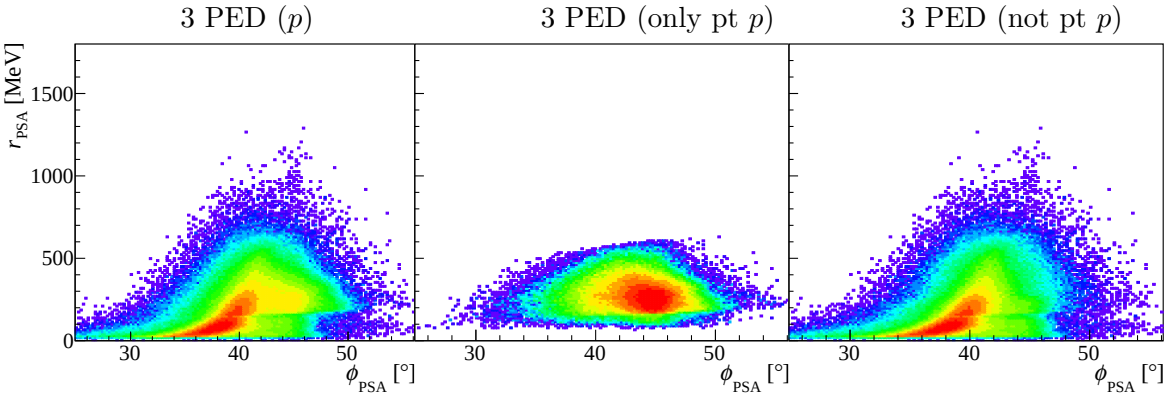

Figure 5.66: The PSA spectrum of proton candidates is shown for the $p\pi^0$ final state (left). The spectrum can be divided into a part containing only punch-through (pt) protons (middle) and low energetic protons that are stopped in the TAPS detector (right). The pt protons are selected using a TCutG on the measured and calculated kinetic energy of the proton candidates (see Figure 5.67). Note: All PSA spectra are plotted in logarithmic scale.

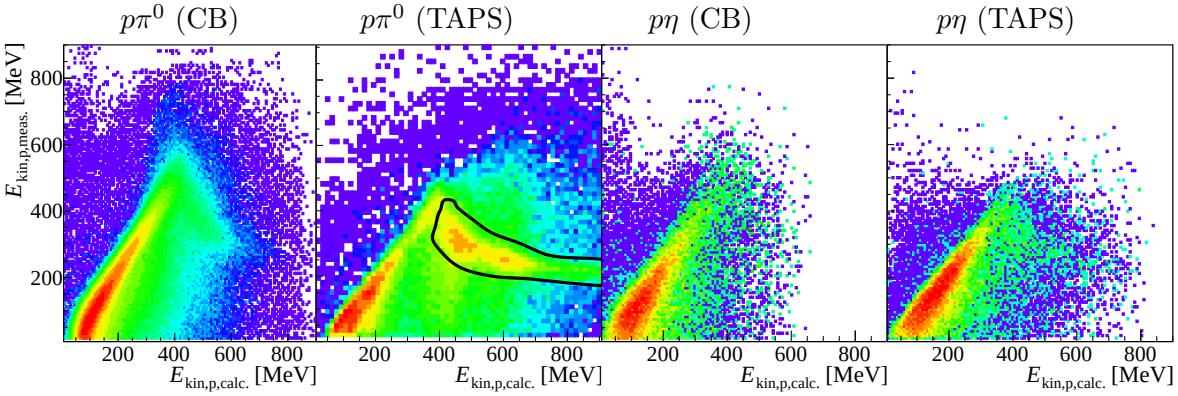

Figure 5.67: The measured and calculated kinetic energy of the selected proton candidates are shown for the cases that the protons are detected in the Crystal Ball (CB) and in the TAPS detector and for both $p\pi^0$ and $p\eta$ final state. The punch-through protons can be selected by the area marked by the black line for the $p\pi^0$ final state. Note: All spectra are plotted in logarithmic scale.

Punch-through protons were identified by comparing the measured and calculated kinetic energy of the proton candidates which is shown in Figure 5.67 for protons detected in the Crystal Ball or TAPS detector and for both final states. The punch-through protons detected in the TAPS

detector were selected within the area marked by the black line for the $p\pi^0$ final state. Since the punch through protons are located at $\phi_{\mathrm{PSA}} > 40°$ in the PSA spectrum, a clean separation of nucleons from photons is not possible here[5]. In order to reduce contamination from photons, an anti-cut was placed on the PSA spectrum of proton candidates which is marked by the black line in Figure 5.64 and 5.65 on the right.

5.3.2.5 Cluster size cut

As already mentioned a charge cut could not be applied in this analysis. To avoid false identification of particles, the different cluster sizes of photons and protons were utilized. The cluster size is depicted for photon and proton candidates of 3 PED events for the $p\pi^0$ final state in Figure 5.68 and for the $p\eta$ final state in Figure 5.69. In both Figures the plotted data points are butanol data. Since the cluster size is only dependent on the final state particles, it is not necessary to discuss butanol and *carbon+helium* data separately.

Photons create a shower in the calorimeters and deposit their energy in several crystals whereas protons deposit their energy in only a few crystals. The photon cluster size is limited to thirteen due to the used clustering algorithm of the Crystal Ball detector (see Section 3.2.2.2). In general the detected photon cluster size is smaller for the TAPS detector than for the Crystal Ball detector. The reason for this lies in the thresholds that were set for each crystal. While the Crystal Ball LED thresholds were set below 2 MeV during data taking, the TAPS CFD thresholds were set at around 5 MeV[6]. In addition, the granularity of both calorimeters is different. 90% of all proton candidates have a cluster size of one or two in the Crystal Ball detector and 85% in the TAPS detector. Neutrons or charged pions make similar small cluster sizes [Die15; Spi19]. Therefore, the cluster size can be used to distinguish between different particles.

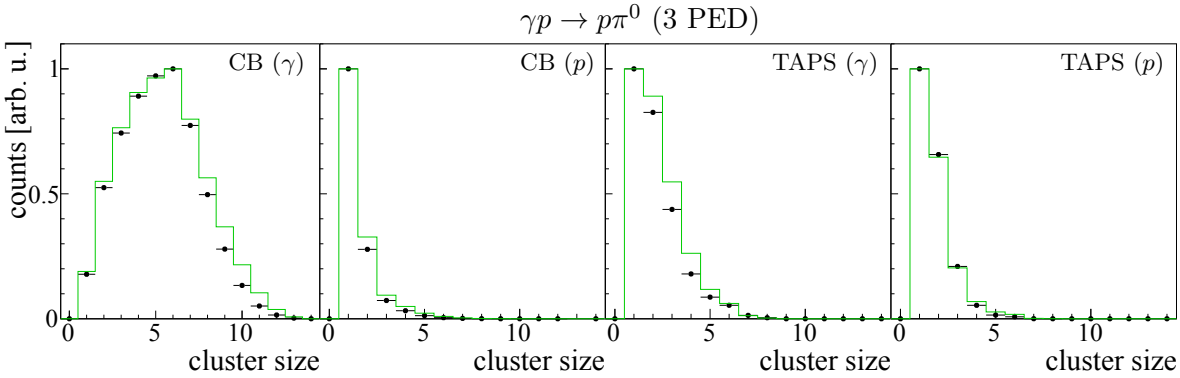

Figure 5.68: The cluster size of photon and proton candidates is depicted for the 3 PED events of the $p\pi^0$ final state (A2 data) after applying the time, invariant and missing mass, coplanarity, polar angle difference and PSA cut. The butanol data is represented by the black points and the MC spectra by the green line. The MC spectra are scaled to the maximum of the data spectra.

A comparison of the butanol data and the MC data is shown as well. Qualitatively, the cluster sizes of the MC data matches the one of the data. However, differences are observed, especially for protons of the $p\eta$ selection. These differences are most likely caused by not taking into

[5] This is the reason why a PSA cut was not applied in the analysis of CBELSA/TAPS data.
[6] A smaller value would have been desirable but could not be set during the beamtimes.

consideration e.g. the channel by channel differences of the set TAPS CFD thresholds in the simulation. Nevertheless, based on the already discussed spectra of the invariant mass, the missing mass, the coplanarity, the polar angle difference and the PSA spectra, a cut on the cluster size was not applied for the 3 PED events of both final states as these events are already selected well without much background contamination.

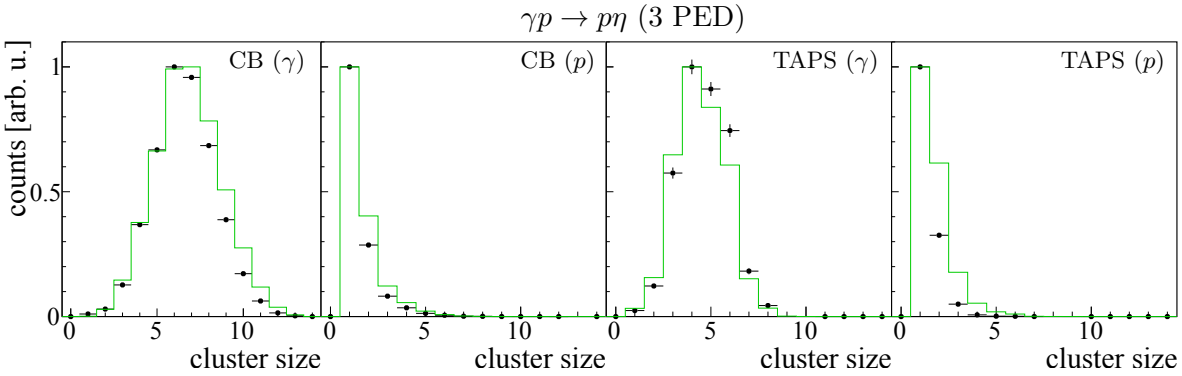

Figure 5.69: The cluster size of photon and proton candidates is depicted for the 3 PED events of the $p\eta$ final state (A2 data) after applying the time, invariant and missing mass, coplanarity, polar angle difference and PSA cut. The butanol data is represented by the black points and the MC spectra by the green line. The MC spectra are scaled to the maximum of the data spectra.

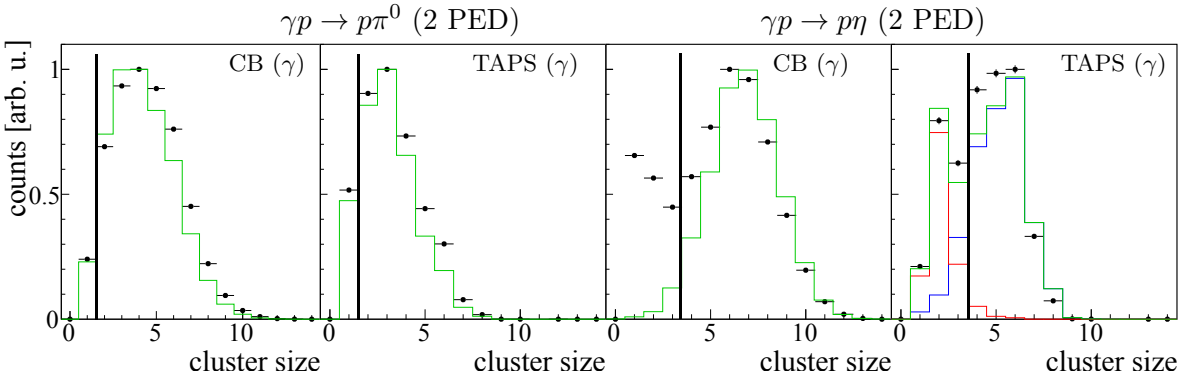

Figure 5.70: The cluster size of photons are depicted for the 2 PED events of the $p\pi^0$ (first two plots from the left) and of the $p\eta$ final state (first two plots from the left) after applying the time, invariant and missing mass, coplanarity, polar angle difference and PSA cut. The butanol data is represented by the black points and the MC spectra by the green line. The MC spectra are scaled to the maximum of the data spectra for the $p\pi^0$ final state and for the photons detected in CB for the $p\eta$ final state. For the photons detected in TAPS of the $p\eta$ final state, the MC of $p\eta$ (blue) and of $p\pi^0$ (red) are used to fit the cluster size spectra. The sum of both MC spectra is plotted in green.

The situation is different for the 2 PED events. Due to the lack of angular cuts, the selection of the photon candidates is not as clean as for the 3 PED events which can also be observed by the PSA spectra (see Figures 5.64 and 5.65). The cluster size of the photons of the 2 PED events is depicted in Figure 5.70 for both final states. A conservative cut at cluster size > 1 was applied for the photon candidates of the $p\pi^0$ final state to reduce background contamination from nucleons. The MC spectra of the $p\eta$ final state show that the photon cluster sizes are mostly above 3.

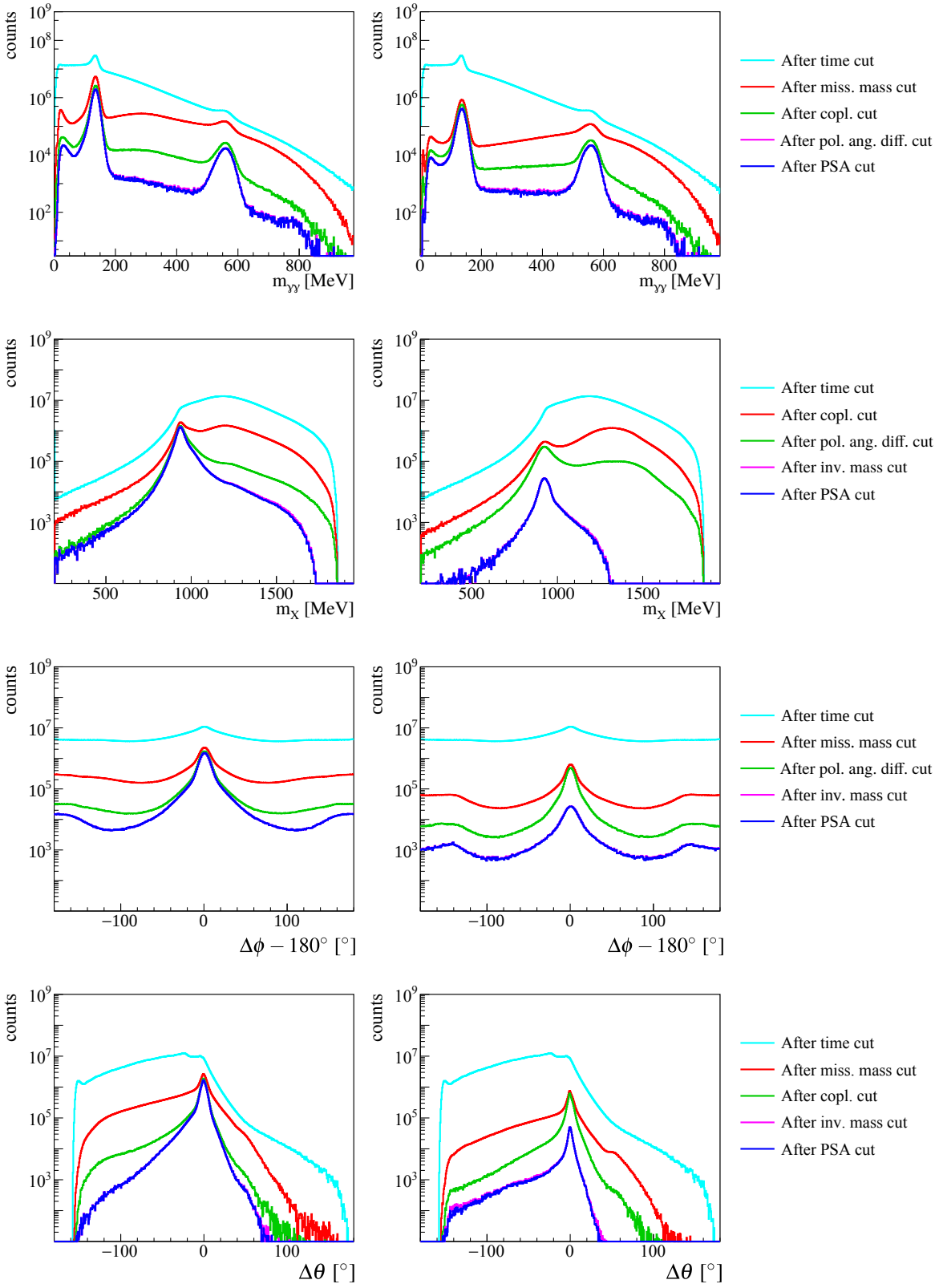

Figure 5.71: The impact of each kinematic constraint on each kinematic variable (invariant mass (first row), missing mass (second row), coplanarity (third row) and polar angle difference (bottom row)) are demonstrated for the 3 PED events and for both final states $p\pi^0$ on the left and $p\eta$ on the right. All shown spectra were taken with the butanol target.

To reduce the background from e.g. the $p\pi^0$ final state, a cluster size cut at cluster size > 3 was applied for the photons. The $p\pi^0$ background can be suppressed by $\sim 95\%$ in TAPS and only 13% $p\eta$ events are lost.

The influence of each cut on each of the four variables: invariant mass, missing mass, coplanarity and polar angle difference is depicted in Figure 5.71 for the 3 PED events and in Figure 5.72 for the 2 PED events. The signal to background ratio is significantly increased after applying all cuts to the data. The cluster size cut improves the signal to background ratio for the 2 PED events further, especially for the $p\eta$ final state.

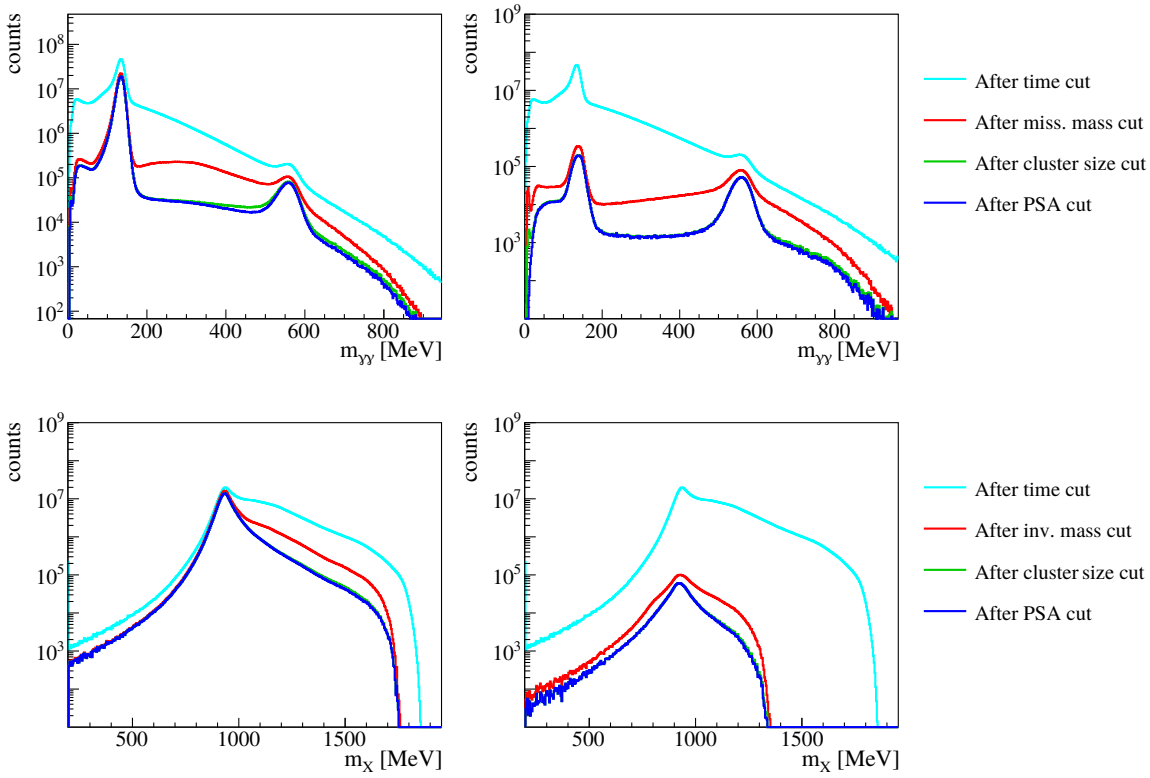

Figure 5.72: The impact of each kinematic constraint on each kinematic variable (invariant mass (first row), missing mass (second row)) are demonstrated for the 2 PED events and for both final states $p\pi^0$ on the left and $p\eta$ on the right. All shown data were taken with the butanol target.

5.3.2.6 $\Delta E - E$ spectra

The deposited energies in either the PID and the Crystal Ball detector or in the TAPS vetoes and the TAPS detector can be used to get an additional check whether the selected proton candidate is indeed a proton. As already mentioned, the PID was not working well during the November 2013 and May 2014 beamtimes (see Figure A.3). Thus, the $\Delta E - E$ spectra were not used to apply a cut. Nevertheless, the $\Delta E - E$ spectra are shown for the PID-Crystal Ball and TAPS vetoes-TAPS detectors for the September 2015 beamtime in Figure 5.73 and 5.74, respectively. The left plot shows the spectra before any cuts are applied to the 3 PED events. Apart from the banana shape signal stemming from low energetic protons, clear signals from

electrons and charged pions are seen as well. While electrons are found at small ΔE_{PID} or $\Delta E_{\mathrm{TAPS\ VETO}}$ and E_{CB} or E_{TAPS}, charged pions lie in an almost flat band below the proton banana. Charged pions exhibit only a small energy dependence as they are almost minimum ionizing when detected in the Crystal Ball detector. Most of the charged pions detected in the TAPS detector are minimum ionizing and leave an almost constant energy of 180 MeV. Minimum ionizing protons leave an energy of about 250 MeV in the TAPS detector and are present to a small fraction in the $p\pi^0$ final state. After applying all the previously discussed kinematic cuts to the data, only the proton banana remains for both $p\pi^0$ and $p\eta$ final states, indicating a successful selection of proton candidates and that a $\Delta E - E$ cut is not necessary for the selection of the 3 PED events.

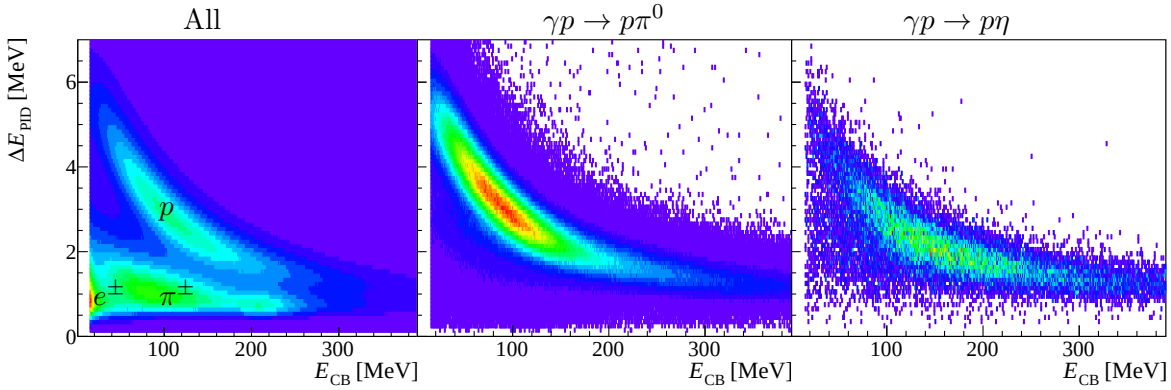

Figure 5.73: The deposited energy of the PID ΔE_{PID} is plotted as a function of the deposited energy in the Crystal Ball detector E_{CB} for all data (left), for selected $p\pi^0$ (middle) and selected $p\eta$ events after applying the time, invariant and missing mass, coplanarity, polar angle difference, PSA and cluster size cuts. Note: The z-axis is chosen differently for all three plots since the statistics is different.

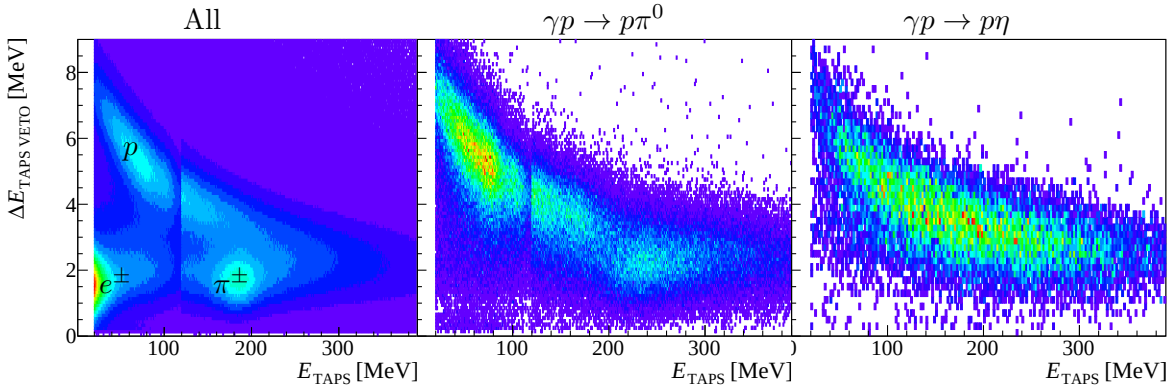

Figure 5.74: The deposited energy of the TAPS vetoes $\Delta E_{\mathrm{TAPS\ VETO}}$ is plotted as a function of the deposited energy in the TAPS detector E_{TAPS} for all data (left), for selected $p\pi^0$ (middle) and selected $p\eta$ events after applying the time, invariant and missing mass, coplanarity, polar angle difference, PSA and cluster size cuts. Note: The z-axis is chosen differently for all three plots since the statistics is different. The LED 1 TAPS trigger threshold at 120 MeV is visible in the spectra.

5.3.3 Quality of event selection

The detection, reconstruction and event selection acceptance is depicted in Figure 5.75 on the left for the $p\pi^0$ and on the right for the $p\eta$ final state. The efficiency can be estimated using the detection and reconstruction efficiency of photons 95% and the efficiency of 2σ broad cuts on the invariant, missing, coplanarity and polar angle difference cuts which retain 95% of the events, 3σ cut on the PSA spectra retaining 99% of the events and the cluster size cut in case of the 2 PED events (90% of the events are kept on average). Thus, the efficiency is given for the 2 and 3 PED events:

$$\epsilon = \begin{cases} 0.95^2 \cdot 0.95^2 \cdot 0.99 \cdot 0.90 \approx 0.73, & \text{2 PED events} \\ 0.95^2 \cdot 0.95^4 \cdot 0.99 \approx 0.64, & \text{3 PED events} \end{cases} \tag{5.17}$$

The maximum acceptance of the 2 PED events below 500 MeV amounts to around 70% for the $p\pi^0$ final state which is in good agreement to the estimated efficiency. Furthermore, the maximum efficiency of the 3 PED events is around 63% which is in accordance with the estimation. The acceptance is reduced in very backward and very forward direction due to the lack of $PbWO_4$ used in the analysis. An acceptance gap is produced by the space between Crystal Ball and TAPS detectors which also decreases the acceptance in certain angular bins. Additionally, the acceptance decreases towards higher beam photon energies, which can be traced back to reconstruction inefficiencies caused by e.g. split-offs, overlapping clusters etc. In case of the $p\eta$ final state, the acceptance reaches its maximum at around 50% since the kinematic acceptance of the $p\eta$ final state is smaller than for the $p\pi^0$ final state.

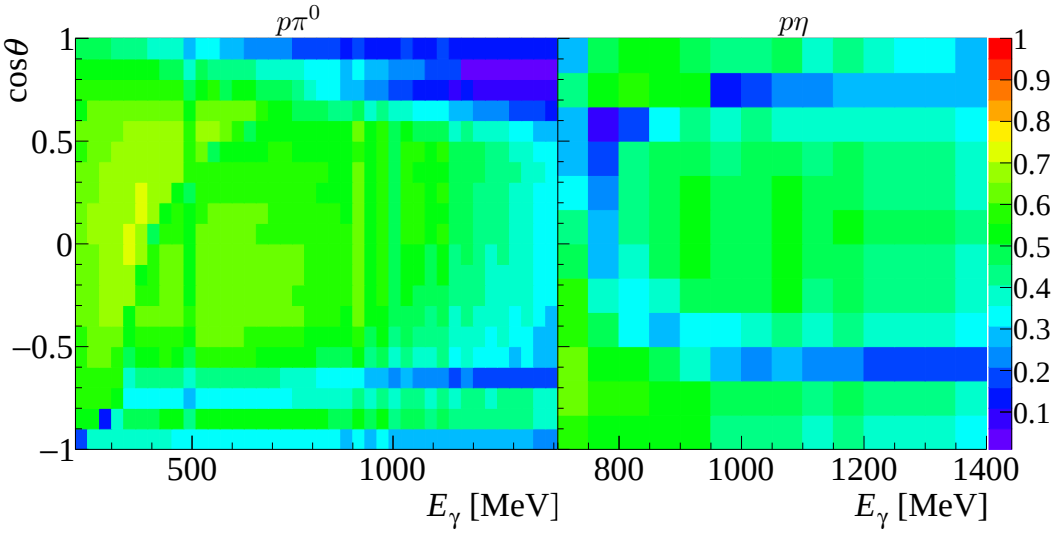

Figure 5.75: The total detection, reconstruction and analysis acceptance $\epsilon(E_\gamma, \cos\theta)$ (see Equation (5.12)) is shown as a function of the beam photon energy and $\cos\theta$ on the left for the $p\pi^0$ final state and on the right for the $p\eta$ final state. The 2 PED events are only added in the forward angular region.

Table 5.3 lists the total number of selected events for the $p\pi^0$ and $p\eta$ final state for each beamtime. In total, 14×10^6 3 PED events of the $p\pi^0$ final state and 3.2×10^5 3 PED events

of the $p\eta$ final state were selected from all the available butanol runs.

beamtime	**target**	**radiator**	**event class**	$\gamma\mathbf{p} \to \mathbf{p}\pi^{\mathbf{0}}$	$\gamma\mathbf{p} \to \mathbf{p}\eta$
November 2013	butanol	diamond	3 PED	1.5×10^6	2.5×10^4
			2 PED	1.8×10^7	6.3×10^4
		Møller	3 PED	1.5×10^5	3.3×10^3
			2 PED	2.0×10^6	8.0×10^3
May 2014	butanol	diamond	3 PED	1.1×10^7	3.9×10^4
			2 PED	5.5×10^6	1.0×10^5
		Møller	3 PED	5.3×10^5	1.4×10^4
			2 PED	4.9×10^6	3.4×10^4
May 2015	butanol	diamond	3 PED	3.8×10^6	1.0×10^5
			2 PED	3.3×10^7	2.6×10^5
		Møller	3 PED	1.1×10^6	2.5×10^4
			2 PED	1.2×10^7	6.3×10^4
September 2015	butanol	diamond	3 PED	4.4×10^6	8.3×10^4
			2 PED	3.5×10^7	2.1×10^5
		Møller	3 PED	1.4×10^6	3.5×10^4
			2 PED	1.6×10^7	9.0×10^4
all beamtimes	butanol	diamond	3 PED	10.8×10^6	2.5×10^5
			2 PED	91×10^6	6.3×10^5
		Møller	3 PED	3.2×10^6	7.7×10^4
			2 PED	35×10^6	1.9×10^5
September 2015	*carbon+helium*	diamond/Møller	3 PED	3.0×10^5	9.5×10^3
			2 PED	1.0×10^7	8.8×10^4

Table 5.3: This table gives an overview about the number of selected events of the butanol data for each beamtime after all cuts are applied to the data.

As a last step, the amount of background contamination in the selected data was determined for both final states. For this purpose, the *carbon+helium* subtracted invariant mass spectra were fitted using a Novosibirsk function to describe the signal peak in combination with a linear function to describe the flat background underneath the invariant mass peak. Example fit results are shown for one energy bin in Figure 5.76 for the $p\pi^0$ final state and in Figure 5.77 for the $p\eta$ final state. The background contamination within the $\pm 2\sigma$ cut ranges are depicted as a function of the beam photon energy and the center of mass angle $\cos\theta$ in Figure 5.78 for the $p\pi^0$ and in Figure 5.79 for the $p\eta$ final state, respectively. The background contamination is mostly below 1% for the 3 PED events of the $p\pi^0$ final state. Small background contributions in the order of 2% - 8% are found in the forward angular region of the meson since here, the 2 PED events contribute. At $\cos\theta \approx 0.95$ background is observed which peaks at around $m_{\gamma\gamma} \approx 50\,\text{MeV}$. However, it is far enough away to justify a linear fit for the background description underneath the π^0 peak. In case of the $p\eta$ final state, background below 1% is visible until 1000 MeV, where the $p\eta$ unpolarized cross section is at its maximum. At higher energies, the background contamination amounts to 2% - 10% and is largest at very backward and forward angles just like in the case of the CBELSA/TAPS data. All in all, the background is kept low using the event selection described in this chapter.

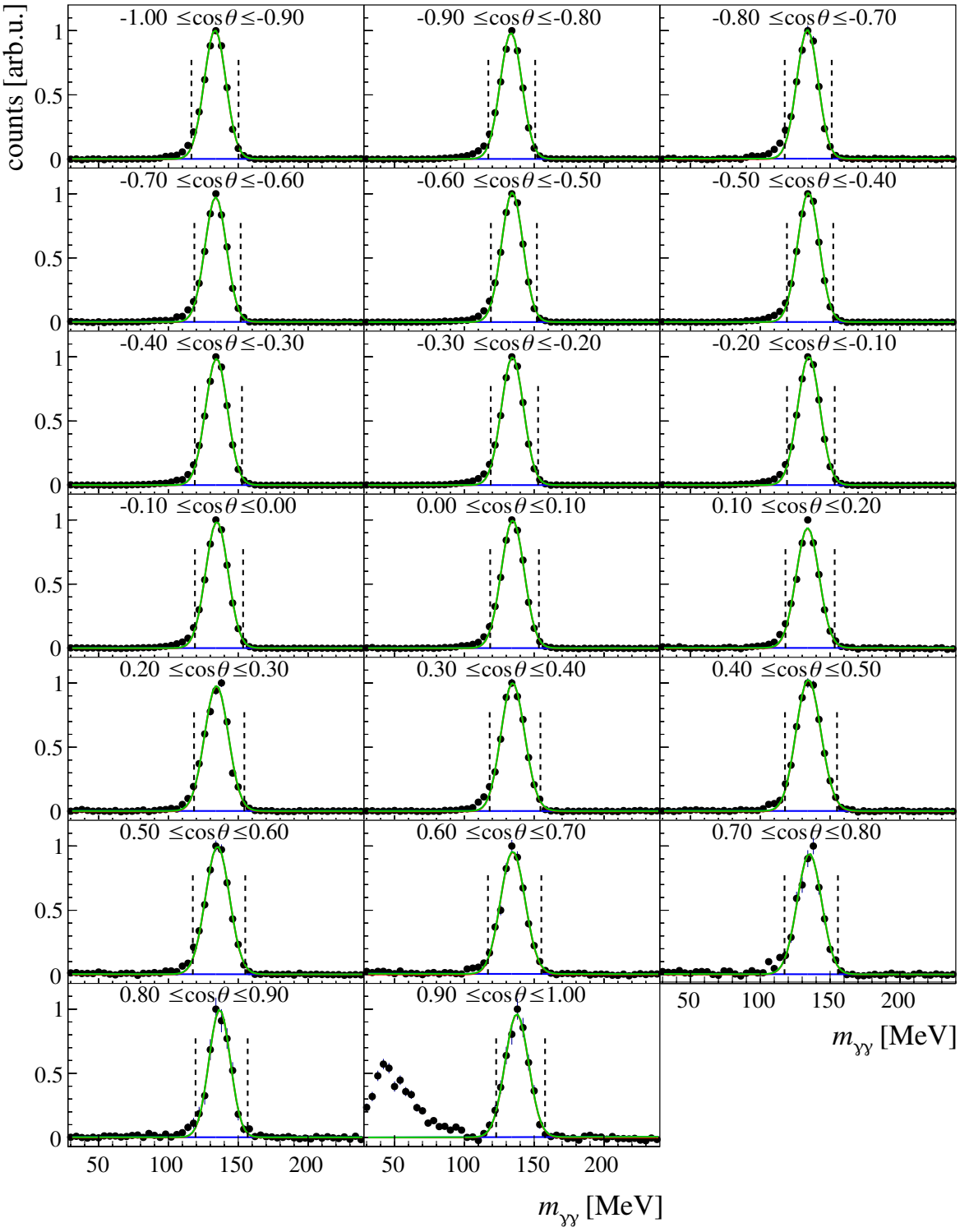

Figure 5.76: Invariant mass spectra of the *carbon+helium* subtracted data (black points) are shown as a function of the center of mass angle $\cos\theta$ for the energy bin ($450\,\text{MeV} \leq E_\gamma < 480\,\text{MeV}$) and for the $p\pi^0$ final state. The red line represents a Novosibirsk function, the blue line a linear function and the green line the total fit function.

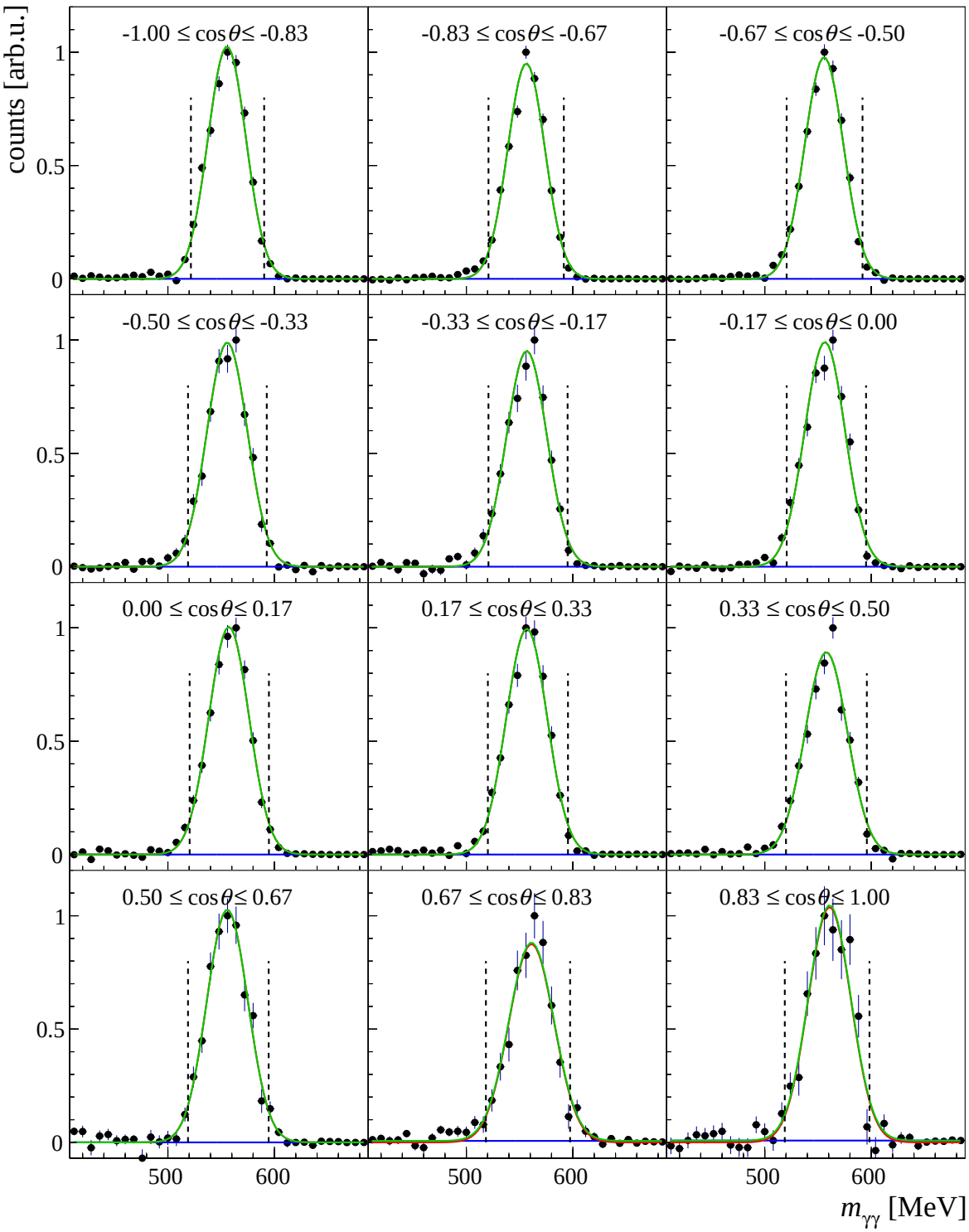

Figure 5.77: Invariant mass spectra of the *carbon+helium* subtracted data (black points) are shown as a function of the center of mass angle $\cos\theta$ for the energy bin (800 MeV $\leq E_\gamma <$ 900 MeV) and for the $p\eta$ final state. The red line represents a Novosibirsk function, the blue line a linear function and the green line the total fit function.

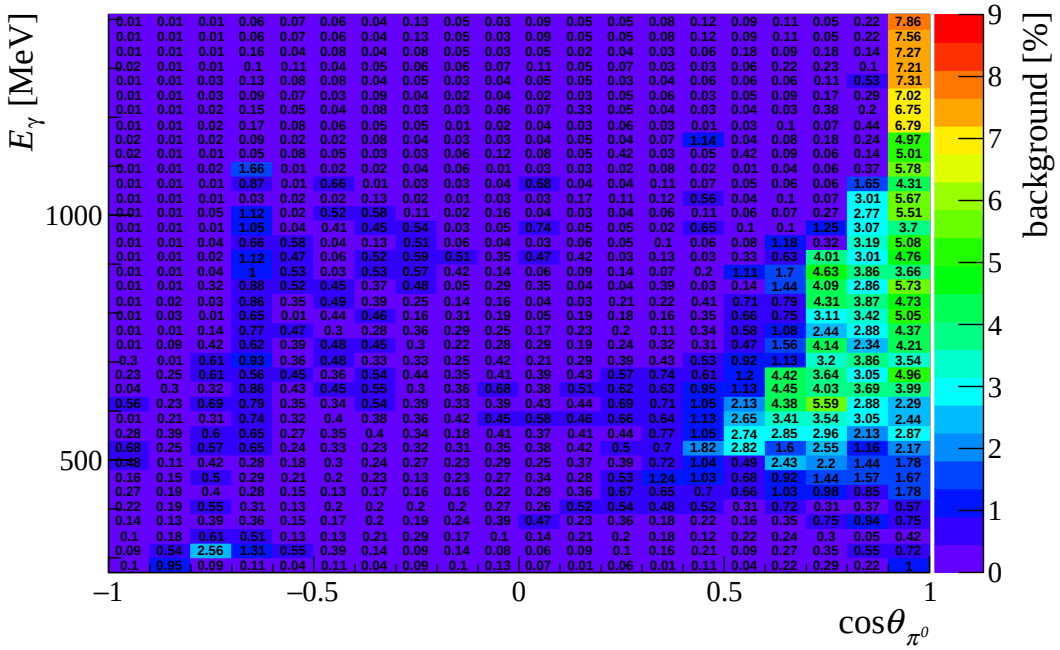

Figure 5.78: The background contributions are shown as a function of the beam photon energy E_γ and the center of mass angle $\cos\theta_{\pi^0}$ for the $p\pi^0$ final state.

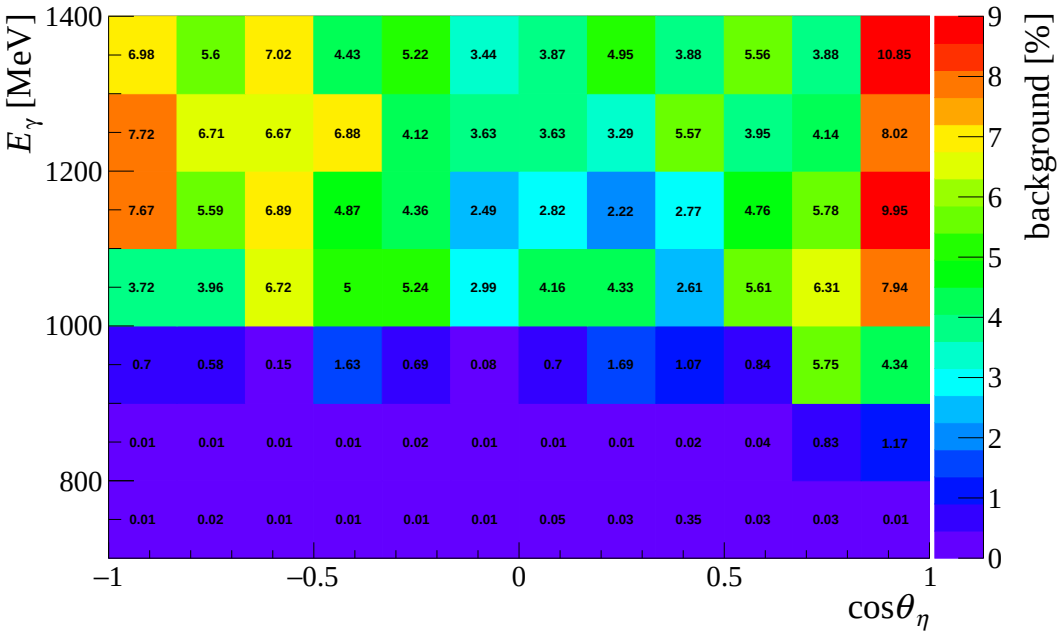

Figure 5.79: The background contributions are shown as a function of the beam photon energy E_γ and the center of mass angle $\cos\theta_\eta$ for the $p\eta$ final state.

6 Determination of the beam asymmetry

Using a linearly polarized photon beam in combination with an unpolarized liquid hydrogen target allows the determination of the single polarization observable Σ, also known as the beam asymmetry. According to [San+11], the polarized cross section is, in contrast to the unpolarized cross section, not ϕ-symmetric but exhibits a cosine modulation as given in Equation (6.1).

$$\frac{d\sigma}{d\Omega_{\mathrm{pol}}} = \frac{d\sigma}{d\Omega_{0}} \left[1 - p_{\gamma}^{\mathrm{lin}} \Sigma \cos(2\varphi)\right] \qquad \text{with} \qquad \varphi = \alpha - \phi. \tag{6.1}$$

$\frac{d\sigma}{d\Omega_0}$ and $\frac{d\sigma}{d\Omega_{\mathrm{pol}}}$ are the unpolarized and polarized cross sections, $p_{\gamma}^{\mathrm{lin}}$ the polarization degree of the linearly polarized photons and φ is the angle between the beam polarization plane and the reaction plane (see Figure 6.1). While the beam polarization plane is defined by the beam photon momentum $\vec{k}$ and the polarization vector $\vec{\epsilon}$, the reaction plane is given by the beam photon and the meson π^0 or η momentum vectors (see Figure 6.1 on the right). The angle φ is related to the measured azimuthal angle ϕ of the final state meson that runs in the x-y plane of the detector system lab frame through the angle α. The latter gives the azimuthal angle of the beam polarization plane (see Figure 6.1 on the left).

The beam asymmetry can be determined by measuring the polarized cross section using Equation (6.1). This method has the disadvantage of requiring a good handling of the flux normalization and detector acceptances in three dimensions $(E_\gamma, \cos\theta, \phi)$. Instead, the measurement of asymmetries can be employed to access the beam asymmetry. Hence, data were not only taken for one α setting but for two orthogonal orientations of the beam polarization plane at $\alpha = \pm 45°$. The values of α can be chosen freely[1] as long as they remain orthogonal to each other.

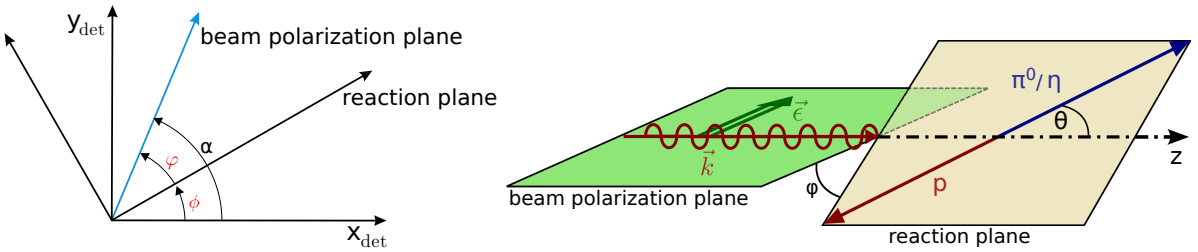

Figure 6.1: Left: Definition of the angles α, ϕ and φ which relate the beam polarization and reaction plane to the detector system lab frame. Adapted from [Har17]. Right: The beam polarization plane is defined by the beam photon momentum $\vec{k}$ and the polarization vector $\vec{\epsilon}$. The reaction plane is given by the final state particles: the recoil proton p and the meson π^0 or η. Adapted from [Gut10].

In this chapter the determination process of the beam asymmetry is explained using the CBELSA/TAPS data, starting with the extraction of the polarization degree (see Section 6.1)

[1] The orientation is chosen in a way which suits best for the given photon beam quality. Due to different large horizontal and vertical beam divergencies the values 0° and 90° are not chosen [Ebe12].

and continuing with the determination of the beam asymmetry applying two different methods: through event yield asymmetries (see Section 6.2) and through an event based maximum likelihood fit (see Section 6.3).

6.1 Polarization degree of the linearly polarized photons

During all four beamtimes runs were taken with a diamond radiator using the data trigger and every forty diamond runs also two runs were taken with an amorphous copper radiator of 50 µm thickness, utilizing an only tagger hit trigger condition. Typical copper and diamond run bremsstrahlung spectra are show in Figure 6.2 on the left and in the middle. Due to the different sizes of the tagger bars and different detection efficiencies of the channels, large fluctuations are visible, especially below an energy of E_γ =1000 MeV. Nevertheless, the $1/E_\gamma$ energy dependence is visible for the bremsstrahlung spectrum of the amorphous radiator, while the spectrum taken with the diamond radiator exhibits the coherent edge structures due to the coherent bremsstrahlung process (see Figure 6.2). Dividing both spectra by each other allows the extraction of the enhancement spectra as demonstrated in Figure 6.4. Thereby, different efficiencies of the different tagger channels are canceled.

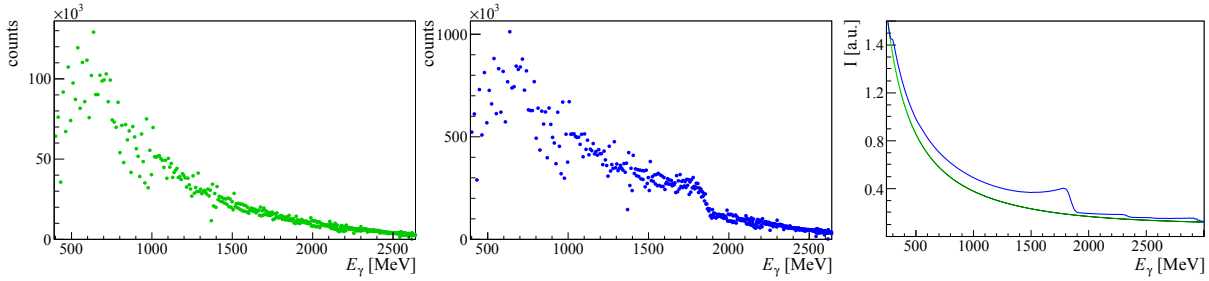

Figure 6.2: The measured beam energy dependence of coincident GIM and tagger hits is shown on the left for a diamond run and in the middle for a copper run. As expected the diamond run shows the coherent edge at 1850 MeV and the copper run the $1/E_\gamma$ energy dependence. The analytically calculated spectra (in blue diamond and in green the amorphous spectrum) using the ANB calculations are shown on the right.

Getting the correct enhancement spectra is a crucial step towards extracting the degree of linear polarization p_γ^{lin} using a software based on the ANB calculations [Nat+03], since the enhancement spectra are directly compared to the analytically calculated spectra of the ANB calculations (see Figure 6.2 on the right). Due to problems that occurred with the GIM detector and the tagger during the beamtimes, this first step represented a challenge which is described in the following.

6.1.1 Extraction of the enhancement spectra

It is important to get the bremsstrahlung spectra of both radiators after the photon beam passes through the collimator since the collimator removes more unpolarized than polarized photons from the photon beam. This can be explained with the strong forward emittance of the coherent bremsstrahlung photons in comparison to the incoherent bremsstrahlung photons. Therefore, it effects the shape of the enhancement spectra and consequently the net degree of linear photon polarization. On average, the collimator increases the polarization degree by

about 8% [Ebe12]. While the tagger counts all electrons that produced bremsstrahlung photons, the GIM detector, which is located at the end of the beamline, counts all photons that have not interacted with the target material. Requiring a time coincidence of the tagger and GIM detector allows to produce the enhancement spectra. Since events that caused the trigger in the diamond runs are different from the events that caused the trigger in the copper runs, they are removed by applying a time cut. Figure 6.3 shows the tagger time plotted against the GIM time. The time coincident events are located on the diagonal. Here, the trigger correlated events are located at the center at (0 ns,0 ns). Events were only retained within the red boxes. Random time background was subtracted using the green sideband areas similarly as described in Section 5.2.1. Figure 6.2 shows the time coincident bremsstrahlung spectrum on the left for the diamond radiator, in the middle for the copper radiator and on the right the calculated diamond and copper spectra as obtained with the ANB calculations.

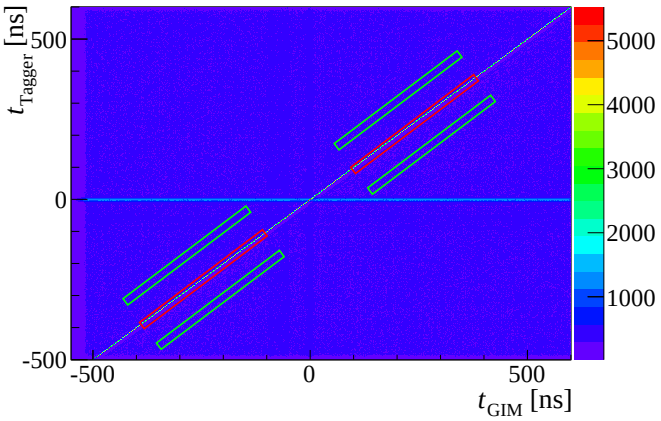

Figure 6.3: The GIM time is plotted against the tagger time. Time coincident hits are located on the diagonal. The not trigger correlated events were chosen within the red rectangular boxes. Random time background was subtracted using the green boxes. Note: Due to the very high rates of around 13 MHz in the GIM detector the prompt peak events at 0 ns are not visible.

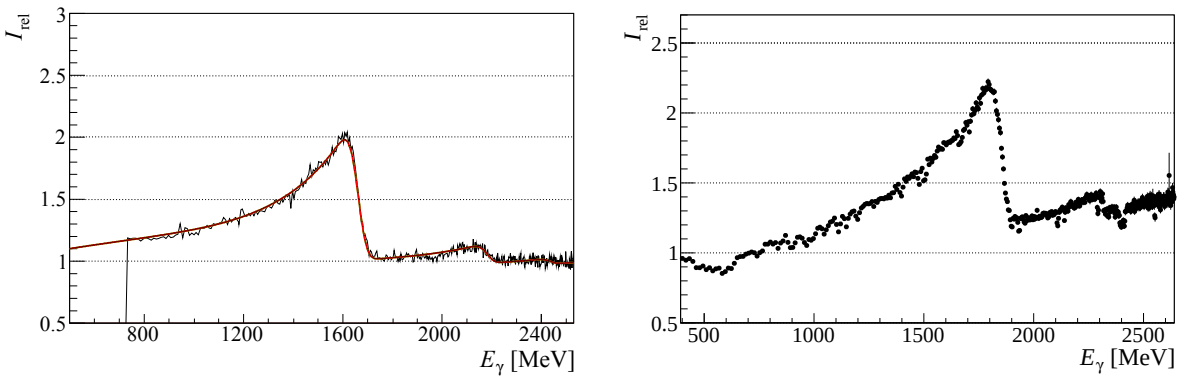

Figure 6.4: Left: Enhancement spectrum measured in an older CBELSA/TAPS beamtime with the coherent edge at around 1650 MeV. The red curve shows the comparison to the ANB calculated spectrum. Adapted from [Els07]. Right: A typical enhancement spectrum for the 1850 MeV coherent edge setting of the September 2013 beamtime. The spectrum is tilted in comparison to the left spectrum.

The resulting enhancement spectrum is depicted in Figure 6.4 on the right. Usually, one expects the enhancement spectrum to lie on a horizontal line, the so-called baseline. The baseline is not visible here since the used collimator diameter of 4 mm is not small enough to separate the visible coherent peaks well enough to see the baseline. However, the depicted enhancement spectrum exemplary for the July - October 2013 beamtimes shows a clear slope from lower to higher energies which, according to the ANB calculations and older measured enhancement spectra (see Figure 6.4 on the left), should not have been present. Since only information of the GIM and the tagger are used for the extraction of the enhancement spectra, both detectors were investigated carefully in cooperation with Jun.-Prof. Dr. A. Thiel [Thi16].

6.1.1.1 Correction of the GIM efficiency using the FluMo detector

Upon investigating the GIM detector, error messages were found regarding the high voltage channel of GIM crystal 7, which is the crystal in the center of the 4×4 GIM matrix and therefore subject to the highest rates of the photon beam. The error messages indicate that the high voltage was ramped up and down during the July - September 2013 beamtimes and in the October beamtime the maximal available voltage was constantly taken. Here, the occurrence of the error messages became more frequent from July to October. Unfortunately, these error messages remained unnoticed until the end of all beamtimes. It was guessed that the very high rates of the GIM detector of around 12 MHz[2] used in the beamtimes may have caused this problem. In a dedicated test beamtime in June 2015 it was attempted to reproduce the GIM error messages using very low to very high rates, but without success. It is not clear until now what exactly caused the problems with the high voltage system. Nevertheless, after more investigation it was found that the GIM hardware problems lead to problems with the GIM efficiency.

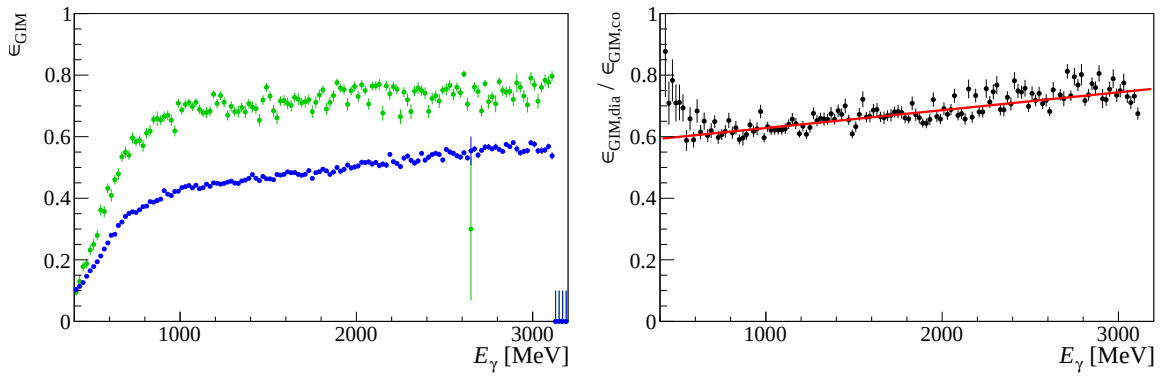

Figure 6.5: Left: The GIM efficiency ϵ_{GIM} is plotted as a function of the beam photon energy for a typical diamond run in blue and a copper run in green. Right: The ratio of the GIM efficiency of diamond runs $\epsilon_{GIM,dia}$ and of copper runs $\epsilon_{GIM,co}$ is plotted as a function of the beam photon energy. The red line shows the linear fit to the ratio.

The GIM efficiency can be determined utilizing the FluMo detector which on the one hand did not exhibit any problems during the beamtime and on the other hand is well suited for high rates. Taking the ratio of coincident hits of the tagger, the GIM and the FluMo detector to

[2] Such high rates were used for the first time in a CBELSA/TAPS experiment.

coincident hits of the tagger and the FluMo gives the GIM efficiency as a function of the beam photon energy. More information are given in [Har17].

$$\epsilon_{\mathrm{GIM}} = \frac{N_{\mathrm{tagger}} \wedge N_{\mathrm{FluMo}} \wedge N_{\mathrm{GIM}}}{N_{\mathrm{tagger}} \wedge N_{\mathrm{FluMo}}} \tag{6.2}$$

Figure 6.5 shows on the left the GIM efficiency in blue for a diamond run and in green for a copper run. The rise of the GIM efficiency until about 700 MeV is due to the influence of the set discriminator thresholds. However, at higher energies the efficiency is unexpectedly not flat but has a linear slope indicating a rate dependence since the rates are higher at lower beam photon energies. More importantly the observed slope is different for the diamond and copper radiator. This can be attributed to the different thicknesses of the diamond (500 µm) and copper (50 µm) foil, which correspond to slightly different radiation lengths. Therefore, the GIM detector was subject to different high rates depending on the choice of radiator. When taking the ratio between diamond and copper spectra the ratio of the GIM efficiency does not cancel out as it is not 1 (see Figure 6.5 on the right). Thus, the GIM efficiency was determined for each diamond and copper run and a linear correction could be applied to the enhancement spectra.
The effect of the GIM problems related linear correction on the enhancement spectrum is depicted in Figure 6.6. A significant reduction of the initially observed slope from low to high energies is observed. Nevertheless, a slope from lower to higher beam photon energies is still visible, indicating that the GIM detector problems do not entirely explain the slope of the enhancement spectra.

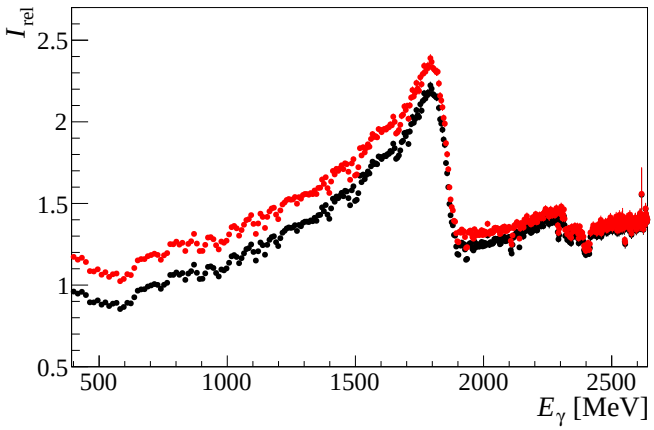

Figure 6.6: The enhancement spectrum is shown with the linear correction due to the GIM efficiency in red and the enhancement spectrum without any correction in black.

6.1.1.2 Rate dependent effects of the tagger

In addition to the GIM detector, the tagger was investigated for any rate dependent effects. First of all the tagger bars and fibers were looked at separately. In general, the tagger bars are subject to higher rates compared to the tagger fibers due to their larger size. Therefore, it was decided to only use the tagger fibers for the creation of the enhancement spectra. Moreover, a dead time correction was performed for each tagger fiber channel. The dead time is given

by approximately 40 ns for most fibers. At lower beam photon energies some fibers exhibited increased dead time values that were corrected for. However, the dead time correction did not show a large dependence on the chosen radiator and therefore did not significantly change the enhancement spectra [Thi16].
Moreover, it was investigated whether the used tagger fiber discriminators have a rate dependency. The tagger fibers had registered rates of up to 1.2 MHz during the beamtimes. Figure 6.7 shows typical rates for the tagger fibers for a diamond and copper run. In order to investigate the rate dependence of the discriminators, they were fed with signals using different input rates and measuring the output rate. Thereby, the signals were randomly distributed in time. Figure 6.7 shows the input and output rates of one discriminator. A clear linear dependent decrease of the output rate is observed in comparison to the input rate towards higher rates. Thus, a correction was applied to the enhancement spectra depending on the rate of each fiber channel. This correction mostly effects the low beam photon energy range and has only little influence at higher energies. The result of the corrected enhancement spectrum is depicted in Figure 6.8.

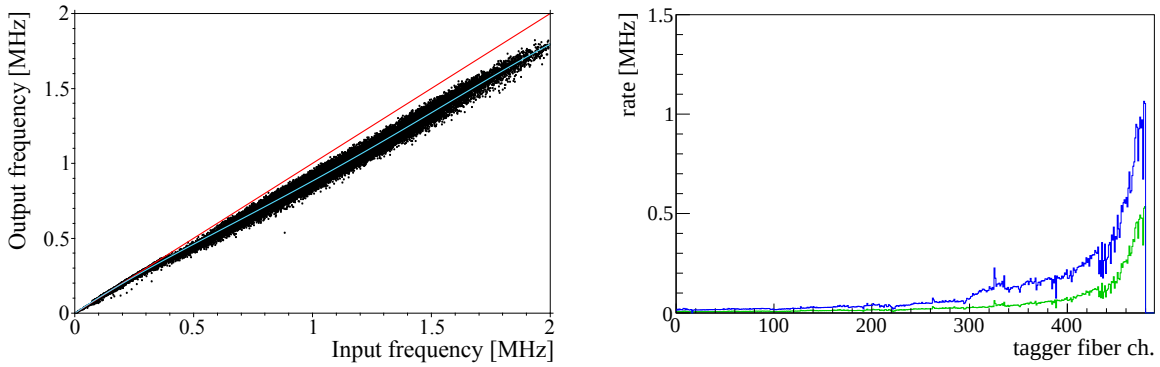

Figure 6.7: Left: The output rate is shown as a function of the input rate for one discriminator. A deviation from the diagonal (red line) is visible. The light blue line is a fit to the data. Taken from [Thi16]. Right: The tagger fiber rates are plotted for a diamond run (blue) and for a copper run (green) as a function of the tagger fiber channel. Note: Small channel numbers correspond to high beam photon energies and large channel numbers to small beam photon energies.

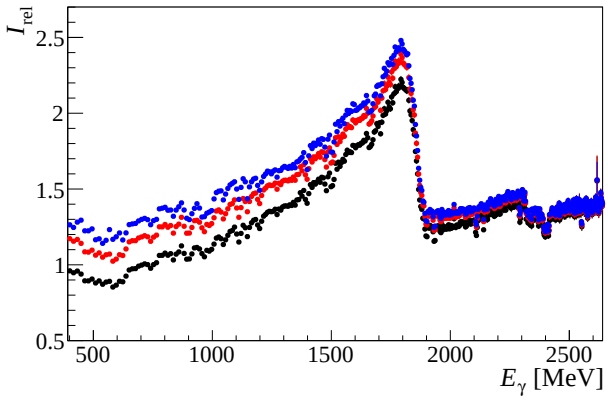

Figure 6.8: The enhancement spectrum is shown without any correction in black, with the linear correction due to the GIM efficiency in red and with the additional tagger rate correction in blue.

6.1.2 Extraction of the polarization degree

After applying the GIM and tagger related corrections to the enhancement spectra, they were subsequently used to determine the polarization degree separately for both $\alpha = \pm 45°$ settings. As already mentioned, the coherent bremsstrahlung process and therefore the coherent peak structures visible in the enhancement spectra can be analytically calculated [Nat+03]. The calculation needs as input parameters the thickness of the diamond crystal, the collimator radius and length, the distance from the collimator to the radiator target and beam divergence properties. The application procedure of the software is described in [Ebe12]. A comparison of the ANB calculated to the measured enhancement spectrum is depicted in Figure 6.9 in the upper row for one spectrum of the 1750 MeV and in the lower row for one spectrum of the 1850 MeV coherent edge setting.

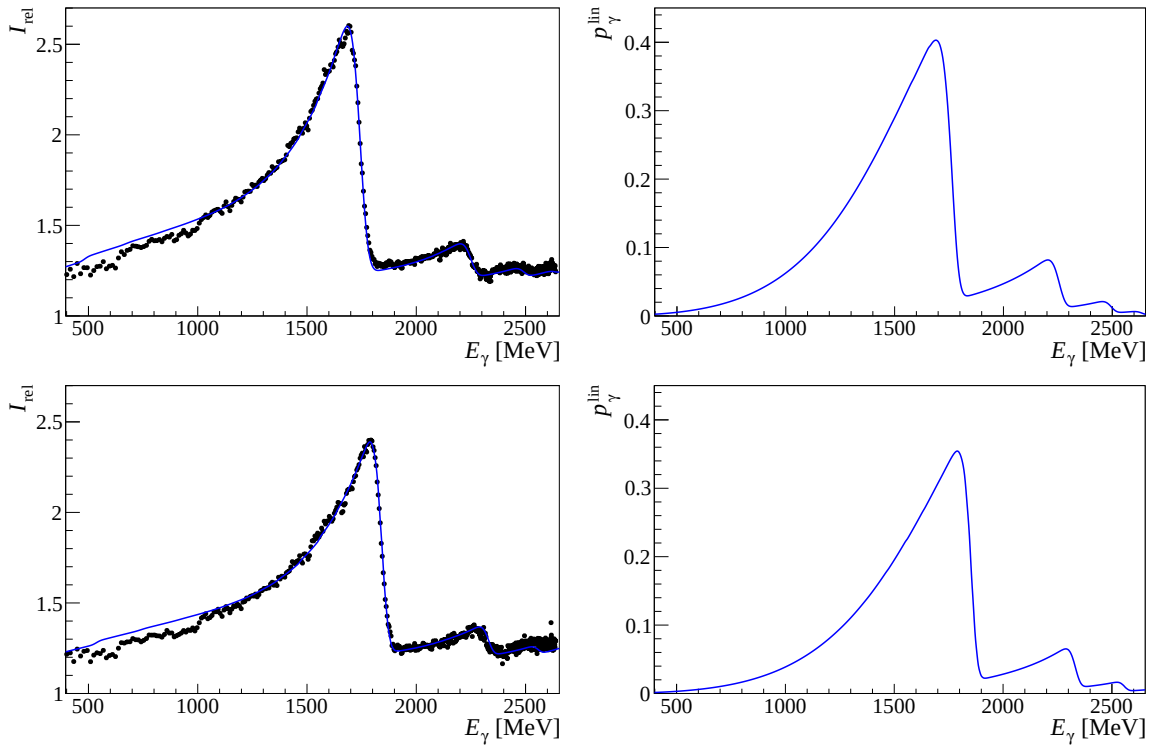

Figure 6.9: The ANB calculated enhancement spectra (blue) are compared to the measured enhancement spectra (black data points). The calculated polarization degree is shown in the right column. The upper row shows the the plots for the 1750 MeV coherent edge setting and the lower row the plots for the 1850 MeV coherent edge setting.

The resulting polarization degree values are plotted as a function of the beam photon energy in the right column. The maximum achieved polarization values are 40 % for the 1750 MeV coherent edge setting and 35 % for the 1850 MeV coherent edge setting. Only events with a polarization degree higher than 10 % are retained for the determination of the beam asymmetry Σ. This corresponds to beam photon energies higher than 1130 MeV for the 1750 MeV coherent edge setting and 1250 MeV for the 1850 MeV coherent edge setting. Small shifts of the coherent edge position can occur during a beamtime due to small drifts of the photon beam position. Whenever larger deviations occurred, the photon beam position was corrected by the ELSA

operator. Due to these shifts the data is divided into subsets and new polarization values are determined for each subset. All calculated enhancement spectra for both coherent edge settings and for both α settings are depicted in Figure 6.10. The coherent edge position remained stable within 20 MeV during the beamtimes. Since the coherent edge position is not exactly the same for both α settings and since large changes of the polarization degree occur at the position of the coherent edge, all events are rejected that lie above 1670 MeV or 1770 MeV, respectively for the 1750 MeV and 1850 MeV coherent edge settings.

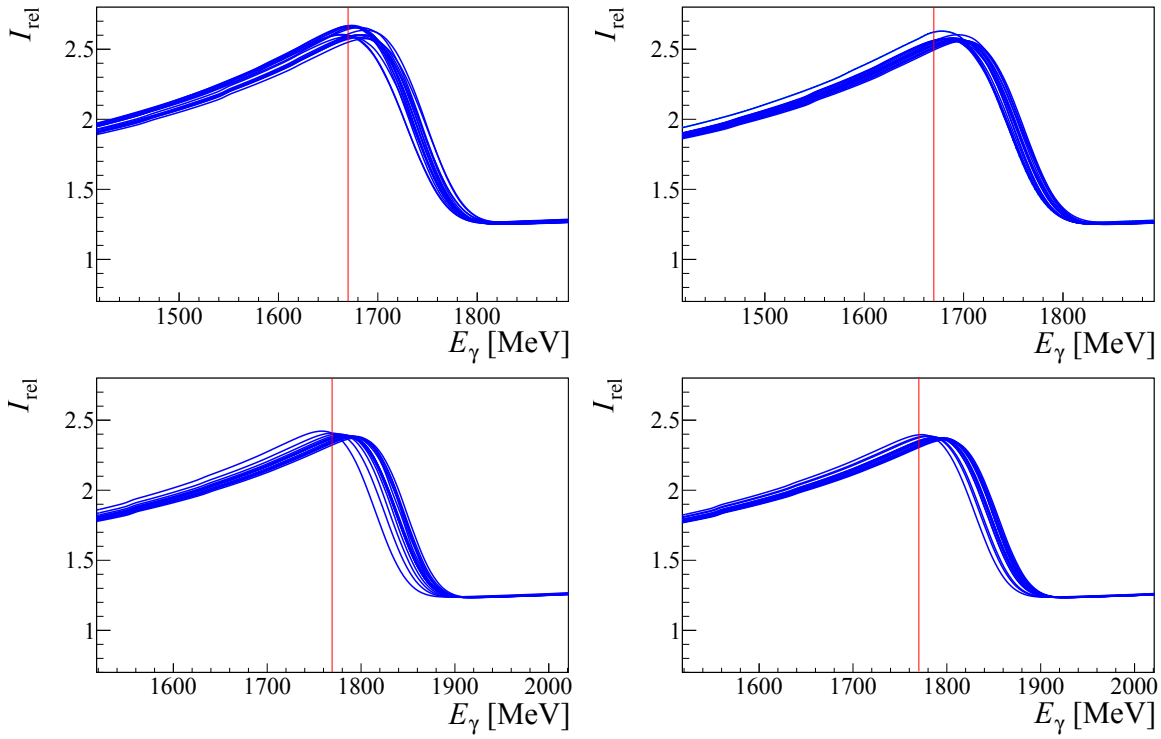

Figure 6.10: All calculated ANB enhancement spectra (blue) of the 1750 MeV (upper row) and of the 1850 MeV coherent edge setting are plotted. The coherent edge position drifted during the beamtime by up to 20 MeV. The left column shows the spectra for $\alpha = -45°$ and the right column for $\alpha = 45°$. The red line marks the upper cut on the energy range that is used to determine the beam asymmetry.

To estimate the relative systematic error of the polarization degree the ratio of the ANB calculated to the measured enhancement spectrum was taken. One example is shown in Figure 6.11 on the right. The deviations are contained within a relative error of $\pm 5\,\%$ in the beam photon energy region of interest. This error estimation represents the accuracy with which the ANB calculations can describe the data. Due to the uncertainty introduced by adding data of an entire day or even more before comparing it to ANB calculations, small shifts of the coherent edge position are not accurately taken into consideration. Therefore, a larger error of $\pm 8\%$ has to be estimated near the coherent edge maximum ($E_\gamma > 1600$ MeV or $E_\gamma > 1700$ MeV, respectively) [Har17]. For energies below 1000 MeV larger deviations are observed. They are possibly caused by tagger rate issues that could not be fully corrected[3]. However this energy region is not used and therefore, the observed deviations are irrelevant for the beam asymmetry

[3] The tagger rate correction is based on measurements performed on a few discriminators. There is a possibility that some discriminators need a higher correction.

determination.

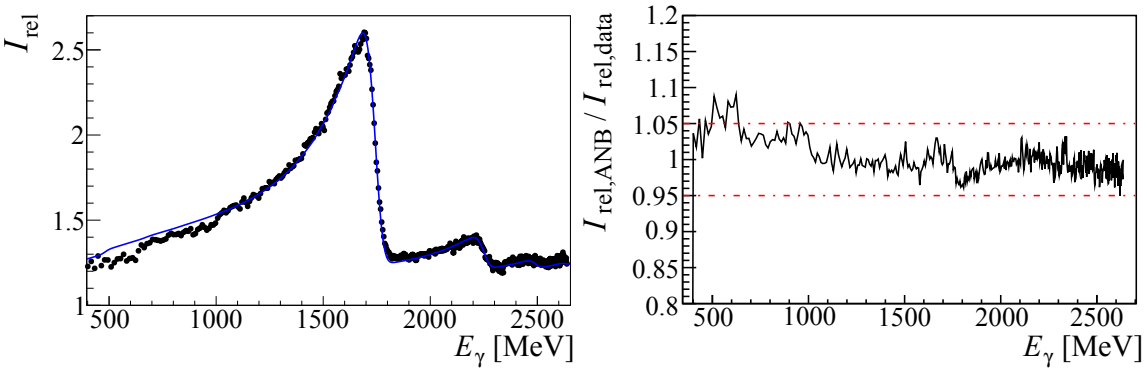

Figure 6.11: Left: The ANB calculated enhancement spectrum (blue) is compared to the measured enhancement spectrum (black data points). Right: The relative deviation of the calculated and measured enhancement spectrum is plotted as a function of the beam photon energy. The relative ±5 % deviation points are marked by the dashed-dotted red line.

6.2 Determination of Σ using event yield asymmetries

The beam asymmetry Σ can be obtained from the data by performing fits. The question arises whether to use a binned or an unbinned fit, which are the most common used fit methods. Two approaches were tested, a binned χ^2-fit and an unbinned maximum likelihood fit, which are both appropriate fit methods for the analyzed data. The advantages and disadvantages of both methods are discussed in the following, starting with the binned χ^2-fit using event yield asymmetries.

6.2.1 Method

The polarized cross sections $\frac{d\sigma}{d\Omega}^{\parallel}_{\text{pol}}$ and $\frac{d\sigma}{d\Omega}^{\perp}_{\text{pol}}$ are given according to Equation (6.1) for the two different settings of $\alpha = \pm 45°$ by

$$\frac{d\sigma}{d\Omega}^{\parallel}_{\text{pol}} = \frac{d\sigma}{d\Omega}_0 \left[1 - p_\gamma^{\parallel} \Sigma \cos\left(2\left(\alpha^{\parallel} - \phi\right)\right)\right], \tag{6.3}$$

$$\begin{aligned}
\frac{d\sigma}{d\Omega}^{\perp}_{\text{pol}} &= \frac{d\sigma}{d\Omega}_0 \left[1 - p_\gamma^{\perp} \Sigma \cos\left(2\left(\alpha^{\perp} - \phi\right)\right)\right] && (6.4)\\
&= \frac{d\sigma}{d\Omega}_0 \left[1 - p_\gamma^{\perp} \Sigma \cos\left(2\left(\alpha^{\parallel} - \phi\right) + 180°\right)\right] && (6.5)\\
&= \frac{d\sigma}{d\Omega}_0 \left[1 + p_\gamma^{\perp} \Sigma \cos\left(2\left(\alpha^{\parallel} - \phi\right)\right)\right], && (6.6)
\end{aligned}$$

with the azimuthal angle of the polarization vector $\alpha^{\parallel} = -45°$, $\alpha^{\perp} = \alpha^{\parallel} + 90° = 45°$, and $p_\gamma^{\parallel}$ and $p_\gamma^{\perp}$ the polarization degrees of the according settings, which do not necessarily have to be the same. In order to take this into account when calculating the asymmetry of the polarized

cross sections, the average polarization degree $\bar{p}_\gamma = 1/2(p_\gamma^\perp + p_\gamma^\parallel)$ is used for the difference of the polarized cross sections (see Equation (6.7)).

$$\frac{d\sigma}{d\Omega_{\text{pol}}}^{\perp} - \frac{d\sigma}{d\Omega_{\text{pol}}}^{\parallel} = \frac{d\sigma}{d\Omega_0}\left(p_\gamma^\perp + p_\gamma^\parallel\right)\Sigma\cos\left(2\left(\alpha^\parallel - \phi\right)\right) \tag{6.7}$$

$$= \frac{d\sigma}{d\Omega_0} 2\bar{p}_\gamma\Sigma\cos\left(2\left(\alpha^\parallel - \phi\right)\right), \tag{6.8}$$

In addition, the sum of both polarized cross sections has to be weighted with the factors a and b in the following way:

$$a\cdot\frac{d\sigma}{d\Omega_{\text{pol}}}^{\perp} + b\cdot\frac{d\sigma}{d\Omega_{\text{pol}}}^{\parallel} = \frac{d\sigma}{d\Omega_0}\left[a + b + \left(a\cdot p_\gamma^\perp - b\cdot p_\gamma^\parallel\right)\Sigma\cos\left(2\left(\alpha^\parallel - \phi\right)\right)\right] \tag{6.9}$$

$$\stackrel{!}{=} 2\frac{d\sigma}{d\Omega_0}. \tag{6.10}$$

Here, it holds for the factors a and b:

$$a + b \stackrel{!}{=} 2, \qquad a\cdot p_\gamma^\perp - b\cdot p_\gamma^\parallel \stackrel{!}{=} 0 \qquad \Leftrightarrow \quad a = \frac{2p_\gamma^\parallel}{p_\gamma^\perp + p_\gamma^\parallel}, \quad b = \frac{2p_\gamma^\perp}{p_\gamma^\perp + p_\gamma^\parallel}. \tag{6.11}$$

The beam asymmetry is then accessible through the asymmetry $A(\phi)$

$$A(\phi) := \frac{1}{\bar{p}_\gamma}\cdot\frac{\frac{d\sigma}{d\Omega_{\text{pol}}}^{\perp} - \frac{d\sigma}{d\Omega_{\text{pol}}}^{\parallel}}{a\frac{d\sigma}{d\Omega_{\text{pol}}}^{\perp} + b\frac{d\sigma}{d\Omega_{\text{pol}}}^{\parallel}} = \Sigma\cos\left(2\left(\alpha^\parallel - \phi\right)\right), \tag{6.12}$$

whereby Equation (6.12) can be simplified further by exchanging the cross sections with the normalized event yields $N^\parallel$ and $N^\perp$, since the detection efficiencies are the same for the nominator and denominator. Therefore, it holds

$$A(\phi) = \frac{1}{\bar{p}_\gamma}\cdot\frac{N^\perp - N^\parallel}{aN^\perp + bN^\parallel} = \frac{N^\perp - N^\parallel}{p_\gamma^\parallel N^\perp + p_\gamma^\perp N^\parallel} = \Sigma\cos\left(2\left(\alpha^\parallel - \phi\right)\right). \tag{6.13}$$

The event yields are normalized by integrating over the entire azimuthal angular range for each E_γ and $\cos\theta$ bin. The statistical error bars of $A(\phi)$ were calculated according to Gaussian error propagation.

6.2.2 Application of method to toy Monte Carlo samples

To test the correct working principle of the method and test the quality of the fits, it is prudent to first apply the event yield method on a sample of generated toy Monte Carlo events. For this purpose, different samples of toy MC were generated as listed in Table 6.1. Toy MC sample 1 represents the ideal case, that the same statistics and polarization degree values for both α settings are present and assumes an evenly distributed detection efficiency over the entire azimuthal angular range and no background contributions. The samples 2 and 3 consider cases where the polarization degree and the statistics is different for both α settings. In addition,

toy MC sample 4 simulates a not perfect detection efficiency which, in the worst case, leads to a strong inefficiency at a certain angular range. Here, a detection efficiency of 0 was chosen for $0° < \phi \leq 15°$[4]. Moreover, background contributions from other reaction channels were taken into consideration for the worst case scenario of the background beam asymmetry Σ^{bg} to be at ± 1. The different MC samples allow to study what influence different statistics, different polarization degree values, detection inefficiencies and background contributions from other reaction channels may have on the obtained results.

sample No.	events/bin for $\alpha^{\perp}$	events/bin for $\alpha^{\parallel}$	$p_{\gamma}^{\perp}$	$p_{\gamma}^{\parallel}$	det. inefficiency	background
1	5000	5000	30 %	30 %	-	-
2	5000	5000	30 %	25 %	-	-
3	5000	4000	30 %	25 %	-	-
4	5000	4000	30 %	25 %	yes	-
5	5000	4000	30 %	25 %	yes	yes ($\Sigma^{bg} = +1$, 10%)
6	5000	4000	30 %	25 %	yes	yes ($\Sigma^{bg} = -1$, 10%)

Table 6.1: Six different toy MC samples were generated. This table gives the number of generated events per bin for each α setting, the chosen polarization degree values and whether or not detection inefficiencies and 10% background contribution with different Σ^{bg} values are taken into account or not. For each sample, the experiment was carried out 10000 times.

The generated events were distributed according to

$$N^{\perp} = N_0 \left[1 - p_{\gamma}^{\perp} \Sigma \cos\left(2\left(\alpha^{\perp} - \phi\right)\right)\right], \tag{6.14}$$

$$N^{\parallel} = N_0 \left[1 - p_{\gamma}^{\parallel} \Sigma \cos\left(2\left(\alpha^{\parallel} - \phi\right)\right)\right], \tag{6.15}$$

using $\Sigma = 0.5$ and reasonable values for $p_{\gamma}^{\parallel}, p_{\gamma}^{\perp}, N^{\parallel}$ and $N^{\perp}$ as given in Table 6.1 to mimic the situation in real data as accurately as possible. Two example ϕ-distributions for $N^{\parallel}$ and $N^{\perp}$ are depicted in Figure 6.13. Here, the chosen azimuthal angle of the polarization plane α is indicated by the blue line.

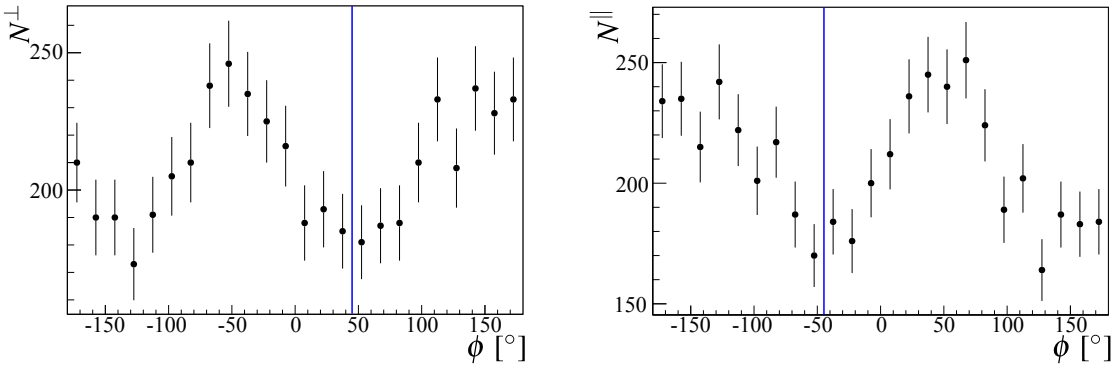

Figure 6.12: Example generated toy MC ϕ-distributions are plotted for the polarization plane being at +45° (left) and at −45° (right), using Equations (6.14) and (6.15). The polarization plane is indicated with a blue line. Both ϕ-distributions are from MC sample 1 (see Table 6.1).

[4] Larger detection inefficiencies can be ruled out for the data and were therefore not considered here.

Utilizing Equation (6.13), the asymmetry $A(\phi)$ was calculated for the generated toy MC events. A binned χ^2- fit was used to obtain the beam asymmetry Σ. The chosen number of bins for $A(\phi)$ ensures that all bins have more entries than 5, so that a Gaussian error can be assumed and a χ^2-fit can be performed. The fit function $f(\phi)$ is given by

$$f(\phi) = p_0 \cdot \cos\left(2\left(\alpha^{\parallel} - \phi\right)\right) + p_1, \tag{6.16}$$

with the fit parameter p_0 giving the beam asymmetry value Σ, p_1 describing an offset value, which is needed if strong detection inefficiencies are present in the data. After checking if parameter p_1 is consistent with 0, the parameter p_1 can be fixed at 0 and the fit repeated. In addition, $\alpha^{\parallel}$ was fixed at $-45°$ for all fits. Figure 6.13 shows the asymmetry $A(\phi)$ together with the fit results for a few toy MC bins. In total 10000 toy MC bins were generated and fitted with a fit function as given in Equation 6.16 in order to evaluate the fit results with statistical significance.

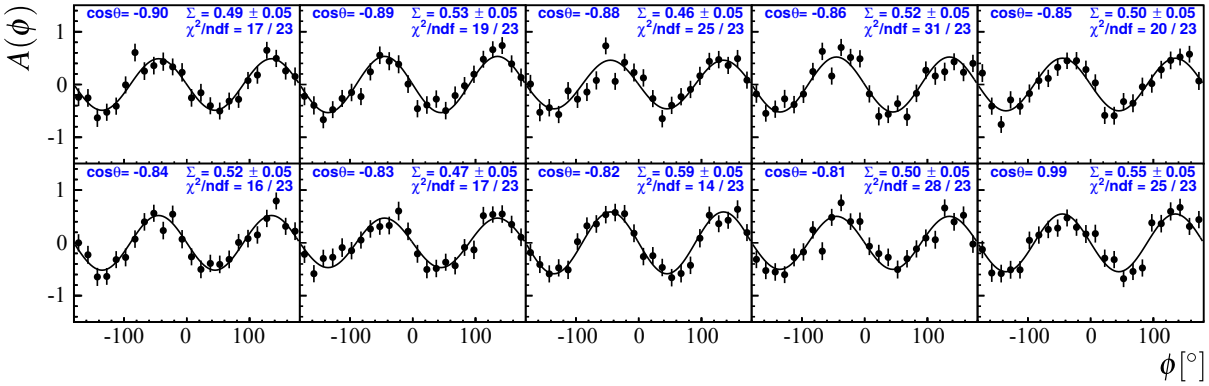

Figure 6.13: The asymmetry $A(\phi)$ (see Equation (6.13)) is plotted for generated toy MC sample 1 (black points) as a function of the azimuthal angle ϕ for several bins. Each distribution is fitted using Equation (6.16) (black line). The fit results are given on the top, whereby p_1 is consistent with 0. All fluctuations are of statistical nature.

The fit quality for the fit parameter $\Sigma_{\text{estimated}}$ can be evaluated by looking at the normalized residuals p:

$$p := \frac{\Sigma_{\text{estimated}} - \Sigma_{\text{true}}}{\sigma_{\Sigma_{\text{estimated}}}}, \tag{6.17}$$

where $\Sigma_{\text{estimated}}$ and $\sigma_{\Sigma_{\text{estimated}}}$ are the fit parameter p_0's value and statistical error as given by the fit. Σ_{true} is 0.5 for toy MC samples 1-4, while for toy MC sample 5 and 6 it is $\Sigma_{\text{true}}^{\text{MC5}} = 0.5 \cdot 0.9 + 1 \cdot 0.1 = 0.55$ and $\Sigma_{\text{true}}^{\text{MC6}} = 0.5 \cdot 0.9 - 1 \cdot 0.1 = 0.35$ due to the 10% assumed background contamination. The fit is unbiased and the statistical errors are correctly estimated if the mean of the normalized residuals is equal to 0 and the width corresponds to 1 [Bar89]. Figure 6.14 shows the normalized residuals for all six toy MC samples. All samples are in agreement with a normal distribution with width 1 within 1σ or 2σ error, indicating a correct estimation of the error bars. As a rule of thumb, the bias is negligible compared to the statistical uncertainty if the mean/$\sigma < 0.25$ [ET94], which is the case for all six toy MC samples.

The determined beam asymmetry values are depicted in Figure 6.15. The results of toy MC

1-4 agree well with the generated value of $\Sigma_{\text{true}} = 0.5$. The statistical errors of the beam asymmetry, which are given by the width σ of the Gaussian, are increased with decreased polarization degree values, and, needless to say, with less statistics for one of the α settings. As expected the detection inefficiencies cancel out when calculating the asymmetry $A(\phi)$ and have no influence on the results, except for causing a slightly larger statistical error. Having background contributions leads to a systematic shift from the true signal value. The shift is largest when the background asymmetry has the opposite sign of the signal beam asymmetry. This needs to be considered for the systematic error (see Section 6.5).

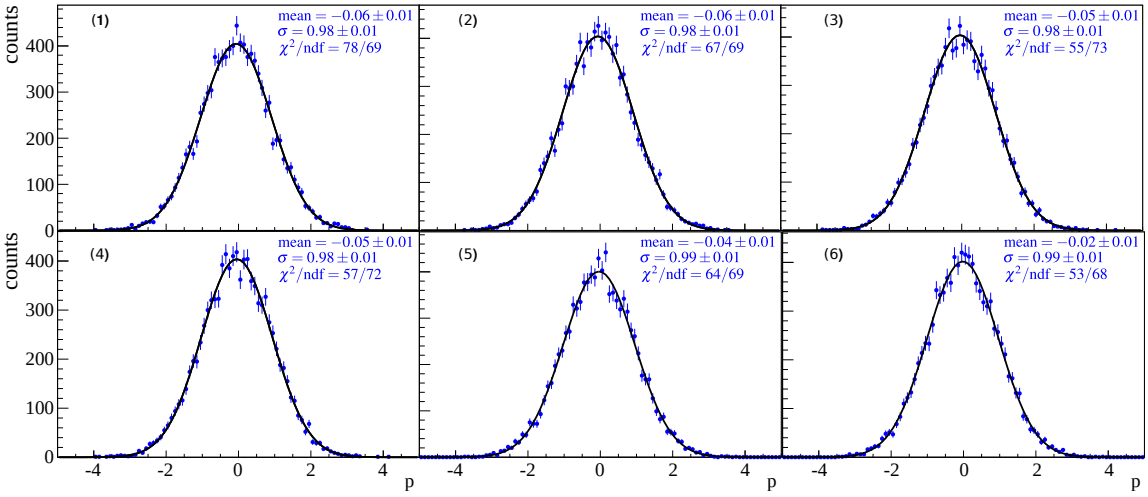

Figure 6.14: The normalized residuals are shown for toy MC samples 1-6 (see Table 6.1) when applying the event yield method (blue points). Gaussian fits were performed to the data (black line) with the results of the fits are given on the right.

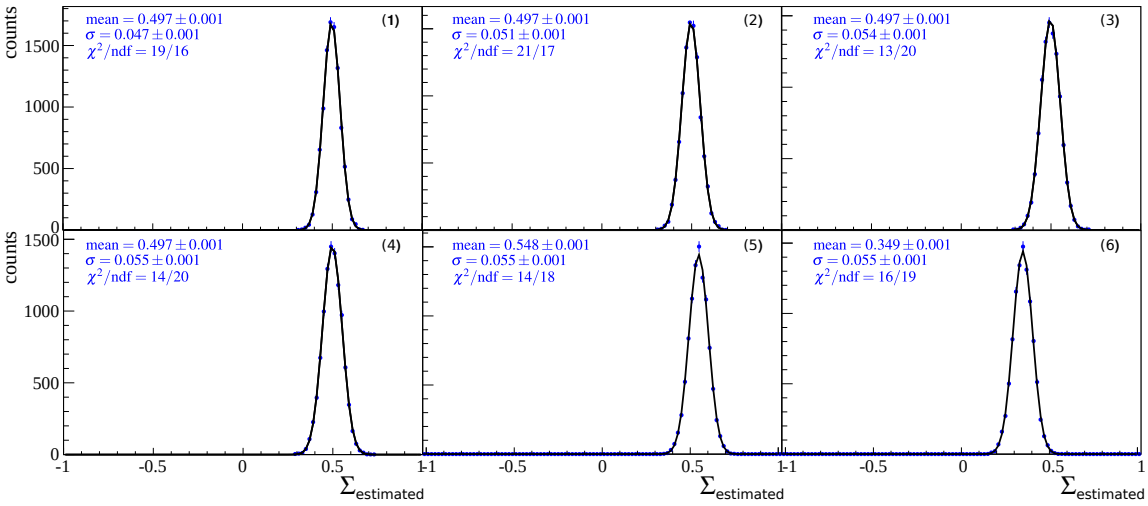

Figure 6.15: Fit values for toy MC sample 1-6 (see Table 6.1) when applying the event yield method (blue points). Gaussian fits were performed to the data (black line) with the results of the fits are given on the left.

A great advantage of the binned χ^2-fit method is the availability of a goodness of fit measure directly from the fit. Figure 6.16 shows the χ^2/ndf values for the fits performed on MC sample 3. On average the χ^2/ndf is 1.0, indicating a correct error estimation. Another parameter to check is the confidence level. As depicted in Figure 6.16 on the right the slope of the confidence level is consistent with 0 which also demonstrates a correct estimation of the statistical errors.

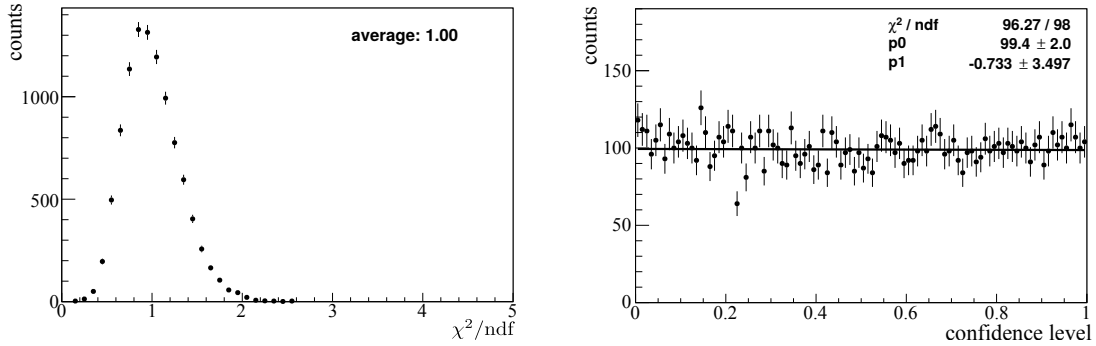

Figure 6.16: Left: χ^2/ndf values are plotted for all 10000 fits of toy MC sample 3. On average the χ^2/ndf value is 1.0. Right: The confidence level for all 10000 fits of toy MC sample 3. The distribution is flat as confirmed by a polynomial fit of first degree.

6.2.3 Application of method to data

Figure 6.17 shows the event yields $N^{\perp}$ and $N^{\parallel}$ as a function of the azimuthal angle ϕ for one $(E_\gamma, \cos\theta)$ bin of the $p\pi^0$ final state. The position of the polarization plane is indicated with the blue line.

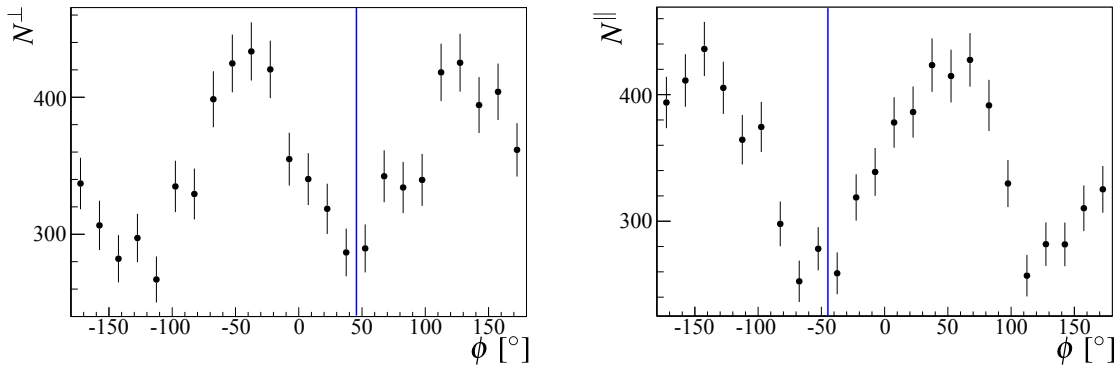

Figure 6.17: Example ϕ-distributions are plotted for the polarization plane being at +45° (left) and at −45° (right) for the $p\pi^0$ final state. The polarization plane is indicated with a blue line.

The choice of binning takes into account on the one hand that the binning is not too large that sensitivity to resonances with large orbital angular momentum L are lost (see Chapter 8) and on the other hand the binning is not too small, that the counts per bin is less than 5 and thus, a χ^2-fit can not be performed any more. As a compromise, a binning of (36 MeV in E_γ, 0.1 in $\cos\theta$, 15° in ϕ) was chosen for the $p\pi^0$ and a binning of (60 MeV in E_γ, 0.17 in $\cos\theta$, 30° in

ϕ) was selected for the $p\eta$ final state. Figure 6.18 shows the counts for each $(E_\gamma, \cos\theta, \phi)$ bin on the left for the $p\pi^0$ and on the right for the $p\eta$ final state. Every bin of the $p\pi^0$ final state and almost every bin of the $p\eta$ final state contains more than 5 counts[5]. Thus, the underlying Poisson statistics of the data can be approximated with a Gaussian distribution.

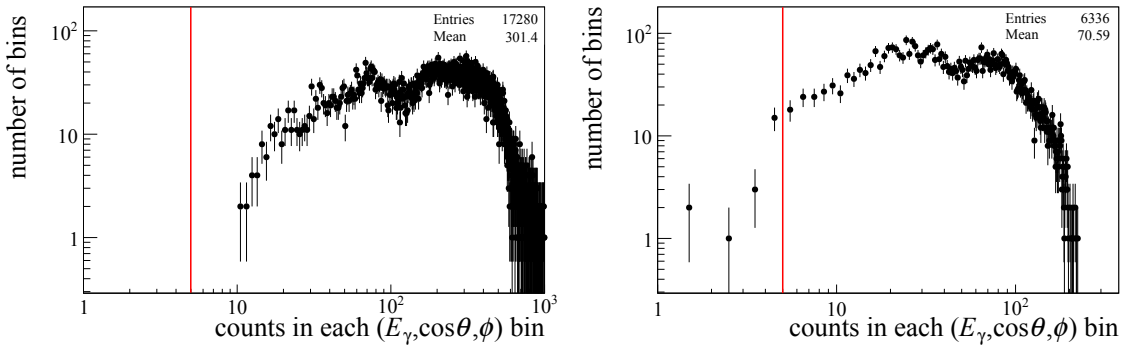

Figure 6.18: The number of counts for the chosen $(E_\gamma, \cos\theta, \phi)$ binning is depicted on the left for the $p\pi^0$ and on the right for the $p\eta$ final state. Almost all of the bins have more than 5 counts which is marked with the red line.

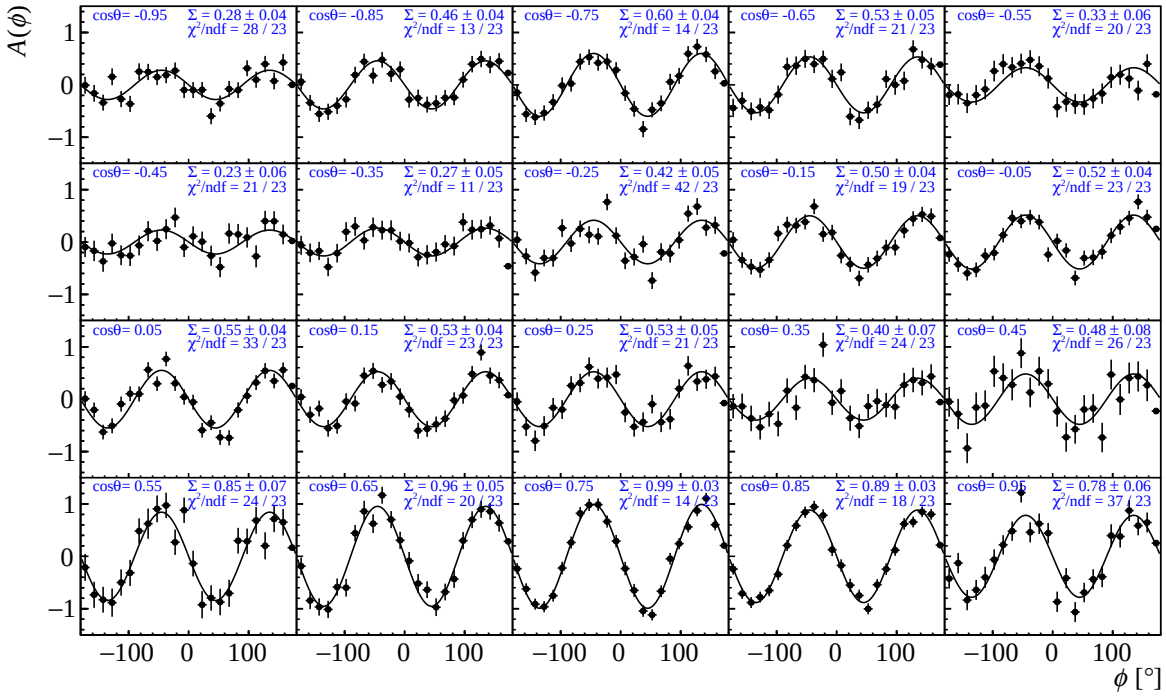

Figure 6.19: The asymmetry $A(\phi)$ (see Equation (6.13)) is plotted for the $p\pi^0$ final state (black points) as a function of the azimuthal angle ϕ for the energy bin 1455 MeV $\leq E_\gamma <$1491 MeV and all its $\cos\theta$ bins. Each distribution was fitted using Equation (6.16) (black line). The fit results are given on the top.

[5] For the bins, where this condition is not fulfilled, no beam asymmetry could be extracted.

Figure 6.19 and 6.20 show for one energy bin and for all its $\cos\theta$-bins the asymmetry $A(\phi)$ (see Equation (6.13)) distributions together with the fit results for the beam asymmetry for the $p\pi^0$ and $p\eta$ final states, respectively. A clear $\cos(2(\alpha^{\parallel} - \phi))$ modulation is visible with the height being directly correlated to the beam asymmetry Σ value.

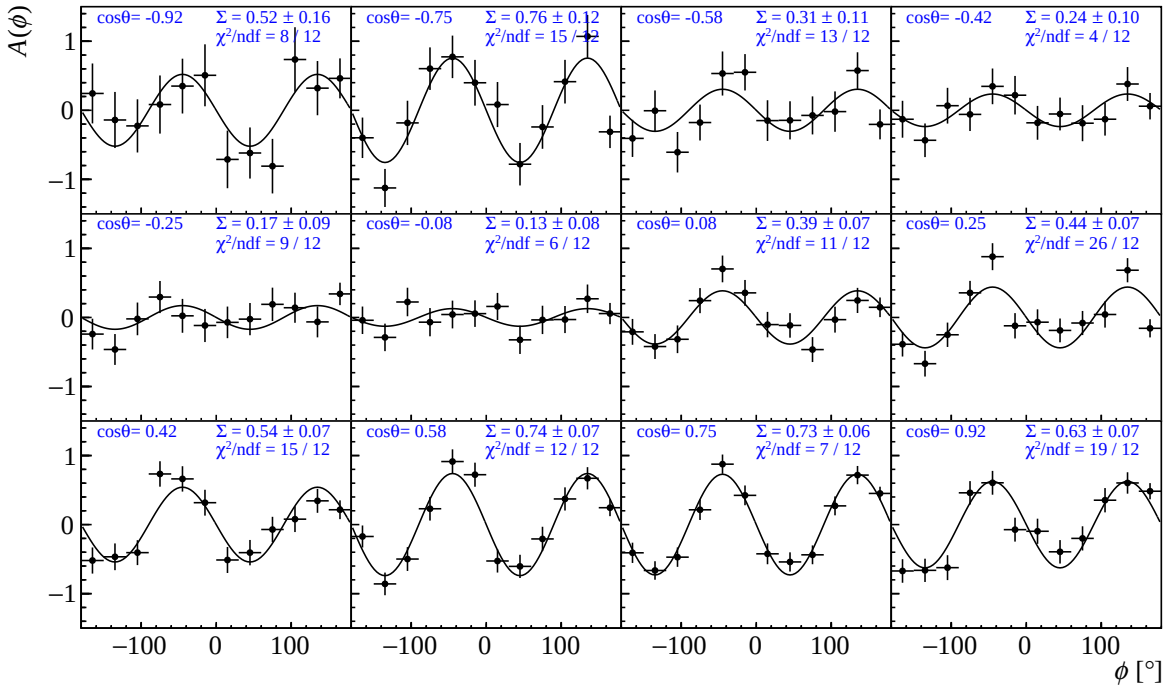

Figure 6.20: The asymmetry $A(\phi)$ (see Equation (6.13)) is plotted for the $p\eta$ final state (black points) as a function of the azimuthal angle ϕ for the energy bin $1610\,\text{MeV} \leq E_\gamma < 1670\,\text{MeV}$ and all its $\cos\theta$ bins. Each distribution was fitted using Equation (6.16) (black line). The fit results are given on the top.

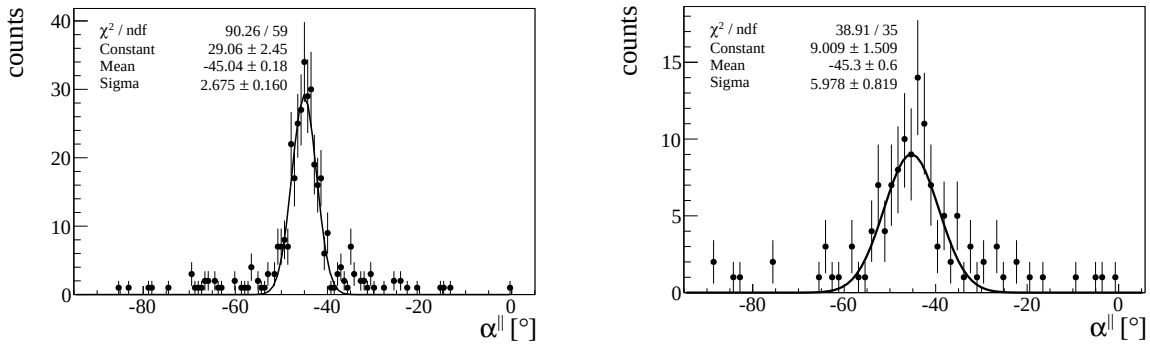

Figure 6.21: The fit results for the parameter $\alpha^{\parallel}$ is depicted on the left for the $p\pi^0$ and on the right for the $p\eta$ final state fits. A Gaussian fit, which is drawn as a black line, confirms that $\alpha^{\parallel}$ is consistent with $-45°$.

Each $(E_\gamma, \cos\theta)$ bin was fitted using a binned χ^2-fit and utilizing the fit function as given in

Equation (6.16). Thereby, $\alpha^{\parallel}$ was first left as an open fit parameter. The fit results for $\alpha^{\parallel}$, as obtained during the initial fit, are given in Figure 6.21 on the left for the $p\pi^0$ and on the right for the $p\eta$ final state. Within the error bars, $\alpha^{\parallel}$ is consistent with $-45°$ for both final states and could, therefore, be fixed for later fits. The same procedure was repeated for the offset parameter p_1. The parameter is consistent with the expected value of 0 for both final states, as shown in Figure 6.22.

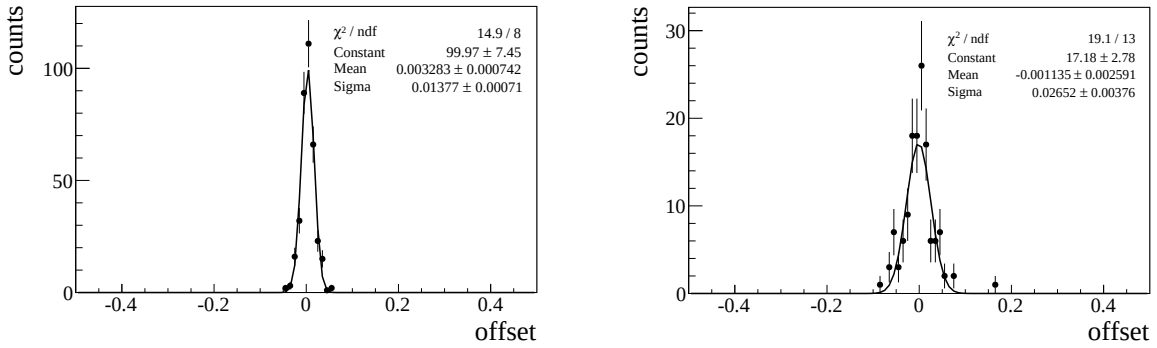

Figure 6.22: The offset parameter is depicted on the left for the $p\pi^0$ and on the right for the $p\eta$ final state fits. A Gaussian fit, which is drawn as a black line, confirms that the offset parameter is consistent with 0.

Finally, the beam asymmetry values were determined through fits with fixed values for $\alpha^{\parallel} = -45°$ and $p_1 = 0$ according to Equation (6.16). The obtained results for the beam asymmetry Σ using the event yield asymmetry method are depicted for one energy bin of the $p\pi^0$ and one energy bin of the $p\eta$ final state in Figure 6.23. The error bars consist of only statistical errors as obtained from the binned χ^2-fit.

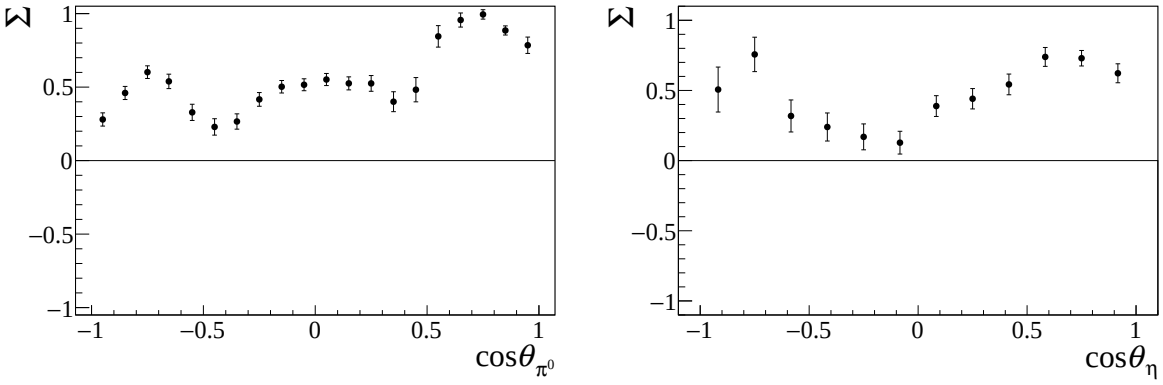

Figure 6.23: The results for the beam asymmetry Σ obtained with the event yield method are shown for $1455\,\text{MeV} \leq E_\gamma < 1491\,\text{MeV}$ of the $p\pi^0$ (left) and for $1610\,\text{MeV} \leq E_\gamma < 1670\,\text{MeV}$ of the $p\eta$ final state (right). The error bars represent statistical errors only.

To gain an estimation of the goodness of the fit the χ^2/ndf and the confidence level distributions are shown in Figure 6.24 for the $p\pi^0$ and in Figure 6.25 for the $p\eta$ final state. On average, the χ^2/ndf values are close to 1 for both final states, whereby the average value of the $p\pi^0$ final

state is closest to 1. Probably, the higher amount of low statistical bins existing for the $p\eta$ final state is responsible for a slightly higher average value of 1.08. The slope of the confidence levels are consistent with 0 within 1.5σ error for the $p\pi^0$ and within 1σ error for the $p\eta$ final state. It is noteworthy, that the polynomial fits were performed with a binned maximum likelihood fit due to the low number of events per bin. All in all, the χ^2/ndf values and confidence level demonstrate a successful extraction of the beam asymmetry values and its statistical error bars using the event yield method.

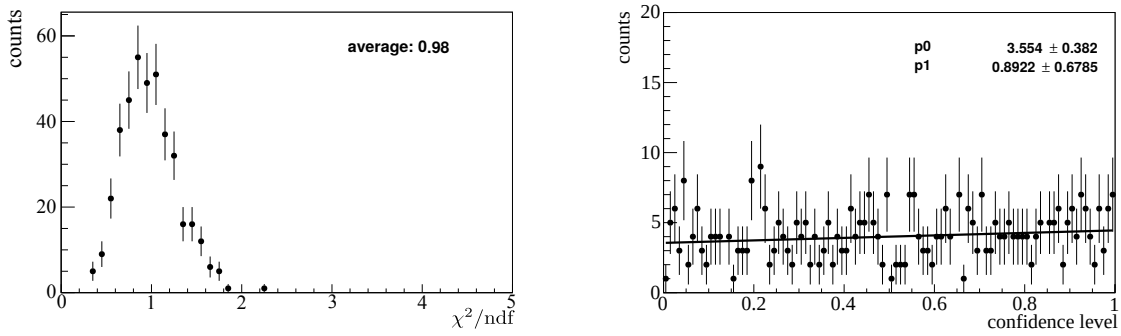

Figure 6.24: Left: The χ^2/ndf values are plotted for all performed fits of the $p\pi^0$ final state. On average the χ^2/ndf value is 0.98. Right: The confidence level for $p\pi^0$ final state. The distribution is flat as confirmed by a polynomial fit of first degree within 1.5σ error. A binned maximum likelihood fit was used.

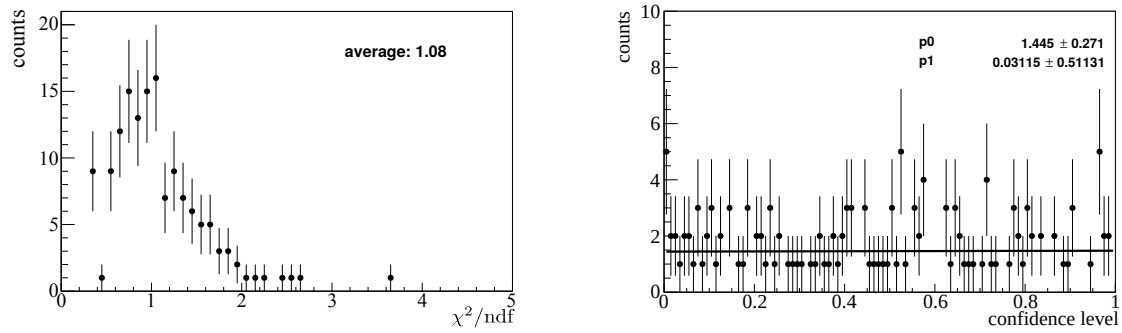

Figure 6.25: Left: The χ^2/ndf values are plotted for all performed fits of the $p\eta$ final state. On average the χ^2/ndf value is 1.08. Right: The confidence level distribution for $p\eta$ final state. The distribution is flat as confirmed by a polynomial fit of first degree within 1σ error. A binned maximum likelihood fit was used.

6.3 Determination of Σ using an unbinned maximum likelihood fit

As already mentioned, it is possible to estimate the beam asymmetry values utilizing an event based maximum likelihood fit. This has two main advantages over the χ^2-fit. Firstly, there is no need to bin the data in ϕ, and therefore no information is lost. Secondly, the statistical errors are calculated exact according to a Poisson distribution which is the underlying distribution of the data. The latter is especially important for low statistic-data (e.g. data of the $p\eta$ final state), as no approximation to a Gaussian distribution is necessary. However, no estimation of the goodness of the fit is available. Therefore, a study with toy MC is indispensable for this method.

6.3.1 Method

The probability density function (pdf) $p^{||/\perp}(\phi, \Sigma)$ of a measured event in a certain $(E_\gamma, \cos\theta)$ bin is given by

$$p^{||/\perp}(\phi, \Sigma) = \left[1 \mp p_\gamma^{||/\perp} \Sigma \cos\left(2(\alpha^{||} - \phi)\right)\right]. \tag{6.18}$$

A sign change occurs depending on the α setting $||$ or $\perp$ of the event.
The pdf, as formulated in Equation (6.18), is incomplete since it does not consider the detector acceptance. Unlike in the case of the event yield asymmetries, the detector acceptance does not cancel out. To parametrize the detector acceptance $\epsilon(\phi)$, a fourier series of the following form [Har17]

$$\epsilon(\phi) = \sum_{k=0}^{4} a_k \sin(k\phi) + b_k \cos(k\phi) \tag{6.19}$$

was used, since any occurring form for the detector acceptance function can be described by it. Even though the series is truncated at 4, the detector acceptance can be accurately described as demonstrated in reference [Har17]. This limits the number of fit parameters to eight detector acceptance coefficients a_k and b_k.
Additionally, the pdf needs to be normalized for an unbinned fit, which is achieved by integrating over the entire azimuthal angular range. The complete normalized pdf $\tilde{p}^{||/\perp}(\phi, \Sigma)$ is given by

$$\tilde{p}^{||/\perp}(\phi, \Sigma) = \frac{p^{||/\perp}(\phi, \Sigma) \cdot \epsilon(\phi)}{\frac{1}{2\pi}\int_0^{2\pi} p^{||/\perp}(\phi, \Sigma) \cdot \epsilon(\phi) d\phi} \tag{6.20}$$

$$= \frac{\left(1 \mp p_\gamma^{||/\perp} \Sigma \cos\left(2(\alpha^{||} - \phi)\right)\right) \cdot \left(\sum_{k=0}^{4} a_k \sin(k\phi) + b_k \cos(k\phi)\right)}{1 \pm \frac{1}{2} a_2 p_\gamma^{||/\perp} \Sigma}, \tag{6.21}$$

where the normalization factor is given by the denominator which has a different sign for the corresponding α setting. Due to the different sign, the correlation of the beam asymmetry Σ and the coefficient a_2 can be removed and both parameters can be determined independently. For convenience, the polarization values of $p_\gamma^{||}$ are multiplied with (-1), so that one general pdf can be written for all events as

$$\tilde{p}(\phi, \Sigma) = \frac{(1 + p_\gamma \Sigma \cos(2(\alpha - \phi))) \cdot \left(\sum_{k=0}^{4} a_k \sin(k\phi) + b_k \cos(k\phi) \right)}{1 - \frac{1}{2} a_2 p_\gamma \Sigma}, \tag{6.22}$$

with α being fixed at $-45°$ (see Figure 6.21).

Since the data is not binned, a sideband subtraction of random time background, as described in 5.2.1, is not possible. Instead, both the prompt peak and sideband background events have to be fitted simultaneously. The prompt peak events consist of signal events and to a small fraction of random time background events that are located underneath the prompt peak. The fraction of signal events in the selected prompt peak range f_{sig} is described by

$$f_{\text{sig}} = \frac{N_{\text{prompt}} - \sum_{i=1}^{7} s_i N_{i,\text{sideband}}}{N_{\text{prompt}}}, \tag{6.23}$$

where N_{prompt} and $N_{i,\text{sideband}}$ are the total number of prompt peak and sideband events within the respective chosen time cut windows. The factors s_i give the ratio of the chosen prompt peak time cut window to sideband time cut window[6] (see Table 5.1). Prompt peak events are weighted by 1, while the sideband events by s_i.
This leads to the following prompt peak p_{prompt} and sideband p_{sideband} pdfs:

$$p_{\text{prompt}} = f_{\text{sig}} \cdot \tilde{p}(\phi, p_\gamma, \Sigma, a_1 \dots a_4, b_1 \dots b_4) + (1 - f_{\text{sig}}) \cdot \tilde{p}(\phi, p_\gamma, \Sigma^{\text{bg}}, a_1^{\text{bg}} \dots a_4^{\text{bg}}, b_1^{\text{bg}} \dots b_4^{\text{bg}}) \tag{6.24}$$

$$p_{\text{sideband}} = \tilde{p}(\phi, p_\gamma, \Sigma^{\text{bg}}, a_1^{\text{bg}} \dots a_4^{\text{bg}}, b_1^{\text{bg}} \dots b_4^{\text{bg}}). \tag{6.25}$$

The joint probability density function of all events is described by the likelihood function $\mathcal{L}$:

$$\mathcal{L} = \prod_{i=1}^{n} p_{\text{prompt}}(\phi_i, p_{i,\gamma}, \Sigma, a_1 \dots a_4, b_1 \dots b_4) \prod_{j=1}^{m} p_{\text{sideband}}(\phi_j, p_{j,\gamma}, \Sigma^{\text{bg}}, a_1^{\text{bg}} \dots a_4^{\text{bg}}, b_1^{\text{bg}} \dots b_4^{\text{bg}}), \tag{6.26}$$

with n being the total number of prompt peak and m the total number of sideband events in a given $(E_\gamma, \cos\theta)$ bin. The beam asymmetry values and the detector acceptance coefficients of the signal and background are acquired by maximizing $\mathcal{L}$, or for computational convenience by minimizing $-\ln(\mathcal{L})$:

$$-\ln(\mathcal{L}) = \sum_{i=1}^{n} -\ln\left(p_{\text{prompt}}(\phi_i, p_{i,\gamma}, \Sigma, a_1 \dots a_4, b_1 \dots b_4)\right) + \tag{6.27}$$

$$\sum_{j=1}^{m} -\ln\left(p_{\text{sideband}}(\phi_j, p_{j,\gamma}, \Sigma^{\text{bg}}, a_1^{\text{bg}} \dots a_4^{\text{bg}}, b_1^{\text{bg}} \dots b_4^{\text{bg}})\right). \tag{6.28}$$

[6] Since the time cut is applied detector dependent, seven different cases exist, each with a different factor s_i and different amount of sideband events $N_{i,\text{sideband}}$.

The fit function is a non-linear function containing eighteen fit parameters, since it holds $a_0 = 0$ and $b_0 = 1$. The unbinned fit was implemented in two different ways. On the one hand, the *ROOT* library offers the function *TTree::UnbinnedFit* for data filled in a *TTree* [ROO]. On the other hand, the *RooFit* library [VK03] is a useful tool for the formulation of pdfs and for applying an unbinned maximum likelihood fit to the data. Both possibilities were tested and both implementations gave the same results.
During the fitting procedure, *MINUIT* [JR75] carries out the minimizing procedure to finding the global minimum. There are three steps involved: first the *MIGRAD* minimization technique [Fle70] is utilized to obtain the minimum position. As a second step all second derivatives and the full error covariance matrix is calculated to estimate the fit parameter errors according to *HESSE*. Here, *HESSE* assumes a parabolic shape for the $\ln(\mathcal{L})$ function and gives symmetric errors. However, according to the central limit theorem only for large statistics ($n \to \infty$), the likelihood $\mathcal{L}$ becomes a Gaussian and the $\ln(\mathcal{L})$ function a parabola [Bar89; Bra99]. An equivalent definition of 1σ error of a Gaussian is for a parabola the points where it holds: $-\ln(\mathcal{L}_{\max}) \to -\ln(\mathcal{L}_{\max}) + 0.5$ [Bar89; Bra99]. If there are deviation from a parabolic shape, the errors become asymmetric. These asymmetric errors are obtained in a last step using the *MINOS* technique [JR75], if needed.

6.3.2 Application of method to toy Monte Carlo samples

To test the unbinned maximum likelihood fit method, different toy Monte Carlo samples were generated. While the effects of different statistics and different polarization degree values for the different α settings are already discussed in Section 6.2.2, the focus is put here on checking whether an unbiased fit and correct error estimation is obtained, when simultaneously fitting prompt peak and sideband background events. Additionally, it is investigated whether a correct description of the detector acceptance is achieved by the formulated likelihood function (see Equation (6.27)).

For this purpose, each of the thrown toy MC experiments consist of prompt peak and sideband events for each α setting. The total number of events for $N^{\perp}$ and $N^{\parallel}$ were chosen to match roughly the $p\eta$ final state statistics in the data. Since the data follows a Poisson distribution, the generated numbers follow a Poisson distribution as well. The ratio of signal events to total prompt peak events f_{sig} was chosen to be $f_{\text{sig}} = 0.95$ and the same seven ratios of prompt peak to sideband cut windows $s_1 \dots s_7$ were selected as in the data. Therefore, seven times signal events, background in prompt peak events and sideband events were generated. For the signal and background beam asymmetry, the values $\Sigma = 0.5$ and $\Sigma^{\text{bg}} = -0.5$ were utilized. Additionally, polarization degree values of $p_\gamma^{\perp} = 0.3$ and $p_\gamma^{\parallel} = 0.25$ were chosen. Moreover, two different arbitrary efficiency functions were used, one mimicking the occurrence of small detection inefficiencies (ϵ_1), and one of large detection inefficiencies (ϵ_2). Table 6.2 gives a full overview of the toy Monte Carlo characteristics.

chosen values	$\Sigma = 0.5$, $\Sigma^{\text{bg}} = -0.5$, $N^{\perp} = \text{Poisson}(1000)$, $N^{\parallel} = \text{Poisson}(800)$, $p_{\gamma}^{\perp} = 0.3$, $p_{\gamma}^{\parallel} = 0.25$, $f_{\text{sig}} = 0.95$, $s_1 = \frac{15}{210}$, $s_2 = \frac{8}{210}$, $s_3 = \frac{4}{210}$, $s_4 = \frac{10}{210}$, $s_5 = \frac{14}{210}$, $s_6 = \frac{6}{210}$, $s_7 = \frac{11}{210}$
calculated values	$N^{\perp/\parallel}_{\text{sig in prompt}} = N^{\perp/\parallel}/7 \cdot f_{\text{sig}}$ $N^{\perp/\parallel}_{\text{bg in prompt}} = N^{\perp/\parallel}/7 \cdot (1 - f_{\text{sig}})$ $N^{\perp/\parallel}_{i,\text{sideband}} = N^{\perp/\parallel}/7 \cdot (1 - f_{\text{sig}}) \cdot 1/s_i$
efficiency function	$\epsilon_1(\phi) = 1./10.5 \cdot (9.3 + 0.28 \cdot \cos(\phi) + 0.24 \cdot \sin(3\phi))$ $\epsilon_2(\phi) = 1./10.5 \cdot (6.3 + \sin(\phi) + 3 \cdot \cos(2\phi) + 0.3 \cdot \sin(3\phi) + 0.8 \cdot \cos(4\phi) + 0.4 \cdot \sin(4\phi))$

Table 6.2: Overview of the chosen parameter values for the two toy MC samples. The distribution of the total number of events of both α settings $N^{\perp/\parallel}$ to signal in prompt peak ($N^{\perp/\parallel}_{\text{sig in prompt}}$), background in the prompt peak ($N^{\perp/\parallel}_{\text{bg in prompt}}$) and sideband ($N^{\perp/\parallel}_{\text{sideband}}$) events are given in the second row. Toy MC sample 1 is generated using the efficiency function $\epsilon_1(\phi)$ and toy MC sample 2 using $\epsilon_2(\phi)$. The remaining parameter are the same for both samples.

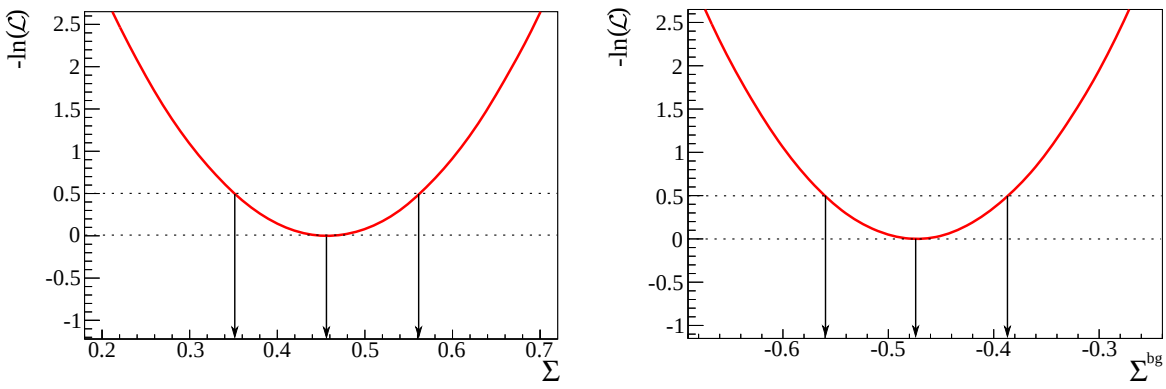

Figure 6.26: The $-\ln(\mathcal{L})$ function is shown for the signal events (left) and the sideband background events (right) for one toy MC experiment. It has the shape of a parabola. The error bars are given by the points where it holds: $-\ln(\mathcal{L}_{\text{max}}) \rightarrow -\ln(\mathcal{L}_{\text{max}}) + 0.5$ which are marked with the left and the right arrows. The found minimum using an unbinned maximum likelihood fit with *RooFit* agrees well with the generated values ($\Sigma_{\text{true}} = 0.5$ and $\Sigma^{\text{bg}} = -0.5$) within the respective error bars. Note: The minimum is shifted to 0 on the y-axis.

Figure 6.26 depicts for one toy MC experiment the obtained $-\ln(\mathcal{L})$ for the signal Σ and background beam asymmetry Σ^{bg} using Equation (6.27) and the *RooFit* library. In both cases exactly one minimum exists and the $-\ln(\mathcal{L})$ function has the form of a parabola. The error bars are given by the two points according to $-\ln(\mathcal{L}_{\text{max}}) \rightarrow -\ln(\mathcal{L}_{\text{max}}) + 0.5$. The crossing points are marked by two arrows. The obtained results are well in agreement with the generated

values of $\Sigma = 0.5$ and $\Sigma^{\mathrm{bg}} = -0.5$ within their error bars.

In total 10000 toy MC experiments for each sample were fitted, utilizing the unbinned maximum likelihood method. The resulting normalized residuals for the signal and background beam asymmetry are shown in Figure 6.27. All normalized residuals are consistent with a normal distribution as confirmed by Gaussian fits. Thus, the unbinned maximum likelihood fit is unbiased and gives a correct error estimation for the fit parameters. The fit values for Σ and Σ^{bg} are plotted in Figure 6.28. They are distributed around the true generated values of $\Sigma = 0.5$ and $\Sigma^{\mathrm{bg}} = -0.5$.

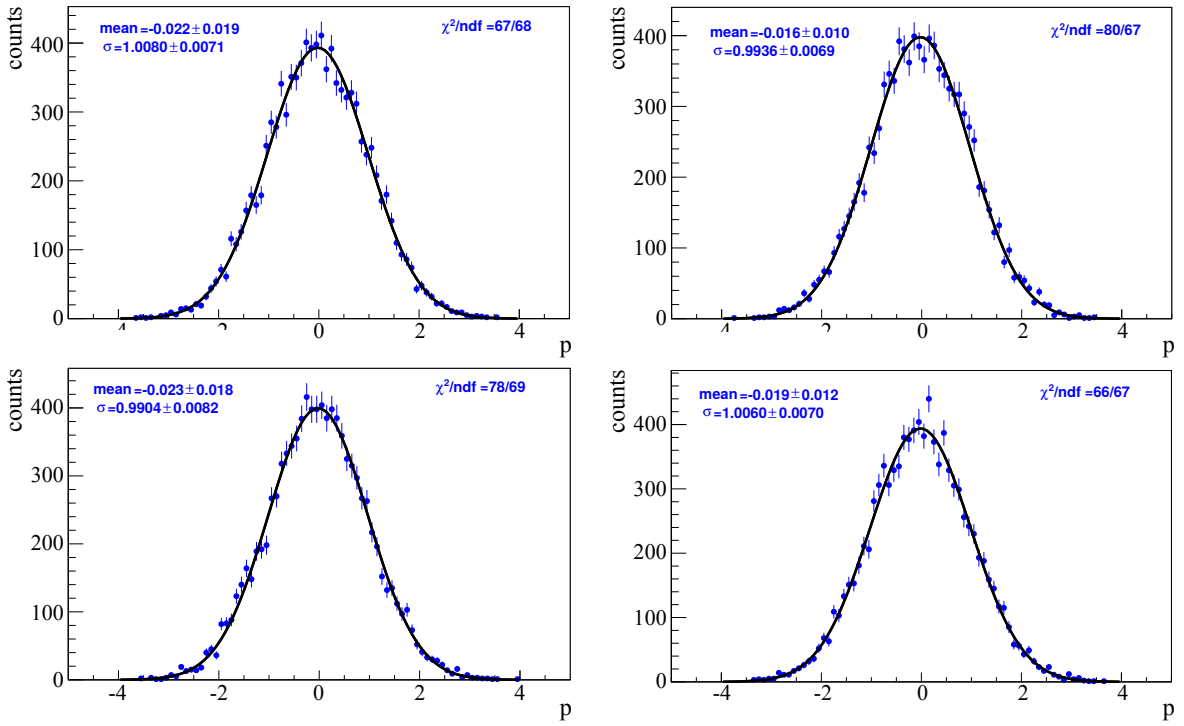

Figure 6.27: Normalized residuals of 10000 toy MC experiments are shown for sample 1 (upper row) and for sample 2 (lower row) for the signal beam asymmetry (left column) and for the sideband background beam asymmetry (right column). All four distributions are in agreement with a normal distribution.

To compare the found detection efficiency function by the unbinned maximum likelihood fit with the toy MC data, the sum of $N^{\perp}$ and $N^{\parallel}$ is plotted using 24 ϕ-bins (see Figure 6.29). In case of a detection efficiency of 1, a flat distribution is expected for the sum. However, if detection inefficiencies exist, it will be visible in the sum distribution. Figure 6.29 shows two examples with small detection inefficiencies (left using ϵ_1) and large detection inefficiencies (right using ϵ_2). In both cases, the unbinned maximum likelihood fit describes the sum distribution very well (blue curve). Thus, an accurate description of the detection efficiency is ensured by the likelihood function as given in Equation (6.27). Even when large detection inefficiencies exist the unbinned maximum likelihood method succeeds to estimate Σ and gives a correct error estimation. The extreme case of a detector acceptance hole being present ($\epsilon(\phi) = 0$), is accurately described by the formulated likelihood as demonstrated in reference [Har17].

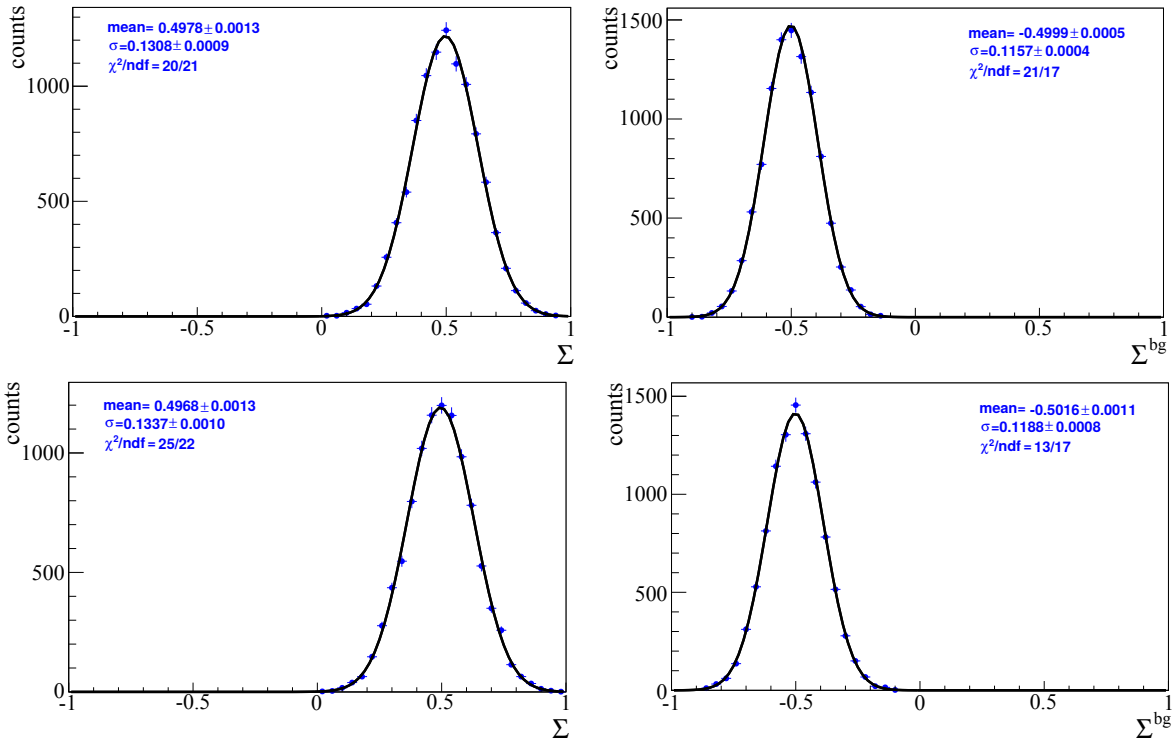

Figure 6.28: The obtained fit values of Σ and Σ^{bg} using an unbinned maximum likelihood fit for toy MC sample 1 (upper row) and sample 2 (lower row). The fit values are distributed around the generated values of $\Sigma_{\mathrm{true}} = 0.5$ for the signal events (left) and of $\Sigma^{\mathrm{bg}}_{\mathrm{true}} = -0.5$ for the sideband background events.

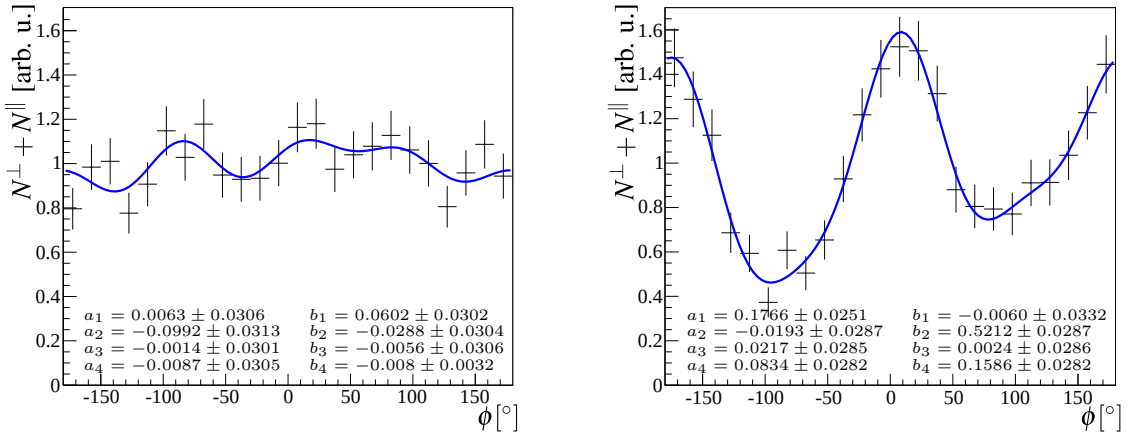

Figure 6.29: The sum of $N^{\perp}$ and $N^{\parallel}$ is plotted together with the efficiency function (blue line) as obtained from an unbinned maximum likelihood fit for two different toy MC samples. The one on the left describes small detection inefficiencies and the one on the right large detection inefficiencies. In both cases the unbinned maximum likelihood fit succeeds in describing accurately the sum distributions.

6.3.3 Application of method to data

After testing the unbinned maximum likelihood fit method on toy MC data, the method is applied to data as well, using the negative log likelihood function as given in Equation (6.27). Figure 6.30 shows as an example two likelihood functions as obtained from the fit. The plot on the left shows the projection of the likelihood function for the fit parameter Σ for the $p\pi^0$ final state and for the bin ($1455\,\text{MeV} \leq E_\gamma < 1491\,\text{MeV}$, $\cos\theta = -0.75$) and the plot on the right for the $p\eta$ final state and for the bin ($1610\,\text{MeV} \leq E_\gamma < 1670\,\text{MeV}$, $\cos\theta = -0.58$). In both cases the likelihood function has a parabolic curve with exactly one minimum that marks the estimated value of Σ. The statistical errors are again obtained from the crossing points of the likelihood function at $-\ln(\mathcal{L}_{\max}) \rightarrow -\ln(\mathcal{L}_{\max}) + 0.5$. Since the asymmetric *MINOS* errors are almost exactly the same and the shape of the likelihood function is a parabolic for all fits, the symmetric *HESSE* errors are given for the statistical error bars.

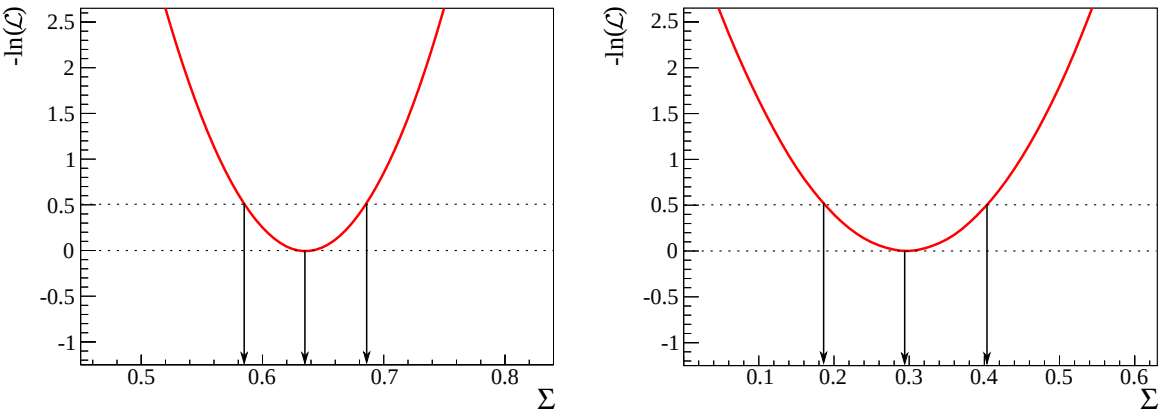

Figure 6.30: The projection of the $-\ln(\mathcal{L})$ function for Σ is shown for one bin ($1455\,\text{MeV} \leq E_\gamma < 1491\,\text{MeV}$, $\cos\theta = -0.75$) of the $p\pi^0$ final state on the left and for one bin ($1610\,\text{MeV} \leq E_\gamma < 1670\,\text{MeV}$, $\cos\theta = -0.58$) of the $p\eta$ final state on the right. The error bars are given by the points where it holds: $-\ln(\mathcal{L}_{\max}) \rightarrow -\ln(\mathcal{L}_{\max}) + 0.5$ which are marked with the left and the right arrows. Note: The minimum is shifted to 0 on the y-axis.

The comparison of the sum distribution ($N^{\perp} + N^{\parallel}$) and the obtained efficiency function (blue line) is plotted in Figure 6.31. An example bin ($1455\,\text{MeV} \leq E_\gamma < 1491\,\text{MeV}$, $\cos\theta = -0.75$) is shown for the $p\pi^0$ final state on the left and one bin ($1610\,\text{MeV} \leq E_\gamma < 1670\,\text{MeV}$, $\cos\theta = -0.58$) for the $p\eta$ final state on the right. The unbinned fit succeeds in both cases to describe the detection efficiencies. Only small detection inefficiencies exist in the data which are even smaller than the simulated inefficiencies of ϵ_1 (see Figure 6.29). This is also indicated by the detection efficiency fit parameter values which are shown in Figure 6.32 for both $p\pi^0$ (black) and $p\eta$ final states (blue). The mean of all parameters is close to zero.

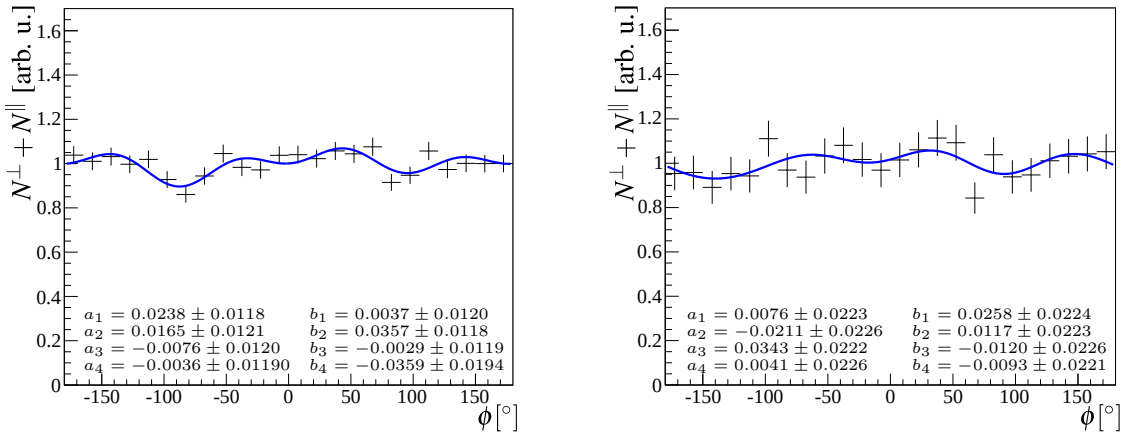

Figure 6.31: The sum of $N^{\perp}$ and $N^{\parallel}$ is plotted together with the efficiency function (blue line) as obtained from an unbinned maximum likelihood fit for one bin (1455 MeV $\leq E_{\gamma} <$ 1491 MeV, $\cos\theta = -0.75$) of the $p\pi^0$ final state on the left and for one bin (1610 MeV $\leq E_{\gamma} <$ 1670 MeV, $\cos\theta = -0.58$) of the $p\eta$ final state.

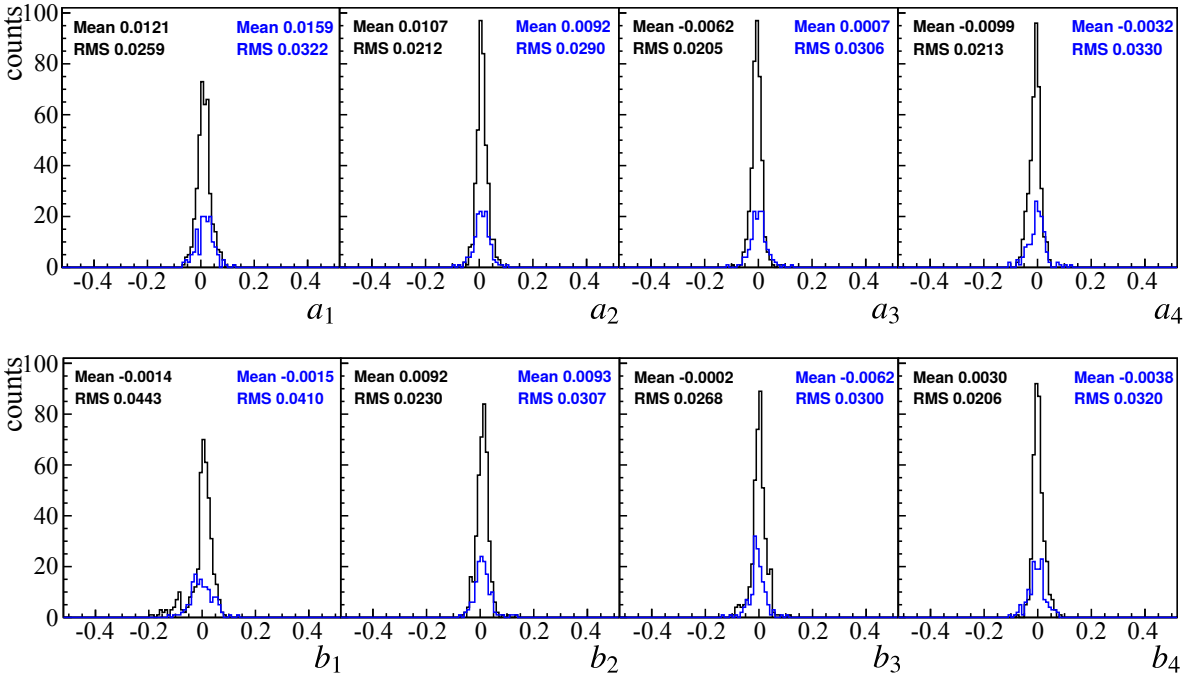

Figure 6.32: The fit coefficients $a_1 \ldots a_4$ and $b_1 \ldots b_4$ as obtained by the unbinned maximum likelihood fit for the $p\pi^0$ final state (black) and for the $p\eta$ final state (blue) are shown. The values are distributed around 0 indicating an almost flat detector acceptance over the azimuthal angle ϕ.

The results for the beam asymmetry Σ using the unbinned maximum likelihood fit method as described in Section 6.3 are shown for one energy bin in Figure 6.33 for the $p\pi^0$ and for the $p\eta$

final state. The error bars consist only of statistical errors.

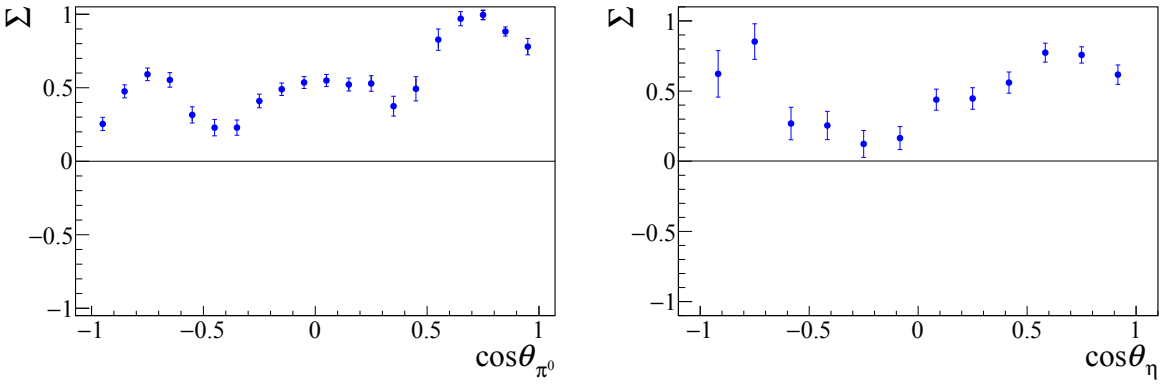

Figure 6.33: The results for the beam asymmetry Σ obtained with the unbinned maximum likelihood fit method are shown for the energy range of 1455 MeV $\leq E_\gamma <$ 1491 MeV for the $p\pi^0$ final state (left) and for the energy range of 1610 MeV $\leq E_\gamma <$ 1670 MeV for the $p\eta$ final state (right). The error bars represent statistical errors only.

6.4 Comparison of both methods

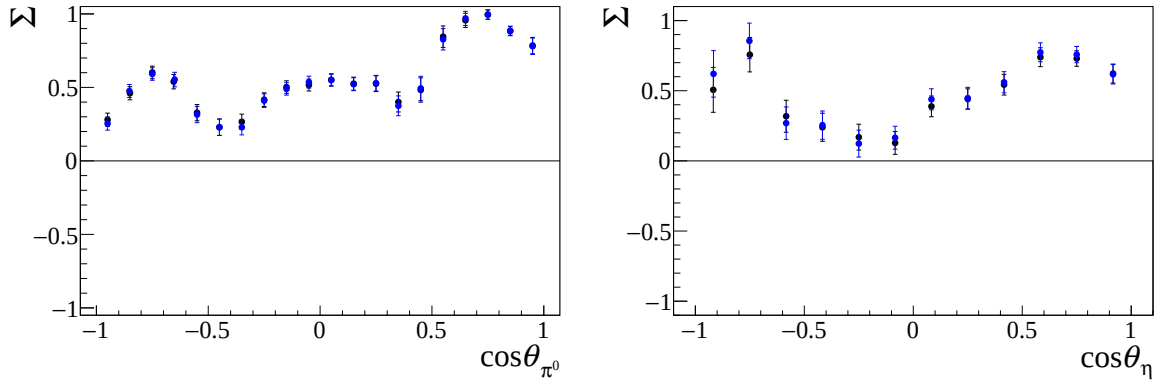

Figure 6.34: Comparison of Σ obtained with a binned χ^2-fit (black) and an unbinned maximum likelihood fit (blue) for the $p\pi^0$ final state on the left and for the $p\eta$ final state on the right.

A comparison of the beam asymmetry results using the event yield and maximum likelihood fit method is depicted in Figure 6.34 for both final states. Within the statistical error bars, both methods yield consistent results. A systematic effect is not introduced by the choice of method that is used to obtain the beam asymmetry. The unbinned maximum likelihood fit method gives a more correct estimation of the statistical error bars using Poisson statistics. In addition, the statistical error bars tend to be slightly smaller in the order of 10% when utilizing the unbinned maximum likelihood fit method. Therefore, only the results obtained with this method will be shown from here on.

6.5 Systematic error

The systematic error is mainly dominated by the contribution from the polarization degree of the linearly polarized photon beam. As discussed in Section 6.1.2, the relative systematic error of the linear polarization degree is given by 5%, except for the region close to the falling edge where it has to be increased to 8%. It holds

$$\frac{\Delta p_\gamma}{p_\gamma} = \begin{cases} 0.05, & \text{if } E_\gamma < 1600\,\text{MeV}, \\ 0.08, & \text{otherwise.} \end{cases} \tag{6.29}$$

The measured value of the beam asymmetry Σ^{real} is given by the real value $\Sigma^{\text{meas.}}$ and the beam asymmetry value of the background Σ^{bg} in the selected data:

$$\Sigma^{\text{meas.}} = \Sigma^{\text{real}} \cdot \left(1 - \delta^{\text{bg}}\right) + \delta^{\text{bg}} \cdot \Sigma^{\text{bg}} \tag{6.30}$$

However, the background beam asymmetry is an unknown parameter and is not easy to determine since the background can stem from different final states and moreover, it is so small that an attempt to determine it e.g. using events around the π^0 or η peak, would lead to a very high statistical error. Therefore, the measured value can not be corrected to the real value. Hence, a systematic error is caused by the background contamination in the selected data as demonstrated with toy MC samples (see Section 6.2.2). It is prudent to assume that the absolute systematic error of the beam asymmetry due to the background is in the order of the relative background contamination in the selected data δ^{bg} as discussed in reference [Har17]:

$$\Delta\Sigma^{\text{bg, abs}} \lesssim \delta^{\text{bg}} \tag{6.31}$$

The relative background contamination in the selected data δ^{bg} is shown for each energy and angular bin of both final states in Figures 5.39 and 5.40 in Chapter 5.

Thus, the total absolute systematic error of the beam asymmetry is given by

$$\Delta\Sigma^{\text{sys, abs}} = \sqrt{\left(\frac{\Delta p_\gamma}{p_\gamma} \cdot \Sigma^{\text{meas.}}\right)^2 + \left(\delta^{\text{bg}}\right)^2} \tag{6.32}$$

Uncertainties of $\alpha^{\parallel}$ and the offset parameter p_1 are negligibly small ($< 1\%$).

6.6 Results

Figure 6.35 and Figure 6.36 show the new CBELSA/TAPS data for the beam asymmetry Σ of the $p\pi^0$ final state, covering an energy range of $E_\gamma = (1131\,\text{MeV} - 1779\,\text{MeV})$. The error bars correspond to the statistical errors. The systematic errors are depicted as well. Similar, Figure 6.37 shows the results for the $p\eta$ final state, showing an energy range of $E_\gamma = (1130\,\text{MeV} - 1790\,\text{MeV})$.

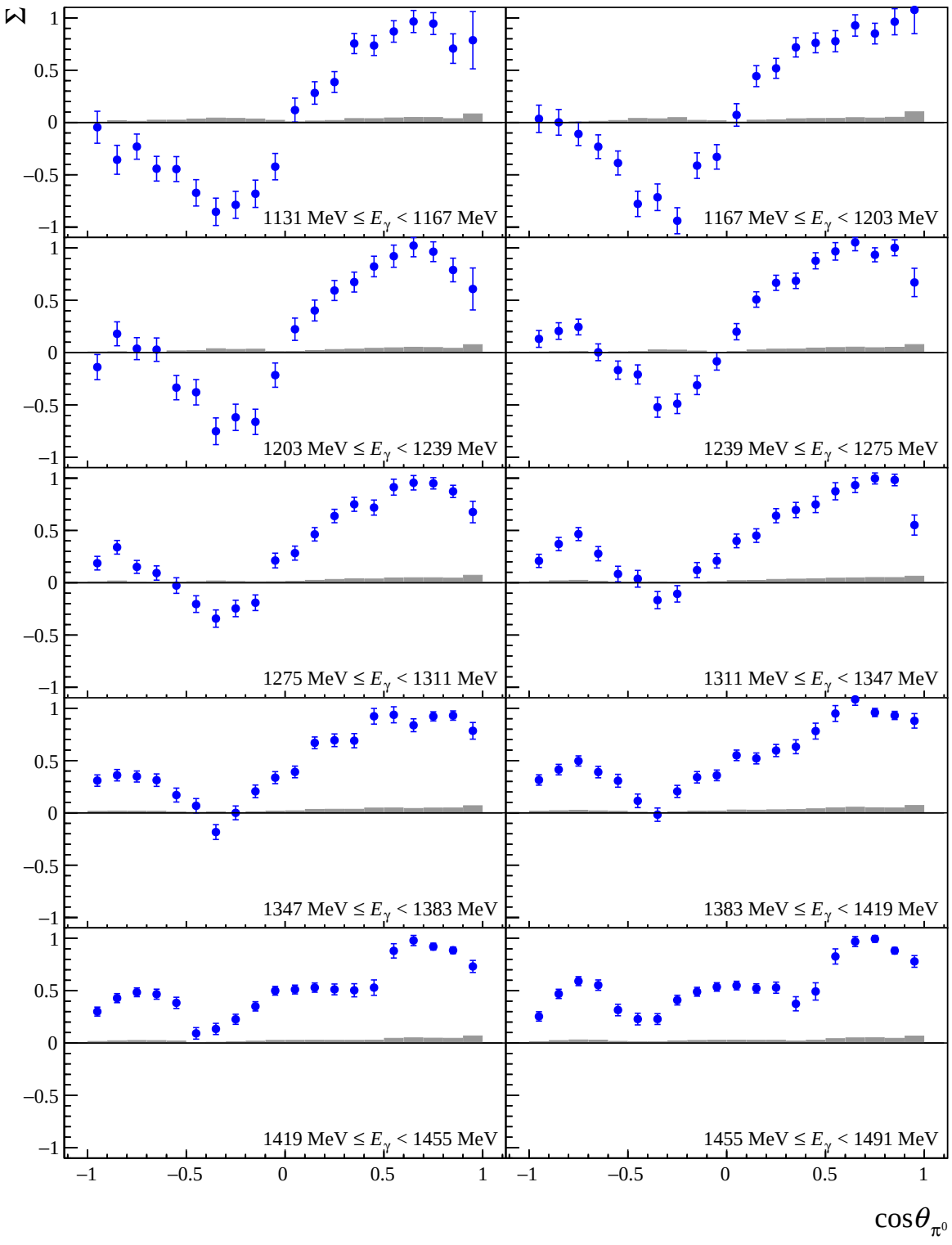

Figure 6.35: The new CBELSA/TAPS data for the beam asymmetry Σ of the $p\pi^0$ final state are shown for the energy range of E_γ = (1131 MeV - 1491 MeV). The error bars show only the statistical errors. The systematic errors are depicted in gray.

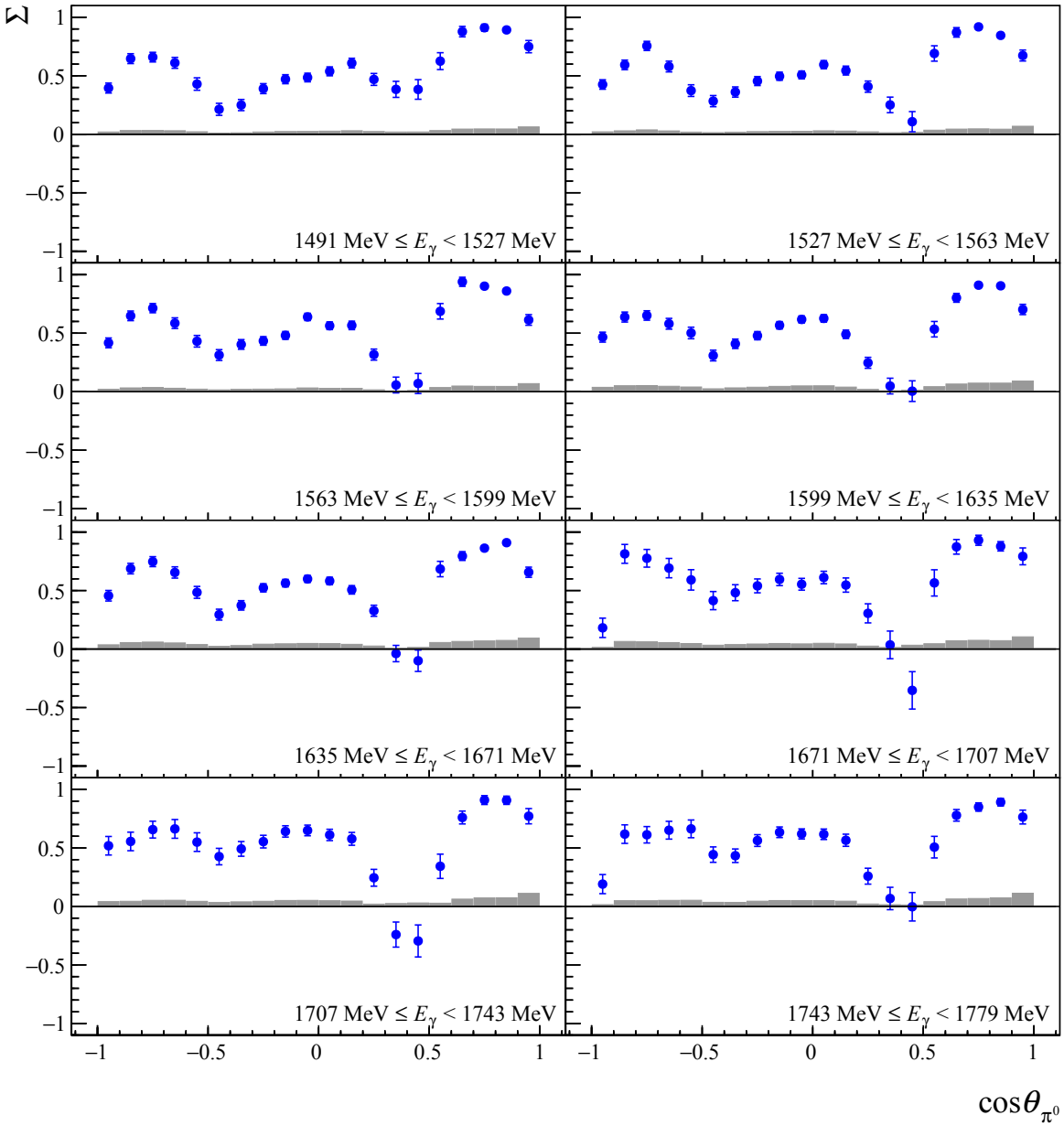

Figure 6.36: The new CBELSA/TAPS data for the beam asymmetry Σ of the $p\pi^0$ final state are shown for the energy range of E_γ = (1491 MeV - 1779 MeV). The error bars show only the statistical errors. The systematic errors are depicted in gray.

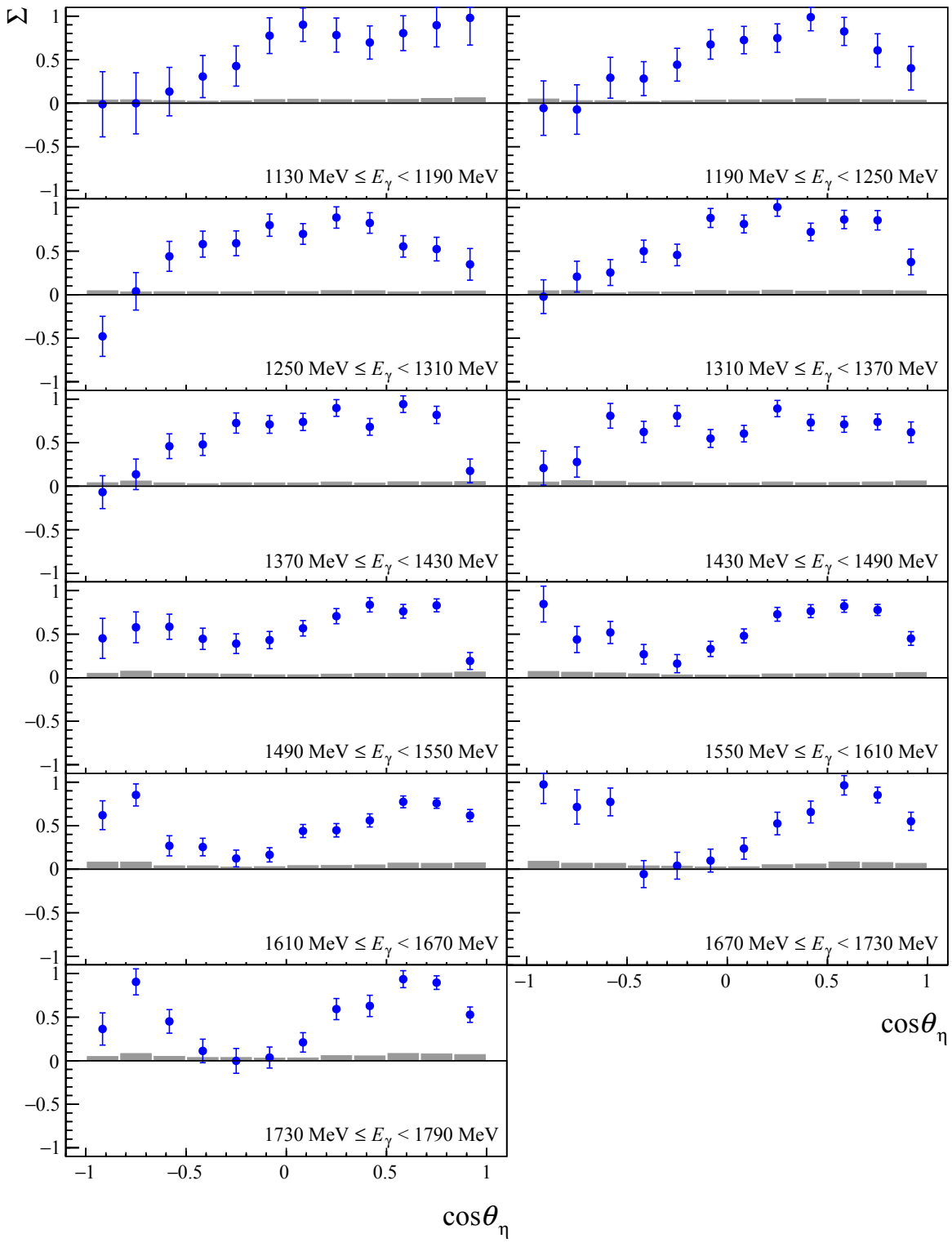

Figure 6.37: The new CBELSA/TAPS data for the beam asymmetry Σ of the $p\eta$ final state are shown for the energy range of E_γ = (1130 MeV - 1790 MeV). The error bars show only the statistical errors. The systematic errors are depicted in gray.

7 Determination of the helicity asymmetry

The A2 data was measured with an elliptically polarized photon beam and a longitudinally polarized target. The polarized differential cross section $\frac{d\sigma}{d\Omega}_{\mathrm{pol}}(E_\gamma, \cos\theta, \phi)$ is given by [San+11]

$$\frac{d\sigma}{d\Omega}_{\mathrm{pol}}(E_\gamma, \cos\theta, \phi) = \frac{d\sigma}{d\Omega}_{0}(E_\gamma, \cos\theta)\left[1 - p_\gamma^{\mathrm{lin}}\Sigma\cos(2(\alpha-\phi)) + p_T p_\gamma^{\mathrm{lin}} G\sin(2(\alpha-\phi)) - p_T p_\gamma^{\mathrm{circ}} E\right], \tag{7.1}$$

where $\frac{d\sigma}{d\Omega}_{0}(E_\gamma, \cos\theta)$ is the unpolarized cross section, the angles α and ϕ are defined in the same way as introduced in Chapter 6, p_γ^{lin} is the degree of linear polarization, p_γ^{circ} is the degree of circular polarization, p_T is the degree of target polarization, Σ is the beam asymmetry and G and E are two double polarization observables. The data were taken with two perpendicular α settings, denoted with $\perp$ and $\parallel$ analog to the convention used in Chapter 6. Additionally, the helicity of the photon beam was switched at a rate of 1 Hz between $h = +1$ ($\uparrow_H$) and $h = -1$ ($\downarrow_H$). Moreover, the longitudinal target polarization orientation was changed from $+z$ ($\uparrow_T$) to $-z$ ($\downarrow_T$). In total, eight different polarized cross sections can be formulated using Equation (7.1). It holds e.g. for $\frac{d\sigma}{d\Omega}^{\uparrow_H,\uparrow_T,\parallel}$ and $\frac{d\sigma}{d\Omega}^{\uparrow_H,\uparrow_T,\perp}$:

$$\begin{aligned}\frac{d\sigma}{d\Omega}^{\uparrow_H,\uparrow_T,\parallel/\perp}(E_\gamma, \cos\theta, \phi) = \frac{d\sigma}{d\Omega}_{0}(E_\gamma, \cos\theta)\Big[1 \mp p_\gamma^{\parallel/\perp}\Sigma\cos(2(\alpha^\parallel - \phi)) \\ \pm p_T^{\uparrow} p_\gamma^{\parallel/\perp} G\sin(2(\alpha^\parallel - \phi)) - p_T^{\uparrow} p_\gamma^{\uparrow} E\Big].\end{aligned} \tag{7.2}$$

To access only the helicity asymmetry E and eliminate the contributions from Σ and G one has to sum over both α settings and integrate over the entire azimuthal angle ϕ. Equation (7.2) simplifies to[1]

$$2\frac{d\sigma}{d\Omega}^{\uparrow_H,\uparrow_T}(E_\gamma, \cos\theta) = \frac{1}{2\pi}\int_0^{2\pi} \frac{d\sigma}{d\Omega}^{\uparrow_H,\uparrow_T,\parallel}(E_\gamma, \cos\theta, \phi) + \frac{d\sigma}{d\Omega}^{\uparrow_H,\uparrow_T,\perp}(E_\gamma, \cos\theta, \phi) \quad d\phi \tag{7.3}$$

$$= 2\frac{d\sigma}{d\Omega}_{0}(E_\gamma, \cos\theta)\left[1 - p_T^{\uparrow} p_\gamma^{\uparrow} E\right]. \tag{7.4}$$

Using Equation (7.3), the differential cross sections $\frac{d\sigma}{d\Omega}^{\uparrow_H,\downarrow_T}$, $\frac{d\sigma}{d\Omega}^{\downarrow_H,\uparrow_T}$ and $\frac{d\sigma}{d\Omega}^{\downarrow_H,\downarrow_T}$ can be obtained as well. Note: A change of the helicity or target polarization direction leads to a sign change in Equation (7.4). The double polarization observable E describes the asymmetry between the state where the photon and proton spins are aligned anti-parallel ($\frac{d\sigma}{d\Omega}^{1/2}$) to the state where the photon and proton spins are aligned parallel ($\frac{d\sigma}{d\Omega}^{3/2}$). The difference of the helicity dependent cross sections leads to

$$\frac{d\sigma}{d\Omega}^{1/2} - \frac{d\sigma}{d\Omega}^{3/2} = \frac{1}{2}\left(\frac{d\sigma}{d\Omega}^{\uparrow_H,\downarrow_T} + \frac{d\sigma}{d\Omega}^{\downarrow_H,\uparrow_T}\right) - \frac{1}{2}\left(\frac{d\sigma}{d\Omega}^{\uparrow_H,\uparrow_T} + \frac{d\sigma}{d\Omega}^{\downarrow_H,\downarrow_T}\right) \tag{7.5}$$

[1] A complete cancellation of Σ and G is only ensured in the ideal case of a flat detection efficiency over the entire azimuthal angle ϕ or in the ideal case of $p_\gamma^\parallel = p_\gamma^\perp$. This is discussed in detail in Section 7.3.2.5.

$$= \frac{1}{2}\frac{d\sigma}{d\Omega_0} E \left(p_T^{\downarrow} p_\gamma^{\uparrow} + p_T^{\uparrow} p_\gamma^{\downarrow} + p_T^{\uparrow} p_\gamma^{\uparrow} + p_T^{\downarrow} p_\gamma^{\downarrow} \right) \tag{7.6}$$

$$= 2\frac{d\sigma}{d\Omega_0} E \bar{p}_T \bar{p}_\gamma^{\text{circ}}, \tag{7.7}$$

where $\bar{p}_\gamma^{\text{circ}} \bar{p}_T$ are the event yield weighted average circular and target polarization degrees. Similar, it holds for the sum

$$\frac{d\sigma}{d\Omega}^{1/2} + \frac{d\sigma}{d\Omega}^{3/2} = \frac{1}{2}\left(\frac{d\sigma}{d\Omega}^{\uparrow_H,\downarrow_T} + \frac{d\sigma}{d\Omega}^{\downarrow_H,\uparrow_T} \right) + \frac{1}{2}\left(\frac{d\sigma}{d\Omega}^{\uparrow_H,\uparrow_T} + \frac{d\sigma}{d\Omega}^{\downarrow_H,\downarrow_T} \right) \tag{7.8}$$

$$= 2\frac{d\sigma}{d\Omega_0} \left(1 + p_T^{\downarrow} p_\gamma^{\uparrow} E + p_T^{\uparrow} p_\gamma^{\downarrow} E - p_T^{\uparrow} p_\gamma^{\uparrow} E - p_T^{\downarrow} p_\gamma^{\downarrow} E \right) \tag{7.9}$$

$$= 2\frac{d\sigma}{d\Omega_0} \left(1 + (p_T^{\downarrow} - p_T^{\uparrow}) \cdot (p_\gamma^{\uparrow} - p_\gamma^{\downarrow}) \cdot E \right) \tag{7.10}$$

$$\overset{p_\gamma^{\uparrow} \approx p_\gamma^{\downarrow}}{=} 2\frac{d\sigma}{d\Omega_0}. \tag{7.11}$$

Only if either the target or the circular polarization degrees are equal does the sum reduce to Equation (7.11). Figure 7.35 shows that this is fulfilled for the circular polarization degrees but not for the target polarization degrees. The helicity asymmetry E is defined as [San+11]:

$$E := \frac{\frac{d\sigma}{d\Omega}^{1/2} - \frac{d\sigma}{d\Omega}^{3/2}}{\frac{d\sigma}{d\Omega}^{1/2} + \frac{d\sigma}{d\Omega}^{3/2}}. \tag{7.12}$$

The unpolarized differential cross section is dependent on the event yield $N(E_\gamma, \cos\theta)$, the detection efficiency $\epsilon(E_\gamma, \cos\theta)$, the photon flux $n_\gamma(E_\gamma)$, the target area density n_T, the branching ratio for the final state Γ_i/Γ and the solid angle coverage $\Delta\Omega$:

$$\frac{d\sigma}{d\Omega_0}(E_\gamma, \cos\theta) = \frac{N(E_\gamma, \cos\theta)}{\epsilon(E_\gamma, \cos\theta) \cdot n_\gamma(E_\gamma) \cdot n_T \cdot \Gamma_i/\Gamma \cdot \Delta\Omega}. \tag{7.13}$$

Using Equation (7.13) and inserting it in Equation (7.12), the double polarization observable E is given by

$$E = \frac{N^{1/2} - N^{3/2}}{N^{1/2} + N^{3/2}} \cdot \frac{1}{\bar{p}_\gamma^{\text{circ}} \bar{p}_T}, \tag{7.14}$$

where $N^{1/2}$ is the combined event yield of $N^{\uparrow_H,\downarrow_T}$ and $N^{\downarrow_H,\uparrow_T}$ and $N^{3/2}$ of $N^{\uparrow_H,\uparrow_T}$ and $N^{\downarrow_H,\downarrow_T}$. It is immediately clear that the constant parameters n_T, Γ_i/Γ and $\Delta\Omega$ cancel, when calculating the asymmetry (see Equation (7.14)). However, neither the photon flux nor the detection efficiency are in general the same for different target polarization orientations: $n_\gamma^{\uparrow_T} \neq n_\gamma^{\downarrow_T}$ as this data consists of different runs taken at different times. But since runs with positive and negative target polarization orientation are summed up before calculating E (see Equations 7.5 and 7.8), it holds for the combined flux: $n_\gamma^{\uparrow_H,\downarrow_T+\downarrow_H,\uparrow_T} \approx n_\gamma^{\uparrow_H,\uparrow_T+\downarrow_H,\downarrow_T}$ and for the detection efficiency: $\epsilon_\gamma^{\uparrow_H,\downarrow_T+\downarrow_H,\uparrow_T} \approx \epsilon_\gamma^{\uparrow_H,\uparrow_T+\downarrow_H,\downarrow_T}$. The only requirement is that the photon flux for both helicity states is the same which is approximately fulfilled since the helicity is switched with 1 Hz. Therefore, the photon flux and the detection efficiency cancel out in the asymmetry. Thus, the helicity asymmetry E can be determined using an event yield asymmetry.

7.1 Dilution factor

So far, all given equations ignore the fact that the A2 data was taken with a butanol target containing polarizable free protons of the hydrogen nuclei and unpolarized contributions from bound carbon and oxygen nuclei. Thus, the unpolarized butanol differential cross section $\frac{d\sigma}{d\Omega}_{0,\mathrm{but}}(E_\gamma, \cos\theta)$ can be divided into a free and a bound part: $\frac{d\sigma}{d\Omega}_{0,\mathrm{but}}(E_\gamma, \cos\theta) = \frac{d\sigma}{d\Omega}_{0,\mathrm{free}}(E_\gamma, \cos\theta) + \frac{d\sigma}{d\Omega}_{0,\mathrm{bound}}(E_\gamma, \cos\theta)$. The amount of polarizable free protons contained in the selected butanol data is given by the so called dilution factor d. It is defined as

$$d(E_\gamma, \cos\theta) := \frac{\frac{d\sigma}{d\Omega}_{0,\mathrm{free}}(E_\gamma, \cos\theta)}{\frac{d\sigma}{d\Omega}_{0,\mathrm{free}}(E_\gamma, \cos\theta) + \frac{d\sigma}{d\Omega}_{0,\mathrm{bound}}(E_\gamma, \cos\theta)} \tag{7.15}$$

$$= 1 - \frac{\frac{d\sigma}{d\Omega}_{0,\mathrm{bound}}(E_\gamma, \cos\theta)}{\frac{d\sigma}{d\Omega}_{0,\mathrm{free}}(E_\gamma, \cos\theta) + \frac{d\sigma}{d\Omega}_{0,\mathrm{bound}}(E_\gamma, \cos\theta)} \tag{7.16}$$

Taking the butanol target into account, Equation (7.1) needs to be modified in the following way:

$$\frac{d\sigma}{d\Omega}_{\mathrm{but}}(E_\gamma, \cos\theta, \phi) = \frac{d\sigma}{d\Omega}_{0,\mathrm{free}}(E_\gamma, \cos\theta)\Big[1 - p_\gamma^{\mathrm{lin}}\Sigma_{\mathrm{free}}\cos(2(\alpha-\phi)) + p_T p_\gamma^{\mathrm{lin}} G\sin(2(\alpha-\phi)) \tag{7.17}$$

$$- p_T p_\gamma^{\mathrm{circ}} E\Big] + \frac{d\sigma}{d\Omega}_{0,\mathrm{bound}}(E_\gamma, \cos\theta)\Big[1 - p_\gamma^{\mathrm{lin}}\Sigma_{\mathrm{bound}}\cos(2(\alpha-\phi))\Big]$$

$$= \frac{d\sigma}{d\Omega}_{0,\mathrm{free}}(E_\gamma, \cos\theta) + \frac{d\sigma}{d\Omega}_{0,\mathrm{bound}}(E_\gamma, \cos\theta) \tag{7.18}$$

$$- p_\gamma^{\mathrm{lin}}\cos(2(\alpha-\phi))\left(\frac{d\sigma}{d\Omega}_{0,\mathrm{free}}\Sigma_{\mathrm{free}} + \frac{d\sigma}{d\Omega}_{0,\mathrm{bound}}\Sigma_{\mathrm{bound}}\right)$$

$$+ \frac{d\sigma}{d\Omega}_{0,\mathrm{free}}(E_\gamma, \cos\theta)\left[p_T p_\gamma^{\mathrm{lin}} G\sin(2(\alpha-\phi)) - p_T p_\gamma^{\mathrm{circ}} E\right]$$

$$= \frac{d\sigma}{d\Omega}_{0,\mathrm{but}}(E_\gamma, \cos\theta)\Big[1 - (d\cdot\Sigma_{\mathrm{free}} + (1-d)\Sigma_{\mathrm{bound}})p_\gamma^{\mathrm{lin}}\cos(2(\alpha-\phi)) \tag{7.19}$$

$$+ p_T p_\gamma^{\mathrm{lin}} d\cdot G\sin(2(\alpha-\phi)) - p_T p_\gamma^{\mathrm{circ}} d\cdot E\Big]$$

$$= \frac{d\sigma}{d\Omega}_{0,\mathrm{but}}(E_\gamma, \cos\theta)\Big[1 - p_\gamma^{\mathrm{lin}}\Sigma_{\mathrm{but}}\cos(2(\alpha-\phi)) \tag{7.20}$$

$$+ p_T p_\gamma^{\mathrm{lin}} d\cdot G\sin(2(\alpha-\phi)) - p_T p_\gamma^{\mathrm{circ}} d\cdot E\Big].$$

It is noteworthy that the measured beam asymmetry Σ_{but} consists also of two components: Σ_{free}, which is compatible to the beam asymmetry as defined in Chapter 6, and a beam symmetry Σ_{bound} which is measured for reactions off bound carbon and oxygen nuclei.

In order to determine the dilution factor additional data were taken with a carbon foam target[2].

[2] According to [Mac+97], the carbon and the oxygen photoabsorption cross sections are approximately the same and do not need to be considered separately.

Using Equation (7.13) the dilution factor is simplified to

$$d(E_\gamma, \cos\theta) = 1 - \frac{n_T^{\text{but}} \cdot n_\gamma^{\text{but}}(E_\gamma) \cdot \epsilon^{\text{but}}(E_\gamma, \cos\theta) \cdot N^C(E_\gamma, \cos\theta)}{n_T^C \cdot n_\gamma^C(E_\gamma) \cdot \epsilon^C(E_\gamma, \cos\theta) \cdot N^{\text{but}}(E_\gamma, \cos\theta)} \tag{7.21}$$

$$= 1 - s^C(E_\gamma, \cos\theta) \cdot \frac{N^C(E_\gamma, \cos\theta)}{N^{\text{but}}(E_\gamma, \cos\theta)}, \tag{7.22}$$

where $N^{\text{but}}(E_\gamma, \cos\theta)$ and $N^C(E_\gamma, \cos\theta)$ are the event yields measured with the butanol and the carbon target, respectively. The scaling factor $s^C(E_\gamma, \cos\theta)$ describes the ratio of photon flux, detection efficiency and target area density of both targets which are not the same.

The dilution factor needs to be included in Equation (7.4), resulting in

$$2\frac{d\sigma}{d\Omega}_{\text{but}}^{\uparrow_H,\uparrow_T}(E_\gamma, \cos\theta) = 2\frac{d\sigma}{d\Omega}_{0,\text{but}}(E_\gamma, \cos\theta)\left[1 - p_T^\uparrow p_\gamma^\uparrow \cdot d \cdot E\right] \tag{7.23}$$

and consequently the helicity asymmetry formula is finally given by

$$E = \frac{N^{1/2} - N^{3/2}}{N^{1/2} + N^{3/2}} \cdot \frac{1}{d} \cdot \frac{1}{\bar{p}_\gamma^{\text{circ}} \bar{p}_T} \tag{7.24}$$

$$= \frac{N^{1/2} - N^{3/2}}{N^{1/2} + N^{3/2} - s^C N^C} \cdot \frac{1}{\bar{p}_\gamma^{\text{circ}} \bar{p}_T}. \tag{7.25}$$

Apart from the unpolarized carbon background contribution in the butanol target there is another source of background. The butanol target is cooled down with a ^{3}He/^{4}He mixture. Reactions can also happen off the helium nuclei which are unpolarized like the carbon nuclei. Therefore, dedicated tests were performed in the September 2015 beamtime investigating the different background contributions. This is discussed in the following section before explaining how the scaling factor s^C is determined from the data.

7.1.1 Comparison of butanol, carbon and helium spectra

As already mentioned, data were taken using different target materials which were inserted into the same Teflon target cell cylinder and cryostat as used for the butanol target. These target materials consist of

- a carbon foam target without the usage of helium. It is referred to as the *only carbon* data,
- a carbon foam target with the usage of helium in the same way as it is used for the butanol data (6% ^{3}He and 94% ^{4}He) to cool down the target. It is called in the following *carbon+helium* data and
- the Teflon target cell was filled only with helium and is referred to as the *only helium* data.

A comparison of the coplanarity spectra is shown in Figure 7.1 on the left for the $p\pi^0$ and on the right for the $p\eta$ final state. The width of the coplanarity spectra differs largely for the different target materials. The butanol spectrum is comprised of two distributions, one dominating thin

and one broader distribution. The *only helium*, *carbon+helium* and *only carbon* spectra are significantly broader. Here, the deviations are more pronounced for the $p\pi^0$ final state than for the $p\eta$ final state. Additionally, a comparison of the missing mass distributions is given in Figure 7.2. The missing mass spectra of *only helium*, *carbon+helium* and *only carbon* are shifted towards higher masses compared to the one measured with the butanol target. The observed differences between the different target spectra can be explained with nuclear effects like Fermi motion with Fermi momentum p_F and Final State Interaction (FSI).

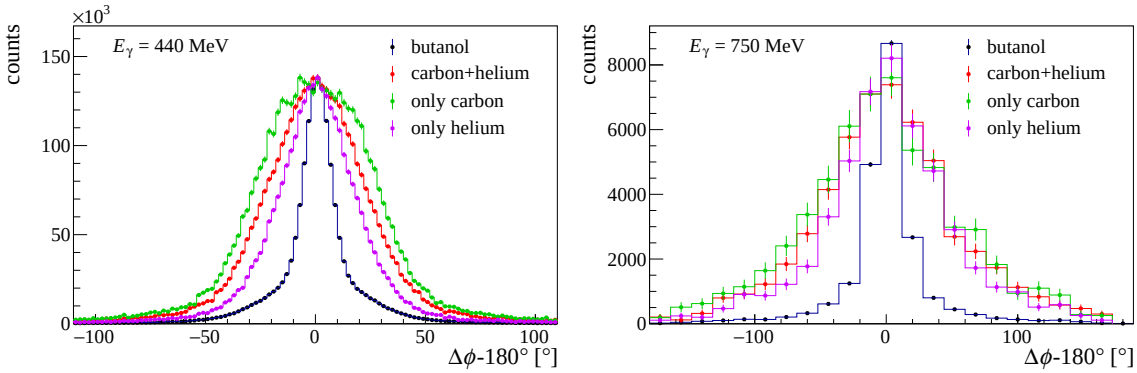

Figure 7.1: Comparison of coplanarity spectra of the $p\pi^0$ final state on the left and of the $p\eta$ final state on the right. The spectra were measured with different targets: butanol (black), carbon target cooled with helium in the same way as the butanol target (red), carbon target without helium (green) and the target cell filled only with helium. The spectra are scaled to the same maximum value for better comparison.

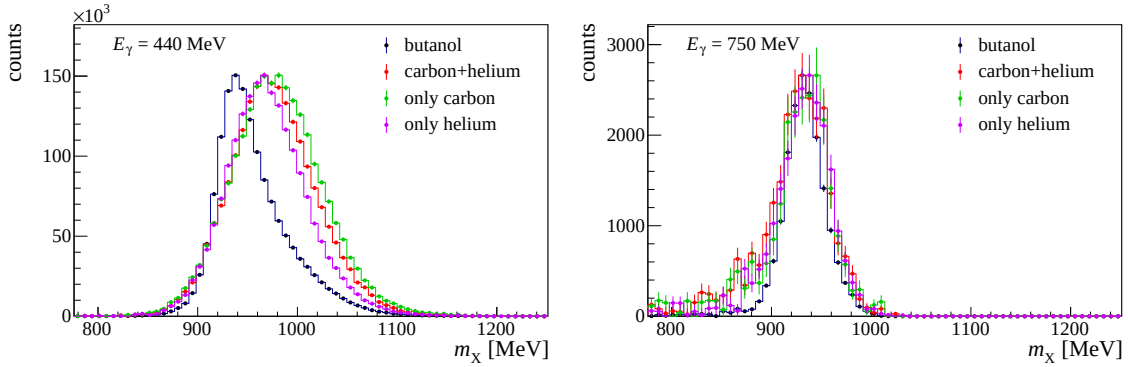

Figure 7.2: Comparison of missing mass spectra of the $p\pi^0$ final state on the left and of the $p\eta$ final state on the right. The spectra were measured with different targets: butanol (black), carbon target cooled with helium in the same way as the butanol target (red), carbon target without helium (green) and the target cell filled only with helium. The spectra are scaled to the same maximum value for better comparison.

In the initial state, the free protons of the hydrogen nuclei are at rest. However, the bound nuclei of carbon and helium have a non-negligible initial momentum due to Fermi motion and FSI. Due to the additional momentum, it is expected that the missing mass distributions

measured with carbon or helium are shifted towards higher masses compared to the distribution measured off free protons, since for its calculation an initial momentum of zero is assumed (see Equation (5.6)). Moreover, the initial momentum of the bound nuclei leads to a broadening of the spectra. Therefore, the coplanarity and missing mass spectra are broader for helium and carbon than for hydrogen. The applied kinematic cut ranges are chosen to select mainly the free hydrogen part of the butanol data (see Section 5.3.2). Thus, the butanol coplanarity spectrum consists dominantly of the free hydrogen part that has a significantly smaller width than the carbon and helium spectra and which sits on a broader distribution due to the contributing reactions off bound carbon and helium nuclei. The observed differences of the spectra are more pronounced at beam photon energies near the photoproduction threshold of the meson than at higher energies, e.g. $E_\gamma \geq 960\,\text{MeV}$, since at these energies the proton momentum is much higher compared to the Fermi momentum. Here, the width of the coplanarity spectra of the *carbon+helium* and *only carbon* become similar (see Figure B.1 in the appendix).
A comparison of the Fermi momentum distributions for carbon and helium is depicted in Figure 7.3. ^{4}He nuclei have the largest Fermi momentum followed by carbon and then by ^{3}He. Based on the Fermi momentum distributions (Figure 7.3) the coplanarity spectrum of *only helium* data should be broader than the one measured with *only carbon*. However, the opposite is observed here which can be explained when taking FSI effects into account.

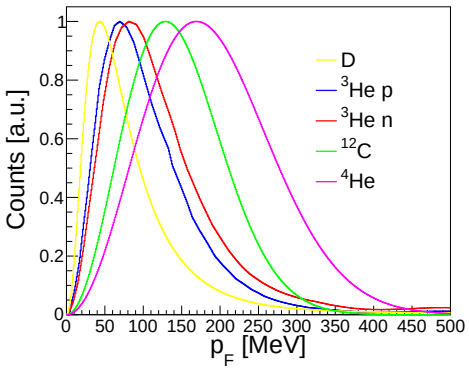

Figure 7.3: Comparison of Fermi momentum p_F distributions as calculated using [Lac+81; Arr+12; Nak+76; MSW77]. Taken from [Wit15].

The produced mesons, e.g. π^0 or η can interact with the nucleons before escaping the nucleus. This leads to a change of the kinematics and also to a broadening of the measured spectra. The higher the number of nucleons in a nucleus, the higher the interaction is expected to be. Here, FSI effects play a more important role for carbon with twelve nucleons than for helium with three or four nucleons. In addition, the FSI is expected to be highly dependent on the analyzed reaction [Kru05; Kru11]. According to the Boltzmann-Uehling-Uhlenbeck (BUU) model calculations [Hom+95; Kru05] the π^0 meson has a high probability around the $\Delta(1232)$ resonance energy region of being absorbed and re-emitted from the nucleus before escaping the nucleus which leads to a change of the $p\pi^0$ kinematics. Only about 5% of all escaped π^0 have not been absorbed at all. It is different for the η meson near its photoproduction threshold [Kru05]. About 90% of all escaped η mesons are not reabsorbed [Kru05]. Thus, the kinematics of $p\eta$ does not change much due to FSI effects. This is indicated in the comparison of the coplanarity spectra which do not deviate in the width as much as the ones of the $p\pi^0$ final state.

To perform a consistency check, the *only carbon* and *only helium* data were scaled in a fit to describe the sum of the *carbon+helium* data. This is demonstrated in Figure 7.4 on the left for the $p\pi^0$ final state. The sum (light blue) of the *only carbon* (green) and of the *only helium* (violet) coplanarity distributions agrees well with the *carbon+helium* (red) coplanarity spectrum. For a correct determination of the amount of bound nuclei contributions in the butanol data, the *carbon+helium* spectrum (and with it all the spectra shown on the left as well) was scaled with s^C to the butanol spectrum (see Figure 7.4 on the right). Since it is desired to know the total amount of bound nuclei, independent of whether they originate from carbon or helium, from now on only the *carbon+helium* spectra will be shown.

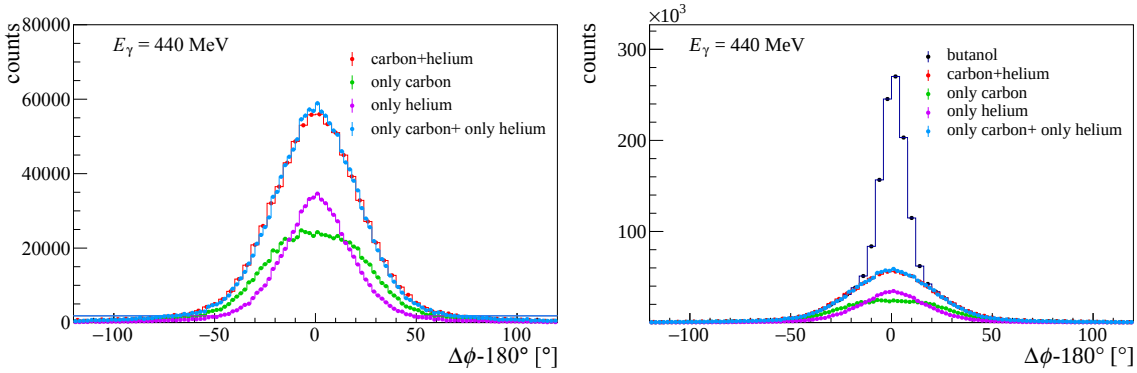

Figure 7.4: Left: The sum (light blue) of the *only carbon* (green) and *only helium* (violet) spectra can describe very well the coplanarity spectrum taken with the *carbon+helium* target (red). Right: The *carbon+helium* spectrum is scaled with s^C to the butanol spectrum (dark blue) to demonstrate the different background contributions in the selected butanol data.

7.1.2 Determination of the scaling factor

To identify the amount of bound nuclei in the butanol data, the data taken with the *carbon+helium* target were utilized and scaled to the butanol data. The scaling factor is needed to take into account the different photon fluxes, target area densities and detector acceptances during data taking of the *carbon+helium* and butanol beamtimes. The scaling factor s^C can be determined either directly, using the photon flux, target area density and detector acceptances (see Section 7.1.2.1), or indirectly by comparing the *carbon+helium* and butanol spectra and scaling them to each other. The latter method consists of scaling the *carbon+helium* spectra to the butanol spectra in a region where the *carbon+helium* contribution dominates and the hydrogen contribution is essentially null. This region is referred to as the non-hydrogen region. Here, it holds

$$s^C \cdot N^C_{\text{non-hydrogen region}} = N^{\text{but}}_{\text{non-hydrogen region}} \tag{7.26}$$

$$s^C = \frac{N^{\text{but}}_{\text{non-hydrogen region}}}{N^C_{\text{non-hydrogen region}}}, \tag{7.27}$$

where $N^{\text{but}}_{\text{non-hydrogen region}}$ and $N^C_{\text{non-hydrogen region}}$ are the event yields of the butanol or the *carbon+helium* data in the non-hydrogen region, respectively. To get the scaling factor, either the

coplanarity or the missing mass spectra are suitable[3]. Since it is easier to scale if no additional background contributions of other reaction channels are present (e.g. multi π^0 background exists for higher missing masses in the $p\eta$ channel), the coplanarity spectra are the preferable choice for the scaling of the 3 PED events.
It was reported in [Har17; Mül18] that the non-hydrogen range should be chosen at least 3σ away from the colanarity peak position in order to avoid any non-hydrogen cut range dependence of the scaling factor. Therefore, the non-hydrogen regions were set for the coplanarity spectra as $(-120°, -36°)$ and $(36°, 120°)$ for the $p\pi^0$ final state and as $(-90°, -36°)$ and $(36°, 90°)$ for the $p\eta$ to the butanol spectra. The cut at $\pm 36°$ ensures that the non-hydrogen range starts at least more than 3σ away from the peak position since the largest colanarity width is $\sigma_{\text{copl.}} \approx 12°$ (see Section 5.3.2.3). However, the entire coplanarity region up to $\pm 180°$ was not utilized due to possible background channels that contribute to the hydrogen component, e.g. the $p\pi^0$ channel in the $p\eta$ analysis (see Section 5.3.2.3).

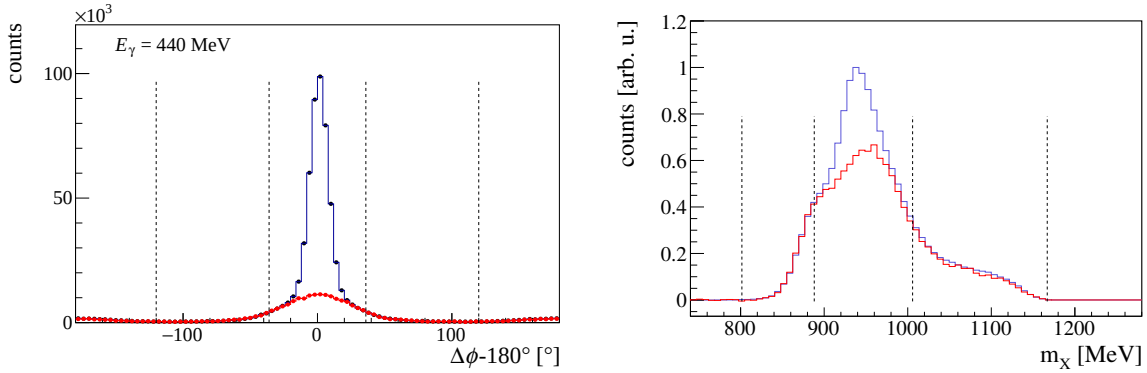

Figure 7.5: The scaling procedure is demonstrated for the $p\pi^0$ final state for 3 PED (left) and 2 PED events (right). Dark blue points represent the butanol data and red the *carbon+helium* data. The non-hydrogen regions are marked for the coplanarity spectrum (left) and missing mass spectrum (right) with dashed black lines.

Assuming that the detector acceptance of the butanol and *carbon+helium* data is approximately the same since the same target cell and cryostat were used, the scaling factors were determined beam photon energy E_γ dependent using the coplanarity spectra of the 3 PED events. Since the *carbon+helium* data of the September 2015 beamtime were taken with the 850 MeV coherent edge setting while the butanol data were taken with six different coherent edge settings, a strong energy dependence according to the coherent edge settings is expected.

In general, the determined scaling factors should work equally well for the 3 PED and 2 PED events. However, due to the different energy sum trigger thresholds, the scaling factors had to be determined separately for the 2 PED events of the $p\pi^0$ final state (see Section 7.1.2.2). Here, the missing mass spectra were used for scaling purposes. Since the shape of the missing mass spectra changes with the beam photon energy E_γ and the center of mass angle $\cos\theta$, the non-hydrogen regions of the missing mass spectra were set carefully for each energy and angular

[3] The invariant mass spectra of hydrogen and *carbon+helium* look similar as shown in Section 5.3.2.1. In principle, the theta difference can be used as well, but this parameter is very sensitive to the target position and is therefore not utilized.

bin (see Figure 7.5 on the right).

7.1.2.1 Direct calculation of the scaling factor

The scaling factor can also be determined through direct calculation of the photon fluxes, the detector acceptances and the target area densities, as follows:

$$s^C(E_\gamma, \cos\theta) = \frac{\epsilon^{\text{but}}(E_\gamma, \cos\theta) \cdot n_\gamma^{\text{but}}(E_\gamma) \cdot n_T^{\text{but}}}{\epsilon^C(E_\gamma, \cos\theta) \cdot n_\gamma^C(E_\gamma) \cdot n_T^C} \tag{7.28}$$

$$s^C(E_\gamma) \approx \frac{n_\gamma^{\text{but}}(E_\gamma) \cdot n_T^{\text{but}}}{n_\gamma^C(E_\gamma) \cdot n_T^C}, \tag{7.29}$$

where $\epsilon^{\text{but}}(E_\gamma, \cos\theta)$ and $\epsilon^C(E_\gamma, \cos\theta)$ are the detector acceptances, n_γ^{but} and n_γ^C are the photon fluxes and n_T^{but} and n_T^C are the target area densities of the butanol and *carbon+helium* data, respectively. Assuming no significant differences occurred for the detector acceptances, the scaling factors depend only on the photon fluxes and the target area densities.

The photon flux gives the number of photons that are incident on the target. It is calculated using the total number of hits registered in each tagger channel N_{e^-} and the tagging efficiency as measured with the pair spectrometer $\epsilon_{\text{tagg}}^{PS}$:

$$n_\gamma(E_\gamma) = \epsilon_{\text{tagg}}^{PS} \cdot N_{e^-} \cdot f^{\text{livetime}}. \tag{7.30}$$

Since the VUPROM tagger scalers are free running and not gated with the trigger signal, the total livetime of the data acquisition f^{livetime} has to be taken into account as well. The livetime is determined by taking the ratio of a trigger signal inhibited clock to a free running clock. The photon flux was determined for each beamtime by Peter Pauli. Detailed information about the photon flux determination process can be found in [Pau16]. Figure 7.6 shows an example of the photon flux as a function of the beam photon energy for all Møller runs and all diamond runs, with the 450 MeV coherent edge setting, of the September 2015 beamtime. The $1/E_\gamma$ dependence is well visible in the Møller spectrum while the diamond spectrum shows the enhancement due to the coherent edge.

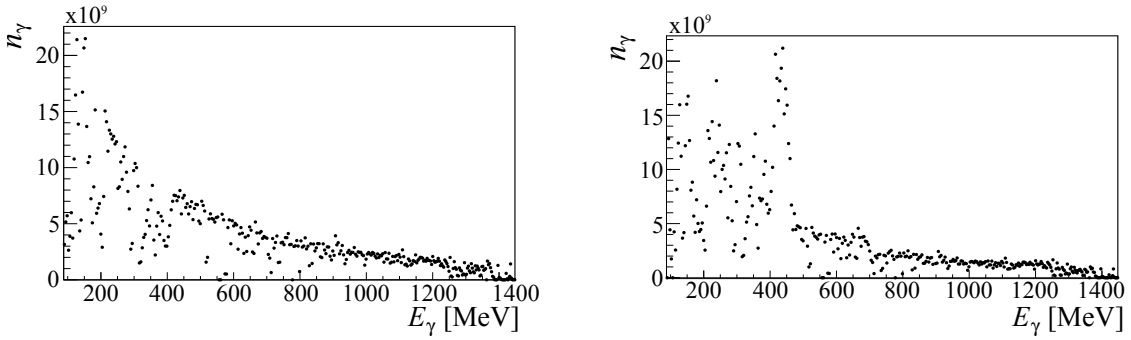

Figure 7.6: The photon flux n_γ is plotted on the left for all Møller runs and on the right for all diamond runs, with the coherent edge at 450 MeV, of the September 2015 beamtime.

To calculate the target area density n_T, the density of the target material ρ, the effective length

of the target l_{eff}, the molar mass m_{mol} and the number of nucleons per molecule N need to be known:

$$n_T = \frac{\rho \cdot l_{\text{eff}} \cdot N \cdot N_A}{m_{\text{mol}}}, \tag{7.31}$$

where N_A is the Avogadro constant. Since the frozen spin target is filled with butanol beads, the effective length of the target is given by the actual target length times the filling factor f^{fill}. It is estimated to be $f^{\text{fill}} = 0.6$ for the butanol beads [Tho]. The helium can flow between the beads and is also present at the 2 mm gap to the endcap downstream of the target cell. Therefore, the effective length of helium is given by $l_{\text{eff}} = (2.0 \cdot (1 - f^{\text{fill}}) + 0.2)$ cm. All target parameters are listed in Table 7.1.

parameters	**butanol beads in FST**	**helium in FST**	**carbon foam**
ρ [g/cm^3]	0.94	0.14	0.57
l_{eff} [cm]	$2.0 \cdot 0.6$	$2.0 \cdot 0.4 + 0.2$	1.98
m_{mol} [g/mol]	74.1	4.0	12.0
N (free+bound)	10+64	4	12
n_T [barn^{-1}] (free)	0.0918		
n_T [barn^{-1}] (bound)	0.5875	0.0843	0.6798
n_T [barn^{-1}] (total)	0.6793	0.0843	0.6798

Table 7.1: Overview of the different parameters and resulting target area density n_T of the butanol beads and helium in the frozen spin butanol target (FST) and the carbon foam target. Values are taken from [Tho].

The length and density of the carbon foam target were chosen to match roughly all contributing bound nucleons in the frozen spin butanol target (carbon, oxygen and helium). The scaling factor s^C has to scale the *carbon+helium* data spectra to the bound nucleons contributions of the butanol data spectra. Therefore, it holds for the ratio of the target area densities

$$\frac{n_T^{\text{but}}}{n_T^C} = \frac{n_T^{\text{but,bound}}}{n_T^C} = \frac{0.5875 + 0.0843}{0.6798 + 0.0843} \approx 0.88, \tag{7.32}$$

assuming the same amount of helium is present in the butanol target and in the carbon target. It is however not exactly known. The contributions of the Teflon target cell is the same for the *carbon+helium* and butanol data and is therefore not considered here.

A comparison of the scaling factors as obtained using the photon fluxes and target area densities and as determined using the coplanarity spectra is shown in Figure 7.7 in the upper row for the 450 MeV coherent edge data and in the lower row for the 850 MeV coherent edge data of the September 2015 beamtime. Since for the *carbon+helium* data a coherent edge position of 850 MeV was set, the resulting scaling factor for the 850 MeV diamond butanol data is almost constant over the entire energy range. In contrast to this, the scaling factor needed for the 450 MeV diamond butanol data shows a strong energy dependence and the shape of the coherent edge setting of the butanol and carbon data is clearly visible.

Within the statistical error bars both methods give the same results for both $p\pi^0$ and $p\eta$ final

states. Larger deviations, e.g. at 220 MeV for the 450 MeV coherent edge data of the $p\pi^0$ final state, were traced back to bad tagger channels that fluctuated a lot during the beamtime.

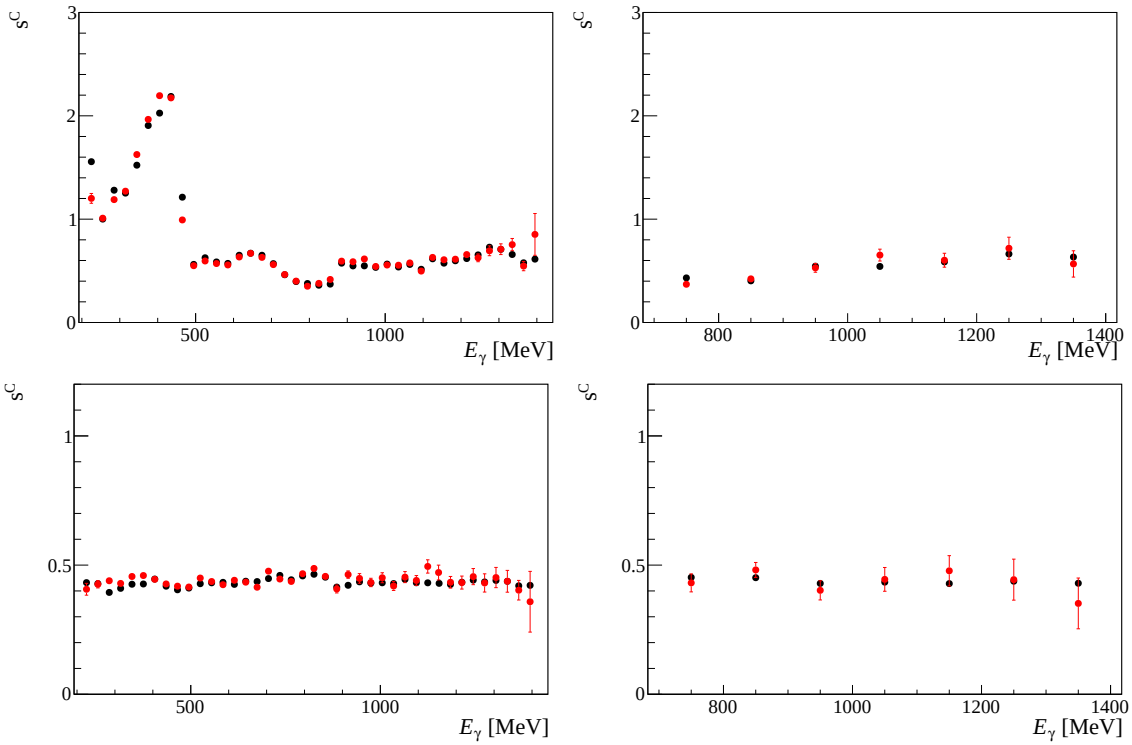

Figure 7.7: The scaling factor is plotted as a function of the beam photon energy on the upper row for the 450 MeV coherent edge data and on the bottom row for the 850 MeV coherent edge data of the September 2015 beamtime. The left column shows the scaling factor for the $p\pi^0$ and the right column for the $p\eta$ final state. The red points represent the method using the coplanarity spectra and the black points the photon flux and target area density method.

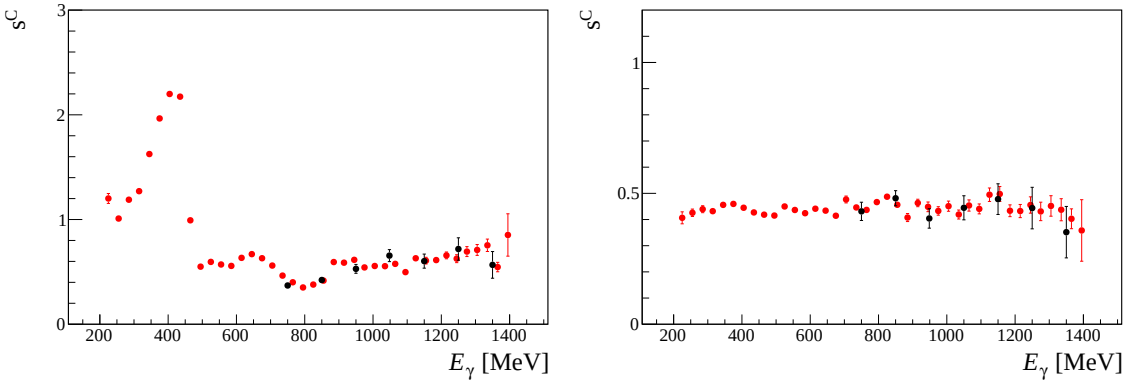

Figure 7.8: The scaling factors of both final states, the $p\pi^0$ final state in red and the $p\eta$ final state in black, are compared on the left for the 450 MeV coherent edge data and on the right for the 850 MeV coherent edge data of the September 2015 beamtime. Both data points were determined with the coplanarity spectra method.

According to Equation (7.29), the scaling factor does not depend on the final state. Figure 7.8

shows a direct comparison of the scaling factors of the $p\pi^0$ and $p\eta$ final state for the 450 MeV and 850 MeV coherent edge data of the September 2015 beamtime. The scaling factors are consistent with each other and fulfill the expectation.

While both scaling factor extraction methods are in agreement for the September 2015 beamtime, this is not the case for the other three beamtimes. A systematic, near constant, offset is visible between the methods, e.g. for the May 2015 beamtime (see Figure 7.9).

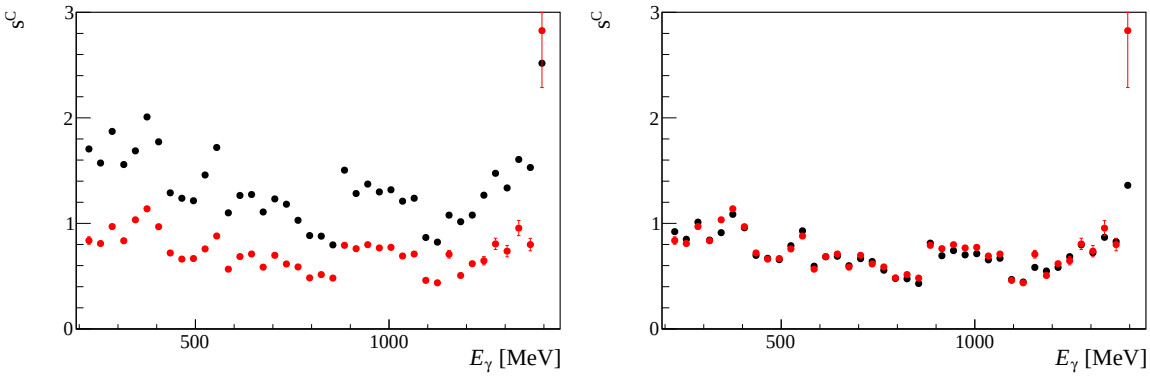

Figure 7.9: The scaling factor extraction methods are compared for the May 2015 beamtime. On the left the total livetime correction factor of the *carbon+helium* September data is applied according to Table 7.2. A clear offset is visible between the two methods. On the right the total livetime of the May 2015 beamtime is corrected as well. Colors are the same as described in Figure 7.7.

After investigating the problem, it became evident that the total livetime was not always correctly recorded during data acquisition. Thus, the photon flux is determined incorrectly by a constant factor when using the free running VUPROM scalers. The livetime problem can be traced back to problems with the configured trigger settings used in the analyzed data and the data acquisition system. Figure 7.10 shows the measured livetimes of all individual detectors and the recorded total livetime of the experiment for all four beamtimes. It is striking, that the total livetime is higher than some of the detector's livetimes for the May 2014, May 2015 and September 2015 beamtimes, indicating a wrong total livetime estimation. Since in the November 2013 and May 2014 beamtimes the FASTBUS scalers were additionally used that are gated with the trigger, the real livetime can be determined by taking the ratio of trigger gated to free running scalers for those beamtimes. Comparing the recorded and real livetimes, it is concluded, that the November 2013 beamtime is not affected by the livetime problem. However, for the May 2014 beamtime the recorded total livetime $f^{\text{livetime}}_{\text{recorded}}$ needs to be corrected by a factor of around $1.2 - 1.4$ to obtain the real total livetime $f^{\text{livetime}}_{\text{real}}$ in the following way:

$$f^{\text{livetime}}_{\text{real}} = f^{\text{livetime}}_{\text{recorded}} / f^{\text{livetime}}_{\text{corr}}. \tag{7.33}$$

The correction factor $f^{\text{livetime}}_{\text{corr}}$ is not constant over the beamtime as it depends on the set trigger thresholds and rates. Starting from June 2014, the FASTBUS scalers were not utilized any longer and therefore correction factors for the total livetime had to be determined differently for the May 2015 and September 2015 beamtimes. One possibility is to use the comparison between the scaling factor extraction methods and utilize the found offset factors of the November 2013 and May 2014 beamtimes to get the correction factor for the total livetime of the *carbon+helium* (and butanol) data of the September 2015 beamtime.

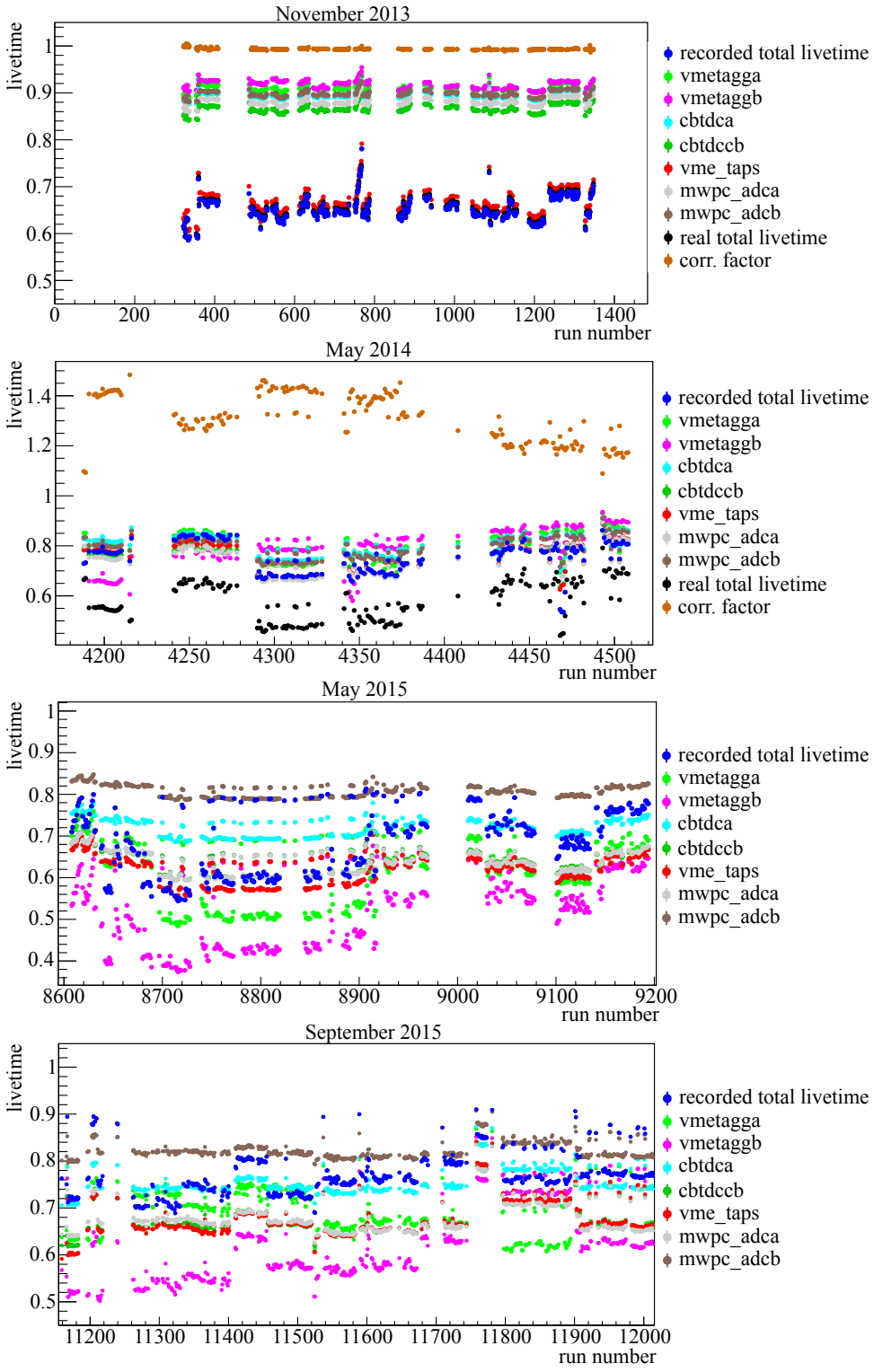

Figure 7.10: The livetimes of all individual detectors (tagger (vmetagga and vmetaggb), Crystal Ball (cbtdca and cbtdcb), TAPS (vme_taps), MWPCs (mwpc_adca and mwpc_adcb)) are plotted as a function of the run number. The total livetime is measured with free running VUPROM scalers for all four beamtimes. In addition trigger gated FASTBUS scalers were used in the November 2013 and May 2014 beamtimes. The total livetime has to the decreased by the correction factor for the May 2014 beamtime.

In a last step, the average correction factor for the May 2015 beamtime was determined. Table 7.2 lists the average correction factors for all beamtimes that need a correction.

beamtime	$\mathbf{f_{corr}^{livetime}}$
May 2014	1.3
May 2015	1.9
September 2015	1.7

Table 7.2: The average total livetime correction factor $f_{\text{corr}}^{\text{livetime}}$ is listed for the May 2014, May 2015 and September 2015 beamtimes.

It is noteworthy that the livetime problems and therefore the incorrect estimated photon flux has no consequence for the calculation of the helicity asymmetry E as the photon flux cancels out in the asymmetry. The correct livetime is however needed for a direct determination of the helicity dependent cross sections $\sigma^{1/2}$ and $\sigma^{3/2}$ (see e.g. [Pau16]). Thus, the helicity asymmetry E was not extracted by directly calculating the helicity dependent cross sections.

Due to the livetime problems that occurred and the observed sensitivity to bad tagger channels, the direct calculation method using the photon fluxes and target area densities was not utilized for the determination of the scaling factor s^C. Nevertheless, the comparison of both methods based on the September 2015 beamtime allows for an estimation of the relative systematic error of the scaling factor. The deviations between the methods are less than 3%.

7.1.2.2 Investigation of the $\cos\theta$ dependence of s^C

According to Equation (7.29), it was assumed that the acceptance of the butanol and *carbon+helium* data is approximately the same since in both data sets the same target cell within the same target cryostat was used. This section discusses the validity of this assumption.

First, it was investigated if anything in the detector geometry changed from the first November 2013 to the last September 2015 beamtime. It is stressed here that the *carbon+helium* beamtime was taken only in September 2015 and thus, it is important to check for differences between the older butanol beamtimes and the September 2015 beamtime. There are two main aspects that changed over the years and lead to differences in the detector acceptance: Not all Crystal Ball PMTs were functioning during data acquisition, which results in acceptance holes for specific angular ranges. Figure 7.11 shows the polar and azimuthal angle of detected Crystal Ball clusters. The number and position of broken PMTs changed over the two years. Thus, the acceptance changed. Furthermore, it is noticeable that the acceptance holes of the first two and last two beamtimes are similar.

In addition, comparisons of MC and data spectra revealed that a change of the target position occurred from around $z = 0\,\text{mm}$ in the November 2013 and in the May 2014 to $z = -3\,\text{mm}$ in the May 2015 and in the September 2015 beamtimes. Is is assumed that alignment problems between the Crystal Ball and the MWPCs before the May 2015 beamtime caused an imprecise calibration of the MWPCs, which are used as a reference for a precise target positioning. More details about the MWPCs calibration problems are given in [Spi19].

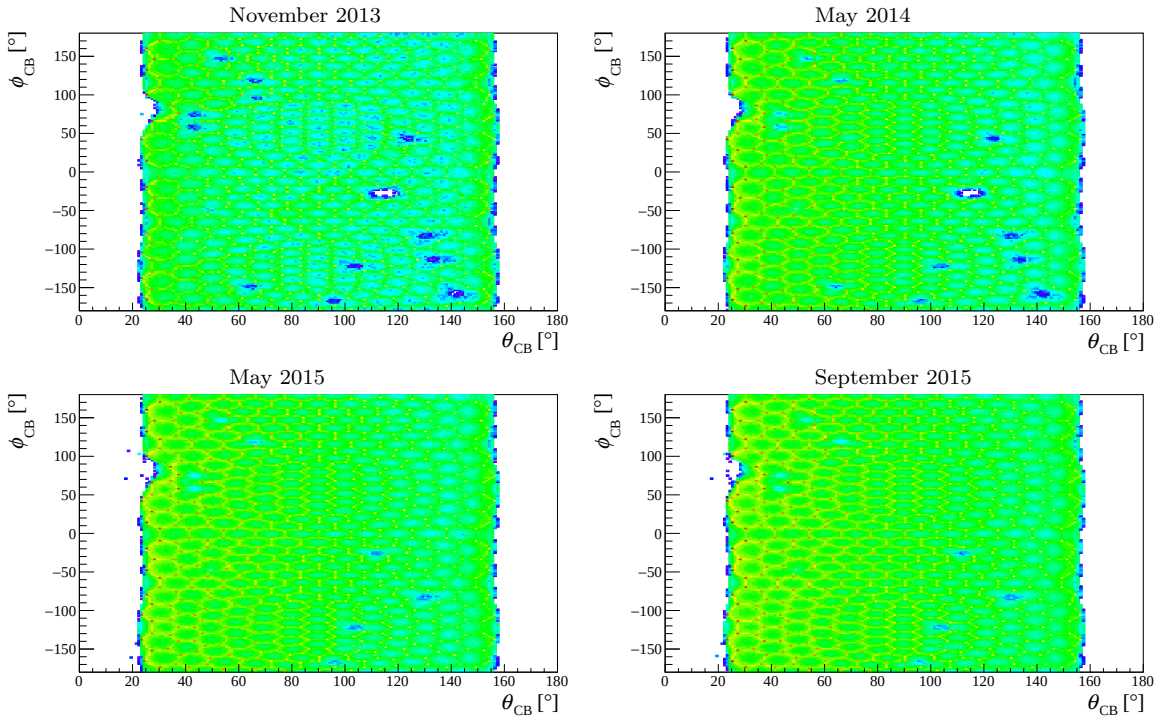

Figure 7.11: Overview of malfunctioning Crystal Ball PMTs over the four different beamtimes. These PMTs cause a hole in the Crystal Ball acceptance for certain polar and azimuthal angles of detected Crystal Ball clusters. Some broken PMTs were replaced between the beamtimes.

The influence of both, the Crystal Ball acceptance holes and the different target positions, were studied carefully with MC data.

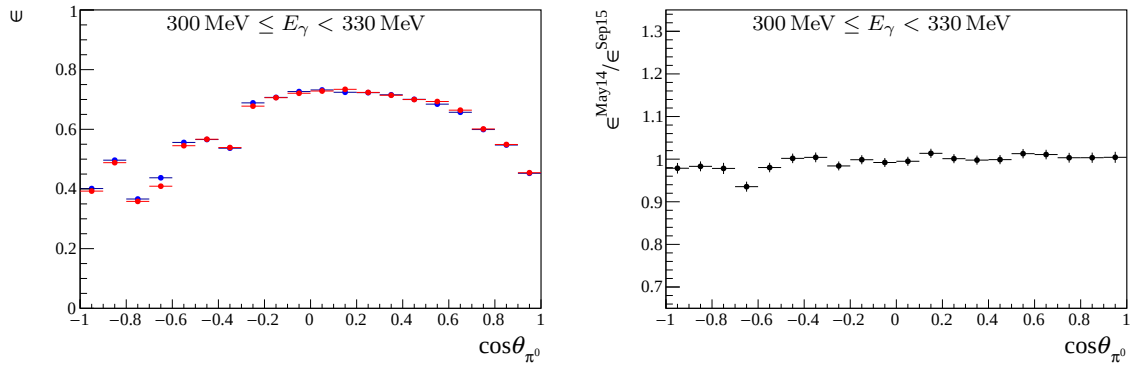

Figure 7.12: Left: The acceptance is plotted as a function of $\cos\theta_{\pi^0}$ for the energy bin 300 MeV $\leq E_\gamma <$ 330 MeV. The MC data were generated with a target position at $z = 0$ mm and by switching off the Crystal Ball elements with broken PMTs of the May 2014 beamtime (red) and at $z = -3$ mm and using the CB holes of the September 2015 beamtime (blue). Right: The ratio of the acceptances is plotted.

Figure 7.12 depicts the reconstruction and selection acceptance for one energy bin of the $p\pi^0$ final state using the target position and switching off Crystal Ball elements with broken PMTs, once for the May 2014 and once for the September 2015 beamtime. Taking the ratio of both acceptances, the $\cos\theta_{\pi^0}$ dependent scaling factor can be determined using the energy dependent

scaling factor $s^C(E_\gamma)$ and the ratio of acceptances in the following way:

$$s^C(E_\gamma, \cos\theta) = s^C(E_\gamma) \cdot \frac{\epsilon^{\text{but}}(E_\gamma, \cos\theta)}{\epsilon^C(E_\gamma, \cos\theta)} \tag{7.34}$$

The acceptance correction is a minor correction in the order of 2 - 6%. It is especially sensitive to the different target position of the butanol and carbon beamtimes in the transitional region between the Crystal Ball and the TAPS detector, which corresponds to $\cos\theta \approx -0.7$. This correction was applied for the November 2013 and May 2014 beamtimes. The acceptance differences between the May 2015 and September 2015 are negligibly small. An alternative approach would be scaling directly with energy and $\cos\theta$ dependence. However, this option was not chosen due to the limited *carbon+helium* data statistics, especially at higher beam photon energies.

Further parameters that did not remain consistent between the butanol and *carbon+helium* beamtimes, are the trigger thresholds of the Crystal Ball energy sum and the individual TAPS LED1 thresholds (see Table 2.4).

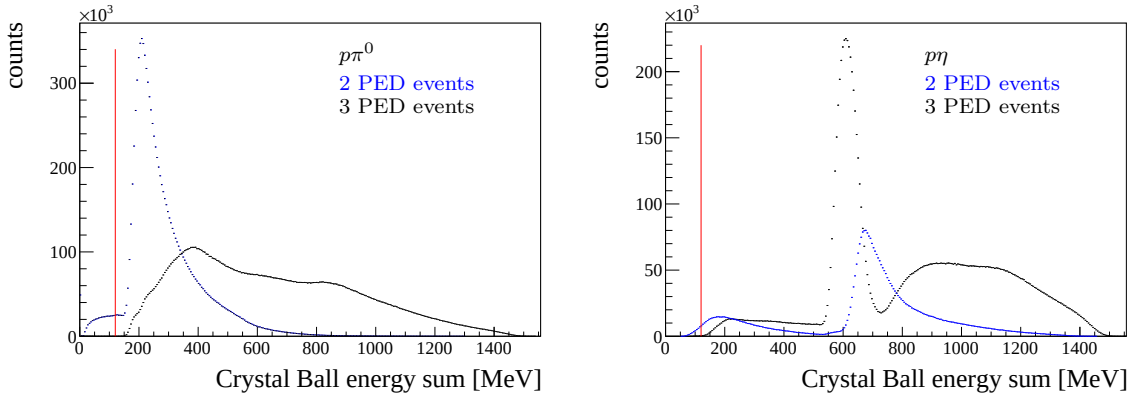

Figure 7.13: The Crystal Ball energy sum of 2 PED events (blue) and 3 PED events (black) is shown for MC data and for the $p\pi^0$ final state on the left and for the $p\eta$ final state on the right. The red line marks the highest chosen energy sum threshold of 120 MeV in the May 2015 beamtime.

The Crystal Ball energy sum is depicted in Figure 7.13 for 2 PED and 3 PED events and for both final states. The highest chosen energy sum threshold of 120 MeV was set during the May 2015 beamtime. The energy sum of the 3 PED events of both final states start at higher energies than 120 MeV and are therefore not sensitive to the trigger threshold. However, a portion of the 2 PED events were already rejected at trigger level. Since the measured energy sum has a strong $\cos\theta$ dependence, it was decided to determine the scaling factor of the 2 PED events with energy and $\cos\theta$ dependence using the missing mass spectra of each $(E_\gamma, \cos\theta)$ bin. Due to these trigger dependent problems, the non-hydrogen range of the missing mass spectra was selected carefully mostly on the left side of the missing mass peak for the November 2013 and May 2014 beamtimes, since low energy sum values correspond to high missing mass values.

7.1.2.3 Consistency check of the dilution factor

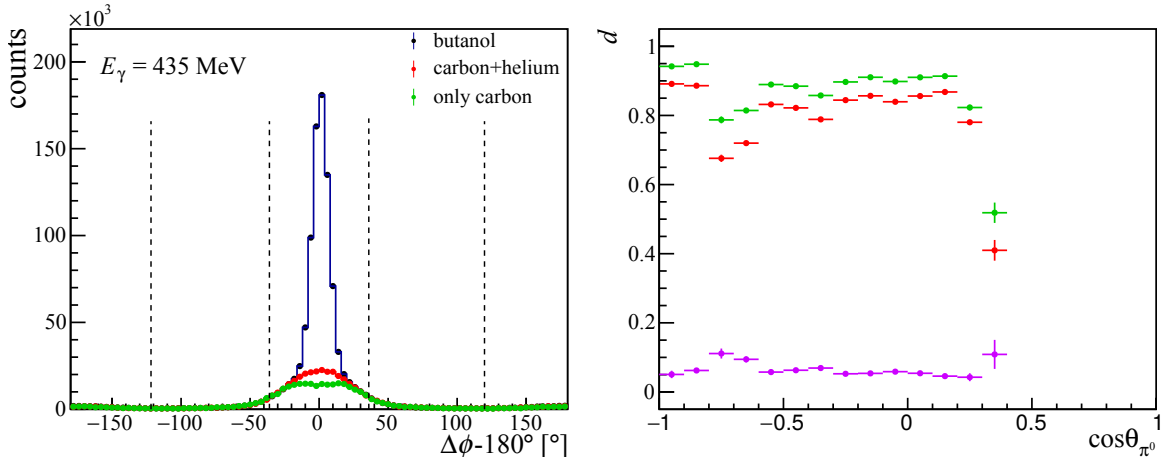

Figure 7.14: Left: The coplanarity spectra of the butanol data (dark blue) is shown together with the scaled *carbon+helium* (red) and *only carbon* (green) data using the non-hydrogen ranges, which are marked by the dashed lines. Right: The dilution factor is plotted as a function of $\cos\theta_{\pi^0}$ for 3 PED events when using *carbon+helium* (red) or *only carbon* (green) data. The absolute difference between both dilution factors is shown in violet. Above $\cos\theta_{\pi^0} > 0.4$ no more 3 PED events are present.

The dilution factor gives the fraction of polarizable hydrogen nucleons that are present in the selected data for each $(E_\gamma, \cos\theta)$ bin. The dilution factor can be increased from the naively assumed $\frac{10}{74} = 13.5\%$, which is based on the number of free hydrogen to bound carbon and oxygen nucleons in butanol (C_4H_9OH), to significantly higher values through a skillful choice of cut ranges (see Section 5.3). Values of up to 98% were achieved for 3 PED events of the $p\pi^0$ final state at low energies as shown in Figure 7.14. Due to the different widths of the coplanarity spectra for helium and carbon, it is important to use the *carbon+helium* data for a correct determination of the scaling factor and thus, the dilution factor (see Section 7.1.1). Utilizing the *only carbon* data leads to a systematically high dilution factor since the scaling factor s^C is determined systematically low. The absolute error that is done in this process is up to 10%. Therefore, all shown dilution factors were obtained with the *carbon+helium* data.

In a last step, the dilution factors of all four butanol beamtimes are compared to each other. Since the exact same cuts are applied to the data of all four beamtimes, it is expected to get the same dilution factors for all beamtimes. This consistency check of the dilution factors between the four beamtimes is depicted in Figures 7.15-7.18 for the $p\pi^0$ final state and in Figure 7.19 for the $p\eta$ final state. The dilution factors of the 3 and 2 PED events are in very good agreement for all four beamtimes for the $p\pi^0$ and the $p\eta$ final states as expected. The dilution factor is very high from over 90% at $E_\gamma = 285\,\text{MeV}$ and around 60% at $E_\gamma = 1400\,\text{MeV}$ for the 3 PED events. A dashed line marks the point where the 2 PED events start to contribute in each energy bin. Here, the dilution factor drops dramatically to 10% - 30% because the angular cuts can not be applied for the 2 PED events and, hence, the bound nuclei contribution can not be as efficiently removed from the data as for the 3 PED events. The drop at $\cos\theta_{\pi^0} \approx -0.7$ or $\cos\theta_\eta \approx -0.3$ corresponds to the transitional region between the Crystal Ball and the TAPS detector for the proton.

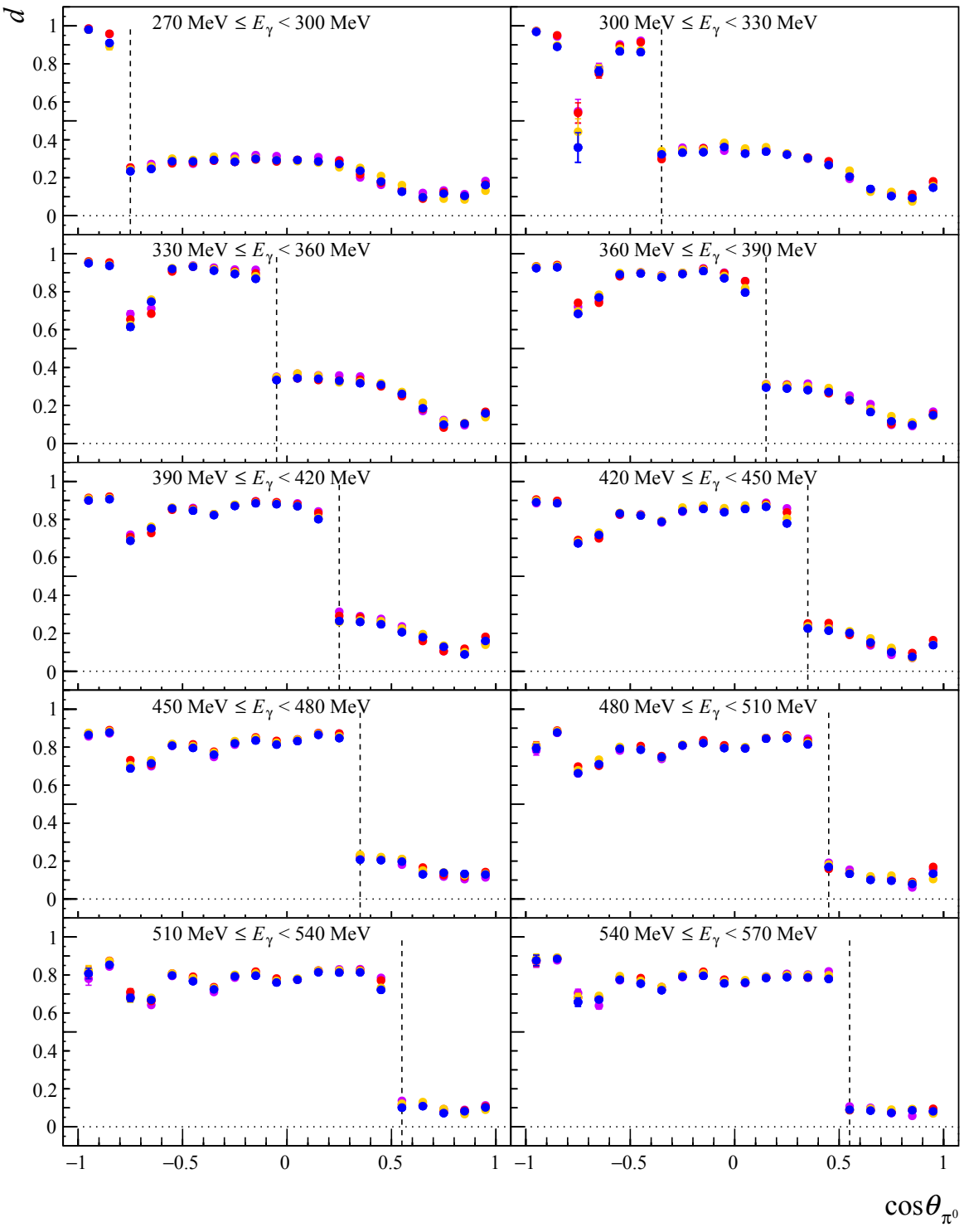

Figure 7.15: The dilution factor is depicted for the energy range of 270 MeV $\leq E_\gamma <$ 570 MeV as a function of $\cos\theta_{\pi^0}$ for the $p\pi^0$ final state and for the November 2013 (red), May 2014 (violet), May 2015 (yellow) and September 2015 (blue) beamtimes. The dashed line marks the starting point of the 2 PED events.

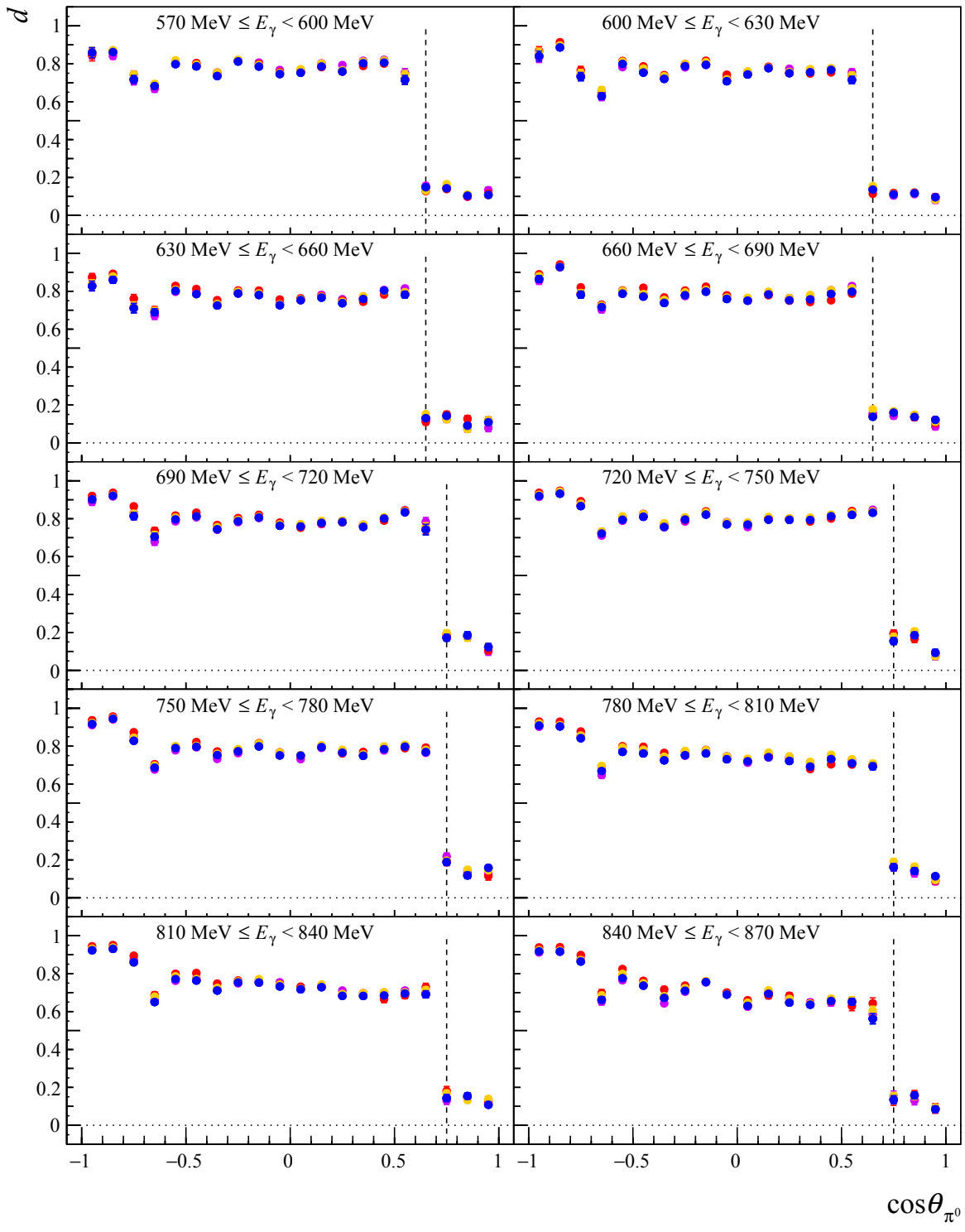

Figure 7.16: The dilution factor is depicted for the energy range of 570 MeV $\leq E_\gamma <$ 870 MeV as a function of $\cos\theta_{\pi^0}$ for the $p\pi^0$ final state and for the November 2013 (red), May 2014 (violet), May 2015 (yellow) and September 2015 (blue) beamtimes. The dashed line marks the starting point of the 2 PED events.

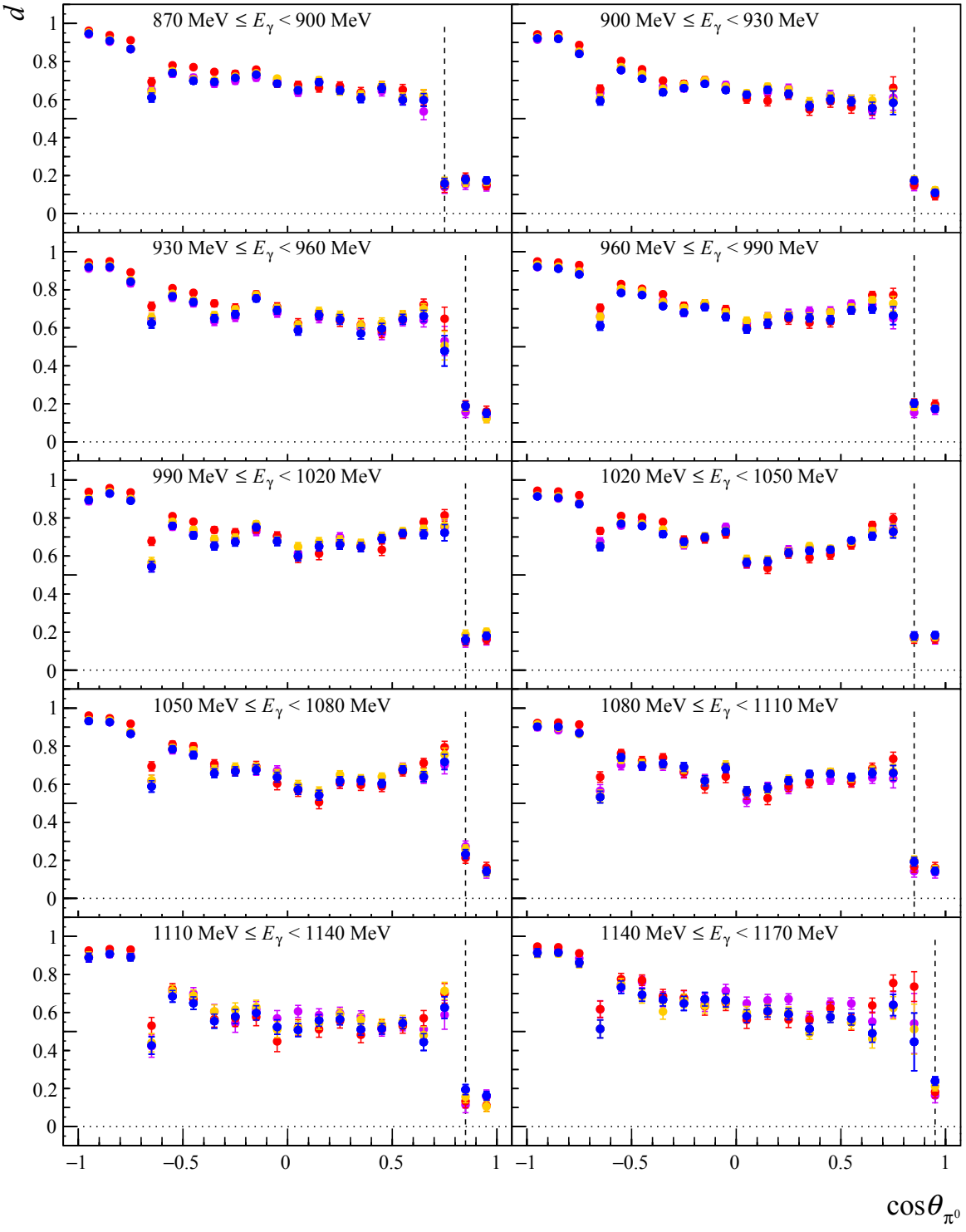

Figure 7.17: The dilution factor is depicted for the energy range of 870 MeV $\leq E_\gamma <$ 1170 MeV as a function of $\cos\theta_{\pi^0}$ for the $p\pi^0$ final state and for the November 2013 (red), May 2014 (violet), May 2015 (yellow) and September 2015 (blue) beamtimes. The dashed line marks the starting point of the 2 PED events.

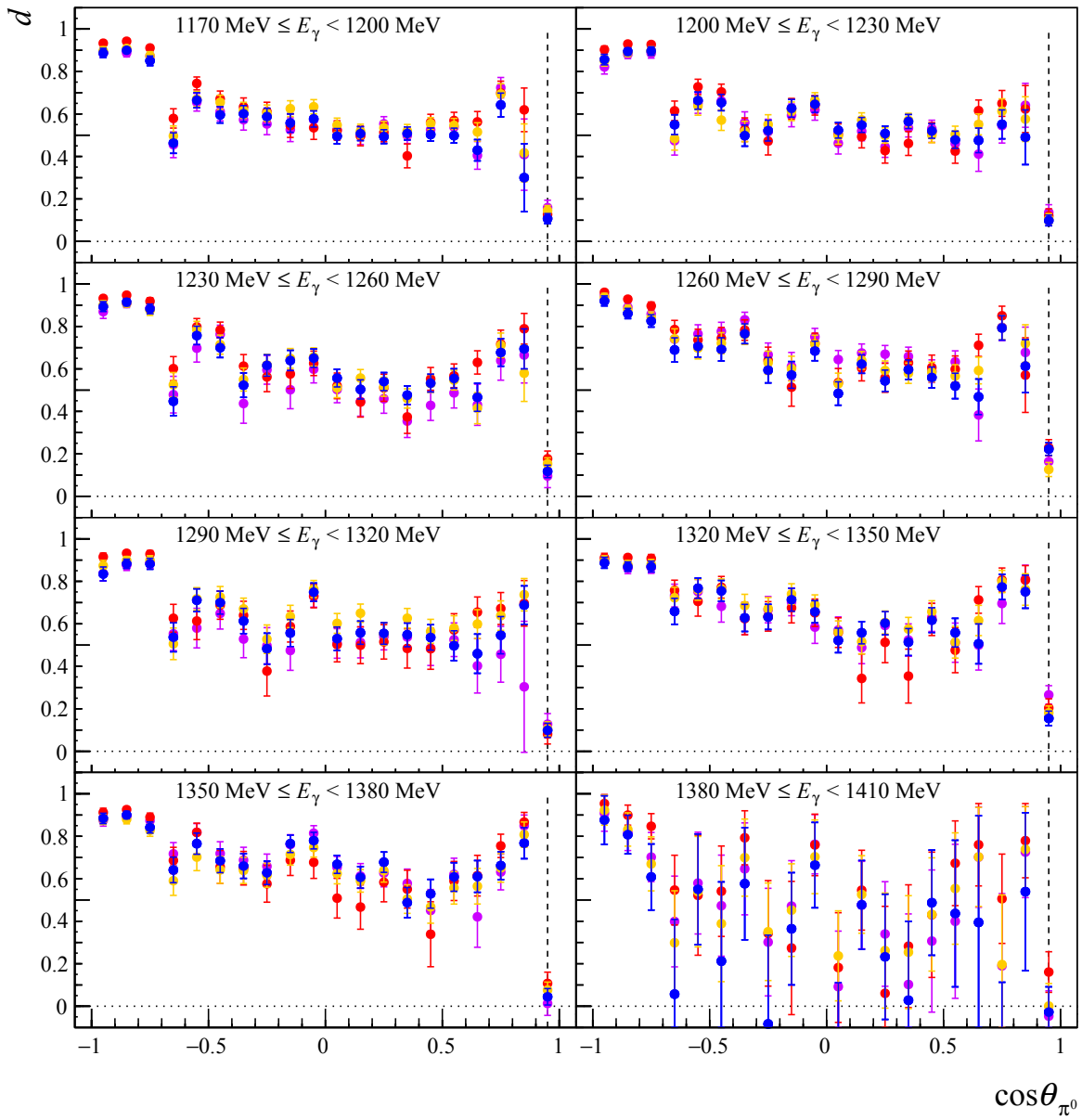

Figure 7.18: The dilution factor is depicted for the energy range of 1170 MeV $\leq E_\gamma <$ 1410 MeV as a function of $\cos\theta_{\pi^0}$ for the $p\pi^0$ final state and for the November 2013 (red), May 2014 (violet), May 2015 (yellow) and September 2015 (blue) beamtimes. The dashed line marks the starting point of the 2 PED events.

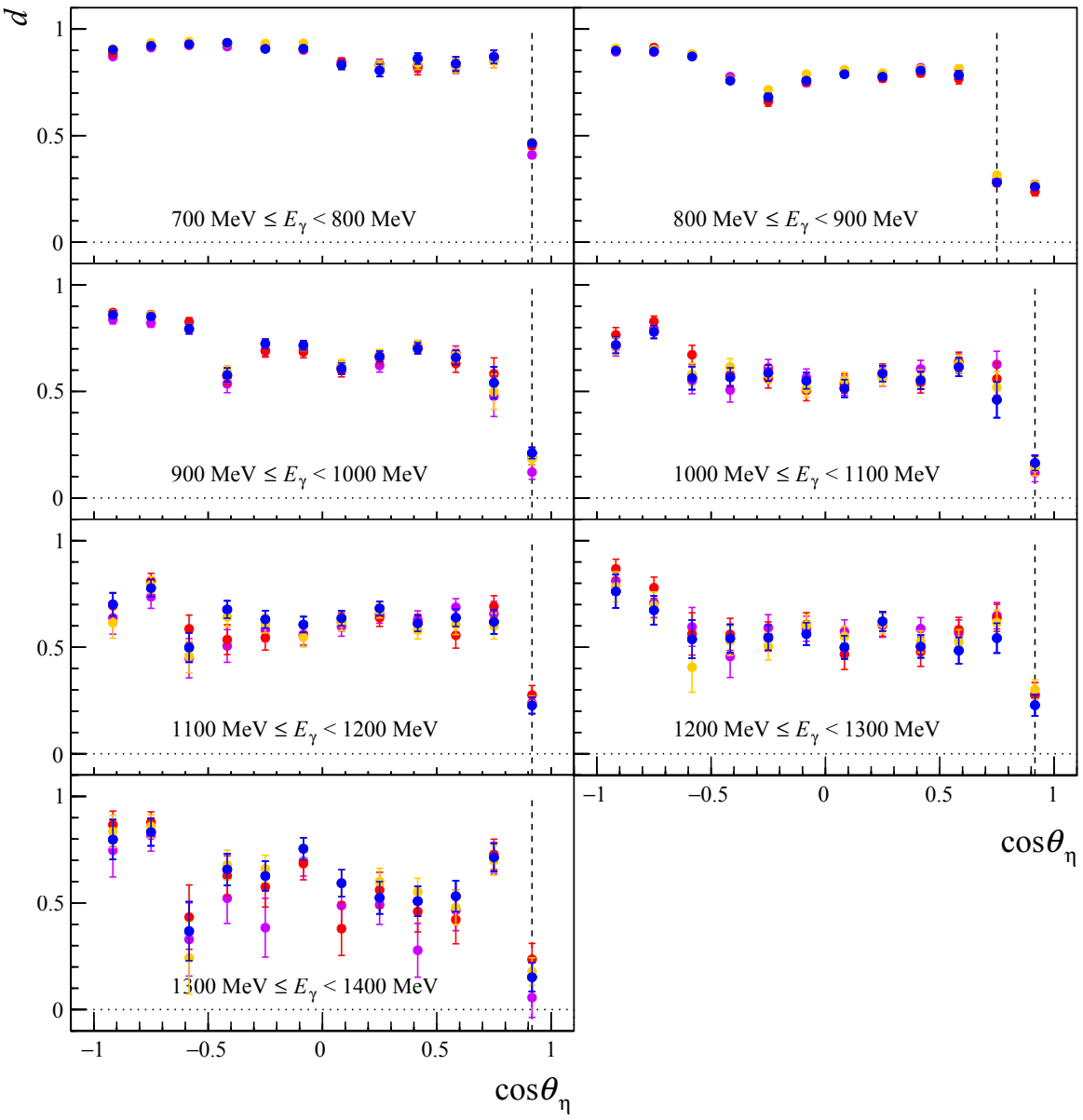

Figure 7.19: The dilution factor is depicted for the energy range of 700 MeV $\leq E_\gamma <$ 1400 MeV as a function of $\cos\theta_\eta$ for the $p\eta$ final state and for the November 2013 (red), May 2014 (violet), May 2015 (yellow) and September 2015 (blue) beamtimes. The dashed line marks the starting point of the 2 PED events.

7.2 Beam and target polarization degree

In order to determine the double polarization observable E, the knowledge of the circular polarization degree and the target polarization degree are needed. This section gives an overview of how the circular polarization degree (see Section 7.2.1) and the target polarization degree (see Section 7.2.2) were determined during data taking.

7.2.1 Circular polarization degree

The circular polarization degree is determined using the beam photon energy E_γ, the initial MAMI electron energy E_0 and the polarization degree of the longitudinally polarized electron p_e according to Equation (2.13). As already explained, either a Mott (see Section 2.2.3) or a Møller (see Section 2.2.4) polarimeter can be utilized to determine the longitudinal electron polarization degree.

7.2.1.1 Mott measurement

During each beamtime a Mott measurement was performed on a daily basis. The measured left-right asymmetry A by the MAMI operator, the Wien filter rotation angle $\phi_{\text{Wien}} = 81°$, the effective Sherman function $S_{\text{eff}} = 0.3930$ [Ott12] and the correction factor due to a small transverse polarization component $f_{\text{trans}}^{\text{corr}} = 1.0551$ [Ott12] determine the longitudinal electron polarization degree in the following way:

$$p_e = \frac{A}{\sin(\phi_{\text{Wien}}) \cdot S_{\text{eff}}} \cdot f_{\text{trans}}^{\text{corr}} \tag{7.35}$$

$$= \frac{A}{\sin(81°) \cdot 0.3930} \cdot 1.0551. \tag{7.36}$$

The Mott asymmetry A was measured for both helicity states. Since the two asymmetry values did not deviate by more than 0.5%, the average of the electron polarization degree of both helicity states was taken. Therefore, it holds

$$p_\gamma^\uparrow = p_\gamma^\downarrow. \tag{7.37}$$

The obtained values for the average longitudinal electron polarization degree using Equation (7.36) are depicted in Figure 7.20 for all beamtimes. On average, the longitudinal polarization degree of the electrons is 80% for the November 2013, 82% for the May 2014, 74% for the May 2015 and 77% for the September 2015 beamtimes. Within only 30 minutes of measurement it is possible to obtain a value for the longitudinal electron polarization degree with less than 0.2% statistical error. A linear fit is used to interpolate in between the Mott measurements. At the end of the September 2015 beamtime, the GaAs crystal had to be changed, which lead to a change of the polarization degree. Therefore, two separate linear fits were performed for the September 2015 beamtime.

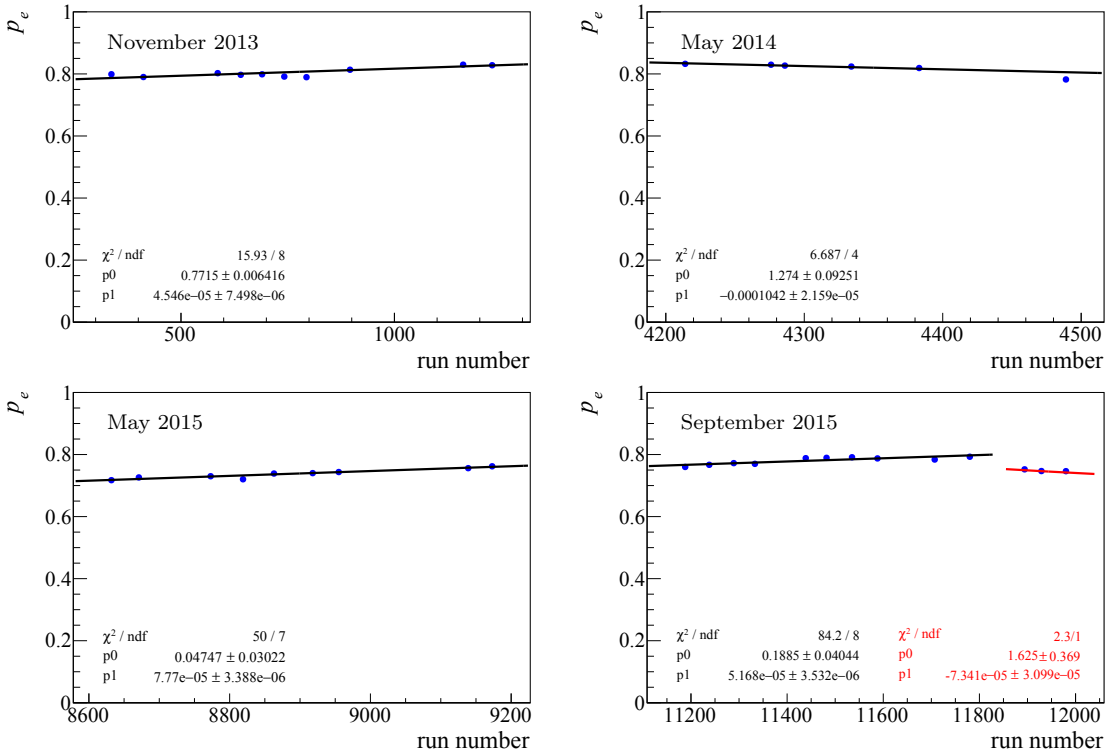

Figure 7.20: The polarization degree of the longitudinally polarized MAMI electrons is plotted for all four beamtimes (blue points) as a function of the run number using the Mott measurements. The measurements were taken approximately once per day. Therefore, a linear fit was used to interpolate between the measurements (black line). The statistical errors are plotted, but are negligibly small.

The relative systematic error of the longitudinal electron polarization degree is given by the following three points [Ott15; TAR11]:

- 1.1% due to the necessary deflection of the electron beam by ±3.1° at 1557 MeV from the accelerator plane shortly before reaching the A2 experimental hall,
- 2.2% because of small contributions from the transverse electron polarization degree and
- 1.0% is the estimated uncertainty of the Sherman function, the thickness of the Mott foil and background contributions during the Mott measurement.

Systematic effects concerning ϕ_{Wien} are negligibly small [TAR11]. Adding the above mentioned error contributions in quadrature, this leads to a total relative systematic error of 2.7% when using a Mott measurement.

7.2.1.2 Cross check with Møller measurement

In addition to the Mott measurements, data runs were taken with a Møller radiator in regular time intervals. Dr. S. Costanza [Cos14] determined the longitudinal electron polarization degree from the Møller runs using Equation (2.18). Here, data were used from a beamtime which took place between the November 2013 and the May 2014 beamtimes[4]. A direct comparison of the

[4] This February 2014 beamtime was taken with almost the same experimental conditions as the analyzed beamtimes here with the exception that a d-butanol target was used.

obtained polarization degree values using Mott and Møller scattering is shown in Figure 7.21. The statistical error bars of the Møller measurement are significantly larger and deflect the obtained statistics with the Møller radiator.

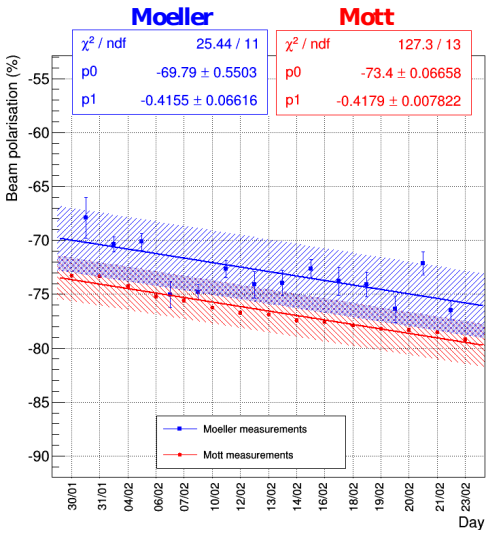

Figure 7.21: The longitudinal polarization degree of the MAMI electrons is depicted as obtained from daily Mott measurements (red points) and from Møller measurements (blue points) using all Møller runs in between the Mott measurements. The respective systematic errors are depicted as striped areas. The results are in agreement within their systematic errors. Taken from [Cos14].

The sources for systematic errors during the Møller measurements consist of the Møller foil polarization degree, the uncertainty of the rotational angle α of the Møller foil (see Section 2.2.4) and the tagger energy calibration since certain tagger channels are used to measure the Møller asymmetry [Cos14]. In total, the relative systematic error of the longitudinal electron polarization degree obtained with the Møller measurements is approximately 3% [Cos14]. The systematic errors are drawn as striped areas in Figure 7.21. Within their respective systematic errors the results of the Mott and Møller measurements are in agreement.

Since the Møller measurements have significantly larger statistical and systematic errors, the average electron polarization degree values of the Mott measurements were used to calculate the circular beam photon polarization degree according to Equation (2.13).

7.2.2 Target polarization degree

The target polarization degree can be measured using a NMR technique [Lin14]. For this purpose a coil has to be placed around or inside the target cell, which corresponds to a series LC circuit. When the radio frequency is equal to the Lamor frequency of protons, a NMR signal is measured. The area under the NMR signal A is proportional to the polarization degree of the butanol target. The signal is calibrated using the NMR signal A_{TE} measured at thermal equilibrium (TE):

$$p_T = \frac{p_{\mathrm{TE}}}{A_{\mathrm{TE}}} A. \tag{7.38}$$

The polarization degree at thermal equilibrium p_{TE} is given for spin 1/2 particles by [Ave+99]:

$$p_{\mathrm{TE}} = \tanh\left(\frac{\mu_p B}{2k_B T}\right), \tag{7.39}$$

where μ_p is the magnetic moment of the proton, k_B the Boltzmann constant, B the magnetic field strength and T the temperature. The NMR measurement takes place before the start of the beamtime, directly after the polarization process. Further measurements are performed if necessary during the beamtime to monitor when repolarization of the target is required and at the end of the beamtime. Thus, the target polarization degree can not be obtained during a normal data run when the target is in the frozen spin mode. Using the measured initial and final target polarization degree values p_T^i and p_T^f and assuming that the target cell temperature and the magnetic field of the holding coil are stable in between, it is possible to calculate the relaxation time τ and the target polarization degree of each run p_T^{run}:

$$p_T^{\mathrm{run}} = p_T^i e^{-\frac{\Delta t}{\tau}} \qquad \text{with} \qquad \tau = \frac{\Delta t_{if}}{\ln(p_T^i/p_T^f)}, \tag{7.40}$$

with Δt_{if} being the time span between the initial and final polarization measurement and Δt being the time span between the measurement of p_T^i and the time in the middle of the run. Since the relaxation time is much larger ($\tau \approx 1000\,\mathrm{h}$, see Table 7.3) than the time span of one run ($\approx 30\,\mathrm{min}$), a single polarization value is assigned to each run. The temperature of the target cell was stable within $\pm 0.2\,\mathrm{mK}$ [Mac17], which is shown in Figure 7.22. All measured values of p_T^i and p_T^f and the calculated relaxation times τ are listed in Table 7.3 for all beamtimes. The polarization degree values are plotted as a function of the run number in Figure 7.23.

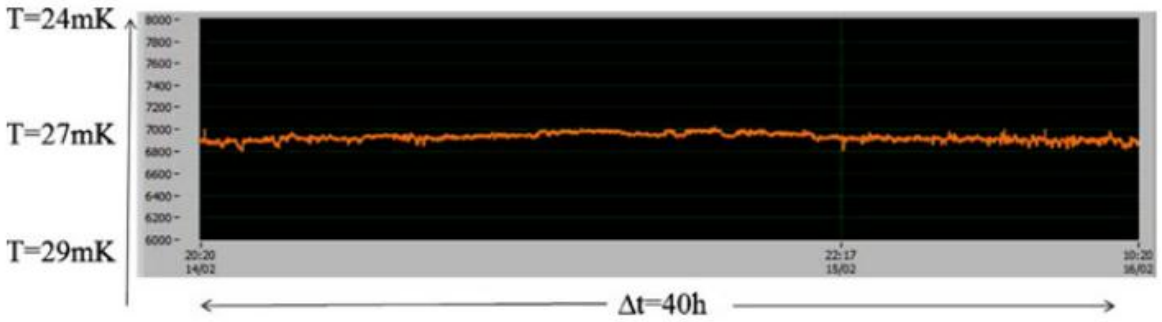

Figure 7.22: The monitored temperature of the frozen spin butanol target is depicted as a function of time span of almost two days. Taken from [Mac17].

beamtime	run number	p_T^i [%]	p_T^f [%]	τ [h]
November 2013	320	63.00	59.25	3707
	860	-64.69	-53.14	1223
May 2014	4181	-64.50	-53.17	1082
May 2015	8607	70.50	66.40	472
	8642	66.40	52.75	307
	8790	64.20	54.70	699
	9030	66.10	58.30	548
	9098	-70.50	-66.90	995
	9178	-66.90	-65.44	974
September 2015	11159	-84.90	-81.65	1038
	11203	-80.50	-73.90	1038
	11390	87.15	79.02	1736

Table 7.3: Overview of all measured initial and final target polarization degree values p_T^i and p_T^f as obtained by the target group. Additionally, the run number, that was taken directly after the polarization measurement, is given. The relaxation times τ were calculated according to Equation (7.40) (the values for November 2013 and May 2014 are taken from [Lin14]). Note: During the May 2015 beamtime a small helium leak existed in the target cryostat which led to smaller relaxation times compared to the other beamtimes. The leak was fixed at the end of the beamtime when the target polarization direction was changed.

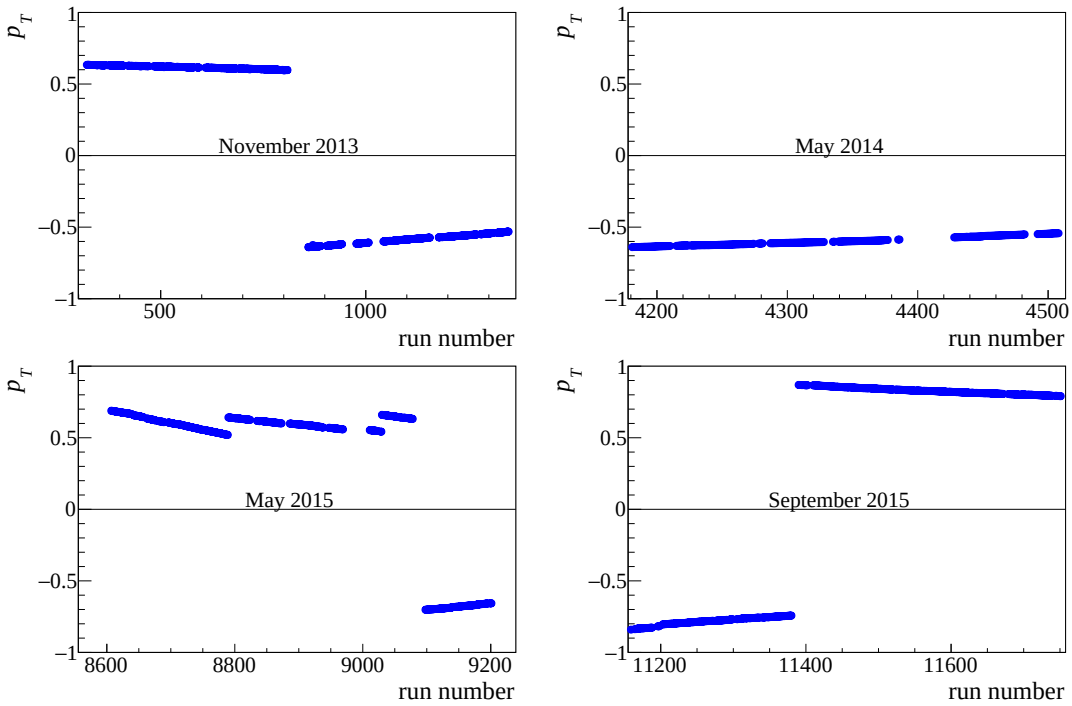

Figure 7.23: The target polarization degree values are plotted as a function of the run number for all utilized runs of all four beamtimes.

7.2.2.1 Problems with the target polarization values

Using the event yields $N^{1/2}$ and $N^{3/2}$, the dilution factor d, and the circular and target polarization degrees, the helicity asymmetry E can be determined according to Equation (7.24). The results of the double polarization observable E exhibit systematic offsets between the four different butanol beamtimes (November 2013, May 2014, May 2015 and September 2015). Figure 7.24 shows the results of E for the November 2013 and the September 2015 beamtimes for nine selected energy bins of the $p\pi^0$ final state, out of which six are near the $\Delta(1232)\frac{3}{2}^+(P_{33})$ resonance region ($E_\gamma = 200\,\text{MeV}$ - $450\,\text{MeV}$). It is noticeable that the results of the September 2015 beamtime are in agreement with the PWA solutions, while the results of the November 2013 beamtime are located below the expected PWA solutions. The results of the November 2013 beamtime are surprising considering that the $\Delta(1232)\frac{3}{2}^+(P_{33})$ resonance is well known and all PWA solutions predict the same parabola curve as expected for a P_{33} resonance contribution. Additionally, some of the data points of the November 2013 beamtime lie in an unphysical region below -1.

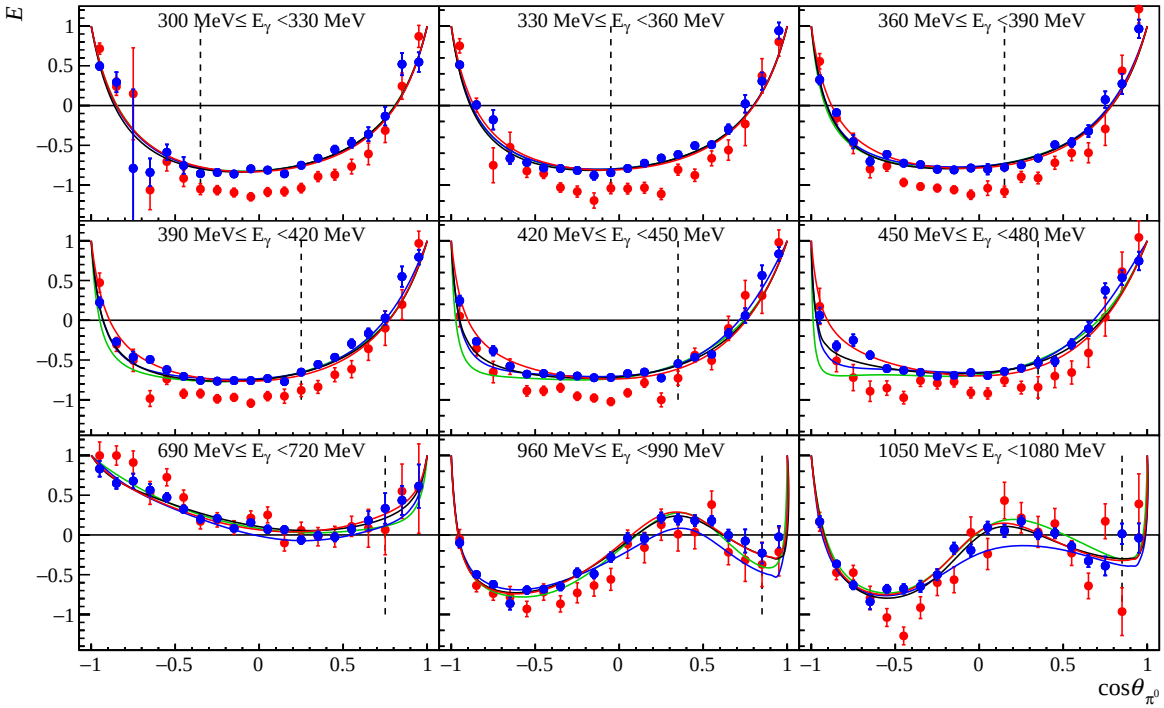

Figure 7.24: Comparison of the E results as obtained from the November 2013 data (red points) and from the September 2015 data (blue points) for selected energy bins of the $p\pi^0$ final state. Systematic deviations are observed. Whenever the values of E are negative, the November 2013 data lie below the September 2015 data points and if the values are positive, the opposite is observed. PWA solution of the BnGa-2014-01 (black line), BnGa-2014-02 (red line) [Gut+14], JüBo-2016 (green line) [Ani+16] and SAID-CM12 (blue line) [Wor+12] are plotted as well. Note: the first three PWA solutions are fits to existing CBELSA/TAPS data (for $E_\gamma > 600\,\text{MeV}$) and therefore agreement to the extracted data is expected. The dashed line marks the point where the 2 PED events start.

This systematic is not only present near the $\Delta(1232)\frac{3}{2}^+(P_{33})$ resonance region, but persists throughout all energy bins. Three examples are given in the third row of Figure 7.24 as well. A

comparison of all energy bins of each of the November 2013, May 2014 and May 2015 beamtime results to the September 2015 beamtime results are depicted for the $p\pi^0$ final state in Figures C.1 - C.20 in the appendix.

Similar problems exist for the $p\eta$ results as well. Here, the results of the November 2013 beamtime are located significantly higher, at approximately 1.3, than the expected value of 1 near the $p\eta$ photoproduction threshold (due to the dominant $N(1535)\frac{1}{2}^-(S_{11})$ resonance contribution). These results also lie in an unphysical region and are therefore not correct. Further investigations indicated that the results of the November 2013 beamtime systematically deviate from the results of the September 2015 beamtime by a constant factor independent of E_γ and $\cos\theta$. In addition, the same factor is present in both the $p\pi^0$ and $p\eta$ final states. The results of the May 2014 and May 2015 beamtimes reveal the same problems in comparison to the September 2015 beamtime albeit with different large systematics (see Figures C.1 - C.20 in the appendix). The observed systematic problems of the November 2013, May 2014 and May 2015 beamtimes led to an investigation of each of the components used for the determination of the helicity asymmetry E. Since the asymmetry is too large in the November 2013 beamtime, it was concluded that one of the parameters used to determine E was estimated too low. Probable reasons for the observed problems and the accepted solution are discussed in the following.

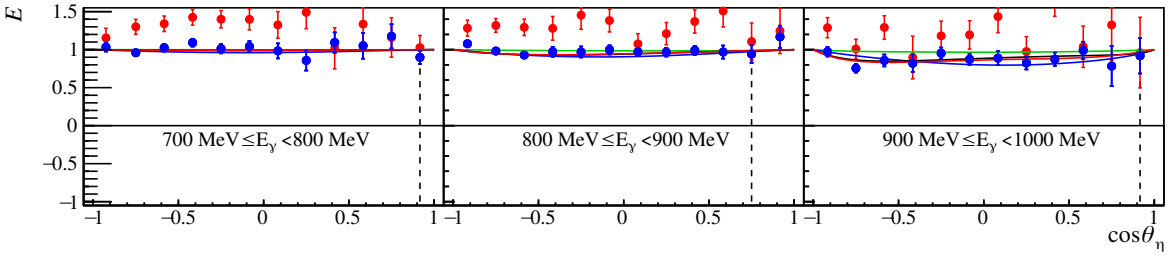

Figure 7.25: Comparison of the E results as obtained from the November 2013 data (red points) and from the September 2015 data (blue points) for selected energy bins of the $p\eta$ final state. Systematic deviations are observed. PWA solution of the BnGa-2014-01 (black line), BnGa-2014-02 (red line) [Gut+14], JüBo-2016 (green line) [Ani+16] and SAID-GE09 (blue line) [Bri+] are plotted as well. The dashed line marks the point where the 2 PED events start.

- **diamond runs**: One of the main goals of the analyzed A2 data is to measure the double polarization observables G and E simultaneously, which had not been attempted before. Therefore, one has to contemplate the possibility that the main assumption, that E can be measured with longitudinally polarized electrons and a diamond radiator in the same way as with an amorphous radiator, is not valid. Since some data were taken with the Møller radiator during each beamtime, the double polarization observable E was also determined using data obtained with the Møller radiator. The results obtained with the Møller radiator are shown for the May 2014 beamtime in Figure 7.26 for the $p\pi^0$ and Figure 7.27 for the $p\eta$ final state. The extracted helicity asymmetry E using the Møller radiator exhibits the same problems as the results obtained with the diamond radiator. Therefore, it can be excluded that the data taken with the diamond radiator are posing a problem[5].

[5] A more detailed discussion of the comparison of Møller and diamond data follows in Chapter 8

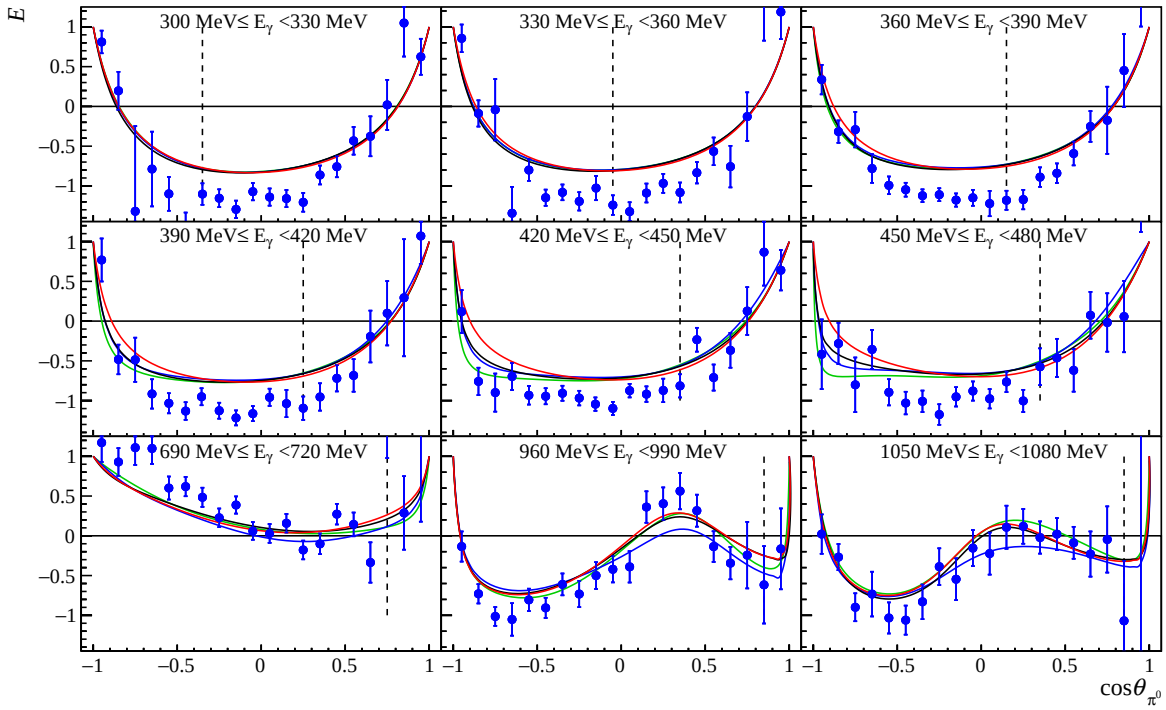

Figure 7.26: The helicity asymmetry E is depicted for the May 2014 Møller runs (blue points) for selected energy bins of the $p\pi^0$ final state. PWA solution of the BnGa-2014-01 (black line), BnGa-2014-02 (red line) [Gut+14], JüBo-2016 (green line) [Ani+16] and SAID-CM12 (blue line) [Wor+12] are plotted as well.

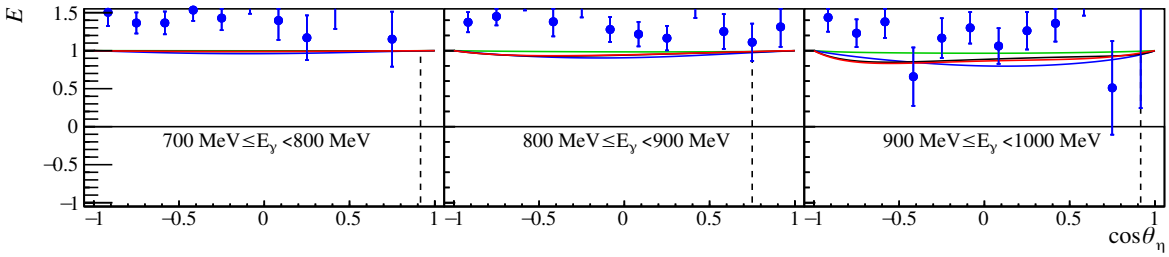

Figure 7.27: The helicity asymmetry E is depicted for the May 2014 Møller runs (blue points) for selected energy bins of the $p\eta$ final state. PWA solution of the BnGa-2014-01 (black line), BnGa-2014-02 (red line) [Gut+14], JüBo-2016 (green line) [Ani+16] and SAID-GE09 (blue line) [Bri+] are plotted as well.

- **event yield difference and helicity information**: If the helicity information is not correct e.g. because the MAMI electron helicity bit was set incorrectly in the data, it could lead to an incorrect event yield difference $N^{1/2} - N^{3/2}$, where events would have been assigned to the wrong helicity state and therefore to the wrong event yield. Indeed, this scenario occurred for a few runs of the November 2013 and the May 2015 beamtimes. The helicity bit was set incorrectly to 0 for all events of these runs (see Figure 7.28). All these runs were rejected from the analysis. The case, that a few data runs with a wrong

helicity information were overlooked in the analysis, can be excluded as well, since the $p\pi^0$ results would suggest therefore that too many events are incorrectly assigned to the $N^{3/2}$ event yield, whereas the $p\eta$ results would indicate that too many events are assigned incorrectly to the $N^{1/2}$ event yield. However, this can not occur at the same time.

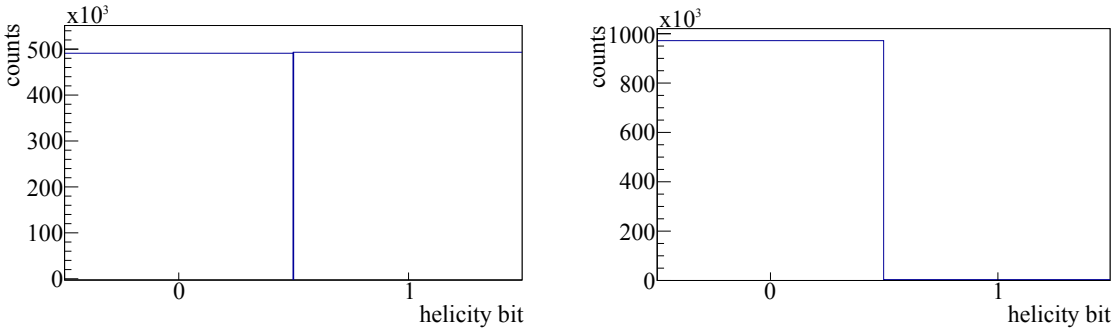

Figure 7.28: Left: The helicity bit information of a normal run with an almost equal amount of data for both helicity states (0 corresponds to the $\downarrow_H$ and 1 to the $\uparrow_H$ helicity state). Right: Typical run with wrong helicity bit information.

- **background**: In the case that a large amount of background exists in the selected data, it could lead to incorrect event yields and therefore incorrect helicity asymmetry results. However, as shown in Section 5.3.3, the background contribution is below 5% for the $p\pi^0$ channel and below 10% in the $p\eta$ channel. Besides, the background is not constant over E_γ and $\cos\theta$, and is not the same for both final states. Therefore, the remaining background contributions after the event selection are not the reason for the observed problematic results.

- **dilution factor**: Another possibility lies in the dilution factor being estimated too small. This would solve the problem for both $p\pi^0$ and $p\eta$ results. Figures 7.15 - 7.19 show the dilution factors for all four beamtimes. It is evident that the dilution factors of all four beamtimes are consistent with each other. No significant differences/systematic offsets exist between the four beamtimes regarding the dilution factors. Moreover, even if the dilution factor was estimated incorrectly, it can not be higher than 100%. However, this would be needed to solve the problematic results of the November 2013 beamtime for example, since the dilution factors of the 3 PED events lie mostly between 80% - 97% below 600 MeV for the $p\pi^0$ final state and below 900 MeV for the $p\eta$ final state. Therefore, the dilution factor can be ruled out as a possible source of the problematic results.

Additionally, Prof. Paolo Pedroni extracted the difference of the helicity dependent cross sections $\Delta\sigma = \sigma_{3/2} - \sigma_{1/2}$ for the $p\pi^0$ final state. The advantage of this method is that it does not need any carbon background subtraction as it cancels out in the difference. The obtained results are compared to existing GDH data [Tho06] (see Figure 7.29) and show the same systematic deviations from existing data as the results of E.

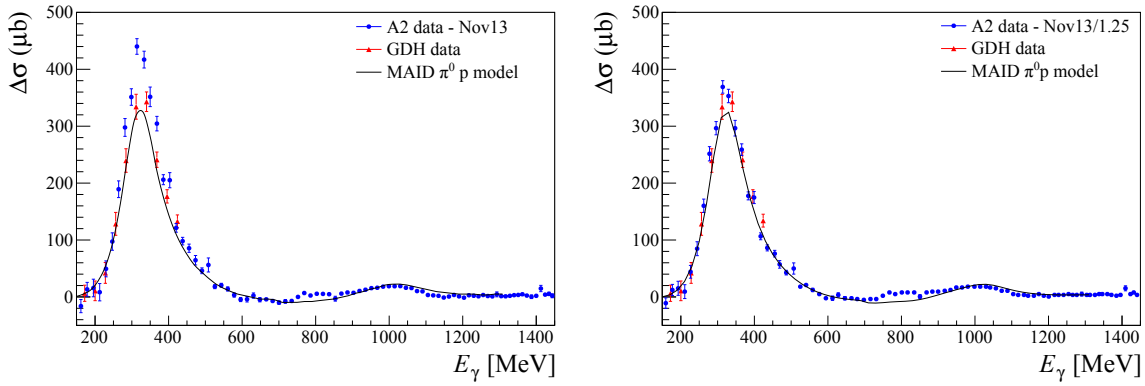

Figure 7.29: The difference of the helicity dependent cross sections $\Delta\sigma = \sigma_{3/2} - \sigma_{1/2}$ is plotted as a function of the beam photon energy. The blue data points represent the results for the $p\pi^0$ final state obtained using the November 2013 beamtime data. They are compared to existing GDH data [Tho06]. The black line shows the PWA solution of MAID 2007. Left: The results are shown using the measured target polarization degree values. Right: The target polarization degree is increased by a factor of ≈1.25. Taken from [Ped].

- **circular polarization degree**: The circular polarization degree strongly depends on the determined MAMI electron beam polarization degree. As discussed in Sections 7.2.1.1 and 7.2.1.2, both Mott and Møller measurement give consistent results. It is not very probable that both methods lead to wrong results. Additionally, increasing the circular polarization degree values by a factor of roughly 1.4, as needed for the May 2014 beamtime, leads to unphysical polarization values that are higher than 100%. Furthermore, the results of the double polarization observable G [Spi19] also indicate systematic deviations between the November 2013, May 2014 and May 2015 beamtimes to the September 2015 beamtime. However, G is obtained using linearly polarized photons and does not depend on the circular polarization degree. Thus, the circular polarization degree can be safely ruled out as the reason for the observed problems.

- **target polarization degree**: Excluding all the above mentioned parameters, the most probable explanation for the results is that the target polarization degree values, as obtained from the NMR measurements, were estimated too low in the November 2013, May 2014 and May 2015 beamtimes. Dr. Andreas Thomas and Dr. Gerhard Reicherz conducted an investigation of whether problems could occur during the NMR measurement, which took place before the start of the September 2015 beamtime [Rei]. Tests were performed with the NMR coil wound on the outside of the target cell container as depicted in Figure 7.30 on the right. This configuration of the NMR coil resembled the chosen configuration of the November 2013, May 2014 and May 2015 beamtimes. According to Dr. Andreas Thomas a small ice coat can form on the NMR coil during the time when the target material with the target cell is inserted into the cryostat. This ice affects the NMR signal since the ice hydrogen nuclei have the same Lamor frequency as the hydrogen nuclei of the butanol target. Since the ice nuclei are unpolarized, the measured NMR signal is falsified and does not represent the NMR signal of only the hydrogen nuclei of the butanol target. Thus, the NMR signal is decreased and measurements of p_T^i and p_T^f are too small. The target group estimated that an ice coat on the NMR coil can lead to a decrease of

the polarization degree by around 10%. However, it is difficult to determine a correction factor in retrospect, since it is not possible to know how much ice was located on the NMR coil during the, already taken, data of the November 2013, May 2014 and May 2015 beamtimes. Dr. Andreas Thomas and Dr. Gerhard Reicherz were able to resolve the issue with the ice by winding the NMR coil on the inside of the target cell as demonstrated in Figure 7.30. Utilizing this configuration, no ice coat can be formed and the polarization degree is measured at the center, where the photon beam goes through the target during normal data taking. Therefore, this configuration gives the best estimation of the target polarization degree and was used for the last September 2015 beamtime.

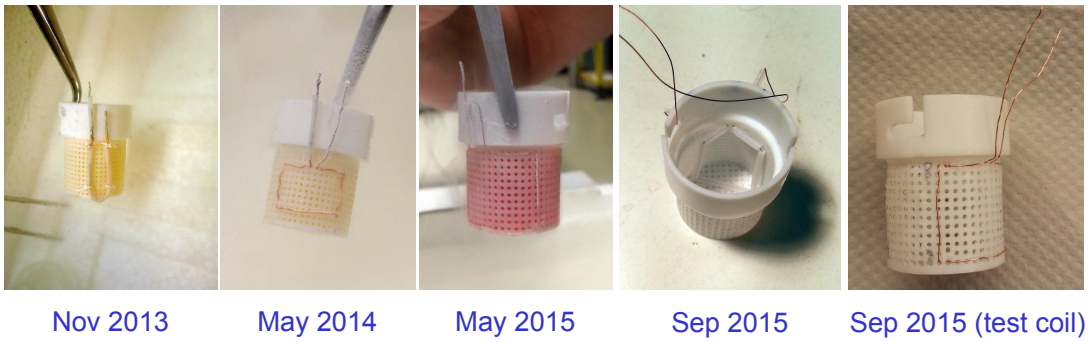

Figure 7.30: The NMR coils were wound around the target cell during the November 2013, May 2014 and May 2015 beamtimes. The NMR coil configuration was changed to have the NMR coil at the beam position during the last September 2015 beamtime. The first four pictures from the left are taken from [Rei].

7.2.2.2 Determination of target polarization correction factors

As already explained it was necessary to determine correction factors for the target polarization degree values of the November 2013, May 2014 and May 2015 beamtimes. Assuming that a similar amount of ice was located on the NMR coil during one beamtime, it means that the determined relaxation times stay the same, but a constant correction factor needs to be determined for each beamtime. Since the September 2015 beamtime is not affected by the problem, correction factors f^{corr} could be determined by comparing the results of E for each beamtime to the results of the September 2015 beamtime. This procedure was done for the $p\pi^0$ and for the $p\eta$ final state. The results for the three ratios $E_{\text{Nov13}}/E_{Sep15}$, $E_{\text{May14}}/E_{\text{Sep15}}$ and $E_{\text{May15}}/E_{\text{Sep15}}$ are depicted in Figure 7.31 in the upper row for the $p\pi^0$ and in the lower row for the $p\eta$ final state.

It is noteworthy that the ratio distributions do not correspond to a perfect Gaussian, as many data points with different statistical error bars contribute. The distribution of the ratios were fitted with a Gaussian, restricting the fit range to the dominant Gaussian peak. The Gaussian peak position gives the needed correction factor. The obtained correction factors are listed in Table 7.4.

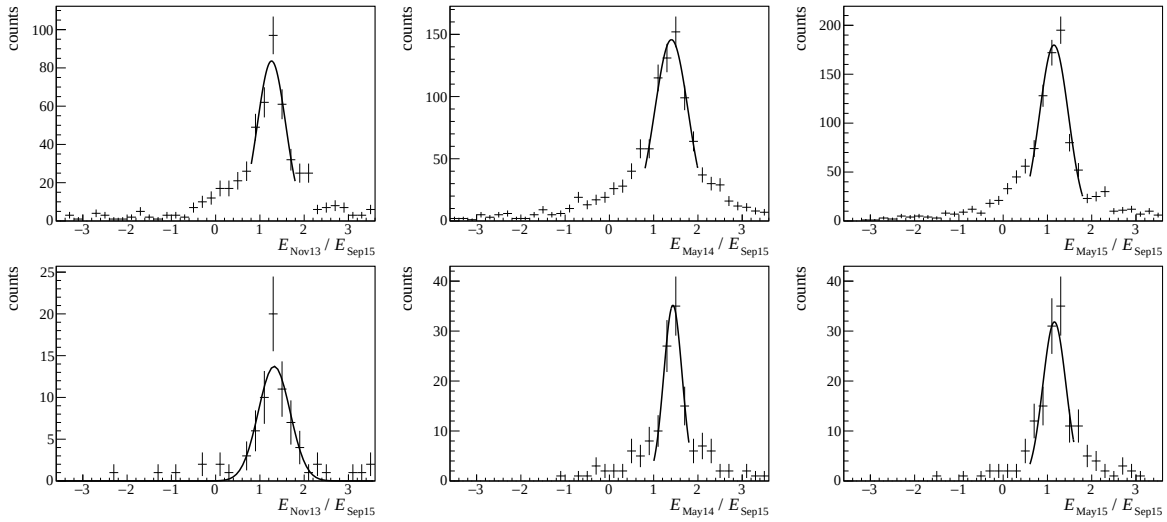

Figure 7.31: The target polarization correction factors are determined from the ratios $E_{\mathrm{Nov13/Sep15}}, E_{\mathrm{May14/Sep15}}$ and $E_{\mathrm{May15/Sep15}}$ for the $p\pi^0$ final state (upper row) and for the $p\eta$ final state (lower row). The black lines show Gaussian fits to the data. The fit results are given in Table 7.4.

channel/beamtime	**November 2013**	**May 2014**	**May 2015**
$p\pi^0$	1.27 ± 0.03	1.40 ± 0.03	1.15 ± 0.02
$p\eta$	1.30 ± 0.05	1.39 ± 0.04	1.17 ± 0.03
mean	1.29 ± 0.02	1.40 ± 0.01	1.16 ± 0.02

Table 7.4: The target polarization correction factors f^{corr} are listed for both analyzed channels and for the November 2013, May 2014 and May 2015 beamtimes.

The correction factors of the $p\pi^0$ and $p\eta$ channels, as obtained by Gaussian fits, are consistent within their statistical errors. The mean values of both results were taken as the final correction factor for each beamtime. Each target polarization value has to be multiplied by its target correction factor. Thus, the equation for the double polarization observable E is modified in the following way:

$$E = \frac{N^{1/2} - N^{3/2}}{N^{1/2} + N^{3/2} - s^C N^C} \cdot \frac{1}{f^{\mathrm{corr}} \cdot p_T \cdot p_\gamma^{circ}}. \tag{7.41}$$

It holds that $f^{\mathrm{corr}} := 1$ for the September 2015 beamtime. The corrected target polarization degree values are depicted in Figure 7.32. After the application of the correction factors, the maximal target polarization degree reads 84% for the November 2013, 89% for the May 2014 and 81% for the May 2015 beamtimes. These values are in the same order as the maximal value of 87% of the September 2015 beamtime, which was measured with the inner coil configuration.

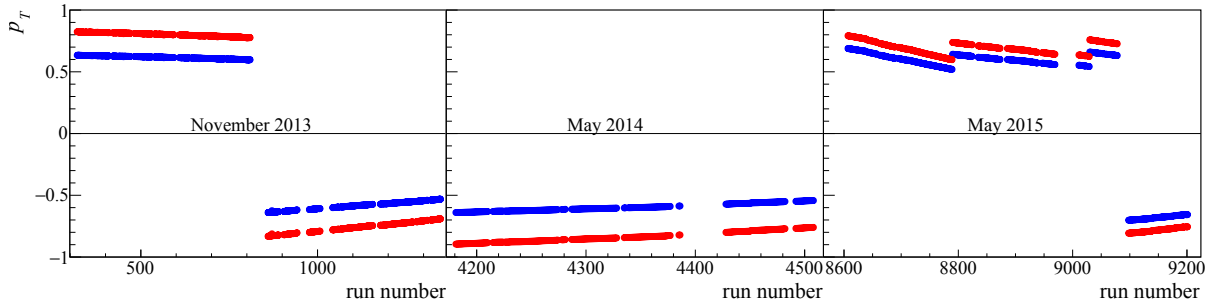

Figure 7.32: The target polarization degree is plotted with (red) and without (blue) the inclusion of the correction factors f^{corr} (see Table 7.4).

Figures 7.33 and 7.34 show the corrected November 2013 results in comparison to the September 2015 beamtime results for the $p\pi^0$ and for the $p\eta$ final state, respectively. Applying the target correction factors leads to consistent results of all beamtimes. Thus, all four butanol beamtimes can be merged together.

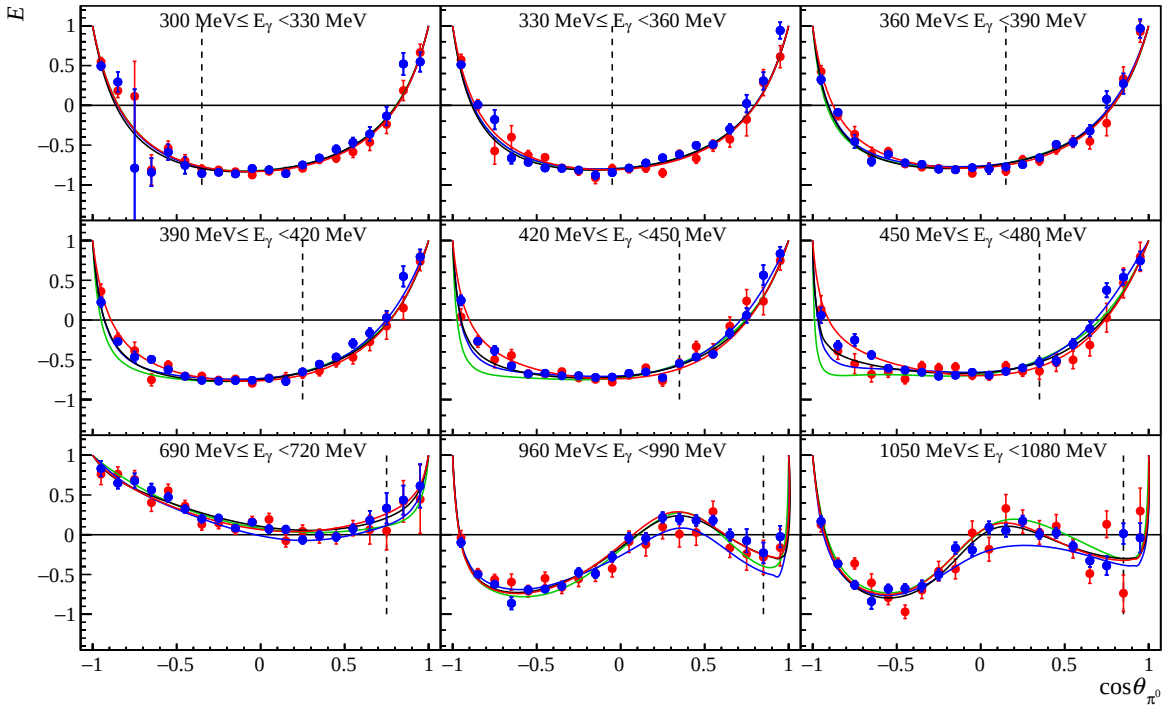

Figure 7.33: Comparison of the E results as obtained from the November 2013 data with the corrected target polarization degree (red points) and from the September 2015 data (blue points) for selected energy bins of the $p\pi^0$ final state. PWA solution of the BnGa-2014-01 (black line), BnGa-2014-02 (red line) [Gut+14], JüBo-2016 (green line) [Ani+16] and SAID-CM12 (blue line) [Wor+12] are plotted as well. The dashed line marks the point where the 2 PED events start.

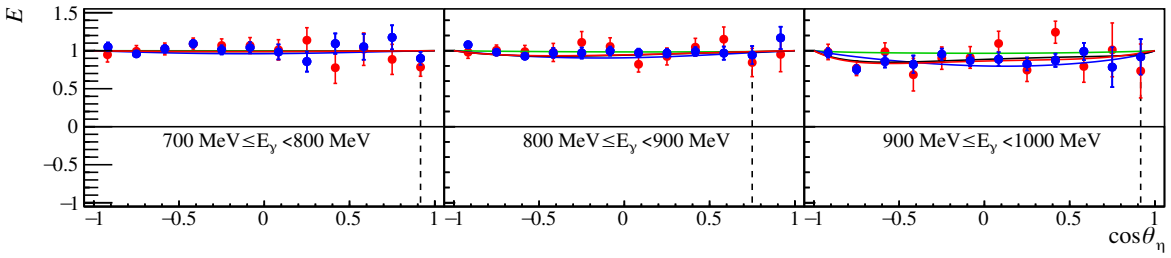

Figure 7.34: Comparison of the E results as obtained from the November 2013 data with the corrected target polarization degree (red points) and from the September 2015 data (blue points) for selected energy bins of the $p\eta$ final state. PWA solution of the BnGa-2014-01 (black line), BnGa-2014-02 (red line) [Gut+14], JüBo-2016 (green line) [Ani+16] and SAID-GE09 (blue line) [Bri+] are plotted as well. The dashed line marks the point where the 2 PED events start.

7.2.3 Comparison of all four polarization settings

A comparison of all four possible polarization combinations $p_T^{\downarrow}p_\gamma^{\uparrow}$, $p_T^{\uparrow}p_\gamma^{\downarrow}$, $p_T^{\uparrow}p_\gamma^{\uparrow}$ and $p_T^{\downarrow}p_\gamma^{\downarrow}$ is shown in Figure 7.35 for all beamtimes. Here, the target polarization correction factors are applied. It holds: $p_T^{\downarrow}p_\gamma^{\uparrow} = p_T^{\downarrow}p_\gamma^{\downarrow}$ and $p_T^{\uparrow}p_\gamma^{\uparrow} = p_T^{\uparrow}p_\gamma^{\downarrow}$ as already explained in Section 7.2.1.1.

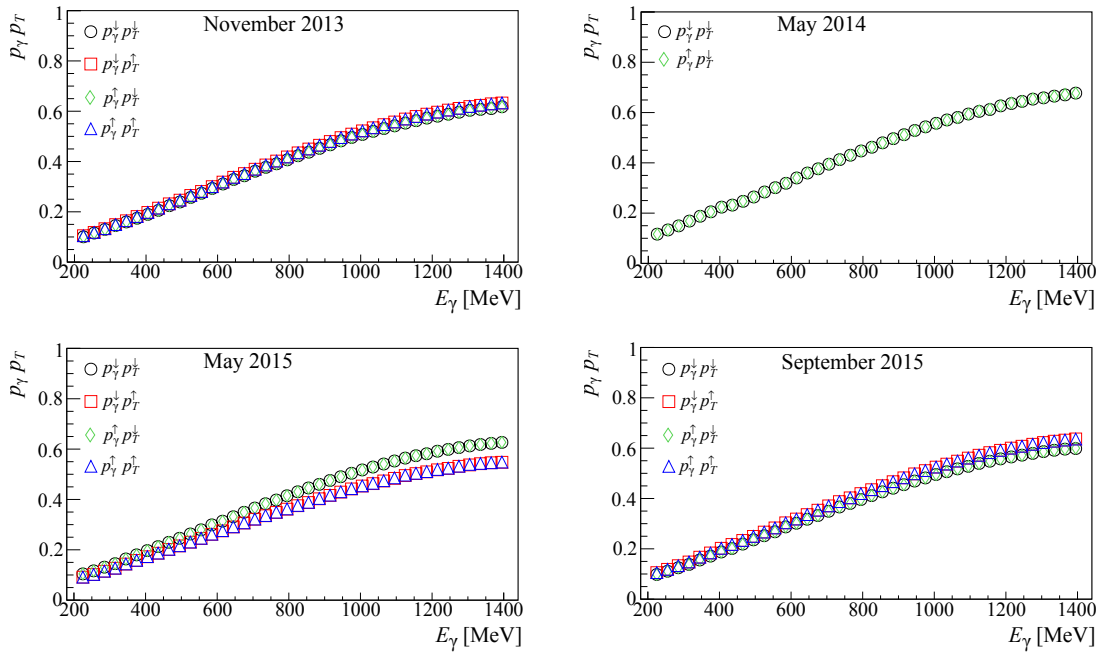

Figure 7.35: Comparison of all four polarization settings of $p_\gamma p_T$. The energy dependence of the circularly polarized photons is clearly visible (see Equation (2.13)).

7.3 Error analysis

7.3.1 Statistical error

The statistical error of the helicity asymmetry E is dominated for each of the four beamtimes by the statistical errors of the event yields $\Delta N^{1/2}$ and $\Delta N^{3/2}$, which were taken with the butanol target. In addition, the statistical error of the scaling factor Δs^C and the event yield of the *carbon+helium* data ΔN^C contribute as well. As all of these parameters are uncorrelated, the total statistical error of E amounts to

$$\Delta E_{\text{stat}} = \sqrt{\left(\frac{\partial E}{\partial N^{1/2}}\Delta N^{1/2}\right)^2 + \left(\frac{\partial E}{\partial N^{3/2}}\Delta N^{3/2}\right)^2 + \left(\frac{\partial E}{\partial N^C}\Delta N^C\right)^2 + \left(\frac{\partial E}{\partial s^C}\Delta s^C\right)^2}. \quad (7.42)$$

The statistical error of the circular polarization degree is negligibly small (see Section 7.2.1) and does not need to be considered here. The error of the target polarization degree only contributes to the systematic error.

As already mentioned, all four butanol beamtimes were merged together to obtain the smallest possible statistical error bars using an error weighted average E_{average} as follows:

$$E_{\text{average}} = \frac{\sum_{i=1}^{4} E_i/\Delta E_{i,\text{stat}}^2}{\sum_{i=1}^{4} 1/\Delta E_{i,\text{stat}}^2} \qquad \text{with} \qquad \Delta E_{\text{average}} = \sqrt{\frac{1}{\sum_{i=1}^{4} 1/\Delta E_{i,\text{stat}}^2}}, \quad (7.43)$$

where E_i is the helicity asymmetry of beamtime i with its statistical error $E_{i,\text{stat}}$.

7.3.2 Systematic error

7.3.2.1 Background contribution in event yields

The relative background contaminations in the event yields δ^{bg} after the event selection process are shown in Figures 5.78 and 5.79. As explained in Section 6.5, these lead to an absolute systematic error $\Delta E^{\text{bg, abs}}$ of

$$\Delta E^{\text{bg, abs}} \lesssim \delta^{\text{bg}}. \quad (7.44)$$

7.3.2.2 Dilution factor d

The relative systematic error of the dilution factor $\frac{\Delta d}{d}$ is correlated to the relative systematic error of the scaling factor $\frac{\Delta s^C}{s^C}$:

$$\frac{\Delta d}{d} = \frac{1-d}{d}\frac{\Delta s^C}{s^C}. \quad (7.45)$$

A systematic deviation of around 3% was found for the method of determining the scaling factor (see Section 7.1.1). An additional source of systematic uncertainty is given by the uncertainty of the filling factor and the uncertainty of whether the same amount of helium was present in the *carbon+helium* and butanol data. According to Rohlof and Dutz [Roh03], an error of 1.5% is reported for the filling factor. Thus, the total systematic error of the scaling factor $\frac{\Delta s^C}{s^C}$ is given by both components added up in quadrature:

$$\frac{\Delta s^C}{s^C} = \sqrt{(0.03)^2 + (0.015)^2} \approx 0.034. \tag{7.46}$$

If the dilution factor is high as in the case for the 3 PED events, the systematic error of the dilution factor is negligible (see Equation (7.45)). However, for the 2 PED events, the systematic error due to the dilution factor is the largest contribution of the total systematic error.

7.3.2.3 Circular polarization degree

The circular polarization degree is determined according to Equation (2.13). The relative error for E_γ and E_0 are negligibly small. Therefore, the relative systematic error of the circular polarization degree is given by the relative systematic error of the longitudinally polarized electrons as determined from the Mott measurement (see Section 7.2.1.1). It holds

$$\frac{\Delta p_\gamma^{\text{circ}}}{p_\gamma^{\text{circ}}} = 2.7\%. \tag{7.47}$$

Furthermore, it needs to be investigated whether Equation (2.13) is valid for a diamond radiator as well, since this equation was derived for an amorphous radiator. If the linear polarization component influences the circular polarization degree, additional systematic effects could occur. However, no additional systematic error needs to be considered here as discussed in Section 7.4.1.

7.3.2.4 Target polarization degree

The relative systematic error of the target polarization degree consists mainly of the NMR signal evaluation at thermal equilibrium which is estimated to be around 1%. Further sources that need to be considered are the temperature, electronics and non-linearities. The systematic error of the target polarization degree is 2%. Due to the problems that occurred with the NMR measurement (see Section 7.2.2.1), the relative systematic error has to increased due to the uncertainty of the target polarization correction factor f^{corr}. Based on the estimated average correction factors, an additional 2% relative error is assumed. The total relative error of the target polarization degree is

$$\frac{\Delta p_T}{p_T} = \sqrt{(2\%)^2 + (2\%)^2} = 2.8\%. \tag{7.48}$$

7.3.2.5 Contributions of Σ and G on the E results

As already mentioned it is necessary to integrate over the entire azimuthal angle ϕ in order to access only the helicity asymmetry E and eliminate the contributions from Σ and G. However, a complete cancellation of Σ and G is only ensured in the ideal case of a flat detection efficiency over the entire azimuthal angle ϕ. In general this can not be assumed. Any arbitrary ϕ-dependent detection efficiency $\epsilon(\phi)$ can be described using a fourier series as given in Equation (6.19) whereby a truncation of the series is not needed. It holds for the ϕ-independent differential cross section $\frac{d\sigma}{d\Omega}^{\uparrow_H,\uparrow_T,\parallel/\perp}(E_\gamma, \cos\theta)$:

$$\frac{d\sigma}{d\Omega}^{\uparrow_H,\uparrow_T,\parallel/\perp}(E_\gamma, \cos\theta) = \frac{1}{2\pi}\int_0^{2\pi} \frac{d\sigma}{d\Omega}^{\uparrow_H,\uparrow_T,\parallel/\perp}(E_\gamma, \cos\theta, \phi) \cdot \epsilon(\phi) \quad d\phi \tag{7.49}$$

$$= \frac{d\sigma}{d\Omega}_0 (E_\gamma, \cos\theta) \left[1 \pm \frac{1}{2} p_\gamma^{\parallel/\perp} \Sigma \cdot a_2 \mp \frac{1}{2} p_\gamma^{\parallel/\perp} p_T^\uparrow G \cdot b_2 - p_\gamma^\uparrow p_T^\uparrow E\right] \quad (7.50)$$

with a_2 and b_2 being detection efficiency parameters which are zero only for the case of a flat detection efficiency. Similarly, it holds for the other differential cross sections

$$\frac{d\sigma}{d\Omega}^{\uparrow_H,\downarrow_T,\parallel/\perp} (E_\gamma, \cos\theta) = \frac{d\sigma}{d\Omega}_0 (E_\gamma, \cos\theta) \left[1 \pm \frac{1}{2} p_\gamma^{\parallel/\perp} \Sigma \cdot a_2 \pm \frac{1}{2} p_\gamma^{\parallel/\perp} p_T^\downarrow G \cdot b_2 + p_\gamma^\uparrow p_T^\downarrow E\right] \quad (7.51)$$

$$\frac{d\sigma}{d\Omega}^{\downarrow_H,\uparrow_T,\parallel/\perp} (E_\gamma, \cos\theta) = \frac{d\sigma}{d\Omega}_0 (E_\gamma, \cos\theta) \left[1 \pm \frac{1}{2} p_\gamma^{\parallel/\perp} \Sigma \cdot a_2 \mp \frac{1}{2} p_\gamma^{\parallel/\perp} p_T^\uparrow G \cdot b_2 + p_\gamma^\downarrow p_T^\uparrow E\right] \quad (7.52)$$

$$\frac{d\sigma}{d\Omega}^{\downarrow_H,\downarrow_T,\parallel/\perp} (E_\gamma, \cos\theta) = \frac{d\sigma}{d\Omega}_0 (E_\gamma, \cos\theta) \left[1 \pm \frac{1}{2} p_\gamma^{\parallel/\perp} \Sigma \cdot a_2 \pm \frac{1}{2} p_\gamma^{\parallel/\perp} p_T^\downarrow G \cdot b_2 - p_\gamma^\downarrow p_T^\downarrow E\right]. \quad (7.53)$$

The differential cross sections for the total helicity state 1/2 and 3/2 are given by

$$\frac{d\sigma}{d\Omega}^{1/2} = \frac{1}{4} \left(\frac{d\sigma}{d\Omega}^{\uparrow_H,\downarrow_T,\parallel} + \frac{d\sigma}{d\Omega}^{\uparrow_H,\downarrow_T,\perp} + \frac{d\sigma}{d\Omega}^{\downarrow_H,\uparrow_T,\parallel} + \frac{d\sigma}{d\Omega}^{\downarrow_H,\uparrow_T,\perp} \right) \quad (7.54)$$

$$= \frac{d\sigma}{d\Omega}_0 \left[1 + \frac{1}{4} \Sigma a_2 (p_\gamma^\parallel - p_\gamma^\perp) + \frac{1}{8} G b_2 (p_T^\downarrow - p_T^\uparrow) \cdot (p_\gamma^\parallel - p_\gamma^\perp) + \frac{1}{2} E (p_\gamma^\downarrow p_T^\uparrow + p_\gamma^\uparrow p_T^\downarrow)\right] \quad (7.55)$$

$$\frac{d\sigma}{d\Omega}^{3/2} = \frac{1}{4} \left(\frac{d\sigma}{d\Omega}^{\uparrow_H,\uparrow_T,\parallel} + \frac{d\sigma}{d\Omega}^{\uparrow_H,\uparrow_T,\perp} + \frac{d\sigma}{d\Omega}^{\downarrow_H,\downarrow_T,\parallel} + \frac{d\sigma}{d\Omega}^{\downarrow_H,\downarrow_T,\perp} \right) \quad (7.56)$$

$$= \frac{d\sigma}{d\Omega}_0 \left[1 + \frac{1}{4} \Sigma a_2 (p_\gamma^\parallel - p_\gamma^\perp) + \frac{1}{8} G b_2 (p_T^\downarrow - p_T^\uparrow) \cdot (p_\gamma^\parallel - p_\gamma^\perp) - \frac{1}{2} E (p_\gamma^\uparrow p_T^\uparrow + p_\gamma^\downarrow p_T^\downarrow)\right] \quad (7.57)$$

Taking the difference and sum of the helicity dependent cross sections leads to

$$\frac{d\sigma}{d\Omega}^{1/2} - \frac{d\sigma}{d\Omega}^{3/2} = 2 \frac{d\sigma}{d\Omega}_0 \bar{p}_\gamma^{\text{circ}} \bar{p}_T E \quad (7.58)$$

$$\frac{d\sigma}{d\Omega}^{1/2} + \frac{d\sigma}{d\Omega}^{3/2} = 2 \frac{d\sigma}{d\Omega}_0 \left[1 + \frac{1}{4} \Sigma a_2 (p_\gamma^\parallel - p_\gamma^\perp) + \frac{1}{8} G b_2 (p_T^\downarrow - p_T^\uparrow) \cdot (p_\gamma^\parallel - p_\gamma^\perp)\right] \quad (7.59)$$

In the difference (see Equation (7.58)) the contributions of Σ and G cancel out completely independent of whether detection inefficiencies or differences in the linear polarization degrees exist or not. However, in the sum (see Equation (7.59)) the contributions only vanish if either the detection efficiency coefficients a_2 and b_2 are zero or if the linear polarization degrees are the same for both α settings (or in case of G if the difference between the target polarization degrees is zero).

Figure 7.36 shows the detection efficiency coefficients as determined by K. Spieker [Spi19]. The relevant coefficients are $a_2 \approx 0.012$ and $b_2 \approx 0.038$ [Spi19], the difference in the linear polarization degree is approximately given as 2% and the difference in the target polarization degree is maximally 10% for the May 2015 beamtime (see Figure 7.35). This allows an estimation of an upper limit for the contribution of Σ and G considering that the largest values Σ and G can take are ± 1:

$$\frac{1}{4}\Sigma a_2(p_\gamma^{\parallel} - p_\gamma^{\perp}) \leq \frac{1}{4} \cdot (\pm 1) \cdot 0.012 \cdot 0.02 \approx 6 \times 10^{-5} \tag{7.60}$$

$$\frac{1}{8}Gb_2(p_T^{\downarrow} - p_T^{\uparrow}) \cdot (p_\gamma^{\parallel} - p_\gamma^{\perp}) \leq \frac{1}{8} \cdot (\pm 1) \cdot 0.038 \cdot 0.10 \cdot 0.02 \approx 1 \times 10^{-5}. \tag{7.61}$$

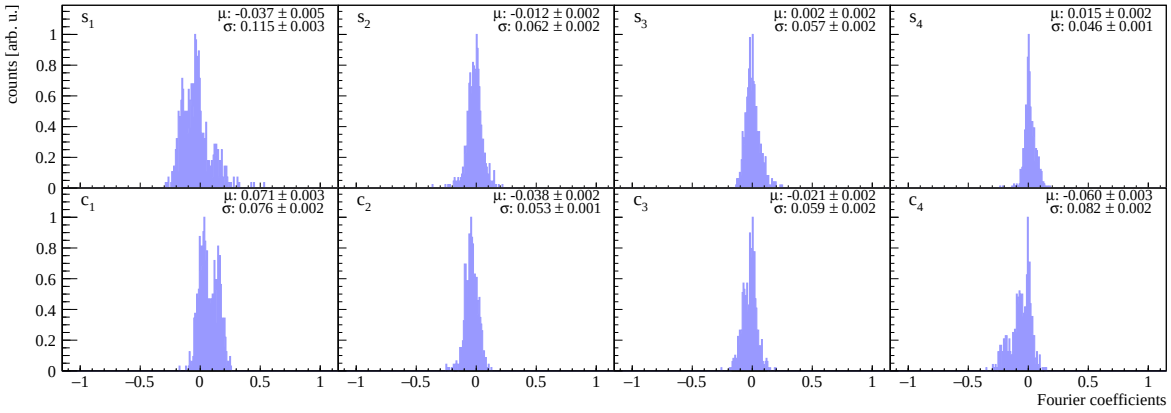

Figure 7.36: The fit coefficients $s_1 \dots s_4$ and $c_1 \dots c_4$ (the notation corresponds to $a_1 \dots a_4$ and $b_1 \dots b_4$ of this work) are shown as obtained from an unbinned maximum likelihood fit for the $p\pi^0$ final state. The unbinned maximum likelihood fit was used to obtain the double polarization observable G. The coefficients describe the detection efficienies of the A2 data. Taken from [Spi19].

Therefore, the contributions of Σ and G on the helicity asymmetry E are negligibly small and no further systematics need to be considered.

7.3.2.6 Total systematic error

The total absolute systematic error of the helicity asymmetry $\Delta E^{\text{sys,abs}}$ consists of four contributions from the dilution factor, the circular and the target polarization degrees and the background. Since these four components are not correlated to each other, they are added up in quadrature:

$$\Delta E^{\text{sys,abs}} = \sqrt{\left[\left(\frac{\Delta d}{d}\right)^2 + \left(\frac{\Delta p_\gamma^{\text{circ}}}{p_\gamma^{\text{circ}}}\right)^2 + \left(\frac{\Delta p_T}{p_T}\right)^2\right] \cdot E^2 + (\delta^{\text{bg}})^2}. \tag{7.62}$$

7.4 Results

7.4.1 Comparison of diamond and Møller data

One of the main goals of this work is to test whether or not it is possible to determine the double polarization observable E utilizing longitudinally polarized electrons on a diamond radiator, producing elliptically polarized photons with a linear and circular polarization component. According to [Bos] the degree of circular polarization of the coherent bremsstrahlung can be approximately calculated in the same way as for incoherent bremsstrahlung when using an

amorphous radiator [Nad76]. In a full calculation dips are expected to appear in the energy dependence of the degree of circular polarization at the position of the coherent edges (see Figure 7.37). As a consequence the degree of circular polarization reduces slightly according to a model calculation [Bos], e.g. for a coherent edge at $E_\gamma \approx E_0/2$ with a maximum degree of linear polarization of around 40%, the polarization degree reduces relatively by 2%[6].

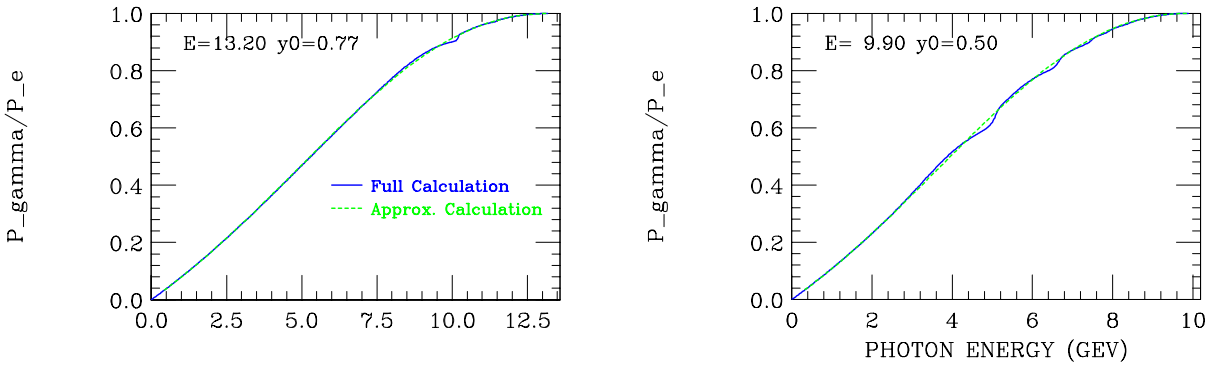

Figure 7.37: The degree of circular polarization relative to the electron polarization degree is plotted as a function of the beam photon energy E_γ for two different electron beam energies $E_0 = 13.20\,\text{GeV}$ (left)and $E_0 = 9.90\,\text{GeV}$ (right) for the SLAC E159 experiment. The coherent edge positions are given by $y_0 = E_\gamma/E_0$. The green dashed line shows the calculation of the polarization degree according to Equation (2.13) for incoherent bremsstrahlung. The blue solid line represents the full calculation for the circular polarization component of the coherent bremsstrahlung. Taken from [Bos].

To investigate these effects, data taken with the diamond radiator were compared to data taken with the amorphous Møller radiator. In order to ensure that any observed deviations are stemming from the degree of circular polarization and not any other systematic effects (see Section 7.3.2), only small subsets of data can be compared with each other, requiring the same overall data taking conditions, especially the same trigger settings. This is only fulfilled for data taken within one beamtime, e.g. the diamond data of the September 2015 beamtime with the 450 MeV coherent edge data and the Møller data, that was taken directly afterwards in time. Therefore, it is assumed that both data sets are subject to the same systematic effects and observed deviations of diamond to Møller data can be interpreted to be present due to a slightly wrong calculation of the degree of circular polarization for the diamond data.

The highest deviation between the diamond and Møller data is expected to be for data taken with the diamond radiator and with the coherent edge at 450 MeV with a maximum linear polarization degree of around 70%[7] and the lowest effect for the coherent edge at 850 MeV with a maximum linear polarization degree of around 35% (see Figure 2.16). Figure 7.38 shows the comparison of the helicity asymmetry E of the $p\pi^0$ final state for the diamond data with the 450 MeV coherent edge position and the Møller data of the September 2015 beamtime. A good agreement between both results for beam photon energies around 100 MeV below the coherent edge position is visible within the statistical error bars.

[6] This estimation was done based on Figure 7.37 and the information given in [Bos].
[7] Data with the coherent edge at 350 MeV of the November 2013 beamtime could not be used here due to insufficient statistics of the Møller data of the November 2013 beamtime.

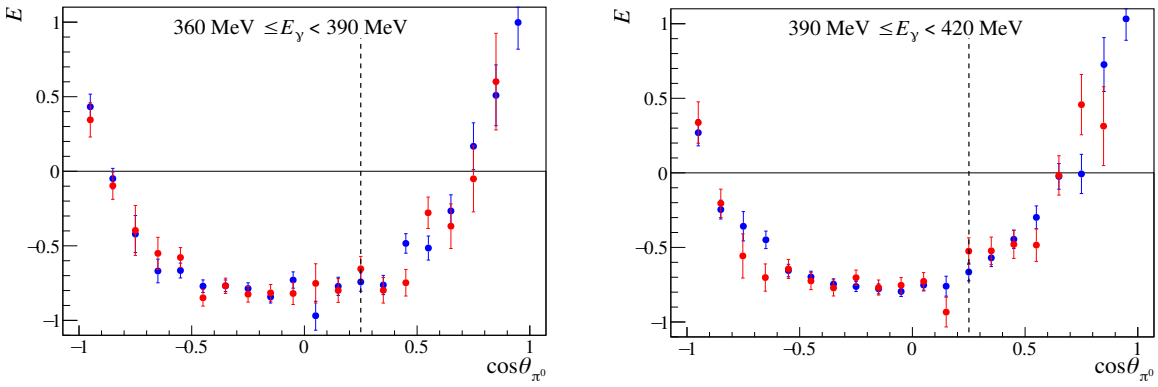

Figure 7.38: Two example angular distributions are given for the comparison of the helicity asymmetry E (of the $p\pi^0$ final state) for diamond data with the coherent edge at 450 MeV (blue) and Møller data (red) of the September 2015 beamtime.

To quantify how good the agreement between the data sets is, the ratio of both results is taken $E_{\text{diamond}}/E_{\text{Møller}}$. This is depicted in Figure 7.39. A Gaussian fit to the ratio confirms that both data sets are in very good agreement (1.02 ± 0.03) with each other within the statistical precision of the data. This result is the first experimental evidence that the degree of circular polarization can be calculated in the same way for a diamond radiator as it is done for an amorphous radiator in a first approximation. Thus, the double polarization observable E can be determined using a longitudinally polarized electron beam which is incident on a diamond radiator. Additionally, the diamond and the Møller data can be combined to increase the overall statistics of the results (see next section).

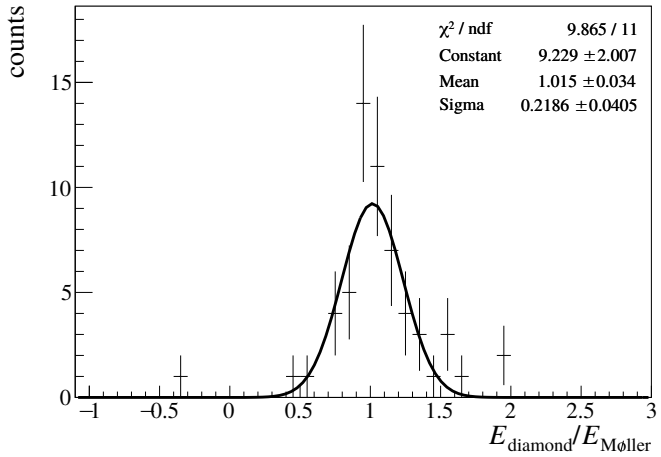

Figure 7.39: The ratio of the helicity asymmetry E results for diamond data with the coherent edge at 450 MeV and Møller data for energies below the coherent edge position is shown. A Gaussian fit confirms that both data sets are in very good agreement (1.02 ± 0.03) with each other within the statistical precision of the data.

7.4.2 Results of the complete butanol data

The results of the new A2 data for the helicity asymmetry E are depicted for all butanol data (diamond and Møller data) of all four beamtimes according to Equation (7.43) in Figures 7.40 - 7.43 for the $p\pi^0$ final state and in Figure 7.44 for the $p\eta$ final state. The error bars correspond to statistical errors, while the gray bars represent the systematic errors.

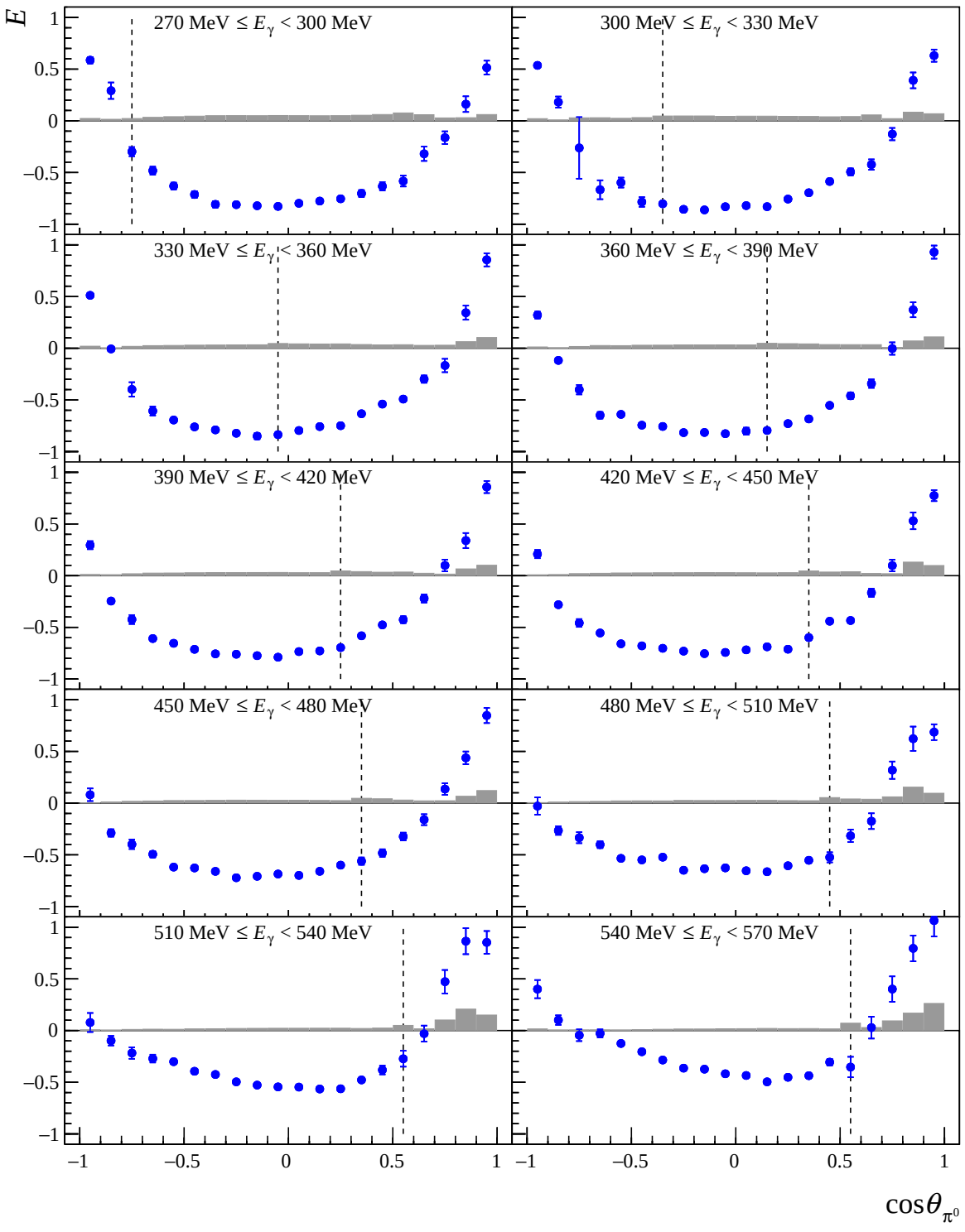

Figure 7.40: The double polarization observable E is plotted as a function of $\cos\theta_{\pi^0}$ for the beam photon energy range from 270 MeV $\leq E_\gamma <$ 570 MeV. The black dashed line marks the point where the 2 PED events are added to the 3 PED events. The error bars show only the statistical errors. The systematic errors are depicted in gray.

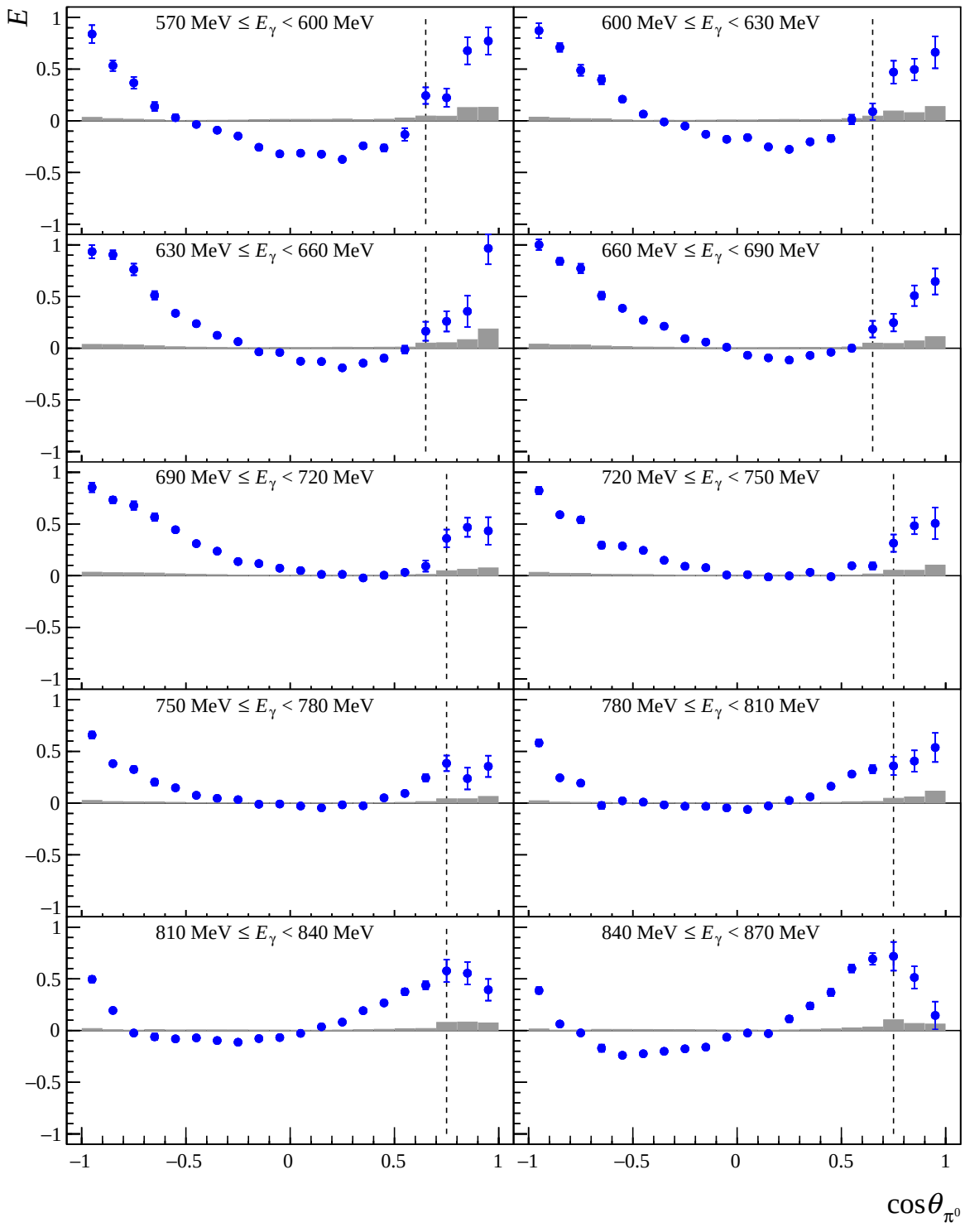

Figure 7.41: The double polarization observable E is plotted as a function of $\cos\theta_{\pi^0}$ for the beam photon energy range from 570 MeV $\leq E_\gamma <$ 870 MeV. The black dashed line marks the point where the 2 PED events are added to the 3 PED events. The error bars show only the statistical errors. The systematic errors are depicted in gray.

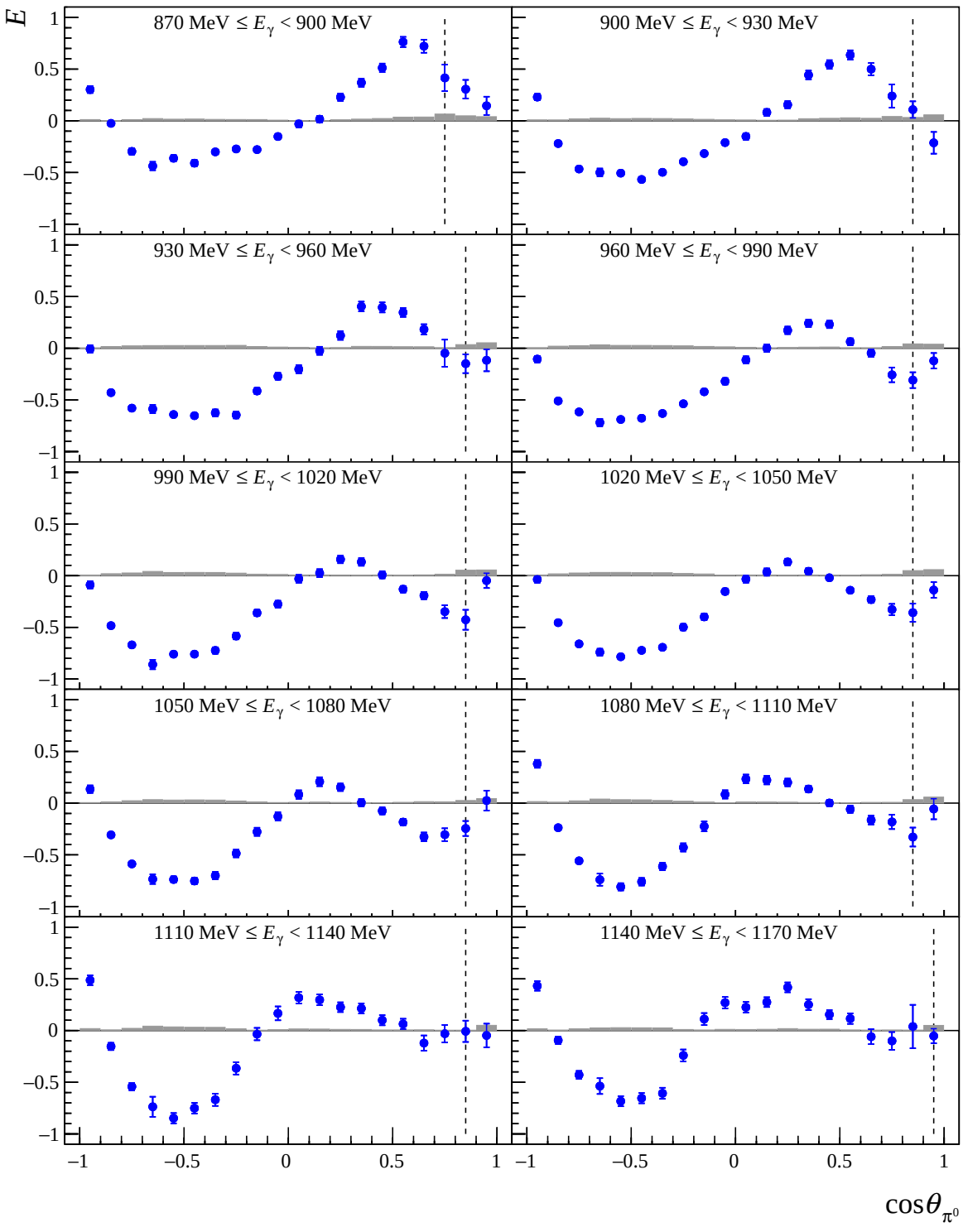

Figure 7.42: The double polarization observable E is plotted as a function of $\cos\theta_{\pi^0}$ for the beam photon energy range from 870 MeV $\leq E_\gamma <$ 1170 MeV. The black dashed line marks the point where the 2 PED events are added to the 3 PED events. The error bars show only the statistical errors. The systematic errors are depicted in gray.

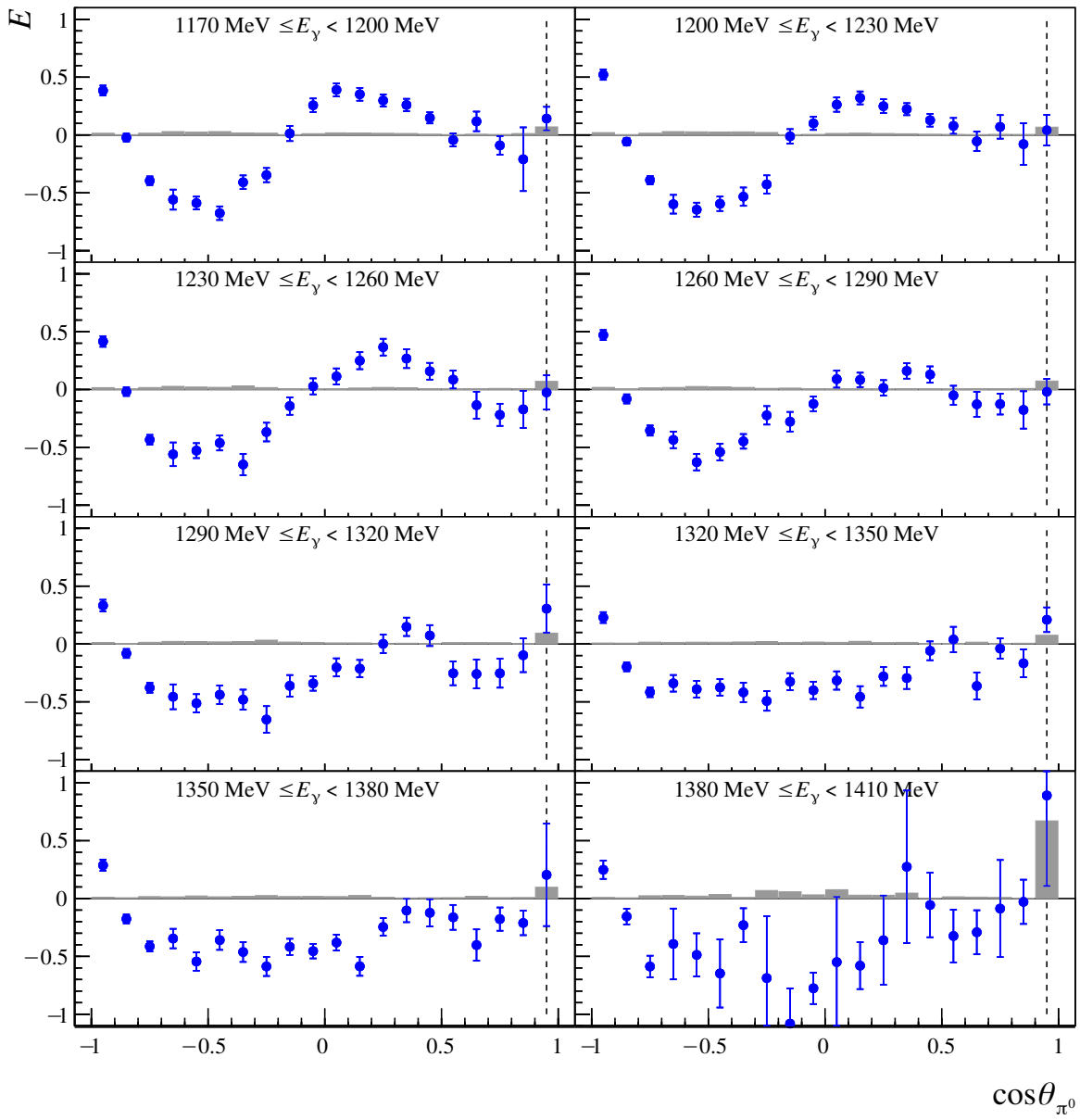

Figure 7.43: The double polarization observable E is plotted as a function of $\cos\theta_{\pi^0}$ for the beam photon energy range from 1170 MeV $\leq E_\gamma <$ 1410 MeV. The black dashed line marks the point where the 2 PED events are added to the 3 PED events. The error bars show only the statistical errors. The systematic errors are depicted in gray.

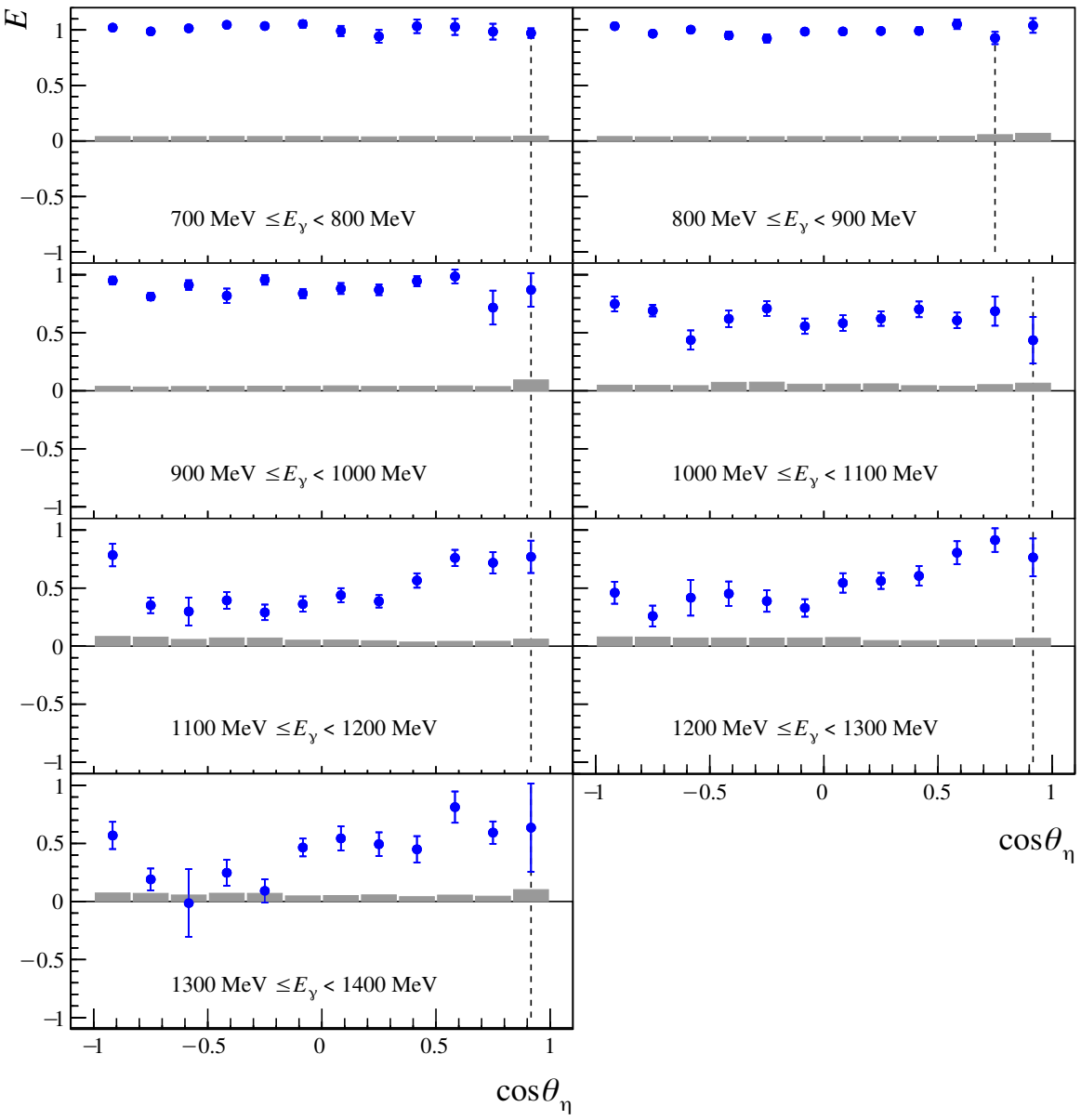

Figure 7.44: The double polarization observable E is plotted as a function of $\cos\theta_\eta$ for the beam photon energy range from 700 MeV $\leq E_\gamma <$ 1400 MeV. The black dashed line marks the point where the 2 PED events are added to the 3 PED events. The error bars show only the statistical errors. The systematic errors are depicted in gray.

8 Discussion of results

The obtained results for the beam asymmetry Σ using the CBELSA/TAPS data and the helicity asymmetry E utilizing the A2 data are discussed in this chapter. First, the results are compared to already existing data (see Section 8.1). Afterwards, the dominant partial wave contributions are determined based on the measured angular distributions (see Section 8.2). In the end, comparisons to different PWA models are given (see Section 8.3).

8.1 Comparison of results to existing data

8.1.1 Beam asymmetry Σ

8.1.1.1 $p\pi^0$ final state

The new CBELSA/TAPS data for the beam asymmetry Σ of the $p\pi^0$ final state are depicted in Figures 8.1 and 8.2. They are compared to three different existing data sets: the GRAAL data [Bar+05a], the CLAS data [Dug+14] and the LEPS data [Sum+07]. Until $E_\gamma < 1491\,\text{MeV}$, a good agreement is visible between the CBELSA/TAPS, the CLAS and the GRAAL data. However, in certain angular ranges (e.g. $0.2 \leq \cos\theta_{\pi^0} \leq 0.8$), the GRAAL data lie systematically below the other two data sets. A very good agreement is present between the CLAS and the CBELSA/TAPS data within their respective statistical error bars in this energy region. Above $E_\gamma = 1500\,\text{MeV}$, the CBELSA/TAPS data can mainly be compared to the CLAS data. Here, both data sets are in good agreement as well. However, it can be noticed that the CBELSA/TAPS data lie slightly systematically below the CLAS data over the entire angular range, especially when progressing to the highest available energy of $E_\gamma = 1779\,\text{MeV}$. Given the high precision quality of the CBELSA/TAPS and CLAS data, the systematic effects due to the polarization degree of the linearly polarized photons play an important role. Within the estimated systematic error of 8% for the polarization degree in this energy range (CBELSA/-TAPS data) and the given 4% systematic error of the CLAS data [Dug+14], both data sets are well in agreement when taking the systematic errors into account for the angular ranges of $-0.6 < \cos\theta_{\pi^0} < 0.3$ and $0.5 < \cos\theta_{\pi^0} < 1$.
Apart from that, deviations between the different data sets are visible in the angular range of $-0.9 \leq \cos\theta_{\pi^0} \leq -0.6$, which are most dominant in the highest energy bin. Due to the angular dependence of these deviations, the most probable source of systematic error is background contamination, which was investigated thoroughly (see Section 5.2.5) and which is very small for the analyzed CBELSA/TAPS data ($< 1\%$). The LEPS data lie systematically below the CLAS and the CBELSA/TAPS data, but agree well with the CBELSA/TAPS data in the highest energy bin. It is noteworthy, that both the CLAS data and the LEPS data rely on the measurement of the proton using a spectrometer and reconstruct the meson as a missing particle. In the angular range of $-0.9 \leq \cos\theta_{\pi^0} \leq -0.6$, protons fly towards forward angles in the LAB frame, where background from e^+e^- events dominates. The advantage of the CBELSA/TAPS experiment lies in the fact that two calorimeters are used to reconstruct the π^0 and therefore,

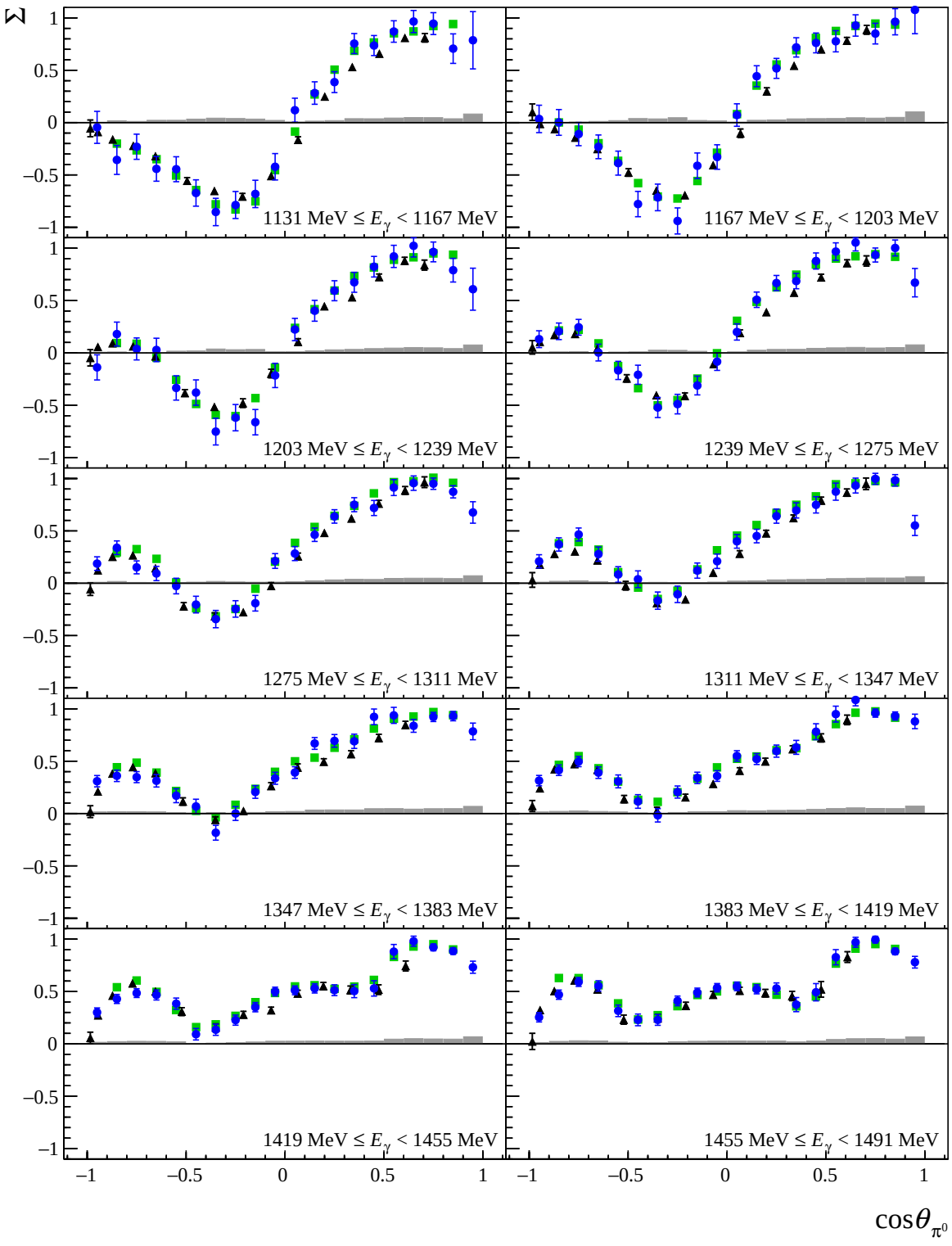

Figure 8.1: Comparison of the new CBELSA/TAPS results for the beam asymmetry Σ of the $p\pi^0$ final state (blue points) to data from the GRAAL collaboration [Bar+05a] (black triangle) and the CLAS collaboration [Dug+14] (green square) are shown as a function of $\cos\theta_{\pi^0}$ for the energy range of (1131 MeV $\leq E_\gamma <$ 1491 MeV). The systematic errors of the new CBELSA/TAPS data are depicted in gray.

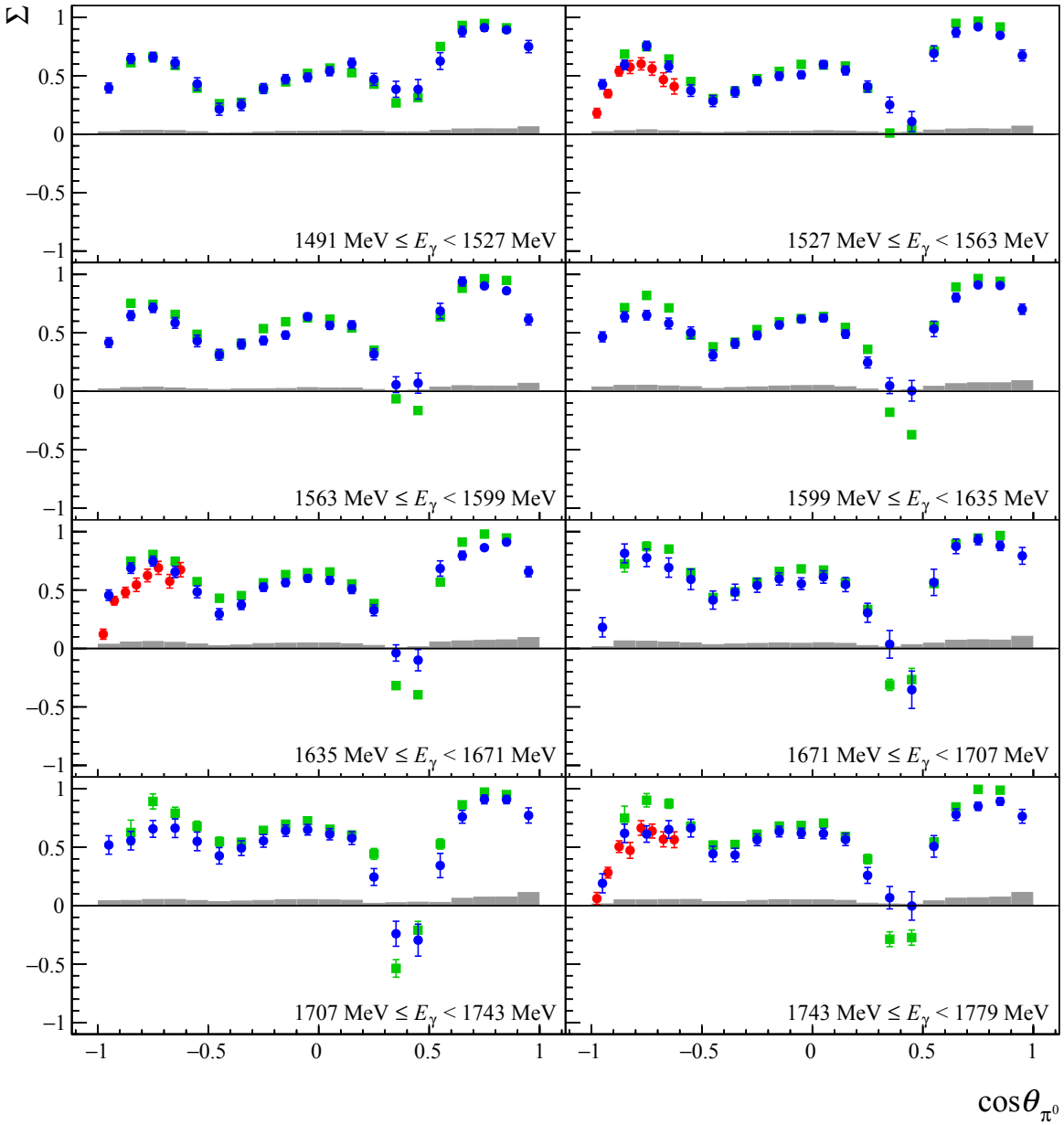

Figure 8.2: Comparison of the new CBELSA/TAPS results for the beam asymmetry Σ of the $p\pi^0$ final state (blue points) to data from the GRAAL collaboration [Bar+05a] (black triangle), the CLAS collaboration [Dug+14] (green square) and the LEPS collaboration (red points) [Sum+07] are shown as a function of $\cos\theta_{\pi^0}$ for the energy range of (1491 MeV $\leq E_\gamma <$ 1779 MeV). The systematic errors of the new CBELSA/TAPS data are depicted in gray.

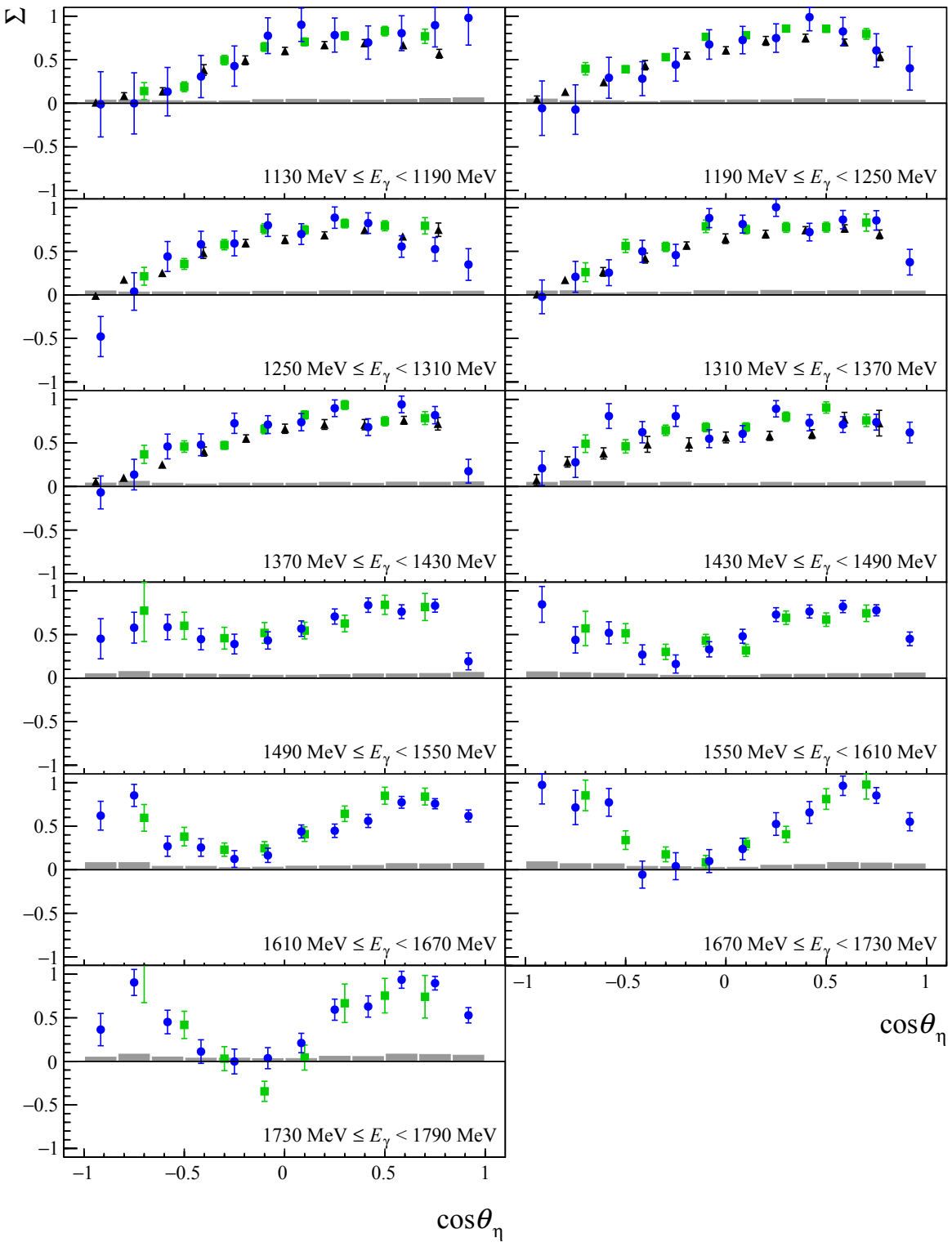

Figure 8.3: Comparison of the new CBELSA/TAPS results for the beam asymmetry Σ of the $p\eta$ final state (blue points) to data from the GRAAL collaboration [Bar+07a] (black triangle) and the CLAS collaboration [Col+17] (green square) are shown as a function of $\cos\theta_\eta$ for the energy range of (1130 MeV $\leq E_\gamma <$ 1790 MeV). The systematic errors of the new CBELSA/TAPS data are depicted in gray.

background contamination can be better suppressed in comparison to the CLAS and the LEPS experiments. The LEPS collaboration reports background contaminations of up to 12% [Sum+07] which is significantly higher than what has been found in this work ($< 1\%$, see Figure 5.39). The sharp structures in the angular range of $0.3 < \cos\theta_{\pi^0} < 0.5$ are more pronounced for the CLAS data than the CBELSA/TAPS data. Here, the angular resolution of the spectrometer of the CLAS experiment, which is used to detect the protons, is better than the angular resolution of the photons in the Crystal Barrel and TAPS detector ($< 3°$ for the polar angle of one decay photon [Wit15]). Furthermore, it should be kept in mind that small deviations could also occur due to the different energy binning of the different data sets. The compared data lie within $\pm$ 12 MeV from the center bin energy of the CBELSA/TAPS data of this work. All in all, the newly obtained CBELSA/TAPS data set is in good agreement with previously measured data and the systematic effects are understood. The new data offers the largest angular coverage for energies above $E_\gamma = 1500$ MeV (see Figure 8.2).

8.1.1.2 $p\eta$ final state

The new CBELSA/TAPS data for the beam asymmetry Σ of the $p\eta$ final state are depicted in Figure 8.3 together with data from the GRAAL collaboration [Bar+07a] and the CLAS collaboration [Col+17]. All three data sets are consistent with each other within the statistical error bars. Since the statistical errors are larger than for the $p\pi^0$ final state, systematic effects are not playing an important role here. Similar to the $p\pi^0$ final state, the new CBELSA/TAPS data has a larger angular coverage in comparison to the CLAS data with better precision at the very forward and backward angles.

8.1.2 Helicity asymmetry E

8.1.2.1 $p\pi^0$ final state

Figures 8.6 - 8.8 show the new results of the helicity asymmetry E for the $p\pi^0$ final state using the A2 data in comparison to the existing data of the CBELSA/TAPS collaboration [Got13; Got+14], starting from $E_\gamma = 270$ MeV to $E_\gamma = 1410$ MeV. Below $E_\gamma = 600$ MeV, no previously measured data for comparison are present until now[1]. The same energy binning was chosen as for the CBELSA/TAPS data. However, above $E_\gamma = 1260$ MeV, the CBELSA/TAPS energy binning changes to a 60 MeV binning and is therefore not compared to the A2 data anymore. A very good agreement is visible within the statistical error bars between both data sets throughout all energy bins. The existing database is improved through the angular bins in forward direction ($\cos\theta > 0.7$), which are not available for the existing CBELSA/TAPS data and which are of paramount importance to get sensitivity to multipoles of high angular momentum ($l > 3$, see Section 8.2) [WA+17]. In addition, the statistical error bars could be decreased by roughly a factor of 4 in the new A2 data set. Here, the advantage of measuring with elliptically polarized photons by using longitudinally polarized electrons on a diamond radiator becomes apparent. Using a diamond radiator to obtain E and hence, due to the presence of different coherent edges during data taking, the statistics can be increased significantly in comparison to the CBELSA/TAPS data where an amorphous radiator was used. The comparison of E of both data sets shows that measuring with elliptically polarized photons leads to the same results as using only a circularly polarized photon beam.

[1] Data points for the helicity dependent cross sections ($\sigma^{3/2} - \sigma^{1/2}$) are available [Ahr+02; Ahr+04], but not directly for the helicity asymmetry E.

8.1.2.2 $p\eta$ final state

Figure 8.9 depicts the new results of the helicity asymmetry E for the $p\eta$ final state utilizing the A2 data. They are compared to existing data of the CBELSA/TAPS collaboration [Mül18] and the CLAS collaboration [Sen+16]. While the CLAS data only covers half of the complete angular range, the CBELSA/TAPS data cover a similar angular range as the A2 data. The newly measured A2 data offers, similar as for the $p\pi^0$ final state, the highest available statistics and largest angular coverage of all available data sets. It is noteworthy, that the CLAS data lie systematically below the CBELSA/TAPS data, most evidently in the energy bin of 900 MeV $\leq E_\gamma <$ 1000 MeV. The obtained A2 data have overall a better agreement to the CBELSA/-TAPS data.

The estimated systematic errors can be tested independently by looking at the energy range close to the η photoproduction threshold ($E_\gamma = 708$ MeV). Here, the helicity asymmetry is expected to be 1 due to the dominating $N(1535)\frac{1}{2}^-$ (S_{11}) resonance which can only contribute to the helicity dependent cross section $\sigma^{1/2}$. The estimated systematic error mainly consists of the polarization degrees of the circularly polarized photons and the target, since background contributions (see Figure 5.79) and the systematic error due to the dilution factor are negligibly small in this energy range. Therefore, it holds (see Sections 7.3.2.3 and 7.3.2.4):

$$E^{\text{sys}} = \sqrt{0.027^2 + 0.028^2} \approx 4\%. \tag{8.1}$$

Figure 8.4 shows the results for the helicity asymmetry E at the η photoproduction threshold. Within the statistical and systematic errors the results are consistent with 1, indicating a correct estimation of the systematic errors.

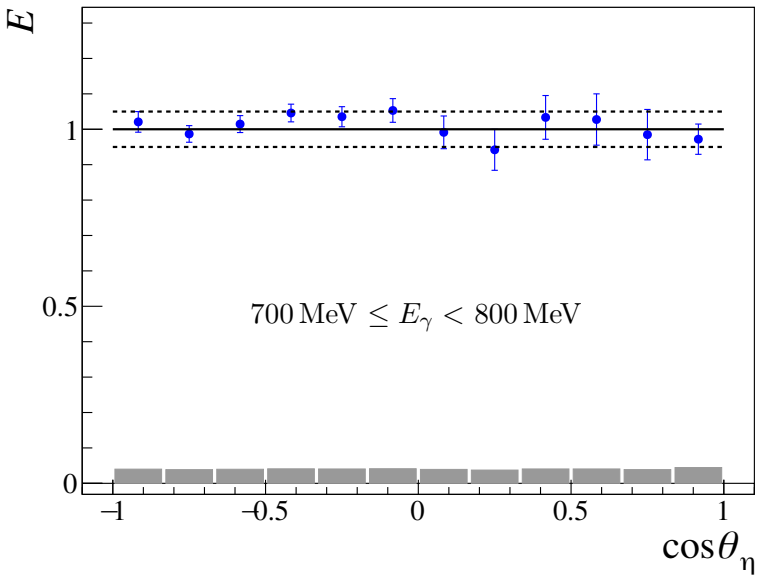

Figure 8.4: The new A2 data for the helicity asymmetry E is shown at the η photoproduction threshold, where it is expected to be 1. The systematic errors are shown in gray. The dashed horizontal lines indicate the ±4% systematic error range.

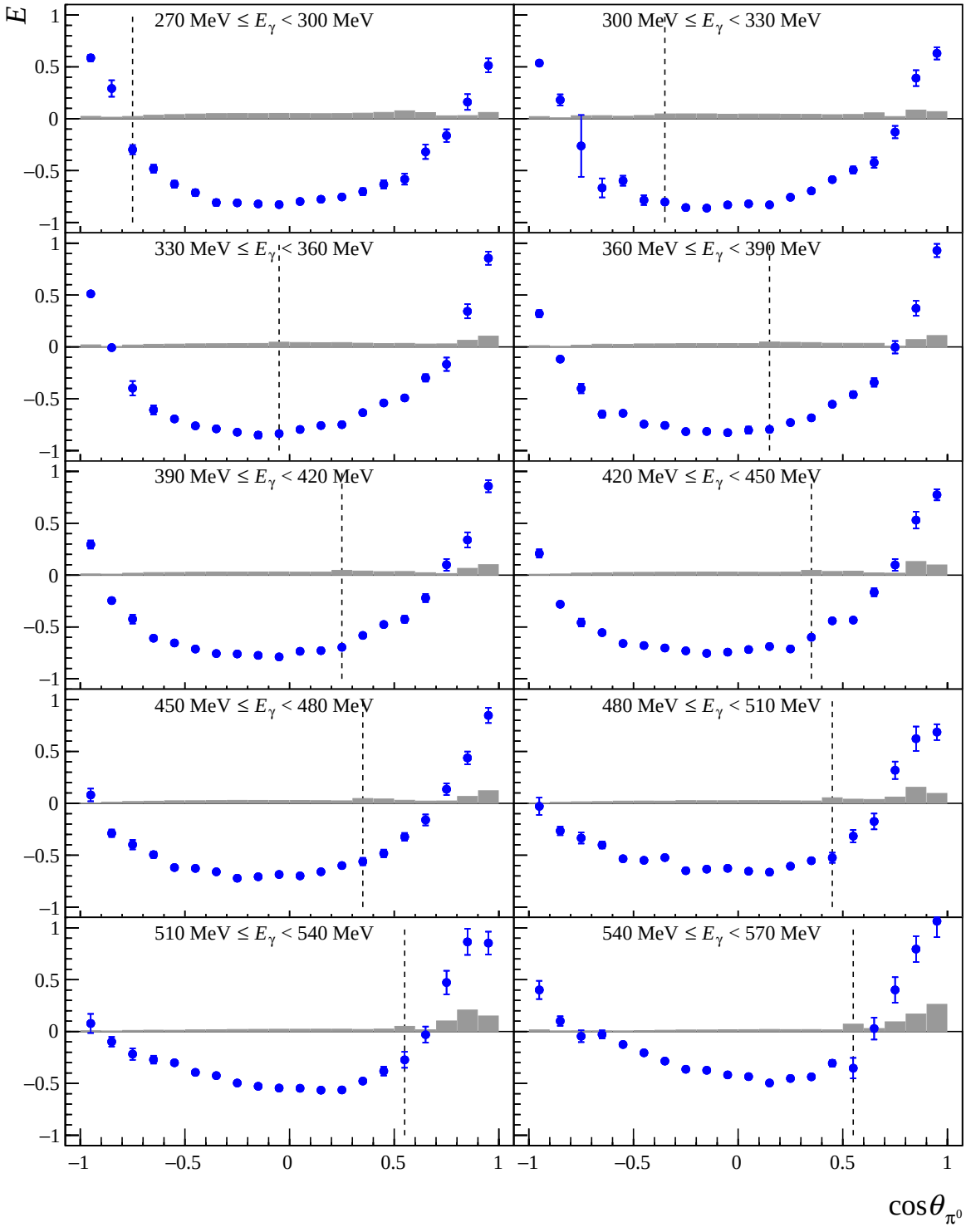

Figure 8.5: The new A2 data for the helicity asymmetry E of the $p\pi^0$ final state (blue points) are shown as a function of $\cos\theta_{\pi^0}$ for the energy range of (270 MeV $\leq E_\gamma <$ 570 MeV). The black dashed line marks the point where the 2 PED events are added to the 3 PED events. The systematic errors of the new A2 data are depicted in gray.

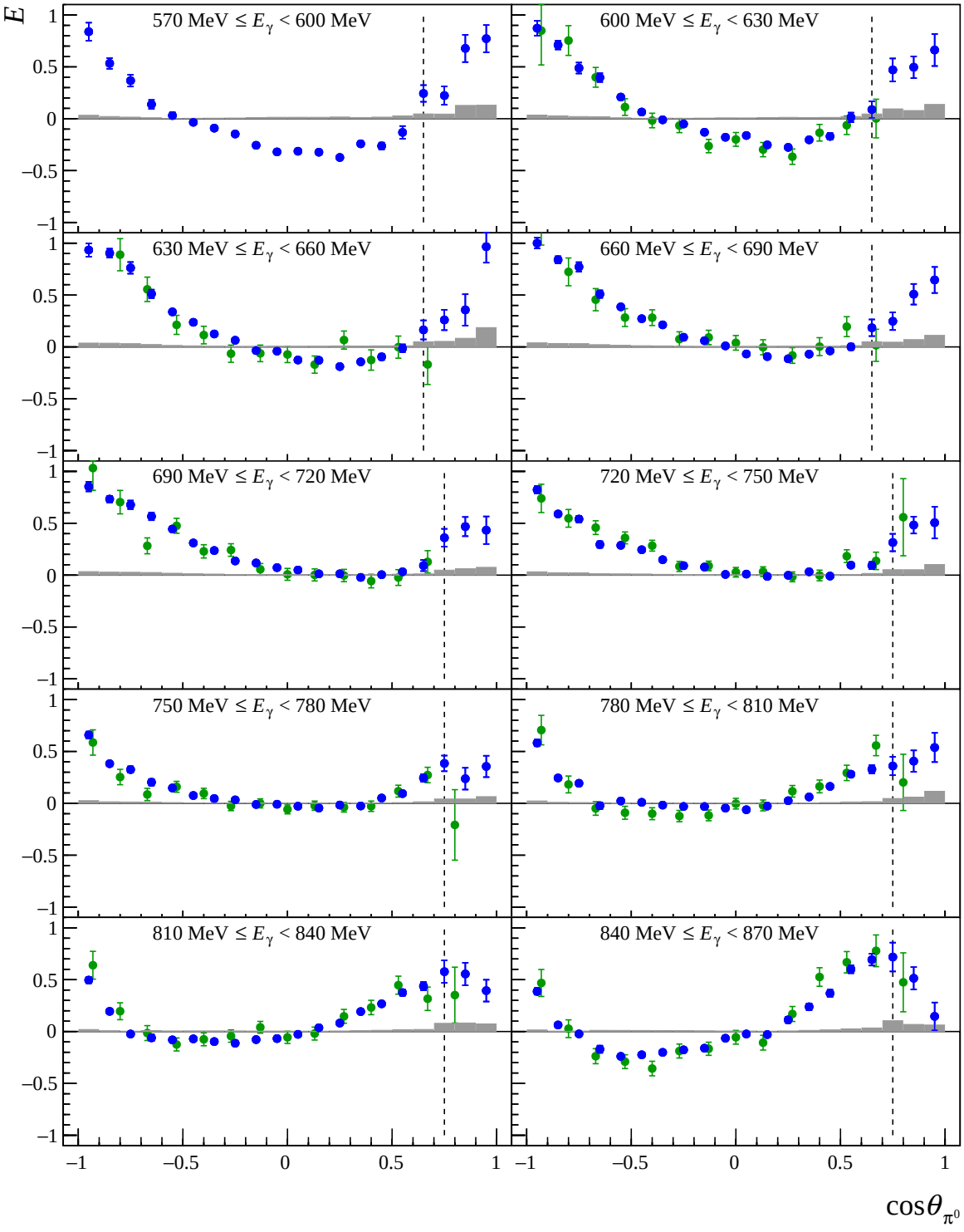

Figure 8.6: Comparison of the new A2 data for the helicity asymmetry E of the $p\pi^0$ final state (blue points) to data from the CBELSA/TAPS collaboration [Got13; Got+14] (green points) are shown as a function of $\cos\theta_{\pi^0}$ for the energy range of (570 MeV $\leq E_\gamma <$ 870 MeV). The black dashed line marks the point where the 2 PED events are added to the 3 PED events. The systematic errors of the new A2 data are depicted in gray.

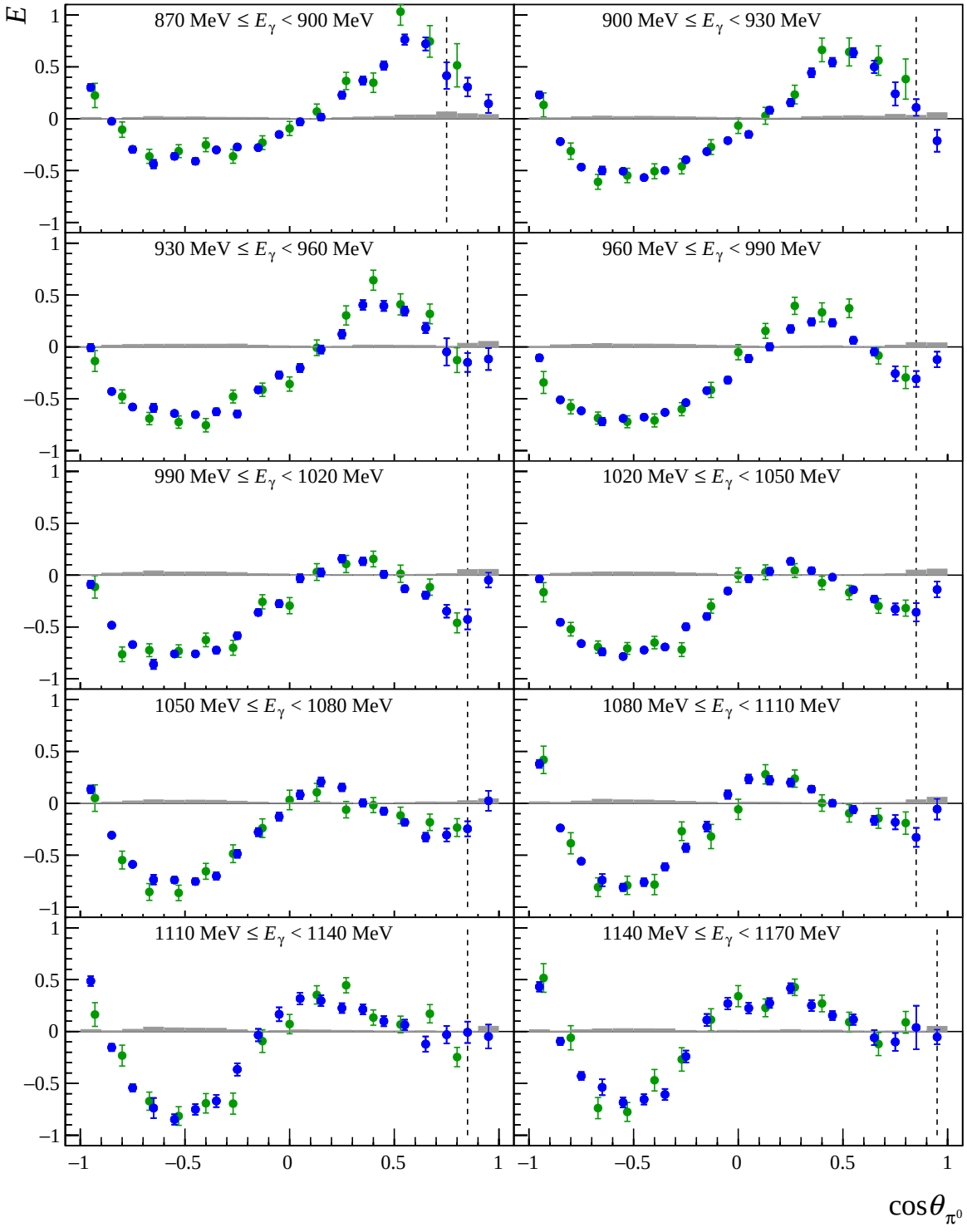

Figure 8.7: Comparison of the new A2 data for the helicity asymmetry E of the $p\pi^0$ final state (blue points) to data from the CBELSA/TAPS collaboration [Got13; Got+14] (green points) are shown as a function of $\cos\theta_{\pi^0}$ for the energy range of (870 MeV $\leq E_\gamma <$ 1170 MeV). The black dashed line marks the point where the 2 PED events are added to the 3 PED events. The systematic errors of the new A2 data are depicted in gray.

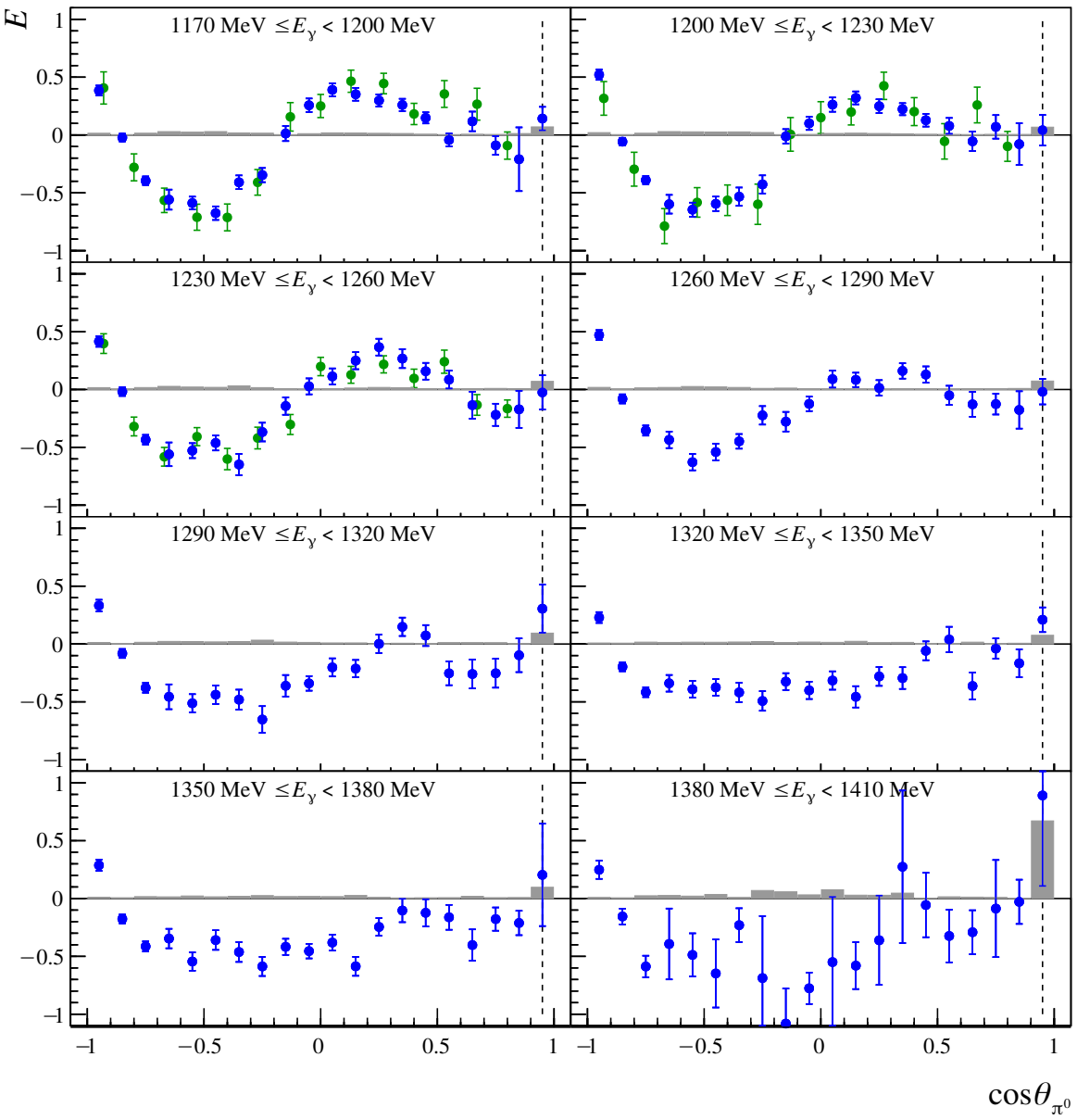

Figure 8.8: Comparison of the new A2 data for the helicity asymmetry E of the $p\pi^0$ final state (blue points) to data from the CBELSA/TAPS collaboration [Got13; Got+14] (green points) are shown as a function of $\cos\theta_{\pi^0}$ for the energy range of (1170 MeV $\leq E_\gamma <$ 1410 MeV). The black dashed line marks the point where the 2 PED events are added to the 3 PED events. The systematic errors of the new A2 data are depicted in gray.

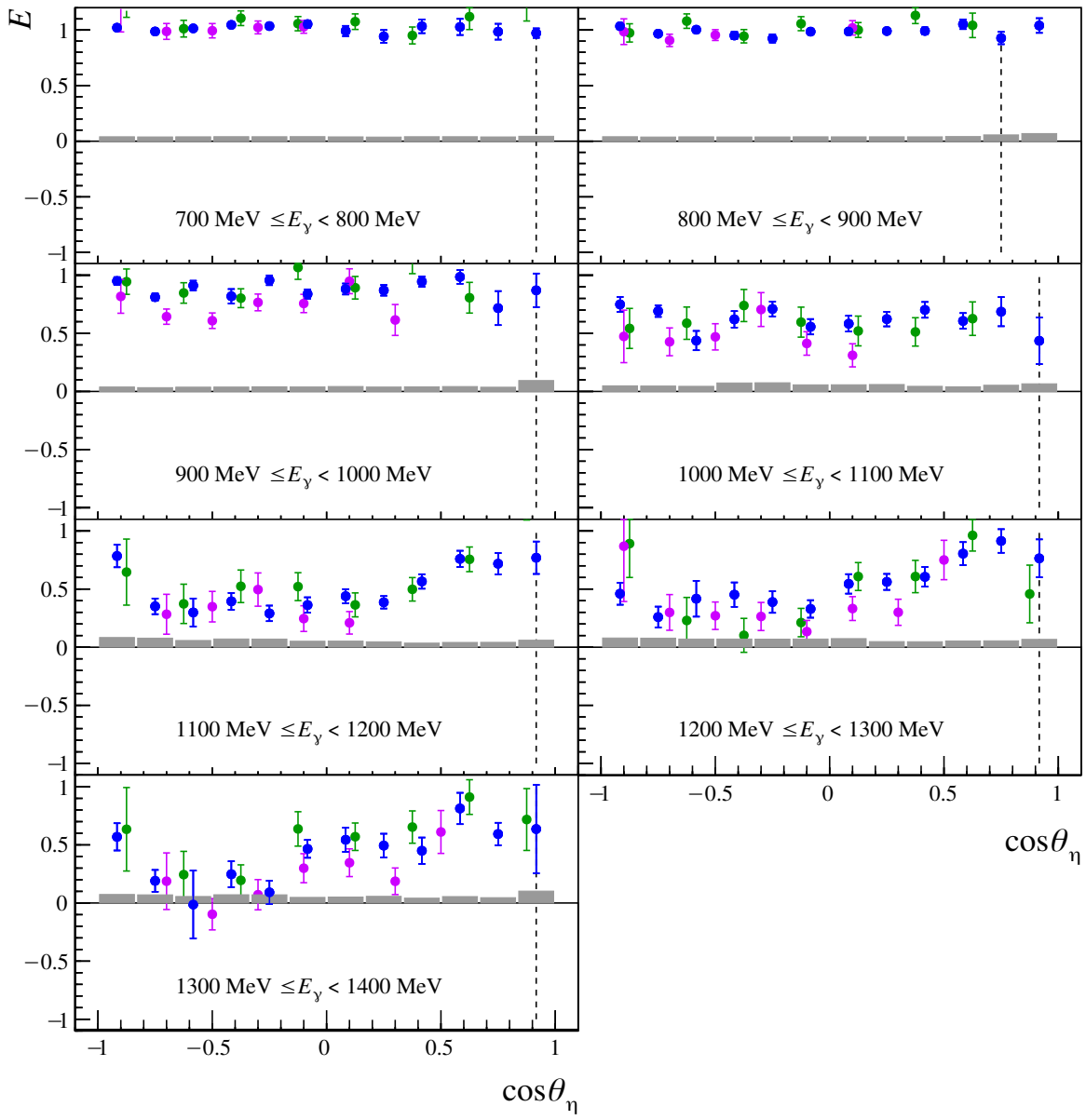

Figure 8.9: Comparison of the new A2 data for the helicity asymmetry E of the $p\eta$ final state (blue points) to data from the CBELSA/TAPS collaboration [Mül18] (green points) and from the CLAS collaboration [Sen+16] (magenta points) are shown as a function of $\cos\theta_\eta$ for the energy range of ($700\,\text{MeV} \leq E_\gamma < 1400\,\text{MeV}$). The black dashed line marks the point where the 2 PED events are added to the 3 PED events. The systematic errors of the new A2 data are depicted in gray.

8.2 Dominant partial wave contributions

In order to obtain knowledge about the dominantly contributing partial waves, the measured angular distributions of the determined beam and helicity asymmetries are further investigated. First, the profile functions $\check{\Sigma} = \Sigma \cdot \frac{d\sigma}{d\Omega}$ and $\check{E} = E \cdot \frac{d\sigma}{d\Omega}$ are obtained by multiplying the measured dimensionless polarization observables with the differential cross section. For this purpose, the BnGa-2014-02 PWA solution [Gut+14] was utilized, since it includes a fit to all existing data points of the differential cross section published until the year 2014. Thus, no experimental errors need to be considered for the cross section. As explained in Section 1.4.2, the profile functions can be expressed in a truncated PWA in the following way [WA+17]:

$$\check{\Sigma}(W,\theta) = \rho \sum_{l=2}^{2\mathrm{L}_{\max}} (a_{\mathrm{L}_{\max}})_l^{\check{\Sigma}}(W)\, P_l^2(\cos\theta)\,, \tag{8.2}$$

$$\check{E}(W,\theta) = \rho \sum_{l=0}^{2\mathrm{L}_{\max}} (a_{\mathrm{L}_{\max}})_l^{\check{E}}(W)\, P_l(\cos\theta)\,, \tag{8.3}$$

where ρ is the phase space factor, $(a_{\mathrm{L}_{\max}})_l^{\check{\Sigma}}$ and $(a_{\mathrm{L}_{\max}})_l^{\check{E}}$ are the Legendre coefficients for a given truncation at $\mathrm{L}_{\max}$ and $P_l^2(\cos\theta)$ and $P_l(\cos\theta)$ are associated Legendre polynomials which describe the angular dependence of the profile functions. The Legendre coefficients are Hermitean forms of the multipoles. They are given by the Hermitean matrices $\mathcal{C}_l^{\check{\Omega}}$ and multipole vectors of dimension $4\mathrm{L}_{\max}$ and depend only on the center of mass energy W [WA+17]:

$$(a_{\mathrm{L}_{\max}})_l^{\check{\Omega}}(W) = \langle \mathcal{M}_{\mathrm{L}_{\max}}(W)|\, \mathcal{C}_l^{\check{\Omega}}\, |\mathcal{M}_{\mathrm{L}_{\max}}(W)\rangle\,. \tag{8.4}$$

$\mathrm{L}_{\max} = 1$ means that only S- and P-wave contributions are taken into consideration. For $\mathrm{L}_{\max} = 2$ D-waves and accordingly for $\mathrm{L}_{\max} = 3$ F-waves, for $\mathrm{L}_{\max} = 4$ G-waves and for $\mathrm{L}_{\max} = 5$ H-waves are included additionally. To clarify, the S-wave contains the multipole E_{0+}, the P-waves the E_{1+}, M_{1+}, M_{1-}, the D-waves the $E_{2+}, E_{2-}, M_{2+}, M_{2-}$, F-waves the $E_{3+}, E_{3-}, M_{3+}, M_{3-}$, G-waves the $E_{4+}, E_{4-}, M_{4+}, M_{4-}$ and the H-waves the $E_{5+}, E_{5-}, M_{5+}, M_{5-}$ multipoles. Since each Legendre coefficient consists of a sum of bilinear products of multipoles, which can result in a lengthy expression, a compact notation is given. For instance the expression $\langle P, P\rangle$ is a sum of bilinear products of multipoles with $l = 1$. For more detailed information, see [WA+17].

The values of χ^2/ndf for the different $\mathrm{L}_{\max}$-fits indicate which $\mathrm{L}_{\max}$ is needed to accurately describe the profile functions within their statistical precision. In addition, it is advantageous to determine the energy dependent Legendre coefficients, as they are sensitive to different interference terms of multipoles. Furthermore, higher order coefficients show exclusively sensitivity to higher l multipoles. Figure 8.10 shows as an example two Legendre coefficients $(a_4)_2^{\check{E}}$ and $(a_4)_6^{\check{E}}$ for the $p\pi^0$ final state. While the coefficient $(a_4)_2^{\check{E}}$ is dominated by the large contributions of $\langle P, P\rangle$ due to the $\Delta(1232)\frac{3}{2}^+$ (P_{33}) resonance, all interference terms involving only S-, P- and D-waves are switched off for the coefficient $(a_4)_6^{\check{E}}$. Here, direct sensitivity to the F-waves is visible. It is noteworthy, that the terms from higher order l multipoles are roughly an order of magnitude smaller in comparison to the lower order multipoles, e.g. in the $p\pi^0$ channel the $\langle P, P\rangle$ term is by a factor of thirty larger than the $\langle F, F\rangle$ term. This puts a high demand on the

data: it needs to have a very high statistical precision and in addition the full angular coverage with a good angular resolution is needed to obtain the sensitivity to higher order multipoles [WA+17].

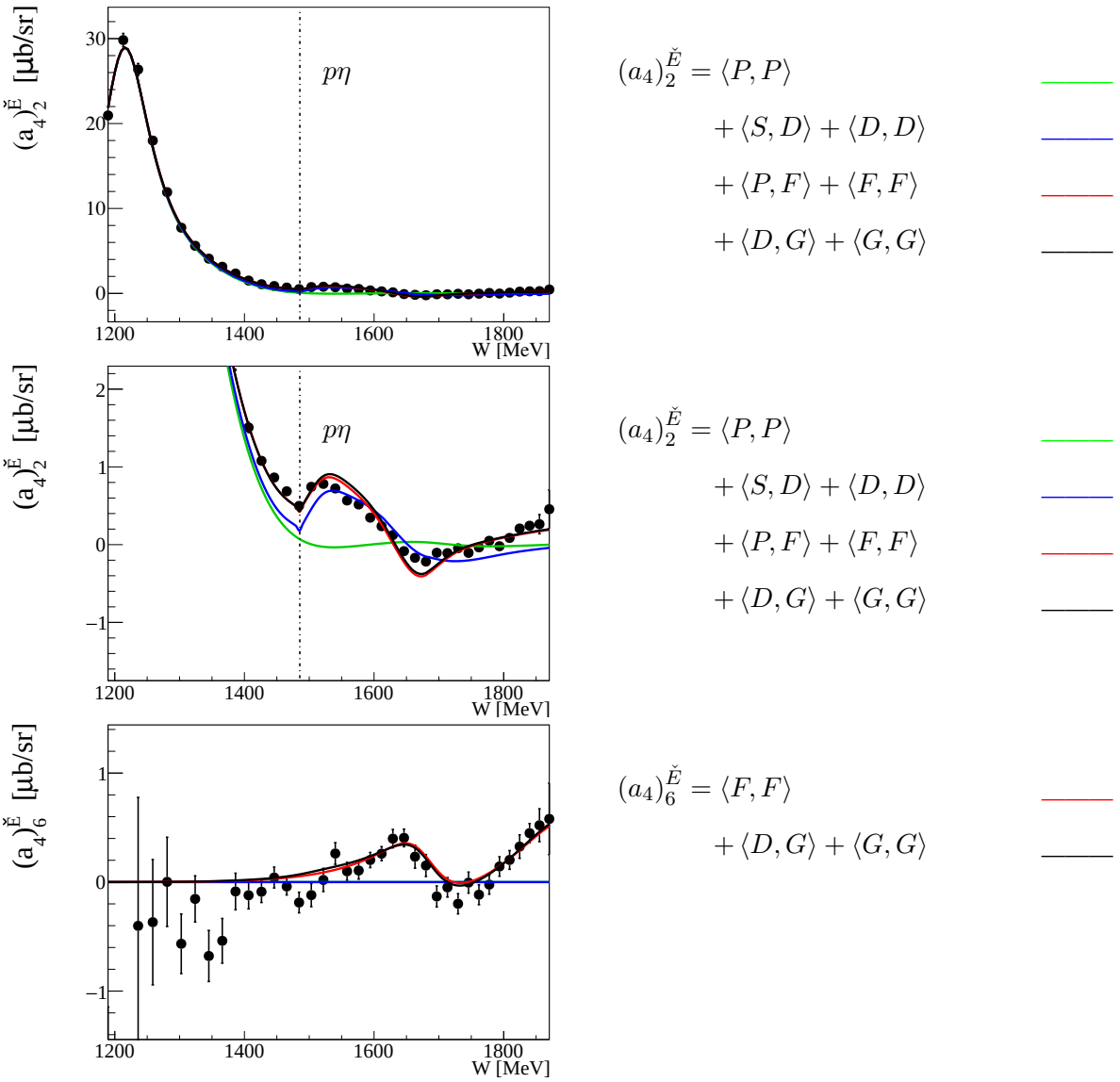

Figure 8.10: Two Legendre coefficients $(a_4)_2^{\check{E}}$ (upper and middle rows) and $(a_4)_6^{\check{E}}$ as obtained from fits to the angular distributions of the profile function $\check{E}$ of the $p\pi^0$ final state are shown. They are compared to continuous curves stemming from the BnGa-2014-02 model solution [Gut+14], which are truncated at different L_{max} ($L_{max} = 1$ (green line), $L_{max} = 2$ (blue line), $L_{max} = 3$ (red line) and $L_{max} = 4$ (black line)). The dashed line indicates the $p\eta$ photoproduction threshold.

If one looks closer at the coefficient $(a_4)_2^{\check{E}}$ (see second row in Figure 8.10), one can see a sudden, discontinuous change in the high precision data as well as in the BnGa-2014-02 curves at $W = 1486\,\text{MeV}$, which is known as the $p\eta$ cusp-effect [Dör+09; DN10]. Since the η meson is mainly produced by the $N(1535)\frac{1}{2}^-$ (S_{11}) resonance at threshold, the cusp-effect is expected to be visible whenever an interference with the S-wave is present. This is why the cusp-effect is first

visible in the blue BnGa-2014-02 curve, which includes the $\langle S, D\rangle$ interference term.

The next two sections discuss the dominant partial wave contributions found in both analyzed reactions $\gamma p \to p\pi^0$ and $\gamma p \to p\eta$ for the beam asymmetry Σ and the double polarization observable E.

8.2.1 Reaction $\gamma p \to p\pi^0$

Figure 8.11 shows six angular distributions of the profile function $\check{E}$ together with the performed fit functions using associated Legendre polynomials according to Equation (8.3) and truncating the partial wave expansion at $\mathrm{L}_{\max} = 1, \ldots, 4$. At $W = 1281\,\mathrm{MeV}$, the parabolic shape of the angular distribution is well described truncating at $\mathrm{L}_{\max} = 1$. This is not surprising since in this energy region the $\Delta(1232)\frac{3}{2}^+$ (P_{33}) resonance, which has $l = 1$ and contributes to the P-wave, strongly contributes to the $p\pi^0$ final state. According to the χ^2/ndf values, a truncation of $\mathrm{L}_{\max} = 1$ is not good enough starting from $W = 1350\,\mathrm{MeV}$ until $W = 1550\,\mathrm{MeV}$. Here, clear contributions from D-waves are visible (see also the angular distribution at $W = 1406\,\mathrm{MeV}$). This energy region ($1350\,\mathrm{MeV} \lesssim W \lesssim 1600\,\mathrm{MeV}$) is also known as the second resonance region (see Figure 1.10), where the $N(1520)\frac{3}{2}^-$ (D_{13}) resonance dominates [Pat+16]. In the third ($1600\,\mathrm{MeV} \lesssim W \lesssim 1800\,\mathrm{MeV}$) and fourth ($1800\,\mathrm{MeV} \lesssim W \lesssim 2250\,\mathrm{MeV}$) resonance regions, two F-wave resonances, the $N(1680)\frac{5}{2}^+$ (F_{15}) and the $\Delta(1950)\frac{7}{2}^-$ (F_{37}), dominate [Pat+16]. This is mirrored in the angular distributions which can only be described well with $\mathrm{L}_{\max} = 3$-fits. It is most evident in the angular distribution of $W = 1855\,\mathrm{MeV}$. Within the statistical precision of the double polarization observable E data, no significant indications for G-waves or higher order partial wave contributions are found for this observable and in this energy range.

Figures 8.12 - 8.14 show the energy dependence of the Legendre coefficients as obtained from a $\mathrm{L}_{\max} = 4$-fit to the angular distributions of the profile function. The Legendre coefficients are compared to different BnGa-2014-02 PWA solution curves, which are truncated at different $\mathrm{L}_{\max}$. The BnGa-2014-02 PWA solution has included the existing data for the double polarization observable E of the CBELSA/TAPS collaboration [Got13; Got+14] in their multi-channel fit and offers the opportunity to demonstrate the sensitivity of the different coefficients to different multipole interference terms according to their model.
The coefficient $(a_4)_0^{\check{E}}$ is sensitive exclusively to interference terms of the same l and furthermore, it is sensitive to the absolute value squared of the multipoles. Since these terms are well determined by the unpolarized cross section, it is not surprising that this coefficient is perfectly described by the BnGa-2014-02 PWA curves. As previously discussed, the $\langle P, P\rangle$-term dominates until $W = 1350\,\mathrm{MeV}$ due to the $\Delta(1232)\frac{3}{2}^+$ (P_{33}) resonance contribution and the BnGa-2014-02 curve for $\mathrm{L}_{\max} = 1$ is sufficient to describe the data. For most of the higher energies, the $\mathrm{L}_{\max} = 3$ curve, which includes F-wave contributions, is needed. The $\langle P, P\rangle$ interference term dominates also the coefficient $(a_4)_2^{\check{E}}$. Starting from coefficient $(a_4)_3^{\check{E}}$, pure S- and/or P-wave interference terms do not contribute anymore. Here, interference terms involving D- and or F-wave become important, e.g. $(a_4)_3^{\check{E}}$ is sensitive to the $\langle P, D\rangle$ interference term until $W = 1500\,\mathrm{MeV}$ and later to the $\langle S, F\rangle$ and the $\langle D, F\rangle$ interference terms since the BnGa-2014-02 curves truncated at $\mathrm{L}_{\max} = 2$ and $\mathrm{L}_{\max} = 3$ describe the data well in the according energy ranges. The coefficients $(a_4)_4^{\check{E}}$ to $(a_4)_6^{\check{E}}$ all show that F-wave contributions can not be ignored for the double polarization observable E. This can be seen most predominantly

in the coefficient $(a_4)_6^{\check{E}}$, since this coefficient would be consistent with 0 if no significant F-wave contributions existed. Instead, one can observe two structures which can be cautiously associated with the F-wave resonances $N(1680)\frac{5}{2}^+$ (F_{15}) and the $\Delta(1950)\frac{7}{2}^-$ (F_{37}). Since both resonances are well-established four star resonances [Pat+16], the coefficients $(a_4)_4^{\check{E}}$ and $(a_4)_6^{\check{E}}$ are well described by the BnGa-2014-02 model curves. However, modifications are needed for the coefficient $(a_4)_5^{\check{E}}$, which is sensitive to the interference term $\langle D, F\rangle$. Considering that the F-wave resonances are well described by the BnGa-2014-02 model, this may indicate that modifications are needed for the D-waves of the BnGa model. Small indications for G-wave contributions are present for the coefficient $(a_4)_7^{\check{E}}$. However, the statistical precision is not high enough to be certain, see e.g. also coefficient $(a_4)_8^{\check{E}}$ which is sensitive to the $\langle G, G\rangle$ interference term and is consistent with zero within the statistical error bars.

As already mentioned, the $p\eta$ cusp-effect is visible for some coefficients. The $p\eta$ cusp is first visible in the coefficient $(a_4)_0^{\check{E}}$ due to the interference term $\langle S, S\rangle$. In the coefficient $(a_4)_2^{\check{E}}$ the cusp is much stronger visible because of the $\langle S, D\rangle$ interference term. Furthermore, the cusp behavior is again enhanced by the interference term $\langle S, F\rangle$ in the coefficient $(a_4)_3^{\check{E}}$. Both the D- and the F-waves are the dominating waves in the $p\pi^0$ channel around the $p\eta$ photoproduction threshold around $W = 1486\,\text{MeV}$. The cusp is not visible anymore for the higher order coefficients because the S-wave interference terms are not contributing anymore.

Almost every coefficient is well described by the BnGa2014-02 solution. However, it is striking that the coefficient $(a_4)_1^{\check{E}}$ shows a significant deviation from the BnGa-2014-02 PWA solution below $W = 1400\,\text{MeV}$. This energy region is not covered by any double polarization observables for the $p\pi^0$ final state until now. The deviations indicate that most likely the interference term $\langle S, P\rangle$ (since no modifications are present through the higher order interference terms) may not be described accurately by the BnGa-2014-02 PWA solution in this energy region. Similar deviations of data to the BnGa2014-02 PWA solution were found for the differential cross section fit coefficient $(a_4)_1^{\sigma_0}$ [WA+17] in the $\Delta(1232)\frac{3}{2}^+$ (P_{33}) resonance region. This coefficient is described by similar interference terms. A comparison to the SAID-PR15 model [Adl+15] for the coefficient $(a_4)_1^{\sigma_0}$ showed a good agreement to the data which means the observed deviations to the BnGa-2014-02 PWA solution for $\check{E}$ and the differential cross section around the $\Delta(1232)\frac{3}{2}^+$ (P_{33}) resonance region can be interpreted as deficiencies of the BnGa PWA model, at least for the solution BnGa-2014-02, and do not mean that the well known $\Delta(1232)\frac{3}{2}^+$ (P_{33}) resonance parameters need modification. Probably, the E_{0+} multipole needs to be modified in the BnGa model.

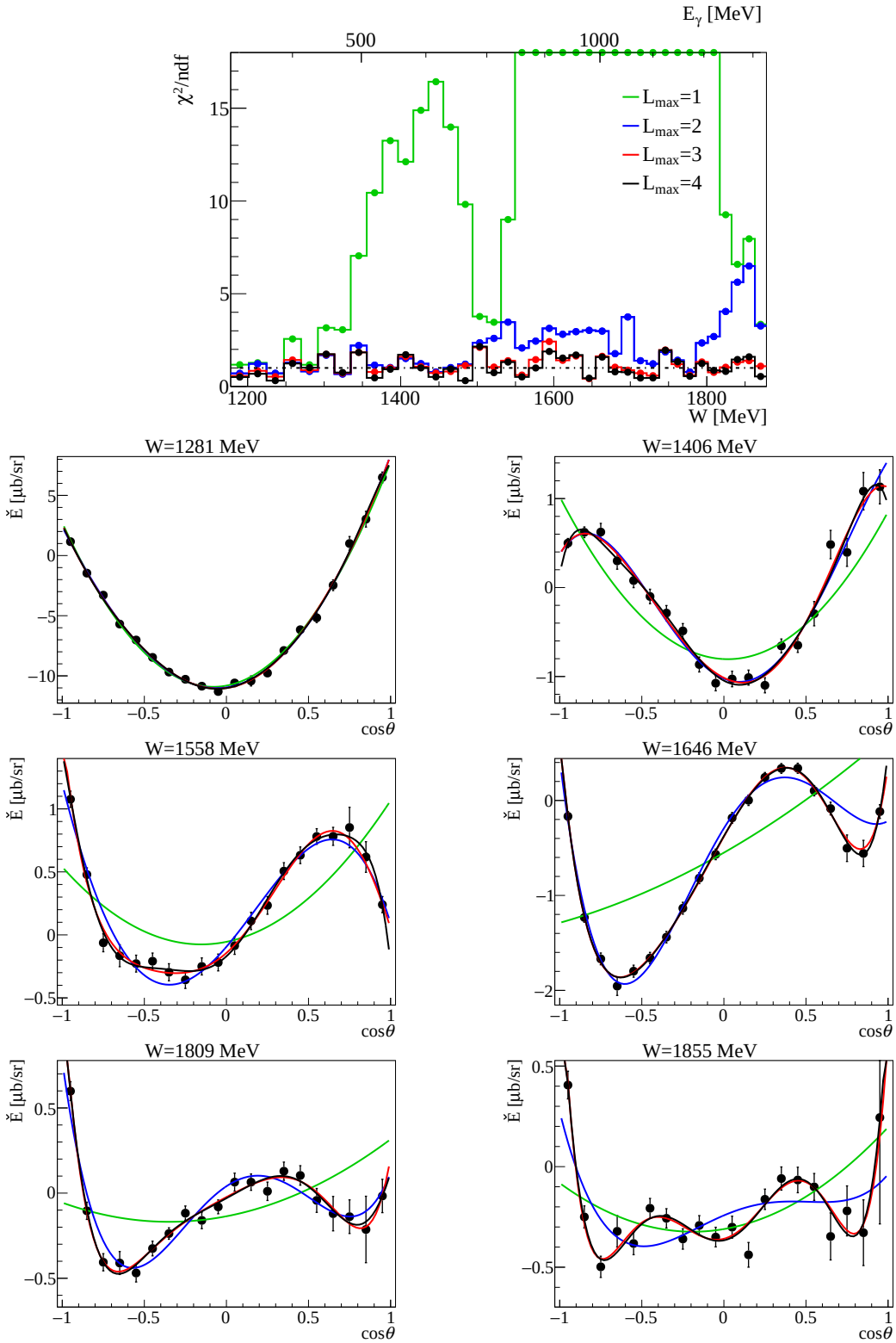

Figure 8.11: The angular distributions of the profile function $\check{E}$ of the $p\pi^0$ final state (A2 data) were fitted utilizing associated Legendre polynomials according to Equation (8.3). Thereby, the partial wave expansion was truncated at different L_{max} ($L_{max} = 1$ (green line), $L_{max} = 2$ (blue line), $L_{max} = 3$ (red line) and $L_{max} = 4$ (black line)). The χ^2/ndf values of the different L_{max}-fits are given at the top as a function of the center of mass and lab energies. Additionally, six angular distributions (black points) are shown in comparison with the different L_{max}-fits.

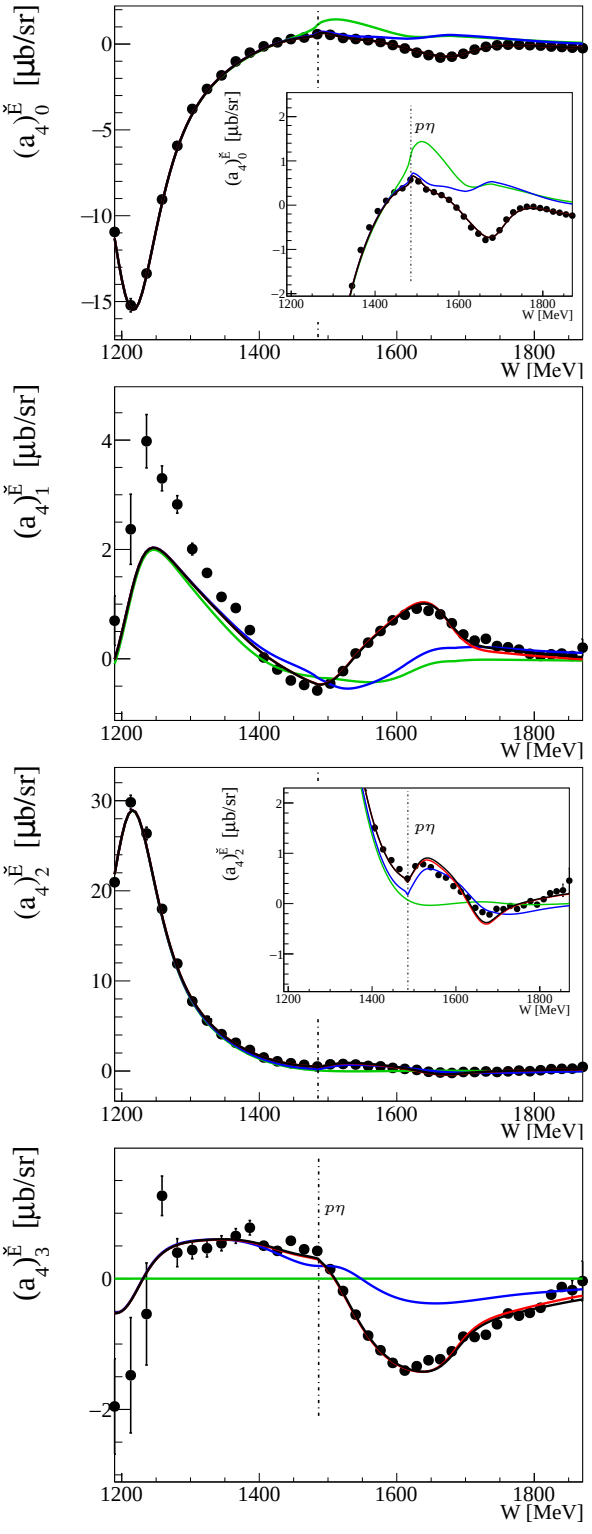

$$(a_4)_0^{\check{E}} = \langle S,S\rangle + \langle P,P\rangle + \langle D,D\rangle + \langle F,F\rangle + \langle G,G\rangle$$

$$(a_4)_1^{\check{E}} = \langle S,P\rangle + \langle P,D\rangle + \langle D,F\rangle + \langle F,G\rangle$$

$$(a_4)_2^{\check{E}} = \langle P,P\rangle + \langle S,D\rangle + \langle D,D\rangle + \langle P,F\rangle + \langle F,F\rangle + \langle D,G\rangle + \langle G,G\rangle$$

$$(a_4)_3^{\check{E}} = \langle P,D\rangle + \langle S,F\rangle + \langle D,F\rangle + \langle P,G\rangle + \langle F,G\rangle$$

Figure 8.12: Left: The obtained fit coefficients $(a_4)_{0\ldots3}^{\check{E}}$ of the $p\pi^0$ final state are plotted (black points). They are compared to continuous curves evaluated from the BnGa-2014-02 model solution [Gut+14], which are truncated at different L_{max} ($L_{max} = 1$ (green line), $L_{max} = 2$ (blue line), $L_{max} = 3$ (red line) and $L_{max} = 4$ (black line)). Right: All contributing partial wave interference terms are given in a compact notation up to $L_{max} = 4$. The green line of the BnGa-2014-02 model contain contributions from S- and P-wave interference terms contributions, the blue line additionally D-wave, the red line additionally F-wave and the black line additionally G-wave contributions. The dashed-dotted line marks the $p\eta$ photoproduction threshold.

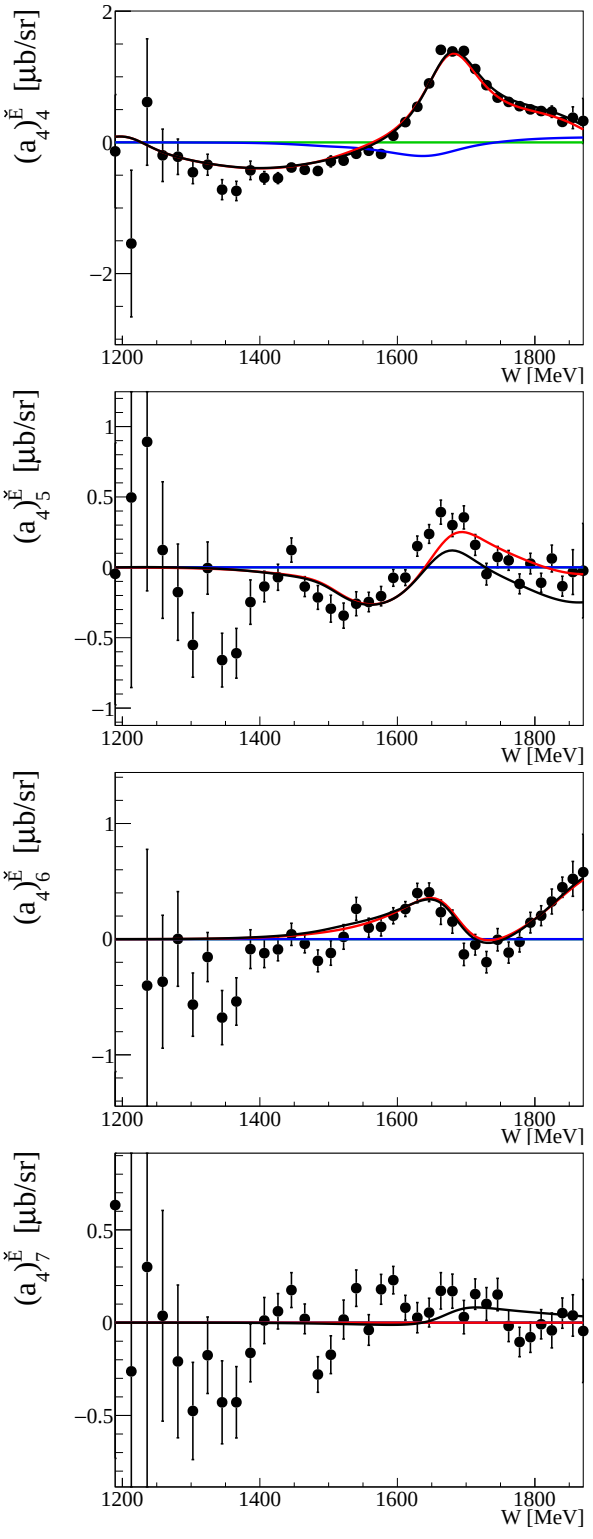

$$(a_4)^{\check{E}}_4 = \langle D, D\rangle + \langle P, F\rangle + \langle F, F\rangle + \langle S, G\rangle + \langle D, G\rangle + \langle G, G\rangle$$

$$(a_4)^{\check{E}}_5 = \langle D, F\rangle + \langle P, G\rangle + \langle F, G\rangle$$

$$(a_4)^{\check{E}}_6 = \langle F, F\rangle + \langle D, G\rangle + \langle G, G\rangle$$

$$(a_4)^{\check{E}}_7 = \langle F, G\rangle$$

Figure 8.13: Left: The obtained fit coefficients $(a_4)^{\check{E}}_{4\ldots7}$ of the $p\pi^0$ final state are plotted (black points). They are compared to continuous curves evaluated from the BnGa-2014-02 model solution [Gut+14], which are truncated at different L_{max} ($L_{max} = 1$ (green line), $L_{max} = 2$ (blue line), $L_{max} = 3$ (red line) and $L_{max} = 4$ (black line)). Right: All contributing partial wave interference terms are given in a compact notation up to $L_{max} = 4$. The green line of the BnGa-2014-02 model contain contributions from S- and P-wave interference terms contributions, the blue line additionally D-wave, the red line additionally F-wave and the black line additionally G-wave contributions.

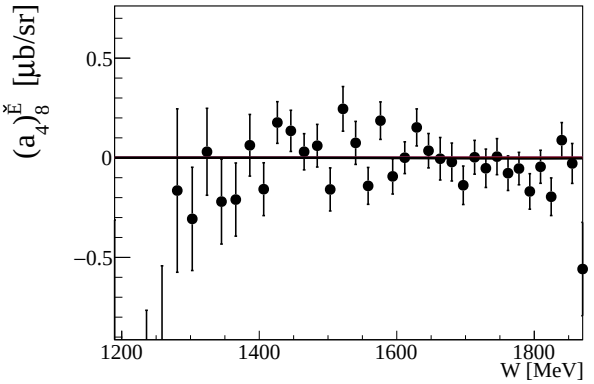

$(a_4)_8^{\check{E}} = \langle G, G \rangle$

Figure 8.14: Left: The obtained fit coefficient $(a_4)_8^{\check{E}}$ of the $p\pi^0$ final state is plotted (black points). It is compared to continuous curves evaluated from the BnGa-2014-02 model solution [Gut+14], which are truncated at different L_{max} ($L_{max} = 1$ (green line), $L_{max} = 2$ (blue line), $L_{max} = 3$ (red line) and $L_{max} = 4$ (black line)). Right: All contributing partial wave interference terms are given in a compact notation up to $L_{max} = 4$. The green line of the BnGa-2014-02 model contain contributions from S- and P-wave interference terms contributions, the blue line additionally D-wave, the red line additionally F-wave and the black line additionally G-wave contributions.

Figure 8.15 shows, for six energy bins, the angular distributions of the profile function $\check{\Sigma}$ of the $p\pi^0$ final state together with the associated Legendre fit functions truncated at different L_{max} according to Equation (8.2). The angular distributions and the χ^2/ndf values of the beam asymmetry data shows sensitivity up to the G-waves ($l = 4$) for almost the entire covered energy range starting at $W = 1800\,\text{MeV}$, which is only possible due to the high statistical precision and large angular coverage of the data. This is well demonstrated with the angular distributions of the profile function $\check{\Sigma}$ starting from $W = 1855\,\text{MeV}$ as only very small statistical error bars allow to distinguish between the fit functions for $L_{max} = 3$ and $L_{max} = 4$ within the angular range of $-0.7 < \cos\theta < 0.7$. In addition, the angular distributions demonstrate the importance of measuring the extreme angular regions $\cos\theta < -0.7$ and $\cos\theta > 0.7$ in order to be sensitive to higher order multipoles.

The Legendre coefficients of the profile function $\check{\Sigma}$ are given in Figures 8.16 and 8.17. The comparison to the BnGa-2014-02 PWA curves, where the beam asymmetry data of the CLAS collaboration [Dug+14] are included and which are truncated at different L_{max}, reveals that F-wave contributions play an important role in the energy range covered by the beam asymmetry. Here, the dominant contributing resonances are the $\Delta(1905)\frac{5}{2}^+$ (F_{35}) and the $\Delta(1950)\frac{7}{2}^-$ (F_{37}) resonances [Pat+16]. Thus, the Legendre coefficients are very sensitive to interference terms involving F-waves, e.g. the coefficient $(a_4)_3^{\check{\Sigma}}$ is sensitive to $\langle S, F \rangle$ and the coefficient $(a_4)_4^{\check{\Sigma}}$ to $\langle P, F \rangle$ and $\langle F, F \rangle$ interference terms. The inclusion of G-wave contributions improves slightly the description of the coefficients $(a_4)_4^{\check{\Sigma}}$ and $(a_4)_6^{\check{\Sigma}}$. However, the largest evidence for G-wave contributions is given by the coefficient $(a_4)_7^{\check{\Sigma}}$, which is not equal to zero. Contributions from H-waves improve slightly the description of the coefficients $(a_4)_7^{\check{\Sigma}}$ and $(a_4)_8^{\check{\Sigma}}$. Large deviations between data and the BnGa-2014-02 curves are visible for the coefficient $(a_4)_5^{\check{\Sigma}}$, where the interference term $\langle D, F \rangle$ plays an important role. Similar to the $\check{E}$ data, this indicates again that probably modifications for the D-waves are needed for the BnGa-2014-02 solution.

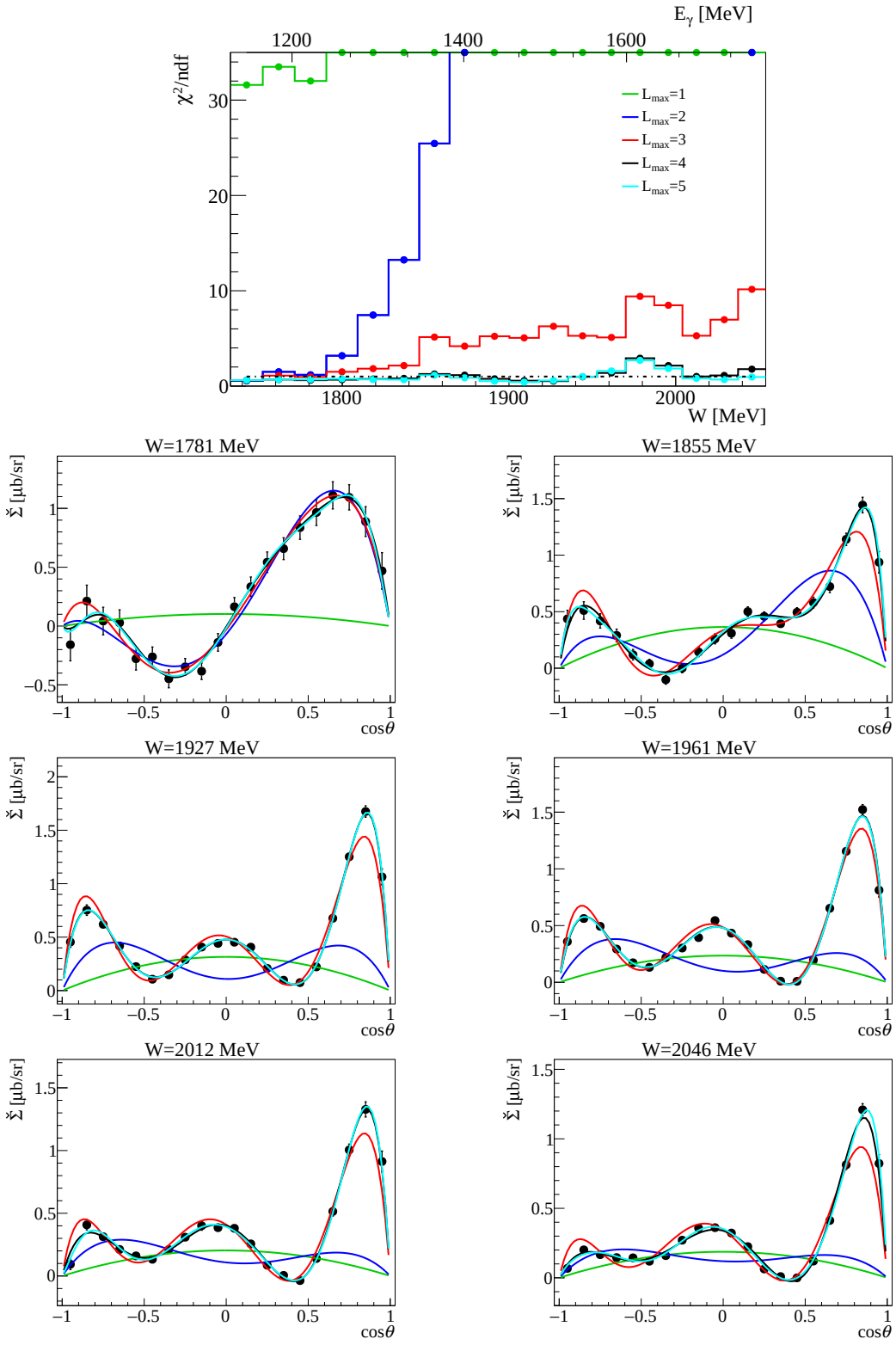

Figure 8.15: The angular distributions of the profile function $\check{\Sigma}$ of the $p\pi^0$ final state (CBELSA/TAPS data) were fitted utilizing associated Legendre polynomials according to Equation (8.2). Thereby, the partial wave expansion was truncated at different L_{max} ($L_{max} = 1$ (green line), $L_{max} = 2$ (blue line), $L_{max} = 3$ (red line), $L_{max} = 4$ (black line) and $L_{max} = 5$ (turquoise)). The χ^2/ndf values of the different L_{max}-fits are given at the top as a function of the center of mass and lab energies. Additionally, six angular distributions (black points) are shown in comparison with the different L_{max}-fits.

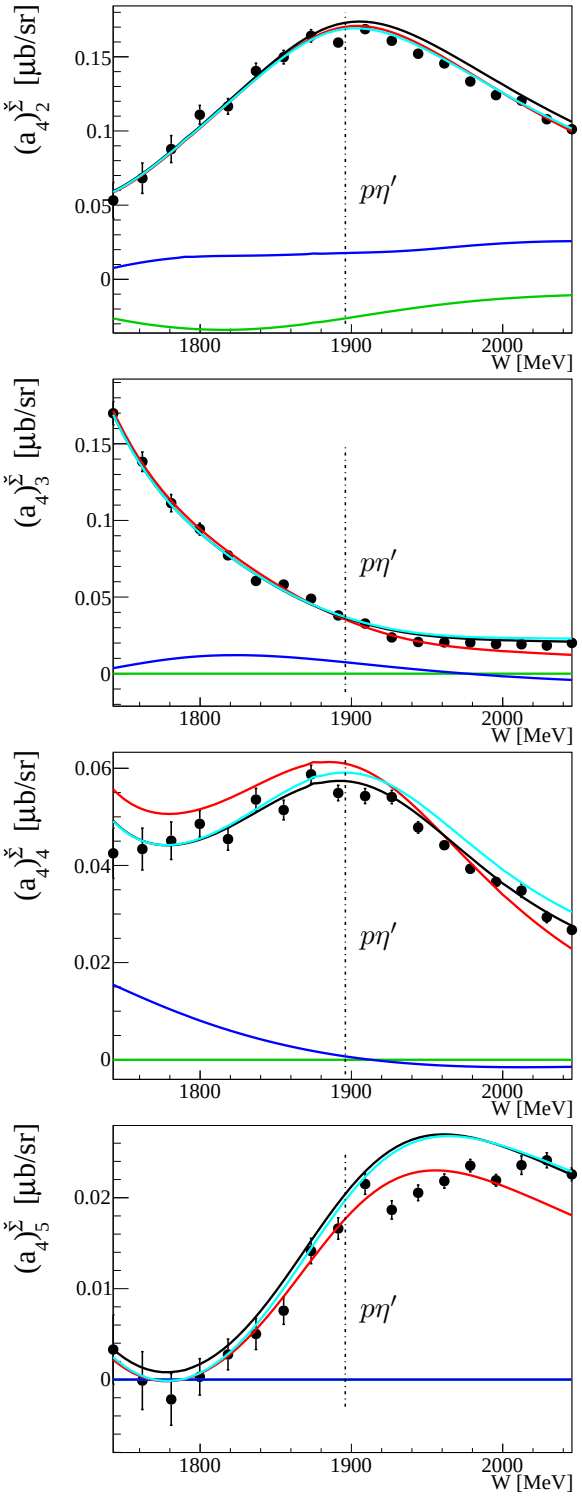

$$(a_5)^{\check{\Sigma}}_2 = \langle P,P\rangle + \langle S,D\rangle + \langle D,D\rangle + \langle P,F\rangle + \langle F,F\rangle + \langle D,G\rangle + \langle G,G\rangle + \langle F,H\rangle + \langle H,H\rangle$$

$$(a_5)^{\check{\Sigma}}_3 = \langle P,D\rangle + \langle S,F\rangle + \langle D,F\rangle + \langle P,G\rangle + \langle F,G\rangle + \langle D,H\rangle + \langle G,H\rangle$$

$$+(a_5)^{\check{\Sigma}}_4 = \langle D,D\rangle + \langle P,F\rangle + \langle F,F\rangle + \langle S,G\rangle + \langle D,G\rangle + \langle G,G\rangle + \langle P,H\rangle + \langle F,H\rangle + \langle H,H\rangle$$

$$(a_5)^{\check{\Sigma}}_5 = \langle D,F\rangle + \langle P,G\rangle + \langle F,G\rangle + \langle S,H\rangle + \langle D,H\rangle + \langle G,H\rangle$$

Figure 8.16: Left: The obtained fit coefficients $(a_4)^{\check{\Sigma}}_{2\ldots5}$ of the $p\pi^0$ final state are plotted (black points). They are compared to continuous curves evaluated from the BnGa-2014-02 model solution [Gut+14], which are truncated at different L_{max} ($L_{max} = 1$ (green line), $L_{max} = 2$ (blue line), $L_{max} = 3$ (red line), $L_{max} = 4$ (black line) and $L_{max} = 5$ (turquoise line)). Right: All contributing partial wave interference terms are given in a compact notation up to $L_{max} = 5$. The green line of the BnGa-2014-02 model contain contributions from S- and P-wave interference terms contributions, the blue line additionally D-wave, the red line additionally F-wave, the black line additionally G-wave and the turquoise line additionally H-wave contributions. The dashed-dotted line mark the $p\eta'$ photoproduction threshold.

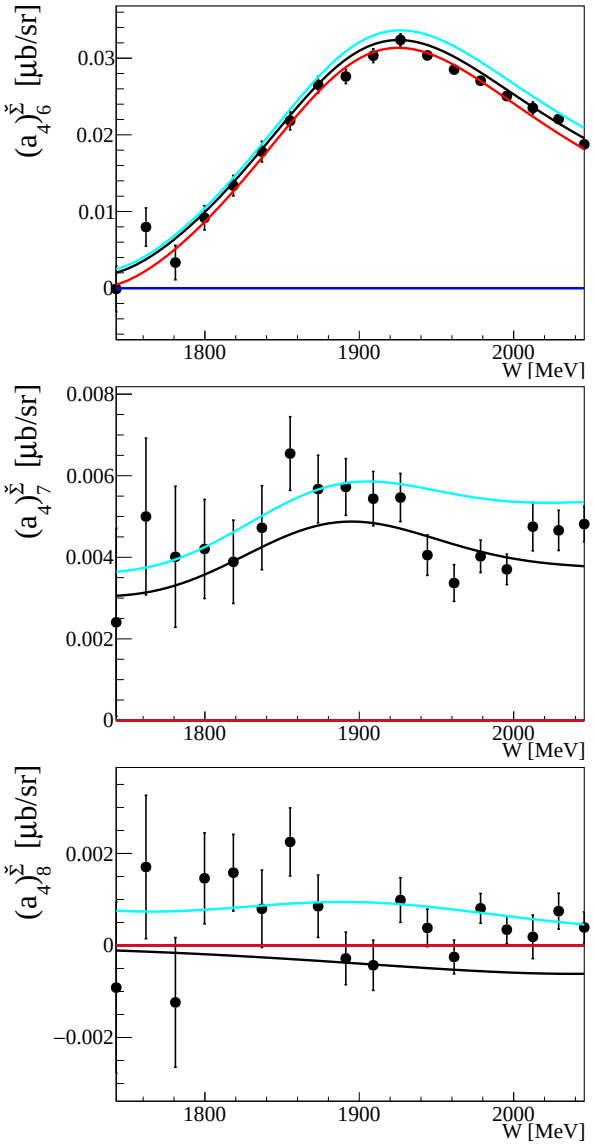

$$(a_5)^{\check{\Sigma}}_6 = \langle F, F\rangle + \langle D, G\rangle + \langle G, G\rangle + \langle P, H\rangle + \langle F, H\rangle + \langle H, H\rangle$$

$$(a_5)^{\check{\Sigma}}_7 = \langle F, G\rangle + \langle D, H\rangle + \langle G, H\rangle$$

$$(a_5)^{\check{\Sigma}}_8 = \langle G, G\rangle + \langle F, H\rangle + \langle H, H\rangle$$

Figure 8.17: Left: The obtained fit coefficients $(a_4)^{\check{\Sigma}}_{6\cdots8}$ of the $p\pi^0$ final state are plotted (black points). They are compared to continuous curves evaluated from the BnGa-2014-02 model solution, which are truncated at different L_{max} ($L_{max} = 1$ (green line), $L_{max} = 2$ (blue line), $L_{max} = 3$ (red line), $L_{max} = 4$ (black line) and $L_{max} = 5$ (turquoise line)). Right: All contributing partial wave interference terms are given in a compact notation up to $L_{max} = 5$. The green line of the BnGa-2014-02 model contain contributions from S- and P-wave interference terms contributions, the blue line additionally D-wave, the red line additionally F-wave, the black line additionally G-wave and the turquoise line additionally H-wave contributions.

8.2.2 Reaction $\gamma p \to p\eta$

The same fitting procedure was repeated for the profile functions $\check{E}$ and $\check{\Sigma}$ of the $p\eta$ final state. In this section the fit results of the $p\eta$ final state are presented.

The double polarization observable E covers the center of mass energy range from $W \approx 1500\,\text{MeV}$ to $W \approx 1880\,\text{MeV}$, starting directly at the η photoproduction threshold ($W = 1486\,\text{MeV}$). Figure 8.18 shows six angular distributions together with the fit functions truncated at different L_{max} up to $\text{L}_{\text{max}} = 3$ and the values for χ^2/ndf. Due to the low number of data points, the fit for $\text{L}_{\text{max}} = 4$ was not performed. The Legendre coefficients are given in Figure 8.19 and 8.20 together with BnGa-2014-02 PWA predictions truncated at different L_{max}. According to the values for χ^2/ndf (see Figure 8.18), the entire covered energy range is described well when truncating at $\text{L}_{\text{max}} = 1$. This shows that the dominating resonances in the $p\eta$ final state are the $N(1535)\frac{1}{2}^-$ (S_{11}) and the $N(1650)\frac{1}{2}^-$ (S_{11}) resonances [Pat+16], which both contribute to the S-wave (see Figure 1.10).

As already mentioned, starting from the η photoproduction threshold to $W \approx 1900\,\text{MeV}$, the $N(1535)\frac{1}{2}^-$ (S_{11}) and the $N(1650)\frac{1}{2}^-$ (S_{11}) resonances play a dominant role [Pat+16]. Therefore, the interference terms involving the S-wave are important in order to accurately describe the Legendre coefficients, e.g. the coefficient $(a_3)_0^{\check{E}}$ shows sensitivity to the absolute value squared of the E_{0+} multipole due to the term $\langle S, S\rangle$, which agrees well with the curves of the BnGa-2014-02 model, since differential cross section data of the $p\eta$ final state are included in the fitted database of the BnGa model. The coefficient $(a_3)_1^{\check{E}}$ is sensitive to the interference term $\langle S, P\rangle$. Also here, the data is already described well using a truncation at $\text{L}_{\text{max}} = 1$. Contributions from D-waves become evident when looking at the coefficient $(a_3)_2^{\check{E}}$, where corrections from the interference terms $\langle S, D\rangle$ and $\langle D, D\rangle$ are needed to describe the data. Here, the $N(1520)\frac{3}{2}^-$ (D_{13}), the $N(1700)\frac{3}{2}^-$ (D_{13}), the $N(1875)\frac{3}{2}^-$ (D_{13}) and the $N(1675)\frac{5}{2}^-$ (D_{15}) resonances [Pat+16] contribute to the D-waves in this energy region. Furthermore, the coefficient $(a_3)_2^{\check{E}}$ shows the $K\Sigma$ cusp-effect at $W = 1686\,\text{MeV}$. Looking at the angular distributions, the sensitivity to F-waves is not well visible for this observable and this energy range. A higher statistical precision and higher angular coverage is needed in the future. Nevertheless, the coefficient $(a_3)_3^{\check{E}}$ suggests that modifications are probably needed for the $\langle P, D\rangle$ and/ or the $\langle S, F\rangle$ and/ or the $\langle D, F\rangle$ interference term to get a better description of the data above $W = 1700\,\text{MeV}$. The BnGa-2014-02 solution predicts a different sign for the contributions from the interference terms $\langle S, F\rangle$ and $\langle D, F\rangle$.

The measured beam asymmetry Σ data has, like the helicity asymmetry E data, twelve data points for each angular distribution. However, according to Equation (8.2), the number of fit coefficients is reduced by two for each L_{max} fit. Therefore, it is possible to perform fits up to $\text{L}_{\text{max}} = 4$. The fit results for six angular distributions and all values for χ^2/ndf are shown in Figure 8.21 and the fit coefficients are given in Figures 8.19 and 8.20. The values for χ^2/ndf demonstrate that a truncation at $\text{L}_{\text{max}} = 2$ is satisfactory until $W = 1850\,\text{MeV}$ and at $\text{L}_{\text{max}} = 3$ until $W = 1950\,\text{MeV}$. For higher energies a truncation at $\text{L}_{\text{max}} = 4$ is needed (see also the angular distribution at $W = 2045\,\text{MeV}$ in Figure 8.21).

In contrast to the helicity asymmetry data, the beam asymmetry data can not be described

well when truncating at $L_{max} = 1$ (compare the angular distributions in Figure 8.21). The D-wave contributions are best visible in the coefficient $(a_4)_2^{\check{\Sigma}}$, where the $\langle S, D\rangle$ interference term plays an important role. Above $W = 1850\,\text{MeV}$, the angular distributions indicate F-wave contributions as the fit with $L_{max} = 3$ is needed to achieve a good agreement with the data. This is further demonstrated for the coefficient $(a_4)_3^{\check{\Sigma}}$, where a good description is achieved with the BnGa-2014-02 PWA, if one takes the interference terms $\langle S, F\rangle$ and $\langle D, F\rangle$ into account. The coefficient $(a_4)_4^{\check{\Sigma}}$ shows the largest deviations from the BnGa-2014-02 PWA curves. The BnGa-2014-02 PWA curves are lying by a factor of around 2 below the data above the η' photoproduction threshold ($W = 1896\,\text{MeV}$), indicating that the interference terms $\langle D, D\rangle$, $\langle S, G\rangle$ and/or $\langle P, F\rangle$ are insufficiently described by the BnGa model. In addition, the Legendre coefficient $(a_4)_4^{\check{\Sigma}}$ indicates the $p\eta'$ cusp-effect at $W = 1896\,\text{MeV}$ in the data. However, the BnGa-2014-02 solution does not show a bend in the energy dependence of the $< S, G >$ interference term (black curve), indicating that the energy dependence of the $p\eta'$ cusp-effect is missing in the S-wave of the BnGa-2014-02 solution.

Furthermore, the data even shows sensitivity for G-wave contributions above $W = 1950\,\text{MeV}$ (compare the χ^2/ndf values), which is also indicated in the coefficient $(a_4)_7^{\check{\Sigma}}$, which is not consistent with zero in this energy range.

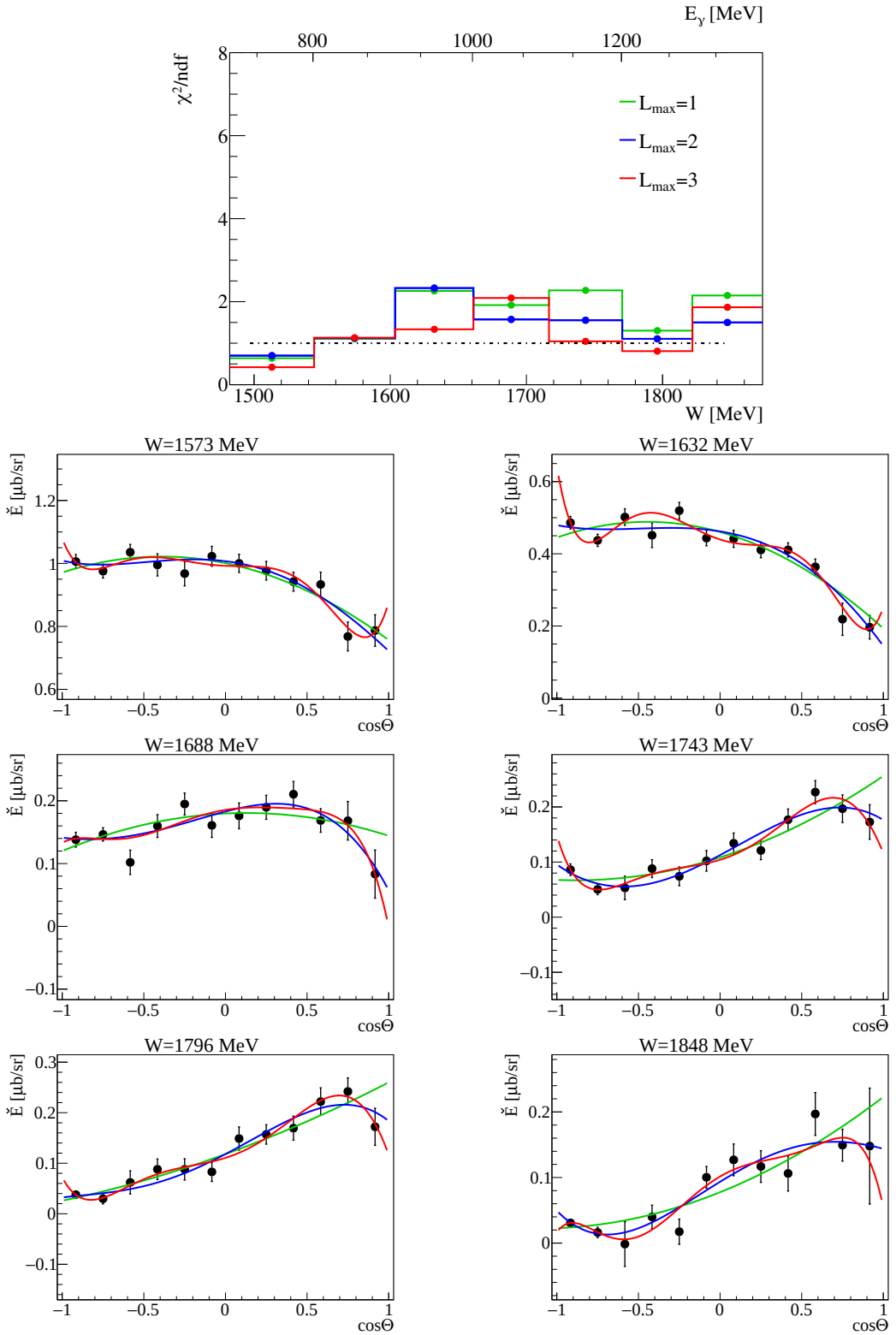

Figure 8.18: The angular distributions of the profile function $\check{E}$ of the $p\eta$ final state (A2 data) were fitted utilizing associated Legendre polynomials according to Equation (8.3). Thereby, the partial wave expansion was truncated at different L_{max} ($L_{max} = 1$ (green line), $L_{max} = 2$ (blue line) and $L_{max} = 3$ (red line)). The χ^2/ndf values of the different L_{max}-fits are given at the top as a function of the center of mass and lab energies. Additionally, six angular distributions (black points) are shown in comparison with the different L_{max}-fits.

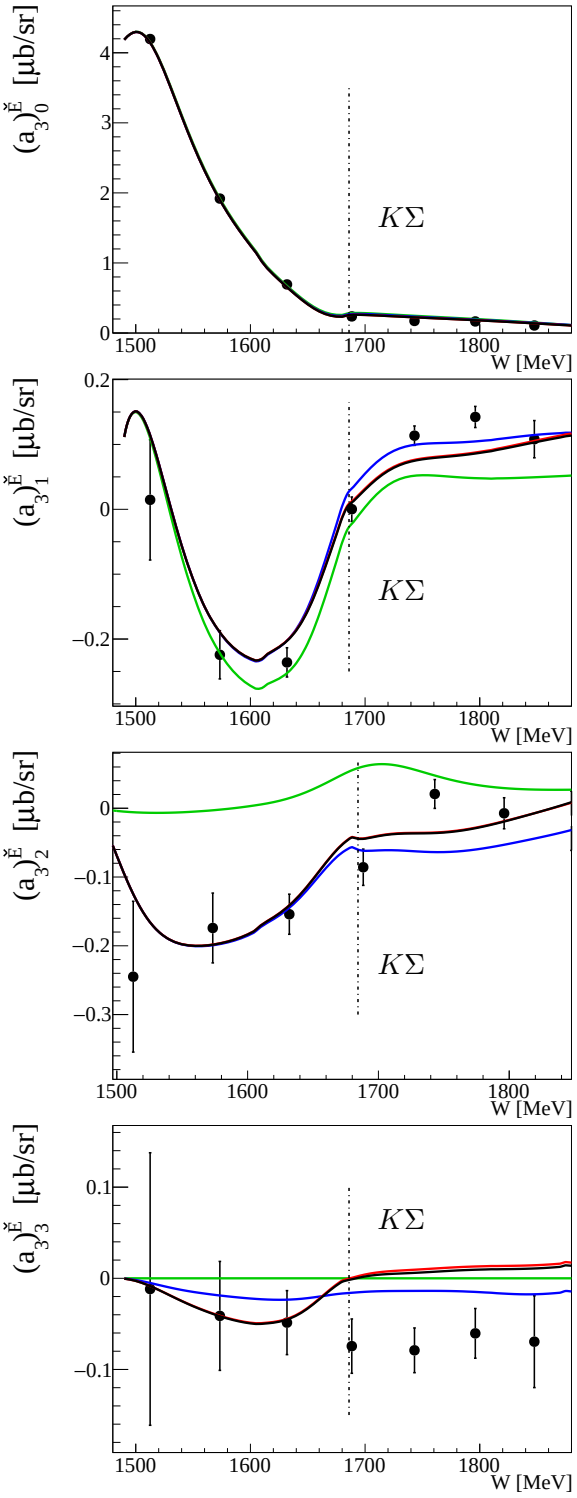

$$(a_4)_0^{\check{E}} = \langle S,S\rangle + \langle P,P\rangle + \langle D,D\rangle + \langle F,F\rangle + \langle G,G\rangle$$

$$(a_4)_1^{\check{E}} = \langle S,P\rangle + \langle P,D\rangle + \langle D,F\rangle + \langle F,G\rangle$$

$$(a_4)_2^{\check{E}} = \langle P,P\rangle + \langle S,D\rangle + \langle D,D\rangle + \langle P,F\rangle + \langle F,F\rangle + \langle D,G\rangle + \langle G,G\rangle$$

$$(a_4)_3^{\check{E}} = \langle P,D\rangle + \langle S,F\rangle + \langle D,F\rangle + \langle P,G\rangle + \langle F,G\rangle$$

Figure 8.19: Left: The obtained fit coefficients $(a_4)_{0\cdots3}^{\check{E}}$ of the $p\eta$ final state are plotted (black points). They are compared to continuous curves evaluated from the BnGa-2014-02 model solution [Gut+14], which are truncated at different L_{max} ($L_{max} = 1$ (green line), $L_{max} = 2$ (blue line), $L_{max} = 3$ (red line) and $L_{max} = 4$ (black line)). Right: All contributing partial wave interference terms are given in a compact notation up to $L_{max} = 4$. The green line of the BnGa-2014-02 model contain contributions from S- and P-wave interference terms contributions, the blue line additionally D-wave, the red line additionally F-wave and the black line additionally G-wave contributions. The dashed-dotted line marks the $K\Sigma$ photoproduction threshold.

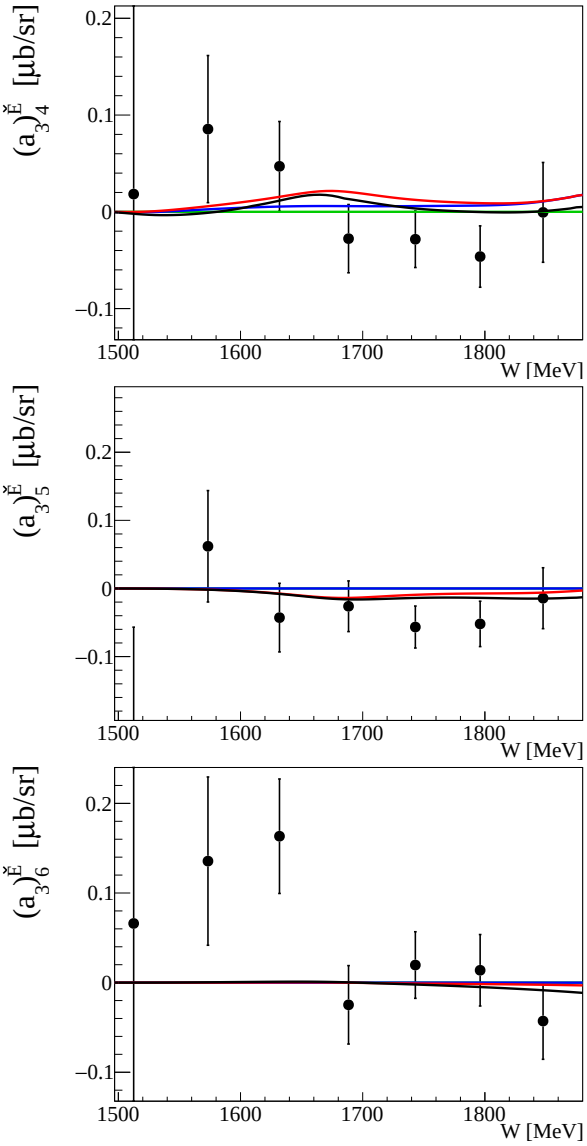

$$(a_4)^{\check{E}}_4 = \langle D, D\rangle$$
$$+ \langle P, F\rangle + \langle F, F\rangle$$
$$+ \langle S, G\rangle + \langle D, G\rangle + \langle G, G\rangle$$

$$(a_4)^{\check{E}}_5 = \langle D, F\rangle$$
$$+ \langle P, G\rangle + \langle F, G\rangle$$

$$(a_4)^{\check{E}}_6 = \langle F, F\rangle$$
$$+ \langle D, G\rangle + \langle G, G\rangle$$

Figure 8.20: Left: The obtained fit coefficients $(a_4)^{\check{E}}_{4\ldots6}$ of the $p\eta$ final state are plotted (black points). They are compared to continuous curves evaluated from the BnGa-2014-02 model solution [Gut+14], which are truncated at different L_{max} ($L_{max} = 1$ (green line), $L_{max} = 2$ (blue line), $L_{max} = 3$ (red line) and $L_{max} = 4$ (black line)). Right: All contributing partial wave interference terms are given in a compact notation up to $L_{max} = 4$. The green line of the BnGa-2014-02 model contain contributions from S- and P-wave interference terms contributions, the blue line additionally D-wave, the red line additionally F-wave and the black line additionally G-wave contributions.

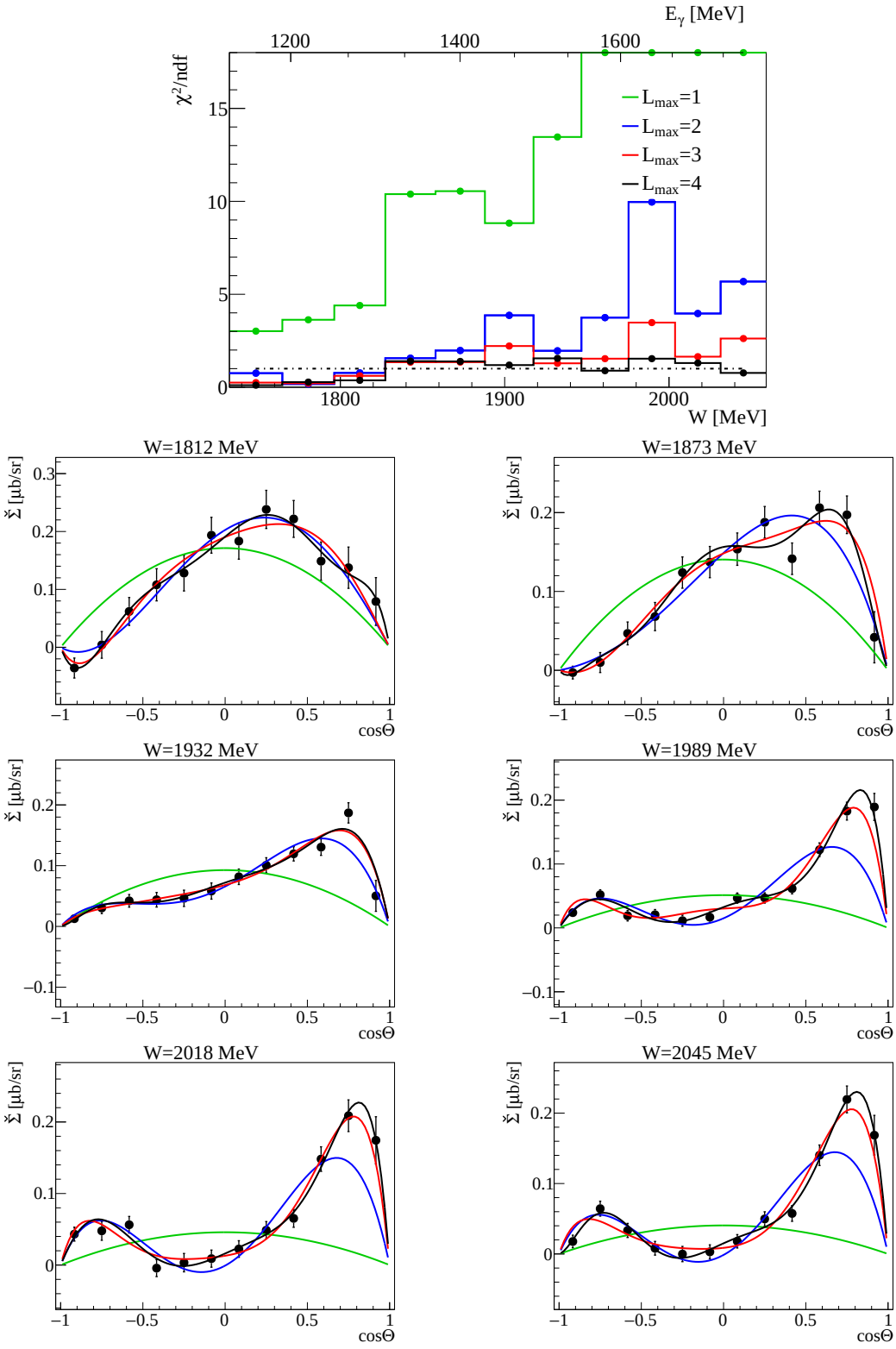

Figure 8.21: The angular distributions of the profile function $\check{\Sigma}$ of the $p\eta$ final state (CBELSA/TAPS data) were fitted utilizing associated Legendre polynomials according to Equation (8.2). Thereby, the partial wave expansion was truncated at different L_{max} ($L_{max} = 1$ (green line), $L_{max} = 2$ (blue line), $L_{max} = 3$ (red line) and $L_{max} = 4$ (black line)). The χ^2/ndf values of the different L_{max}-fits are given at the top as a function of the center of mass and lab energies. Additionally, six angular distributions (black points) are shown in comparison with the different L_{max}-fits.

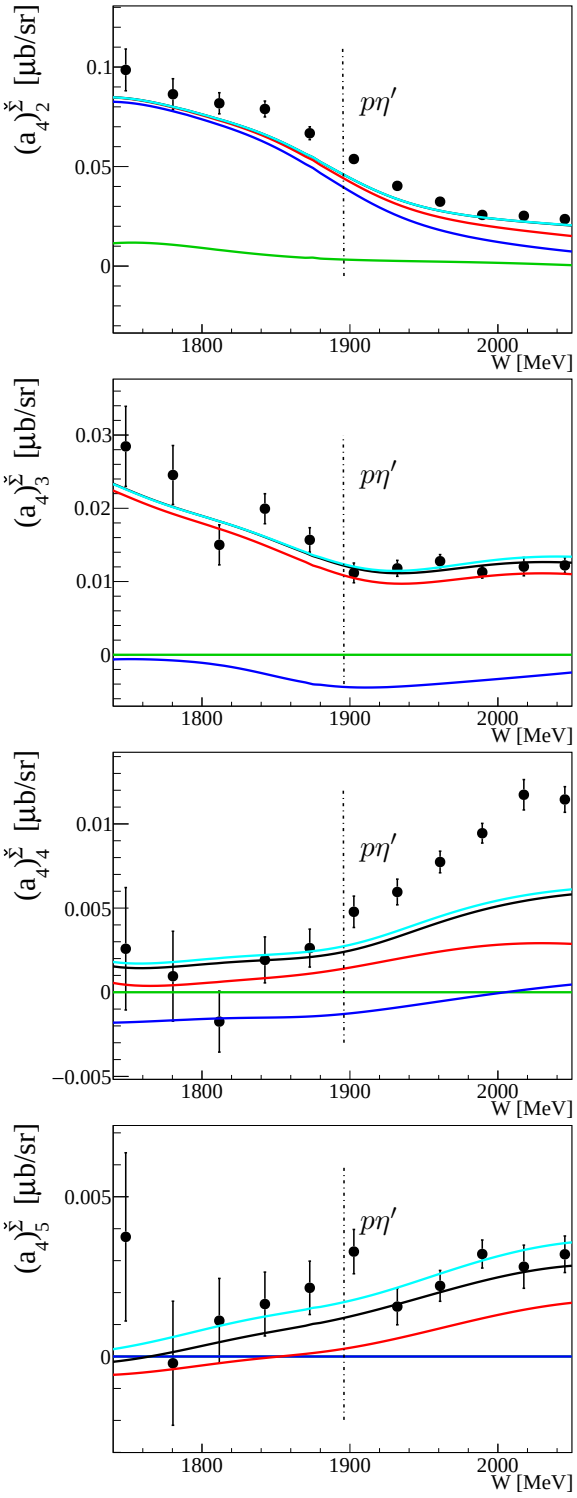

$$(a_5)^{\check{\Sigma}}_2 = \langle P,P\rangle + \langle S,D\rangle + \langle D,D\rangle + \langle P,F\rangle + \langle F,F\rangle + \langle D,G\rangle + \langle G,G\rangle + \langle F,H\rangle + \langle H,H\rangle$$

$$(a_5)^{\check{\Sigma}}_3 = \langle P,D\rangle + \langle S,F\rangle + \langle D,F\rangle + \langle P,G\rangle + \langle F,G\rangle + \langle D,H\rangle + \langle G,H\rangle$$

$$(a_5)^{\check{\Sigma}}_4 = \langle D,D\rangle + \langle P,F\rangle + \langle F,F\rangle + \langle S,G\rangle + \langle D,G\rangle + \langle G,G\rangle + \langle P,H\rangle + \langle F,H\rangle + \langle H,H\rangle$$

$$(a_5)^{\check{\Sigma}}_5 = \langle D,F\rangle + \langle P,G\rangle + \langle F,G\rangle + \langle S,H\rangle + \langle D,H\rangle + \langle G,H\rangle$$

Figure 8.22: Left: The obtained fit coefficients $(a_4)^{\check{\Sigma}}_{2\ldots5}$ of the $p\eta$ final state are plotted (black points). They are compared to continuous curves evaluated from the BnGa-2014-02 model solution [Gut+14], which are truncated at different L_{max} ($L_{max} = 1$ (green line), $L_{max} = 2$ (blue line), $L_{max} = 3$ (red line), $L_{max} = 4$ (black line) and $L_{max} = 5$ (turquoise line)). Right: All contributing partial wave interference terms are given in a compact notation up to $L_{max} = 5$. The green line of the BnGa-2014-02 model contain contributions from S- and P-wave interference terms contributions, the blue line additionally D-wave, the red line additionally F-wave, the black line additionally G-wave and the turquoise line additionally H-wave contributions. The dashed-dotted line marks the $p\eta'$ photoproduction threshold.

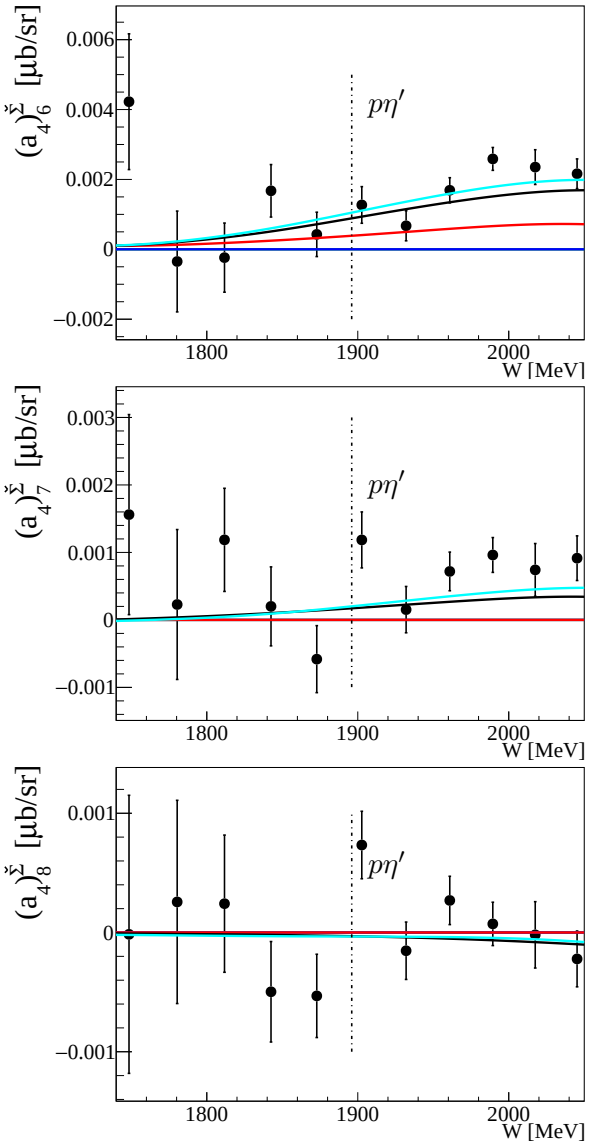

$$(a_5)^{\check{\Sigma}}_6 = \langle F, F\rangle$$
$$+ \langle D, G\rangle + \langle G, G\rangle$$
$$+ \langle P, H\rangle + \langle F, H\rangle + \langle H, H\rangle$$

$$(a_5)^{\check{\Sigma}}_7 = \langle F, G\rangle$$
$$+ \langle D, H\rangle + \langle G, H\rangle$$

$$(a_5)^{\check{\Sigma}}_8 = \langle G, G\rangle$$
$$+ \langle F, H\rangle + \langle H, H\rangle$$

Figure 8.23: Left: The obtained fit coefficients $(a_4)^{\check{\Sigma}}_{6\cdots8}$ of the $p\eta$ final state are plotted (black points). They are compared to continuous curves evaluated from the BnGa-2014-02 model solution [Gut+14], which are truncated at different L_{max} ($L_{max} = 1$ (green line), $L_{max} = 2$ (blue line), $L_{max} = 3$ (red line) and $L_{max} = 4$ (black line)). Right: All contributing partial wave interference terms are given in a compact notation up to $L_{max} = 5$. The green line of the BnGa-2014-02 model contain contributions from S- and P-wave interference terms contributions, the blue line additionally D-wave, the red line additionally F-wave, the black line additionally G-wave and the turquoise line additionally H-wave contributions. The dashed-dotted line marks the $p\eta'$ photoproduction threshold.

8.3 Comparison to PWA models

After determining the dominant partial wave contributions observed in the data, the data are compared to the different PWA models in this section in order to assess the impact of the measured polarization observables.

8.3.1 Reaction $\gamma p \to p\pi^0$

Figures 8.25 - 8.28 show the comparison of the new A2 data for the double polarization observable E of the $p\pi^0$ final state to PWA predictions, that existed prior to any data for the double polarization observable E, namely the BnGa-2011-02 [Ani+12], JüBo-2015-FitB [Rön+15], SAID-CM12 [Wor+12] and MAID2007 [DKT07] model solutions. In addition, the latest PWA solutions of the BnGa (BnGa-2017 [Ani+18])[2] and JüBo (JüBo-2017 [RDM18]) groups are plotted as well, which have already fitted the CBELSA/TAPS data for E. [Got13; Got+14]. The double polarization observable E is strongly negative and shows a parabolic angular dependence from $E_\gamma = 270\,\text{MeV}$ to $420\,\text{MeV}$ due to the $\Delta(1232)\frac{3}{2}^+$ (P_{33}) resonance, which contributes to the M_{1+} multipole and thus, to the P-waves. Therefore, and since differential cross section and beam asymmetry data already exist in this energy range, the angular dependence is well described by all PWA groups. In the energy range from $E_\gamma = 420\,\text{MeV}$ to $630\,\text{MeV}$, most of the PWA solutions describe the data overall well. However, the SAID-CM12 and JüBo-2015-FitB PWA predictions show deviations to the data for $\cos\theta_{\pi^0} < -0.5$. The latest JüBo-2017 PWA solution achieves a much better description for this angular region. Starting from $E_\gamma = 660\,\text{MeV}$, the MAID2007 PWA prediction shows a large deviation from the data as well as from the other PWA solutions and above $E_\gamma = 900\,\text{MeV}$, the different PWA solutions deviate from each other and the data a lot, especially at forward angles of $\cos\theta_{\pi^0} > 0.5$. Here, the new A2 data of this work provides a full angular coverage and will help to constrain the different PWA solutions further. Starting from E_γ =1260 MeV, small deviations between the data and the latest PWA solutions JüBo-2017 and BnGa-2017 are present. Here, the A2 data provides a finer energy binning and overall a better statistical precision in comparison to the CBELSA/-TAPS data and will help to extract the resonance parameters more precisely.

The comparison of the beam asymmetry data of the $p\pi^0$ final state to the different PWA solutions are shown in Figures 8.29 and 8.30. Since the GRAAL data existed prior to all of these PWA solutions, the different PWA solutions are consistent with each other and describe the data mostly well until $E_\gamma = 1450\,\text{MeV}$. Nonetheless, small deviations between the PWA solutions are visible for $\cos\theta_{\pi^0} > 0.7$, where neither the GRAAL nor the CLAS data (for $\cos\theta_{\pi^0} > 0.8$) exist. Above $E_\gamma = 1450\,\text{MeV}$, the different PWA solutions deviate stronger from each other and from the data, especially the SAID-CM12 and the MAID2007 solutions. In this energy range, the data shows a strong angular dependence with two minima, indicating sensitivity to higher order multipoles. This is consistent with the found G-wave sensitivity in the Legendre coefficient $(a_4)_7^{\check{\Sigma}}$ (see Figure 8.17). Both the JüBo-2015-FitB and the JüBo-2017 as well as the BnGa-2017 solution used the CLAS data [Dug+14] in their database. At the very forward angles $\cos\theta_{\pi^0} > 0.7$, the JüBo-2017 solution achieves a better description of the data than the BnGa-2017 solution.

[2] Comparisons with the BnGa-2014-02 solution are shown in the appendix (see Figures D.1-D.6). The new BnGa-2017 solution is very similar to the BnGa-2014-02 solution, at least regarding the $p\pi^0$ channel.

The impact of the measured single and double polarization observables E, G, H, T and P for the $p\pi^0$ final state has been investigated and reported in reference [Ani+16]. For this purpose, the multipole amplitudes of the BnGa, JüBo and SAID PWA solutions were compared before and after including the polarization observables into their fit. The new polarization data leads to a convergence of the multipole amplitudes of the different PWA groups. This is demonstrated by the combined variance of the three analyses, which is significantly reduced through the new polarization observables in the covered energy range of the observables (see Figure 8.24). Here, the variance between two models 1 and 2 is given by [Ani+16]:

$$\mathrm{var}(1,2) = \frac{1}{2}\sum_{i=1}^{16} \left(M_1(i) - M_2(i)\right)\left(M_1^*(i) - M_2^*(i)\right), \tag{8.5}$$

where $M_1(i)$ and $M_2(i)$ are the 16 complex multipoles up to $l = 4$ of PWA model 1 and 2, respectively. The largest contribution of the improvement was traced back to the E_{0+} multipole [Ani+16]. A large variance remains for the multipole amplitudes below $W = 1500\,\mathrm{MeV}$. Here, the new A2 data could play an important role in the future as it closes the gap in the database of double polarization observables for this energy range. The Legendre coefficient $(a_4)_1^{\check{E}}$ (see Figure 8.12), which is sensitive to the $< S, P >$ interference term, indicates that further improvements for the E_{0+} multipole are probably needed, at least for the BnGa-2014-02 model solution. In addition, discrepancies are observed between the PWA solutions at the $p\eta$ and $K\Sigma$ photoproduction thresholds, where the new A2 data could help to reduce the variance between the PWA solutions further.

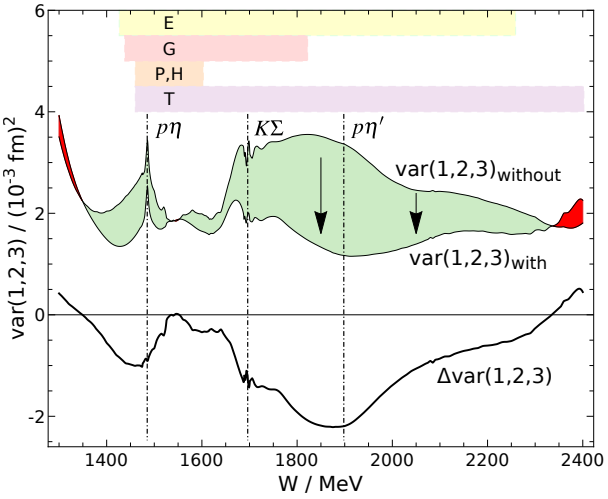

Figure 8.24: The combined variance of the BnGa, JüBo and SAID analyses is given for the sum of all $p\pi^0$ final state multipoles up to $l = 4$ before and after the inclusion of the double polarization observables. The green area marks the reduction of the variance due to the new double polarization data. In addition, the covered energy ranges of the polarization observables are shown at the top. The dashed-dotted lines indicate the $p\eta$, the $K\Sigma$ and the $p\eta'$ photoproduction thresholds. Taken from [Ani+16].

Furthermore, the BnGa group performed a new fit based on polarization observables of the $p\pi^0$ and $n\pi^+$ final states. The latter final state is of importance in order to perform an isospin separation. It is reported in reference [Ani+17], that this new fit gives evidence for the existence

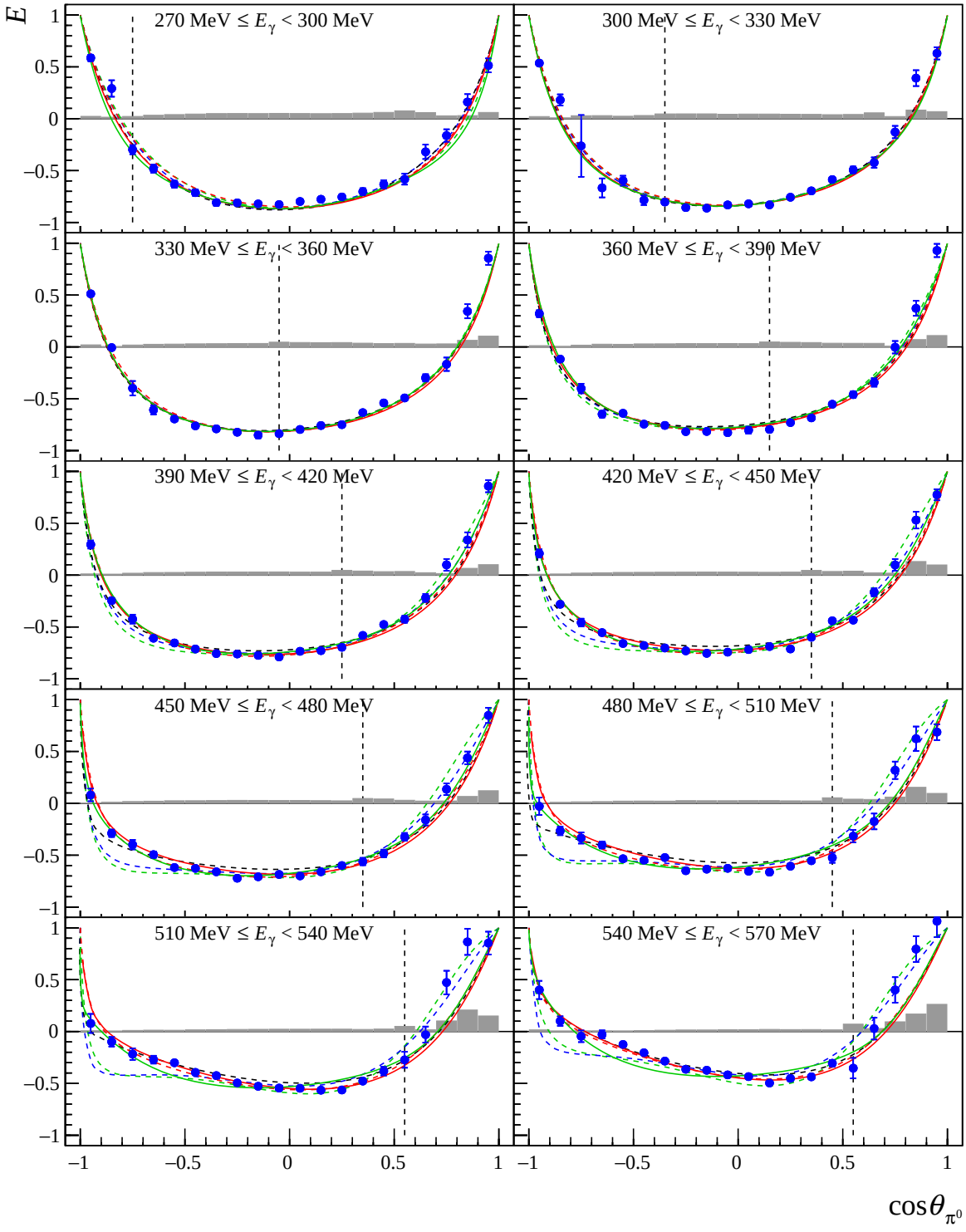

Figure 8.25: The new A2 data for the double polarization observable E are plotted as a function of $\cos\theta_{\pi^0}$ for the beam photon energy range of 270 MeV $\leq E_\gamma <$ 570 MeV. The black dashed line marks the point where the 2 PED events are added to the 3 PED events. The error bars show only the statistical errors. The systematic errors are depicted in gray. The data is compared to the following PWA solutions: BnGa-2011-02 (red, dashed line) [Ani+12], BnGa-2017 (red, solid line) [Ani+18], JüBo-2015-FitB (green, dashed line) [Rön+15], JüBo-2017 (green, solid line) [RDM18], SAID-CM12 (blue, dashed line) [Wor+12] and MAID2007 (black, dashed line) [DKT07].

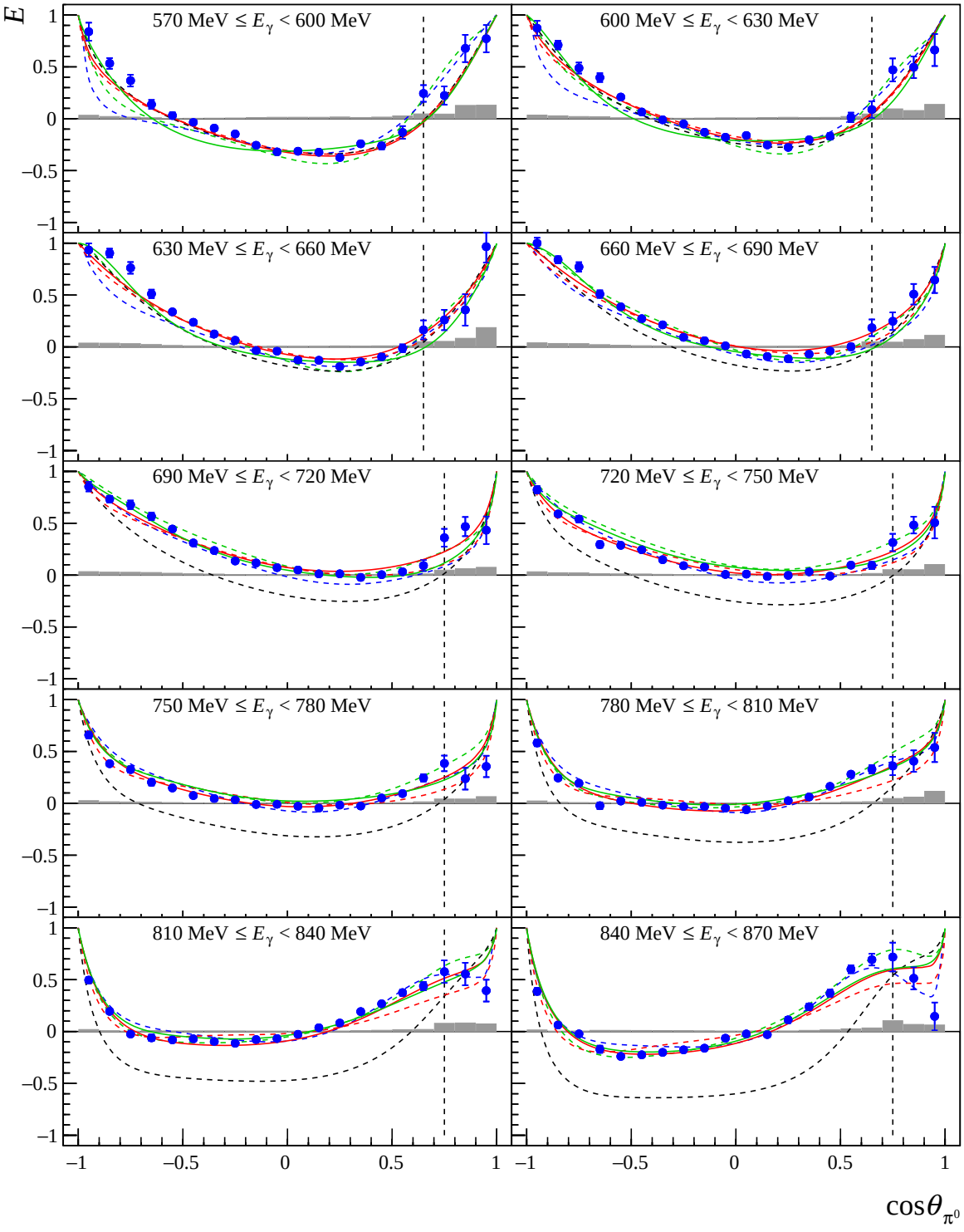

Figure 8.26: The new A2 data for the double polarization observable E are plotted as a function of $\cos\theta_{\pi^0}$ for the beam photon energy range of 570 MeV $\leq E_\gamma <$ 870 MeV. The black dashed line marks the point where the 2 PED events are added to the 3 PED events. The error bars show only the statistical errors. The systematic errors are depicted in gray. The data is compared to the following PWA solutions: BnGa-2011-02 (red, dashed line) [Ani+12], BnGa-2017 (red, solid line) [Ani+18], JüBo-2015-FitB (green, dashed line) [Rön+15], JüBo-2017 (green, solid line) [RDM18], SAID-CM12 (blue, dashed line) [Wor+12] and MAID2007 (black, dashed line) [DKT07].

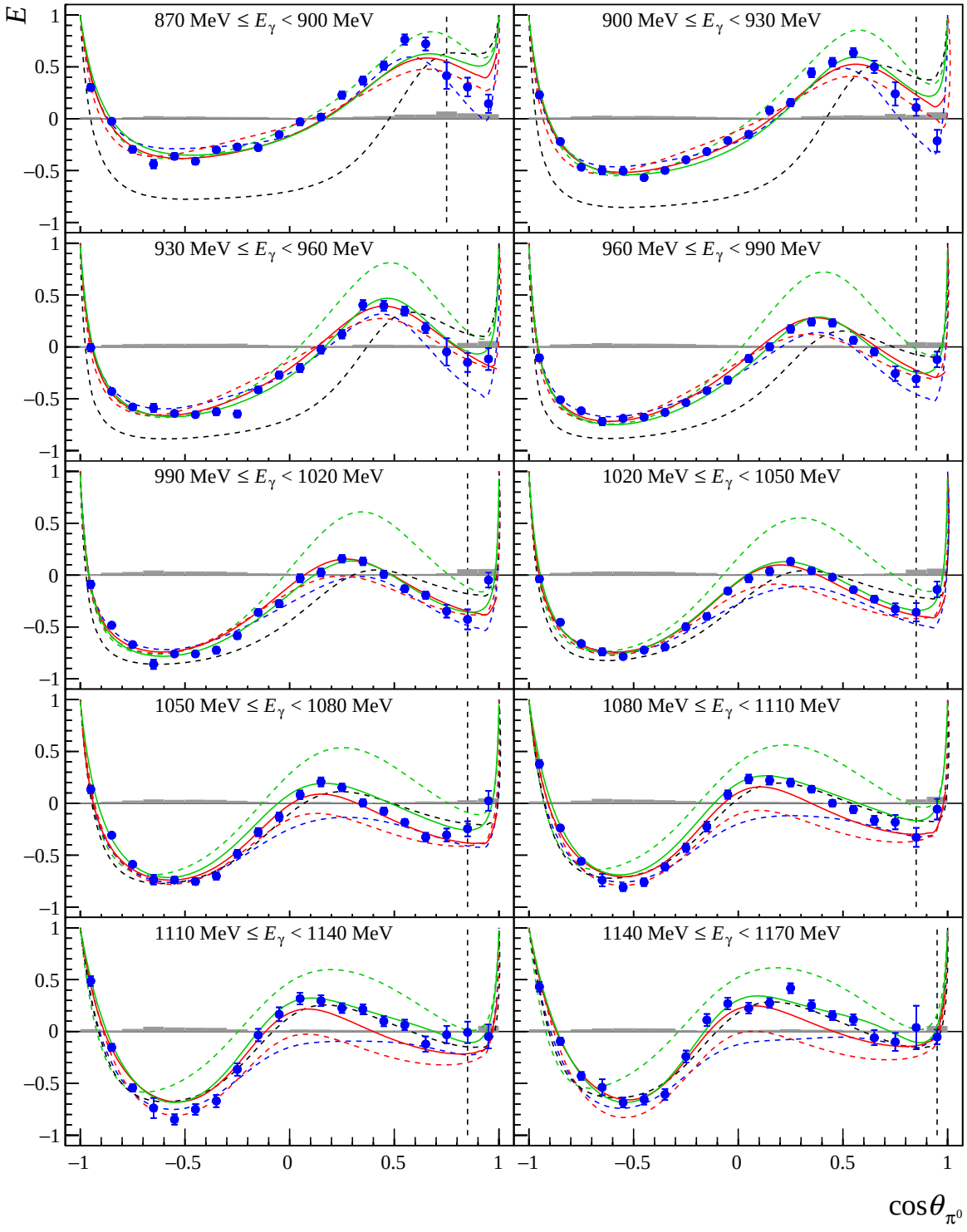

Figure 8.27: The new A2 data for the double polarization observable E are plotted as a function of $\cos\theta_{\pi^0}$ for the beam photon energy range of 870 MeV $\leq E_\gamma <$ 1170 MeV. The black dashed line marks the point where the 2 PED events are added to the 3 PED events. The error bars show only the statistical errors. The systematic errors are depicted in gray. The data is compared to the following PWA solutions: BnGa-2011-02 (red, dashed line) [Ani+12], BnGa-2017 (red, solid line) [Ani+18], JüBo-2015-FitB (green, dashed line) [Rön+15], JüBo-2017 (green, solid line) [RDM18], SAID-CM12 (blue, dashed line) [Wor+12] and MAID2007 (black, dashed line) [DKT07].

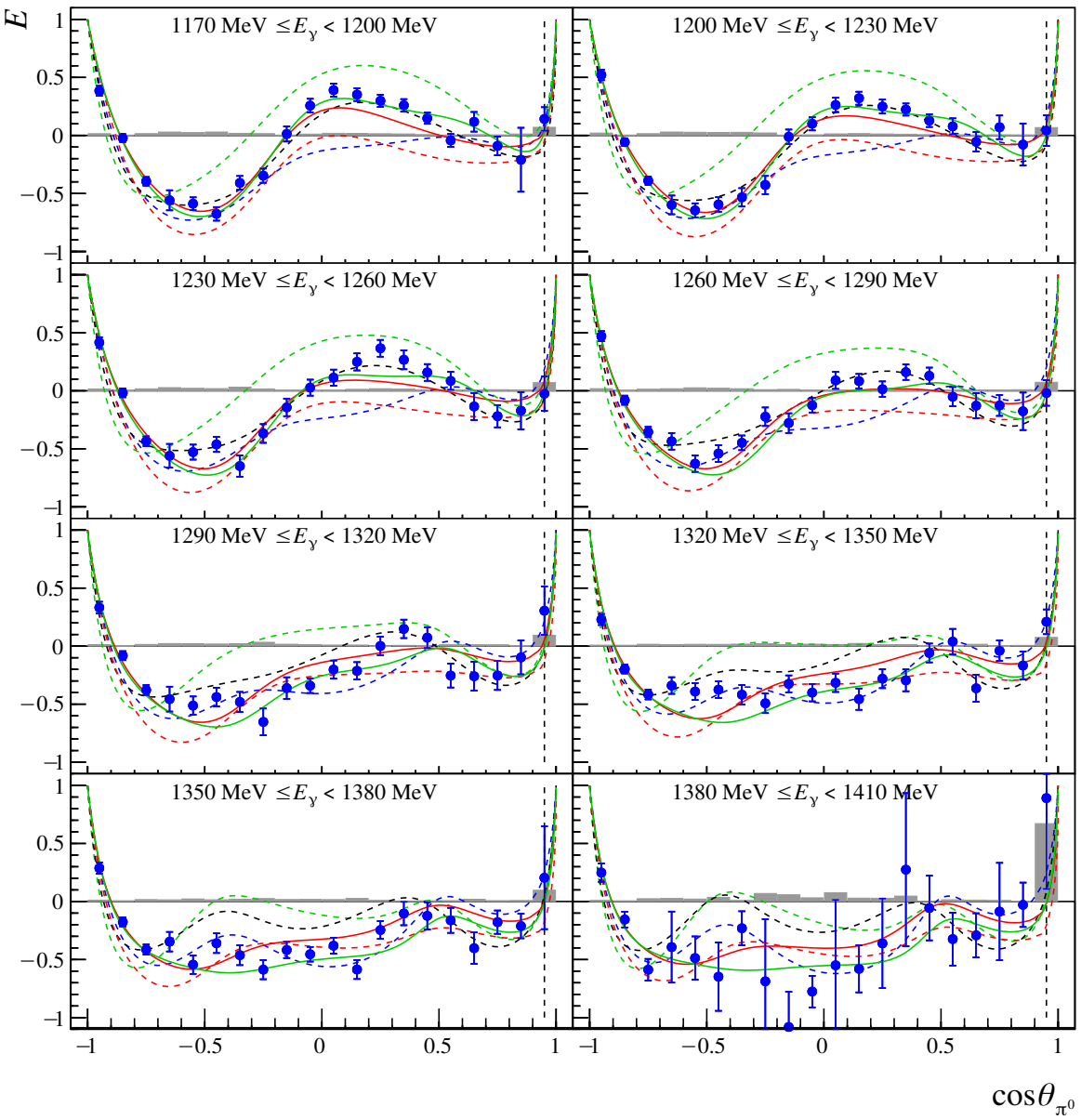

Figure 8.28: The new A2 data for the double polarization observable E are plotted as a function of $\cos\theta_{\pi^0}$ for the beam photon energy range of 1170 MeV $\leq E_\gamma <$ 1410 MeV. The black dashed line marks the point where the 2 PED events are added to the 3 PED events. The error bars show only the statistical errors. The systematic errors are depicted in gray. The data is compared to the following PWA solutions: BnGa-2011-02 (red, dashed line) [Ani+12], BnGa-2017 (red, solid line) [Ani+18], JüBo-2015-FitB (green, dashed line) [Rön+15], JüBo-2017 (green, solid line) [RDM18], SAID-CM12 (blue, dashed line) [Wor+12] and MAID2007 (black, dashed line) [DKT07].

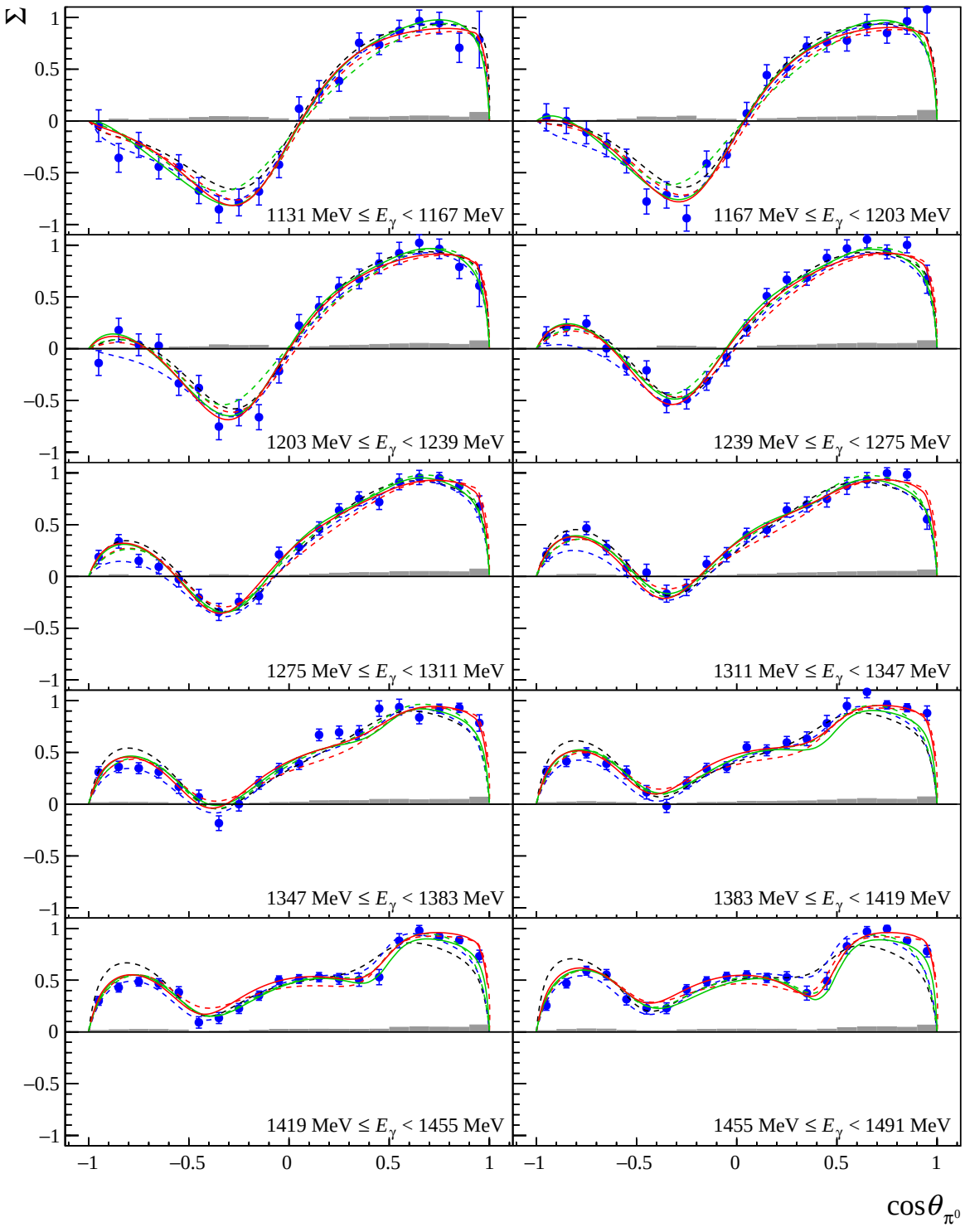

Figure 8.29: The new CBELSA/TAPS data for the beam asymmetry Σ of the $p\pi^0$ final state are shown for the energy range of E_γ = (1131 MeV - 1491 MeV). The error bars show only the statistical errors. The systematic errors are depicted in gray. The data is compared to the following PWA solutions: BnGa-2011-02 (red, dashed line) [Ani+12], BnGa-2017 (red, solid line) [Ani+18], JüBo-2015-FitB (green, dashed line) [Rön+15], JüBo-2017 (green, solid line) [RDM18], SAID-CM12 (blue, dashed line) [Wor+12] and MAID2007 (black, dashed line) [DKT07].

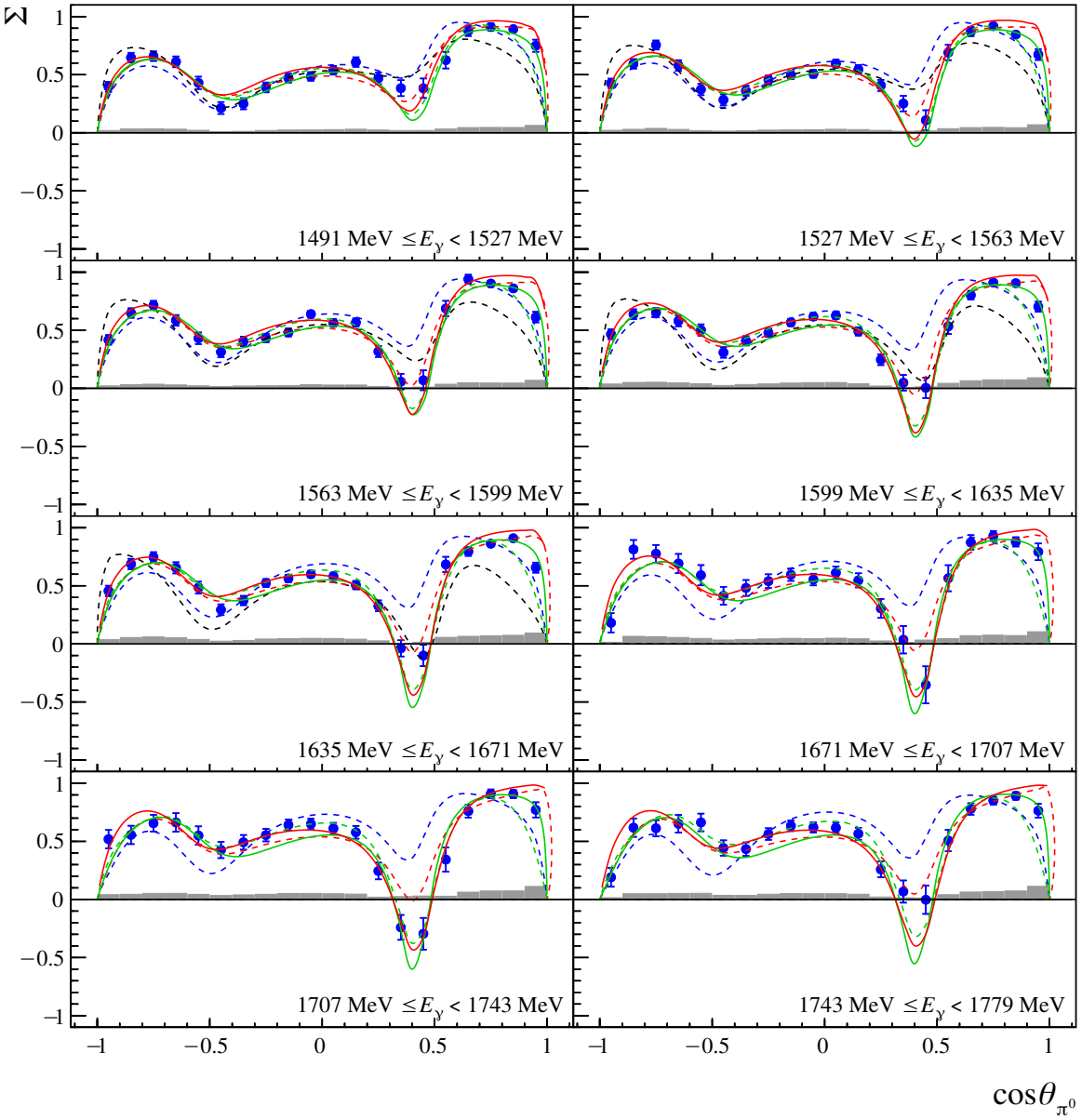

Figure 8.30: The new CBELSA/TAPS data for the beam asymmetry Σ of the $p\pi^0$ final state are shown for the energy range of E_γ = (1491 MeV - 1779 MeV). The error bars show only the statistical errors. The systematic errors are depicted in gray. The data is compared to the following PWA solutions: BnGa-2011-02 (red, dashed line) [Ani+12], BnGa-2017 (red, solid line) [Ani+18], JüBo-2015-FitB (green, dashed line) [Rön+15], JüBo-2017 (green, solid line) [RDM18], SAID-CM12 (blue, dashed line) [Wor+12] and MAID2007 (black, dashed line) [DKT07].

of the G-wave resonance $\Delta(2200)\frac{7}{2}^-$ (G_{37}), which is listed as a one star resonance in the PDG [Pat+16]. The mass of this resonance is too far away for the resonance to be considered as the parity partner of the four star resonance $\Delta(1950)\frac{7}{2}^+$ (F_{37}) and no indications for an additional Δ resonance were found. This result is in favor of the quark model, where no parity doublets are predicted and does not support a chiral symmetry restoration at high masses [EHM09].

8.3.2 Reaction $\gamma p \to p\eta$

Figure 8.31 depicts the new A2 data for the double polarization observable E of the $p\eta$ final state together with the different PWA predictions: BnGa-2014-02 [Gut+14], JüBo-2015-FitB [Rön+15], SAID-GE09 [Bri+] and ηMAID [Chi+02] as well as the latest PWA solutions (BnGa-2017 [Ani+18], JüBo-2017 [RDM18] and ηMAID-2018 [Tia+18]). Starting from the η photoproduction threshold until $E_\gamma = 900\,\text{MeV}$, the E data lies around 1 as expected, since the $N(1535)\frac{1}{2}^-$ (S_{11}) resonance dominates in this energy region and since this resonance contributes only to the helicity dependent cross section $\sigma^{1/2}$ and since the helicity asymmetry E is defined as [San+11]

$$E = \frac{\sigma^{1/2} - \sigma^{3/2}}{\sigma^{1/2} + \sigma^{3/2}}. \tag{8.6}$$

All PWA solutions are in agreement with the data in the threshold energy region. However, large discrepancies exist between the PWA predictions towards higher energies, especially the SAID-GE09 solution predicts a completely different angular dependence for the double polarization observable E. Here, the new acquired data of the CLAS, the CBELSA/TAPS and the A2 collaboration (this work) help to constrain the different PWA solutions. The new data of the CLAS collaboration [Sen+16] were fitted by the JüBo and the MAID group. Due to the limited angular coverage of the CLAS data, deviations of the new JüBo-2017 and ηMAID-2018 solutions to the E data are visible, especially for $\cos\theta > -0.2$.

The latest BnGa-2017 PWA solution has included the latest CBELSA/TAPS data [Mül18] in their fitted database. Nevertheless, a completely satisfactory description of the E data is still not present. This could indicate problems with one or more data sets of the database included in their fit, as the BnGa PWA group performs a simultaneous multi-channel PWA. According to the BnGa group, the latest E data of the CBELSA/TAPS data [Mül18] help to determine new or more precise branching ratios and helicity amplitudes of several resonances, e.g. the branching ration of the $N(1650)\frac{1}{2}^-$ (S_{11}) resonance was determined as 0.32 ± 0.04 and is no longer in conflict with the branching ratio of the $N(1535)\frac{1}{2}^-$ (S_{11}) resonance with 0.42 ± 0.04 [Mül18]. The new A2 data has a higher precision than the CBELSA/TAPS data and is expected to reduce the uncertainties of the resonance parameters further in new PWA fits.

Figure 8.32 shows the comparison of the different PWA solutions to to the new beam asymmetry Σ data of the CBELSA/TAPS collaboration in the $p\eta$ final state. All PWA solutions agree well with each other until $E_\gamma = 1400\,\text{MeV}$ and describe the data since all PWA solutions had included the existing GRAAL data from the year 2007 [Bar+07a] to their database. However, above $E_\gamma = 1400\,\text{MeV}$, the PWA solutions BnGa-2014-02 [Gut+14], JüBo-2015-FitB [Rön+15], SAID-GE09 [Bri+] and ηMAID [Chi+02] predict very different behaviors for the angular dependence. None of these predictions are capable of describing the beam asymmetry data satisfactorily. In particular, none of the PWA solutions predict the emerging structure at backward angles

$-1 < \cos\theta < -0.5$. Here, the latest published data of the CLAS collaboration [Col+17] and the data of this work provide an important contribution towards achieving a convergence of all different PWA solutions to one single, common solution.
The latest ηMAID2018 model explains the angular dependence of the beam asymmetry data at backward angles through an interference of the $N(2120)\frac{3}{2}^-$ (D_{13}) and the $N(2060)\frac{5}{2}^-$ (D_{13}) resonances [KTO17], which corresponds to the interference term $\langle D, D\rangle$. This is one of the possible explanations to account for the observed deviations of the Legendre coefficient $(a_4)_4^{\check{\Sigma}}$ (see Figure 8.22)[3]. The JüBo group reports finding changes in the P-wave, e.g. the helicity couplings of the $N(1720)\frac{3}{2}^+$ (P_{13}) needed to be changed in order to describe the latest beam asymmetry data [Col+17]. In addition, they include the $N(1900)\frac{3}{2}^+$ (P_{13}) and $N(2060)\frac{5}{2}^-$ (D_{15}) resonances in their latest solution JüBo-2017 [RDM18], which were not present in their solution JüBo-2015-FitB. These resonances are listed as a three and a two star resonance in the PDG [Pat+16], respectively. The latest BnGa-2017 PWA solution [Ani+18] has included the CLAS data and the data of this work in their fit, together with new data from multi-meson final states. This solution is now also capable of describing the beam asymmetry data. The changes for the resonance parameters from the BnGa-2014-02 to the BnGa-2017 PWA solution will be discussed in an upcoming publication [Nik18].

[3] Even though the comparison of the Legendre coefficient $(a_4)_4^{\check{\Sigma}}$ is shown to the BnGa-2014-02 solution, similar deviations are also present when comparing to the other PWA models.

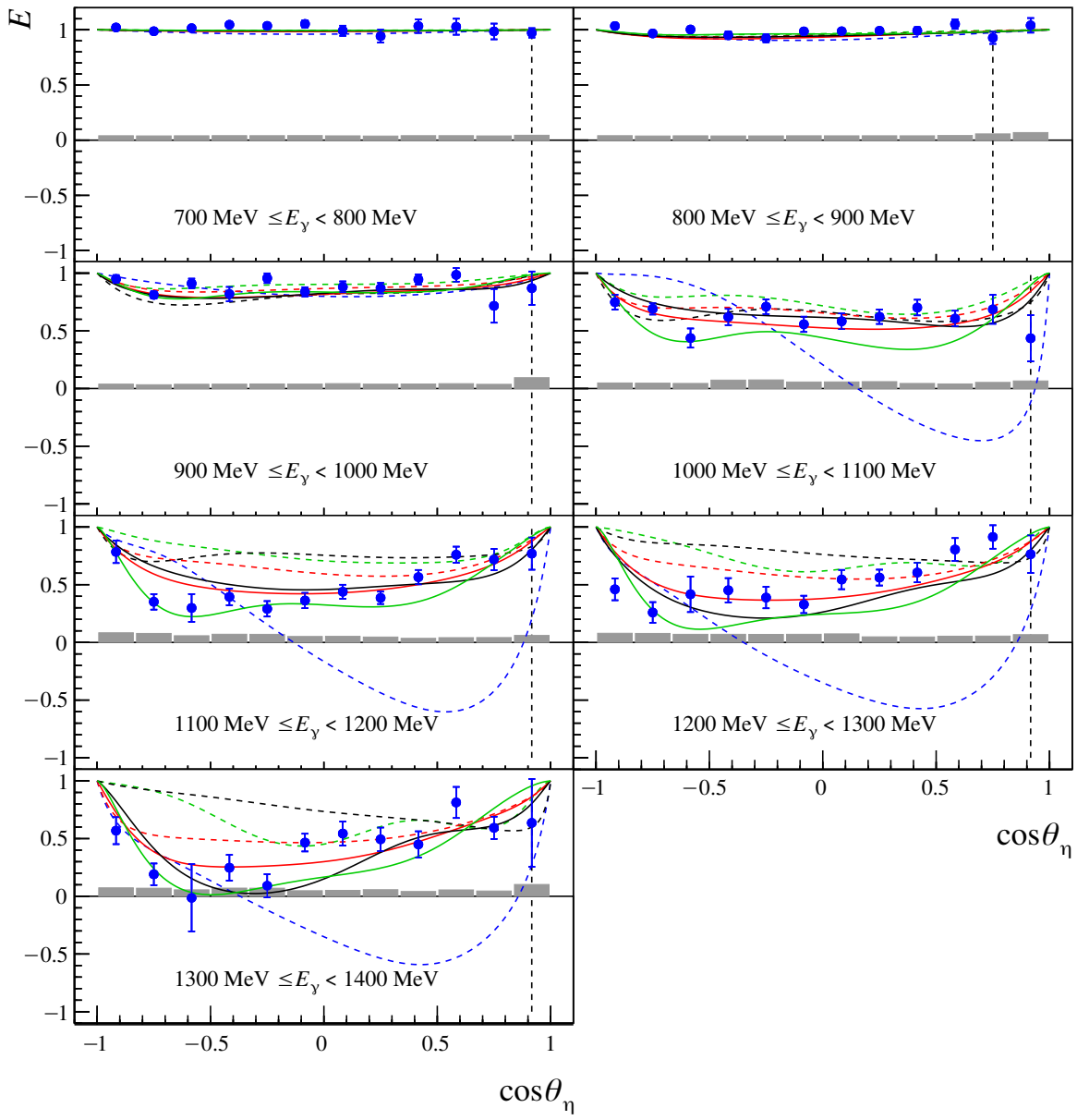

Figure 8.31: The new A2 data for the double polarization observable E are plotted as a function of $\cos\theta_\eta$ for the beam photon energy range of 700 MeV $\leq E_\gamma <$ 1400 MeV. The black dashed line marks the point where the 2 PED events are added to the 3 PED events. The error bars show only the statistical errors. The systematic errors are depicted in gray. The data is compared to the following PWA solutions: BnGa-2014-02 (red, dashed line) [Gut+14], BnGa-2017 (red, solid line) [Ani+18], JüBo-2015-FitB (green, dashed line) [Rön+15], JüBo-2017 (green, solid line) [RDM18], SAID-GE09 (blue, dashed line) [Bri+], ηMAID (black, dashed line) [Chi+02] and ηMAID-2018 (black, solid line) [Tia+18].

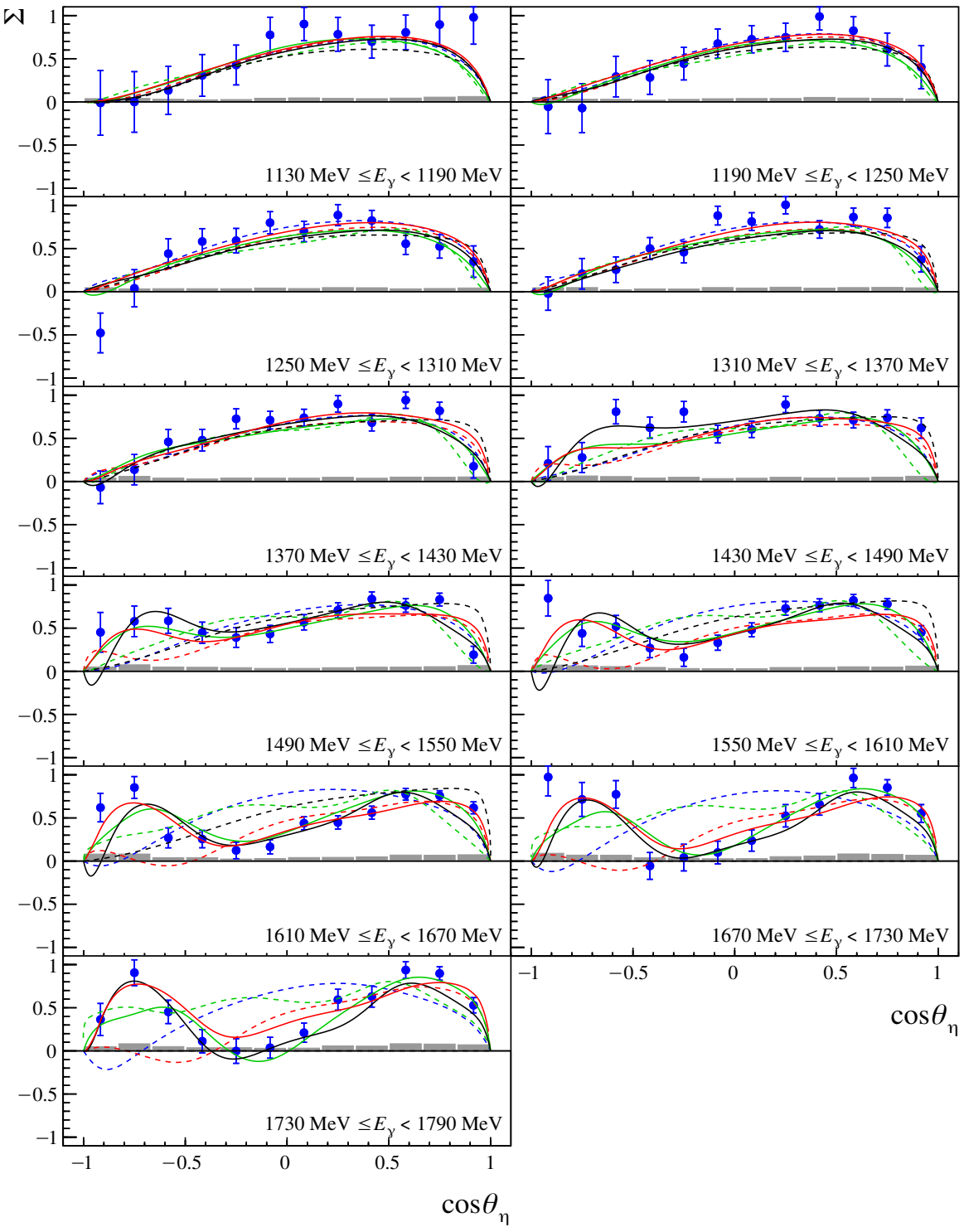

Figure 8.32: The new CBELSA/TAPS data for the beam asymmetry Σ of the $p\eta$ final state are shown for the energy range of E_γ = (1130 MeV - 1790 MeV). The error bars show only the statistical errors. The systematic errors are depicted in gray. The data is compared to the following PWA solutions: BnGa-2014-02 (red, dashed line) [Gut+14], BnGa-2017 (red, solid line) [Ani+18], JüBo-2015-FitB (green, dashed line) [Rön+15], JüBo-2017 (green, solid line) [RDM18], SAID-GE09 (blue, dashed line) [Bri+], ηMAID (black, dashed line) [Chi+02] and ηMAID-2018 (black, solid line) [Tia+18].

9 Summary and outlook

Data were taken with a linearly polarized photon beam and a liquid hydrogen target with the CBELSA/TAPS experiment at the electron stretcher accelerator ELSA, covering an energy range of 1130 MeV $< E_\gamma <$ 1790 MeV. The $p\pi^0$ and $p\eta$ final states were selected using the decay modes $\pi^0 \to \gamma\gamma$ and $\eta \to \gamma\gamma$ with background contributions below 2% and 6% almost over the entire angular range, respectively. In total, 6.28×10^6 $p\pi^0$ and 5.24×10^5 $p\eta$ events were retained. The beam asymmetry Σ was extracted from the data employing two different methods: firstly, by using event yield asymmetries and performing a χ^2-binned fit and secondly, by using an unbinned maximum likelihood fit, which results in an improved statistical error estimation by 10%. The dominant contribution to the systematic error was found to be the uncertainty of the polarization degree of the linearly polarized photons with 5-8%. The beam asymmetry was determined with high statistical precision and the results cover the full angular range for both final states, a feature which is lacking in most of the already existing data sets. Utilizing a simple method of fitting a truncated expansion of associated Legendre polynomials to the angular distributions, a sensitivity up to G-waves was obtained for both final states and indications for the $p\eta'$ cusp were found.

Using the A2 experiment at the Mainz microtron MAMI data were taken with a longitudinally polarized electron beam which was incident on a diamond radiator, resulting in an elliptically polarized photon beam. In addition, a longitudinally polarized butanol target was used. This allowed the simultaneous determination of two double polarization observables: G (linearly polarized photons on a longitudinally polarized target) and E (circularly polarized photons on a longitudinally polarized target), which has not been attempted so far. In this work, the focus was put on the helicity asymmetry E. Similar to the CBELSA/TAPS data analysis, the $p\pi^0$ and $p\eta$ final states were selected using the same decay modes with less than 5% and 7% background over a large angular range, respectively. Here, in total 140×10^6 $p\pi^0$ and 1.1×10^6 $p\eta$ events were retained for the butanol data. For the determination of the double polarization observable E, the fraction of polarizable hydrogen nuclei in the selected butanol data is needed. Therefore, a careful study of the unpolarized background stemming from carbon, oxygen and helium nuclei was conducted utilizing different targets: *only carbon*, *only helium* and *carbon+helium*. It was found that the carbon and helium background contributions do not behave in the same way due to different Fermi momentum distributions and Final State Interaction effects. Thus, it is necessary to measure the unpolarized background using a carbon foam target together with helium in the same way as it is done during the measurement with the butanol target, which was not done in past measurements at MAMI. The helicity asymmetry E was extracted from the data within the energy ranges starting near the respective $p\pi^0$ and $p\eta$ photoproduction thresholds until E_γ =1400 MeV, covering the full angular range. The new A2 data improves the existing statistics by a factor of 4 and will improve the precision of resonance parameters in this energy region. Furthermore, the precise data of the $p\pi^0$ final state allow an observation of the $p\eta$ cusp-effect in the data. In addition, a good agreement was observed between data taken with the diamond and data taken with an amorphous radiator, indicating that elliptically

polarized photons can be used to measure the helicity asymmetry E and the double polarization observable G at the same time. This has an important impact on future experiments since it means that it is possible to measure all polarization observables of the beam-target category within two beamtimes, exchanging only the target polarization orientation from longitudinal to transverse.

During the time frame of this thesis, the CBELSA/TAPS readout electronics was upgraded in order to achieve better trigger capabilities for final states involving neutrons and to overall increase the data taking rates. First beamtimes have been successfully completed with the aim of increasing the existing database of single and double polarization observables for photoproduction reactions off protons and neutrons. This will help to further decrease inconsistencies between different partial wave analyses and help to understand the nucleon excitation spectra. The knowledge gained in this thesis regarding the analysis of the data, can be applied for future data analyses.

Appendices

A Additional plots of the event selection

This section shows additional plots that are helpful to understand the event selection process (see Chapter 5) better.

A.1 Event selection of CBELSA/TAPS data

Figure A.1 depicts the time difference between the beam photons and the recoil proton candidates, in case the recoil proton candidates are detected in the forward detector crystals (FD) and in the forward detector vetoes. The peak at around 5 ns for the time difference between beam photons and recoil protons detected in the forward detector crystals, which is also shown in Figure 5.7, is not understood since time of flight effects would result in negative time difference values and since, additionally, Figure 5.3 demonstrates that most of the recoil protons detected in the forward detector are punch-though protons. However, the time difference of the beam photons and recoil protons detected in the forward detector vetoes shows a time difference of around 0 ns as expected for punch-through protons. Therefore, these events are not rejected, justifying the chosen cut limits in Figure 5.7.

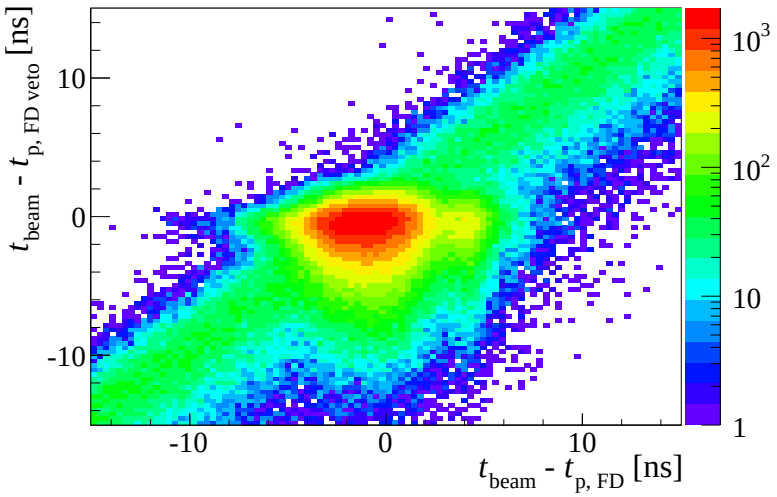

Figure A.1: Comparison of the time difference between the beam photon and the recoil proton time in case the time is provided by the forward detector crystals or the forward detector vetoes.

Figure A.2 shows the angular distributions of the unpolarized differential cross section $\frac{d\sigma}{d\Omega}$ for one energy bin of the $p\pi^0$ and $p\eta$ final state. The differential cross section of the $p\pi^0$ final state exhibits two minima which are reflected in the angular dependence of the kinematic variables (see e.g. the invariant mass in Figure 5.9), while the $p\eta$ differential cross section rises from $\cos\theta = -1$ to $\cos\theta = +1$ (see also Figure 5.10).

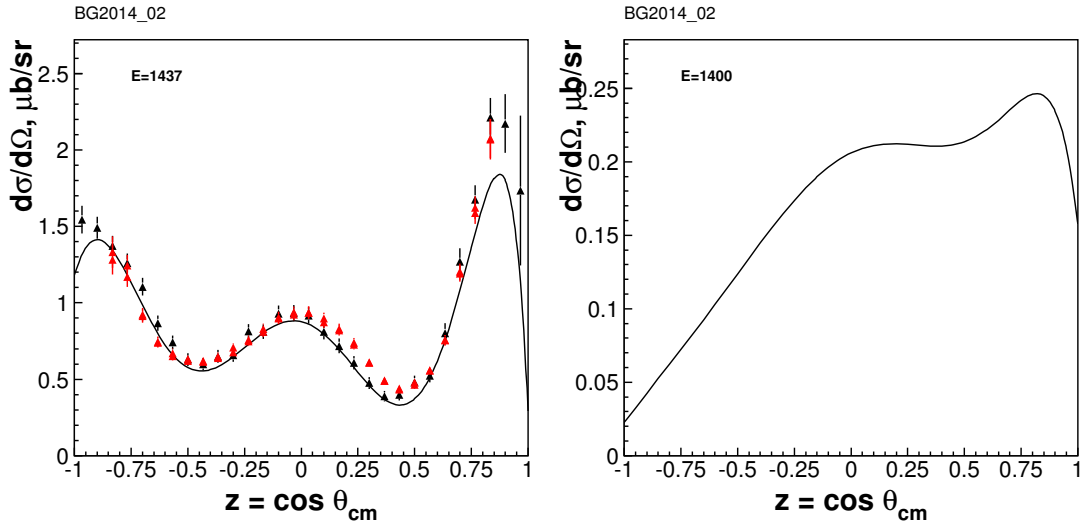

Figure A.2: The unpolarized differential cross section of the $p\pi^0$ final state is shown for an energy of $E_\gamma = 1437\,\text{MeV}$ (data from [Adl+15] and curve: BnGa-2014-02 solution [Gut+14]) and of $p\eta$ for an energy of $E_\gamma = 1400\,\text{MeV}$ (black curve: BnGa-2014-02 solution [Gut+14]). Both plots are taken from [AKN+].

A.2 Event selection of A2 data

Due to gate timing problems with the PID signals during the November 2013 and May 2014 beamtimes of the A2 data, the $\Delta E - E$ spectra could not be used in the analysis. A typical spectrum of the May 2014 beamtime is shown in Figure A.3. The expected behavior of protons, charged pions and electrons is not at all visible (see Figure 5.73).

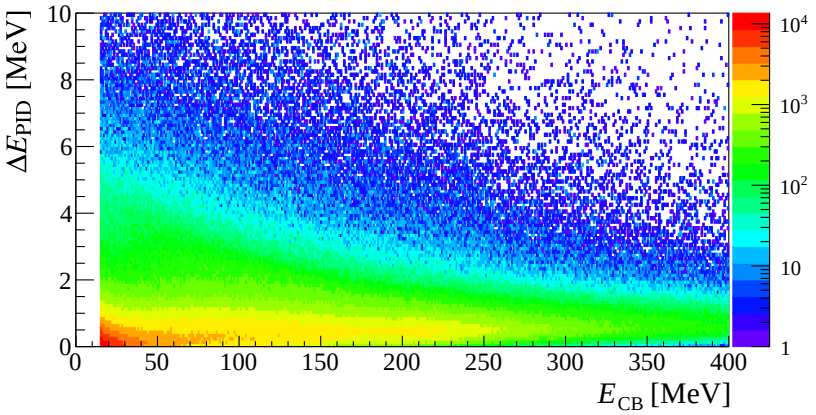

Figure A.3: A typical $\Delta E_{\text{PID}} - E_{\text{CB}}$ spectrum of the May 2014 beamtime is shown. The proton band is not visible at all and merges with the charged pion band.

While in Section 5.3.2.1 example plots of the invariant mass and in Section 5.3.2.2 of the missing mass are shown for lower beam photon energies, Figures A.4 - A.7 show example plots for the high energy region from 1000 MeV - 1400 MeV.

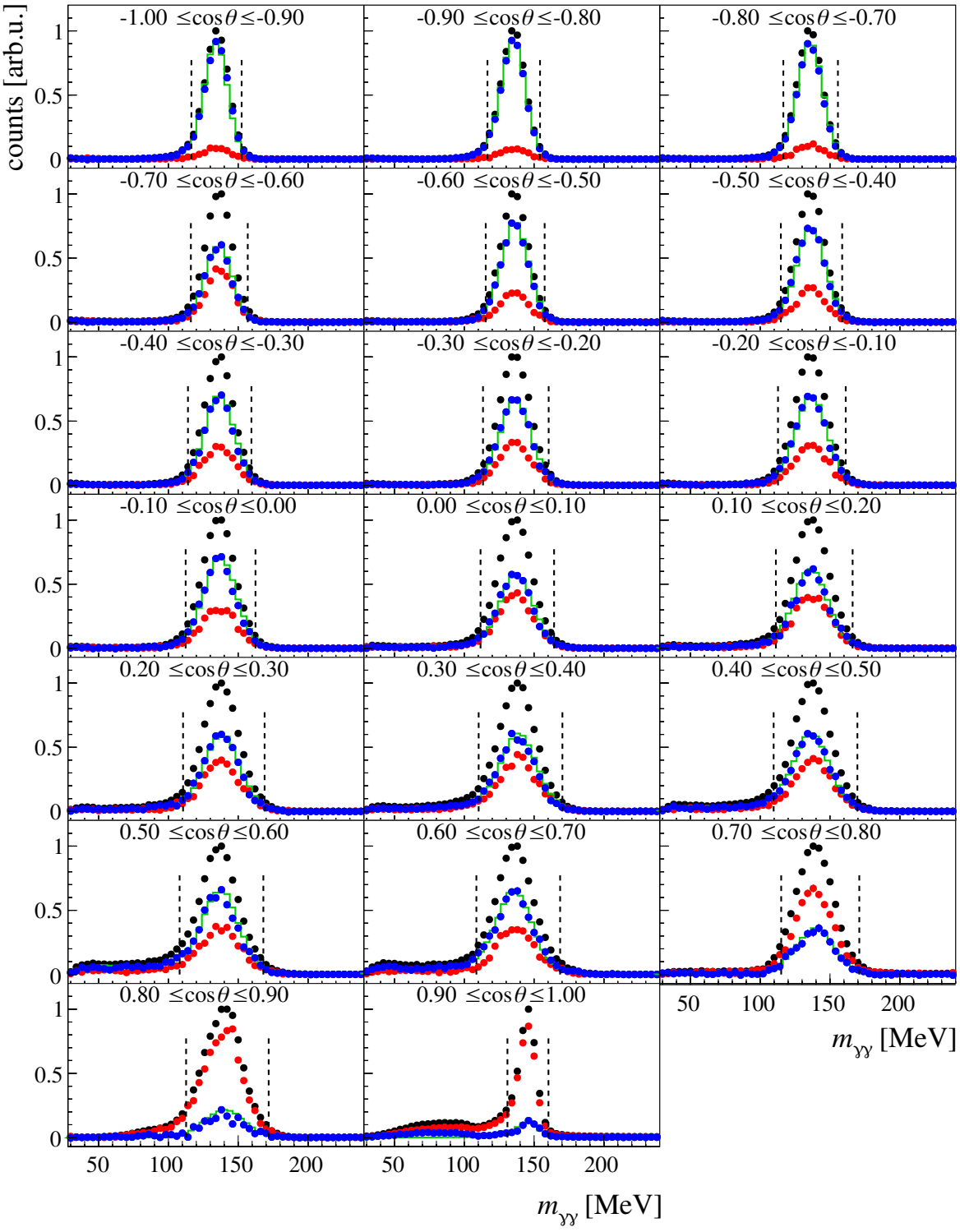

Figure A.4: Invariant mass spectra are shown for the $p\pi^0$ final state and for the energy 1000 MeV $\leq E_\gamma <$1400 MeV and for all $\cos\theta$ bins. All cuts are applied to the data. Black filled circle represent the butanol data and the red points the *carbon+helium* data. The carbon+helium subtracted data is plotted in blue which are compared to Monte Carlo distributions (green). The black line shows the fit to the *carbon+helium* subtracted histogram. The cut ranges are marked as dashed lines.

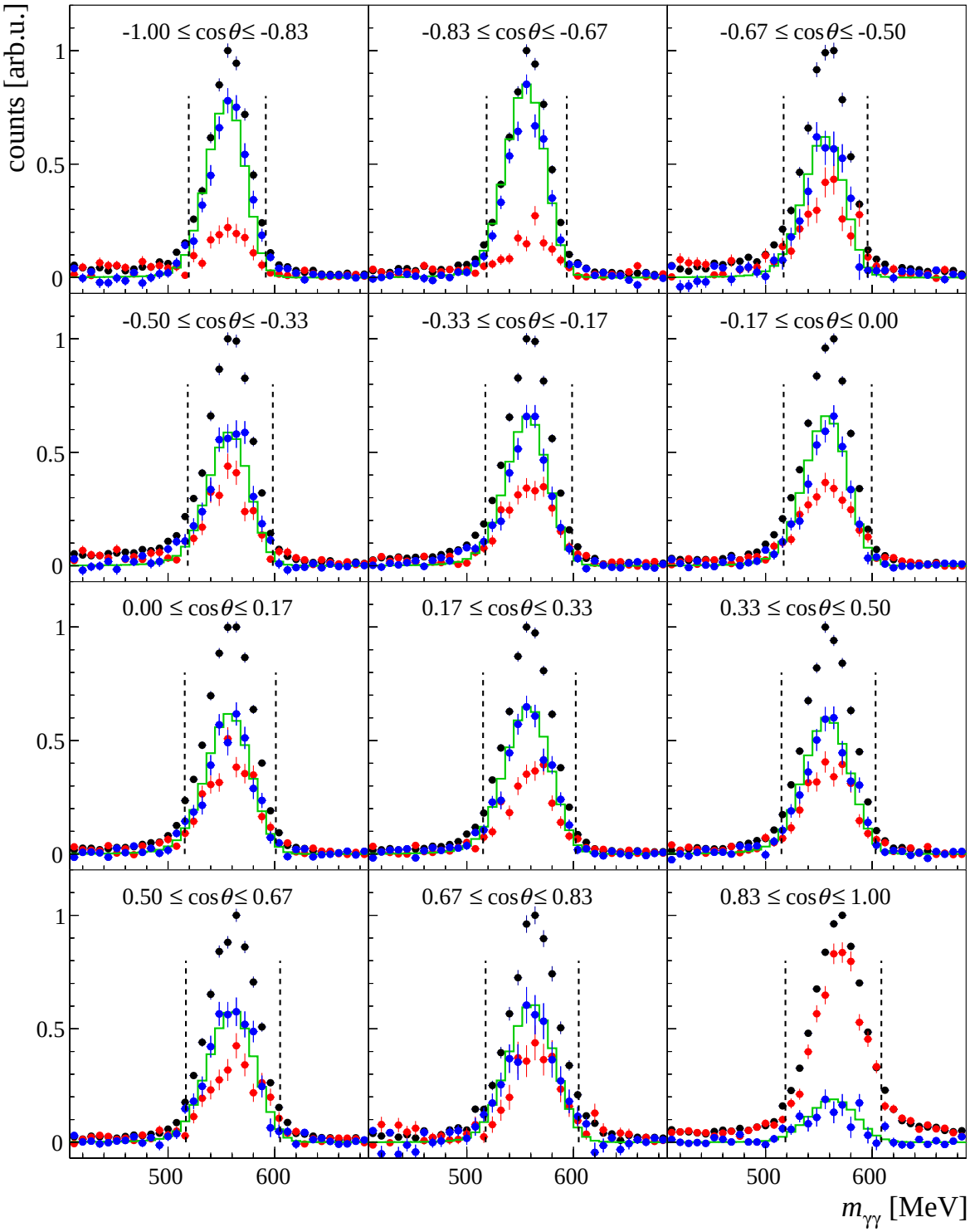

Figure A.5: Invariant mass spectra are shown for the $p\eta$ final state and for 1000 MeV $\leq E_\gamma <$1400 MeV and for several $\cos\theta$ bins. All cuts are applied to the data. Black filled circle represent the butanol data and the red points the *carbon+helium* data. The *carbon+helium* subtracted data is plotted in blue which are compared to Monte Carlo distributions (green). The black line shows the fit to the *carbon+helium* subtracted histogram. The cut ranges are marked as dashed lines.

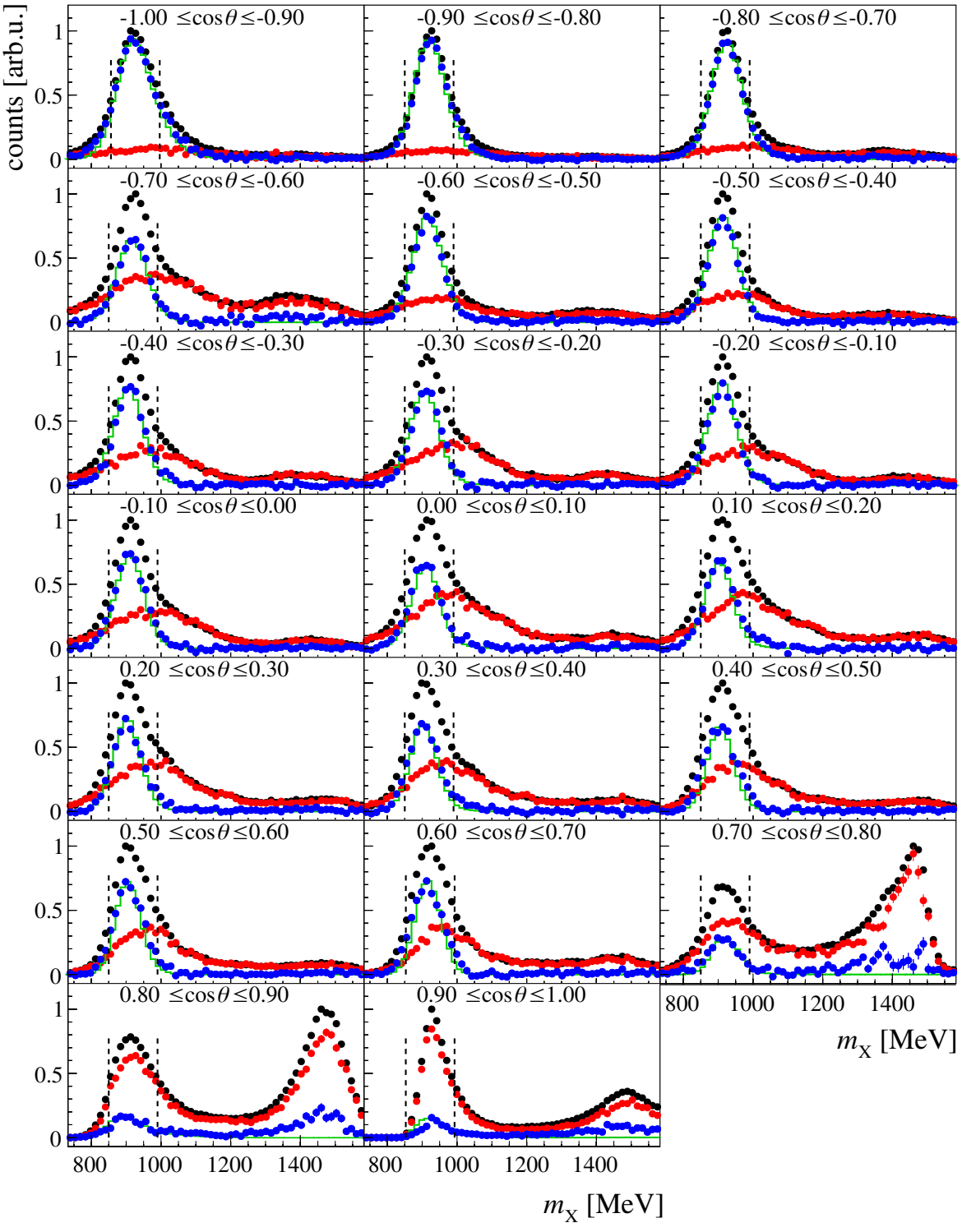

Figure A.6: Missing mass spectra are shown for the $p\pi^0$ final state and for all $\cos\theta$ bins of the energy range 1000 MeV $\leq E_\gamma <$1400 MeV. The selection cuts: time, invariant mass, coplanarity, theta difference, PSA and clustersize cuts are applied to the data. Black points represent the butanol data and the red points the *carbon+helium* data. The *carbon+helium* subtracted data are plotted in blue which are compared to Monte Carlo distributions (green). The cut ranges are marked as dashed lines.

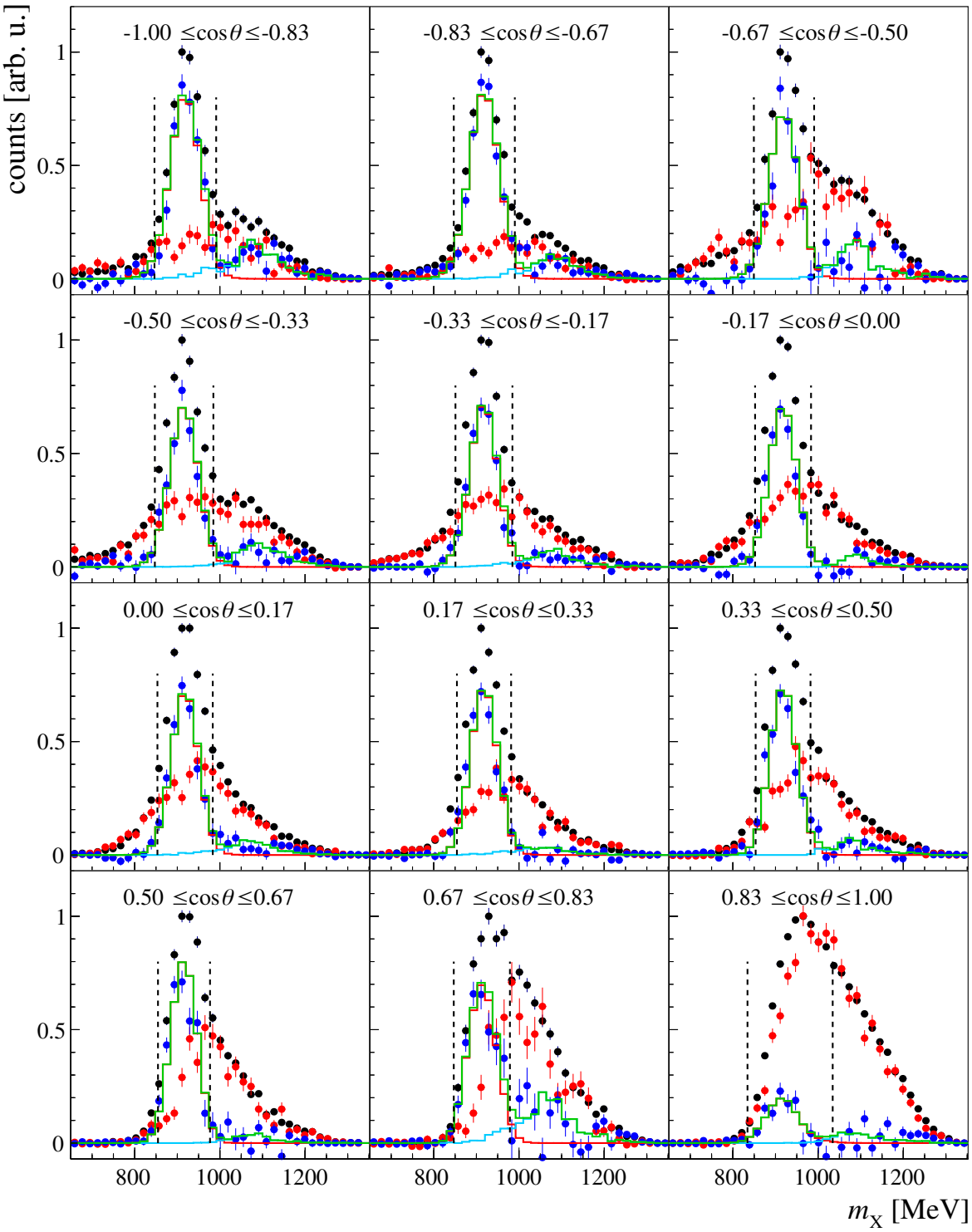

Figure A.7: Missing mass spectra are shown for the $p\eta$ final state and for all $\cos\theta$ bins of the energy range 1000 MeV $\leq E_\gamma <$1400 MeV. The selection cuts: time, invariant mass, coplanarity, theta difference, PSA and clustersize cuts are applied to the data. Black points represent the butanol data and the red points the *carbon+helium* data. The *carbon+helium* subtracted data are plotted in blue which are compared to Monte Carlo distributions (red line: $p\eta$ MC, light blue line: sum of background contributions containing $p\pi^0\eta$, $p\pi^-\eta$, $n\pi^+\eta$ and $p\pi^0\pi^0$ MC and green line: sum of signal and background MC distributions). The cut ranges are marked as dashed lines.

B Dilution factor

The comparison of the coplanarity spectra of data taken with the butanol, the *only helium*, the *only carbon* and the *carbon+helium* is depicted in Figure B.1 for the two energy bins at $E_\gamma = 680\,\text{MeV}$ and $960\,\text{MeV}$ of the $p\pi^0$ final state. As already explained in Section 7.1.1, Fermi momentum and Final State Interactions are responsible for the broader widths of the *only helium*, the *only carbon* and the *carbon+helium* data in comparison to the hydrogen component of the butanol target. The difference between the spectra decreases (see also Figure 7.1) with higher energies as the recoil proton momenta increase. This also leads to a decrease of the dilution factor with higher beam photon energies (see Figures 7.15 - 7.18) because the applied cuts can not remove the non-hydrogen components of the butanol data as efficiently as for lower beam photon energies.

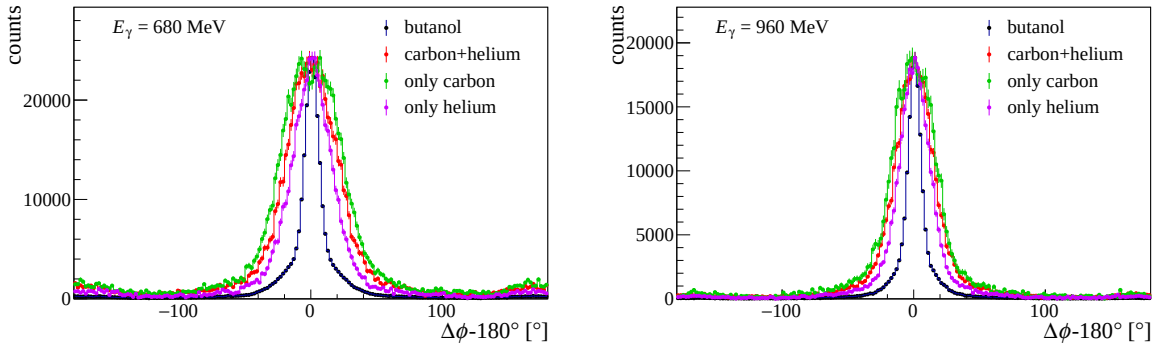

Figure B.1: Comparison of coplanarity spectra of the $p\pi^0$ final state for an energy of $E_\gamma = 680\,\text{MeV}$ (left) and $960\,\text{MeV}$ (right). The blue histogram shows the butanol, the red histogram the *carbon+helium*, the green histogram the *only carbon* and the violet histogram the *only helium* data.

C Comparison of results

As explained in Section 7.2.2.2, the target polarization degree values needed to be corrected for the November 2013, May 2014 and May 2015 beamtimes by a multiplicative constant factor f^{corr}. The following sections show comparison of the helicity asymmetry E for the $p\pi^0$ final state without and with the application of the target polarization correction factor. Section C.1 starts with the comparison of the November 2013 and the September 2015 beamtimes, while Section C.2 shows the comparisons between the May 2014 and the September 2015 beamtimes and finally Section C.3 shows the comparisons between the May 2015 and the September 2015 beamtimes.

C.1 (November 2013 vs. September 2015) for the $p\pi^0$ final state

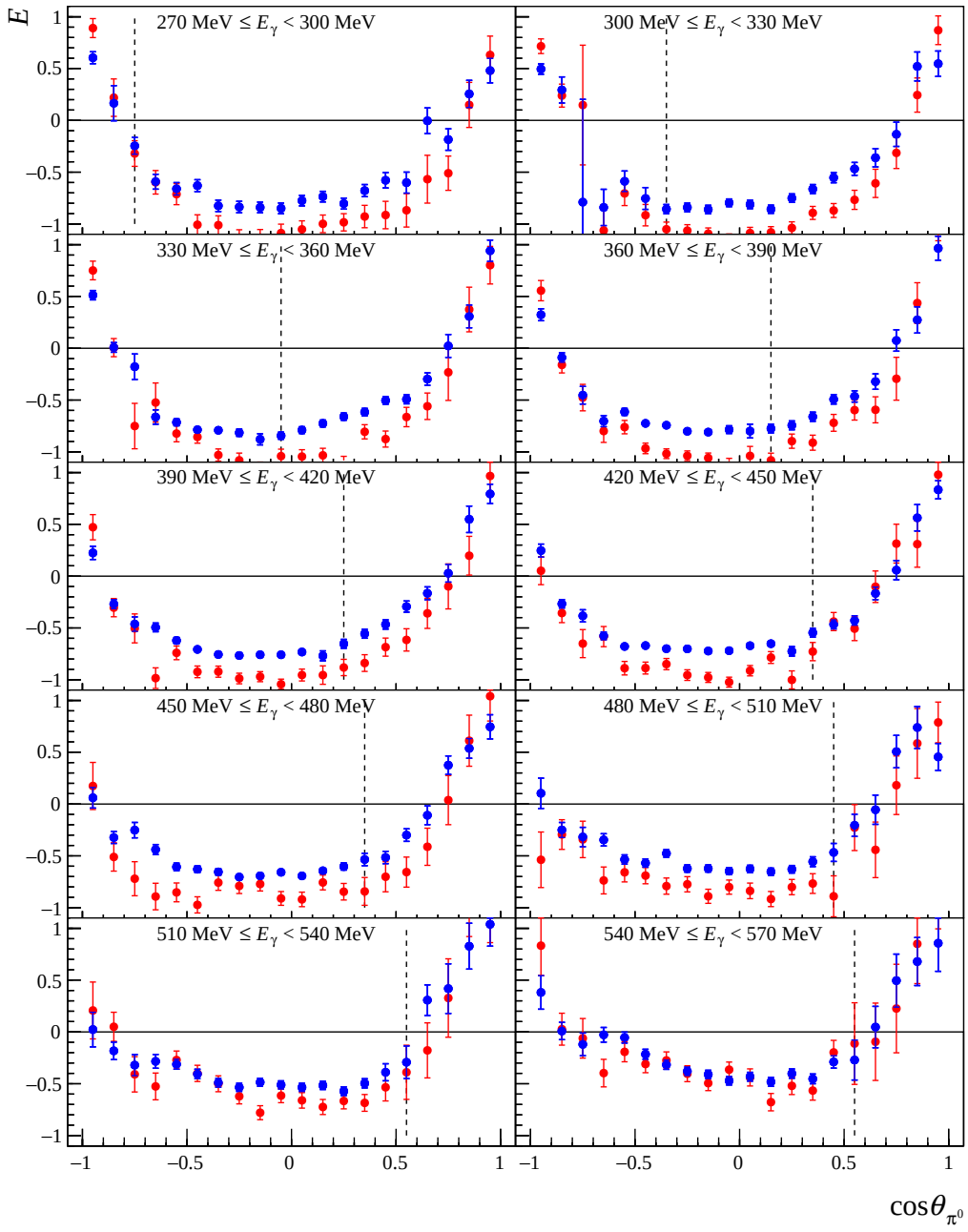

Figure C.1: The double polarization observable E is plotted for the September 2015 (blue) and November 2013 (red) beamtimes as a function of $\cos\theta_{\pi^0}$ for the beam photon energy range from 260 MeV-570 MeV. The black dashed line marks the point where the 2 PED events are added to the 3 PED events. The target polarization correction factor is not applied.

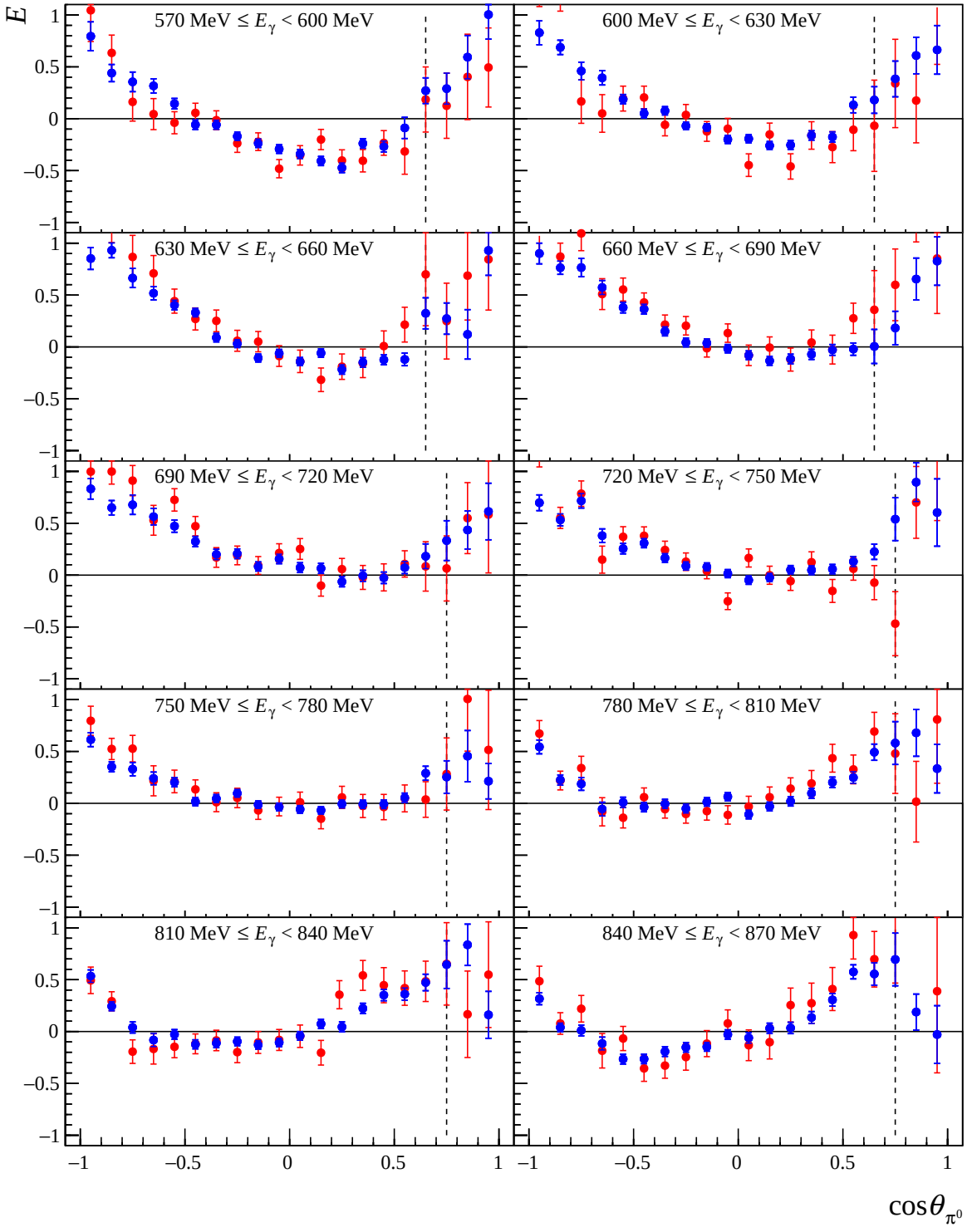

Figure C.2: The double polarization observable E is plotted for the September 2015 (blue) and November 2013 (red) beamtimes as a function of $\cos\theta_{\pi^0}$ for the beam photon energy range from 570 MeV-870 MeV. The black dashed line marks the point where the 2 PED events are added to the 3 PED events. The target polarization correction factor is not applied.

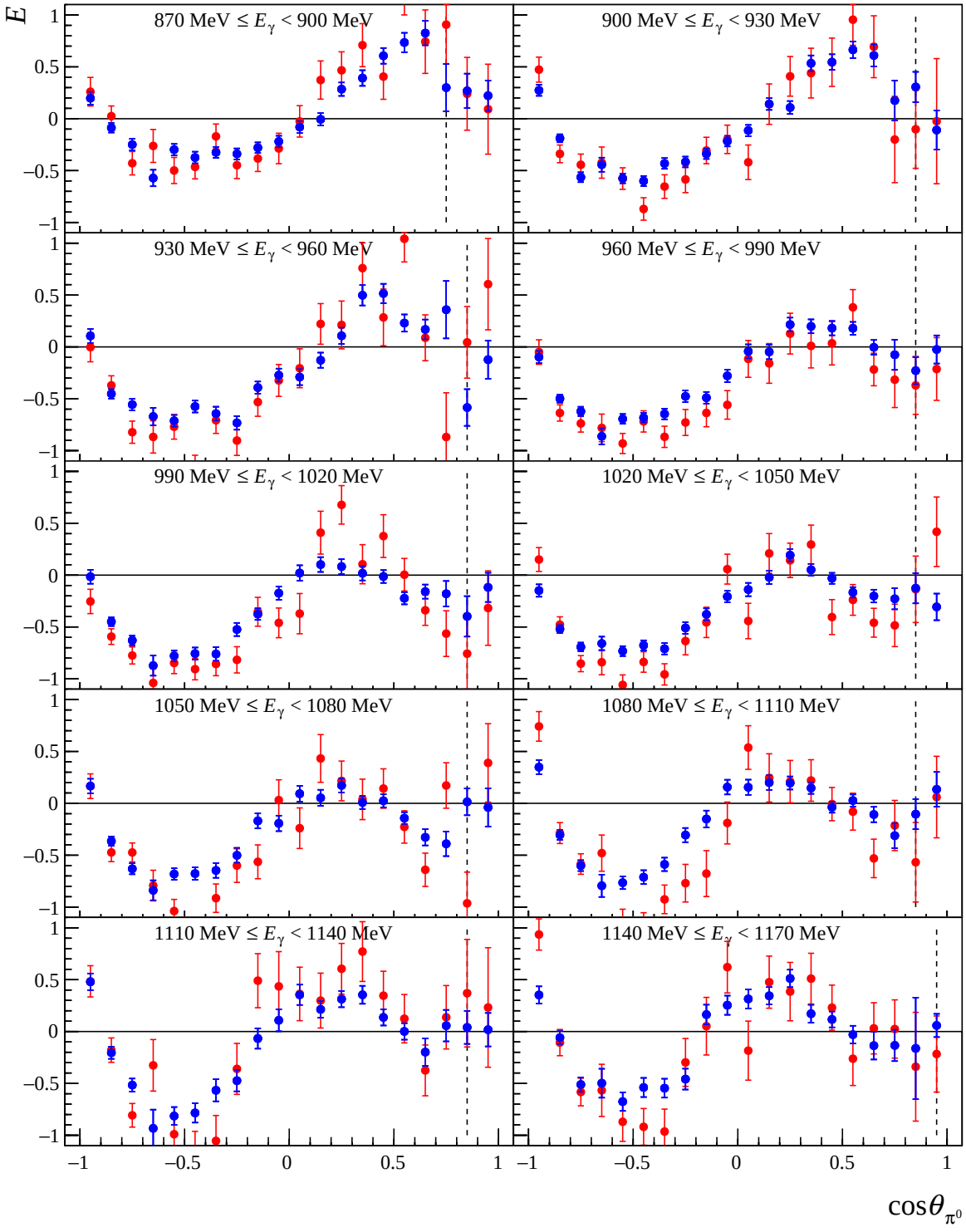

Figure C.3: The double polarization observable E is plotted for the September 2015 (blue) and November 2013 (red) beamtimes as a function of $\cos\theta_{\pi^0}$ for the beam photon energy range from 870 MeV-1170 MeV. The black dashed line marks the point where the 2 PED events are added to the 3 PED events. The target polarization correction factor is not applied.

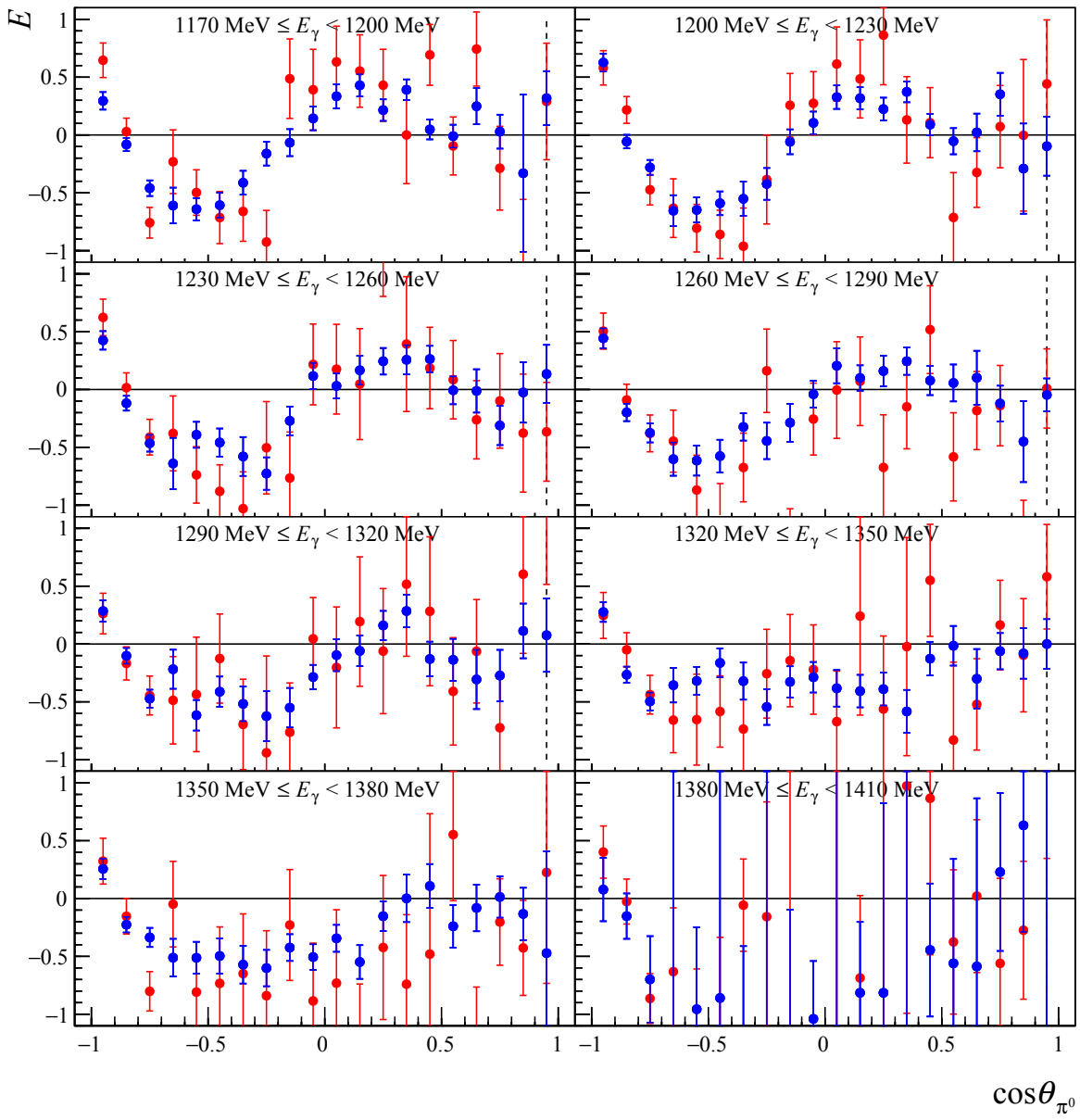

Figure C.4: The double polarization observable E is plotted for the September 2015 (blue) and November 2013 (red) beamtimes as a function of $\cos\theta_{\pi^0}$ for the beam photon energy range from 1170 MeV-1410 MeV. The black dashed line marks the point where the 2 PED events are added to the 3 PED events. The target polarization correction factor is not applied.

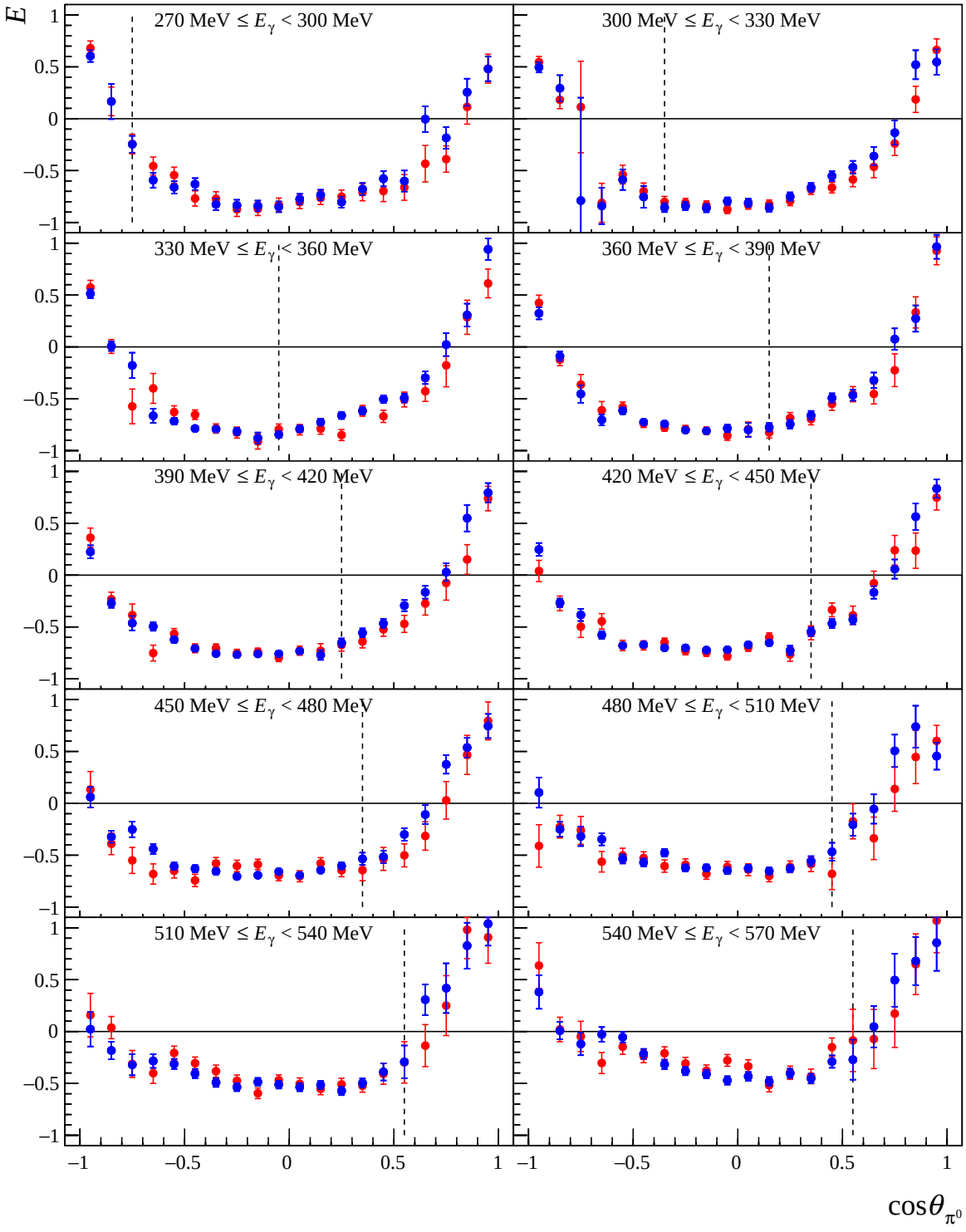

Figure C.5: The double polarization observable E is plotted for the September 2015 (blue) and November 2013 (red) beamtimes as a function of $\cos\theta_{\pi^0}$ for the beam photon energy range from 260 MeV-570 MeV. The black dashed line marks the point where the 2 PED events are added to the 3 PED events. The target polarization correction factor is applied.

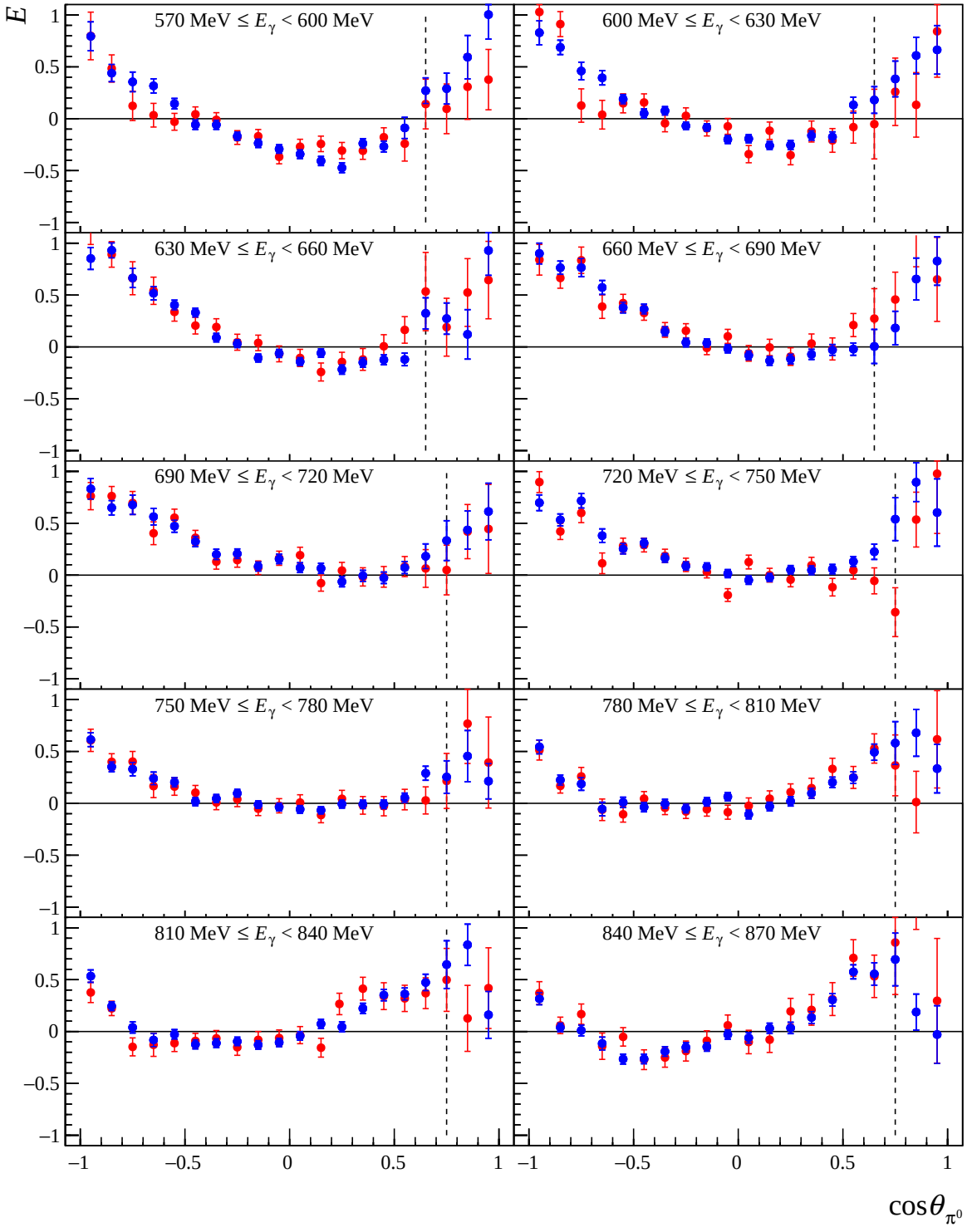

Figure C.6: The double polarization observable E is plotted for the September 2015 (blue) and November 2013 (red) beamtimes as a function of $\cos\theta_{\pi^0}$ for the beam photon energy range from 570 MeV-870 MeV. The black dashed line marks the point where the 2 PED events are added to the 3 PED events. The target polarization correction factor is applied.

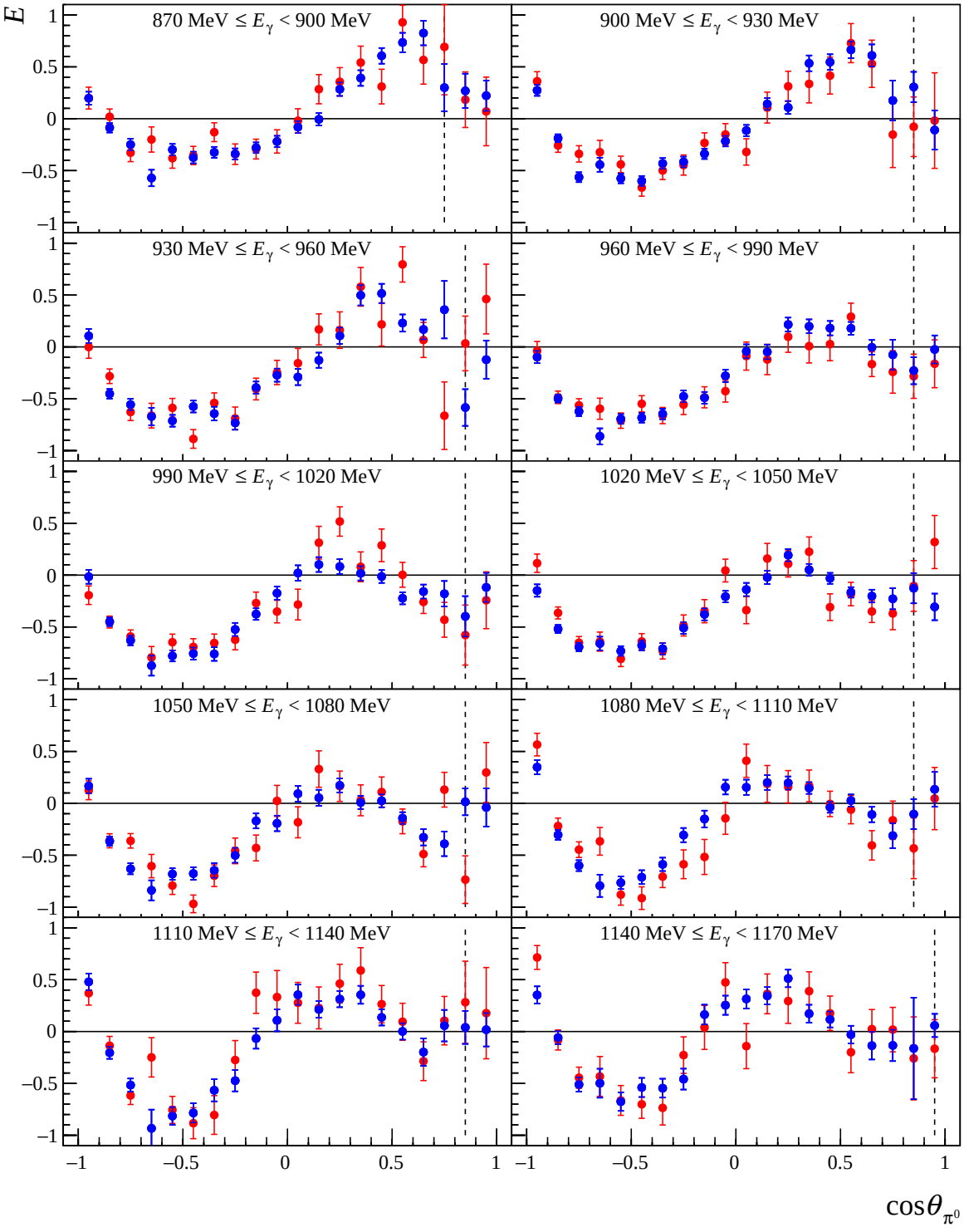

Figure C.7: The double polarization observable E is plotted for the September 2015 (blue) and November 2013 (red) beamtimes as a function of $\cos\theta_{\pi^0}$ for the beam photon energy range from 870 MeV-1170 MeV. The black dashed line marks the point where the 2 PED events are added to the 3 PED events. The target polarization correction factor is applied.

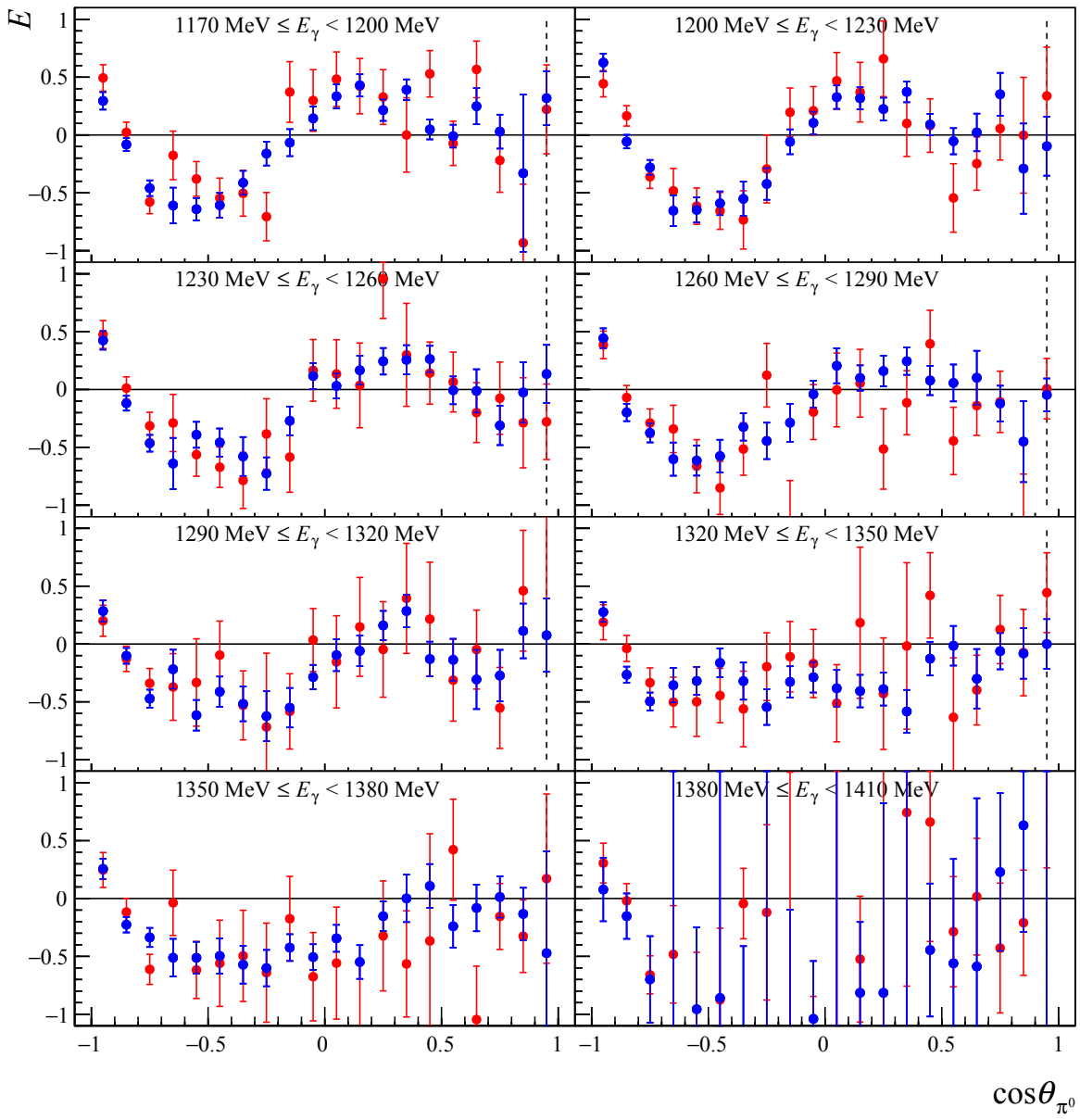

Figure C.8: The double polarization observable E is plotted for the September 2015 (blue) and November 2013 (red) beamtimes as a function of $\cos\theta_{\pi^0}$ for the beam photon energy range from 1170 MeV-1410 MeV. The black dashed line marks the point where the 2 PED events are added to the 3 PED events. The target polarization correction factor is applied.

C.2 (May 2014 vs. September 2015) for the $p\pi^0$ final state

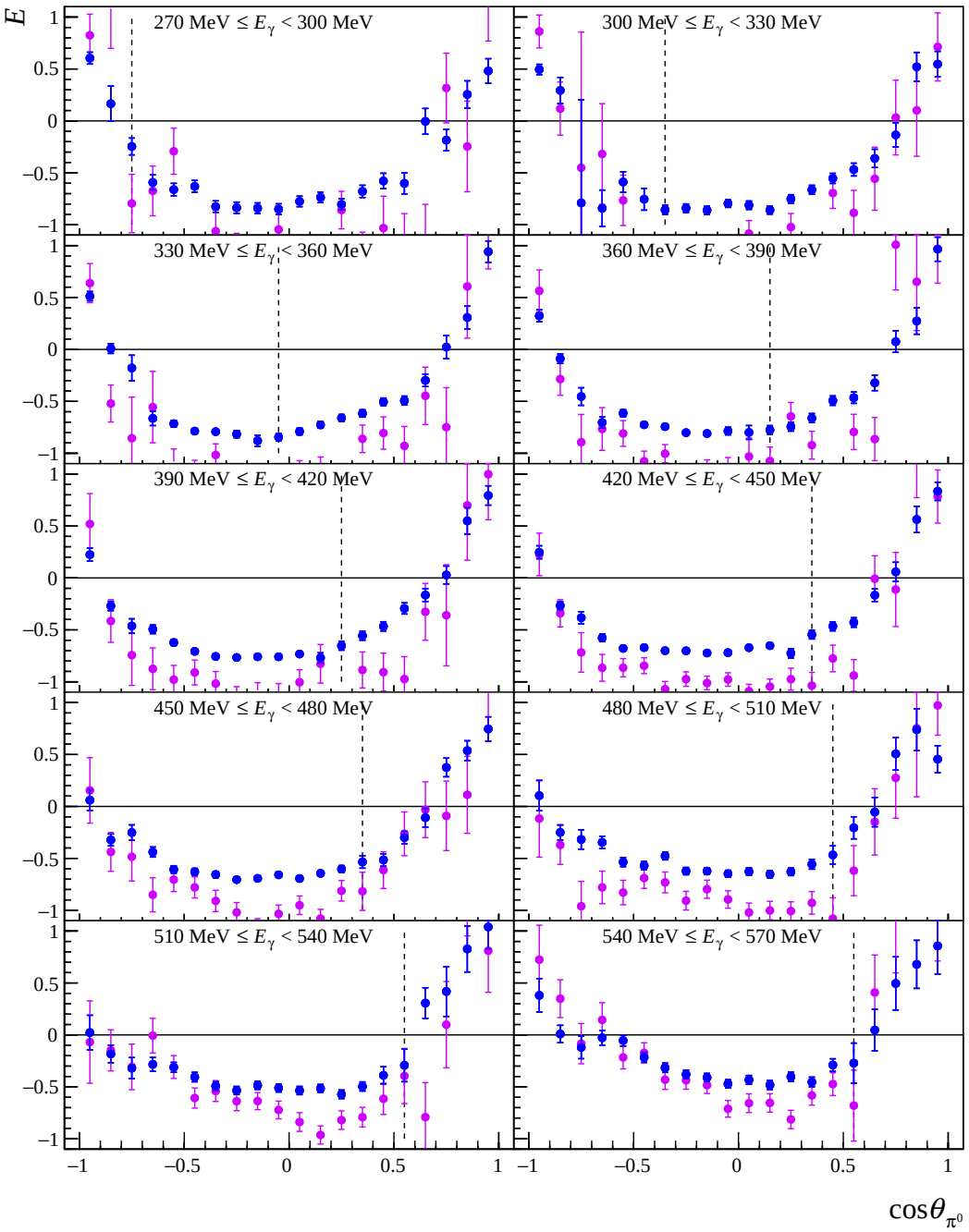

Figure C.9: The double polarization observable E is plotted for the September 2015 (blue) and May 2014 (violet) beamtimes as a function of $\cos\theta_{\pi^0}$ for the beam photon energy range from 260 MeV-570 MeV. The black dashed line marks the point where the 2 PED events are added to the 3 PED events. The target polarization correction factor is not applied.

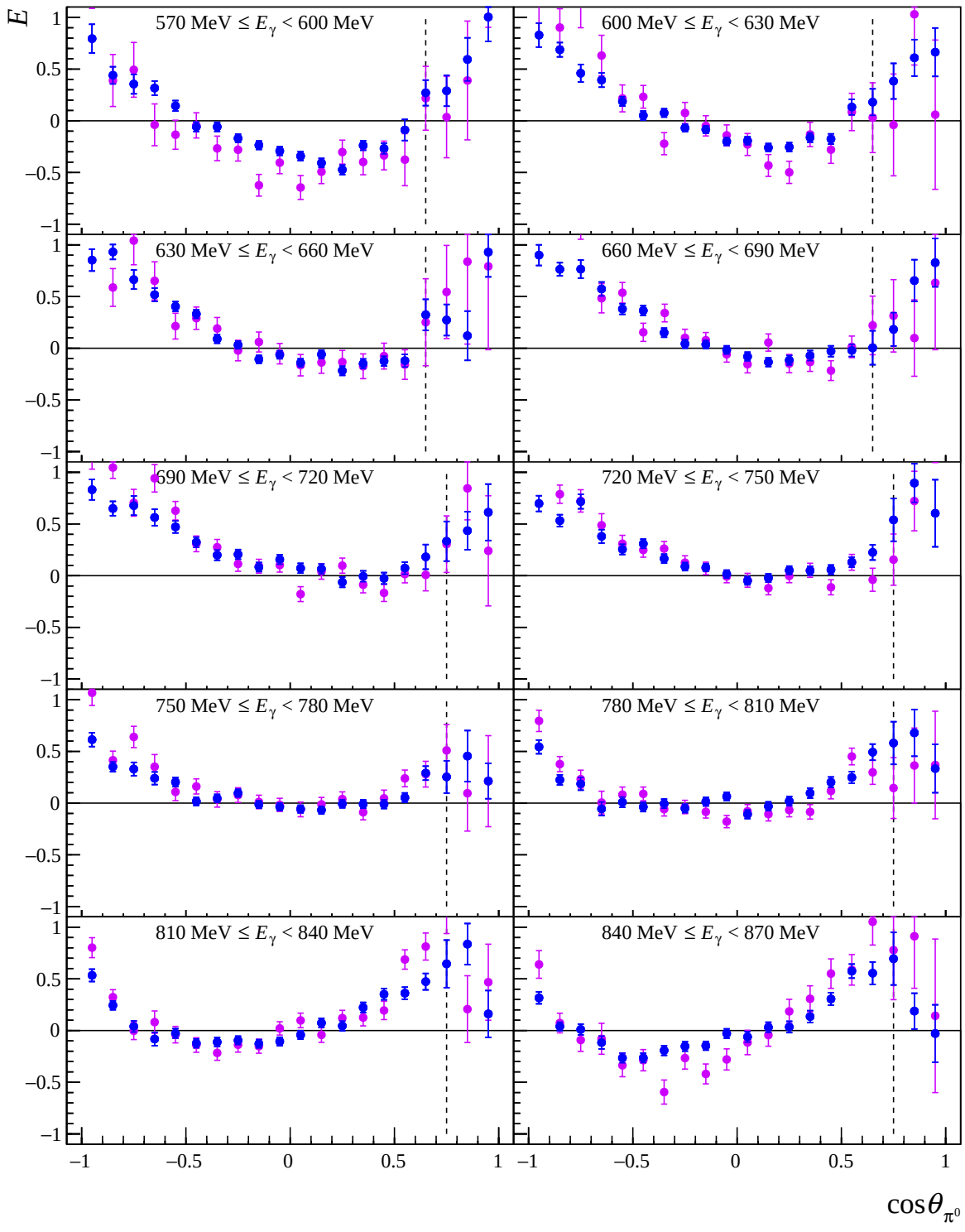

Figure C.10: The double polarization observable E is plotted for the September 2015 (blue) and May 2014 (violet) beamtimes as a function of $\cos\theta_{\pi^0}$ for the beam photon energy range from 570 MeV-870 MeV. The black dashed line marks the point where the 2 PED events are added to the 3 PED events. The target polarization correction factor is not applied.

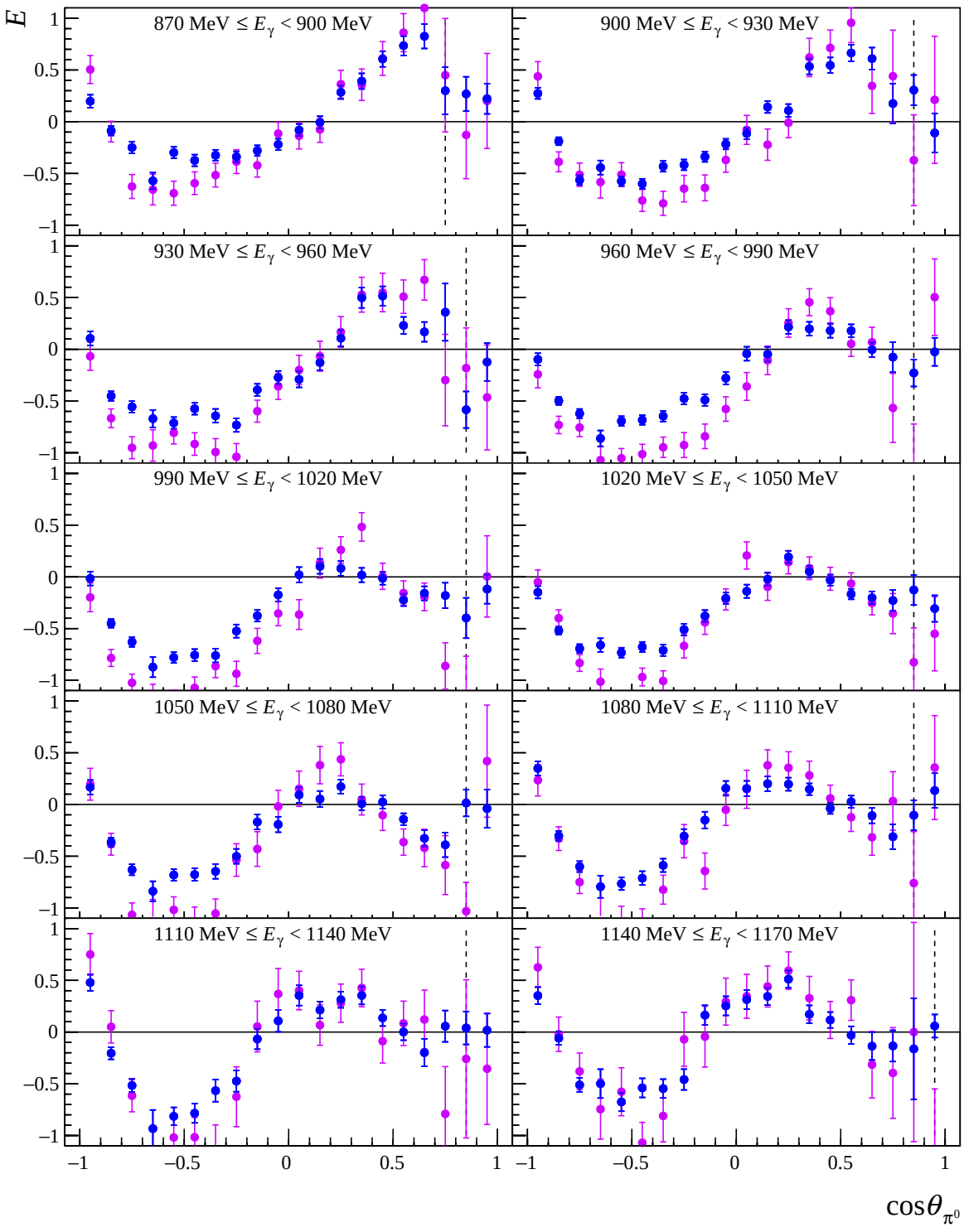

Figure C.11: The double polarization observable E is plotted for the September 2015 (blue) and May 2014 (violet) beamtimes as a function of $\cos\theta_{\pi^0}$ for the beam photon energy range from 870 MeV-1170 MeV. The black dashed line marks the point where the 2 PED events are added to the 3 PED events. The target polarization correction factor is not applied.

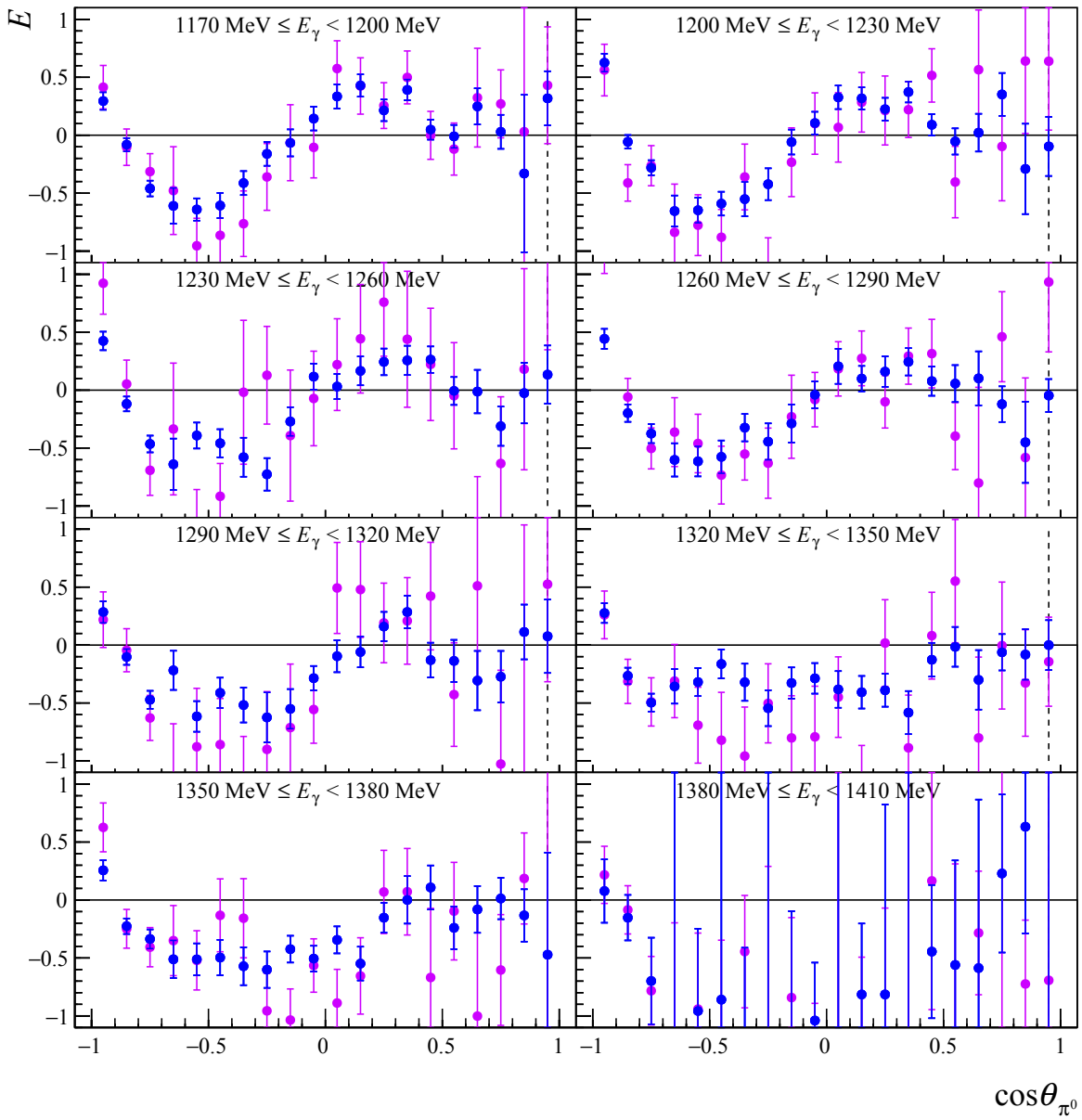

Figure C.12: The double polarization observable E is plotted for the September 2015 (blue) and May 2014 (violet) beamtimes as a function of $\cos\theta_{\pi^0}$ for the beam photon energy range from 1170 MeV-1410 MeV. The black dashed line marks the point where the 2 PED events are added to the 3 PED events. The target polarization correction factor is not applied.

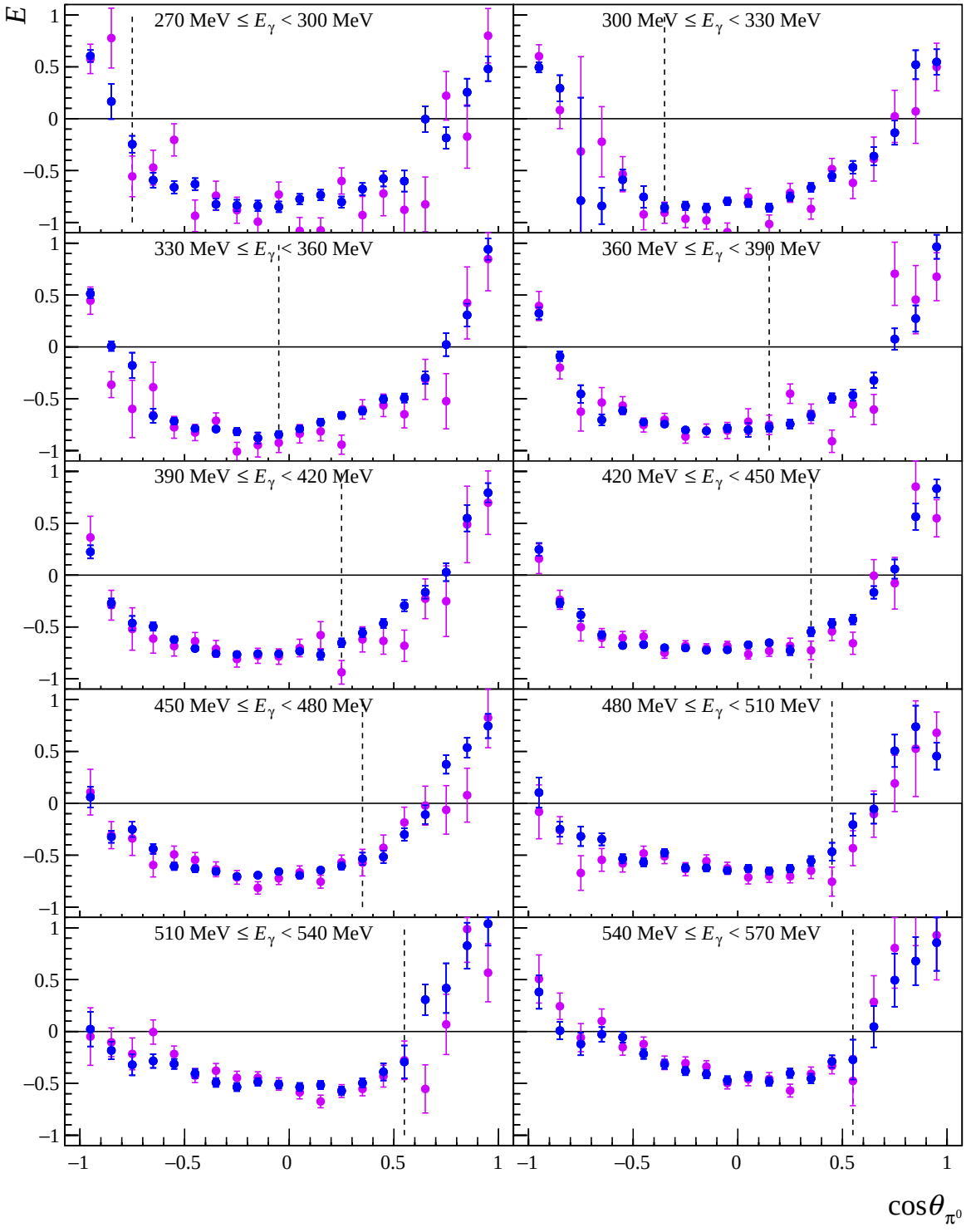

Figure C.13: The double polarization observable E is plotted for the September 2015 (blue) and May 2014 (violet) beamtimes as a function of $\cos\theta_{\pi^0}$ for the beam photon energy range from 260 MeV-570 MeV. The black dashed line marks the point where the 2 PED events are added to the 3 PED events. The target polarization correction factor is applied.

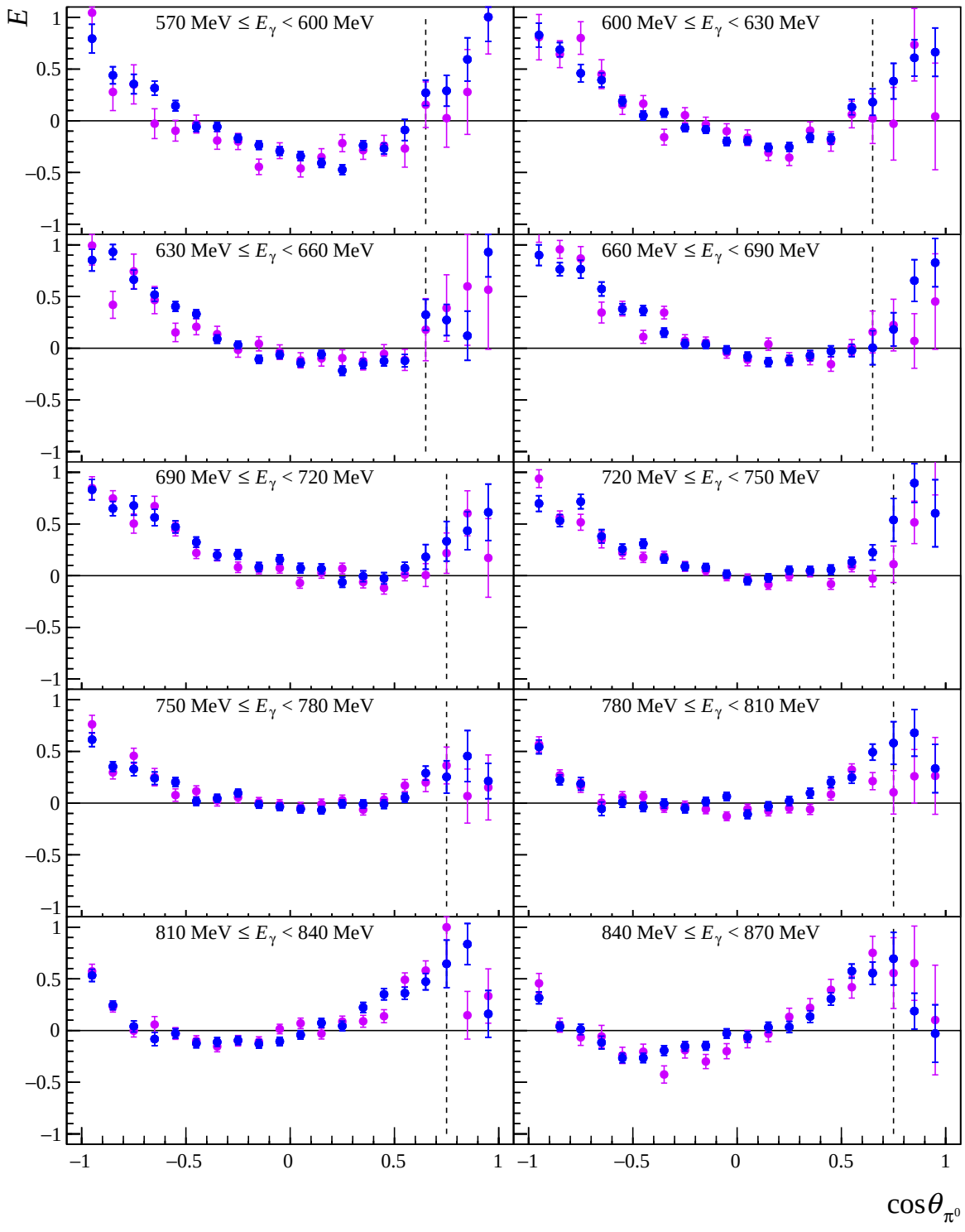

Figure C.14: The double polarization observable E is plotted for the September 2015 (blue) and May 2014 (violet) beamtimes as a function of $\cos\theta_{\pi^0}$ for the beam photon energy range from 570 MeV-870 MeV. The black dashed line marks the point where the 2 PED events are added to the 3 PED events. The target polarization correction factor is applied.

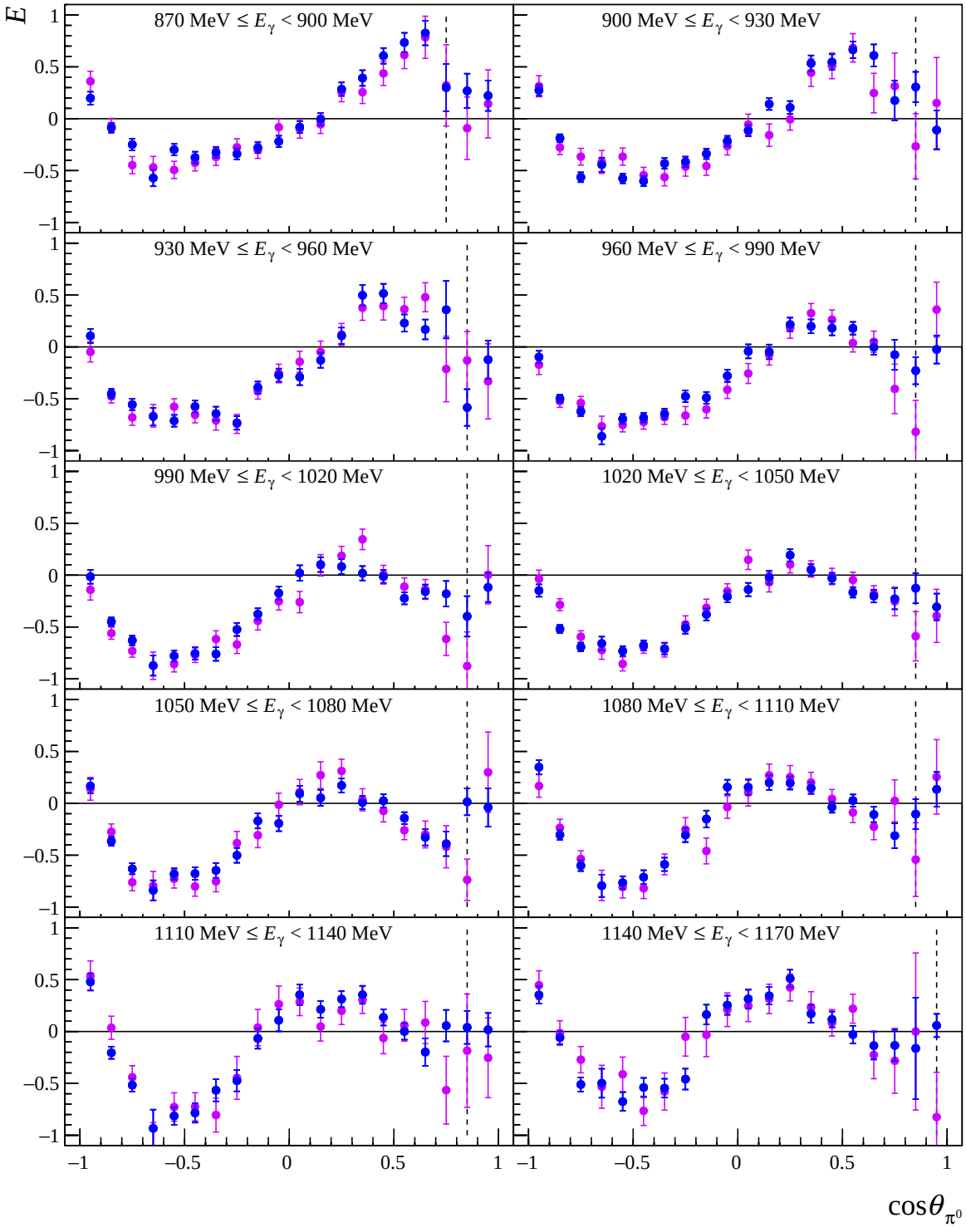

Figure C.15: The double polarization observable E is plotted for the September 2015 (blue) and May 2014 (violet) beamtimes as a function of $\cos\theta_{\pi^0}$ for the beam photon energy range from 870 MeV-1170 MeV. The black dashed line marks the point where the 2 PED events are added to the 3 PED events. The target polarization correction factor is applied.

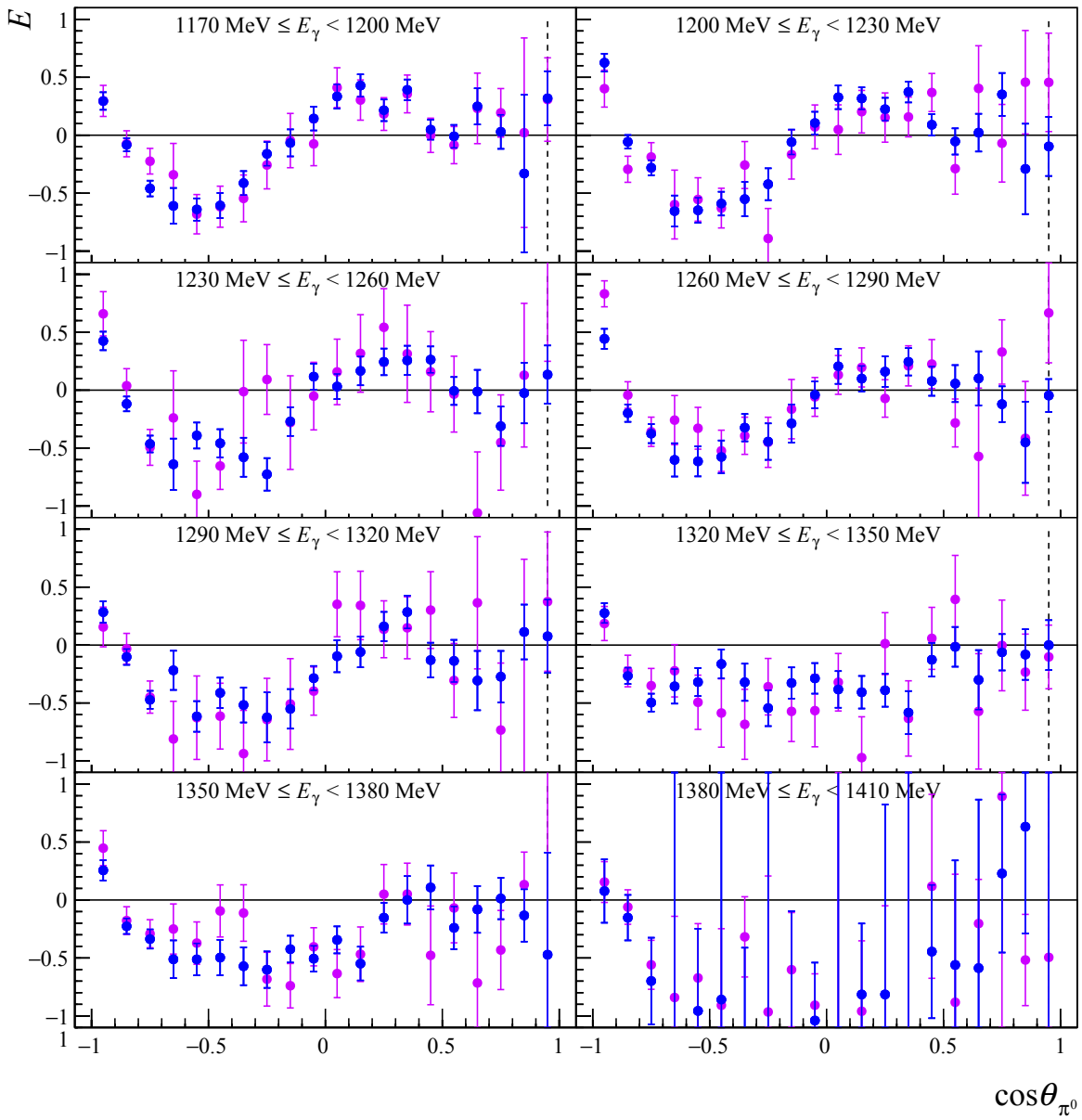

Figure C.16: The double polarization observable E is plotted for the September 2015 (blue) and May 2014 (violet) beamtimes as a function of $\cos\theta_{\pi^0}$ for the beam photon energy range from 1170 MeV-1410 MeV. The black dashed line marks the point where the 2 PED events are added to the 3 PED events. The target polarization correction factor is applied.

C.3 (May 2015 vs. September 2015) for the $p\pi^0$ final state

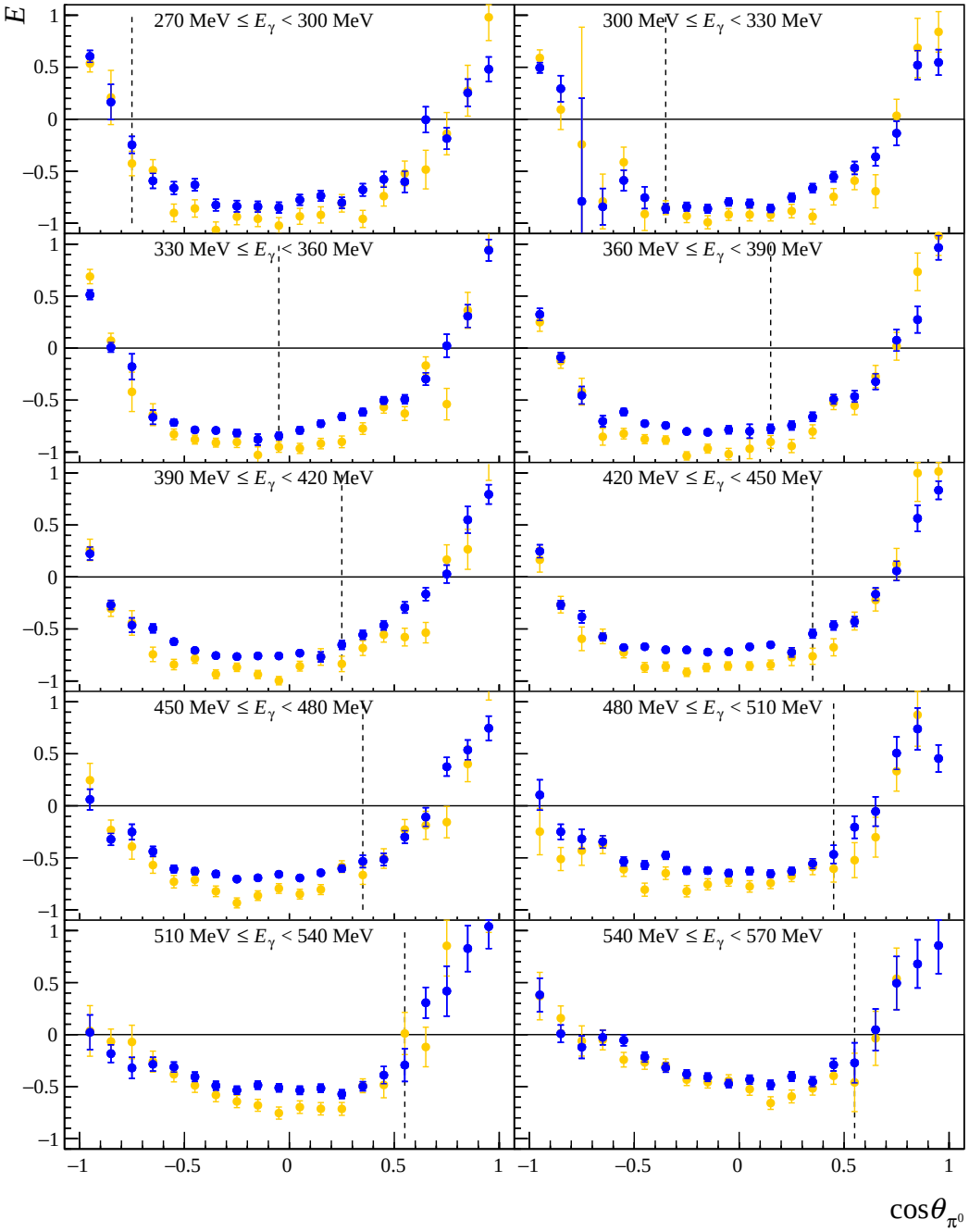

Figure C.17: The double polarization observable E is plotted for the September 2015 (blue) and May 2015 (yellow) beamtimes as a function of $\cos\theta_{\pi^0}$ for the beam photon energy range from 260 MeV-570 MeV. The black dashed line marks the point where the 2 PED events are added to the 3 PED events. The target polarization correction factor is not applied.

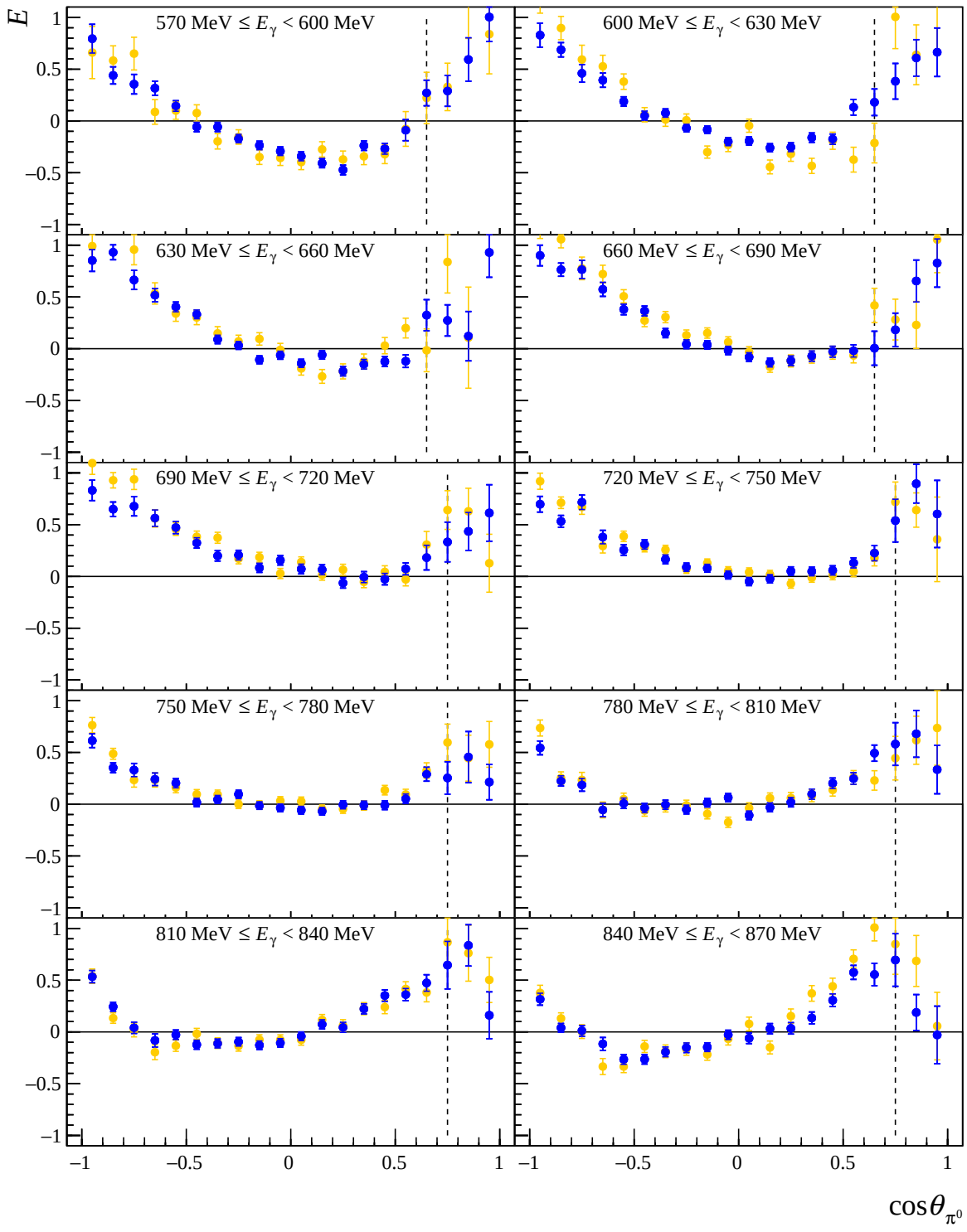

Figure C.18: The double polarization observable E is plotted for the September 2015 (blue) and May 2015 (yellow) beamtimes as a function of $\cos\theta_{\pi^0}$ for the beam photon energy range from 570 MeV-870 MeV. The black dashed line marks the point where the 2 PED events are added to the 3 PED events. The target polarization correction factor is not applied.

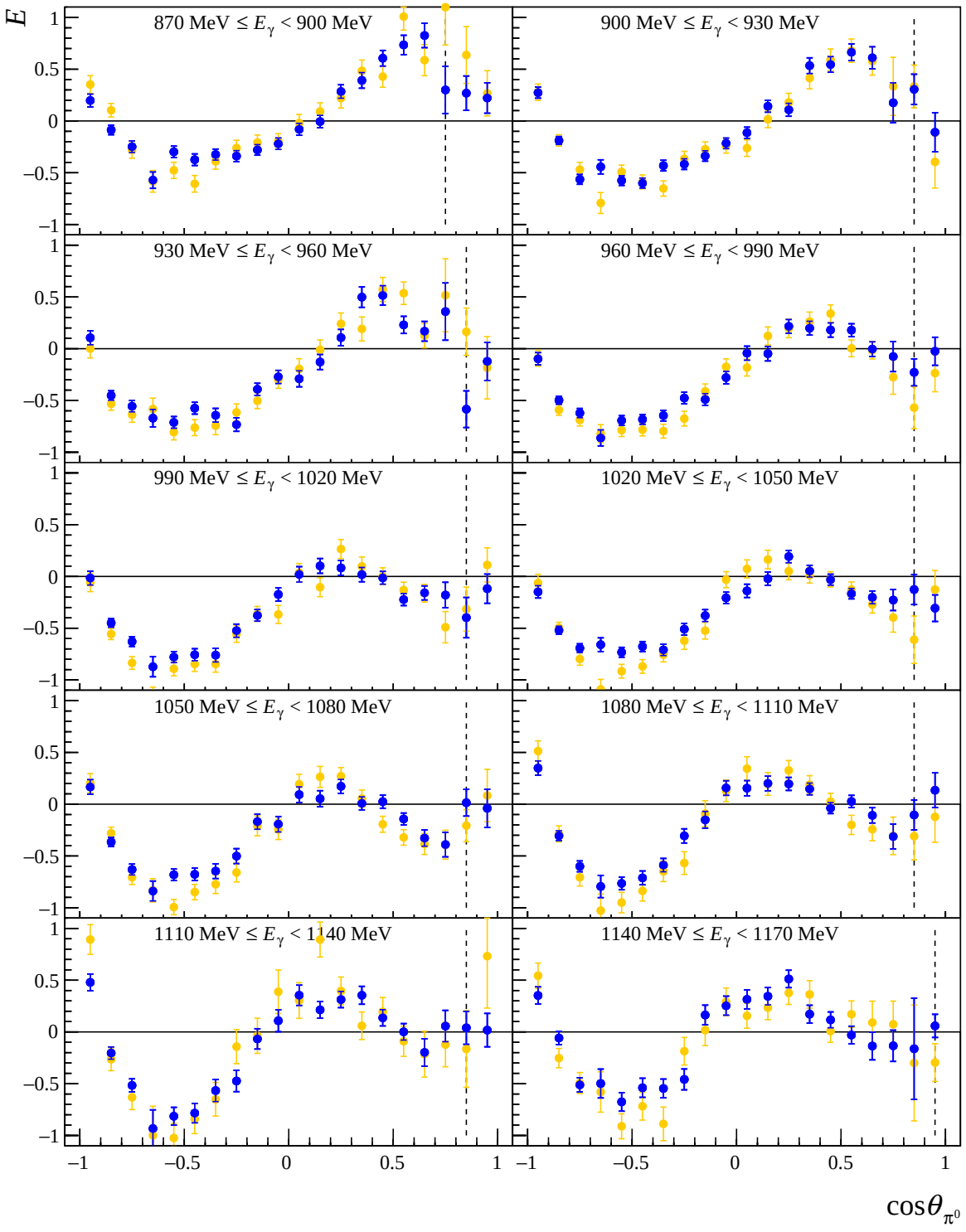

Figure C.19: The double polarization observable E is plotted for the September 2015 (blue) and May 2015 (yellow) beamtimes as a function of $\cos\theta_{\pi^0}$ for the beam photon energy range from 870 MeV-1170 MeV. The black dashed line marks the point where the 2 PED events are added to the 3 PED events. The target polarization correction factor is not applied.

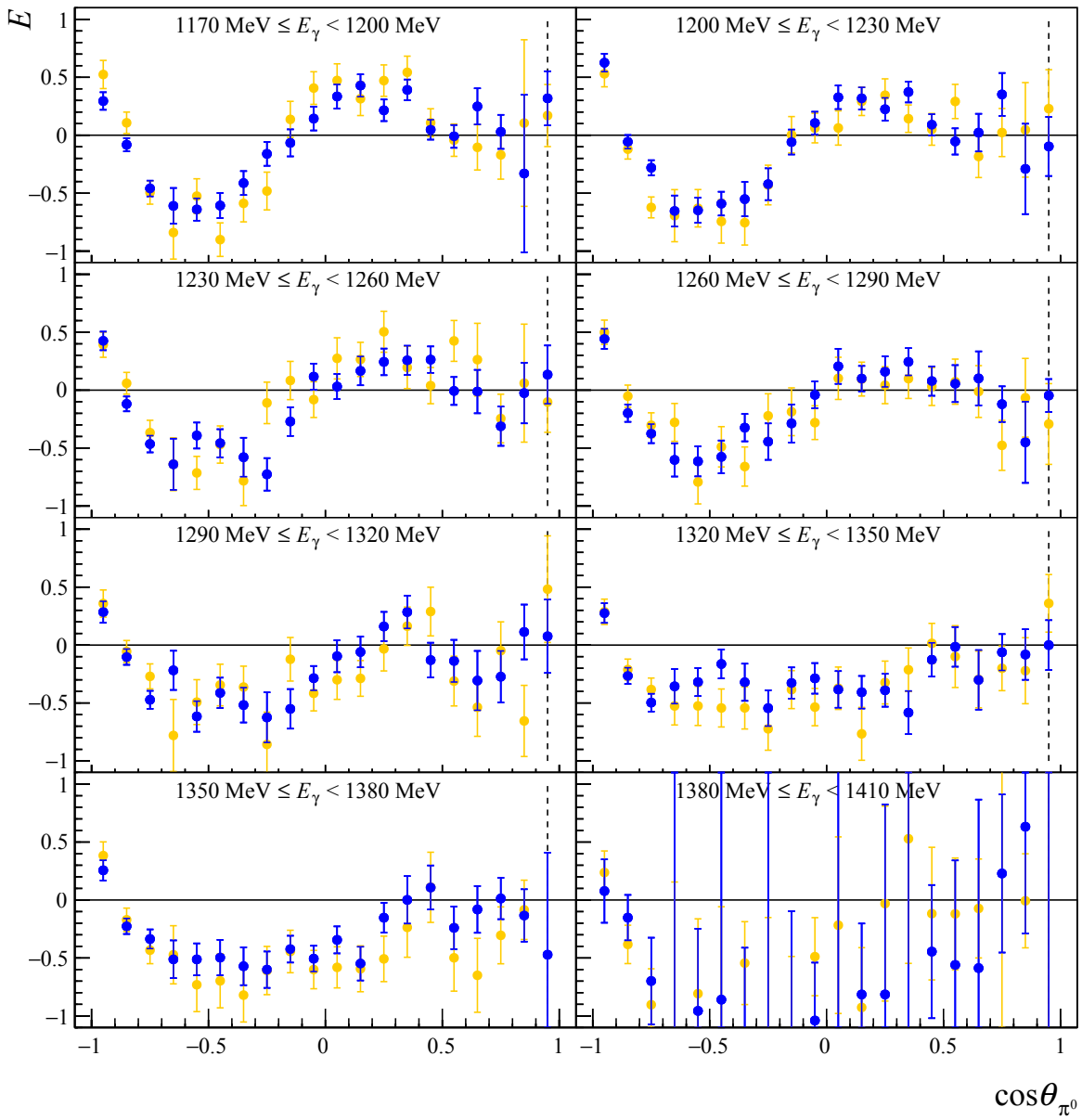

Figure C.20: The double polarization observable E is plotted for the September 2015 (blue) and May 2015 (yellow) beamtimes as a function of $\cos\theta_{\pi^0}$ for the beam photon energy range from 1170 MeV-1410 MeV. The black dashed line marks the point where the 2 PED events are added to the 3 PED events. The target polarization correction factor is not applied.

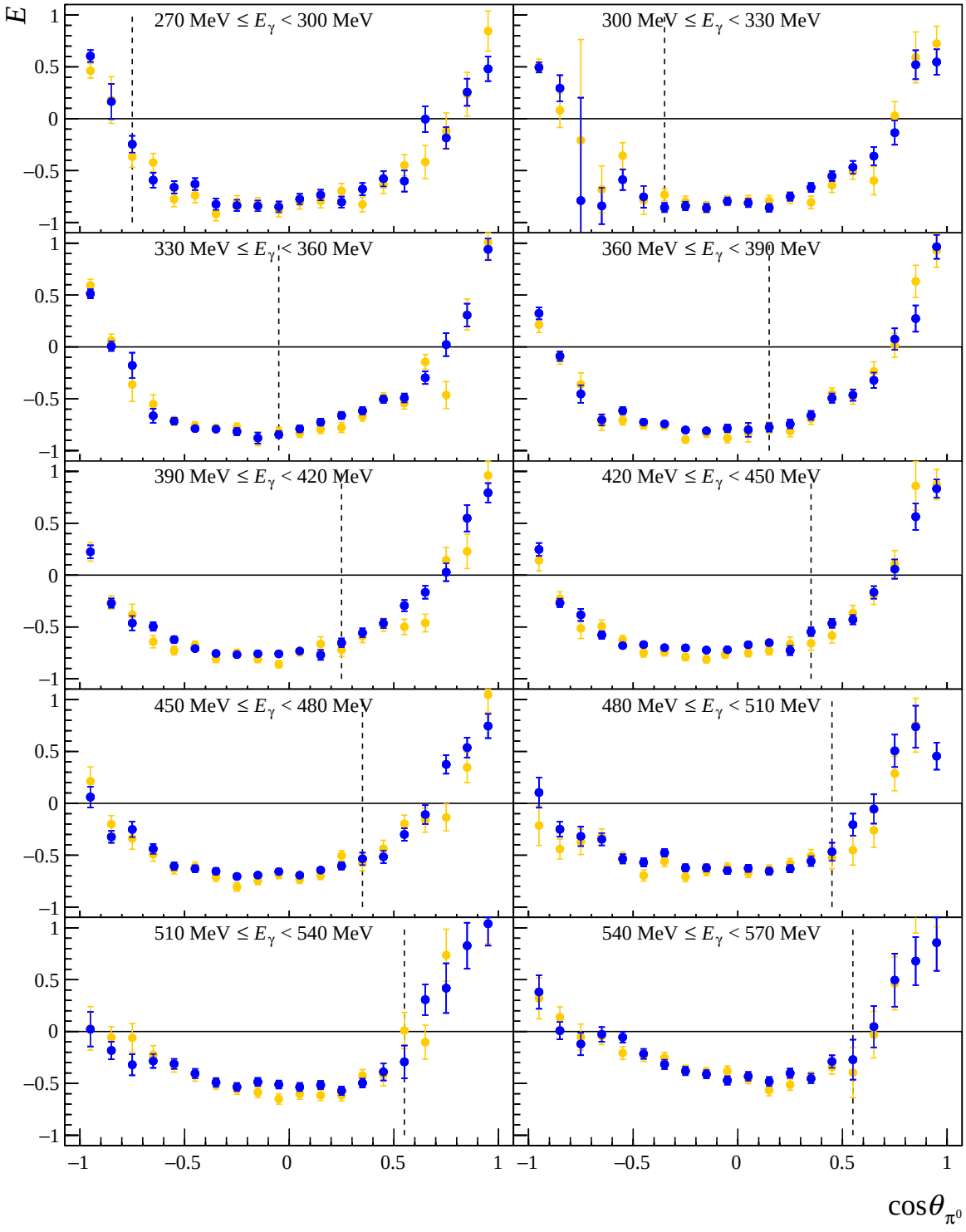

Figure C.21: The double polarization observable E is plotted for the September 2015 (blue) and May 2015 (yellow) beamtimes as a function of $\cos\theta_{\pi^0}$ for the beam photon energy range from 260 MeV-570 MeV. The black dashed line marks the point where the 2 PED events are added to the 3 PED events. The target polarization correction factor is applied.

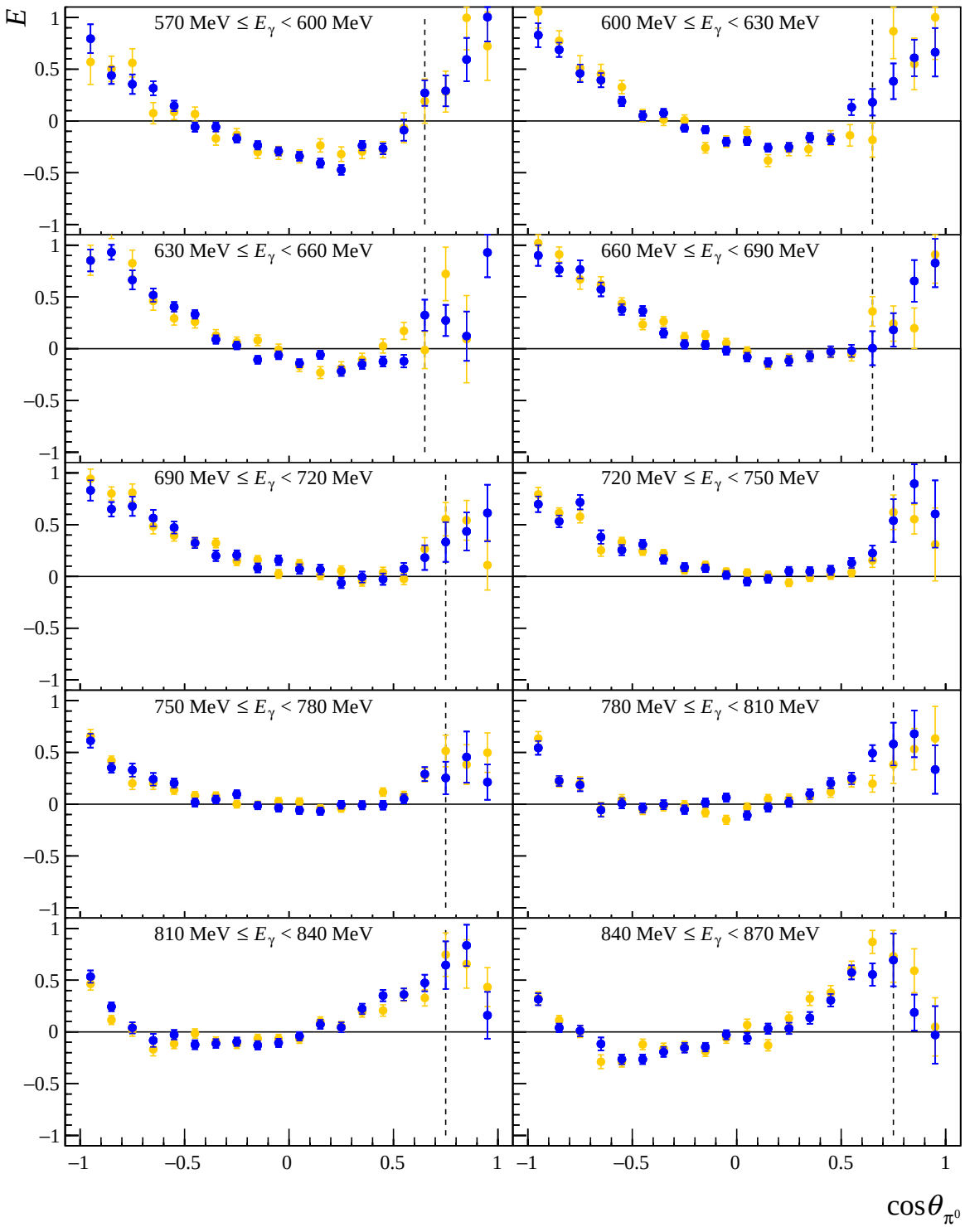

Figure C.22: The double polarization observable E is plotted for the September 2015 (blue) and May 2015 (yellow) beamtimes as a function of $\cos\theta_{\pi^0}$ for the beam photon energy range from 570 MeV-870 MeV. The black dashed line marks the point where the 2 PED events are added to the 3 PED events. The target polarization correction factor is applied.

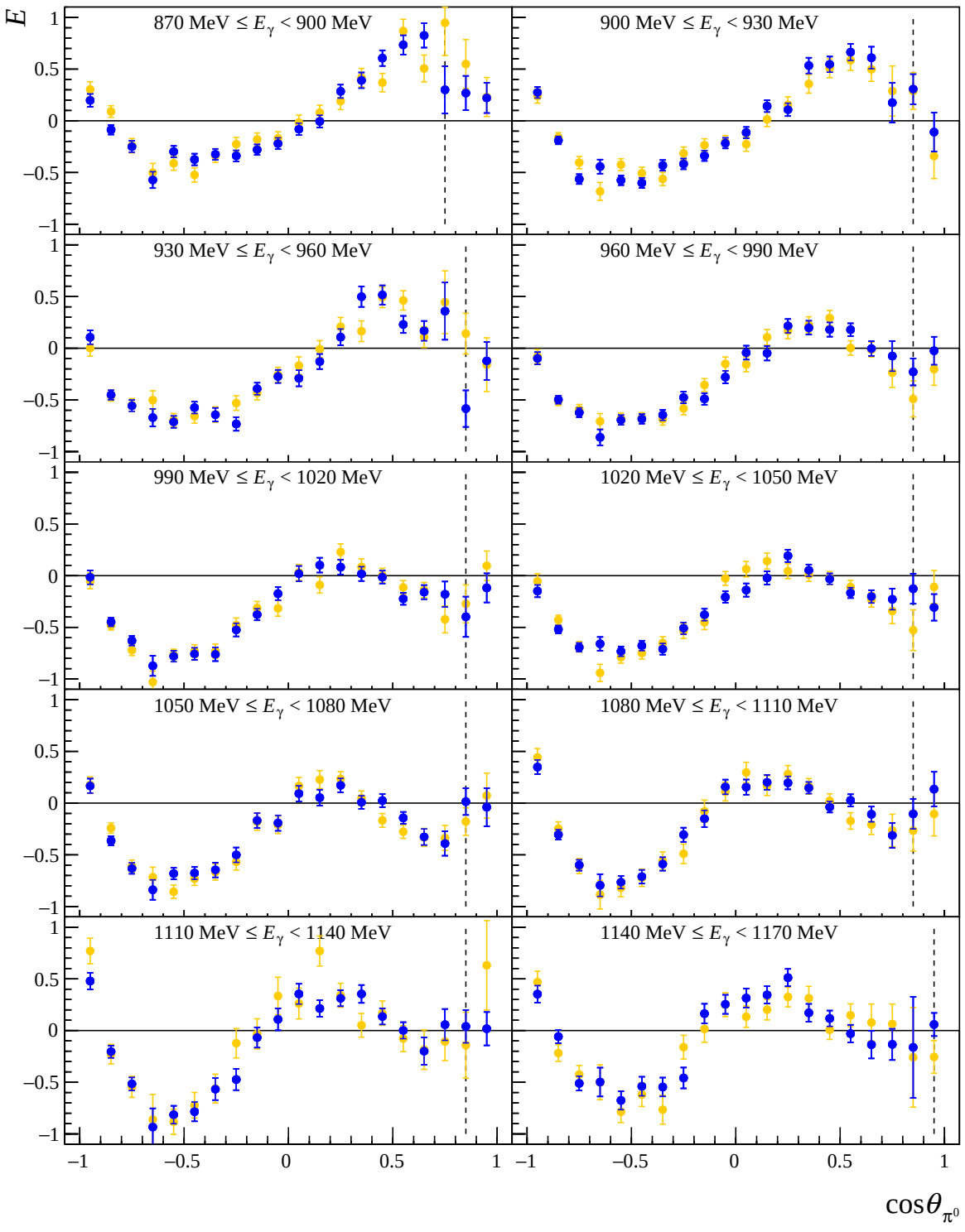

Figure C.23: The double polarization observable E is plotted for the September 2015 (blue) and May 2015 (yellow) beamtimes as a function of $\cos\theta_{\pi^0}$ for the beam photon energy range from 870 MeV-1170 MeV. The black dashed line marks the point where the 2 PED events are added to the 3 PED events. The target polarization correction factor is applied.

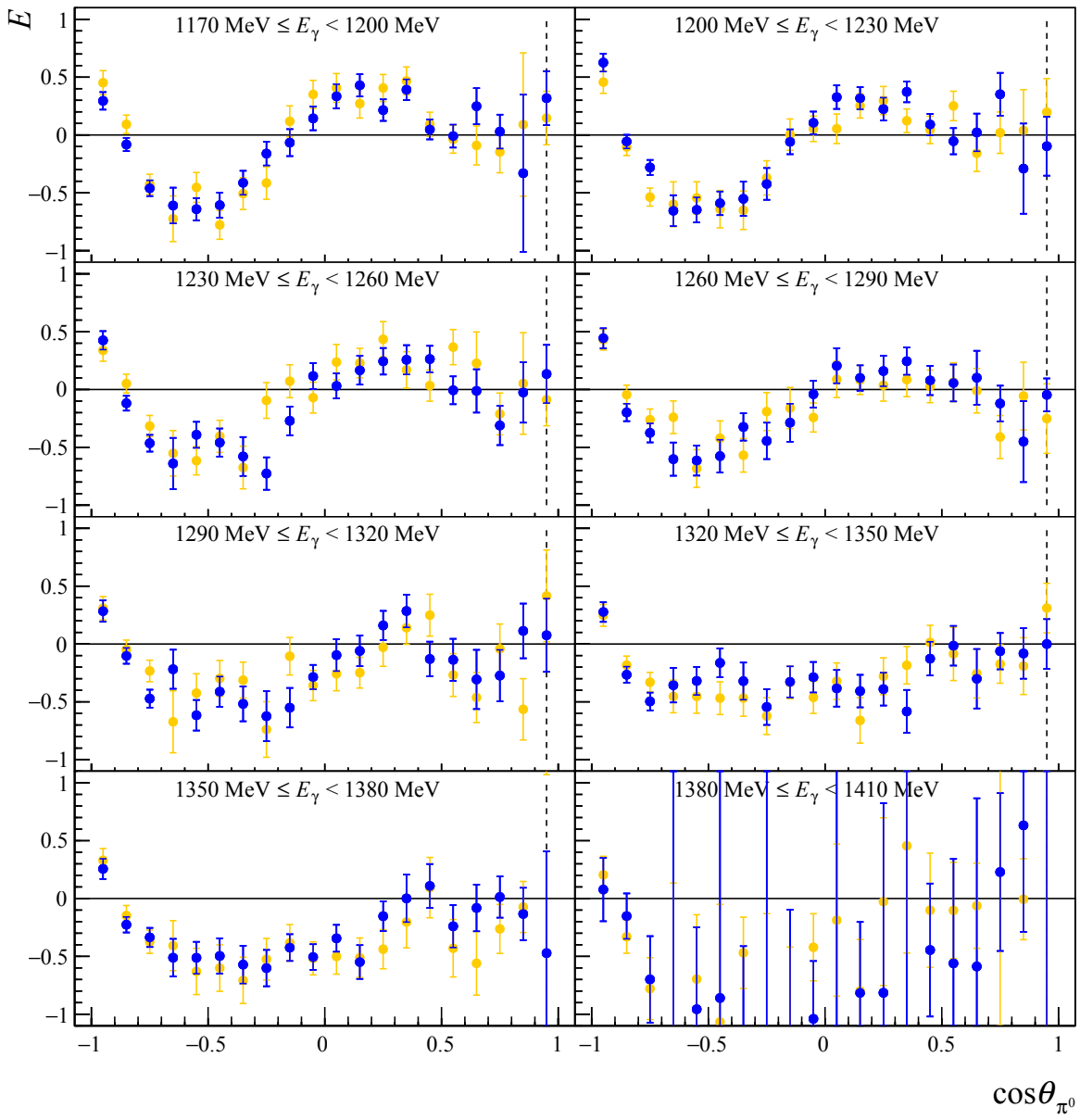

Figure C.24: The double polarization observable E is plotted for the September 2015 (blue) and May 2015 (yellow) beamtimes as a function of $\cos\theta_{\pi^0}$ for the beam photon energy range from 1170 MeV-1410 MeV. The black dashed line marks the point where the 2 PED events are added to the 3 PED events. The target polarization correction factor is applied.

D Comparison of data to PWA solution

The comparison of the helicity asymmetry E to different PWA solutions is given in Figures D.1 - D.4 and for the beam asymmetry Σ in Figures D.5 - D.6. Here, the BnGa-2014-02 solution is depicted in contrast to the Figures 8.25 - 8.30, where the BnGa-2011-02 solution is shown.

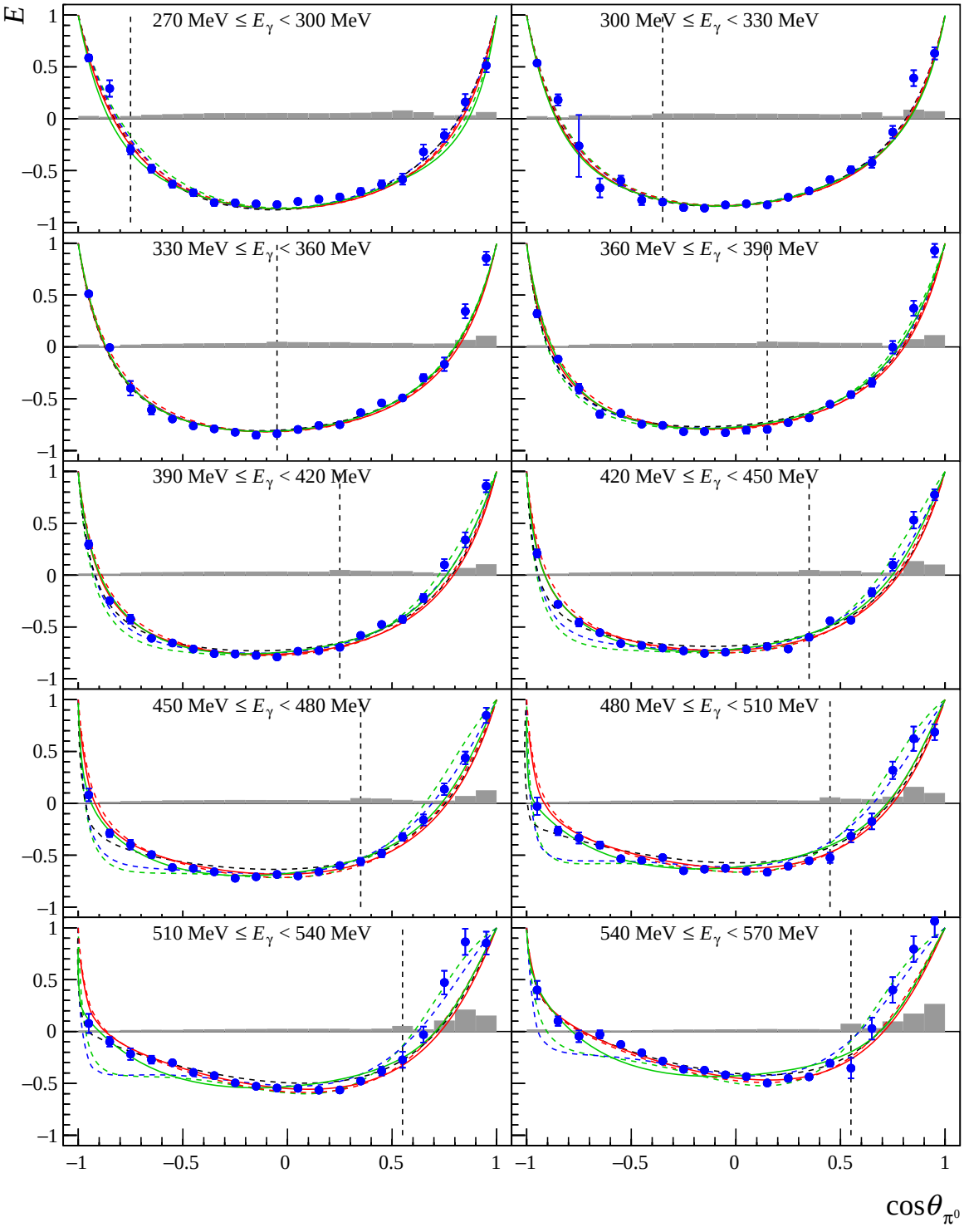

Figure D.1: The double polarization observable E is plotted as a function of $\cos\theta_{\pi^0}$ for the beam photon energy range from 270 MeV $\leq E_\gamma <$ 570 MeV. The black dashed line marks the point where the 2 PED events are added to the 3 PED events. The error bars show only the statistical errors. The systematic errors are depicted in gray. The data is compared to the following PWA solutions: BnGa-2014-02 (red, dashed line) [Ani+12], BnGa-2017 (red, solid line) [Ani+18], JüBo-2015-FitB (green, dashed line) [Rön+15], JüBo-2017 (green, solid line) [RDM18], SAID-CM12 (blue, dashed line) [Wor+12] and MAID2007 (black, dashed line) [DKT07].

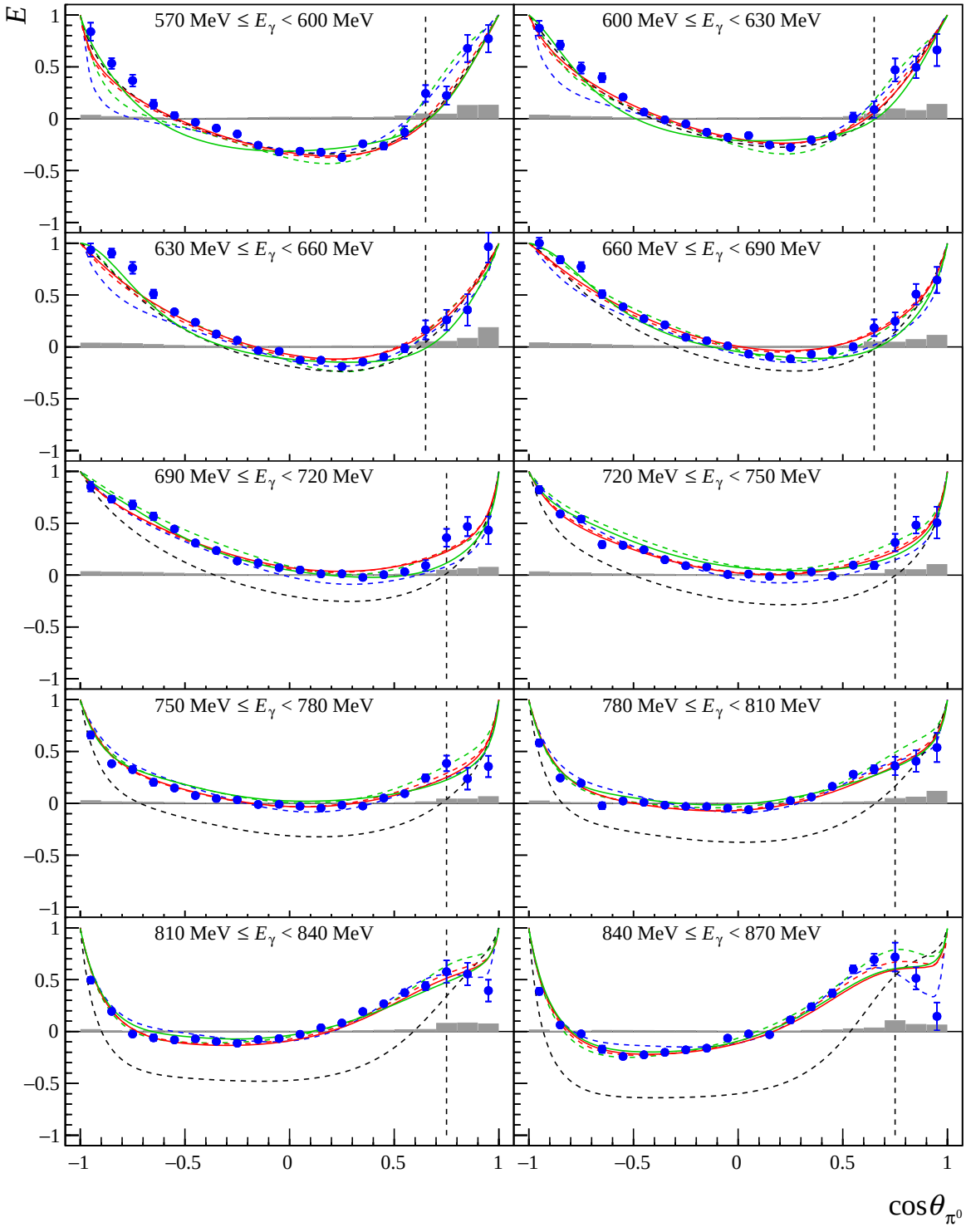

Figure D.2: The double polarization observable E is plotted as a function of $\cos\theta_{\pi^0}$ for the beam photon energy range from 570 MeV $\leq E_\gamma <$ 870 MeV. The black dashed line marks the point where the 2 PED events are added to the 3 PED events. The error bars show only the statistical errors. The systematic errors are depicted in gray. The data is compared to the following PWA solutions: BnGa-2014-02 (red, dashed line) [Ani+12], BnGa-2017 (red, solid line) [Ani+18], JüBo-2015-FitB (green, dashed line) [Rön+15], JüBo-2017 (green, solid line) [RDM18], SAID-CM12 (blue, dashed line) [Wor+12] and MAID2007 (black, dashed line) [DKT07].

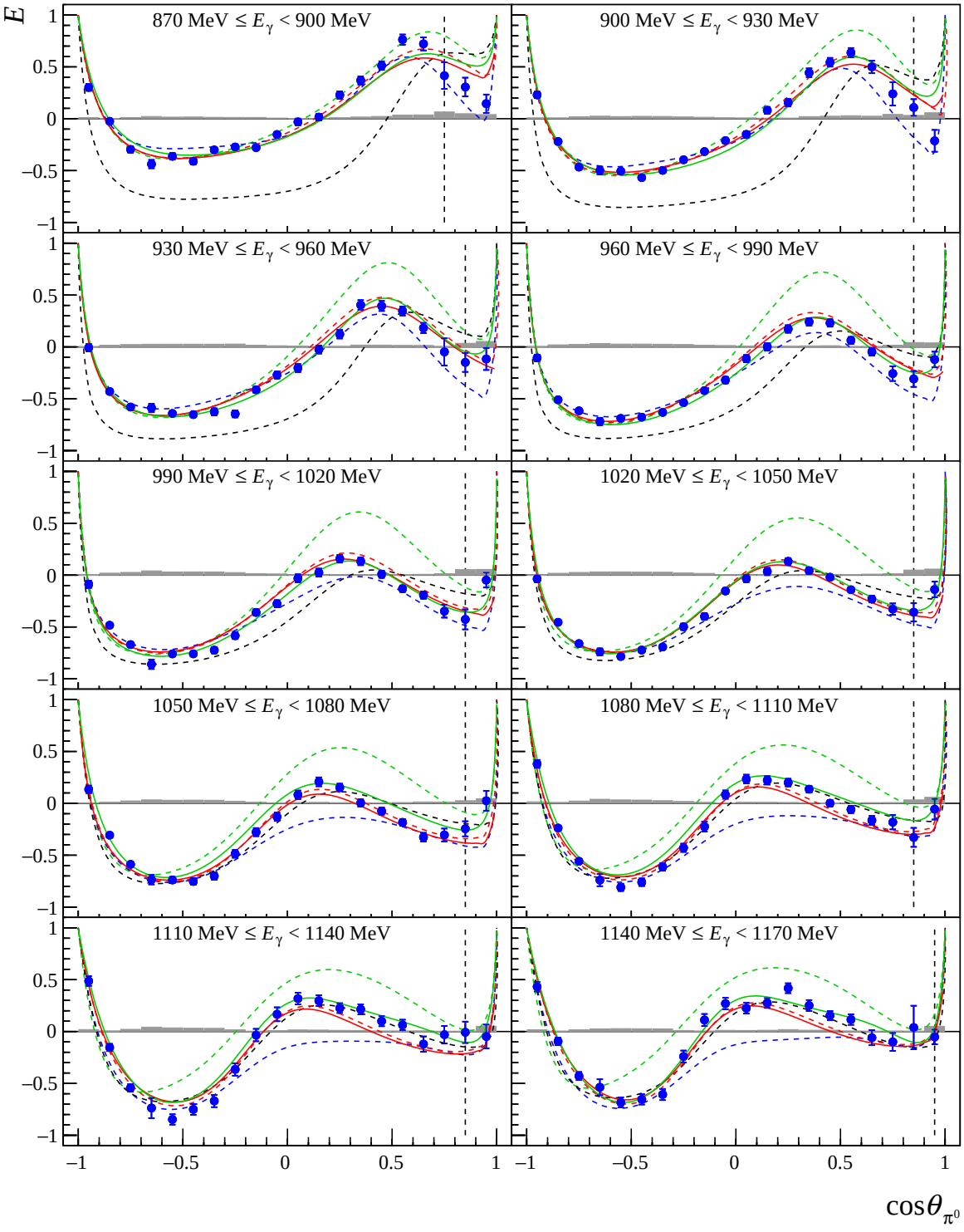

Figure D.3: The double polarization observable E is plotted as a function of $\cos\theta_{\pi^0}$ for the beam photon energy range from 870 MeV $\leq E_\gamma <$ 1170 MeV. The black dashed line marks the point where the 2 PED events are added to the 3 PED events. The error bars show only the statistical errors. The systematic errors are depicted in gray. The data is compared to the following PWA solutions: BnGa-2014-02 (red, dashed line) [Ani+12], BnGa-2017 (red, solid line) [Ani+18], JüBo-2015-FitB (green, dashed line) [Rön+15], JüBo-2017 (green, solid line) [RDM18], SAID-CM12 (blue, dashed line) [Wor+12] and MAID2007 (black, dashed line) [DKT07].

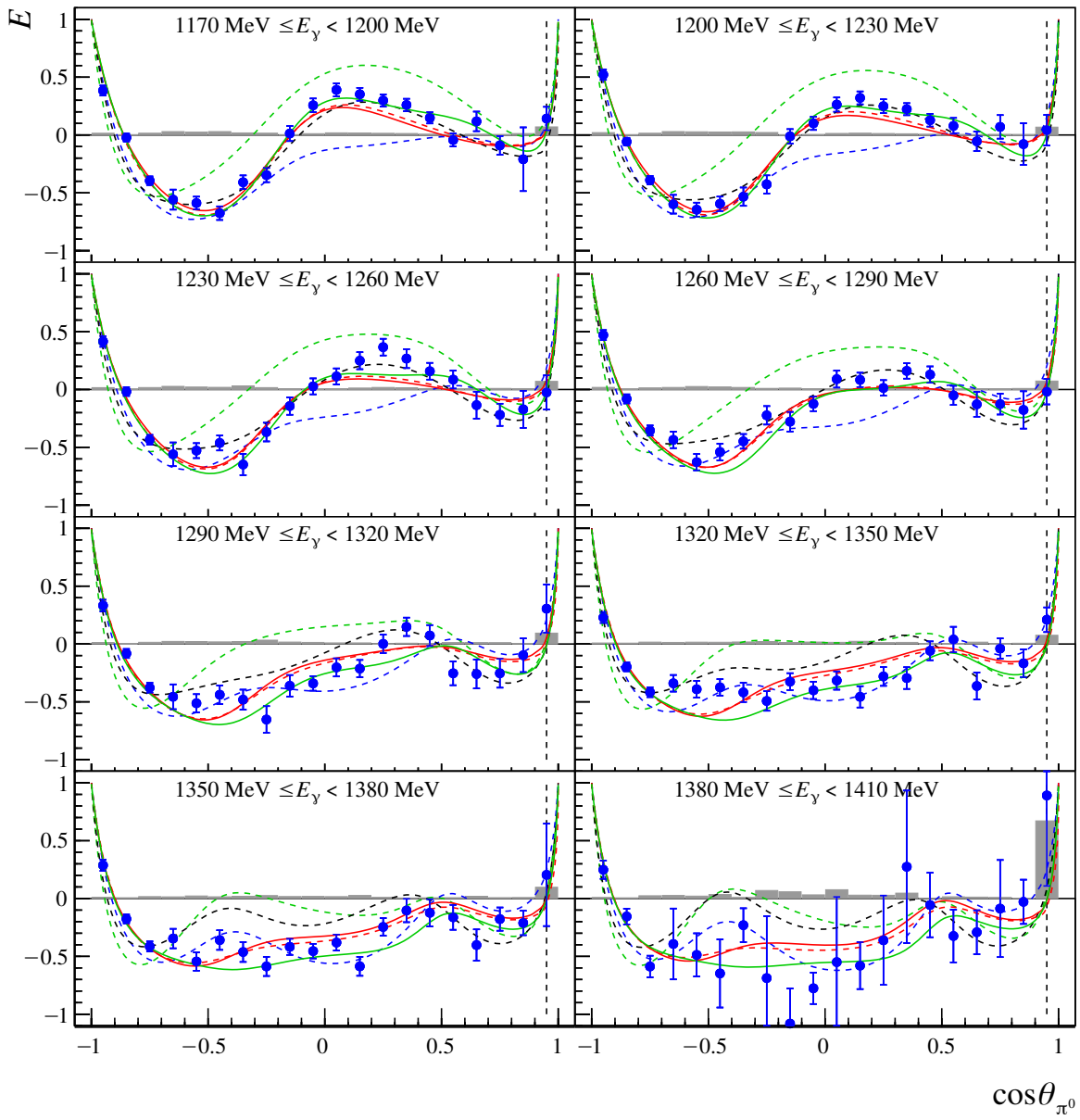

Figure D.4: The double polarization observable E is plotted as a function of $\cos\theta_{\pi^0}$ for the beam photon energy range from 1170 MeV $\leq E_\gamma <$ 1410 MeV. The black dashed line marks the point where the 2 PED events are added to the 3 PED events. The error bars show only the statistical errors. The systematic errors are depicted in gray. The data is compared to the following PWA solutions: BnGa-2014-02 (red, dashed line) [Ani+12], BnGa-2017 (red, solid line) [Ani+18], JüBo-2015-FitB (green, dashed line) [Rön+15], JüBo-2017 (green, solid line) [RDM18], SAID-CM12 (blue, dashed line) [Wor+12] and MAID2007 (black, dashed line) [DKT07].

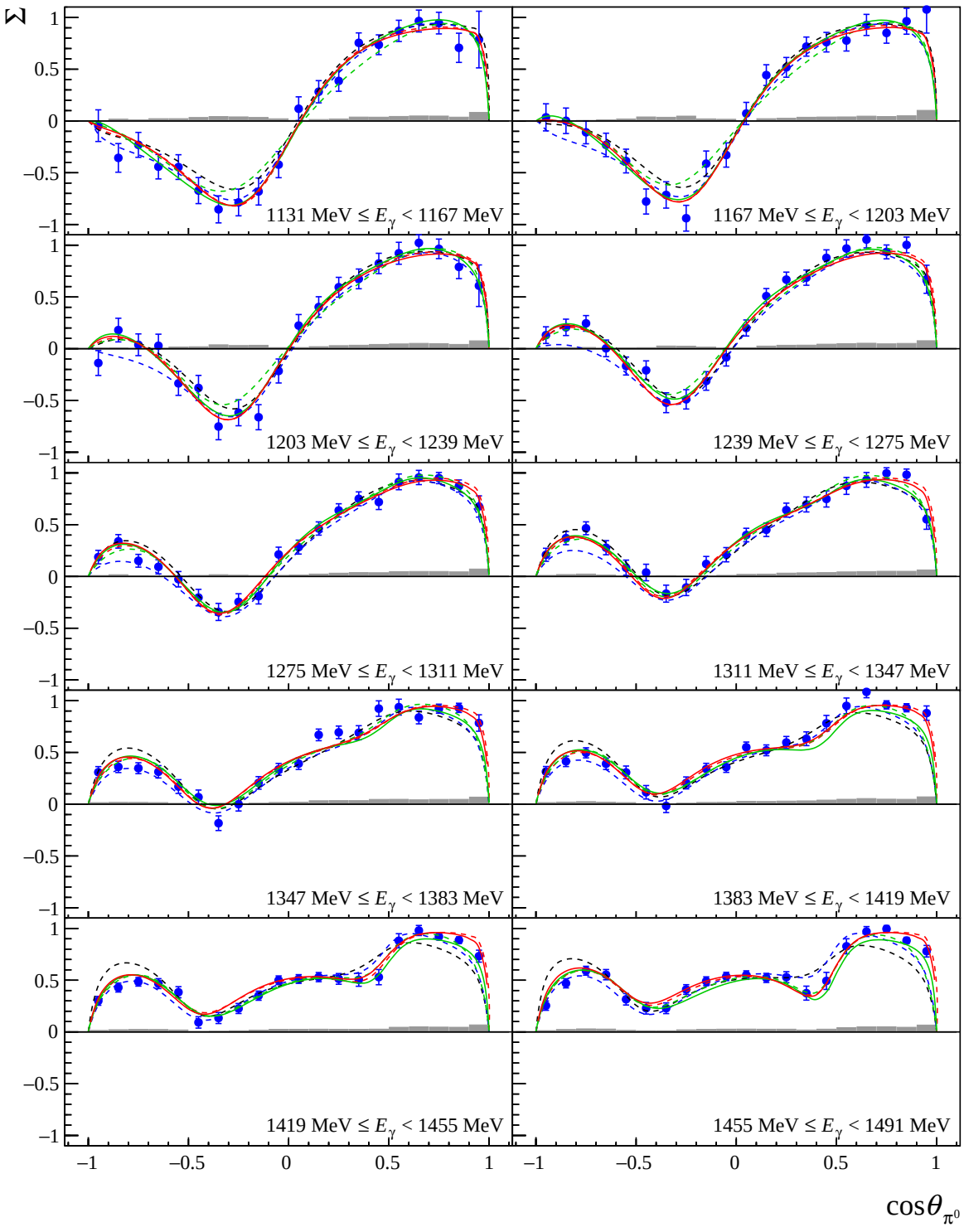

Figure D.5: Results of the beam asymmetry Σ for the $p\pi^0$ final state are shown for the energy range of E_γ = (1131 MeV - 1491 MeV). The error bars show only the statistical errors. The systematic errors are depicted in gray. The data is compared to the following PWA solutions: BnGa-2014-02 (red, dashed line) [Ani+12], BnGa-2017 (red, solid line) [Ani+18], JüBo-2015-FitB (green, dashed line) [Rön+15], JüBo-2017 (green, solid line) [RDM18], SAID-CM12 (blue, dashed line) [Wor+12] and MAID2007 (black, dashed line) [DKT07].

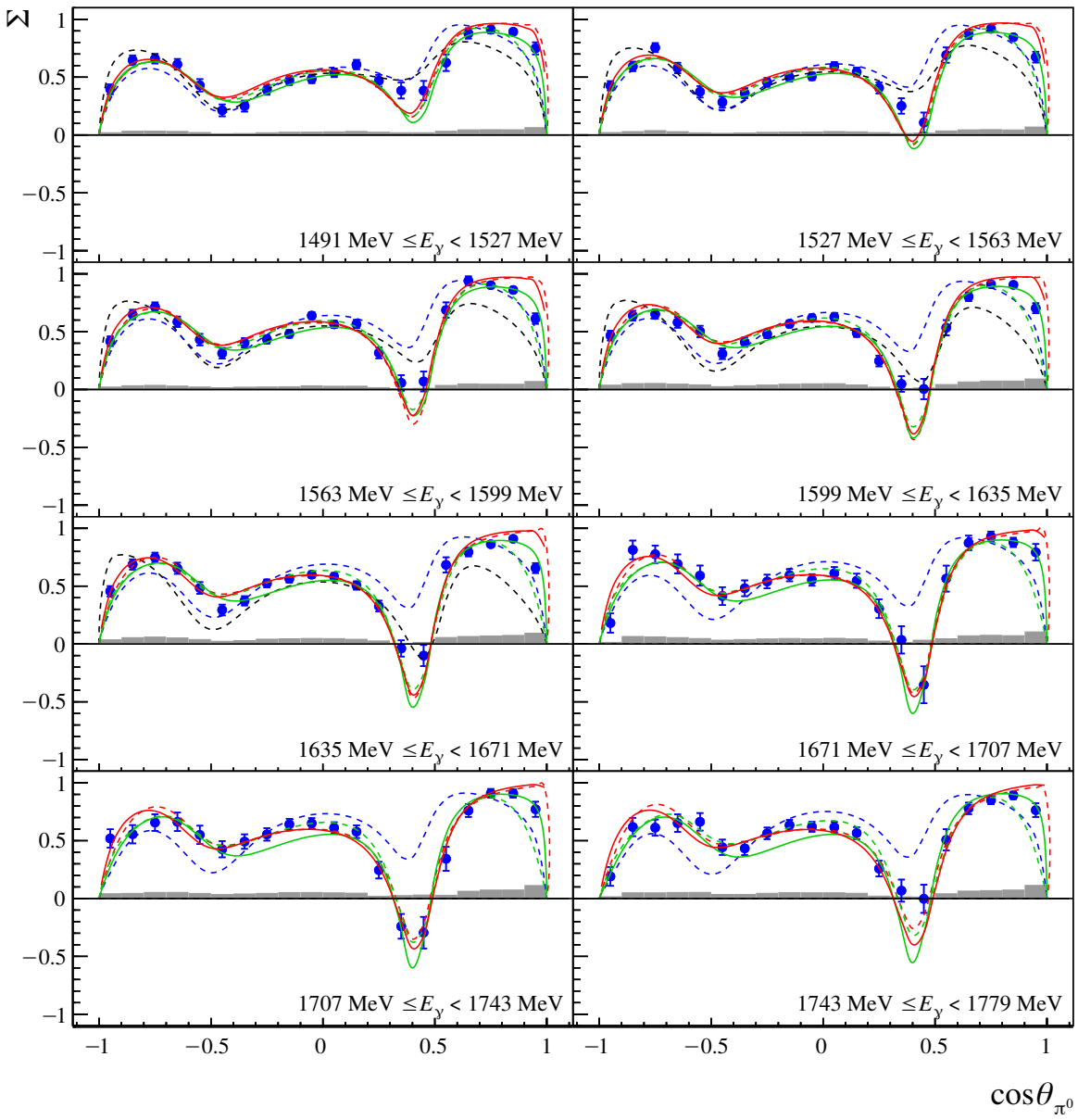

Figure D.6: Results of the beam asymmetry Σ for the $p\pi^0$ final state are shown for the energy range of E_γ = (1491 MeV - 1779 MeV). The error bars show only the statistical errors. The systematic errors are depicted in gray. The data is compared to the following PWA solutions: BnGa-2014-02 (red, dashed line) [Ani+12], BnGa-2017 (red, solid line) [Ani+18], JüBo-2015-FitB (green, dashed line) [Rön+15], JüBo-2017 (green, solid line) [RDM18], SAID-CM12 (blue, dashed line) [Wor+12] and MAID2007 (black, dashed line) [DKT07].

Bibliography

[Aad+12] G. Aad et al., *Observation of a new particle in the search for the Standard Model Higgs boson with the ATLAS detector at the LHC*, Phys. Lett. B **716** (2012) 1–29.

[AG78] A. Abragam and M. Goldman, *Principles of dynamic nuclear polarisation*, Reports on Progress in Physics **41** (1978) 395.

[AP57] A. Abragam and W. G. Proctor, *Experiments on Spin Temperature*, Phys. Rev. **106** (1957) 160–161.

[AS72] M. Abramowitz and I. Stegun, *Handbook of Mathematical Functions*, Dover Publishing, 1972.

[Ach+05] P. Achard et al., *Measurement of the running of the electromagnetic coupling at large momentum-transfer at LEP*, Phys. Lett. B **623** (2005) 26 –36.

[Ada+01] F. V. Adamian et al., *Measurement of the cross section asymmetry of the reaction $\gamma p \to \pi^0 p$ in the resonance energy region $E_\gamma = 0.5 - 1.1$GeV*, Phys. Rev. C **63** (2001) 054606.

[Adl+15] P. Adlarson et al., *Measurement of π^0 photoproduction on the proton at MAMI C*, Phys. Rev. C **92** (2015) 024617.

[Afz12] F. N. Afzal, *Analysis of Crystal Barrel data - Measurement of the double polarization observable E in the reaction $\vec{\gamma}\vec{p} \to \eta' p$*, Master's thesis: Rheinische Friedrich-Wilhelms-Universität Bonn, 2012.

[Afz+16] F. N. Afzal et al., *Measurement of the double polarization observables E and G at the Crystal Ball experiment at MAMI*, *Proceedings of the XVIth International Workshop in Polarized Sources, Targets, and Polarimetry (PSTP2015)*, (Bochum, Germany), PoS, 2016.

[Ago+03] S. Agostinelli et al., *GEANT4: A Simulation toolkit*, Nucl. Instrum. Meth. A **506** (2003) 250–303.

[Ahr+02] J. Ahrens et al., *Helicity Amplitudes $A_{1/2}$ and $A_{3/2}$ for the $D_{13}(1520)$ Resonance Obtained from the $\vec{\gamma}\vec{p} \to p\pi^0$ Reaction*, Phys. Rev. Lett. **88** (2002) 232002.

[Ahr+04] J. Ahrens et al., *Helicity dependence of the $\gamma p \to N\pi$ channels and multipole analysis in the Δ region*, Eur. Phys. J. A **21** (2004) 323–333.

[AH13] I. Aitchison and A. Hey, *Gauge theories in particle physics (Vol. 2)*, Fourth edition, CRC Press, 2013.

[Aja+98] J. Ajaka et al., *New Measurement of Σ Beam Asymmetry for η Meson Photoproduction on the Proton*, Phys. Rev. Lett. **81** (1998) 1797–1800.

[Ake+92] E. Aker et al., *The Crystal Barrel spectrometer at LEAR*, Nucl. Instrum. Meth. A **321** (1992) 69–108.

[Ako+14] C. S. Akondi et al., *Measurement of the Transverse Target and Beam-Target Asymmetries in η Meson Photoproduction at MAMI*, Phys. Rev. Lett. **113** (2014) 102001.

[Alt05] G. Altarelli, *The Standard model of particle physics* (2005).

[ADK16] C. Amsler, T. DeGrand and B. Krusche, *Quark Model*, in: The Review of Particle Physics 2016 [Pat+16] (2016).

[Ams+08] C. Amsler et al., *Review of Particle Physics*, Phys. Lett. B **667** (2008) 1ff.

[AKN+] A. V. Anisovich, E. Klempt, V. A. Nikonov et al., *Bonn-Gatchina Partial Wave Analysis*, URL: `https://pwa.hiskp.uni-bonn.de/` (visited on 27/08/2018).

[Ani+12] A. V. Anisovich et al., *Properties of baryon resonances from a multichannel partial wave analysis*, Eur. Phys. J. A **48** (2012) 15.

[Ani+16] A. V. Anisovich et al., *The impact of new polarization data from Bonn, Mainz and Jefferson Laboratory on $\gamma p \to \pi N$ multipoles*, Eur. Phys. J. A **52** (2016) 284.

[Ani+17] A. V. Anisovich et al., *Evidence for Δ(2200)7/2- from photoproduction and consequence for chiral-symmetry restoration at high mass*, Phys. Lett. B **766** (2017) 357 –361.

[Ani+18] A. Anisovich et al., *Proton-η' interactions at threshold*, Phys. Lett. B **785** (2018) 626 –630.

[Ann+16] J. R. M. Annand et al., *T and F asymmetries in π^0 photoproduction on the proton*, Phys. Rev. C **93** (2016) 055209.

[Ann08] J. Annand, *The Glasgow/Mainz Bremsstrahlung Tagger Operations Manual*, Internal Manual of the A2 collaboration, 2008.

[Ans+93] M. Anselmino et al., *Diquarks*, Rev. Mod. Phys. **65** (1993) 1199–1233.

[Ant+91] I. Anthony et al., *Design of a tagged photon spectrometer for use with the Mainz 840-MeV microtron*, Nucl. Instrum. Meth. A **301** (1991) 230–240.

[Aoy+15] T. Aoyama et al., *Tenth-order electron anomalous magnetic moment: Contribution of diagrams without closed lepton loops*, Phys. Rev. D **91** (2015) 033006.

[Arr+92] J. Arrington et al., *A variable energy Møller polarimeter at the MIT-Bates Linear Accelerator Center*, Nucl. Instrum. Meth. A **311** (1992) 39–48.

[Arr+12] J. Arrington et al., *Hard probes of short-range nucleon-nucleon correlations*, Prog. Part. Nucl. Phys. **67** (2012) 898–938.

[Ash88] J. Ashman, *A measurement of the spin asymmetry and determination of the structure function g_1 in deep inelastic muon-proton scattering*, Phys. Lett. B **206** (1988) 364–370.

[AHK16] D. Asner, C. Hanhart and E. Klempt, *Resonances*, in: The Review of Particle Physics 2016 [Pat+16] (2016).

[Aul11] K. Aulenbacher, *Polarized beams for electron accelerators*, Eur. Phys. J. Spec. Top. **198** (2011) 361.

[Aul+97] K. Aulenbacher et al., *The MAMI source of polarized electrons*, Nucl. Instrum. Meth. A **391** (1997) 498–506.

[Ave+99] T. Averett et al., *A solid polarized target for high-luminosity experiments*, Nucl. Instrum. Meth. A **427** (1999) 440–454.

[Bar+69] G. Barbiellini et al., *Photoproduction of π^0 on Protons by Polarized γ Rays*, Phys. Rev. **184** (1969) 1402–1413.

[BMT59] V. Bargmann, L. Michel and V. L. Telegdi, *Precession of the Polarization of Particles Moving in a Homogeneous Electromagnetic Field*, Phys. Rev. Lett. **2** (1959) 435–436.

[BDS75] I. S. Barker, A. Donnachie and J. K. Storrow, *Complete Experiments in Pseudoscalar Photoproduction*, Nucl. Phys. B **95** (1975) 347–356.

[Bar89] R. J. Barlow, *Statistics: A Guide to the Use of Statistical Methods in the Physical Science*, Wiley, 1989.

[Bar+05a] O. Bartalini et al., *Measurement of π^0 photoproduction on the proton from 550 to 1500 MeV at GRAAL*, Eur. Phys. J. A **26** (2005) 399–419.

[Bar+07a] O. Bartalini et al., *Measurement of η photoproduction on the proton from threshold to 1500 MeV*, Eur. Phys. J. A **33** (2007) 169–184.

[Bar19] C. Bartels, *Efficiency determination of the scintillating fibre detector of the CBELSA/TAPS experiment*, Master's thesis: Rheinische Friedrich-Wilhelms-Universität Bonn, 2019.

[Bar+05b] O. Bartholomy et al., *Neutral-Pion Photoproduction off Protons in the Energy Range* 0.3 GeV $< E_\gamma <$ 3 GeV, Phys. Rev. Lett. **94** (2005) 012003.

[Bar+07b] O. Bartholomy et al., *Photoproduction of eta-mesons off protons*, Eur. Phys. J. A **33** (2007) 133–146.

[Bec+97] R. Beck et al., *Measurement of the $E2/M1$ Ratio in the $N \to \Delta$ Transition using the reaction $p(\gamma,\vec{p})\pi^0$*, Phys. Rev. Lett. **78** (1997) 606–609.

[Bel+83] A. Belyaev et al., *Experimental studies of the Σ, T, P polarization parameters and the $\gamma p \to p\pi^0$ reaction multipole analysis in the first resonance region*, Nucl. Phys. B **213** (1983) 201–222.

[Ber09] R. Berezov, *Investigation to observe spin entanglement from elastic scattering of electrons*, PhD thesis: Johann Wolfgang Goethe Universität Frankfurt, 2009.

[BDS16] S. Bethke, G. Dissertori and G. Salam, *Quantum Chromodynamics*, in: The Review of Particle Physics 2016 [Pat+16] (2016).

[Bla+92] G. Blanpied et al., *$p(\vec{\gamma},\pi^0)$ reaction and the E2 excitation of the Δ*, Phys. Rev. Lett. **69** (1992) 1880–1883.

[Bla+01] G. Blanpied et al., *$N \to \Delta$ transition and proton polarizabilities from measurements of $p(\vec{\gamma}, \gamma)$, $p(\vec{\gamma}, \pi^0)$, and $p(\vec{\gamma}, \pi^+)$*, Phys. Rev. C **64** (2001) 025203.

[Blo+75] E. Bloom et al., *A Proposal For A Large Solid Angle Neutral Detector For Spear 2 (The Crystal Ball)*, SLAC Proposal **SP-024** (1975).

[Bös16] S. Böse, *Aufbau und Test eines Szintillationsfaser-Detektors für das neue Vorwärtsspektrometer an ELSA*,
PhD thesis: Rheinische Friedrich-Wilhelms-Universität Bonn, 2016.

[Bös06] S. Böse, *Modifikation und Test des Lichtpulsersystems für den Crystal Barrel Aufbau an ELSA*,
Diploma thesis: Rheinische Friedrich-Wilhelms-Universität Bonn, 2006.

[Bos] P. E. Bosted, *Experimental Tests of the GDH and other sum rules at SLAC*, *GDH 2002*, ed. by M. Anghinolfi, M. Battaglieri and R. De Vita, World scientific 157–164.

[Bra+99] C. Bradtke et al., *A new frozen-spin target for 4π particle detection*,
Nucl. Instrum. Meth. A **436** (Nov. 1999) 430–442.

[Bra99] S. Brandt, *Datenanalyse: Mit statistischen Methoden und Computerprogrammen*, 4. Auflage, Spektrum, 1999.

[Bri+] W. J. Briscoe et al., *George Washington University Partial Wave Analysis*,
URL: `http://gwdac.phys.gwu.edu/` (visited on 27/08/2018).

[BR97] R. Brun and F. Rademakers, *ROOT: An object oriented data analysis framework*,
Nucl. Instrum. Meth. A **389** (1997) 81–86.

[Bru+87] R. Brun et al., *GEANT3* (1987).

[CR00] S. Capstick and W. Roberts, *Quark models of baryon masses and decays*,
Prog. Part. Nucl. Phys. **45** (2000) S241–S331.

[Cha+12] S. Chatrchyan et al., *Observation of a new boson at a mass of 125 GeV with the CMS experiment at the LHC*, Phys. Lett. B **716** (2012) 30–61.

[Che+57] G. F. Chew et al.,
Relativistic Dispersion Relation Approach to Photomeson Production,
Phys. Rev. **106** (1957) 1345–1355.

[CT97] W.-T. Chiang and F. Tabakin,
Completeness rules for spin observables in pseudoscalar meson photoproduction,
Phys. Rev. C **55** (1997) 2054–2066.

[Chi+02] W.-T. Chiang et al.,
An isobar model for η photo- and electroproduction on the nucleon,
Nucl. Phys. A **700** (2002) 429 –453.

[Chu+95] S. U. Chung et al., *Partial wave analysis in K-matrix formalism*,
Annalen der Physik **507** (1995) 404–430.

[Clo79] F. Close, *An introduction to quarks and partons*, Academic Press, 1979.

[Col15] C. Collicott, *Probing proton structure through single polarisation observables of compton scattering and π^0 photoproduction within the $\Delta(1232)$ region*,
PhD thesis: Dalhousie University, 2015.

[Col+17] P. Collins et al.,
Photon beam asymmetry Σ for η and η' photoproduction from the proton,
Phys. Lett. B **771** (2017) 213–221.

[Cos14] S. Costanza, *Report on the Moeller analysis of the Jan/Feb 2014 beamtime*,
tech. rep. (2014).

[Cre+09] V. Crede et al., *Photoproduction of η and η' mesons off protons*,
Phys. Rev. C **80** (2009) 055202.

[Cre+11] V. Crede et al., *Photoproduction of neutral pions off protons*,
Phys. Rev. C **84** (2011) 055203.

[Cre01] V. Credé, *CBGeant 1.08/01*, CB-Note (2001).

[Dah08] T. Dahlke, *Bestimmung einer winkelabhängigen Energiekorrekturfunktion für das TAPS-Kalorimeter des Crystal-Barrel/TAPS-Experiments an ELSA*,
Diploma thesis: Rheinische Friedrich-Wilhelms-Universität Bonn, 2008.

[Die08] J. Dielmann, *Entwicklung, Aufbau und Test eines Detektors zur Bestimmung des Photonenflusses an der Bonner Photonenmarkierungsanlage*,
Diploma thesis: Rheinische Friedrich-Wilhelms-Universität Bonn, 2008.

[Die15] M. Dieterle, *Measurement of Polarization Observables in π^0 and $\pi^0\pi^0$ Photoproduction from Protons and Neutrons at MAMI and ELSA*,
PhD thesis: University of Basel, 2015.

[DGH14] J. Donoghue, E. Golowich and B. Holstein, *Dynamics of the Standard Model*,
Second edition, Cambridge Univ. Press, 2014.

[DN10] M. Döring and K. Nakayama,
The phase and pole structure of the $N^*(1535)$ in $\pi N \to \pi N$ and $\gamma N \to \pi N$,
Eur. Phys. J. A **43** (2010) 83–105.

[Dör+09] M. Döring et al., *Analytic properties of the scattering amplitude and resonances parameters in a meson exchange model*, Nucl. Phys. **A 829** (2009) 170–209.

[Dow06] E. J. Downie,
Radiative π^0 photoproduction in the region of the $\Delta(1232)$ resonance,
PhD thesis: University of Glasgow, Scotland, 2006.

[DKT07] D. Drechsel, S. Kamalov and L. Tiator, *Unitary isobar model –MAID2007*,
Eur. Phys. J. A **34** (2007) 69.

[DT92] D. Drechsel and L. Tiator, *Threshold pion photoproduction on nucleons*,
J. Phys. G: Nucl. Part. Phys. **18** (1992) 449.

[Dre04] P. Drexler, *Entwicklung und Aufbau der neuen TAPS-Elektronik*,
PhD thesis: Justus-Liebig-Universität Gießen, 2004.

[Dug+02] M. Dugger et al.,
η Photoproduction on the Proton for Photon Energies from 0.75 to 1.95 GeV,
Phys. Rev. Lett. **89** (2002) 249904.

[Dug+07] M. Dugger et al.,
π^0 photoproduction on the proton for photon energies from 0.675 to 2.875 GeV,
Phys. Rev. C **76** (2007) 025211.

[Dug+14] M. Dugger et al., *Beam asymmetry Σ for π^+ and π^0 photoproduction on the proton for photon energies from 1.102 to 1.862 GeV*, Phys. Rev. C **89** (2014) 029901.

[Dür+08] S. Dürr et al., *Ab Initio Determination of Light Hadron Masses*, Science **322** (2008) 1224–1227.

[Ebe12] H. Eberhardt, *Bestimmung von Polarisationsobservablen in der π^0 und ω Photoproduktion am Proton mit dem CBELSA/TAPS-Experiment*, PhD thesis: Rheinische Friedrich-Wilhelms-Universität Bonn, 2012.

[Edw+11] R. G. Edwards et al., *Excited state baryon spectroscopy from lattice QCD*, Phys. Rev. D **84** (2011) 074508.

[ET94] B. Efron and R. J. Tibschirani, *An introduction to the Bootstrap*, Chapman & Hall/CRC, 1994.

[Els07] D. Elsner, *Untersuchung kleiner Partialwellenbeiträge in der Nähe dominierender Resonanzzustände des Protons mit linear polarisierten Photonen*, PhD thesis: Rheinische Friedrich-Wilhelms-Universität Bonn, 2007.

[Els+07] D. Elsner et al., *Measurement of the beam asymmetry in η photoproduction off the proton*, Eur. Phys. J. A **33** (2007) 147–155.

[Els+09] D. Elsner et al., *Linearly polarised photon beams at ELSA and measurement of the beam asymmetry in π^0 photoproduction off the proton*, Eur. Phys. J. A **39** (2009) 373–381.

[EHM09] E. Epelbaum, H.-W. Hammer and U.-G. Meißner, *Modern theory of nuclear forces*, Rev. Mod. Phys. **81** (2009) 1773–1825.

[FTS92] C. G. Fasano, F. Tabakin and B. Saghai, *Spin observables at threshold for meson photoproduction*, Phys. Rev. C **46** (1992) 2430–2455.

[Fle01] H. Flemming, *Entwurf und Aufbau eines Zellularlogik-Triggers für das Crystal-Barrel-Experiment an der Elektronenbeschleunigeranlage ELSA*, PhD thesis: Ruhr-Universität Bochum, 2001.

[Fle70] R. Fletcher, *A new approach to variable metric algorithms*, The Computer Journal **13** (1970) 317–322.

[FP09] K. Fornet-Ponse, *Die Photonenmarkierungsanlage für das Crystal-Barrel/TAPS-Experiment an ELSA*, PhD thesis: Rheinische Friedrich-Wilhelms-Universität Bonn, 2009.

[Fös00] A. Fösel, *Entwicklung und Bau des Innendetektors für das Crystal Barrel Experiment an ELSA/Bonn*, PhD thesis: Friedrich-Alexander-Universität Erlangen-Nürnberg, 2000.

[Fro] F. Frommberger, *Private communication.*

[Fuc+96] M. Fuchs et al., *Neutral pion photoproduction from the proton near threshold*, Phys. Lett. B **368** (1996) 20–25.

[Gab+94] A. R. Gabler et al., *Response of TAPS to monochromatic photons with energies between 45-MeV and 790-MeV*, Nucl. Instrum. Meth. A **346** (1994) 168–176.

[Geh15] S. Gehring, *Test des Szintillationsdetektors zur Identifizierung geladener Teilchen im Crystal-Barrel-Vorwärtsdetektor*,
Bachelor's thesis: Rheinische Friedrich-Wilhelms-Universität Bonn, 2015.

[GM62] M. Gell-Mann, *Symmetries of Baryons and Mesons*,
Phys. Rev. **125** (1962) 1067–1084.

[Gla61] S. L. Glashow, *Partial Symmetries of Weak Interactions*,
Nucl. Phys. **22** (1961) 579.

[Gor+74] V. Gorbenko et al., *Proton polarization in $\gamma + p \to \pi^0 + p$ reaction on a linearly polarized photon beam (In Russian)*, Pisma Zh.Eksp.Teor.Fiz. **19** (1974) 659–662.

[Gor+78] V. Gorbenko et al., *Measurement of Polarization of Secondary Proton from $\gamma p \to \pi^0 p$ Reaction with Polarized Photons at Energies of 360-MeV, 400-MeV, 450-MeV, 500-MeV (In Russian)*, Yad.Fiz. **27** (1978) 1204–1211.

[Got19] L. Gottardi,
Test and improvement of the calibration mechanisms of the MiniTAPS detector,
Master's thesis: Rheinische Friedrich-Wilhelms-Universität Bonn, 2019.

[Got+09] M. Gottschall et al., *Documentation of the TAPS Energy Calibration for the CB-ELSA/TAPS Experiment*, CB-ELSA/TAPS Note (2009).

[Got+14] M. Gottschall et al., *First Measurement of the Helicity Asymmetry for $\gamma p \to p\pi^0$ in the Resonance Region*, Phys. Rev. Lett. **112** (2014) 012003.

[Got13] M. Gottschall, *Bestimmung der Doppelpolarisationsobservablen E für die Reaktion $\gamma p \to p\pi^0$ am CBELSA/TAPS-Experiment*,
PhD thesis: Rheinische Friedrich-Wilhelms-Universität Bonn, 2013.

[Grü18] M. Grüner, *Private communication*, 2018.

[GP08] M. Grüner and D.-M. Piontek, *Hit-Reconstruction in ChaPI*,
CB-TR16 Note 003 (2008).

[GHK64] G. S. Guralnik, C. R. Hagen and T. W. B. Kibble,
Global Conservation Laws and Massless Particles,
Phys. Rev. Lett. **13** (1964) 585–587.

[Gut+14] E. Gutz et al., *High statistics study of the reaction $\gamma p \to p\pi^0\eta$*,
Eur. Phys. J. A **50** (2014) 74.

[Gut10] E. P.-M. Gutz, *Measurement of beam asymmetries in the reaction $\gamma p \to p\pi^0\eta$ with the Crystal Barrel/TAPS experiment at ELSA*,
PhD thesis: Rheinische Friedrich-Wilhelms-Universität Bonn, 2010.

[Hal+96] S. J. Hall et al.,
A focal plane system for the 855-MeV tagged photon spectrometer at MAMI-B,
Nucl. Instrum. Meth. A **368** (1996) 698–708.

[Ham09] C. Hammann, *Aufbau eines Flüssigwasserstofftargets zur Durchführung von Kalibrationsmessungen am Crystal-Barrel Experiment an ELSA*,
Diploma thesis: Rheinische Friedrich-Wilhelms-Universität Bonn, 2009.

[Har17] J. Hartmann, *Measurement of Double Polarization Observables in the Reactions $\gamma p \to p\pi^0$ and $\gamma p \to p\eta$ with the Crystal Barrel/TAPS Experiment at ELSA*,
PhD thesis: Rheinische Friedrich-Wilhelms-Universität Bonn, 2017.

[Har+14] J. Hartmann et al.,
$N(1520)\ 3/2^-$ *Helicity Amplitudes from an Energy-Independent Multipole Analysis Based on New Polarization Data on Photoproduction of Neutral Pions*,
Phys. Rev. Lett. **113** (2014) 062001.

[Har+15] J. Hartmann et al., *The polarization observables T, P, and H and their impact on* $\gamma p \to p\pi^0$ *multipoles*, Phys. Lett. B **748** (2015) 212 –220.

[Har08] J. Hartmann, *Zeitkalibrierung und Photonenflussbestimmung für das Crystal-Barrel-Experiment an ELSA*,
Diploma thesis: Rheinische Friedrich-Wilhelms-Universität Bonn, 2008.

[Hei54] W. Heitler, *The Quantum Theory of Radiation*, Oxford University Press (1954).

[Her18] L. Herrmann, *Bestimmung der energie- und winkelabhängigen Nachweiseffizienz für Protonen im TAPS Detektor*,
Bachelor's thesis: Rheinische Friedrich-Wilhelms-Universität Bonn, 2018.

[Hig64] P. W. Higgs, *Broken Symmetries and the Masses of Gauge Bosons*,
Phys. Rev. Lett. **13** (1964) 508–509.

[Hil06] W. Hillert, *The Bonn Electron Stretcher Accelerator ELSA: Past and future*,
Eur. Phys. J. A **28** (2006) 139–148.

[Hil00] W. Hillert, *Erzeugung eines Nutzstrahls spinpolarisierter Elektronen an der Beschleunigeranlage ELSA*,
Habilitation thesis: Rheinische Friedrich-Wilhelms-Universität Bonn, 2000.

[Hof18] P. Hoffmeister,
Das Datenerfassungssystem für das Crystal-Barrel/TAPS-Experiment an ELSA,
PhD thesis: Rheinische Friedrich-Wilhelms-Universität Bonn, 2018.

[Hof57] R. Hofstadter, *Nuclear and Nucleon Scattering of High-Energy Electrons*,
Annual Review of Nuclear Science **7** (1957) 231–316.

[Hom+95] A. Hombach et al., *Pion and eta photoproduction in nuclei*,
Zeitschrift für Physik A Hadrons and Nuclei **352** (1995) 223–230.

[Hon14] C. Honisch, *Design, Aufbau und Test einer neuen Ausleseelektronik für das Crystal-Barrel-Kalorimeter*,
PhD thesis: Rheinische Friedrich-Wilhelms-Universität Bonn, 2014.

[Hor+09] D. Hornidge et al., *Measurement of the Proton Spin Polarizabilities. An A2 Collaboration Proposal for an Experiment at MAMI* (2009).

[IK77] N. Isgur and G. Karl, *Hyperfine interactions in negative parity baryons*,
Physics Letters B **72** (1977) 109–113.

[IK79] N. Isgur and G. Karl,
Positive-parity excited baryons in a quark model with hyperfine interactions,
Phys. Rev. D **19** (1979) 2653–2677.

[JR75] F. James and M. Roos, *Minuit - a system for function minimization and analysis of the parameter errors and correlations*,
Computer Physics Communications **10** (1975) 343 –367.

[Jan06] A. Jankowiak, *The Mainz Microtron MAMI: Past and future*,
Eur. Phys. J. A **28S1** (2006) 149–160.

[Jan+09] A. Jankowiak et al.,
The first two years of operation of the 1.5 GeV cw electron accelerator MAMI C, *Presented at Particle Accelerator Conference (PAC 09), Vancouver, BC, Canada*, 2009.

[Jun04] J. Junkersfeld,
Kalibration des Crystal-Barrel-ELSA Detektors mit Hilfe der Reaktion $\gamma p \to p\pi^0$,
Diploma thesis: Rheinische Friedrich-Wilhelms-Universität Bonn, 2004.

[Kai] D. Kaiser, *Private communication.*

[Kai07] D. Kaiser, *Aufbau und Test des Gas-Čerenkov-Detektors für den Crystal-Barrel-Aufbau an ELSA*,
Diploma thesis: Rheinische Friedrich-Wilhelms-Universität Bonn, 2007.

[Kai+08] K. H. Kaiser et al.,
The 1.5-GeV harmonic double-sided microtron at Mainz University,
Nucl. Instrum. Meth. A **593** (2008) 159–170.

[Kal11] F. Kalischewski, *Development of a new simulation for the CBELSA/TAPS experiment using Virtual Monte Carlo, Diploma thesis*,
PhD thesis: Rheinische Friedrich-Wilhelms-Universität Bonn, 2011.

[Kam09] S. Kammer, *Strahlpolarimetrie am CBELSA/TAPS Experiment*,
PhD thesis: Rheinische Friedrich-Wilhelms-Universität Bonn, 2009.

[KTO17] V. L. Kashevarov, L. Tiator and M. Ostrick,
η and η' photoproduction with EtaMAID including Regge phenomenology,
Bled Workshops Phys. **18** (2017) 1–5.

[Kas+17] V. L. Kashevarov et al., *Study of η and η' Photoproduction at MAMI*,
Phys. Rev. Lett. **118** (2017) 212001.

[Kes69] J. Kessler,
Electron Spin Polarization by Low-Energy Scattering from Unpolarized Targets,
Rev. Mod. Phys. **41** (1969) 3–25.

[Kla19] P. Klassen,
Entwicklung eines neuen Cluster Finders für das Crystal-Barrel-Kalorimeter,
PhD thesis in preparation: Rheinische Friedrich-Wilhelms-Universität Bonn, 2019.

[KM59] H. W. Koch and J. W. Motz,
Bremsstrahlung Cross-Section Formulas and Related Data,
Rev. Mod. Phys. **31** (1959) 920–955.

[Kru05] B. Krusche,
Photoproduction of mesons from nuclei —in-medium properties of hadrons,
Prog. Part. Nucl. Phys. **55** (2005), International School of Nuclear Physics 26th course 46 –70.

[Kru11] B. Krusche, *Photoproduction of mesons off nuclei - Electromagnetic excitations of the neutron and meson-nucleus interactions*,
Eur. Phys. J. Spec. Top. **198** (2011) 199.

[KS03] B. Krusche and S. Schadmand,
Study of non-strange baryon resonances with meson photoproduction,
Prog. Part. Nucl. Phys. **51** (2003) 399–485.

[Lac+81] M. Lacombe et al.,
Parametrization of the deuteron wave function of the Paris n-n potential,
Phys. Lett. B **101** (1981) 139–140.

[LB14] T. Lancaster and S. J. Blundell, *Quantum Field Theory for the Gifted Amateur*, OUP Oxford, 2014.

[Lan04] M. Lang, *Aufbau des GDH-Experiments und Messung der Helizitätsabhängigkeit von $\vec{\gamma}\vec{p} \to p\pi^+\pi^-$ von der Schwelle*,
PhD thesis: Johannes Gutenberg-Universität Mainz, 2004.

[Lei93] D. B. Leinweber, *Do quarks really form diquark clusters in the nucleon?*,
Phys. Rev. D **47** (1993) 5096–5103.

[Lin14] J. M. Linturi, *Target Polarization for Butanol and D-Butanol Beam-times*,
Internal Manual of the A2 collaboration, 2014.

[Liv09] K. Livingston, *The Stonehenge technique. A method for aligning coherent bremsstrahlung radiators*, Nucl. Instrum. Meth. A **603** (2009) 205 –213.

[LMP01] U. Löring, B. C. Metsch and H. R. Petry,
The light-baryon spectrum in a relativistic quark model with instanton-induced quark forces: The non-strange baryon spectrum and ground-states,
Eur. Phys. J. A **10** (2001) 395–446.

[Mac+97] M. MacCormick et al.,
Total photoabsorption cross section for ^{4}He from 200 to 800 MeV,
Phys. Rev. C **55** (1997) 1033–1038.

[Mac17] R. Macrae, *Polarisation Observables in π^0 Photoproduction at MAMI*,
PhD thesis: University of Glasgow, 2017.

[Man58] S. Mandelstam, *Determination of the Pion-Nucleon Scattering Amplitude from Dispersion Relations and Unitarity. General Theory*,
Phys. Rev. **112** (1958) 1344–1360.

[Mar13] P. Martel,
Measuring proton spin polarizabilities with polarized compton scattering,
PhD thesis: University of Massachusetts Amherst, 2013.

[Mar07] M. Martinez, *Study of the Helicity Dependence of Single Pion Photoproduction on the Deuteron*, PhD thesis: Johannes Gutenberg-Universität Mainz, 2007.

[MSW77] J. S. McCarthy, I. Sick and R. R. Whitney,
Electromagnetic structure of the helium isotopes,
Phys. Rev. C **15** (1977) 1396–1414.

[McG08] W. McGehee, *The Gamma Intensity Monitor at the Crystal-Barrel-Experiment*,
Bachelor's thesis: Massachusetts Institute Of Technology, 2008.

[McG+08] J. C. McGeorge et al.,
Upgrade of the Glasgow photon tagging spectrometer for Mainz MAMI-C,
Eur. Phys. J. A **37** (2008) 129–137.

[McN+10] E. F. McNicoll et al., *Experimental study of the $\gamma p \to \eta p$ reaction with the Crystal Ball detector at the Mainz Microtron (MAMI-C)*, Phys. Rev. C **82** (2010) 035208.

[Mes05] D. Meschede, *Gerthsen Physik*, 23rd ed., Springer Spektrum, 2005.

[MU49] N. Metropolis and S. Ulam, *The Monte Carlo Method*, J. Amer. Stat. Assoc. **44** (1949) 335–341.

[Met08] B. Metsch, *Quark models∗*, Eur. Phys. J. A **35** (2008) 275–280.

[Mol92] K. Molenaar, *Performance of TAPS in the Tagged Photon Beam of MAMI*, PhD thesis: Rijksuniversiteit Groningen, 1992.

[Mül+17] J. Müller et al., *New data on $\vec{\gamma}\vec{p} \to \eta p$ with polarized photons and protons and their implications for $N^* \to N\eta$ decays*, submitted to Phys. Lett. B (2017).

[Mül18] J. Müller, *Bestimmung der Doppelpolarisationsobservablen E in der Reaktion $\gamma p \to p\eta$ am CBELSA/TAPS-Experiment*, PhD thesis: Rheinische Friedrich-Wilhelms-Universität Bonn, 2018.

[Nad76] I. M. Nadzhafov, Bull. Acad. Sci. USSR, Phys. Ser. **14** (1976) 2248.

[Nak+76] K. Nakamura et al., *The reaction 12C(e, e'p) at 700 MeV and DWIA analysis*, Nucl. Phys. A **268** (1976) 381–407.

[Nak+10] K. Nakamura et al., *The Review of Particle Physics*, J. Phys. G **37** (2010) 075021.

[Nar04] S. Narison, *QCD as a theory of hadrons: from partons to confinement*, Cambridge Univ. Press, 2004.

[Nat+03] F. Natter et al., *Monte Carlo simulation and analytical calculation of coherent bremsstrahlung and its polarisation*, Nucl. Instrum. Meth. B **211** (2003) 465 –486.

[Nec93] M. Neckenig, *Theoretische und experimentelle Untersuchungen zur Verbesserung der Zeitstruktur des extrahierten Strahles aus dem Stretcherring ELSA*, PhD thesis: Rheinische Friedrich-Wilhelms-Universität Bonn, 1993.

[Ne'61] Y. Ne'eman, *Derivation of strong interactions from a gauge invariance*, Nucl. Phys. **26** (1961) 222 –229.

[Nik18] V. Nikonov, *Private communication*, 2018.

[Nov91] R. Novotny, *The BaF_2 Photon Spectrometer TAPS*, IEEE Trans. Nucl. Sci. **38** (1991) 379–385.

[OM59] H. Olsen and L. C. Maximon, *Photon and Electron Polarization in High-Energy Bremsstrahlung and Pair Production with Screening*, Phys. Rev. **114** (1959) 887–904.

[Ore81] M. J. Oreglia, *A study of the reactions $\Psi' \to \gamma\gamma\Psi$*, PhD thesis: Stanford University, 1981.

[Ott08] P.-B. Otte, *Aufbau und Test eines Møllerpolarimeters für das Crystal-Ball-Experiment an MAMI-C*, Diploma thesis: Johannes Gutenberg-Universität Mainz, 2008.

[Ott12] P.-B. Otte, *Internal Note: Polarisation Values for complete Frozen Spin Data*, 2012.

[Ott15] P.-B. Otte, *Erste Messung der π^0- Photoproduktion an transversal polarisierten Protonen Nahe der Schwelle*, PhD thesis: Johannes Gutenberg-Universität Mainz, 2015.

[Pat+16] C. Patrignani et al., *The Review of Particle Physics*, Chinese Phys. C **40** (2016) 100001.

[Pau16] P. Pauli, *Investigation of the Absolute Normalisation of the Helicity Dependent Cross Sections $\sigma^{1/2}$ and $\sigma^{3/2}$*, Master's thesis: Rheinische Friedrich-Wilhelms-Universität Bonn, 2016.

[PDG] PDG, *Atomic and Nuclear Properties*, URL: `http://pdg.lbl.gov/2017/AtomicNuclearProperties/index.html` (visited on 27/08/2018).

[Ped] P. Pedroni, *Private communication.*

[Pee+07] H. van Pee et al., *Photoproduction of π^0 Mesons off Protons from the $\Delta(1232)$ Region to $E_\gamma = 3$ GeV*, Eur. Phys. J. A **31** (2007) 61–77.

[Pio07] D.-M. Piontek, *Entwicklung eines Online-Monitors für das Crystal-Barrel-Experiment an ELSA*, Diploma thesis: Rheinische Friedrich-Wilhelms-Universität Bonn, 2007.

[Poc] *Poco Graphite, Inc., Decatur, TX, USA*, URL: `http://www.poco.com/Portals/0/Literature/Semiconductor/78962v2PocoFoamFlyer.pdf` (visited on 27/08/2018).

[Poh+10] R. Pohl et al., *The size of the proton*, Nature **466** (2010) 213–216.

[Pus12] T. Pusch, *Bestimmung von Intensität und Position des extrahierten Elektronenstrahls an ELSA mittels Hochfrequenzresonatoren*, PhD thesis: Rheinische Friedrich-Wilhelms-Universität Bonn, 2012.

[Red55] A. G. Redfield, *Nuclear Magnetic Resonance Saturation and Rotary Saturation in Solids*, Phys. Rev. **98** (1955) 1787–1809.

[Rei] G. Reicherz, *NMR Polarization Measurement*, Talk at the 28th International A2 Collaboration Meeting in Dubrovnik 2016.

[Röb91] M. Röbig, *Eichung des TAPS-Detektorsystems mit Höhenstrahlung*, Diploma thesis: Universität Giessen, 1991.

[Roh03] C. Rohlof, *Entwicklung polarisierter Targets zur Messung der Gerasimov-Drell-Hearn-Summenregel an ELSA*, PhD thesis: Rheinische Friedrich-Wilhelms-Universität Bonn, 2003.

[RDM18] D. Rönchen, M. Döring and U. G. Meißner, *The impact of $K^+\Lambda$ photoproduction on the resonance spectrum*, Eur. Phys. J. A **54** (2018) 110.

[Rön+] D. Rönchen et al., *The Jülich-Bonn dynamical coupled-channel analysis of pion- and photon-induced hadronic reactions*, URL: `http://collaborations.fz-juelich.de/ikp/meson-baryon/juelich_amplitudes.html` (visited on 27/08/2018).

[Rön+15] D. Rönchen et al., *Eta photoproduction in a combined analysis of pion- and photon-induced reactions*, Eur. Phys. J. A **51** (2015) 70.

[RM11] M. Ronninger and B. Metsch,
Effects of a spin-flavour dependent interaction on the baryon mass spectrum,
Eur. Phys. J. A **47** (2011) 162.

[ROO] ROOT, *TTree Class Reference*,
URL: `https://root.cern.ch/doc/v608/classTTree.html#a3e6bf252ab8653b47cc9116950f3ee7b` (visited on 27/08/2018).

[Ros] T. A. Rostomyan, *TAPS*,
Talk at the 25th International A2 Collaboration Meeting in Dubna 2014.

[Ros12] T. A. Rostomyan, *Cherenkov-Manual*, 2012.

[Sal68] A. Salam, *Weak and Electromagnetic Interactions*,
Conf. Proc. **C680519** (1968) 367.

[Sal16] B. W. Salisbury, *Entwicklung einer grafischen Benutzeroberfläche zur Energiekalibrierung des Crystal-Barrel-Kalorimeters*,
Bachelor's thesis: Rheinische Friedrich-Wilhelms-Universität Bonn, 2016.

[San+11] A. M. Sandorfi et al., *Determining pseudoscalar meson photo-production amplitudes from complete experiments*, J. Phys. G **38** (2011) 053001.

[Sei10] T. Seifen, *CB-ELSA/TAPS-Note: Correction of simulated energy deposit of protons in MiniTAPS*, 2010.

[Sen+16] I. Senderovich et al., *First measurement of the helicity asymmetry E in η photoproduction on the proton*, Phys. Lett. B **755** (2016) 64 –69.

[Spa+10] N. Sparks et al.,
Measurement of the beam asymmetry Σ in the forward direction for $\vec{\gamma}p \to p\pi^0$,
Phys. Rev. C **81** (2010) 065210.

[Spi19] K. Spieker, *Measurement of the double polarization observables G and E in neutral and positive pion photoproduction off the proton*, Ph.D. thesis in preparation: Rheinische Friedrich-Wilhelms-Universität Bonn, 2019.

[Sta+01] A. Starostin et al., *Measurement of $K^-p \to \eta\Lambda$ near threshold*,
Phys. Rev. C **64** (2001) 055205.

[Sta16] N. S. Stausberg, *Entwicklung einer Mesonenmassenkorrekturfunktion für das Crystal-Barrel-Kalorimeter*,
Bachelor's thesis: Rheinische Friedrich-Wilhelms-Universität Bonn, 2016.

[Str96] H. Ströher, *Electromagnetic and Hadronic Probes of Nuclear Matter: Portrait of the European Photon Detector TAPS*, Nuclear Physics News **6** (1996) 7–15.

[Suf+05] G. Suft et al.,
A scintillating fibre detector for the Crystal Barrel experiment at ELSA,
Nucl. Instrum. Meth. A **538** (2005) 416–424.

[Sum+07] M. Sumihama et al.,
Backward-angle photoproduction of π^0 mesons on the proton at E_γ =1.5-2.4 GeV,
Phys. Lett. B **657** (2007) 32 –37.

[Thi16] A. Thiel, *Documentation of the linear polarization degree for the hydrogen beam times in 2013*, CBELSA/TAPS Note (2016).

[Thi+12] A. Thiel et al., *Well-Established Nucleon Resonances Revisited by Double-Polarization Measurements*, Phys. Rev. Lett. **109** (2012) 102001.

[Thi+15] A. Thiel et al., *Three-Body Nature of N^* and Δ^* Resonances from Sequential Decay Chains*, Phys. Rev. Lett. **114** (2015) 091803.

[Thi+17] A. Thiel et al., *Double-polarization observable G in neutral-pion photoproduction off the proton*, Eur. Phys. J. A **53** (2017) 8.

[Thi11] A. Thiel, *Bestimmung der Doppelpolarisationsobservablen G in π^0 -Photoproduktion*, PhD thesis: Rheinische Friedrich-Wilhelms-Universität Bonn, 2011.

[Tho] A. Thomas, *Numbers of Nucleons and Nuclei in Butanol Target, Solid Carbon Target, Technical Realisation Carbon 2011*, Internal Manual of the A2 collaboration.

[Tho06] A. Thomas, *The Gerasimov-Drell-Hearn sum rule at MAMI*, Eur. Phys. J. A **28** (2006) 161–171.

[Tho13] A. Thomas, *Review on the last developments on polarized targets at Mainz*, Annual Meeting of the GDR PH-QCD (2013) 1–40.

[Tia12] L. Tiator, *Towards a model-independent partial wave analysis for pseudoscalar meson photoproduction*, AIP Conf. Proc. **1432** (2012) 162.

[Tia+a] L. Tiator et al., *ηMAID Partial Wave Analysis*, URL: `https://maid.kph.uni-mainz.de/eta2018/eta-observ.html` (visited on 27/08/2018).

[Tia+b] L. Tiator et al., *MAID Partial Wave Analysis*, URL: `https://maid.kph.uni-mainz.de/` (visited on 27/08/2018).

[Tia+18] L. Tiator et al., *Eta and Etaprime Photoproduction on the Nucleon with the Isobar Model EtaMAID2018*, Eur. Phys. J. A **54** (2018) 210.

[TV02] V. I. Tikhonov and A. A. Volkov, *Separation of Water into Its Ortho and Para Isomers*, Science **296** (2002) 2363–2363.

[Tim69] U. Timm, *Coherent bremsstrahlung of electrons in crystals*, Fortsch. Phys. **17** (1969) 765–808.

[TA06] V. Tioukine and K. Aulenbacher, *Operation of the MAMI accelerator with a Wien filter based spin rotation system*, Nucl. Instrum. Meth. A **568** (2006) 537–542.

[TAR11] V. Tioukine, K. Aulenbacher and E. Riehn, *A Mott polarimeter operating at MeV electron beam energies*, Rev. Sci. Instrum. **82** (2011) 033303.

[Ü56] H. Überall, *High-Energy Interference Effect of Bremsstrahlung and Pair Production in Crystals*, Phys. Rev. **103** (1956) 1055–1067.

[Uka13] A. Ukawa, *Quantum Chromodynamics on a space-time lattice*, Talk presented at the HPC Summer School, 25th June, New York, USA, 2013.

[Unv04] M. Unverzagt, *Energie-Eichung des Crystal Ball-Detektors am MAMI*, Diploma thesis: Johannes Gutenberg-Universität Mainz, 2004.

[Urb17] M. Urban, *Design eines neuen Lichtpulsersystems sowie Aufbau und Inbetriebnahme der neuen APD Auslese für das Crystal-Barrel-Kalorimeter*, PhD thesis: Rheinische Friedrich-Wilhelms-Universität Bonn, 2017.

[VK03] W. Verkerke and D. P. Kirkby, *The RooFit toolkit for data modeling*, eConf **C0303241** (2003) MOLT007.

[Wag+90] B. Wagner et al., *A Møller polarimeter for CW and pulsed intermediate-energy electron beams*, Nucl. Instrum. Meth. A **294** (1990) 541–548.

[Wal07] D. Walther, *Private communication*, 2007.

[Wat05] D. Watts, *The Crystal Ball and TAPS Detectors at the MAMI Electron Beam Facility*, Calorimetry in Particle Physics - the eleventh international conference (2005) 116–123.

[Wat] D. Watts, *PID II status*, Talk at the 25th International A2 Collaboration Meeting in Dubna 2014.

[Wei67] S. Weinberg, *A Model of Leptons*, Phys. Rev. Lett. **19** (1967) 1264–1266.

[Wen04] C. Wendel, *Entwicklung eines Szintillations-Detektors zur Identifikation geladener Teilchen im Crystal-Barrel Vorwärtsdetektor*, Diploma thesis: Rheinische Friedrich-Wilhelms-Universität Bonn, 2004.

[Wer14] D. Werthmüller, *Experimental study of nucleon resonance contributions to η-photoproduction on the neutron*, PhD thesis: University of Basel, 2014.

[Wer+13] D. Werthmüller et al., *Internal Manual: Calibration procedure of A2 data using the CaLib software*, 2013.

[Wil+09] M. Williams et al., *Differential cross sections for the reactions $\gamma p \to p\eta$ and $\gamma p \to p\eta'$*, Phys. Rev. C **80** (2009) 045213.

[Wil74] K. G. Wilson, *Confinement of quarks*, Phys. Rev. D **10** (1974) 2445–2459.

[Win06] A. Winnebeck, *Entwicklung und Implementierung eines universellen, FPGA basierten Triggermoduls für das Crystal-Barrel-Experiment an ELSA*, Diploma thesis: Rheinische Friedrich-Wilhelms-Universität Bonn, 2006.

[Wit15] L. Witthauer, *Measurement of Cross Sections and Polarisation Observables in η Photoproduction from Neutrons and Protons Bound in Light Nuclei*, PhD thesis: University of Basel, 2015.

[Wit+13] L. Witthauer et al., *Quasi-free photoproduction of η-mesons off ^{3}He nuclei*, Eur. Phys. J. A **49** (2013) 154.

[Wor+12] R. L. Workman et al., *Parameterization dependence of T-matrix poles and eigenphases from a fit to πN elastic scattering data*, Phys. Rev. C **86** (2012) 035202.

[WA+17] Y. Wunderlich, F. Afzal et al., *Determining the dominant partial wave contributions from angular distributions of single- and double-polarization observables in pseudoscalar meson photoproduction*,
Eur. Phys. J. A **53** (2017) 86.

[ZWG15] L. Zana, D. Watts and D. Glazier, *Internal A2 note: A2 Geant4 Simulation*, 2015.

[Zwe64] G. Zweig,
An SU_3 model for strong interaction symmetry and its breaking; Version 1,
tech. rep., CERN, 1964.

List of Figures

List of Tables

Acknowledgements

First of all, I would like to express my utmost gratitude to my supervisor and mentor Prof. Dr. Reinhard Beck for giving me the opportunity to be part of his research group. I am most grateful for his guidance and immense support and confidence throughout my PhD years. I could not have imagined a better mentor for me.

Aside from Prof. Dr. R. Beck, I thank the rest of my thesis committee: Prof. Dr. Bernd Krusche and Prof. Dr. Ulf-G. Meißner.

I would like to thank the Bonn-Cologne-Graduate school for the financial support through my scholarship and thus, giving me opportunities to attend many international conferences.

I also thank Prof. Dr. Paolo Pedroni, Dr. Ken Livingston, Dr. Andreas Thomas and Prof. Dr. Bernd Krusche for their great support and many fruitful discussions regarding the A2 data analysis. Equally, I thank Prof. Dr. Ulrike Thoma for her great guidance during all analysis meetings concerning CBELSA/TAPS data.

I thank Yannick Wunderlich, Annika Thiel, Jan Hartmann, Florian Kalishewski, Tobias Seifen, Dominik Werthmüller, Karsten Spieker and Phil Martel for their good advice and successful collaborations during the last years.

I also want to mention and acknowledge the hard work of the hardware groups in Bonn and Mainz, without whom this thesis would not have been possible. Special thanks to Christian Honisch, Martin Urban, Philipp Hoffmeister, Peter Klassen, Johannes Müllers, Jennifer Wettig, Edoardo Mornacchi, Federico Cividini, Phil Martel and Michael Lang. In addition, one needs to mention the ELSA and MAMI crew for their incredible work.

I thank everyone from the CBELSA/TAPS and A2 collaboration for their general support and for making my PhD years enjoyful, especially Karsten Spieker, Yannick Wunderlich, Annika Thiel, Peter Pauli, Susanna Costanza and Federico Cividini.
Furthermore, I owe particular thanks to all of my past and current office colleagues for their patience and fun time: Karsten Spieker, Sebastian Ciupka, Peter Pauli, Eugenia Fix, Steffen Urban, Fahimeh Jahanbakhsh, Yannick Wunderlich, Luca Gottardi and Vitalij Adam.

Finally, I thank my family: my mother Rakhshinda Jabeen for keeping me alive, my father Muhammad Afzal for being there most of the time, my sister Shazia Samreen Afzal for being the most annoying, irritating, but loving sister (you are and will always be my most favorite person in the world ;P), my uncle Shabbir Hussain and my uncle Muhammad Akmal for simply believing in me and all of my 91 (?) relatives (sorry guys, not sure if I counted everyone, but if you think you are related to me, then I mean you!). Thank you all for your continuous support and encouragement throughout my life.